



UNIVERSITY OF
PLYMOUTH



School of Geography, Earth and Environmental Sciences Theses
Faculty of Science and Engineering Theses

2023

Historic and prehistoric volcanic activity on St Kitts and Nevis, West Indies: Controls on future hazard

Amy Lea Peach-Gibson

Let us know how access to this document benefits you

General rights

All content in PEARL is protected by copyright law. Author manuscripts are made available in accordance with publisher policies. Please cite only the published version using the details provided on the item record or document. In the absence of an open licence (e.g. Creative Commons), permissions for further reuse of content should be sought from the publisher or author.

Take down policy

If you believe that this document breaches copyright please [contact the library](#) providing details, and we will remove access to the work immediately and investigate your claim.

Follow this and additional works at: <https://pearl.plymouth.ac.uk/gees-theses>

Recommended Citation

Peach-Gibson, A. (2023) *Historic and prehistoric volcanic activity on St Kitts and Nevis, West Indies: Controls on future hazard*. Thesis. University of Plymouth. Retrieved from <https://pearl.plymouth.ac.uk/gees-theses/450>

This Thesis is brought to you for free and open access by the Faculty of Science and Engineering Theses at PEARL. It has been accepted for inclusion in School of Geography, Earth and Environmental Sciences Theses by an authorized administrator of PEARL. For more information, please contact openresearch@plymouth.ac.uk.



UNIVERSITY OF
PLYMOUTH

PEARL

PHD

**Historic and prehistoric volcanic activity on St Kitts and Nevis, West Indies:
Controls on future hazard**

Peach-Gibson, Amy Lea

Award date:
2023

Awarding institution:
University of Plymouth

[Link to publication in PEARL](#)

All content in PEARL is protected by copyright law.

The author assigns certain rights to the University of Plymouth including the right to make the thesis accessible and discoverable via the British Library's Electronic Thesis Online Service (EThOS) and the University research repository (PEARL), and to undertake activities to migrate, preserve and maintain the medium, format and integrity of the deposited file for future discovery and use.

Copyright and Moral rights arising from original work in this thesis and (where relevant), any accompanying data, rests with the Author unless stated otherwise*.

Re-use of the work is allowed under fair dealing exceptions outlined in the Copyright, Designs and Patents Act 1988 (amended), and the terms of the copyright licence assigned to the thesis by the Author.

In practice, and unless the copyright licence assigned by the author allows for more permissive use, this means,

That any content or accompanying data cannot be extensively quoted, reproduced or changed without the written permission of the author / rights holder

That the work in whole or part may not be sold commercially in any format or medium without the written permission of the author / rights holder

* Any third-party copyright material in this thesis remains the property of the original owner. Such third-party copyright work included in the thesis will be clearly marked and attributed, and the original licence under which it was released will be specified . This material is not covered by the licence or terms assigned to the wider thesis and must be used in accordance with the original licence; or separate permission must be sought from the copyright holder.

Download date: 28. Oct. 2024

This copy of the thesis has been supplied on condition that anyone who consults it is understood to recognise that its copyright rests with its author and that no quotation from the thesis and no information derived from it may be published without the author's prior consent.



**UNIVERSITY OF
PLYMOUTH**

Historic and prehistoric volcanic activity on St Kitts and Nevis, West Indies:
Controls on future hazard

by

Amy Lea Peach-Gibson

A thesis submitted to the University of Plymouth in partial fulfilment for the
degree of

DOCTOR OF PHILOSOPHY

School of Geography, Earth and Environmental Sciences

June 2023

Acknowledgements

I would like to express my sincere gratitude to the following individuals and groups who have provided invaluable support and guidance throughout the completion of this project:

Firstly, I would like to express my gratitude to my supervisors, Paul, Jenni, Michelle, and Martin. Your expertise, feedback, and support have been instrumental in shaping this work and ensuring its success. Your guidance and mentorship have challenged me to think critically and have undoubtedly shaped the outcome of this project.

I am grateful to the insightful staff at the various archives I visited while researching Chapter 2 of this thesis. Archival work became one of my favourite parts of the project, and it's a skill I carried forward into my job.

Thanks is owed to the PEMC staff, particularly to Lorelei, who found ways to run remote control SEM analysis of my samples when I was unable to carry out lab work during lockdowns. Thanks is also extended to the EPMA technicians at the University of Bristol for giving me a two day whistle-stop tour of the microprobe.

I would like to express my appreciation to the Volcanic and Magmatic Studies Group (VMSG) for the fieldwork grant, although unused due to COVID-19, the offer was greatly appreciated.

Additionally, I give thanks to the National Emergency Management Agency (NEMA) of St. Kitts and Nevis for their insights and assistance during my visit to the islands, and for connecting me with the Planning Department of the Government of St. Kitts to gain access to high quality mapping resources.

I extend my gratitude to my colleagues at work, particularly my manager Hazel. Your support, flexibility, and understanding allowed me to finish this thesis while working what has turned out to be a dream job! I am incredibly lucky to work with such a friendly and supportive group of people.

I would also like to offer my appreciation to the two organisations that helped keep me sane during my PhD studies. Firstly, to the wonderful women and girls of Girlguiding Cornwall. To 1st Boscoppa Brownies, I'm so thankful for your endless optimism, kindness and humour. Tuesday nights with the brownies gave structure to my week, and having fun with the girls provided solace when things became stressful. To the leaders in Redruth North and to 1st Treleigh Brownies, who welcomed me into the district when I moved south for work, and gave me another reason to push this thesis over the finish line. Secondly, I must thank the wonderful Newquay Women's Surf Club, which has provided a much-needed respite during this demanding period, giving me something to focus on when my academic life took a nose dive.

I would also like to express my deepest gratitude to my parents, family and friends, whose love, encouragement and belief in me have been constant sources of motivation. Your belief in me and unwavering support have fuelled my determination to overcome challenges and achieve my goals.

I am deeply grateful to my husband for his unwavering support, patience, and understanding (and yummy food!). Tom, you've stood by me through everything, from the incredible experiences we've had, to the dark times when we struggled to see the light at the end of the tunnel. Soon, we will turn the page on this chapter of our lives, and start the next – it's been a long time coming!

Author's Declaration

At no time during the registration for the degree of Doctor of Philosophy has the author been registered for any other University award without prior agreement of the Doctoral College Quality Sub-Committee.

Work submitted for this research degree at the University of Plymouth has not formed part of any other degree either at the University of Plymouth or at another establishment.

This study was financed by a studentship from the School of Geography, Earth and Environmental Sciences, University of Plymouth. This project was also awarded with a fieldwork grant of £500 from VMSG, although this was not spent due to the COVID-19 pandemic.

Presentations at conferences related to the work in this thesis:

Peach, A. L., Cole, P. D., Barclay, J., Robertson, R. An integrated approach to understanding volcanic hazards on Saint Kitts and Nevis. *VMSG Annual Meeting (Plymouth), Jan 2020*. Poster.

Peach, A. L., Cole, P. D., Barclay, J., Harris, M. Geochemical characterisation of the youngest explosive volcanic activity at St Kitts and Nevis, Lesser Antilles. *VMSG Annual Meeting (Virtual), Jan 2021*. Presentation.

Peach-Gibson, A. L., Cole, P. D., Barclay, J., Harris, M. CRES - An integrated approach to understanding volcanic hazards on Saint Kitts and Nevis. *Centre for Research in Earth Science (CRES) Annual Conference (Plymouth), April 2022*. Presentation.

Word count of main body of thesis: 51,604

Signed: *H. Peach-Gibson*

Date: 20/06/2023

Abstract

Historic and prehistoric volcanic activity on St Kitts and Nevis, West Indies:

Controls on future hazard

Amy Lea Peach-Gibson

Saint Kitts and Nevis lie in the northern part of the Lesser Antilles island arc, an archipelago formed by the subduction of the North American plate beneath the Caribbean plate. An integrated approach was undertaken to understand the most recent volcanic activity on the islands, and to assess likely future eruption styles and scenarios. A new analysis of archival records suggests that there may not have been activity at Mt Liamuiga in historic times. The 1690 activity may have been misattributed to St Kitts instead of Guadeloupe, whereas the 1843 activity remains unconfirmed. A field campaign characterised the nature of the pyroclastic density currents (PDCs) on St Kitts and Nevis. Pyroclastic density currents (PDCs) of pumice and ash flows, and surge deposits characterise the youngest products at both Mt Liamuiga and Nevis Peak, although subordinate lapilli fallout deposits also occur on St Kitts. The geochemistry of the youngest products at Mt Liamuiga, St Kitts and Nevis Peak have been analysed to characterise the nature of the magma storage conditions below both islands, and to understand the styles of the most recent eruptions. These geochemical analyses have shown that open-system processes dominated the magma storage conditions at both St Kitts and Nevis, and recharges of hot, primitive magma into the reservoirs led to mixing and magmatic differentiation. The geochemistry also showed that rapid crystallization, reheating and partial melting occurred in the shallow crust before eruption. Magma mingling occurred shortly before or syn-eruption.

Crystal Size Distribution (CSD) methods allowed decompression and ascent rates to be estimated, providing further evidence for the nature of the youngest eruptions at Mt Liamuiga and Nevis Peak. Ascent rate estimates suggest that the majority of the Mt Liamuiga deposits studied were the products of explosive eruptions, and the estimates calculated for the Nevis samples suggest a much slower decompression and ascent rate indicating a lava dome collapse origin, potentially associated with explosive activity.

Future eruptive scenarios were modelled using VolcFlow based on parameters informed by fieldwork, geochemistry and CSD analysis. This modelling suggests that the main hazard from PDCs is in the northwest of the island, with multiple settlements lying directly in the path of the PDCs modelled, including Old Road Town, Newton Ground, Saddlers Village, and the southern portion of Sandy Point Town in larger volume scenarios.

Contents

Acknowledgements.....	i
Author's Declaration	iii
Abstract.....	v
Contents.....	1
List of Figures	6
List of Tables	14
List of Appendices	16
1. Introduction	18
1.1 Overview	18
1.2 Aims and Objectives.....	22
1.3 Thesis structure.....	23
1.5 Terminology of key deposits.....	24
1.5.1 PDCs	24
1.5.2 Fallout	25
2. A history of disasters on the Islands of St. Kitts and Nevis, 17 th to 20 th Centuries.....	26
2.1 Introduction	26
2.2 Disaster events in chronological order	31
2.2.1 Hurricanes of the 1600s.....	34
2.2.2 Earthquake of 1690 (including the description of the possible volcanic activity, 1692)	36
2.2.3 Mt Liamuiga volcanic activity of 1692	38
2.2.4 Hurricanes of the 1700s.....	41
2.2.5 Droughts of the 1700s	44
2.2.6 Earthquakes of the 1700s	44
2.2.7 Hurricanes and flooding of the 1800s.....	45
2.2.8 Droughts and other disasters of the 1800s	47
2.2.9 Earthquakes of the 1800s	48
2.2.10 Earthquake of 1843.....	49
2.2.11 Hurricanes of the 1900s.....	53
2.2.12 Earthquake of the 1900s.....	55
2.3 Discussion and concluding points	57
2.3.1 General impact of disasters	57
2.3.2 Volcanic hazard	57

2.3.3 Multi-hazard vulnerability	58
2.3.4 Preparedness for future disasters	62
2.3.5 Acknowledgement of historic bias of sources	64
3. Fieldwork.....	65
3.1 Aims of this field study.....	65
3.2 Introduction to the stratigraphy of St Kitts and Nevis.....	65
3.2.1 St Kitts	65
3.2.2 Nevis.....	71
3.3 Methodology.....	75
3.4 St. Kitts	76
3.4.1 Summary of Locations.....	76
3.5 Nevis.....	93
3.6 Interpretation and discussion of field observations.....	96
3.6.1 St Kitts	96
3.6.2 Nevis.....	104
3.7 Conclusions	106
4. Petrography and Geochemistry	107
4.1 Introduction	107
4.1.1 Geochemical background of St Kitts.....	107
4.1.2 Petrography of the St Kitts.....	112
4.1.3 Geochemical and petrographic background of Nevis	113
4.1.4 Microlites	114
4.1.5 Glass compositions	114
4.2 Method	115
4.2.1 Sample selection and preparation.....	115
4.2.2 Petrographic analysis	115
4.2.3 Geochemical analysis.....	115
4.3 Results.....	121
4.3.1 Petrography	121
4.3.2 Whole-rock major and trace element analysis.....	136
4.3.3 Trace element composition	144
4.3.4 Loss on Ignition (LOI).....	149
4.3.5 Interstitial glass compositions	151
4.3.6 Phenocryst composition	154
4.3.7 Microlite composition.....	159

4.4 Interpretation and comparison with published data	161
4.4.1 Origins of the St Kitts and Nevis magmas	161
4.4.2 Implications for magma storage	163
4.4.3 Interpretation of pre- and syn-eruptive processes and style of eruption.....	167
4.4.4 Implications for future eruptions.....	168
4.5 Conclusions	169
5. Crystal Size Distribution Analysis for Mt Liamuiga and Nevis Peak.....	171
5.1 Introduction	171
5.2 Methodology.....	174
5.2.1 Image and data acquisition.....	174
5.2.2 Ascent rates	175
5.2.3 Crystal size distribution (CSD).....	177
5.2.4 Crystallization times and Nucleation rates	177
5.3 Results.....	178
5.3.1 Quantitative microlite analysis	178
5.3.2 Crystal size distributions (CSD)	189
5.3.3 Crystallization times and nucleation rate	200
5.3.4 Magma decompression and ascent rates.....	202
5.4 Discussion.....	209
5.4.1 Microlite textural variations within the youngest deposits on Mt Liamuiga.	209
5.4.2 Crystal Size Distribution (CSD)	216
5.4.3 Ascent rates	220
5.4.4 Amphibole reaction rims	230
5.5 Conclusions	234
6. Hazard Analysis of Pyroclastic Density Currents.....	235
6.1 Introduction	235
6.1.1 Computer models for PDC hazard analysis.....	235
6.1.2 Hazard assessments of Mt Liamuiga.....	238
6.1.3 Towns, Population and infrastructure	242
6.2 Methodology.....	244
6.2.1 Digital elevation model (DEM).....	244
6.2.2 VolcFlow	244
6.2.3 ArcMap.....	249
6.3 Results.....	250
6.3.1 Dense PDC deposits	251

6.3.2 Surge deposits generated by a lower surge production coefficient.....	260
6.3.3 Surge deposits generated by a higher surge production coefficient	266
6.4 Discussion.....	269
6.4.1 Comparison between pumice and ash flows and transitional flows.....	269
6.4.2 Comparison between low and high surge production scenarios models	273
6.4.3 Comparison to field observations.....	275
6.4.4 Factors influencing inundation area and thickness	276
6.4.5 PDC Hazard implications for St Kitts	276
6.4.6 Discussion of VolcFlow.....	282
6.5. Conclusions	284
7. Conclusions	286
7.1 Concluding remarks	286
7.1.1 Historic volcanic activity	286
7.1.2 Prehistoric volcanic activity	286
7.1.3 Future volcanic hazards	288
7.2 Limitations and future work	289
References	292
Appendices.....	316
Appendix 1 - List of Libraries and Archives consulted	316
Appendix 2 - St. Kitts field locations and Latitude/Longitude	317
Appendix 3 - Maximum axis collected from clasts in the upper layer of pumice lapilli at location SK2.....	318
Appendix 4 - Description of the samples chosen for XRF analysis.	319
Appendix 5 – Thin section scans	327
Appendix 6 - XRF whole rock major element data	340
Appendix 7 - Normalised XRF whole rock major element data.....	343
Appendix 8 - Plagioclase phenocryst compositions (An, Ab, Or) calculated from microprobe data	346
Appendix 9 - Pyroxene phenocryst compositions (Wo, En, Fs) calculated from microprobe data	348
Appendix 10 - Microprobe analysis of plagioclase phenocryst compositions.....	350
Appendix 11 - Microprobe analysis of pyroxene phenocryst compositions	355
Appendix 12 - Microprobe analysis of plagioclase microlites, compositions and classifications	358
Appendix 13 - Microprobe analysis of glass compositions.....	360
Appendix 14 - SEM analysis of glass compositions.....	362

Appendix 15 - XRF whole rock trace element compositions	371
Appendix 16 – Growth rate and nucleation rate calculations	374
Appendix 17 - Lower surge production coefficient - dense deposits	376
Appendix 18 - Lower surge production coefficient - surge deposits.....	380
Appendix 19 - Lower surge production coefficient - surge and dense deposits	384
Appendix 20 - Higher surge production coefficient - dense deposits	388
Appendix 21 - Higher surge production coefficient - surge deposits	389
Appendix 22 - Higher surge production coefficient - surge and dense deposits	390

List of Figures

<i>Figure 1.1 - Map of the Lesser Antilles adapted from (Robertson, 2009). The red line represents the axis of the current active volcanic arc, while the blue line represents the axis of the older arc.....</i>	<i>18</i>
<i>Figure 1.2 – The islands of St. Kitts and Nevis showing terrain. Source: Google Maps.....</i>	<i>19</i>
<i>Figure 1.3 – Photos showing A) Mt Liamuiga, St. Kitts. B) Nevis Peak, Nevis.....</i>	<i>20</i>
<i>Figure 2.1 - Map showing the islands surrounding St Kitts and Nevis mentioned in this chapter. Source: Open Street Map (OSM).....</i>	<i>28</i>
<i>Figure 2.2 - Map of St Kitts showing towns and villages as well as infrastructure. Source: Open Street Map (OSM).....</i>	<i>29</i>
<i>Figure 2.3 - Map of Nevis showing towns and villages as well as infrastructure. The location of the destroyed capital Jamestown has been added to the map. Source: Open Street Map (OSM).....</i>	<i>30</i>
<i>Figure 2.4 Passage from A letter from Hans Sloane, M. D. and S. R. S: with several accounts of the earthquakes in Peru October the 20th. 1687. and at Jamaica, February 19th. 1687/8 and June the 7th. 1692 (Sloane, 1694)...</i>	<i>40</i>
<i>Figure 2.5 - Map of central Basseterre showing College Street, Greenland Gut (present day South Olivees river), the Market Hut and Victoria Road.....</i>	<i>46</i>
<i>Figure 2.6 – Timeline of geological and meteorological disaster events that have occurred on St Kitts and Nevis since the arrival of the first settlers in the 17th Century.....</i>	<i>60</i>
<i>Figure 3.1 - Geological map of St. Kitts from Baker (1969). The youngest, northern extent of the island is shown, including the deposits associated with Mt Liamuiga (Mt Misery).....</i>	<i>67</i>
<i>Figure 3.2 - The Mansion Series original type section in the cliffs below Mansion Village, from Baker (1969).....</i>	<i>69</i>
<i>Figure 3.3 - Composite section through the Steel Dust Series, location: Bourke’s Estate, from Baker (1985).....</i>	<i>70</i>
<i>Figure 3.4 - Geological map of Nevis from Hutton (1978) showing the youngest centre on Nevis – Nevis Peak Volcano, the older centres and the identifiable flow deposits.....</i>	<i>73</i>

<i>Figure 3.5 - Mop of Field locations on St. Kitts.....</i>	<i>77</i>
<i>Figure 3.6 – Logs depicting the exposures of block and ash flows at locations SK2, SK10, SK12 and SK13.....</i>	<i>79</i>
<i>Figure 3.7 - Gas escape pipe within the block and ash flow at location SK2. The material within these pipes is poorly sorted and lacking the finer grain ash component.....</i>	<i>81</i>
<i>Figure 3.8 - Block and ash flow at Location SK10. Examples of large, dense blocks and gas escape pipes are shown in this image.....</i>	<i>81</i>
<i>Figure 3.9 - Block and ash flow at location SK12. The upper unit shown is an example of a block and ash flow. This flow sits above the lowermost unit is clast poor. A horizon of soil can be seen beneath the base of the PDC unit... </i>	<i>82</i>
<i>Figure 3.10 - Logs depicting the exposures of pumice and ash flows at locations SK4, SK6 and SK13.....</i>	<i>84</i>
<i>Figure 3.11 - Location SK4, showing two pumice and ash flow units. Gas escape structures can be seen in both units. A lens of breccia and a reddish coloured upper part indicating thermal alteration can be seen in the upper unit.....</i>	<i>85</i>
<i>Figure 3.12 - SK5 MIXED samples collected from SK4. These samples are composed of lighter and darker material.....</i>	<i>87</i>
<i>Figure 3.13 – 0.5 m Section through the steel dust series at SK11, close to Sandy Point Town.....</i>	<i>89</i>
<i>Figure 3.14 - Logs depicting the exposures of fallout deposits at locations SK1, SK2, SK5 and SK12.....</i>	<i>90</i>
<i>Figure 3.15 - Logs depicting the exposures of volcanoclastic deposits at locations SK1 and SK8.....</i>	<i>92</i>
<i>Figure 3.16 - Mop of Fieldwork location on Nevis.....</i>	<i>93</i>
<i>Figure 3.17 - SKN9 showing Unit 1, Unit 2, Unit 3 and surges.....</i>	<i>94</i>
<i>Figure 3.18 - Surge deposits between Unit 1 and Unit 2.....</i>	<i>96</i>
<i>Figure 3.19 – Graphic logs from this study, SK4, SK6, SK10, SK12 & SK13, correlated with logs in similar locations in Roobol et al. (1981), Locations 12, 7, 5 & 11.....</i>	<i>99</i>

Figure 3.20 - The modern day Nevis Peak crater shown open to the west. (Imagery from Google Earth, 2023)....105

Figure 4.1 - Photomicrograph showing sample SK21 in cross polarised light. The two main phenocryst phases, plagioclase and pyroxene, and the glass and crystalline groundmass, are labelled.....123

Figure 4.2 - Photomicrograph showing sample SK30 in cross polarised light. This image shows the typical phenocryst textures observed in the Mt Liamuiga samples; sieve textures, zoning and glomerocrysts.....124

Figure 4.3 – Photomicrograph showing the typical characteristics of plagioclase phenocrysts in SK8 banded in cross-polarised light. Fine oscillatory zoning, sieve texture, reabsorbed crystals and fractured crystals are present.....125

Figure 4.4 – Photomicrograph showing a large glomerocryst found in SK30, in cross polarised light.....125

Figure 4.5 – Photomicrograph of SK8L showing reaction rim around an amphibole phenocryst.....126

Figure 4.6 – Photomicrograph showing the difference in textures between the enclave and juvenile material in SK8, shown in cross polarised light.....128

Figure 4.7 – Photomicrograph showing the difference in groundmass textures between the enclaves and juvenile material (highly crystalline enclave and the glassy juvenile material) in SK1E, shown in cross polarised light.....129

Figure 4.8 – Photomicrograph of SKN18 (top) and SKN19 (bottom) in plane polarised light. This image shows the typical texture of the Nevis Peak samples, including amphibole phenocryst with reaction rims.....131

Figure 4.9 – Photomicrograph showing an amphibole phenocryst in SKN19 surrounded by a reaction rim.....132

Figure 4.10 – FeO*/MgO versus silica diagram showing tholeiitic and calc-alkaline classifications.....136

Figure 4.11 - AMF diagram showing tholeiitic and calc-alkaline classifications.....136

Figure 4.12 – K₂O shown against SiO₂. This diagram shows the tholeiitic and calc-alkaline classifications.....137

Figure 4.13 – Total Alkali-Silica (TAS) diagrams showing the chemical composition of the samples collected on Mt Liamuiga, St Kitts, with comparison to published (Baker, 1968a, 1980, 1984, 1985; Baker and Holland, 1973;

<i>Roobol et al., 1987; Toothill et al., 2007) data . The samples collected are of basaltic andesite, andesitic and dacitic composition.....</i>	<i>137</i>
<i>Figure 4.14 - R1-R2 diagrams (De la Roche et al., 1980) showing the classification of volcanic rocks.....</i>	<i>138</i>
<i>Figure 4.15 – Harker diagrams (Harker, 1909) showing major element trends plotted against SiO₂.....</i>	<i>140</i>
<i>Figure 4.16 – Total Alkali-Silica (TAS) diagrams showing the chemical composition of the samples collected on Nevis Peak, Nevis. The samples collected are of basaltic andesite, andesitic and dacitic composition.....</i>	<i>142</i>
<i>Figure 4.17 - Chondrite normalised REE patterns for the St Kitts (orange) and Nevis (blue) samples.....</i>	<i>144</i>
<i>Figure 4.18 - Relative enrichment compared to mid-ocean ridge basalt (MORB) shown for St Kitts (orange) and Nevis (blue) samples.....</i>	<i>145</i>
<i>Figure 4.19 - Trace elements plotted on Zr/TiO₂ versus Nb/Y (top)), and Zr/TiO₂ versus Ce (bottom) diagrams (Winchester and Floyd, 1977).....</i>	<i>147</i>
<i>Figure 4.20 – Based on Barrett and MacLean (2019), showing Zr versus Y, classifying tholeiitic, traditional and calc-alkaline magmas.....</i>	<i>148</i>
<i>Figure 4.21 – TAS diagrams showing glass compositions for the Mt Liamuiga samples. SEM derived EDS data is shown as crosses, while microprobe derived data is shown as circles.....</i>	<i>152</i>
<i>Figure 4.22 – TAS diagrams showing glass compositions derived from SEM EDS data for the ‘mixed magma’ Mt Liamuiga samples, SK5 and SK8.....</i>	<i>152</i>
<i>Figure 4.23 – TAS diagrams showing glass compositions for the Nevis Peak samples. SEM derived EDS data is shown as crosses, while microprobe derived data is shown as circles.....</i>	<i>154</i>
<i>Figure 4.24 – Feldspar classification diagram (Deer et al., 1992), showing the classification of feldspar phenocrysts for the Nevis (top) and the St Kitts (bottom) samples.....</i>	<i>156</i>
<i>Figure 4.25 – Ternary composition diagram for pyroxene phenocrysts.....</i>	<i>157</i>

<i>Figure 4.26 - An-Ab compositional diagrams for plagioclase phenocrysts transects, shown for the St Kitts and Nevis polished thin sections. The different coloured lines on each plot represent different transects taken on the same sample.....</i>	<i>158</i>
<i>Figure 4.27 - Feldspar classification diagram (Deer et al., 1992), showing the classification of feldspar microlites for the Nevis and the St Kitts samples.....</i>	<i>160</i>
<i>Figure 4.28 - Ternary composition diagram for pyroxene microlites.....</i>	<i>160</i>
<i>Figure 4.29 – Diagrams showing inferred origins of magma a) from Pearce (2008), b) from Pearce et al. (1984).....</i>	<i>163</i>
<i>Figure 4.30 – representative diagrams of plagioclase textures and their suggested interpretations, adapted from Viccaro et al. (2010).....</i>	<i>166</i>
<i>Figure 5.1 - SEM images showing key microlite textures. The mafic crystals are shown as light crystals, while the plagioclase microlites are shown as dark grey.....</i>	<i>179</i>
<i>Figure 5.2 - Mean aspect ratio (S/L) against mean microlite crystal area (μm^2) for both plagioclase and mafic microlites analysed from the Mt Liamuiga and Nevis Peak samples.....</i>	<i>180</i>
<i>Figure 5.3 - Microlite area number density (Na) shown against crystallinity (φ) for Mt Liamuiga and Nevis samples.....</i>	<i>188</i>
<i>Figure 5.4 - CSD plot for plagioclase microlites in the St Kitts samples.....</i>	<i>190</i>
<i>Figure 5.5 - CSD plot for plagioclase microlites in the Nevis samples.....</i>	<i>191</i>
<i>Figure 5.6 - CSD plot for mafic microlites in the St Kitts samples.....</i>	<i>195</i>
<i>Figure 5.7 - CSD plot for mafic microlites in the Nevis samples.....</i>	<i>196</i>
<i>Figure 5.8 - Box plot showing the estimated ascent rates for Mt Liamuiga and Nevis based on A) plagioclase microlites, B) mafic microlites and C) average of the plagioclase and mafic microlites. SK1 & SK11 – Pumice lapilli. SK5D, SK8D and SK31 – Pumice and ash flows. SK20, SK21 & SK30 – Block and ash flows. SK24b & SK27a – Steel dust. SKN18 & SKN19 – Nevis samples.....</i>	<i>208</i>

Figure 5.9 - Modified from Hammer et al. (2000) a) Schematic diagram showing crystallisation paths of erupting lavas. Path 1 shows a nucleation dominated regime, while 2A and 2B show nucleation dominated regimes, followed by a transition to growth dominated regimes. b) Hypothetical curve modified from Swanson (1977) relating N_a and ΔT , showing over low degrees of undercooling, microlite population density is proportional to the rate of undercooling. As ΔT increases, the rate of nucleation peaks then declines, resulting in a much larger potential range of textures produced by explosive eruptions(Swanson, 1977).....211

Figure 5.10 - Microlite number density (N_a) shown against crystallization (ϕ). This graph shows the same values as Figure 5.3, with SK27a and SK30 removed to allow the trends to be seen with more clarity.....211

Figure 5.11 - Comparison of global microlite number volume (N_v) against crystallinity (ϕ), based on (Cashman, 2020). (Cashman and McConnell, 2005; Clarke et al., 2007; Hammer et al., 1999; Martel and Poussineau, 2007; Miwa et al., 2009; Murch and Cole, 2019; Piochi et al., 2005; Preece et al., 2013, 2016; Suzuki et al., 2006; Suzuki and Fujii, 2010; Szramek et al., 2006; Wong and Larsen, 2009).....215

Figure 5.12 - Glass composition shown against microlite number density (N_a) for the Mt Liamuiga samples.....216

Figure 5.13 - Comparison graph showing the relationship between ascent rate and crystallisation time.....223

Figure 5.14 - Ascent rate estimates for different volcanoes, with the bars representing the range of the data, and the x symbols indicating the mean value. Where explosive/extrusive is not specified, the values are combined into one dataset.(Baker, 1968b; Brown and Andrews, 2015; Cassidy et al., 2015; Geschwind and Rutherford, 1995; Hammer et al., 1999; Murch and Cole, 2019; Noguchi et al., 2008; Scott et al., 2012; Szramek et al., 2006).....225

Figure 5.15 – Ascent rate estimates for different volcanoes with the outliers shown in Figure 15 removed, with the bars representing the range of the data, and the x symbols indicating the mean value. Where explosive/extrusive is not specified, the values are combined into one dataset. (Brown, R. J. and Andrews, 2015; Cassidy et al., 2015; Geschwind and Rutherford, 1995; Hammer et al., 1999; Murch and Cole, 2019; Noguchi et al., 2008; Scott et al., 2012; Szramek et al., 2006).....226

Figure 5.16 - Summary diagram showing three microlite evolution pathways and their corresponding eruption styles. The different shades of orange represents different magma types with the potential to mingle at shallow levels of the magma reservoir.....228

Figure 5.17 - Amphibole phenocrysts in SK8L. The thicker reaction rims are visible.....232

Figure 5.18 - Amphibole phenocrysts found in SKN18 and SKN19. A) Amphibole in SKN18 showing no or thin reaction rims. B) Amphibole with a thick reaction rim, other amphibole crystals in the same image show thin reaction rims.....232

Figure 6.1 – Pyroclast flow hazard map for NW St Kitts from Baker (1985).....239

Figure 6.2 - Volcanic hazard map for an explosive eruption at Mt Liamuiga, St. Kitts (Robertson, 2005).....240

Figure 6.3 - Volcanic hazard map for an effusive dome forming eruption at Mt Liamuiga, St. Kitts (Robertson, 2005).....241

Figure 6.4 - Map of Mt Liamuiga showing the source area, a circle with a radius of 650 m centred on the crater, indicated in blue.....250

Figure 6.5 - Topographic map of Northern St Kitts showing the towns and topographic features referenced in this chapter.....251

Figure 6.6 - Maps showing examples of deposits from dense PDCs from the low surge production scenarios with basal part densities of 1200 kg m⁻³. The inundation area and deposit thickness is shown for each scenario, with the respective total deposit volume and basal part densities indicated in the upper left.....252

Figure 6.7 - Maps showing examples of deposits from dense PDCs from the low surge production scenarios with basal part densities of 1400 kg m⁻³. The inundation area and deposit thickness is shown for each scenario, with the respective total deposit volume and basal part densities indicated in the upper left.....253

Figure 6.8 - Maps showing examples of deposits from dense PDCs from the high surge production scenarios with basal part densities of 1400 kg m⁻³. The inundation area and deposit thickness is shown for each scenario, with the respective total deposit volume and basal part densities indicated in the upper left of each map.....254

Figure 6.9 – Maps showing examples of surge deposits from the low surge production scenarios with basal part densities of 1200 kg m⁻³. The inundation area and deposit thickness is shown for each scenario, with the respective total deposit volume and basal part densities indicated in the upper left of each map.....262

Figure 6.10 – Maps showing examples of surge deposits from the low surge production scenarios with basal part densities of 1400 kg m⁻³. The inundation area and deposit thickness is shown for each scenario, with the respective total deposit volume and basal part densities indicated in the upper left of each map.....263

Figure 6.11 - Maps showing examples of surge deposits from the high surge production scenarios with basal part densities of 1400 kg m⁻³.The inundation area and deposit thickness is shown for each scenario, with the respective total deposit volume and basal part densities indicated in the upper left of each map.....267

Figure 6.12 – Combined dense deposits and surge deposits maps from the low surge production scenarios with basal part densities of 1200 kg m⁻³, with the respective total deposit volume and basal part densities indicated in the upper left of each map.....271

Figure 6.13 – Combined dense deposits and surge deposits maps from the low surge production scenarios with basal part densities of 1400 kg m⁻³, with the respective total deposit volume and basal part densities indicated in the upper left of each map.....272

Figure 6.14 – Combined dense deposits and surge deposits maps from the high surge production scenarios with basal part densities of 1400 kg m⁻³, with the respective total deposit volume and basal part densities indicated in the upper left of each map.....274

Figure 6.15 - Map showing the locations of the main settlements, roads and rivers surrounding Mt Liamuiga. The inundation area of PDCs in a small volume scenario is shown.....279

Figure 6.16 - Map showing the locations of the main settlements, roads and rivers surrounding Mt Liamuiga. The inundation area of PDCs in a medium volume scenario is shown.....280

Figure 6.17 - Map showing the locations of the main settlements, roads and rivers surrounding Mt Liamuiga. The inundation area of PDCs in a large volume scenario is shown.....281

List of Tables

<i>Table 2.1 - List of historic disasters for St Kitts & Nevis.....</i>	<i>32</i>
<i>Table 3.1 - Summary of the ¹⁴C dates from the Mansion series, for Mt. Liamuiga, St Kitts. References: 1) Baker (1969) 2) Baker (1985) 3) Roobol et al. (1981) 4) Harkness et al. (1994). (adapted from Lindsay et al. (2005)).....</i>	<i>71</i>
<i>Table 3.2 – Descriptions of the block and ash flows identified from Mt Liamuiga.....</i>	<i>80</i>
<i>Table 3.3 – Descriptions of the pumice and ash flows identified from Mt Liamuiga.....</i>	<i>86</i>
<i>Table 3.4 – Table summarising the locations and descriptions of samples collected from SKN19.....</i>	<i>95</i>
<i>Table 3.5 - Correlation of the locations in this study with the existing stratigraphy for Mt Liamuiga (Baker, 1969, 1985; Harkness et al., 1994; Roobol et al., 1981).....</i>	<i>100</i>
<i>Table 4.1 - Whole rock XRF analysis (major and trace element) for the 'mixed magma' clasts in Roobol et al. (1987). SK-164 is the darker end member and SK-165 is the lighter end member.....</i>	<i>110</i>
<i>Table 4.2 - Settings for the Wroxi applications, for major elements of interest.....</i>	<i>120</i>
<i>Table 4.3 - Table of petrographic analysis of the Mt Liamuiga and Nevis samples. Modal abundances and vesicle areas were estimated based on a visual inspection of the sample. The number of 'x' symbols indicates the relative phenocryst abundance, for example, x = very rare and XXXX = abundant.....</i>	<i>133</i>
<i>Table 4.4 – Whole rock XRF major element data for St Kitts and Nevis samples.....</i>	<i>143</i>
<i>Table 4.5 - Table showing loss on ignition (LOI) as a percentage of sample mass.....</i>	<i>150</i>
<i>Table 5.1 - Comparison of ascent rate estimates using different methods, for Mt St Helens, and Soufriere Hills.....</i>	<i>173</i>
<i>Table 5.2 - Quantitative microlite data for plagioclase microlites.....</i>	<i>182</i>
<i>Table 5.3 - Quantitative microlite data for mafic microlites.....</i>	<i>185</i>
<i>Table 5.4 - Crystal Size Distribution (CSD) data for plagioclase microlites in Mt Liamuiga samples.....</i>	<i>192</i>

<i>Table 5.5 - Crystal Size Distribution (CSD) data for plagioclase microlites in Nevis samples.....</i>	<i>193</i>
<i>Table 5.6 - Crystal Size Distribution (CSD) data for mafic microlites in Mt Liamuiga samples.....</i>	<i>197</i>
<i>Table 5.7 - Crystal Size Distribution (CSD) data for mafic microlites in Nevis samples.....</i>	<i>200</i>
<i>Table 5.8 - Calculated crystallisation times and nucleation rate for the Mt Liamuiga and Nevis samples.....</i>	<i>201</i>
<i>Table 5.9 – Decompression and ascent rates estimated for Mt Liamuiga and Nevis using plagioclase microlites.....</i>	<i>203</i>
<i>Table 5.10 - Decompression and ascent rates estimated for Mt Liamuiga and Nevis using mafic microlites.....</i>	<i>205</i>
<i>Table 6.1 – Parishes and towns in St Kitts, with their respective populations (Department of Statistics, 2011)....</i>	<i>243</i>
<i>Table 6.2 - VolcFlow input parameters chosen for the Mt Liamuiga dense PDC and surge models.....</i>	<i>245</i>

List of Appendices

<i>Appendix 1 - List of Libraries and Archives consulted.....</i>	<i>316</i>
<i>Appendix 2 - St. Kitts field locations and Latitude/Longitude.....</i>	<i>317</i>
<i>Appendix 3 - Maximum axis collected from clasts in the upper layer of pumice lapilli at location SK2.....</i>	<i>318</i>
<i>Appendix 4 - Description of the samples chosen for XRF analysis.....</i>	<i>319</i>
<i>Appendix 5 – Thin section scans.....</i>	<i>327</i>
<i>Appendix 6 - XRF whole rock major element data.....</i>	<i>340</i>
<i>Appendix 7 - Normalised XRF whole rock major element data.....</i>	<i>343</i>
<i>Appendix 8 - Plagioclase phenocryst compositions (An, Ab, Or) calculated from microprobe data.....</i>	<i>346</i>
<i>Appendix 9 - Pyroxene phenocryst compositions (Wo, En, Fs) calculated from microprobe data.....</i>	<i>348</i>
<i>Appendix 10 - Microprobe analysis of plagioclase phenocryst compositions.....</i>	<i>350</i>
<i>Appendix 11 - Microprobe analysis of pyroxene phenocryst compositions.....</i>	<i>355</i>
<i>Appendix 12 - Microprobe analysis of plagioclase microlites, compositions and classifications.....</i>	<i>358</i>
<i>Appendix 13 - Microprobe analysis of glass compositions.....</i>	<i>360</i>
<i>Appendix 14 - SEM analysis of glass compositions.....</i>	<i>362</i>
<i>Appendix 15 - XRF whole rock trace element compositions.....</i>	<i>371</i>
<i>Appendix 16 – Growth rate and nucleation rate calculations.....</i>	<i>374</i>
<i>Appendix 17 - Lower surge production coefficient - dense deposits.....</i>	<i>376</i>
<i>Appendix 18 - Lower surge production coefficient - surge deposits.....</i>	<i>380</i>
<i>Appendix 19 - Lower surge production coefficient - surge and dense deposits.....</i>	<i>384</i>

Appendix 20 - Higher surge production coefficient - dense deposits.....388

Appendix 21 - Higher surge production coefficient - surge deposits.....489

Appendix 22 - Higher surge production coefficient - surge and dense deposits.....390

1. Introduction

1.1 Overview

The volcanic islands of St Kitts and Nevis (Figure 1.1) form part of the Lesser Antilles island chain, an archipelago formed as a result of the crust of both the North and South American plates being subducted beneath the eastern edge of the Caribbean plate (Macdonald *et al.*, 2000; Robertson, 2009; Wadge, 1986).

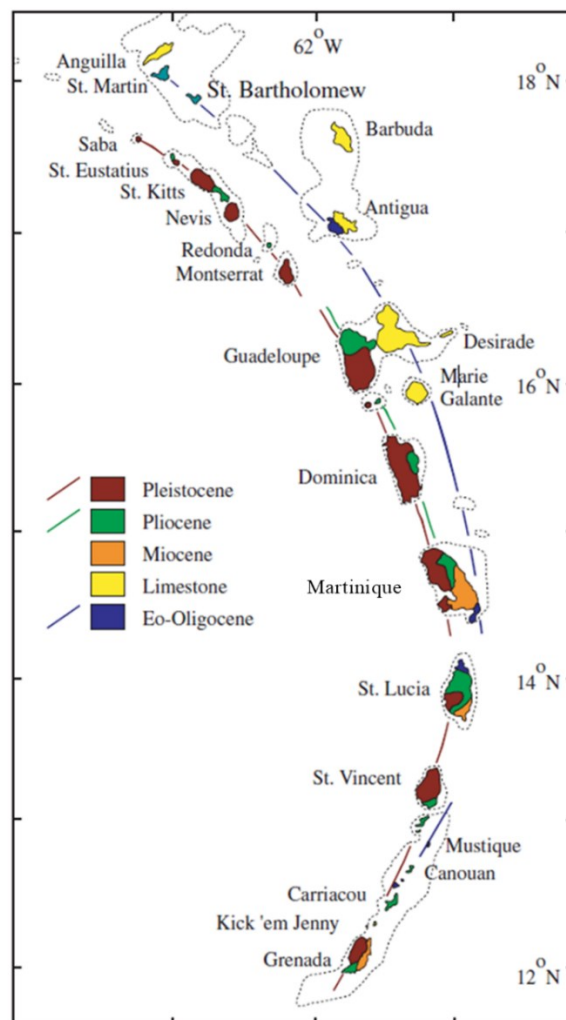


Figure 1.1 - Map of the Lesser Antilles adapted from (Robertson, 2009). The red line represents the axis of the current active volcanic arc, while the blue line represents the axis of the older arc.

These volcanic islands are examples of Small Island Developing States (SIDS), as designated by the United Nations (UN), where social and economic development has been significantly influenced by natural hazards including, but not limited to; hurricanes, floods, landslides, earthquakes, tsunamis and volcanic activity. This multi-hazard threat creates the need for a clear understanding and assessment of all potential hazards. Despite the volcanic nature of both islands, there have been few investigations into the most recent volcanic activity from historic (defined here as recorded history from the arrival of the first Europeans in 1493) and prehistoric times.

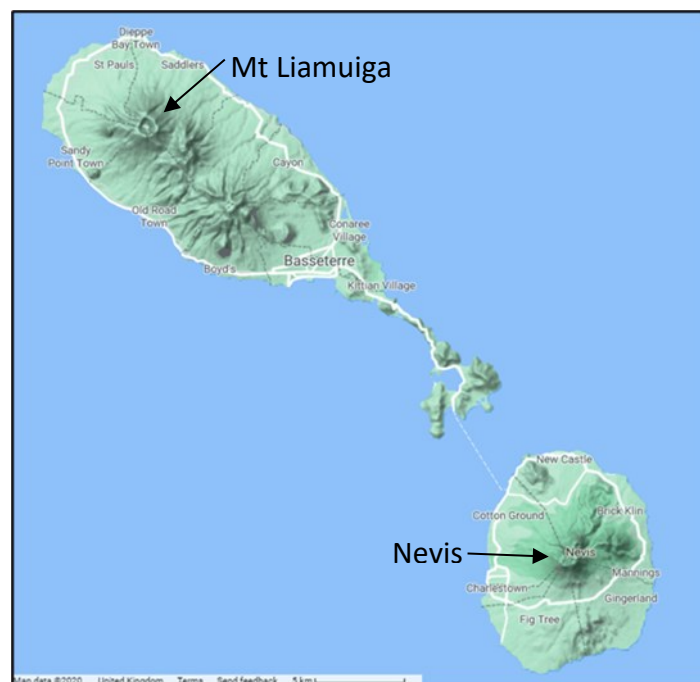


Figure 1.2 – The islands of St. Kitts and Nevis showing terrain. Source: Google Maps.

Two major seismic swarms occurred beneath Mt Liamuiga (Figure 1.2) on St Kitts during 1974 and 1988. These swarms were comparable to those observed on St Vincent before the eruption in St Vincent in 1979 (Simpson, 2005) and on Montserrat before activity of the Soufrière Hills began in 1995 (Luckett *et al.*, 2008; Robertson, 2005). The largest earthquake recorded beneath Mt Liamuiga was larger than any identified at Soufrière Hills, Montserrat,

(magnitude 4.5 and 4.0 respectively: Lockett *et al.*, 2008), suggesting that the volcano on St Kitts remains potentially active (Robertson, 2005).

To understand the potential hazards posed by Mt Liamuiga, and by the other volcanic centres on St Kitts and Nevis, it is important to understand the nature of past activity. Evidence suggests that there may have been activity on St Kitts since it was sighted by Christopher Columbus in 1493, while activity at Nevis (Nevis Peak shown in Figure 1.2) is likely to be significantly older (Simpson, 2005). Understanding past volcanic activity, and establishing the type of activity and any volcanic hazards that have affected the islands previously, is essential to understanding how best to mitigate and manage the risks associated with future eruptions.

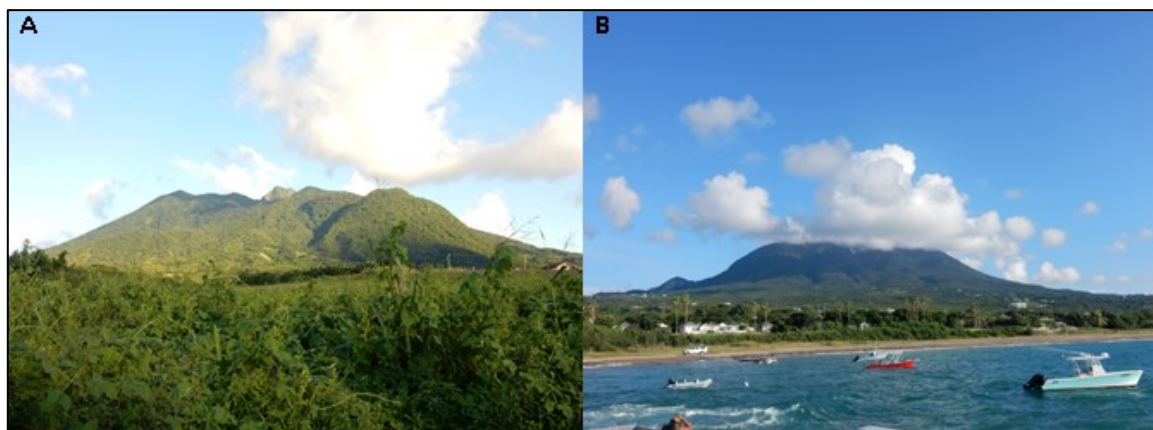


Figure 1.3 – Photos showing A) Mt Liamuiga, St. Kitts. B) Nevis Peak, Nevis.

The geology of St Kitts, particularly Mt Liamuiga (previously known as ‘Mt Misery Volcano’), has been generally well studied, and previous research has focused on the more recent volcanic deposits on Mt Liamuiga (Baker, 1980, 1984, 1985; Baker and Holland, 1973; Roobol *et al.*, 1981, 1985; Roobol *et al.*, 1987; Roobol, 1985). While literature indicates two historical eruptions on St Kitts, 1692 and 1843 (Baker, 1985; Capadose, 1845; Feuillet *et al.*, 2011; Simpson, 2005; Sloane, 1694), these eruptions have not been confirmed and little other work

has investigated historical activity. However, the literature concerning the geology of Nevis is comparatively scarce (Hutton and Nockolds, 1978).

1.2 Aims and Objectives

This project aims to combine the historical and geological evidence of recent eruptions to improve our understanding of the potential hazard and risk posed by volcanic activity at Mt Liamuiga and Nevis Peak, as well as furthering our understanding of the geochemical and petrological profile of the most recent volcanic deposits on St Kitts and Nevis. To achieve this, the project has five primary objectives:

1. To undertake archival work to investigate the 'possible' volcanism since 1493 (the arrival of the first Europeans) including the unconfirmed eruptions in 1692 and 1843, the role the volcanic landscape has played in current settlement patterns, and the influence of other major natural hazards in historical times. A secondary component will be to understand the importance of volcanic activity in the context of other geophysical and hydrometeorological hazards, and to consider the implications these may have on volcanic hazard assessment.
2. To undertake fieldwork on St Kitts and Nevis to document and interpret the critical volcanic products (i.e. deposits from Holocene eruptions) and undertake detailed sub-sampling of key sequences for further analysis.
3. To use geochemical and petrological analysis of samples collected in the field to understand pre- and syn- eruptive processes for the most recent eruptions from Mt Liamuiga and Nevis Peak.
4. To understand the nature of the crystallisation history from storage to eruption, providing insight into potential ascent dynamics.

5. To undertake modelling of the various types of pyroclastic density currents (PDCs) at different eruption volumes to conduct hazard analysis of the threat posed to the islands by PDCs.

1.3 Thesis structure

The thesis will explore these aims and objectives in the following chapters:

- Chapter Two will describe a history of disaster events on St Kitts and Nevis, including hurricanes, floods, earthquakes and volcanic eruptions, to build an understanding of the historic challenges posed to the islands by natural hazards. The two unconfirmed historic volcanic eruptions will be investigated in detail, and the implications of natural hazards for the settlements on St Kitts and Nevis discussed.
- Chapter Three will examine the field evidence for the most recent eruptions on St Kitts and Nevis. The focus of these investigations is the pyroclastic density current deposits (PDCs) and some of the fallout deposits from the most recent eruptions to have occurred on Mt Liamuiga, and on Nevis Peak.
- Chapter Four will investigate the geochemical and petrological characteristics of the samples collected from the fieldwork on St Kitts and Nevis. This will give insights into the magma storage conditions, as well as pre- and syn- eruptive processes.
- Chapter Five will use Crystal Size Distribution (CSD) analysis to gain insights into ascent conditions including possible ascent rates. Comparison of ascent rates and conditions with similar volcanoes will provide insights into the styles of eruptions at Mt Liamuiga and Nevis Peak.
- Chapter Six will use modelling of pyroclastic density currents (PDCs), as well as the knowledge gathered in chapters three to six, to discuss potential future eruptive

scenarios, as well as the hazard implications any future eruptions might pose to the islands,

1.5 Terminology of key deposits

This section will outline definitions of the key volcanic deposits studied in this thesis.

1.5.1 PDCs

Block-and-ash flows refer to the PDCs generated by gravitational collapse of a lava dome. These small volume flows are usually hot, typically 400-600°C, with carbonised remains of plant life common in deposits where flows have travelled across vegetated slopes. The flows have a high-particle concentration and are topography controlled, mostly confined to valleys. The deposits of these flows are poorly sorted and composed of dense to moderately vesicular blocks of fragmented lava derived from the lava dome in a medium to coarse ash matrix. They can be massive, or have prismatic joints and bread crusting, providing evidence for the hot emplacement of juvenile clasts. Explosions at lava domes can lead to flows and deposits rich in pumice along with a significant amount of lithic material originating from the dome. These are also referred to as block-and-ash flows (Brown and Andrews, 2015).

Pumice and ash flows are characteristically similar to block and ash flows, with the exception that they are composed of mainly pumice and ash. These flows can be formed by explosive eruptions, including fountain collapse. These flows are also generally confined by topography. Deposits are commonly lobate and sinuous, and can be deposited at lower temperatures as eruptive material is cooled significantly by the surrounding air (Brown and Andrews, 2015).

Pyroclastic surges are low particle concentration, dilute PDCs. In contrast to the high particle concentration of pyroclastic flows, surges represent the dilute end member. They can have

very low densities and have been seen to travel over water. Pyroclastic surges are typically generated from dense PDCs, and can flow on top of, or detach from, the original PDC. Deposits from surges are less confined by topography than the other PDCs, and often have bedforms and stratified deposits (Brown and Andrews, 2015).

It is important to understand that the term 'pyroclastic density currents (PDCs)' is currently used collectively to describe all gas-pyroclastic flows driven by the density contrast with the surrounding fluid generated by explosions, landslides of hot material or eruption column collapse (Brown and Andrews, 2015). The definitions given above divide PDCs into sub-categories for descriptive purposes, and for the purposes of recognising eruption styles.

1.5.2 Fallout

Fallout refers to any deposits formed by pyroclastic fall or ash-fall. These deposits are created by the sedimentation of pyroclasts through the atmosphere from an eruption plume during an explosive event (Houghton and Carey, 2015).

2. A history of disasters on the Islands of St. Kitts and Nevis, 17th to 20th Centuries

2.1 Introduction

The islands of Kitts and Nevis have one of the longest written histories in the West Indies. In the context of the Leeward Islands (Figure 2.1), the term 'history' refers to the written history commencing at the arrival of the first Europeans, beginning with Christopher Columbus in the 1493. Both islands, now a two-island nation, have played important administrative and tactical roles in both English and French colonial history (Hubbard, 2002a, 2002b), resulting in a well-documented narrative of events as far back as 1620.

Both St Kitts (Figure 2.2) and Nevis (Figure 2.3) are examples of Small Island Developing States (SIDS) where the progress of social and economic development has been significantly influenced by natural hazards including, but not limited to; hurricanes, flooding, landslides, earthquakes, tsunamis and volcanic activity. Records of these events occurring on the islands during the past four centuries can be found preserved in a vast number of sources, from admiralty and colonial office correspondence (e.g. Colonial Office, 1843) to letters and diaries of the ordinary townsfolk (e.g. Anonymous, 1690), and international newspaper articles carrying news of any devastation to fellow colonies (e.g. The Times, 1843) .

Both islands are volcanic in nature, yet, despite the vast documentation of natural hazards preserved the history of St Kitts and Nevis, there have been few investigations into the most recent reports of volcanic activity from historic sources. To understand the potential hazards posed by Mt Liamuiga (St Kitts) and Nevis Peak (Nevis), it is important to understand the nature of past activity. Evidence suggests that there may have been activity on St Kitts since

it was sighted by Christopher Columbus in 1493, while activity at Nevis is likely to be significantly older (Hutton and Nockolds, 1978; Simpson, 2005). While literature quotes two historical eruptions on St Kitts, 1692 and 1843 (Baker, 1985; Capadose, 1845; Feuillet *et al.*, 2011; Simpson, 2005; Sloane, 1694), these eruptions have not been confirmed and little other work has investigated any historical activity. In contrast to St Kitts, there is no suggestion of any historic volcanic activity occurring on Nevis, although swarms of volcanic earthquakes have been recorded. The most significant swarms occurred in 1926, 1947-48, 1950-51 and 1961-63 (Simpson, 2005).

This chapter has three key aims. The first, to compile a list of the types of geological and meteorological hazards to have impacted St Kitts and Nevis over time, and to outline the subsequent consequences for the islands. The second is to investigate any potential historic volcanic activity which may have occurred on the islands and, thirdly, to gain a multi-hazard understanding of the pattern of changes to the impacts and responses through time.

While the overall records for St Kitts and Nevis are reasonably comprehensive, the quality of the records preserved is significantly impacted by the changes between French and English colonial rule. For example, when the French took control of Nevis in 1705, all existing records of the islands from whilst they were under English control were piled into the streets and burned. This conflict between the French and English also resulted in the preferential recording of naval matters over natural hazards. While this may have reduced the amount of detail available in the records, the heavy European naval presence in the Eastern Caribbean during the 17th to 19th Centuries ensured a continuous narrative of events over this period (e.g. Colonial Office, 1843 and Smith, 1835).

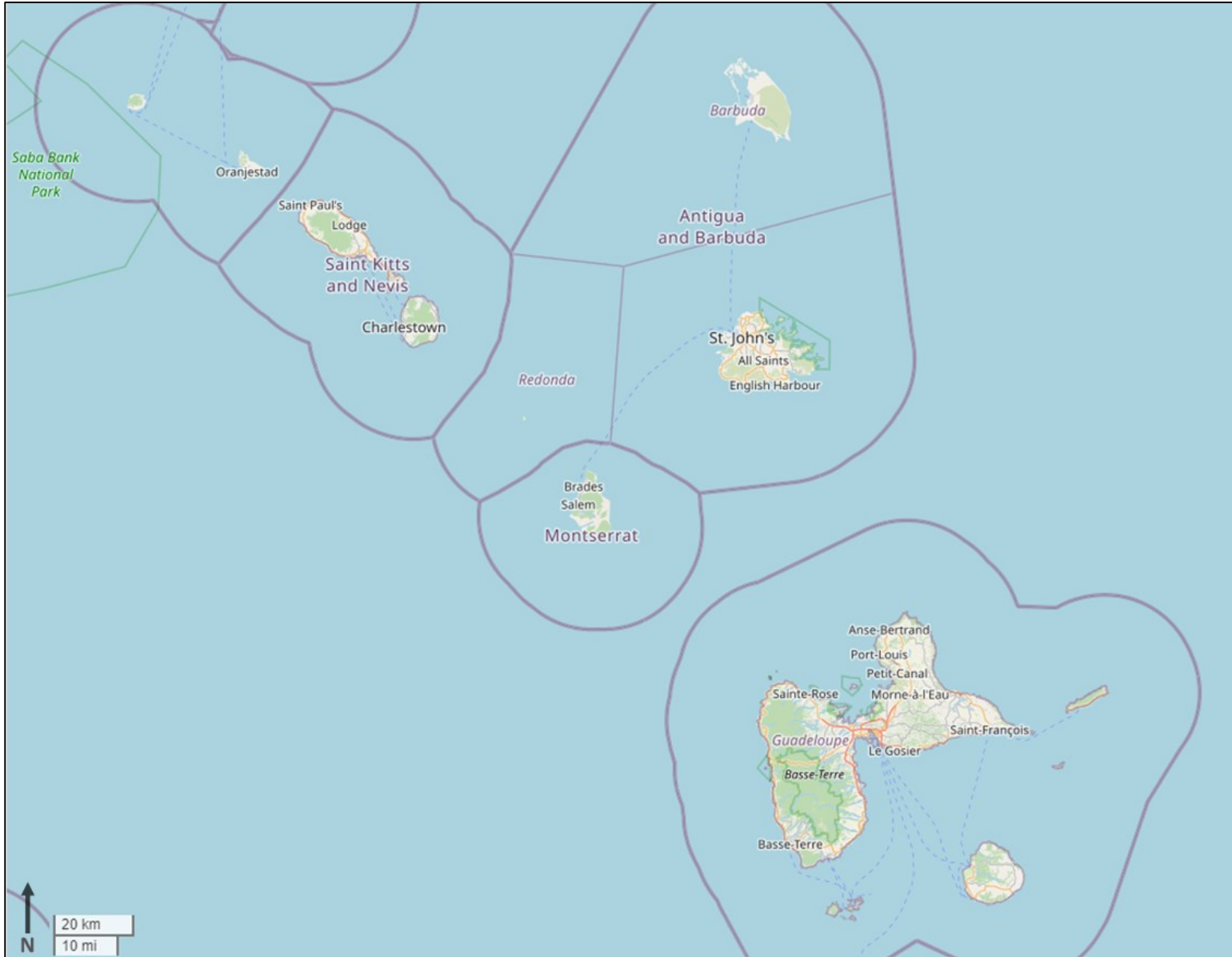


Figure 2.1 - Map showing the islands surrounding St Kitts and Nevis mentioned in this chapter.

Source: Open Street Map (OSM).

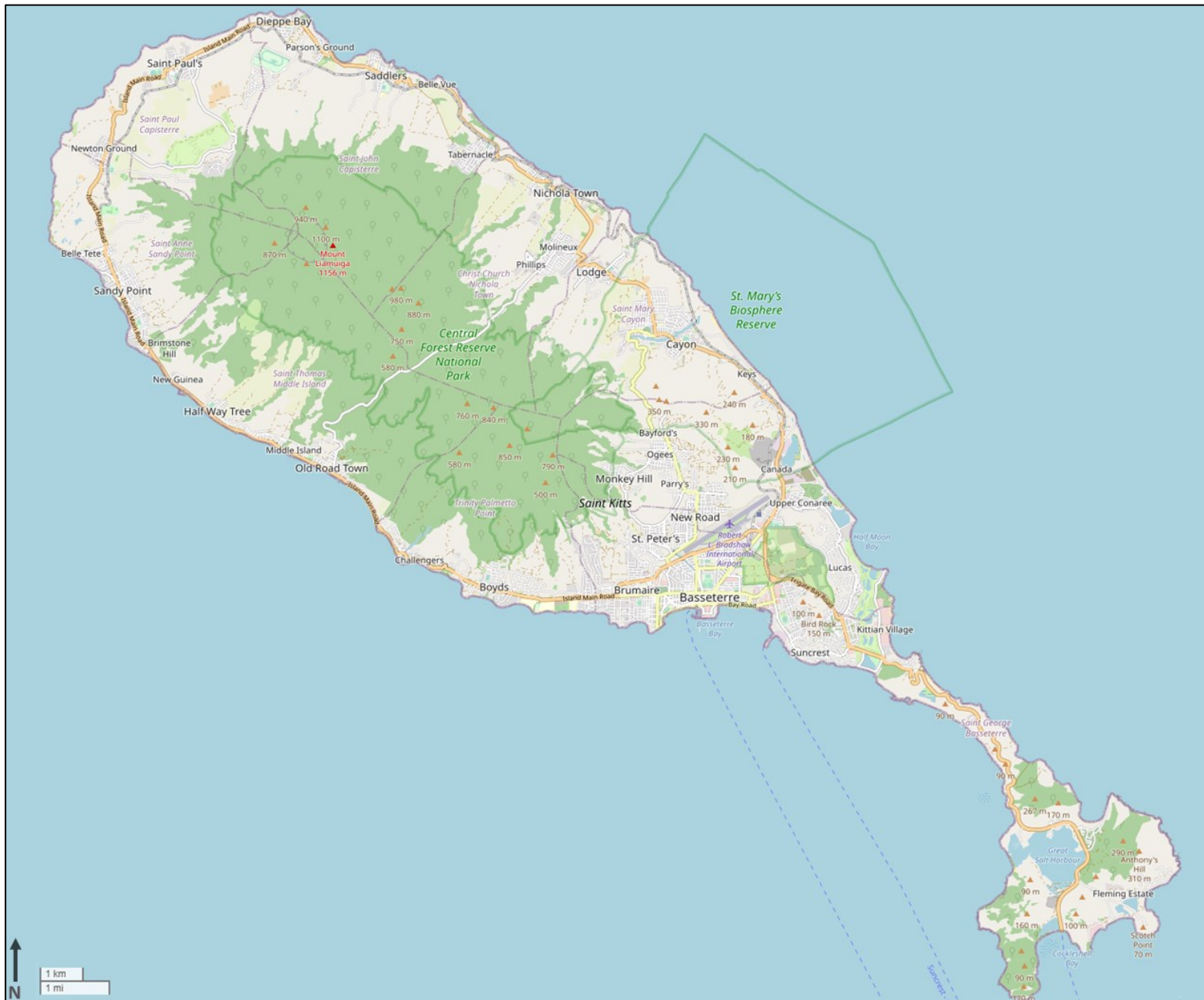


Figure 2.2 - Map of St Kitts showing towns and villages as well as infrastructure. Source: Open Street Map (OSM).



Figure 2.3 - Map of Nevis showing towns and villages as well as infrastructure. The location of the destroyed capital Jamestown has been added to the map. Source: Open Street Map (OSM).

2.2 Disaster events in chronological order

To gain an understanding of the impact of geological and meteorological disasters on the islands of St Kitts and Nevis, this study outlines key details from significant events for which descriptions could be obtained from historical records and publications. In the context of this study, events such as war and disease have been omitted as they are considered irrelevant, except for where they have significant implications for the effects of geological or meteorological events.

Table 2.1 shows a summary list of disasters which have occurred on the islands of St Kitts and Nevis from the seventeenth century, when the first Europeans arrived on the islands, through to the end of the twentieth century. These events have been selected as significant natural hazard events causing serious impacts on one or both of the islands.

Of particular interest are the earthquakes of 1690 and 1843, which both have anecdotal evidence of volcanic activity associated with them (Capadose, 1845; Sloane, 1694). Reports of activity at Mt Liamuiga during these years have appeared widely in published literature, yet reliable evidence for these reports of activity is yet to be found.

Table 2.1 - List of historic disasters for St Kitts & Nevis.

Year	Date	Event	Notes
1624	19 th September	Hurricane	All dwellings destroyed Tobacco and provisional crops destroyed
1626	August	Hurricane	All dwellings destroyed 2 ships lost Tobacco plantations destroyed All provisions lost
1638	August	Hurricane	Damaged many houses 75 dead 5 ships lost
1642	September	Hurricane	Destroyed all houses 600 dead (Guadeloupe, Martinique & St Kitts) 23 ships wrecked Salt ponds overflowed, becoming unproductive Cotton and Tobacco crops destroyed
1667	1 st -6 th September	Hurricane	Majority of buildings on Nevis destroyed Many building on St Kitts destroyed Major flooding Sugar production ceased temporarily Unknown number dead
1681	27 th August 4 th October	Hurricane	Houses and sugar mills damaged/destroyed Provisions lost
1689	Unknown	Hurricane	Yellow fever outbreak Half of Nevis' population perished
1690	5 th /10 th April	Earthquake (& tsunami)	Jamestown (Nevis) destroyed, damage on St Kitts
1707	29 th August	Hurricane	Nevis 'nearly ruined' Outbreak of disease
1747	21 st September 14 th October	Hurricane	32 ships wrecked Crews lost
1772	31 st August	Hurricane (series of three storms)	Caused £500,000 worth of damage Majority of building on St Kitts and Nevis destroyed Sugar mills destroyed Damage to crops and vegetation Several killed and many wounded
1792	April	Flood	Loss of lives Destruction to property

1793	August	Hurricane	30 ships stranded or lost
1804	3 rd September	Hurricane	Destructive hurricane
1821	9 th September	Hurricane	Destructive hurricane
1827	17 th August	Hurricane	Destructive hurricane
1833	8 th /25 th /26 th February	Earthquake	Series of strong earthquakes in February
1835	12 th August	Hurricane	Destructive hurricane
1843	8 th February	Earthquake	Damage across the Lesser Antilles, Volcanic activity at Mt Liamuiga
1871	31 ST August	Hurricane	Destructive hurricane 'General damage'
1876	12 th September	Hurricane	Destructive hurricane 'severe storm'
1880	12 th January	Flood	231 people drowned Loss of property and damage to buildings
1899	7 th August	Hurricane	200 small houses destroyed on St Kitts Considerable damage done to estates 'General destruction' on Nevis 21 dead on Nevis
1924	28 th August	Hurricane	Destructive hurricane
1928	13 th September	Hurricane	Destructive Hurricane
1950s	-	Earthquake	Series of severe earthquakes on Nevis and St Kitts
1974	8 th October	Earthquake	Significant damage Damage to St George's Parish Church
1985	16 th March	Earthquake	6.3mw Significant damage on Nevis
1989	17 th September	Hurricane	Hurricane Hugo Significant damage amounting to \$61 million in St Kitts and \$51 Million in Nevis
1998	21 st September	Hurricane	Hurricane George 90% housing in St Kitts damaged 5 dead 3,000 homeless Damage to major infrastructure US\$497 million worth of damage

2.2.1 Hurricanes of the 1600s

The hurricanes of the 1600s were the encountered by the first European settlers following their arrival on St Kitts and Nevis. The first settlers on St Kitts, a group of no more than 20 English men (Dyde, 2005), modelled their early dwellings on those of the local islanders. These did not stand up to the powerful winds of hurricanes and most collapsed at the first storm (Mulcahy, 2006). The early colonists weren't any safer at sea, where ships were often sunk or wrecked along the coasts of the islands.

On 29th September 1623, a hurricane destroyed the first tobacco crop. The storm wrecked tobacco ships, poisoning the coastal waters surrounding St Kitts and killing thousands of fish. Dead bodies were washed up along the coast from the wrecked ships (Hubbard, 2002a).

The 1624 hurricane destroyed early crops, the early dwellings and the fort built by first English colonists, led by Sir Thomas Warner, on St Kitts (Dyde, 2005). In 1625, French settlers joined the English on St Kitts, dividing the island between the two colonies (Hubbard, 2002a). Less than two years after the 1624 event, another hurricane struck the islands. For the second time in as many years, the early colonists found all of their dwellings destroyed. The tobacco and subsistence crops were ruined, leaving the small colony without essential provisions. Captain John Smith describes how the wind drove two ships, and left the settlers scavenging for food (Mulcahy, 2006; Neely, 2016). The 1626 hurricane sank 2 ships and left the colony to rebuild again. Relief finally arrived for the distressed settlers in October 1627, when the ship the *Hopewell* arrived carrying provisions and weaponry from England, along with the first English women settlers. The first settlers arrived onto Nevis shortly after, in 1628, and by the end of the year over 150 settlers had moved from St Kitts to Nevis, causing resentment on St Kitts (Dyde, 2005).

In 1638, a pamphlet was published in England detailing the impacts of a hurricane on St Kitts in August of the same year. John Taylor's *'Newes and strange Newes from St Christophers of a tempestuous Spirit, which is called by the Indians a Hurry-Cano or whirlwind'* describes how 5 ships were lost, 75 killed and many houses were damaged. Settlers were said to have found safety from the winds hiding in holes, caves, pits, dens and other hollow places (Mulcahy, 2006).

A deadly hurricane struck the Leeward Islands in of 1642. The exact date of this hurricane is unknown, though it is thought to have been in September of that year. According to the Nevis Disaster Management Department (NDMD) website, the storm has been reported to have 'destroyed all houses on St Kitts'. It caused upwards of 600 deaths across Guadeloupe, Martinique and St Kitts (Longshore, 2000). The islands' cotton and tobacco crops were destroyed, the salt ponds overflowed and 23 vessels were wrecked along the coast (Garriott, 1900; Marx, 1987). Several of these ships were carrying tobacco, which subsequently poisoned the water, killing thousands of fish (Neely, 2016).

On 15th August 1666, a hurricane passed through St Kitts leading to the loss of an entire French fleet with 2000 men drowned (Hubbard, 2002a). Just a year later a hurricane described as 'tremendous', swept through St Kitts, Nevis and Virginia over 6 days, from 1st to 6th September 1667, killing an unknown number of people. The residents of St Kitts and Nevis sought shelter 'throwing themselves flat on the ground in the fields (Garriott, 1900; Hubbard, 2002b). Nearly all the buildings on Nevis were flattened, while St Kitts was described as being 'in the most deplorable state'. M. Laurent, the governor, writes in a letter 'there is not a house or sugar works standing, and they cannot hope to make any sugar for 15 months to come'.

In 1681 three hurricanes struck within 37 days (Hubbard, 2002a). The strongest hurricane, once again caused houses and sugar mills on St Kitts to suffer great damage, with all provisions lost during the storm (Garriott, 1900; Mulcahy, 2006). There are reports of another hurricane in 1689, which left half of Nevis' population dead (Garriott, 1900). The deaths are likely to have occurred during a yellow fever outbreak (Zacek, 2010), possibly caused by flooding, although little else is known regarding the impacts of this hurricane.

2.2.2 Earthquake of 1690 (including the description of the possible volcanic activity, 1692)

The Great Leeward Islands Earthquake of 1690 was one of the first seismic events in the West Indies to be recorded in any detail by European settlers. The earthquake shook the islands on 5th April of 1690, although some records of the date are conflicting with the 6th of April most commonly listed as an alternative date (Hubbard, 2002a). On St Kitts and Nevis, the biggest earthquake was felt on the afternoon of the 5th, with a second which may have been felt on the 10th and an earlier small earthquake on the 26th February (Robson, 1964). Feuillard (1985) suggests that the earthquake felt in Guadeloupe was not the same as that which struck St Kitts and Nevis on the 5th or 10th April, and instead occurred on the 16th April (Feuillet *et al.*, 2011; Robson, 1964).

This event is likely to have been a shallow earthquake with an epicentre located between Nevis, Antigua and Montserrat. The earthquake is thought to have ruptured the fault set known as Montserrat-Havers and Redonda, part of the en echelon fault system. From damage reports, the intensities are thought to have been IX on St Kitts, Nevis and Antigua (Feuillet *et al.*, 2011).

During the 1690 earthquake, there were no Englishmen on St Kitts, and reports came from observations made on Nevis. In the August of 1689, the French had seized the English territory

on St Kitts while the English settlers escaped to Nevis. By 16th July 1690, the English had landed a force on St Kitts and forced the French to surrender, deporting French settlers to Santo Domingo (Dyde, 2005; Hubbard, 2002b; Zacek, 2010).

The earthquake on the 5th April caused great damage on both St Kitts and Nevis. On Nevis, one report titled 'An account of the late dreadful earth-quake in the islands of Mevis and St Christophers, &c. Which happen'd in the beginning of April, of this present 1690', in 'a letter to a friend in London' published in 1690 (Anonymous, 1690), describe how all of the stone buildings were 'thrown down' while the structure made of wood were 'no less shaken' but remained standing after the shaking subsided. The letter goes on to describe how the ground opened up in many places, 'hot, bituminous waters' flowed out of some cracks and that trees were uprooted. St Kitts is said to have suffered as badly as Nevis, with wooden structures surviving compared to those built of stone or brick. The island also saw the majority of sugar mills overturned, Jesuit College ruined and 'La Fontaine', the palace of the French governor, destroyed. The palace was never rebuilt.

The destruction listed in 'An account of the late dreadful earth-quake...' is verified in the letter from Governor Codrington to the Lords of Trade and Plantations dated 4th June 1690. Governor Codrington claims a personal loss of £2,000 due to the earthquake, and mentions the collapse of buildings, the damage to the majority of stone works on the island and some persons killed. As the origin of the letter is listed as Antigua, the £2,000 loss is likely to be from the Codrington plantations on Antigua, however, the damage he is referring too could be from Antigua, or the Leeward Islands in general (Dyde, 2005).

A tsunami resulting from the 1690 earthquake is infamously said to have destroyed and sunk Jamestown, the first capital of Nevis. The date of this event is sometimes given as 1680,

although no primary sources quote an earthquake or tsunami occurring in Nevis or St Kitts in that year (Gordon, 1987; Hubbard, 2002b; Zacek, 2010). Soon after the earthquake, the sea is said to have receded three quarters of a mile, exposing the fish covered seabed, before returning at speed. This happened multiple times during the day, with the first rush of water the most powerful (Anonymous, 1690; Hubbard, 2002a). The water is said to have encroached as far as a third of a mile inland (Hubbard, 2002a). Smith (1745) recounts a tale told to him by a parishioner, where ‘the sea retired a good furlong from Charles Town, and in a minute or two, or a little more, came back to its usual bounds’, also noting how the foundation rock of the lower town was damaged as the water burst through, the damage of which could still be observed several decades later. An alternative theory to Jamestown’s disappearance is proposed by Hubbard (2002). It suggests that Jamestown was badly damaged during the 1690 earthquake causing the residents to slowly move out of the town until it become non-existent. Hubbard suggests this accounts for the location of Jamestown remaining on maps of Nevis for many years after the earthquake.

Reports of volcanic activity in 1692, possibly relating to the 1690 earthquake, has been reported on Mt Misery, St Kitts. A single secondary report of this activity was made by Hans Sloane (1694), although when compared to other written accounts from St Kitts and Nevis, it appears unlikely that any activity occurred during this period. Section 2.2.3 below describes the possibilities for the suspected activity in 1692.

2.2.3 Mt Liamuiga volcanic activity of 1692

The potential activity on St Kitts in 1692 was recorded in a secondary account by Hans Sloan in 1692, shown in Figure 2.4 (Sloane, 1694). Sloan’s letter detailed the destruction caused by the 7th June earthquake in Jamaica, the infamous earthquake that sank the pirate town of

Port Royal. The letter describes an eruption on St Kitts after the island was ‘much troubled by earthquakes.’ This single secondary source has been quoted in numerous papers as evidence for the activity in 1692, although the only recorded seismic activity on St Kitts that this could relate to is the 1690 earthquake which shook St Kitts and the surrounding Lesser Antilles.

No other record of the 1692 activity on St Kitts has been found during any past study, nor during this extensive literature search. Due to the busy nature of the island during the seventeenth and eighteenth century as a trade hub, and as an important naval location in the battle against the French, most events on St Kitts have been well documented, as shown by the summary of other disasters. Detailed records exist for the 1692 earthquake, the widespread trade activity and the prevalent naval operations. Considering the extensive records kept at the time, and the extensive descriptions of the earthquake as well as the war taking place at the time, it would be likely that any significant volcanic activity would have been recorded on the island and possibly by passing ships.

One possible explanation for the single account of a sustained eruption at Mt Liamuiga is that it has been misidentified as La Soufriere, Guadeloupe, which was recorded to have erupted in 1690 and showed periods of violent degassing until in 1696 (Komorowski *et al.*, 2005).

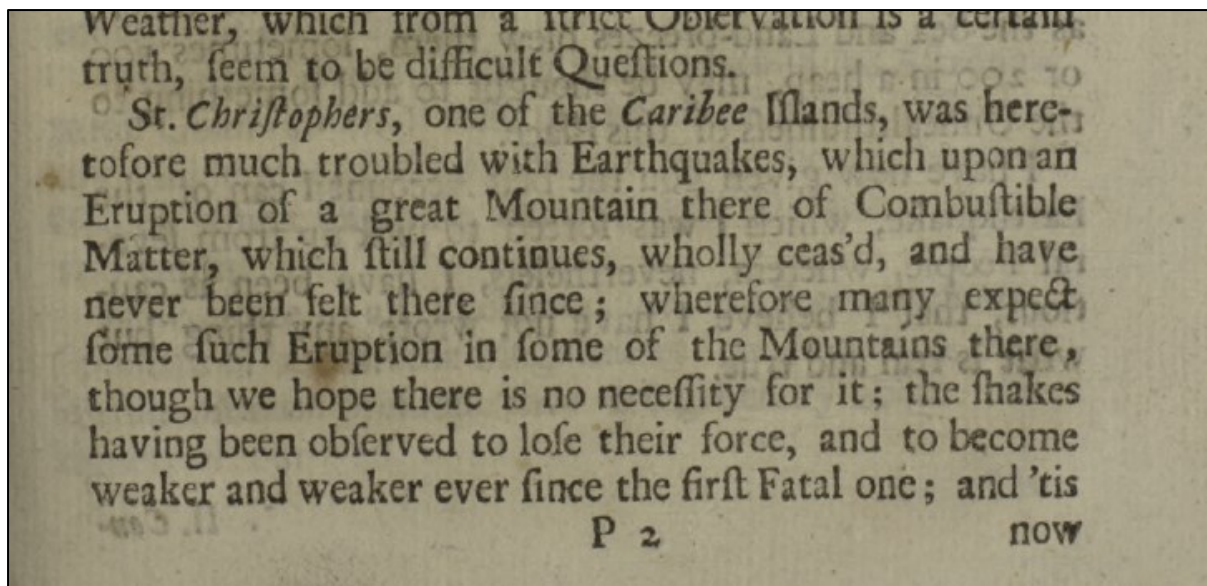


Figure 2.4 Passage from A letter from Hans Sloane, M. D. and S. R. S: with several accounts of the earthquakes in Peru October the 20th. 1687. and at Jamaica, February 19th. 1687/8 and June the 7th. 1692 (Sloane, 1694).

“St Christophers, one of the Caribee Islands, was heretofore much troubled with Earthquakes, which upon an eruption of a great mountain there of combustible matter, which still continues, wholly ceas’d, and have never been felt there since; wherefore many expect some such eruption in some of the mountains there, though we hope there is no necessity for it; the shakes having been observed to lose their force, and to become weaker and weaker ever since the first fatal one;”

- A letter from Hans Sloane, M. D. and S. R. S: with several accounts of the earthquakes in Peru October the 20th. 1687. And at Jamaica, February 19th. 1687/8 and June the 7th. 1692

The passage implies that the eruption happened in the past, ‘...was heretofore much troubled with Earthquakes, which upon an eruption of a great mountain there of combustible matter...’, which could imply that possible activity on St Kitts took place prior to June 1692. An earthquake struck St Kitts and the surrounding Lesser Antilles on 10th April 1690, although

there is no record of any volcanic activity on the island. It is possible that Sloane was referencing the large cracks which opened up in the ground during the 1690 earthquake; these cracks in the Earth were described by Sloane as 'spewing steam' and 'smelling strongly of sulphur'. Whether these continued to vent steam two years after the 1690 earthquake is unknown. While no activity was reported on St Kitts, activity was reported on Guadeloupe immediately after the 1690 earthquake.

The activity on Mt Liamuiga is said to have continued until 1692. At Guadeloupe in 1690, activity on north side of the summit dome indicated that the volcano was in violent state of degassing. La Soufriere Guadeloupe also showed signs of activity between 1690 and 1696, explaining the reference to an 'ongoing' eruption (Komorowski *et al.*, 2005). In this case, the accounts of activity at La Soufriere are a closer fit Sloan's account of the 'St Kitts' eruption, suggesting that the 1962 eruption has been incorrectly attributed to Mt Liamuiga.

2.2.4 Hurricanes of the 1700s

A hurricane on 29th August 1707 set Nevis on its future course, leaving the island 'nearly ruined' just one year after the devastating French invasion in 1706 (Chenoweth, 2006; Hubbard, 2002b; Mulcahy, 2006; Zacek, 2010). The invasion burnt and damaged most of the island's buildings, looted the towns and carried away the majority of plantation workers (Meniketti, 2016). The hurricane caused further damage to the already devastated settlement, bringing a wave of disease, although in some records, distinction is not made between the impacts of the invasion and those of the hurricane. St Kitts also suffered during this storm, with several ships were wrecked off the coast and many buildings damaged (Hubbard, 2002a). Financial help was sent from London for victims of both the incursion and the hurricane (Schwartz, 2015). The French invasion and the 1707 hurricane left Nevis in ruins,

and while the island recovered, it never regained its position as the most prosperous and well-governed of the Leeward Islands (Zacek, 2010).

After the downfall of Nevis due to war and hurricanes, St Kitts grew and became the more significant economic power of the two. Over both the seventeenth and eighteenth centuries, the islands changed hands between the English and the French several times, due to war, disasters and the signing of treaties (Hubbard, 2002b; Zacek, 2010). During the early 1700s, St Kitts grew to become one of the most successful economies of the British crown colonies, with its sugar trade thriving (Meniketti, 2016).

Two violent hurricanes struck St Kitts and Nevis in 1747, the first on September 21st and the Second on October 14th (Garriott, 1900). The latter storm saw 24 vessels lost at Basseterre, all loaded with sugar bound for England (Hubbard, 2002b; Marx, 1987), while eight ships were wrecked off the coast of Nevis (Hubbard, 2002b). Impacts of this hurricane were felt most at sea.

1772 was known as the year of the great hurricane (Gordon, 1987) throughout the West Indies. The hurricane, often known as 'The Alexander Hamilton Hurricane', after Founding Father Alexander Hamilton's poetic description of the storm in a letter, devastated the Leeward Islands. Three storms hit the islands in 1772, the first 'scarcely a house left standing' in Nevis (Hubbard, 2002b). The Oxford Journal of 28th November 1772 reported that 'At Saint Kitts, almost all the estates are destroyed, there being scarce a mill or boiling house left standing'. St Kitts, Nevis and Antigua lost more sugar in a single storm, than the total that was exported to England in the previous year (Cervený, 2016), with the total estimated damage totalling £500,000 (Garriott, 1900; Hubbard, 2002a). Nine hundred people are listed to have

died across Dominica, St Kitts and Cuba (Longshore, 2000), though on St Kitts alone the storm was said to have killed several and wounded many (Garriott, 1900).

The year of 1780 was the worst hurricane season in the 18th century, with eight major hurricanes reaching the Caribbean and American coast, including four deadly hurricanes in October alone (Longshore, 2000; Neely, 2016). St Kitts and Nevis experienced a small storm during August, and escaped the worst of the winds in October, when the great hurricane of 1780, the deadliest hurricane on record, tore through Barbados and caused destruction in other parts of the Lesser Antilles (Hubbard, 2002b; Mulcahy, 2006). In the Great hurricane of 1780, all 100 ships docked in St Kitts were wrecked, with thousands killed on ships and on land (Hubbard, 2002a).

In 1782, the French tried once again to seize St Kitts, and captured the island in February 1782. The island was recognised as British territory in the Treaty of Paris, signed in 1783. Since this time, the island has been associated with the Kingdom of Great Britain (later the UK). St Kitts remained of administrative and economic importance to the British into the next century (Hubbard, 2002b; Zacek, 2010).

In April of 1792, heavy rain caused flooding in Basseterre. Many residents are reported to have lost their lives as the flood carried their belongings and homes out to sea. The English church, Methodist chapel and merchants' cellars were filled with water and mud, ruining large quantities of provisions (Garriott, 1900; Haynes, 1934). An account dated 11th April 1792 describes how the town experienced strong winds and heavy rain, which led to the flood in College Street, the current being 'very rapid' and the water rising higher than the walled fences. The flood toppled fences and walls and brought down a few houses, killing the residents inside. The water carried away several of the town's inhabitants (Day, 1852),

although the exact death toll is unknown. Basseterre was not the only area affected, with properties on Old Road and several estates in St Paul Capisterre parish damaged by floods on the same day. Dieppe Bay in the North of the island was almost completely destroyed, while Sandy Point and the surrounding parish remained the only town to have avoided any damage from the heavy rain and subsequent flooding. Despite the devastation caused, the island recovered from the floods within a year, although respite was short, as by 1793 France and Britain were at war again and there was a call for both St Kitts and Nevis to strengthen defences in preparation for a possible attack from the French (Dyde, 2005).

2.2.5 Droughts of the 1700s

Despite the hurricane and flood hazard on St Kitts and Nevis, periods of drought also posed a threat to the islands, particularly in years of El Niño events. The Leeward Islands existed on agriculture, which made them susceptible to the effects of drought. Short wet seasons followed by long dry seasons, combined with the lack of fresh water available on the islands, could lead to severe droughts which lasted many months. The worst of the droughts in the eighteenth century lasted for four years, from 1718 and 1721. Other droughts occurred in 1726, 1731 and 1736 (Mulcahy, 2006; Zacek, 2010).

2.2.6 Earthquakes of the 1700s

The Reverend William Smith, was resident on the island for five years in the 1730s, experienced at least a dozen earthquakes during his time on Nevis, though does not note any damage (Mulcahy, 2006; Smith, 1745; Zacek, 2010). Smith describes how the residents 'look upon to be caused by these veins of sulphur, brimstone etc. that being over-heated, either blow up on a sudden like a grenade or bomb-shell, at least shake the ground till it gets vent out in the open air, or else burn gradually away, leaving the ground about them so hollow till

it at last drops in'. This quote demonstrates how the settlers of Nevis were aware of a potential volcanic threat, and link the islands earthquakes to the volcanic centres on both St Kitts and Nevis.

2.2.7 Hurricanes and flooding of the 1800s

There appears to be a general lack of documentation of the effects of many of the hurricanes occurring in the 1800s. Several dates and brief descriptions of storms can be found, although little evidence of the effects of these storms exists. Strong hurricanes struck the Leeward Islands, including St Kitts, in 1804, September 1819, and again in 1827.

The 12th August 1835 hurricane hit Antigua, Nevis and St Kitts and was described as being 'destructive' and 'devastating' (Hubbard, 2002b; Smith, 1835). Little detail has been recorded for this hurricane, although it is frequently mentioned as a significant hurricane. Similarly, little is known concerning the hurricane on the 31st August 1871, which passed through the Leeward Islands. The eye of the storm passed directly over St Kitts in the early hours of the morning, with the damage described as being 'quite general' (Garriott, 1900). The 1876 event was described only as a severe storm, which passed the northern end of St Kitts on the 12th September (Garriott, 1900).

On the night of the 11th and 12th January 1880, Basseterre on St Kitts suffered major flooding worse than that of the 1792 floods, as thirty to forty inches of rain fell over the course of 3 hours. The disaster led to the death of almost 240 residents (Dyde, 2005). The flood was reported by many newspapers across the world. The Maitland Mercury and Hunter River General Advertiser, published in Australia on Thursday 1st April 1880, reports on a telegram describing the effects of the flood published first in the New York Times ('The Disastrous Floods at St Kitts', 1880). The flood, reported as having taken place on Sunday 11th January,

occurred after a period of unseasonal high temperatures, followed by a sudden cooling of air temperature. The streams on Mount Misery overflowed their channels and flooded the surrounding land. There was chaos and confusion as the residents tried to evacuate towards the coast, while the water flowed into Basseterre carrying along debris from estates. Sugar fields were destroyed, houses were washed away, and livestock perished in the torrents which swept into the sea.



Figure 2.5 - Map of central Basseterre showing College Street, Greenland Gut (present day South Olives river), the Market Hut and Victoria Road.

The bulk of the water flooded through College Street, Greenland Gut (present day South Olives river), the Market Hut and Victoria Road (Figure 2.5). The flood washed away shops, houses, walls and earth, destroying anything in its path. It also deposited debris from higher

ground, with up to twelve feet of material deposited in places. Relief was provided to the town in the form of emergency food supplies and shelter. £6,000 was spent repairing public buildings, roads, bridges, walls and harbours (Dyde, 2005). While the flood caused great amount of damage in Basseterre, it was a crucial turning point for the town, with the repairs marking the start of a series of major improvements and expansion of the existing structure.

In 1890s, US Meteorological Bureau with the agreement of the St Kitts government, installed a weather monitoring station. This station was put to the test on 7th August 1899 when winds reached 120mph. Four people were killed in St Kitts, which received a telegraph warning in advance. In comparison, Nevis did not receive any warning or data regarding the approaching storm, lost twenty-seven residents (Hubbard, 2002a). The hurricane in 1899 occurred between the 7th and 14th August. The storm swept across the Leeward and onto the Virgin Islands, Porto Rico, the Bahamas and the US (Garriott, 1900). 200 houses were destroyed on St Kitts, and the estates suffered 'considerable damage' (Partagas, 1966).

2.2.8 Droughts and other disasters of the 1800s

Droughts continued to pose a problem for St Kitts and Nevis into the 19th century, with Nevis, the more mountainous of the two, able to obtain fresh water but struggled to distribute it throughout the population (Dyde, 2005). A two year drought, beginning in 1834, proved a complication for emancipation, with famine and protests against apprenticeships leading to unrest on both islands (Hubbard, 2002a, 2002b).

A combination of the hurricane in 1835, the drought of 1836 to 1838 followed by a fire in 1837 devastated Nevis. A fall in sugar prices led workers to leave the island. The earthquake in 1843 followed by the cholera epidemic in 1853-54 only worsened the situation. The cholera

epidemic alone left over 800 people dead on Nevis and 3920 dead on St Kitts (Hubbard, 2002a).

On the 12th January 1880, 'a night of terrific rain in the mountains' caused rain to sweep down College street into Basseterre, drowning 231 residents (Hubbard, 2002a). Twenty-three inches (584mm) of rain is thought to have fallen in four hours of heavy rain during a storm, causing the streams flowing from the mountains to overflow. Many of the residents of Basseterre lived in small, one-storey houses built of light materials, which were quickly washed out to sea in the flood. Many other buildings in the town were damaged and considerable property was lost (Alexander, 1899; 'The Maitland Mercury and Hunter River General Advertiser', 1880). Many people were rescued from their homes in the sea by men in boats (Hubbard, 2002a).

Captain Alexander of the Royal engineers proposed a scheme to prevent a similar event to the 1880 flooding from occurring again. In the 1890s, plans were made to widen streets and line them with masonry walls to channel flood water into the sea. The scheme completed was completed in 1895 at a cost of £7400. Since the installation of such protective measure, effects of flooding events have been significantly less destructive (Hubbard, 2002a).

2.2.9 Earthquakes of the 1800s

Several small earthquakes shook the Leeward Islands during the 19th century, many of these had little impact except to startle the population. Two large earthquakes during the period, one in 1833 and a second in 1843. The 1843 earthquake caused widespread destruction throughout the Leeward Islands and it thought to be associated with minor volcanic activity on St Kitts.

The 1833 earthquake occurred on the evening of February 8th 1833. This was followed by several aftershocks over the next few months, leaving many afraid to stay in their homes. Large waves were observed on the coast and some residents boarded ships docked in the harbour for fear that the low-lying coastal areas would be inundated. People occupied the churches and prayed for their safety as earthquakes continued to occur (*The Christian remembrancer; or, The Churchman's Biblical, ecclesiastical & literary miscellany*, 1844). A large aftershock followed at 8pm on the 8th march, and was said to have 'continued with little intermission' for eight days. Residents were kept in a state of terror, stores were closed, people tried to board ships hoping they would be safer offshore. Several old chimneys and walls were thrown down. The damaged building listed on St Kitts included the church, the Wesleyan Chapel, the Jail, the custom house, the reading room, the Tavern, private dwelling houses. Two estates recorded considerable losses, Spring Lodge Otley's (Cayon Village) and Olivees, while the American Railroad Journal (Minor, 1833) stated that other estates were 'not accounted for'. A 'considerable quantity of bottled liquor' destroyed by first shock, thought to be worth some hundred pounds sterling.

According to 'The Christian remembrancer; or, The Churchman's Biblical, ecclesiastical & literary miscellany', published in 1844, earthquakes shook St Kitts from 8th February through to the 27th March 1833. The 1833 earthquake is mentioned in reports of the 1843 earthquake, having struck almost exactly 10 years prior, and was said to have been much smaller than the 1843 event, however still proved frightening for the islands' residents.

2.2.10 Earthquake of 1843

The earthquake of 1843 struck the Lesser Antilles at approximately 10:30 on Wednesday 8th February (Robson, 1964), and is thought to have lasted around one and a half minutes. It was

thought to be similar in intensity to the 1690 earthquake, which was up to IX in St. Kitts and Nevis (Hubbard, 2002a). This earthquake caused widespread devastation across the islands, including both St Kitts and Nevis, which suffered significant damage. Volcanic activity has been considered to have been associated with this earthquake, described as a plume of white smoke rising from the mountain. Despite the detailed records which exist for this earthquake, there are only two records of this mystery 'white smoke' rising from Mt Liamuiga.

2.2.10.1 Possible volcanic activity associated with the 1843 earthquake

Capadose (1845), described the activity in January 1843 in his writing of a hike to the crater of Mt Liamuiga in 1845. He states '...a spiral cloud of white smoke was seen to ascend, and the sulphureous (sic) spring is said to have bubbled up and overspread the space around. I was also told that the appearance of the crater is changed and the difficulties of the descent much increased.' This account is frequently quoted in published literature despite being a secondary source, with little to no evidence to support these claims (Dobson, 1853).

A second account, claiming to be a published 'eye-witness account', appears to be the only primary source recounting the volcanic activity. The anonymous account (Anonymous, 1690) mentions the observations amongst those of earthquake damage; 'From Mount Misery, the highest point on the island, a long spiral cloud of white smoke was seen to ascend during the tome of the earthquake; and the sulphurous spring, situated in its centre, is said to have bubbled over.'

No other primary or credible secondary reports of volcanic activity have been found in previous studies, nor in this investigation into historical reports. It is likely that the 'eruption' that has been recorded is either heightened fumarolic activity or a small phreatic eruption triggered by the earthquake, or a misinterpretation of dust rising from landslides and other

damage in and around the crater. Based on the descriptions of various landslides around both St Kitts and Nevis, and with the comment written by Capadose (1843) regarding the reported changes to the crater walls, it is reasonable to conclude that the cause of the eruption reports is the observation of dust rising from earthquake damage, possibly a landslide within the crater itself.

2.2.10.2 Effects of the 1843 earthquake, including damage and loss of life on St Kitts and Nevis

Many of the Leeward Islands were badly damaged by the 1843 earthquake, St Kitts and Nevis included. The Governor of Barbados, in letter to the Treasury, informed of a plan to send fifteen thousand dollars to the Leeward Islands after the region suffered 'calamitous' damage. The windward islands on the other hand, felt the shaking intensely, but did not suffer any damage (Treasury, 1843).

An anonymous eyewitness account titled 'A narrative of the late awful and calamitous earthquake in the West India islands of Antigua, Montserrat, Nevis, St Christopher, Guadeloupe &c. &c. on February 8th 1843. Written by an eye-witness' gives a graphic insight into the distressing scenes witnessed on St Kitts. The morning of the earthquake was described as being the usual sunny, blue sky start, with no suggestion of the impending disaster. The arrival of the earthquake was marked with a low rumbling sound, followed soon after by intense shaking. The stone buildings 'crashed and crushed' while the wooden buildings 'waved to and fro'. The author suggests that the earthquake last for three to four minutes. All residents, regardless of their social distinction, sought safety in the open streets and squares, and collectively prayed for their lives. The damage was described as 'immense'. The majority of damage was to stone buildings. St George's Parish Church collapsed, and the gaol was destroyed (Anonymous, 1843; Colonial Office, 1843), both of which were later

rebuilt in 1856 and 1844 respectively. The 'Wall House' and the reading-rooms collapsed and the sugar production facilities were completely destroyed, while the West Indian Bank, Moravian Church and the Wesleyan chapel all suffered damage. Legislation was passed to demolish any damaged buildings which posed an ongoing hazard. This meant that many of the islands stone buildings were rebuilt following the 1843 earthquake (Anonymous, 1843; Hubbard, 2002a).

There are thought to have been a number of deaths as a result of this earthquake, although the exact death toll for St Kitts is unknown. One despatch from Sir Charles A. Fitz Roy to Lord Stanley states that the loss of life was 'miraculously small' for all of the islands (House of Commons Parliamentary Papers, 1843). Three women are known to have died when rocks fell from a ledge above the river where they were washing clothes and crushed them (Anonymous, 1843; The Times, 1843).

On Nevis, the courthouse, which contained the secretary's office, was completely razed to the ground. The bath house was mostly collapsed. The streets were said to resemble ruins, with nearly every stone building either destroyed, or suffered severe damage (Anonymous, 1843). Cliffs are said to have fallen, and cracks two to three inches wide opened up in the ground. A group passing through 'The Narrows' between St Kitts and Nevis observed 'great agitation' of the sea and feared their boat being swamped (Anonymous, 1843).

A smaller earthquake occurred at 20:00 on Friday 14th April 1843. The St Christopher Advertiser (printed 18/4/1843) reported that many people were frightened and ran outdoors (Robson, 1964), likely reminded of the disastrous effect of the earthquake earlier in the year.

2.2.11 Hurricanes of the 1900s

Only seven hurricanes of note struck St Kitts and Nevis in the 20th Century, with a handful of these causing any significant damage. The first of these three hit both islands on the 28th and 29th August 1924. Many houses were affected, from mud filling cellars to complete destruction of property. Damage to the water transport system around the island led to a shortage in supply, eased only by the Sugar factory connecting its own supply to Basseterre's main supply. Recovery efforts were boosted by the employment of labourers to clear the streets of mud and debris, and enabled Basseterre's water supply to be re-established in under a week ('Hurricane damage | National Archives St Kitts & Nevis', n.d.). St Kitts and Nevis escaped the worst of the damage, with neighbouring Montserrat suffering much greater harm and loss of life. As St Kitts, Nevis and Montserrat were all under the same governance in 1924, with no significant differences in development, the distribution of damage is likely due to the location of the worst storm conditions as the Hurricane passed over the Leeward Islands.

St Kitts and Nevis were just two of the many areas to feel the effects of 1928 'Okeechobee' or the 'San Felipe Segundo' hurricane, thought to be one of the deadliest hurricanes to have struck the North Atlantic Basin (Rappaport and Fernandez-Partagas, 1995). The hurricane began on the 6th September off the West African coast, and by 12th September, reached the Leeward Islands as a Category 4 hurricane (Schwartz, 2015). Guadeloupe received a direct hit from the storm, recording the total fatalities at 1,200, the highest death rate in the Caribbean and the Bahamas. St Kitts and Nevis, along with the other Leeward Islands, escaped the worst of the damage, with 9 deaths reported on St Kitts, six from the collapse of a schoolhouse, and 13 deaths occurred on Nevis. A small number of buildings on both St Kitts and Nevis collapsed, although the majority of these were built on wooden foundations. This may have had a

positive effect on the housing quality following the hurricane, as many of these houses were rebuilt with stronger foundations. The hurricane continued to travel up towards the Bahamas, making landfall in Florida on 17th September. By the 18th September 1928, the total damage stood at over \$100 million, with over 4,100 fatalities (Neely, 2014).

Towards the end of the 20th century, St Kitts and Nevis suffered the impact of several hurricanes in quick succession. In September 1989, Hurricane Hugo, caused tremendous damage to St Kitts, amounting to a total US\$46 million, and a single life lost (Case and Mayfield, 1990). Hurricane Luis, on 5th September 1995, impacted both St Kitts and Nevis, causing damage in excess of US\$72,500,000 (Lawrence, 1996). No lives were lost on St Kitts or Nevis during Hurricane Luis.

In the hurricane season of 1998, Hurricane George caused great damage as it passed through the Caribbean and Southern US. On 21st September, George reached St Kitts and Nevis as a Category 3 Hurricane. The hurricane caused over US\$400 million worth of damage to the islands. An address from the Prime Minister, Hon. Dr. Denzil Douglas, on 22nd September declared a state of emergency and summarised the initial damage assessment. The storm caused damage or complete destruction to critical infrastructure, hospitals, schools, utilities, 85% of housing and agricultural land ('St. Kitts declared disaster area with damage over 1 Billion EC dollars - Saint Kitts and Nevis | ReliefWeb', 1998).

A hurricane watch, and later a hurricane warning, was issued for St Kitts and Nevis during the approach of Hurricane Jose in October 1999. The worst of the Storm arrived on the 20th October (Pasch, 1999). The estimated damage to the island exceeded US\$ 3 million. On 18th November 1999, Hurricane Lenny caused severe damage to the Nevis coastline. The Four Seasons Hotel and the deep-water harbours sustained significant damage. Total damages

from Hurricane Lenny amounted to nearly USD \$42 million after the islands saw flooding along the coast and damage to infrastructure ('Post Impact Report #1 - Hurricane Lenny - Anguilla | ReliefWeb', 1999).

2.2.12 Earthquake of the 1900s

A swarm of earthquakes were felt on St Kitts and Nevis in December 1950 to January 1951. The first earthquake occurred on the 27th December, at 18.15 local time. The activity continued into January with minor renewals of activity in March and May 1951. These swarms are thought to be a common preliminary symptom of eruptions in the Lesser Antilles. The colonial office invited Dr P. L. Willmore to monitor the situation on the islands in early January 1951. During the first 30 days of the crisis, over 150 earthquakes were recorded, with the two strongest shocks occurring on the 29th and 31st December. The event on the 29th December was felt most strongly on Nevis, damaging stone buildings. The focus was thought to be offshore, to the west or south-west of Nevis as the damage done to structures was concentrated on the westward side of the island. This earthquake was also felt in Anguilla.

The earthquakes occurring at the end of end of March 1951 are thought have a focus 2-3km from Nevis Peak. Such a small number occurring close Nevis Peak, combined with a lack of earthquake activity from Mt Liamuiga on St Kitts and no noticeable increase in any other volcanic activity, suggested that the swarm was not an emergency. A lack of activity in the months following May 1951 meant that the seismometers installed on the island to monitor the situation were left to fall into disrepair (Willmore, 1952).

On the 8th October 1974, at around 5:55am, a large earthquake shook the Lesser Antilles. The earthquake had a maximum Mercalli intensity of VIII and M_s ranging between 7.1 and 7.6 (Feuillet *et al.*, 2011). The earthquake caused some damage on St Kitts, although the most

widely noted loss was the significant damage done to St George's Parish Church on St Kitts. Nevis escaped comparatively unscathed (Geological Survey, 1974). No deaths were recorded on either island. Another large earthquake struck St Kitts and Nevis on 16th March 1985 (Feuillet *et al.*, 2011). Slight damage was seen on St Kitts and Nevis, with nothing of any significance reported.

2.3 Discussion and concluding points

2.3.1 General impact of disasters

Natural disasters have affected the development of the islands from the first European settlers in the early 1600s. It impeded the speed at which the colony on St Kitts was established and it is clear that the settlements on both St Kitts and Nevis have both been shaped by the disasters they have faced through history. One of the most prominent examples of this was in the early 18th century, when St Kitts 'overtook' Nevis in economic importance. Towards the late 18th century, Nevis suffered a series of bad hurricane seasons, making it the worst period for hurricanes in the island's recorded history (Hubbard, 2002a). Nevis never made up the financial losses of this period, and lost the prominent colonial status it had earned over the previous two centuries.

2.3.2 Volcanic hazard

While it is likely that no eruption occurred at Mt Liamuiga, or anywhere else on the Island of St Kitts during 1692, and that the single record of the eruption has misidentified the activity for that of La Soufriere on Guadeloupe. However, it is possible that a small phreatic eruption associated with the earthquake did occur in 1843. No historical eruptions have taken place on Nevis.

The level of volcanic activity at St Kitts and Nevis is similar to that of neighbouring islands Saba and St Eustatius, located to the northwest of St Kitts. Saba is thought to have had one eruption in 1640, with no other recorded historic activity, while St Eustatius has not exhibited any activity in written history. Similarly the volcanic earthquake swarms observed at St Kitts and Nevis in the 20th century, Saba experienced a swarm in 1992, although no activity was

observed at the surface (Defant *et al.*, 2001). In contrast, Monserrat, located to the southeast of Nevis, experienced several periods of volcanic unrest, with eruptions in 1995-2003, 2004 and 2005-2013 (Barclay *et al.*, 2022; Hincks *et al.*, 2005). The islands of Guadeloupe, Martinique, St. Vincent, Montserrat and Dominica have also experienced more recent volcanic activity, with eruptions occurring since 1900 (Barclay *et al.*, 2022; Barclay, Wilkinson, *et al.*, 2019; Lindsay and Robertson, 2018).

2.3.3 Multi-hazard vulnerability

For hurricanes and large earthquakes, it is difficult to identify specific regions as suffering more than others. In these cases, phrases such as ‘all of the houses fell down’ or ‘the streets were full of ruins’; these generic descriptions may imply that damage was island-wide and no single specific area was hit harder than any other. Floods appear to have a much more localised effect. While many towns suffered during the 1792 flooding, Basseterre and Old Road Town seem to have suffered more often than others. During the earthquake swarms in the 1950s, Nevis experienced significantly more damage to houses on the western side of the island, suggesting that these were localised earthquakes with a focus off the western coast of the island.

Basseterre and Old Road Town appear to be the most frequently impacted towns on St Kitts, while Charlestown is most frequently mentioned in damaged reports for Nevis. The locations of settlements do not appear to have been influenced by their vulnerability to disasters, more so by colonial interests, for example the location of plantations, harbours, defences and the French/English borders. Most towns have adapted to deal with the impact of certain hazards. Basseterre is a good example of this, with the measures introduced to reduce the impacts of

flooding in the 1890s. The exception to this trend is Jamestown, the first settlement on Nevis, which was abandoned in 1690 after it suffered greatly in the 1690 earthquake.

The downfall of Jamestown and the rise of Charlestown as Nevis' primary town is widely thought to have been caused by a tsunami during the 1690 earthquake, which left the town underwater, uninhabitable. An alternative theory to Jamestown's disappearance is proposed by Hubbard (2002), who suggests that Jamestown was badly damaged during the 1690 earthquake causing the residents to migrate from the town until it become non-existent. This would explain the location of Jamestown remaining on maps of Nevis for many years after the earthquake.

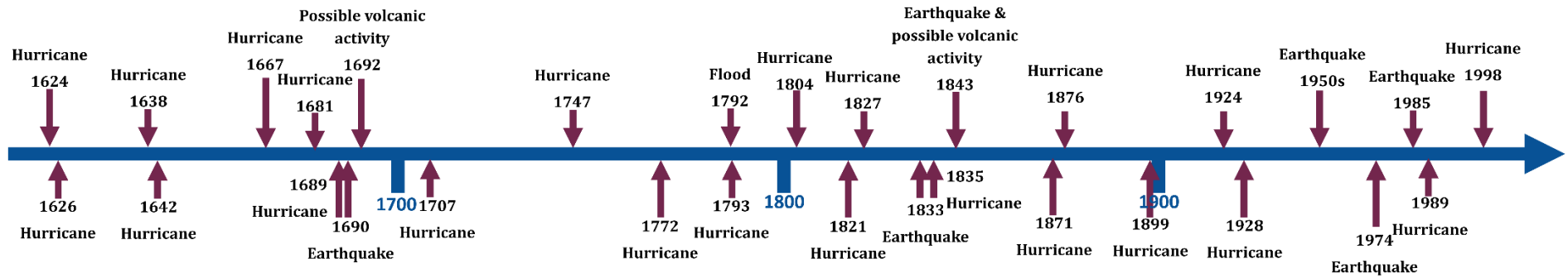


Figure 2.6 – Timeline of geological and meteorological disaster events that have occurred on St Kitts and Nevis since the arrival of the first settlers in the 17th Century.

The building material of a structure has much more impact on whether it will survive than its geographical location on the islands. In a hurricane, the more primitive wooden structures destroyed, while the stone building often remained standing with comparatively little damage. This also applies to floods, where wooden structures are quickly washed away while stone buildings are flooded, but withstand the flow of water and remain standing when flood waters recede. In stark comparison, the opposite is observed during an earthquake. The stone structures crack and collapse while the wooden structures sway with the shaking and remain standing when the shaking ceases.

Location may still have a significant impact on settlements depending on the infrastructure connection with the rest of the island such as, water, electricity, internet and phone, and the road network. The Island Main Road is a single circular road that encircles the island, connecting the major settlements. Based on historic records of landslides, flooding and tsunamis, this road is a vulnerable part of the island's infrastructure, which could easily result in cutting off populated areas once compromised. Nevis also has a similar road network, with its own Island Main Road connecting the island's settlements. This road is likely to be comparably vulnerable to damage. Landslides, flooding, tsunamis and volcanic hazards such as PDCs, rockfalls and lahars all pose a risk to the road network on both St Kitts and Nevis. The water and power distribution systems on St Kitts are as equally vulnerable to the aforementioned hazards, as they generally follow the layout of the road infrastructure, forming a circular network around the island (Stødle *et al.*, 2021).

The move from agriculture as the primary industry to a more diversified economy funded by tourism, offshore banking and light manufacturing suggests a faster recovery from disaster events (Baker *et al.*, 2019). It is faster to repair damaged hotels and factories, and inform the

international community that the country is open for business again, than to completely re-establish lost agricultural land and replenish crops (Sword-Daniels *et al.*, 2014). This may only apply to isolated events, for example, the hurricanes in the latter half of the 1990s reversed a decade of economic growth. This would suggest that *sustained* volcanic activity, depending its nature, may have more of an impact on tourism, manufacturing and export infrastructure and therefore a longer recovery. An example of this scenario was observed following the onset of volcanic activity Soufriere Hills volcano in 1995, on the neighbouring island of Montserrat (Sword-Daniels *et al.*, 2014).

2.3.4 Preparedness for future disasters

While the current population on St Kitts and Nevis has experienced hurricanes, many have never experienced a destructive earthquake, volcanic eruption or tsunami. This lack of experience with disasters is likely to create an underprepared population, with a lack of motivation to prepare for such hazards (Simpson and Shepherd, 2001). The closest volcanic eruption to St Kitts and Nevis took place on neighbouring Montserrat in the 1990s and 2000s (Hincks *et al.*, 2005). The catastrophic impact of the eruptions on Montserrat should serve as a warning to St Kitts and Nevis, although there is little evidence to suggest that any warning has been heeded (Simpson and Shepherd, 2001).

The vulnerability of St Kitts and Nevis can be compared with Montserrat, and with other volcanically active islands such as St Vincent. St Kitt's capital, Basseterre, is at the opposite end of the island to the volcano, and not thought to be at risk from PDCs, although it may be vulnerable to thick ashfall (Robertson, R., 2005). This is more similar to Kingstown on St Vincent rather than Plymouth on Montserrat, which was vulnerable to PDCs (Robertson, R. E. A. *et al.*, 2000; Sword-Daniels *et al.*, 2014). This is likely to mean that governance and

coordination can continue in a crisis. The capital of Nevis, Charlestown, lies close to the crater of Nevis Peak. In the event of a PDC flowing E-SE of the crater, Charlestown may be at risk of a similar fate to Plymouth on Montserrat. Where administration is shared between St Kitts and Nevis, governance may be possible from the opposite island. This may also slow down response times in resources need to be transported between islands.

If the ring roads on St Kitts and Nevis were to be obstructed in two locations, residents may find themselves cut off from help, and marine evacuations may be necessary. While this road is a key weakness in the islands' infrastructure, it provides an escape in two directions, where many towns and villages on Montserrat and on St Vincent could only be evacuated/reached from one direction (Barclay *et al.*, 2019; Graham *et al.*, 2024). Once these roads were cut off, the only options were air or marine evacuation.

Similar to Montserrat, the topography and larger, elongated shape of St Kitts means the opposite end of the island to the volcano is not at risk from PDCs, although may still experience heavy ash fall. In contrast, the topography, circular shape, and smaller size of Nevis leaves the entire island vulnerable to a number of volcanic hazards during an eruption. Whilst residents of northern St Kitts may be evacuated to the south of the island, it is likely that the entire population of Nevis will need to be evacuated if a large eruption were to occur there.

Lessons can be learned from St Kitts and Nevis' history of disaster events. While the settlements on the islands still exist despite geological and meteorological disasters, economic development has been hindered by such events. In the same way that Montserrat's economy all but collapsed after volcanic activity began in 1995 (Barclay *et al.*, 2022; Barclay, Few, *et al.*, 2019; Sword-Daniels *et al.*, 2014), St Kitts and Nevis are likely to be vulnerable to severe economic disruption. Another vulnerability is that St Kitts and Nevis have no historical

eruptions to learn from. While members of the population may have observed other eruptions in the Caribbean, there is no living memory of an eruption, likely leading to complacency over the level of volcanic hazard on the islands. Eruptions on Montserrat seem to have prompted a review of the island's volcanic hazard assessments in the early 2000s, however, these do not appear to have been revised over the last 20 years (Robertson, 2005; Simpson, 2005).

Cascading risk is a problem on St Kitts and Nevis. History shows that flooding is a frequent hazard during heavy rains. If this flooding were to occur during an eruption, lahars could potentially be produced. An eruption during hurricane season could leave the islands particularly vulnerable. Any adverse weather could also prevent aid arriving by sea or air, and may hamper any evacuation attempts.

2.3.5 Acknowledgement of historic bias of sources

It would be wrong not to highlight the possible bias in reporting of these disaster events. Particularly during the early years of St Kitts and Nevis' history, much of the reporting of damage and death comes from European colonists on the islands, with little to no records from the enslaved population. It is also important to mention that the islands were occupied before the arrival of the European colonists. The islands were first settled as early as 3000 years ago, and have changed hand by conflict and invasion on several occasions even before European arrivals. The early settlements built by the English and French were based on the existing structures built by the Island Caribs who occupied the islands at the time, but were later massacred by the Europeans (Hubbard, 2002a, 2002b).

3. Fieldwork

The aim of this chapter is to explore the nature of the youngest deposits on St. Kitts and Nevis, thought to be deposited from the most recent eruptions. These youngest deposits can give an insight into the typical styles of eruption on St Kitts and Nevis, and allow better understanding of the likely characteristics of future eruptions.

3.1 Aims of this field study

The aim of the fieldwork was to document and interpret the youngest volcanic products on St Kitts and Nevis and to undertake detailed sub-sampling of key sequences for further analysis. The collection of this data allows an interpretation of eruption styles typical of Mt Liamuiga (previously known as Mt Misery) and Nevis Peak to be made and used to infer the potential style of future eruptions.

3.2 Introduction to the stratigraphy of St Kitts and Nevis

3.2.1 St Kitts

The island can be thought of as four distinct geomorphological units; the Salt Pond Peninsula, South East Range, Middle Range, and Mt Liamuiga (Baker, 1969). These units are shown in Figure 3.1. The oldest deposits on St. Kitts are found in the South East of the islands, and the geology becomes progressively younger towards the North West.

The Salt Pond Peninsula is the oldest part of the island (Baker, 1985). The peninsula is formed of a chain of at least nine eroded Pelean domes thought to have been active approximately 2.3 million years ago. Canada Hills and Conaree Hills are the remnants of older volcanic centres. The South East Range comprises of a deeply eroded, extinct stratovolcano rising to

900m (Baker, 1969). Four peaks aligned NW-SE and two parasitic domes are located on the flanks, Ottley's Dome and Monkey Hill Dome. The geology of the South East Range is composed of poorly exposed lava flows and volcanoclastic deposits. The predominant feature of the Middle Range is the poorly exposed, jungle covered stratovolcano with a small crater lake at the summit. The Middle Range is geomorphologically distinct to the South East Range, but is partly overlapped by Mt Liamuiga to the North.

Mt Liamuiga is the youngest and only active volcanic centre on the island. Mt Liamuiga is a basaltic to andesitic stratovolcano with an open crater. The crater walls comprise layers of lava flows and coarse pyroclastic breccia (Baker, 1969). The highest point of Mt Liamuiga is a remnant of a dome (Baker, 1985). The volcano has several parasitic domes; two on the upper western flank and one on the lower southwestern flank (known as Brimstone Hill). The lower flanks of the volcano are covered by pyroclastic material > 40m thick, known as the Mansion Series, which blankets most of the northern end of the island (Baker, 1968a; Baker and Holland, 1973).

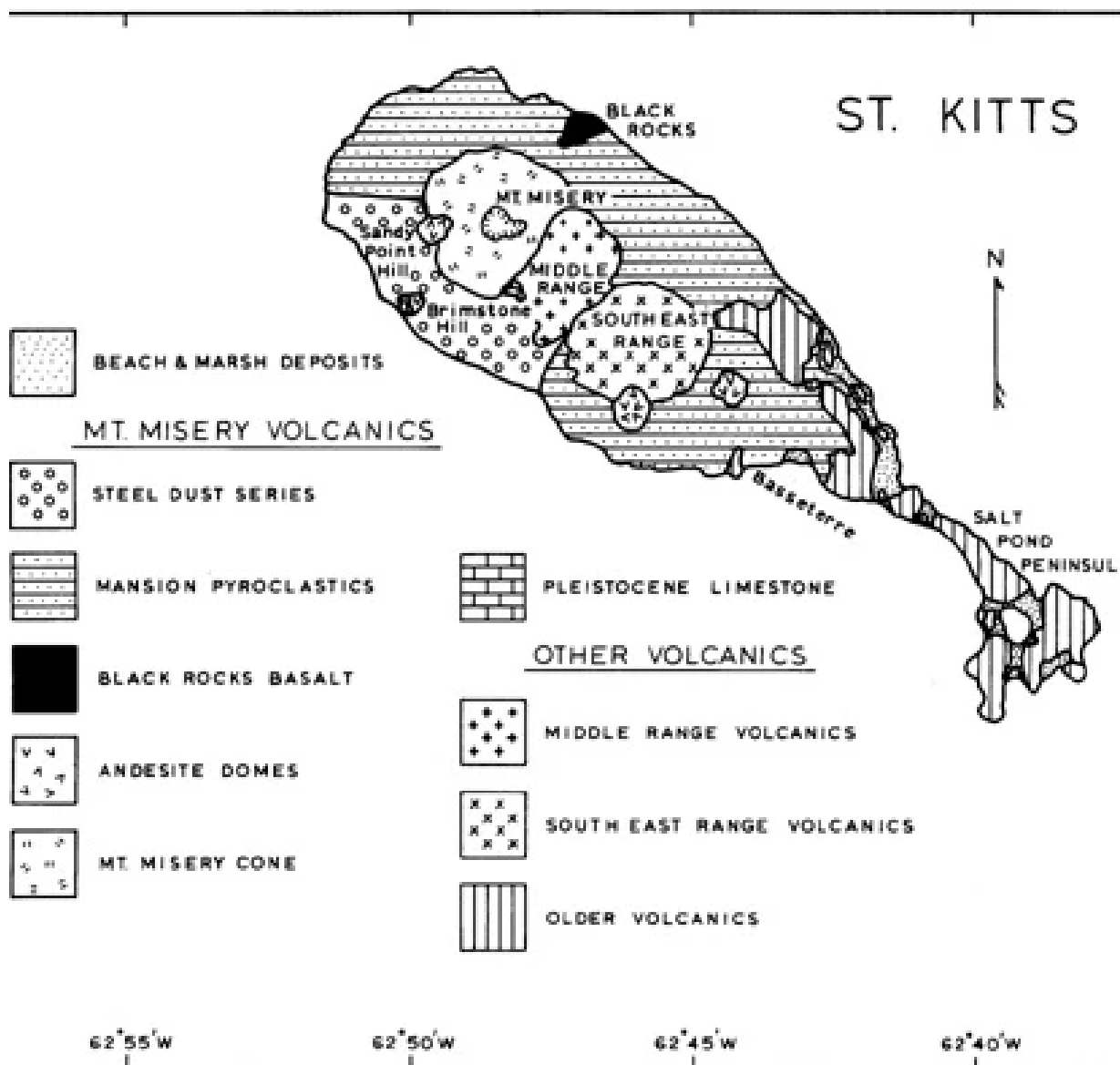


Figure 3.1 - Geological map of St. Kitts from Fink (1975). The youngest, northern extent of the island is shown, including the deposits associated with Mt Liamuiga (Mt Misery).

The Mansion series represents the last major series of eruptions from Mt Liamuiga, and consists of basaltic, basaltic-andesite and andesitic pyroclastic products, with a few interbedded lava flows. The type section for the sequence (Figure 3.2) was described by Baker (1969) in sea cliffs below Mansion village, where the series takes its name from.

Four main zones (or Units) of the Mansion Series were originally recognised: The Pumice Zone, the Upper Green Lapilli Zone, the Cinder Zone and the Lower Green Lapilli Zone. The

Lower Green Lapilli Zone and Upper Green Lapilli Zone are composed of unconsolidated lapilli with a greenish tinge. The Cinder Zone is formed of basaltic cinders, ranging in size from coarse ash to lapilli. Graded bedding is observed in these beds and reddened horizons provide evidence for significant time gaps between eruptions. The Pumice Zone is composed of three beds of white pumice separated by beds of ash and dust containing pumice fragments. Carbonised wood is present in some of these layers (Baker, 1969). These four main zones were later revised into six phases, based on the Baker and Holland (1973) study; Upper Pumice, pyroclastic flows, Lower Pumice, Upper Green Lapilli, Black Cinder and Lower Green Lapilli. This assigned a unit to the PDC deposits observed on the island, and further divided the lapilli and pumice deposits based on geochemical variations (Baker and Holland, 1973; Roobol *et al.*, 1987).

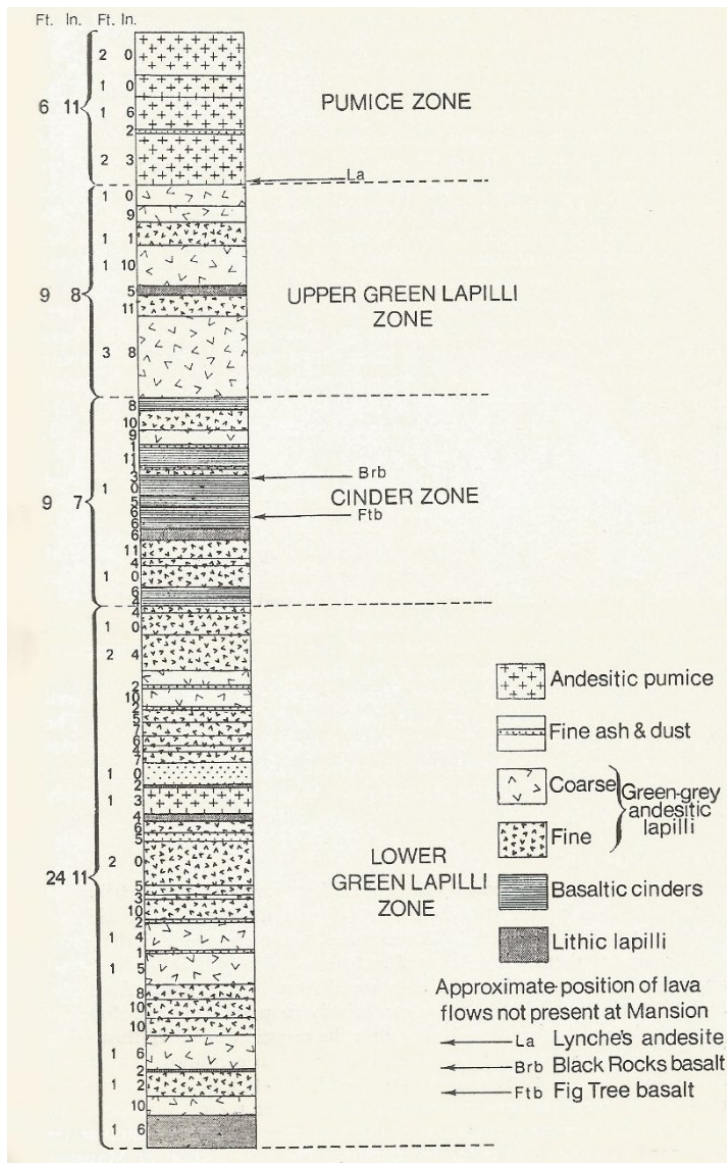


Figure 3.2 - The Mansion Series original type section in the cliffs below Mansion Village, from Baker (1969).

One of the most recent deposits on St. Kitts is the Steel Dust Series, a stratified series ash layers found on the lower western slopes of Mt Liamuiga. A bed of steel-coloured ash within the series gives the deposit its name. The Steel Dust Series is formed from thin beds interpreted as pyroclastic surge deposits and ash fall (Baker, 1969) (Figure 3.3). The observation of deposits exclusively on the western flanks of the volcano suggests that the pyroclastic surge travelled over the lowest part of the crater rim and down the western flanks of the volcano (Baker, 1969, 1985). While earlier publications (Baker, 1969; Roobol *et al.*,

1981) place the Steel Dust Series at the very top of Mt Liamuiga's stratigraphy, Baker (1985) suggests that it may instead lie within the uppermost beds (Pumice Zone shown on Figure 3.2) of the Mansion Series.

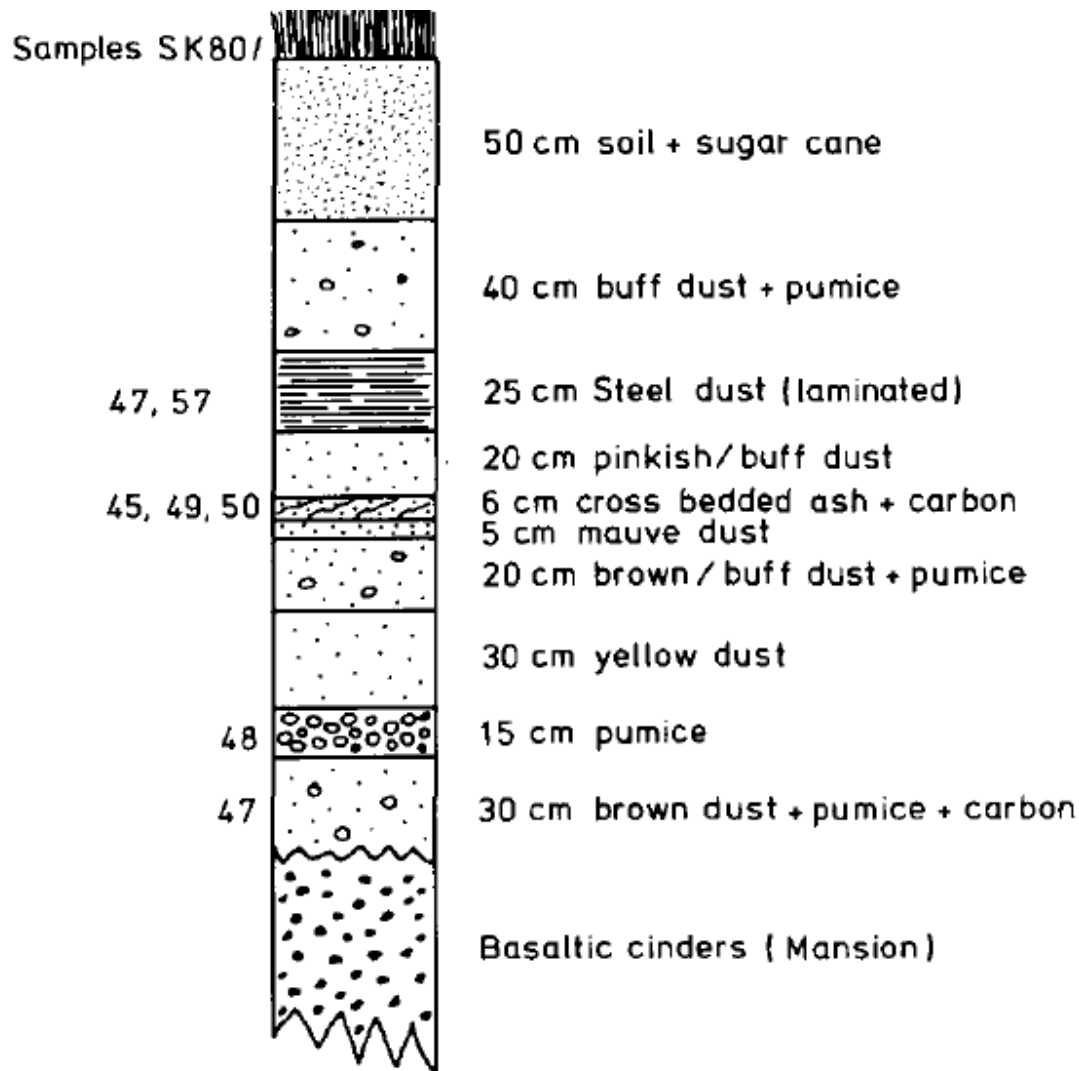


Figure 3.3 - Composite section through the Steel Dust Series, location: Bourke's Estate, from Baker (1985).

Radiocarbon dates have been acquired from charcoal preserved in a number of PDC deposits (Baker, 1985; Harkness *et al.*, 1994; Roobol *et al.*, 1981; Roobol, 1985). The summary Table 3.1 outlines the key dates given for events related to the mansion series.

Table 3.1 - Summary of the ^{14}C dates from the Mansion series, for Mt. Liamuiga, St Kitts. References: 1) Baker (1969) 2) Baker (1985) 3) Roobol et al. (1981) 4) Harkness et al. (1994). (adapted from Lindsay et al., 2005).

Description	Locality	Ages, years B.P.	Reference
Steel Dust Series	Bourke's Estate Mansion	1620±50	2,4
Pyroclastic flow deposit	Upper Lamberts	1710±80	2,4
Andesite pumice surge deposit	Mansion	1750±90	3,4
Dense andesite pyroclastic flow deposit	Newton Ground	1817±38	4
Mixed Magma surge deposit	East side of Sandy Bay	1840±55	4
Mixed magma pyroclastic flow deposit	Coast below Brothersons	1852±27	4
Pyroclastic flow deposit	Godwin Estate	2030±40	2
Pyroclastic flow deposit	Brothersons Estate	2038±21	4
Pyroclastic flow deposit	Dieppe Bay – Hacket Point	2060±40	2
Fine ash and carbon deposit	Church Gut, Lamberts Estate	2070±50	2,4
Dense andesite pyroclastic flow deposit	Crantouns Gut	2280±135	3
Basaltic andesite pyroclastic flow deposit	Headland SE of Sandy Bay	2340±80	3
Dense andesite pyroclastic flow deposit	Masshouse Bay	3060±200	
Ash and carbon deposit	Christchurch	3658±94	1,4
Pyroclastic flow deposit	Charles Fort	4270±170	2,4
Cinder Unit	North of Mt. Pleasant Estate	>41730	3,4
Cinder Unit		>41140	3
Lower Green Lapilli Unit	Mansion	>41420	3,4

3.2.2 Nevis

There are seven volcanic centres on Nevis (oldest to youngest): Round Hill, Cades Bay, Hurricane Hill, Saddle Hill, Butlers Mountain, Red Cliff and Nevis Peak. These range in age from 4.43 ± 0.17 Ma (Round Hill) to 0.98 ± 0.10 Ma (Nevis Peak) (Hutton and Nockolds, 1978;

Simpson, 2005). These centres are shown in Figure 3.4. There are two areas of geothermal activity, Cades Bay, and Farm Estate Soufriere. At Farm Estate, vents which emit steam and H₂S are active at several points, and deposit sulphur and magnetite (Hutton and Nockolds, 1978). The majority of the surface geology observed on Nevis originates from Nevis Peak Volcano, although little is understood about the stratigraphy of these youngest deposits (Hutton and Nockolds, 1978), making correlation of units on Nevis difficult. Nevis Peak is the youngest volcanic centre and is the only centre considered to have the potential to erupt in the future (Simpson, 2005).

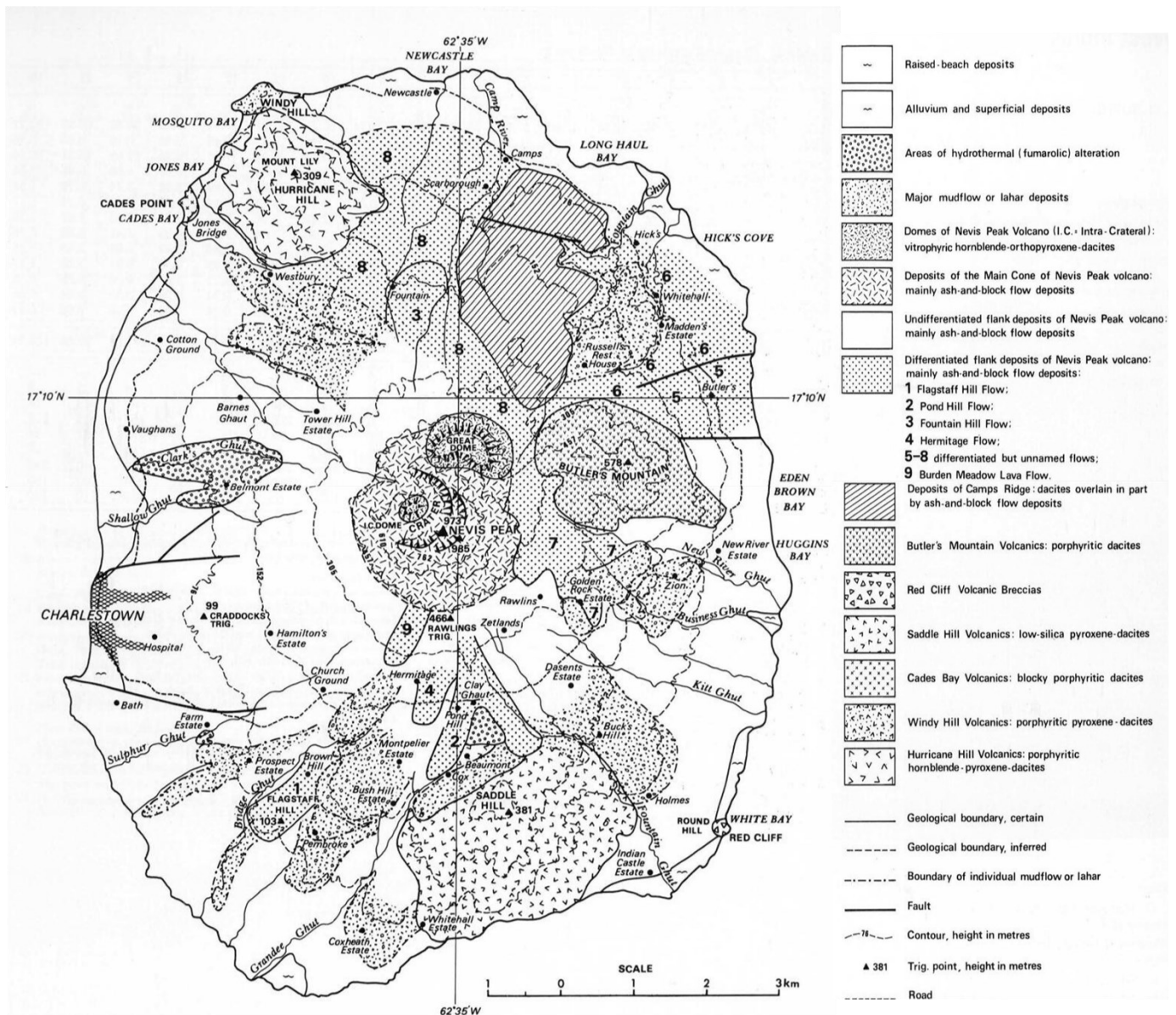


Figure 3.4 - Geological map of Nevis from Hutton (1978) showing the youngest centre on Nevis – Nevis Peak Volcano, the older centres and the identifiable flow deposits.

The majority of the island is made up of upper to lower Pleistocene volcanic rocks. The volcanic deposits on Nevis have a basaltic to dacitic composition. The dominating rock type is block and ash flow deposits, thought to have originated from Nevis Peak. These flows have partly destroyed previous eruptive centres. Nevis Peak consists of a main cone with two associated domes, which lie above the remains of an earlier volcanic centre (Hutton and Nockolds, 1978).

The two domes, one on the main crater floor and the other on the northern outer slopes of the main dome, are of relatively recent origin. These are composed of vitrophyric hornblende orthopyroxene dacites. Hutton and Nockolds (1978) approximated that one third of the surface of Nevis is covered by block and ash flow deposits from the main cone, and from the older volcanic centre located beneath it. The older volcanic centres are enveloped by these deposits. The flows are not easily differentiated into individual flow units in the field, or by petrographic study (Hutton and Nockolds, 1978).

Lava flows from lateral vents or fissures on the lower slopes of Nevis peak have been identified (Simpson, 2005). These consist of glassy dacites, differing from the block and ash flow deposits. Xenoliths are found throughout the primary rock type on Nevis, with varying frequency (Hutton and Nockolds, 1978).

3.3 Methodology

A week of fieldwork was undertaken on the islands of St. Kitts and Nevis in November 2019. The locations were selected based on searches of the literature, alongside consideration of the present day exposure and accessibility. Studied exposures were graphically logged with the accessible units measured, and the more inaccessible unit thicknesses estimated. Unit thicknesses, lithology and interpreted deposit types were recorded, with field sketches and photographs taken where appropriate. Samples were collected where they were thought to be representative of their respective deposit, or due to exhibiting notable features. Descriptions of other relevant geomorphological or hazard related observations, such as the presence of charcoal and the present day topography, were also noted.

The layers of deposits identified were categorised into 4 different deposit types, based on field observations and interpretations; PDCs, fallout, volcanoclastics, and the Steel Dust series. This classification system allowed for correlation and comparison between like deposits in later analysis. The PDCs were identified as deposits that were constrained by topography, confined to valleys and/or thinning out on the sides of valleys. Fallout was classified as well sorted air-fall deposits that evenly blanket topography, having consistent thicknesses. Volcanoclastics were grouped based on evidence for secondary reworking of volcanic material, mostly from water. The Steel Dust unit, a group of variably coloured, layered deposits mentioned frequently in literature (Baker, 1969, 1985; Roobol *et al.*, 1981), was intentionally sought out and studied, and so this unit has been described under its own category.

3.4 St. Kitts

3.4.1 Summary of Locations

Twelve locations on St. Kitts were studied during this campaign (Figure 3.5).

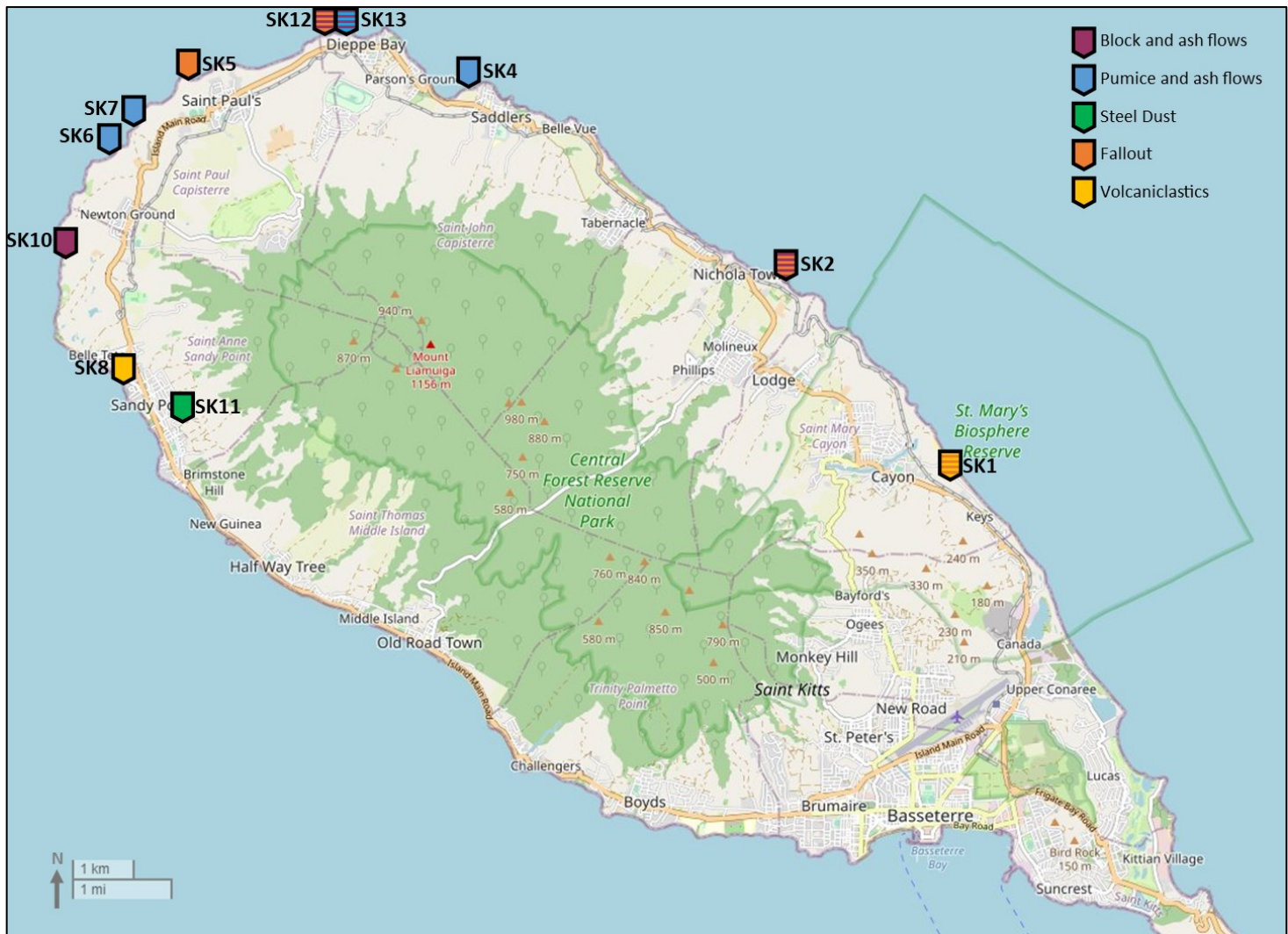


Figure 3.5 - Map of Field locations on St. Kitts

3.4.1.1 Block and ash flows

Block and ash flows were observed in several coastal exposures surrounding the flanks on Mt Liamuiga at locations SK2, SK10, SK12, and SK13 (Figures 3.6 - 3.9). They were poorly sorted and composed of blocks and boulders, in an ash matrix. Large blocks locally occur toward the top of deposits, and can sometimes be seen protruding from the top of the deposits (Figures 3.8 and 3.9). The deposits contained very few vesicular clasts with abundant large, dense blocks being typical. The dense blocks observed were typically homogeneous, dark, and glassy. Gas escape structures (Figure 3.7) were present in many of the block and ash flows, suggesting that the deposits were also hot when emplaced. The finer material in the gas escape structures had been worked out and replaced by coarser material.

Location SK10 is a small cliff above the beach between Newton ground and Fig Tree village, where a 10 metre high exposure of primary PDC deposits can be seen in the cliff face (Figure 3.6). The deposits are block and ash flows, with dense clasts forming 85% of the blocks. Notably larger blocks are observed towards the top of the unit (Figure 3.8). Vesicular clasts form a minor component, approximately 15%. Samples of the dense (SK20) and minor vesicular (SK21) component were collected at SK10.

Location 12 is situated to the west Dieppe Bay, where a block and ash flow can be seen observed in the cliff. This deposit extends along the coastline to towards Location SK13, where a breccia filled channel appears to lie unconformably above, separating the block and ash flow from the pumice and ash flow observed at Location 13. This block and ash flow is likely to be the 'dense andesite pyroclastic flow' identified by Roobol et al. (1981), which has been radiocarbon dated to 3000 ± 200 B.P.

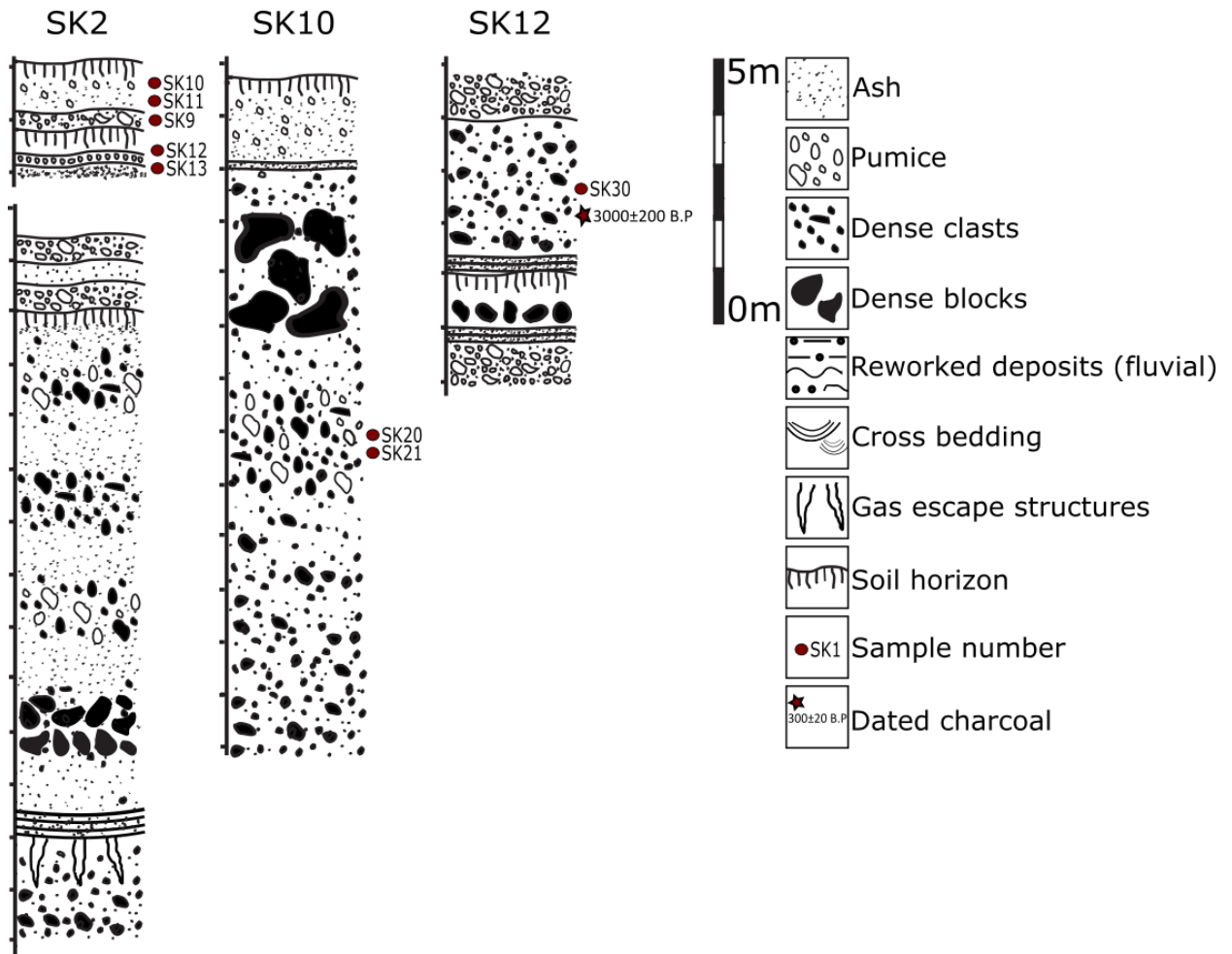


Figure 3.6 – Logs depicting the exposures of block and ash flows at locations SK2, SK10, SK12 and SK13.

Table 3.2 – Descriptions of the block and ash flows identified from Mt Liamuiga.

Location number	Latitude	Longitude	Location description	Outcrop description	Key features	Samples collected	Samples notes
SK2	17.380760	-62.750976	Coastal exposure below Nichola Town	12 metre high section of PDC deposits	Poorly sorted Large dense blocks abundant Smaller clasts of pumice Gas escape structures	SK9 SK10 SK11 SK12 SK13	SK9 - bulk sample Upper unit: SK10 - dense SK11 - pumice Lower unit: SK12 - pumice SK13 - dense
SK10	17.831456	-62.863086	Small cliff above the beach between Newton ground and Fig Tree village	10 metre high exposure of primary PDC deposits in cliff face	Poorly sorted Dense clasts form 85% of the blocks. Notably larger blocks observed towards the top of the unit Vesicular clasts form a minor component, approximately 15% Gas escape structures	SK20 SK21	SK20 - dense SK21 - vesicular
SK12	17.416726	-62.819973	centre of the beach at Dieppe Bay	Block and ash flow in small cliff	Poorly sorted Large dense blocks abundant Smaller clasts of pumice Gas escape structures Charcoal present in deposit	SK30	SK30 - dense
SK13	17.416958	-62.817780	east end of the beach at Dieppe Bay	Block and ash flow in small cliff	Poorly sorted Large dense blocks abundant Smaller clasts of pumice Pumice rich at the top of deposit Gas escape structures Charcoal present in deposit	SK31	SK31 - pumice

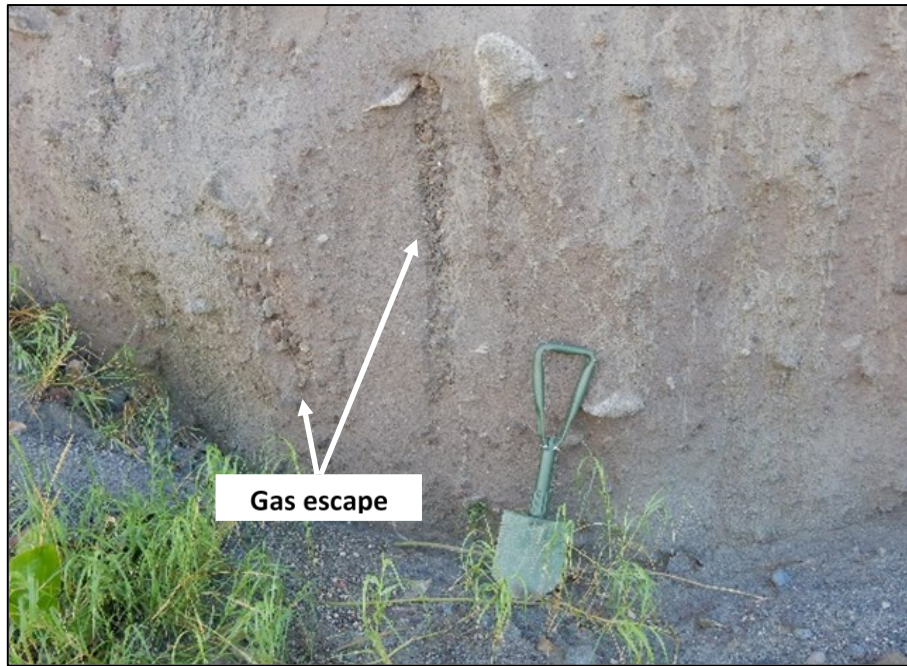


Figure 3.7 - Gas escape pipe within the block and ash flow at location SK2. The material within these pipes is poorly sorted and lacking the finer grain ash component.

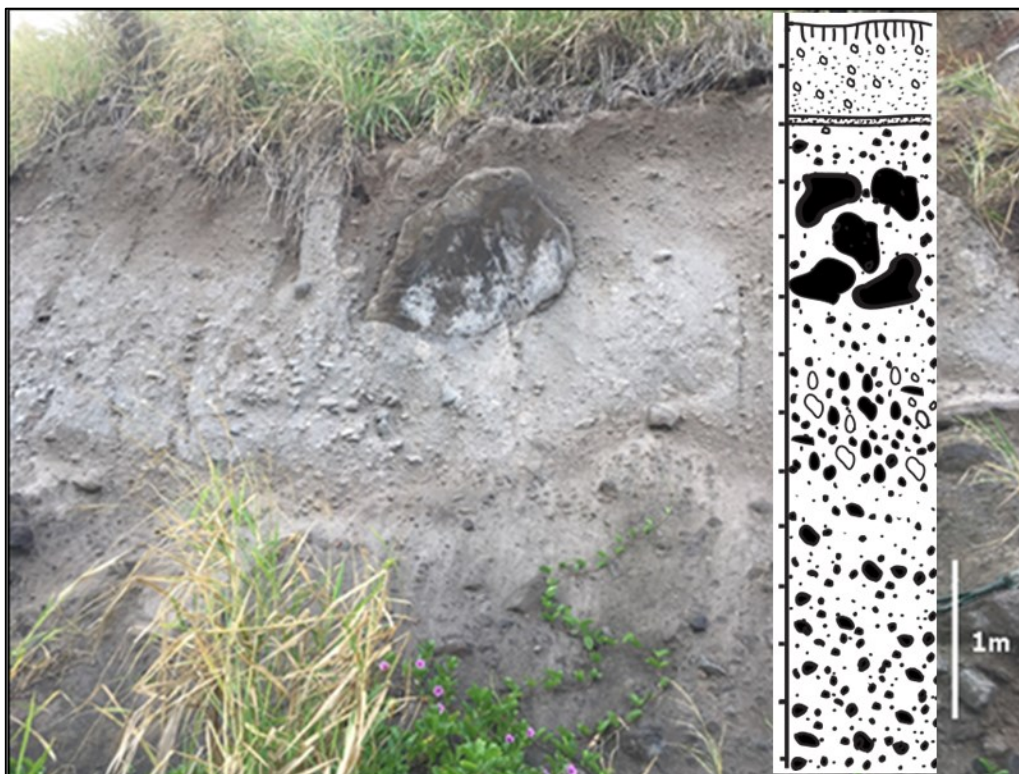


Figure 3.8 - Block and ash flow at Location SK10. Examples of large, dense blocks and gas escape pipes are shown in this image.

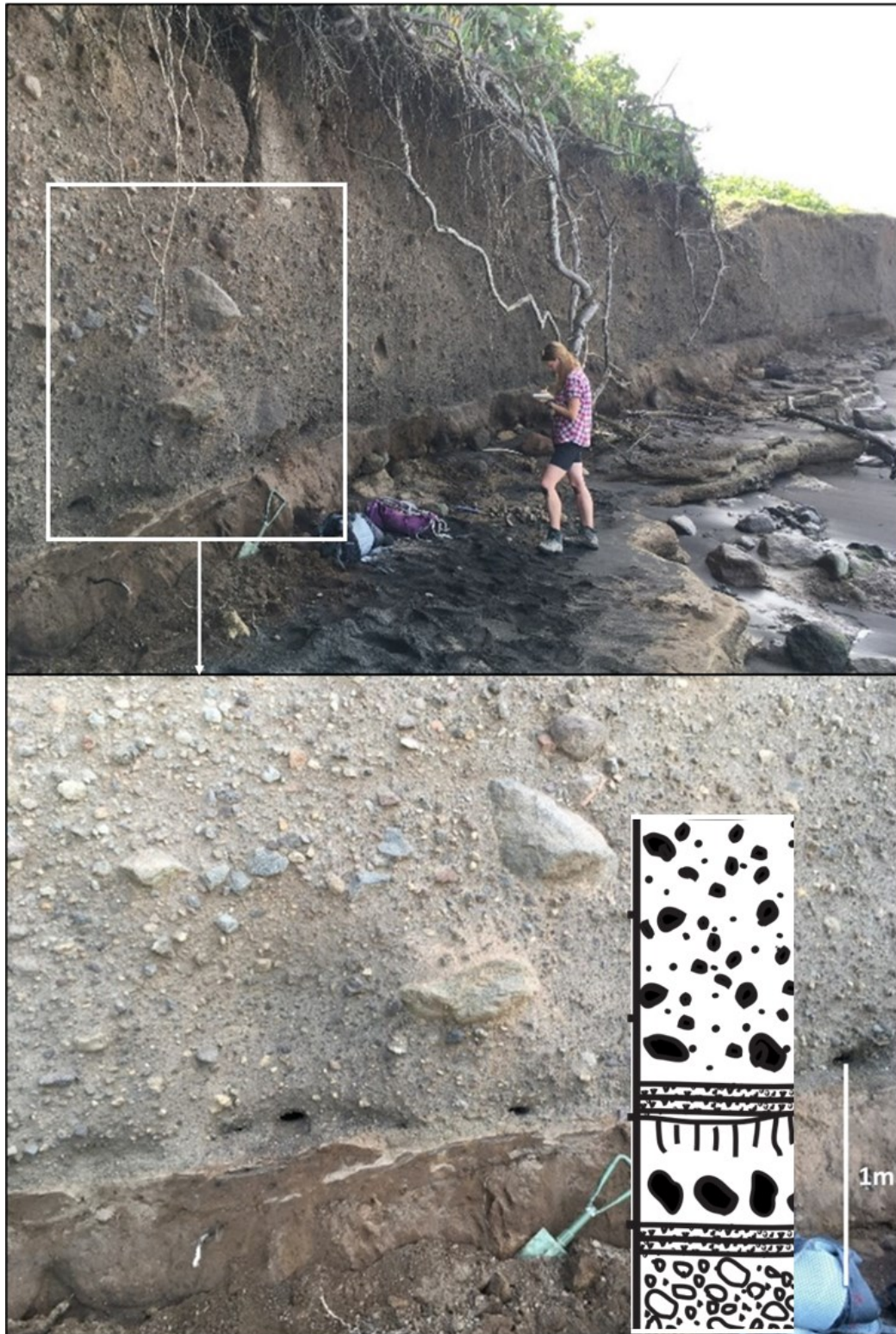


Figure 3.9 - Block and ash flow at location SK12. The upper unit shown is an example of a block and ash flow. This flow sits above the lowermost unit is clast poor. A horizon of soil can be seen beneath the base of the PDC unit.

3.4.1.2 Pumice and ash flows

Pumice and ash flows are characteristically similar to block and ash flows, with the exception that they are composed of mainly pumice and ash. The clasts are typically smaller than those observed in block and ash flows, and are highly vesiculated. Some flows also have lenses of coarse, vesicular clasts. Gas escape structures, vertical pipes of clast supported material depleted in fine ash, were also seen in the pumice and ash flows on St. Kitts. A reddish coloured oxidised surface was sometimes observed surrounding these structures. The gas escape structures and oxidised surfaces indicate that these deposits were emplaced while hot. These we observed at locations SK4, SK5, SK6 and SK13.

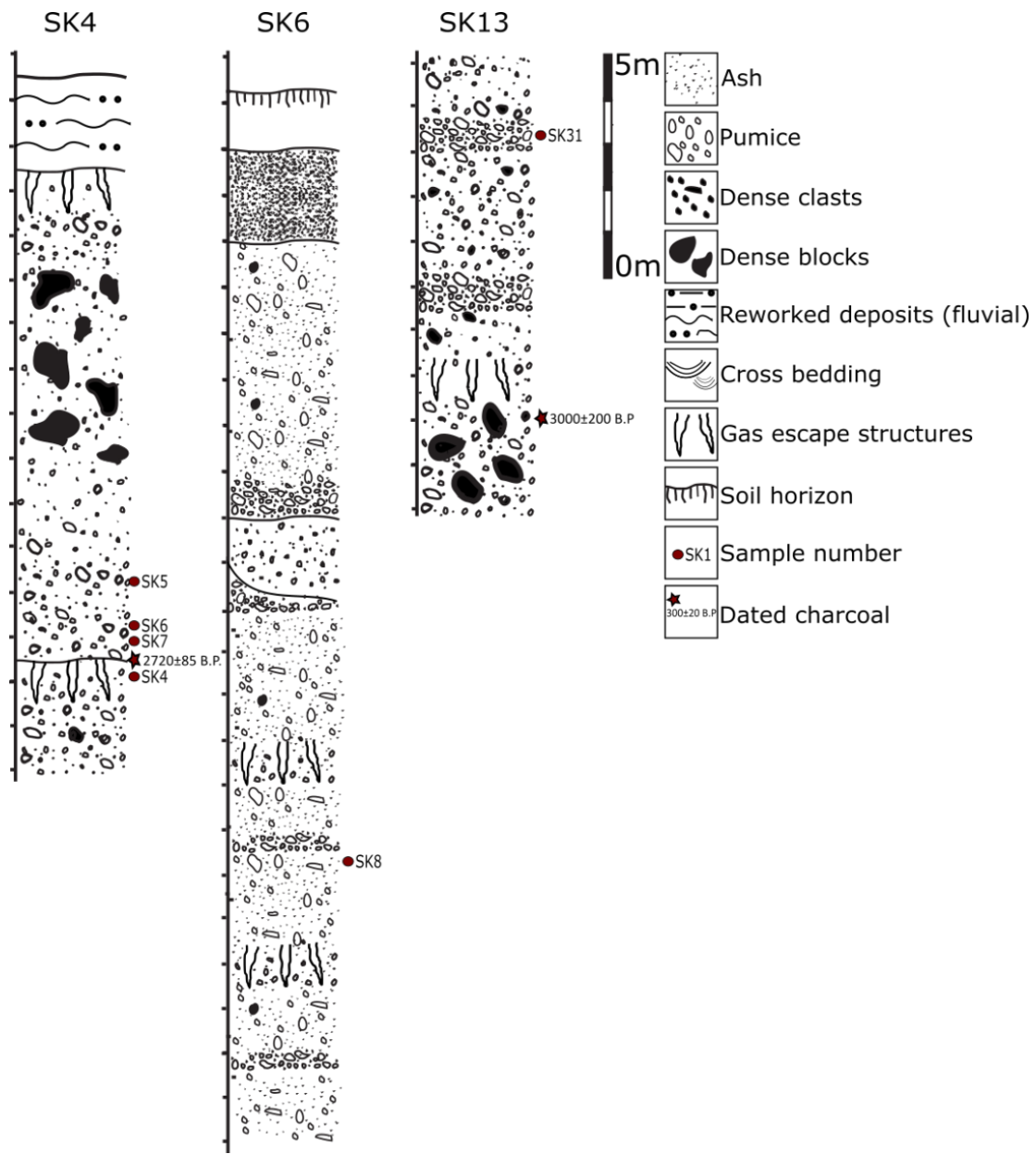


Figure 3.10 - Logs depicting the exposures of pumice and ash flows at locations SK4, SK6 and SK13.



Figure 3.11 - Location SK4, showing two pumice and ash flow units. Gas escape structures can be seen in both units. A lens of breccia and a reddish coloured upper part indicating thermal alteration can be seen in the upper unit.

Table 3.3 – Descriptions of the pumice and ash flows identified from Mt Liamuiga.

Location number	Latitude	Longitude	Location description	Outcrop description	Key features	Samples collected	Samples notes
SK4	17.408393	-62.797731	End of Sandy Bay to below Sadler’s Village	Two units of PDC deposits overlain by a layer of fluvially reworked material. Upper unit has a maximum thickness of 7m. Lower unit has a maximum thickness of 2.5m.	‘Mixed magma’ clasts of pumice Large gas escape structures differentiated the top surface of PDC units. Reddish oxidised surface surrounding gas escape structures. Lithic breccia observed in both units. Normal grading in the visible parts of the lower unit. symmetrical grading (reverse to normal) in the upper unit. Charcoal present in lowest deposits.	SK4 SK5L SK5D SK5 MIXED SK6 SK7	Charcoal: SK4 SK6 SK7 PDC: SK5L - Light SK5D - Dark SK5 MIXED - mixed magma clasts
SK6	17.398266	-62.854530	Cliff above a beach, north east of Newton Ground	Approx. 21m high cliff containing multiple PDC deposits.	Fine ash layer between the two of the units - from surge either preceding or following the pumice and ash flow.	SK8L SK8D SK8 MIXED	SK8L - Light SK8D - Dark SK8 MIXED - mixed
SK7	17.402573	-62.851068	Cliffs below Belmont Estate.	12m outcrop in cliff face.	Massive PDC deposit of pumice clasts in an ash matrix.	No samples collected	n/a
SK13	17.416958	-62.817780	East end of the beach at Dieppe Bay	Two block and ash flows in a 10m cliff section.	Juvenile clasts and vesicular scoria Banded vesicular clasts	SK31	SK31 - vesicular sample

Both PDC units at location SK4 contain 'mixed magma' clasts of pumice, some clasts are dark in colour, others are much lighter, samples of these clasts were collected; SK5 LIGHT, SK5 DARK and SK5 MIXED (Figure 3.12). Some of the clasts appear to be banded. This colour variation may be due to differing geochemical compositions (e.g. more mafic could be darker in colour) or textural differences (e.g. variation in crystallinity or vesicularity). Little variation in texture is observed in the SK5 samples, so the variation in colour may be due to differences in geochemical composition. Charcoal from this unit has been previously dated to 2720 ± 85 B.P. (Baker 1985).



Figure 3.12 - SK5 MIXED samples collected from SK4. These samples are composed of lighter and darker material.

At Location SK6, multiple layers of PDC deposits in the cliffs were observed, separated by gradational boundaries (Figure 3.10). All of these layers appear to be pumice and ash flows.

There is a fine ash layer between the two of the units, which could be a surge deposit from a surge either preceding or following the pumice and ash flow.

Location SK7 was an inaccessible location, where only a brief description could be made from a distance. A 12 m sequence of fallout with cinders, and fine basal PDC. This fallout is overlain by thick coarse pumice fallout, approximately 30 cm deep. Other massive PDC deposits above lie above these fallout deposits.

Location SK13 lies approximately 235 m from Location SK12. A pumice and ash flow lies above the block and ash flow identified at Location SK12, separated by a breccia filled channel visible in the cliff between the two locations. This more vesicular pyroclastic deposit identified at Location 13 contains bands of juvenile clasts, with some vesicular scoria. Some of the vesicular clasts appear to be banded (similar to those from Location SK4, shown in Figure 3.12).

3.4.1.3 Steel Dust Sequence

A sequence of variably coloured, layered deposits were observed at Location SK11. Baker (1969 & 1985) described a sequence in the region of Sandy Point, which lies close to SK11. The descriptions given show significant similarities to the deposits observed at SK11.

The lowermost layer is a preserved soil horizon, which lies below a bed of fine ash which pinches and swells with a minimum thickness of 1 cm to a maximum thickness of 6 cm (Figure 3.13, A). Above this lies a layer, 24 cm thick, of fine ash which shows reverse grading (Figure 3.13, B). Small pieces of charcoal were recovered from this layer. Above this lies a 25 cm thick bed of steel coloured, very fine ash (Figure 3.13, C). This layer is lighter in colour at the base, and pinches and swells. A bed of coarse, poorly sorted material follows the steel coloured ash (Figure 3.13, D). This bed contains accretionary lapilli and other dense clasts. This bed is in

turn overlain by another layer of fine ash (Figure 3.13, E). The last exposed layer consists of accretionary lapilli and clasts of other material (Figure 3.13, F). This sequence is likely to be the ‘Steel Dust’ series noted in Baker (1969 & 1985), Harkness *et al.* (1994) and Roobol *et al.* (1981, 1985).

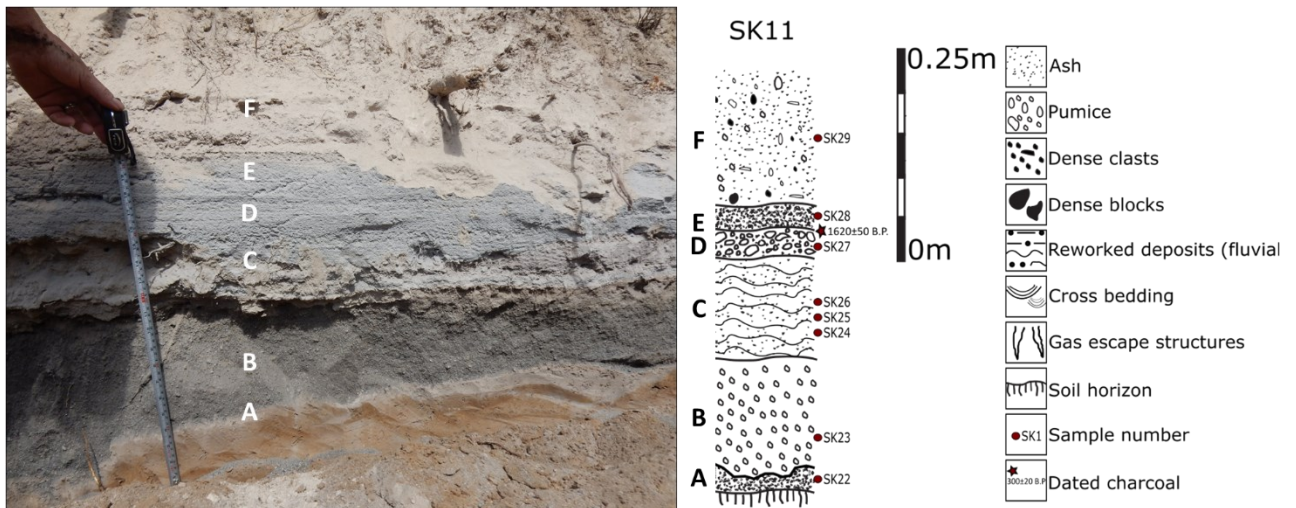


Figure 3.13 – 0.7 m Section through the steel dust series at SK11, close to Sandy Point Town (length of tape measure is 0.5 m).

3.4.1.4 Fallout

The youngest deposits of the Mansion series are lapilli fallout (Baker, 1985; Harkness *et al.*, 1994; Roobol *et al.*, 1981; Toothill *et al.*, 2007). Primary fallout was observed at locations SK1, SK2, SK5 and SK12.

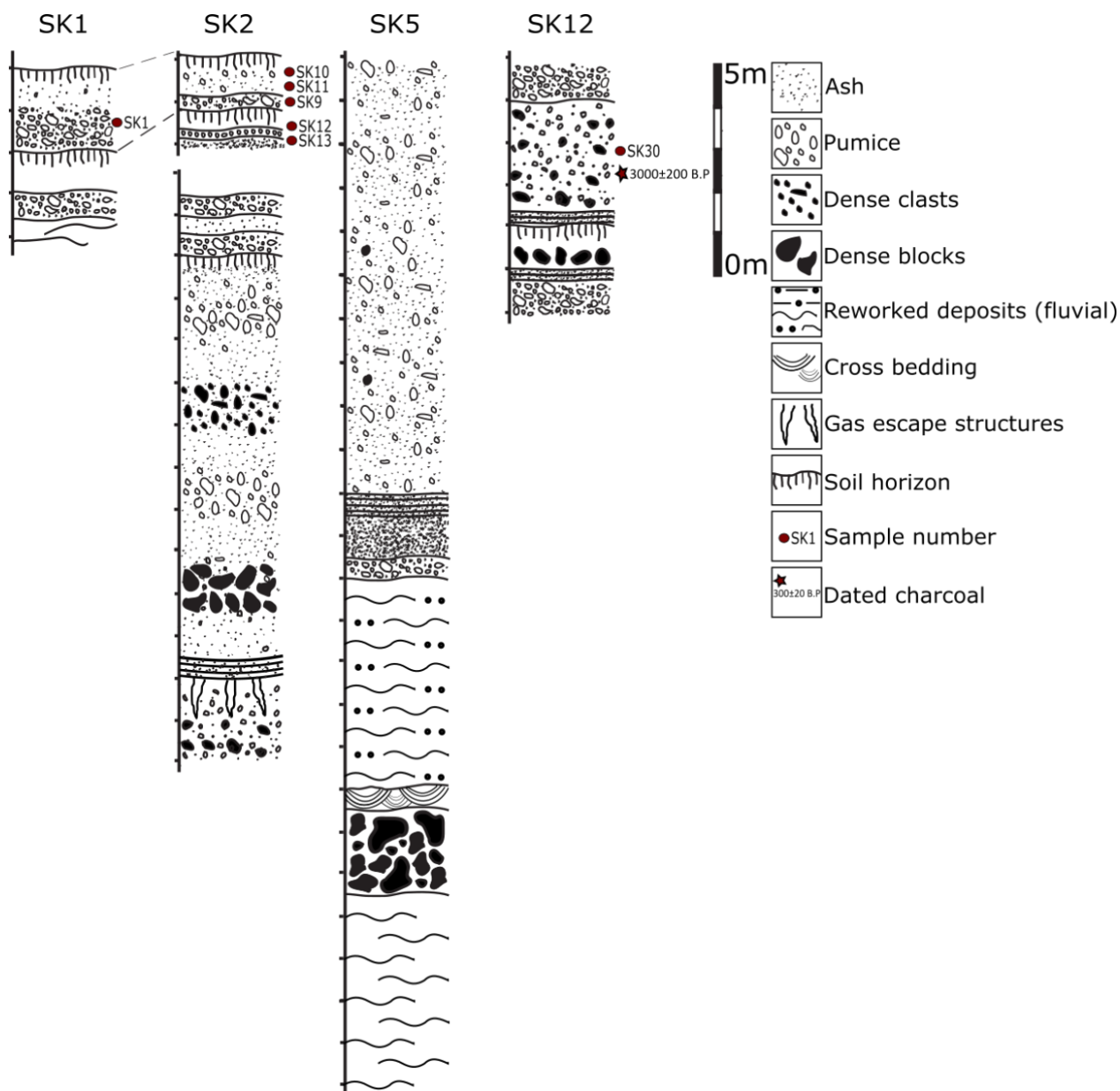


Figure 3.14 - Logs depicting the exposures of fallout deposits at locations SK1, SK2, SK5 and SK12.

At location SK1, many layers of lapilli fallout are present, some interbedded with soil and laharic material. The two layers located towards the top of the outcrop were thought to be

among the younger deposits (Figure 3.14). These deposits are likely to form part of the Upper Pumice zone, the uppermost unit of the mansion series (Baker, 1969; Baker and Holland, 1973). Two types of pumice were collected from the upper lapilli fallout beds of SK1, one white in colour and one grey. Both samples are highly vesicular.

Primary fallout lies above the block and ash flows identified at location SK2 (Figure 3.14). These deposits are made up of the following layers, from the lowermost upwards; ash, reverse graded lapilli, soil horizon, lapilli with the bottom 0.1 m reverse graded, pumice lapilli, topped by modern soil.

Two metres of fallout deposits can be seen in the exposure at location SK5, a sea cliff above a small rocky beach near Heldens (Figure 3.5). These fallout layers can be seen approximately 12 m above fluvial and surge deposits, and are overlain by 10 m of PDC deposits (Figure 3.14). These layers consist of a pumice lapilli fallout, overlain by a fine ash deposit, and an unidentifiable fallout deposit. The fine ash deposit is reddish in colour, and is indurated. This sequence is shown in Figure 3.14.

3.4.1.5 Volcaniclastic deposits

Evidence of reworked volcanic material, most of which has been reworked by fluvial processes or lahars, could be observed on St. Kitts.

These deposits are commonly composed of clasts that range from millimetres, to over a metre in size. They are commonly matrix supported, poorly sorted, and often contain clay or silt in the matrix. The clast shapes vary from rounded to angular, and may be either single or mixed rock types, depending on the source material. Some deposits show features such as cross bedding. Lahars, or material deposited by other fluvial processes, can be distinguished from

PDC deposits from their lack of heat related features, e.g. oxidation evidence or gas escape structures. They may also contain voids, preserved from where bubbles of air were trapped in the matrix material.

Laharic material was identified at Location SK1, SK7 and SK8 (Figure 3.15). Many of the fallout deposits observed at location SK1 were partly reworked, with fallout layers of lapilli, 20-100cm thick clearly interbedded with soils and laharic material. Many of the clasts in these layers show evidence of hydrothermal alteration. Clear evidence of fluvial processes were observed at location SK8, where fluvial and reworked material is cut by a canyon infilled with further fluvial deposits.

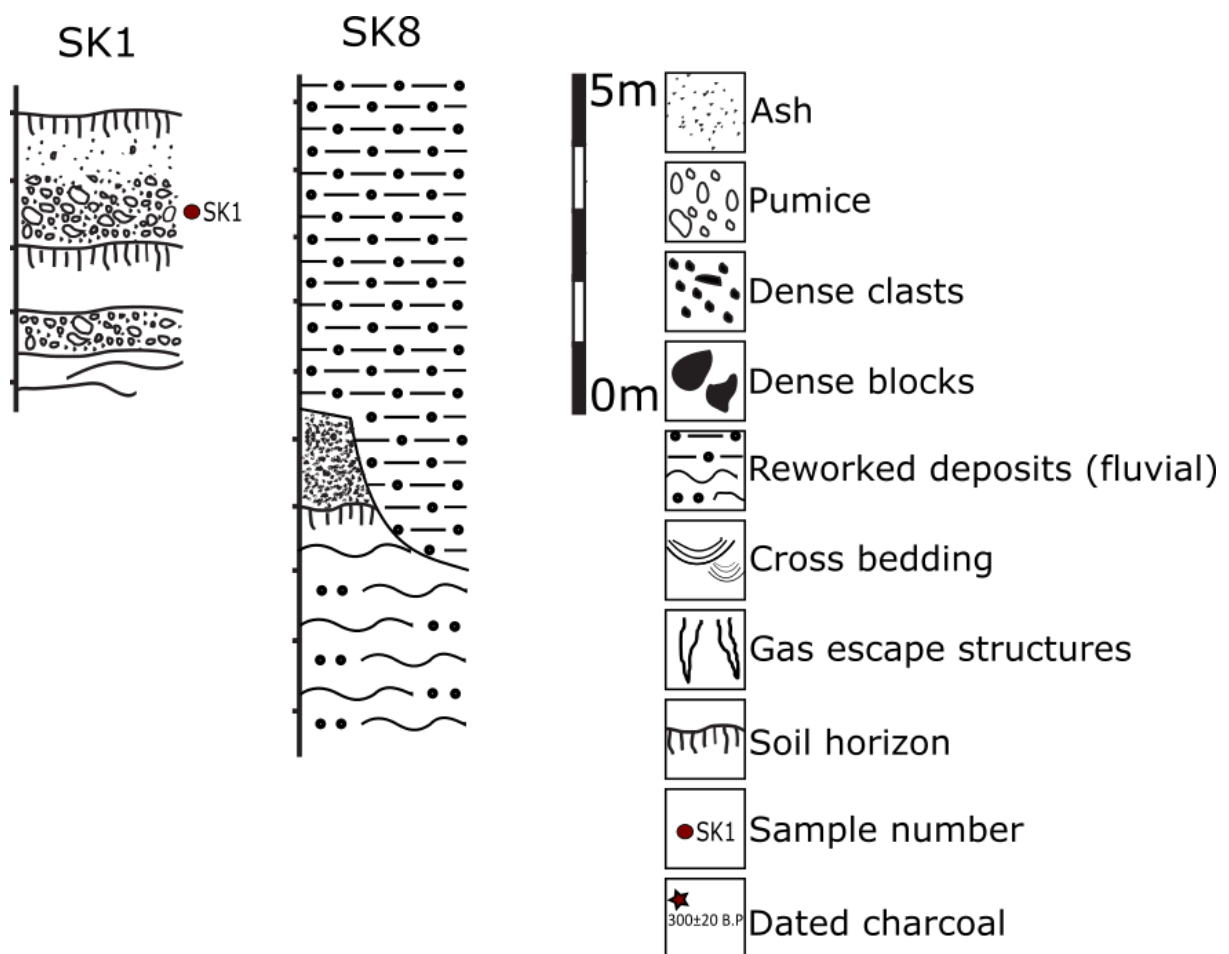


Figure 3.15 - Logs depicting the exposures of volcanoclastic deposits at locations SK1 and SK8.

3.5 Nevis

A single location, SKN9 (Figure 3.16), was studied on Nevis. The exposure was in the sea cliff 400 m SE of Long Point. Three distinct units divided by bedded Pumaceous deposits can be observed at SKN9 (Figure 3.17), in an 8 m high exposure.

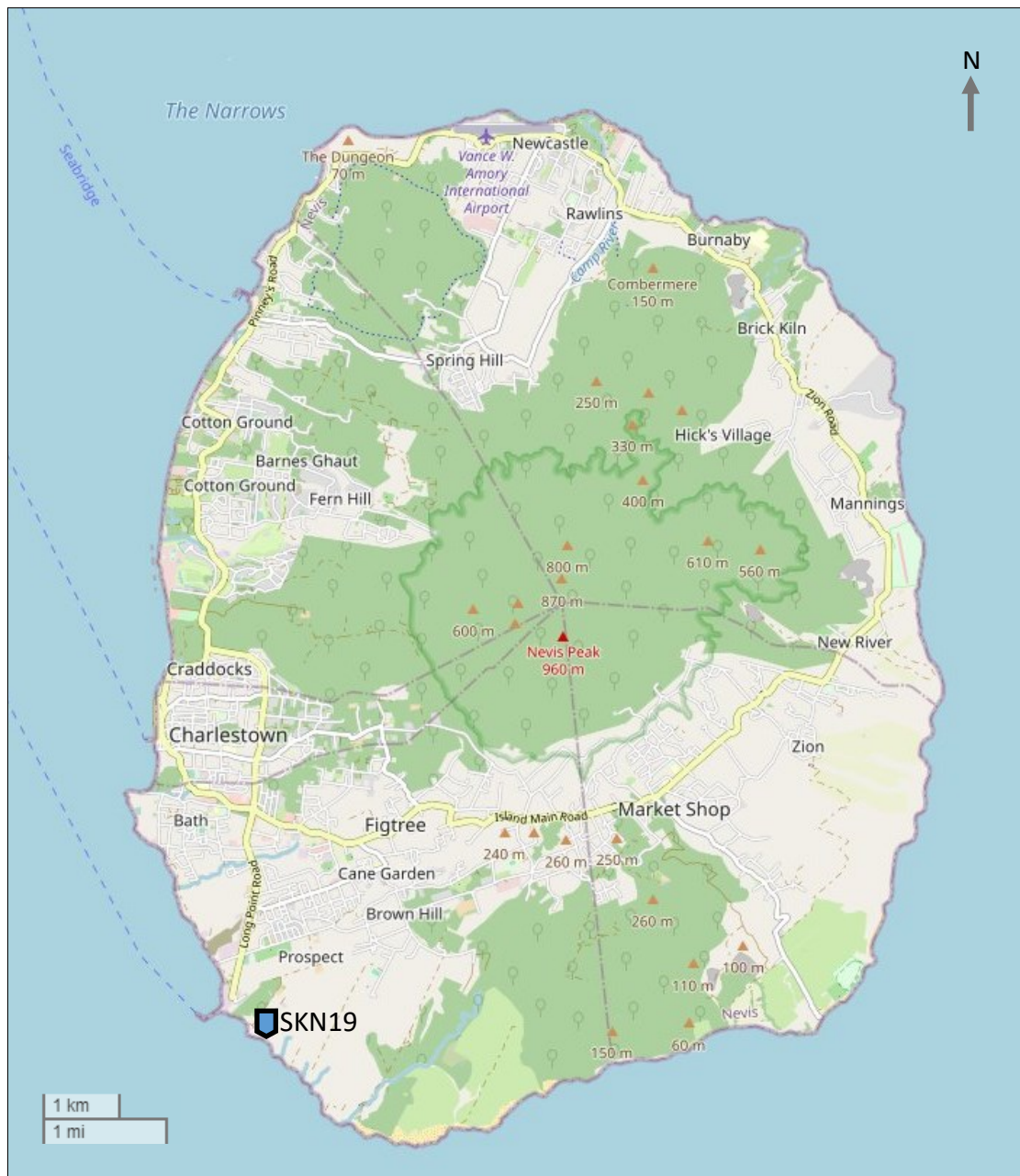


Figure 3.16 - Map of Fieldwork location on Nevis.

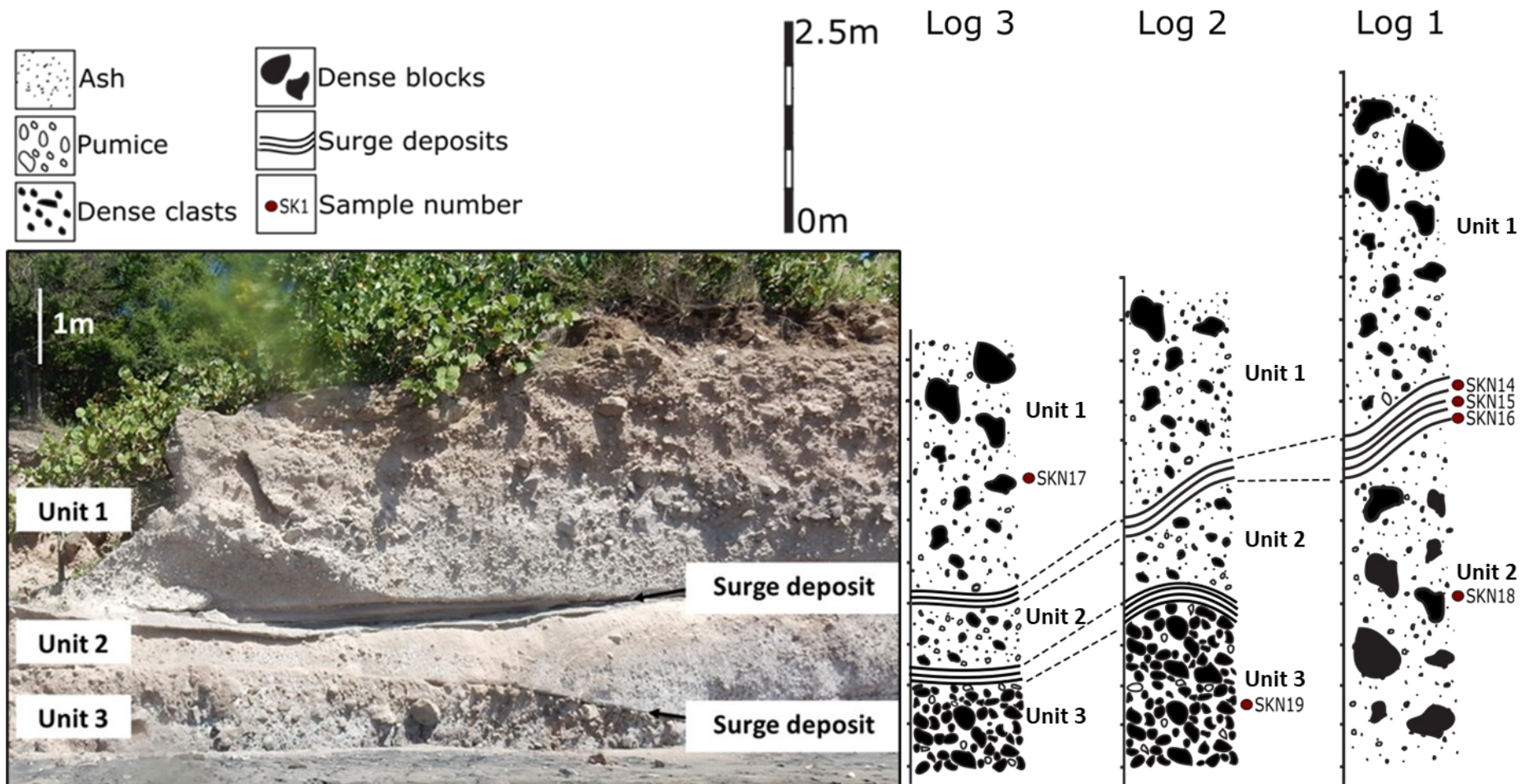


Figure 3.17 - SKN9 showing Unit 1, Unit 2, Unit 3 and surges.

Table 3.4 – Table summarising the locations and descriptions of samples collected from SKN19.

SKN19 – UNIT NUMBER	SAMPLE NUMBERS	SAMPLE NOTES
UNIT 1	SKN17	Dense block from upper section of the unit
SURGE	SKN14 SKN15 SKN16	SKN15 – Bulk matrix sample SKN14 – Pumice from top of deposit SKN16 – Pumice from bottom of deposit
UNIT 2	SKN18	Sample of blocks
UNIT 3	SKN19L SKN19D	SKN19L – Lighter coloured, more vesicular sample SKN19D – Darker coloured, denser sample

Unit 3 is the lowermost deposit observed. This unit has a maximum thickness of 2 m and is poorly sorted, clast supported with a matrix, and large blocks making up the bulk of the deposit. A deposit of pinching and swelling fine ash, up to 0.2 m in thickness, lies above Unit 3. Unit 2 is the middle unit, and has a maximum thickness of 4 m. This unit contains fewer blocks than Unit 2. The blocks lie in a fine ash matrix. Above Unit 2 lies another pinching and swelling deposit of fine ash (Figure 3.17). This deposit is bedded and contains lapilli (Figure 3.18). Unit 1 is the uppermost unit with a maximum thickness of 4 m, and, unlike Units 2 and 3, shows evidence of reverse grading. The unit consists of large dense blocks, with a minor vesicular component in an ash matrix. Units 1, 2, and 3 are dense PDC flow units, while the bedded laminated fine ash between each unit are likely low concentration PDC deposits (surges), identified by the varying thickness, and pinching and swelling of the layers independent to topography (fallout deposits would retain a constant thickness).



Figure 3.18 - Surge deposits between Unit 1 and Unit 2.

3.6 Interpretation and discussion of field observations.

3.6.1 St Kitts

3.6.1.1 Distribution of PDCs from Mt Liamuiga

PDCs from Mt Liamuiga were observed in the North West of St Kitts, located between Brimstone Hill and Saddlers. A PDC deposit was observed at Location SK2, near Nicola Town, and close to the original type locality of the Mansion series first identified by Baker (1969). This deposit was included in the descriptions of block and ash flows, however, on closer examination and correlation of the field data combined with literature, it is likely that this dense PDC unit is older than the PDCs in the mansion series. As shown in the log of SK2 in Figure 3.6, the dense PDC unit lies below the fallout deposits that make up the majority of the Mansion Series. Taking into account the topography, it is also considered unlikely that a dense PDC of the size that typically produces the deposit observed (block and ash flow) would be

capable of overtopping the ridge to the East of Mt Liamuiga to reach the location it was deposited.

3.6.1.2 Correlation with existing stratigraphy for Mt Liamuiga

The units described in the field were correlated to well-described sections recorded in the literature (Baker, 1969, 1985; Harkness *et al.*, 1994; Roobol *et al.*, 1981). The literature was used to inform the studied fieldwork locations, this meant that deposits could initially be correlated based on location. The units were then more precisely correlated based on their textural features, and stratigraphic position within a recognisable sequence (Figure 3.19). Unique characteristics, such as the presence of charcoal, were used to further refine correlations. As the presence of charcoal was relatively rare, its identification within a given deposit would allow that unit to be directly correlated to charcoal-containing deposits noted in the literature (Baker, 1985; Harkness *et al.*, 1994; Roobol *et al.*, 1981).

Table 4.5 shows the correlation of the locations in this study with the existing stratigraphy for Mt Liamuiga. The PDCs and fallout deposits that form the focus of this study are from the Upper Pumice Unit and the Pyroclastic Flows. These beds were given the labels of Unit F and Unit E respectively from Roobol *et al.* (1981). Locations SK5, SK7 and SK8 were unable to be correlated with the other field locations and the stratigraphy due to the isolated nature of the deposits, and the lack of comparable similarities with the locations and characteristics described in the literature.

The PDC deposits identified fall within Unit E (Roobol *et al.*, 1981), or simply the 'pyroclastic flows' of the mansion series (Baker, 1985). Some debate has occurred around the accuracy of radiocarbon dating of charcoal from St Kitts due to the variations in the physical nature of the charcoal preserved in PDC deposits, and their differing susceptibility to contamination. The

radiocarbon dates agreed in Harkness *et al.* (1994), shown in Table 4.5, are considered to be the most accurate dates for the deposits. These suggest that the PDC deposits observed in this study are likely to have erupted approximately 1817 ± 38 and 2038 ± 21 years B.P.

The fallout deposits observed from Mt Liamuiga form part of Unit F (Roobol *et al.*, 1981), or the 'Pumice Zone' of the Mansion Series (Baker, 1969, 1985).

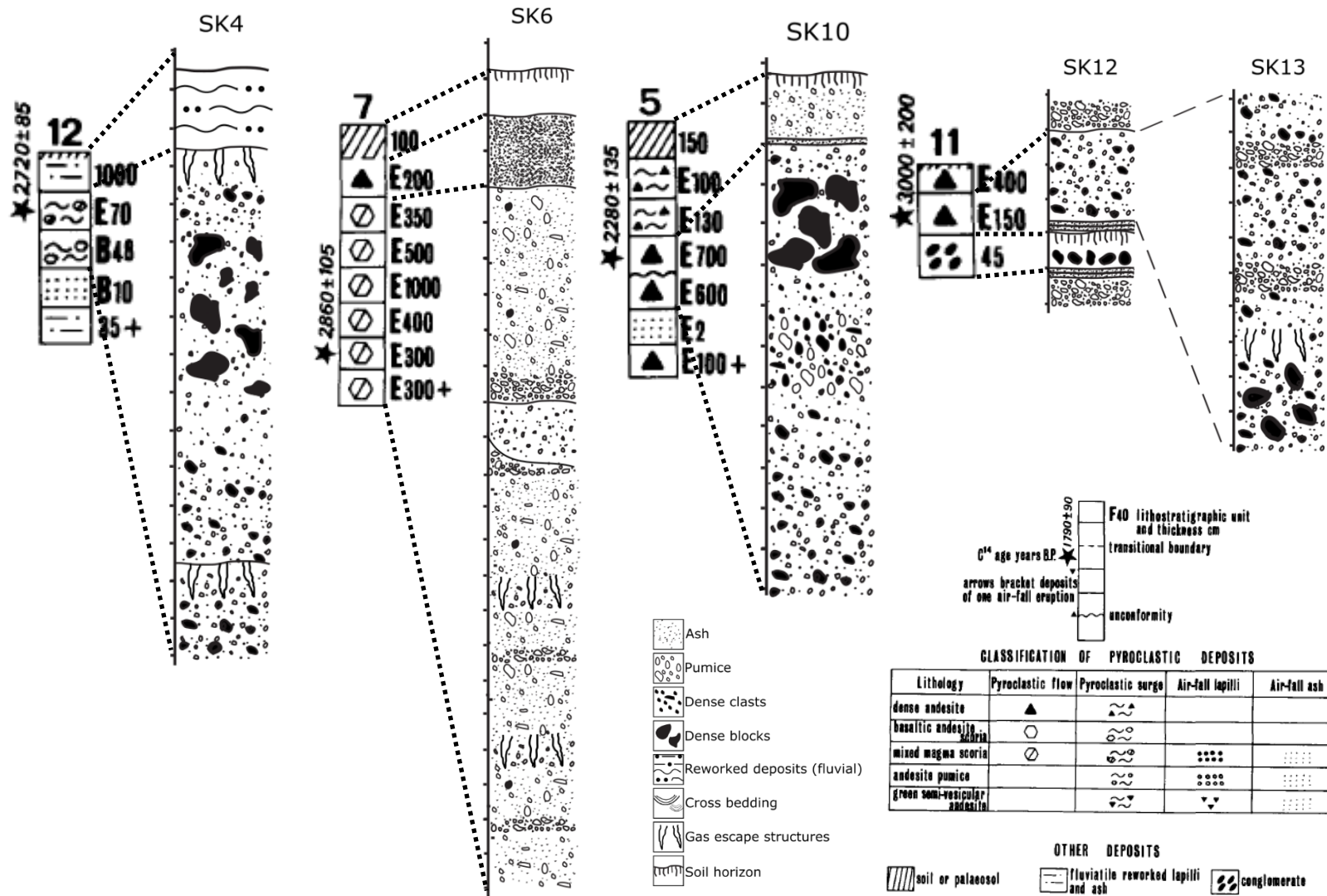


Figure 3.19 – Graphic logs from this study, SK4, SK6, SK10, SK12 & SK13, correlated with logs in similar locations in Roobol et al. (1981), Locations 12, 7, 5 & 11.

Table 3.5 - Correlation of the locations in this study with the existing stratigraphy for Mt Liamuiga (Baker, 1969, 1985; Harkness et al., 1994; Roobol et al., 1981).

Roobol et al. (1981)				Baker (1985) (revised from (Baker (1969)))			Harkness et al. (1994)	Correlation with this study
Unit	Deposit	Example location	Age	Deposit	Example location	Age		Location numbers
	Steel Dust Series							
F	Upper Pumice Unit Mansion series Pumice Pumice Andesite pumice surge Pumice		1750 ± 90	Coarse pumice Pumice Fine ash and carbon Nuée Ardente Pumice Steel Dust Series Pumice	Grange Bay, Mt Pleasant Lynches Lamberts Belmont Lynches, Farm Source Bourkes Estate Mansion, Cranstouns	2070 ± 50 1710 ± 80 1620 ± 50	2070 ± 50 1720 ± 80 1620 ± 50	SK1 and SK2 - Fallout SK11
E	Block/scoria mixed magma scoria ash Dense andesite pyroclast flow Basaltic andesite pyroclast flow Dense andesite pyroclasts flow Mixed magma surge Mixed magma pyroclast flow Dense andesite pyroclast flow	Cranstouns Gut Headland SE of sandy bay Coast below Cranstouns East side of sandy bay Brothersons Masshouse Bay	2280 ± 135 2340 ± 80 2410 ± 120 2720 ± 85 2860 ± 105 3060 ± 200	Pyroclastic flow Pyroclastic flow Pyroclastic flow	Godwin Estate Coast below Brotherson's Dieppe Bay to Hacket Point	2030 ± 40 2050 ± 40 / 2120 ± 40 2060 ± 40	1817 ± 38 1840 ± 55 2038 ± 21 / 1852 ± 21	SK10 SK4 SK6 SK12 and SK13
D	Lower Pumice Unit		3658 ± 94	Pumice Ash and carbon	Christchurch	3658 ± 94	3658 ± 94	
C	Upper Green Lapilli			Pumice falls Pyroclast flow Pyroclast fall Nuée ardente Coarse mud flows Grey nuée and carbon White nuée and pumice Mudflows	Charles Fort Coast between Mansion and Tabernacle Coast between Mansion and Tabernacle Coast between Mansion and Tabernacle Coast between Mansion and Tabernacle Coast between Mansion and Tabernacle Coast between Mansion and Tabernacle	4270 ± 140 24,870 +450/- 430	4270 ± 140	SK2 – PDC deposit
B	Cinder Unit		>41,730 >41,140	Cinder Zone			>41,730	
A	Lower Green Lapilli		>41,420	Lower Green Lapilli Zone			>41,420	

3.6.1.3 Interpretation of PDCs

The PDC deposits observed on St Kitts are categorised into two end members, block and ash flows and pumice and ash flows (Baker, 1985; Baker and Holland, 1973; Roobol *et al.*, 1987; Roobol, 1985). While this classification was used to simplify the terminology used, it is more accurate to describe the flows as transitional, with the pumice and ash flows containing some more denser clasts, whilst the block and ash flows contained a significant volume of pumice (Brown and Andrews, 2015). The overall trend is that all of the flows were towards the pumice and ash end of the scale, with the so called 'block and ash flows' simply containing denser clasts and some blocks without being 'true' block and ash flows (Sections 3.4.1.1 and 3.4.1.1).

PDC deposits containing large amounts of pumice are likely to have originated from explosive activity, where conduit-derived, gas-rich magma has been extruded (Cole *et al.*, 2002, 2014).

This suggests that the pumice and ash-flows observed on Mt Liamuiga were the result of fountain collapse during explosive activity. The suggestion that many of the PDC flows appear to be 'transitional' in nature, with denser clasts found in flows containing pumice, indicates that the explosions may have been related to lava dome growth and collapse. The denser clasts represent fragments of the lava dome caught in the explosion. The block and ash flows are most likely the result of the collapse of an andesitic lava dome. The 'transitional' style flow suggest that the typical style of activity at Mt Liamuiga is likely to include periods of dome building, follow by dome collapse events accompanied by explosions.

The gas escape structures and reddish coloured oxidised surface towards the top of the PDC deposits suggest that the deposits were emplaced at high temperatures. The gas escape structures suggest rapid deposition of PDC deposits (Stinton *et al.*, 2014) over wet or moisture rich ground (Brown and Andrews, 2015). These features may be the result of water

penetrating into the deposit whilst it was hot, flashing to steam and causing alteration to the material in the surrounding area. Whilst water may have penetrated downwards into the deposit whilst it was still hot, for example in heavy rainfall or flooding, another potential scenario is that the PDCs ran into the sea and were emplaced in coastal regions, where the high temperatures of the flows caused sea water to turn to steam, causing the gas escape structures and thermal alteration. The presence of carbonised wood in many of the PDCs suggests that the emplacement temperature was frequently above 300°C (Cole *et al.*, 2002).

3.6.1.4 The Steel Dust Series

The Steel Dust series was originally thought to be the youngest deposits originating from Mt Liamuiga. The radiocarbon dates proposed by 3 papers (Baker, 1985; Harkness *et al.*, 1994; Roobol *et al.*, 1981), suggest this, with the charcoal found in the Steel Dust being dated to 1620 ± 50 year B.P. Baker (1985) later revised the stratigraphy, suggesting that the Steel Dust series lies below several beds of pumice and another PDC. The fieldwork undertaken for this thesis identified a well-preserved section of the Steel Dust series, overlain only by a soil horizon, with no other context of its relative place in the stratigraphy. It does appear to lie at the top, or near to the top of the volcanic deposits observed on Mt Liamuiga, making it one of the products of one of the youngest eruptions at St Kitts.

The nature and origin of the Steel Dust Series is another debated topic. The Steel Dust is thought to have phreatomagmatic origins due to the presence of accretionary lapilli (Baker, 1985). Accretionary lapilli used to be considered exclusively phreatomagmatic, however is now thought to be the result of moisture addition from a range of sources (Burns *et al.*, 2017).

Layers A to D are likely to be pyroclastic surge deposits. Surge deposits are typically thinly bedded, laminated and often wavy-, lenticular- or low angle cross-bedded. They can be highly

variable, with some resembling dunes of medium sized sand. Many contain lenses of well-sorted and well-rounded pumice lapilli. Surge deposits have a more restricted grain size than pyroclastic flow deposits, lacking both the very fine and the coarse fractions (Belousov *et al.*, 2007). Layers are similar to that which may occur in a blast deposit. These blasts are formed by explosions which can generate high energy pyroclastic density currents (Belousov *et al.*, 2007). Most layers were identified as surge deposits, not fallout, as they display too much pinching and swelling. Layers E and F may be of a fallout origin.

3.6.2 Nevis

3.6.2.1 Origins of PDCs

The PDC deposits observed on Nevis were classified as block and ash flows. The typical emplacement mechanism for this type of PDC is from a lava dome collapse, in this case from Nevis Peak, which would have caused massive flows (Brown and Andrews, 2015). The surges observed between the block and ash flow deposits may represent a more buoyant cloud which preceded or followed the dense PDC. However, the block and ash flows observed on Nevis contained a vesicular component, which would not be expected during a dome collapse scenario without explosive activity (Cole *et al.*, 1998, 2002).

All three of the described block and ash flow units contained a minor vesicular component. As block and ash flows contain dense clasts, they are typically associated with dome collapse events, but the presence of vesicular material within them may indicate some explosive activity co-occurred with the dome collapse, producing the vesicular clasts. The block and ash flows described from Nevis may, therefore, have been formed from primarily dome collapse events, with secondary explosive activity associated with them. This style of eruption was observed on multiple occasions on Montserrat, for example in the February 2010 eruptions (Cole *et al.*, 2014; Stinton *et al.*, 2014). This interpretation of primarily dome collapse derived PDCs and surges is broadly in agreement with the past eruptive activity described in the literature (Simpson, 2005).

The surge horizons contained pumice, as shown in Figure 3.18, which indicates that these surges were explosively derived and not from a straightforward dome collapse, similar to those observed on Montserrat (Cole *et al.*, 2014).

3.6.2.2 Morphology of Nevis Peak

The morphology of the Nevis Peak crater rim at the time of the eruptions studied here is not known, although the presence of dome collapse related material to the south suggests that the crater may have been open in that direction. However, there does not appear to be an open amphitheatre collapse scar oriented towards the south, and instead the crater is open to the west at present (Figure 3.20), related to an apparent sector collapse (Koon Koon, 2012). If the crater were open to the west during the time of eruption, as it is today, then an eruption column collapse may have been a mechanism by which the PDCs were able to travel over the crater rim towards the south. A more likely scenario is that the deposits studied are not the product of the most recent activity on Nevis, and that the morphology of the crater differed at the time of their emplacement.



Figure 3.20 - The modern day Nevis Peak crater shown open to the west. (Imagery from Google Earth, 2023).

3.7 Conclusions

The following conclusions can be drawn from this chapter:

- Transitional flows more similar to block and ash flows than pumice and ash flows, were observed in several coastal exposures surrounding the flanks on Mt Liamuiga. These deposits contained few vesicular clasts with more abundant large, dense blocks. The dense blocks observed were typically homogeneous, dark, and glassy.
- Pumice and ash flows are similar to block and ash flows, except that they are composed of mainly pumice and ash. The clasts are typically smaller than those observed in block and ash flows, and were highly vesicular.
- Rather than the end-members of block and ash flow vs pumice and ash flow, St Kitts exhibits more transitional PDCs skewed towards the pumice and ash flow end of the scale.
- The pumice and ash-flows observed on Mt Liamuiga were the result of fountain collapse during explosive activity. Transitional nature PDCs indicate explosions may have been related to lava dome growth and collapse.
- A well-preserved section of the Steel Dust series was identified. Most layers within the Steel Dust series were classified as surge deposits, not fallout, as they display too much pinching and swelling. Two layers at the top of the section may be fallout.
- Nevis block and ash flows formed from primarily dome collapse events, with secondary explosive activity associated with them, evidenced from vesicular components.

4. Petrography and Geochemistry

4.1 Introduction

This chapter will investigate the geochemical and petrological characteristics of the samples collected from fieldwork on Mt Liamuiga, St Kitts and Nevis Peak, Nevis. There are two aims to this chapter; firstly to investigate the magma storage conditions below Mt Liamuiga and Nevis Peak, and secondly, to gain an understanding of the pre-and syn- eruptive processes for the most recent eruptions from the two volcanoes. To achieve these aims, three types of deposit collected during the fieldwork (as discussed in Chapter 3) were analysed; pumice and ash flows, block and ash flows and fallout deposits.

4.1.1 Geochemical background of St Kitts

4.1.1.1 Major elements compositions

The Mt Liamuiga deposits show neither a clear tholeiitic or calc-alkaline trend, with compositional data often plotting on the boundary between the two classifications (Toothill *et al.*, 2007). This is a trend commonly observed in low-K suites of arc volcanoes in the Lesser Antilles (Macdonald *et al.*, 2000).

The SiO₂ composition within the Mansion Series ranges from 48% SiO₂ (basalt) to 62% SiO₂ (andesite) (Baker, 1980; Baker and Holland, 1973). There are no dacites on St. Kitts, and no rhyolites originating from Mt Liamuiga (Baker, 1984). According to Baker (1984), basalt comprises 9% of the total volcanic deposits on St. Kitts, all of which are associated with Mt Liamuiga and occur as lava flows, or as layers of basaltic cinders in the lower units of the Mansion Series.

Baker and Holland (1973) state that the pyroclastic deposits (fallout and PDCs) of the Mansion Series are basaltic andesite in composition, and suggest that this is evidence to indicate that Mt. Liamuiga is prone to explosive activity when the magma has a basaltic andesite composition. The PDCs deposits were identified as having a composition of basaltic andesite to andesite, in the range of 55 to 60% SiO₂, with a mean of 57.2% (Baker, 1985).

The lapilli layers in the upper Mansion Series have an andesitic composition, ranging from 59.75 to 61.52% SiO₂ (Baker, 1980). The compositional analysis of the Mansion lapilli layers in Baker (1980) aided the correlation of these lapilli units across the island, although Baker (1980) attributed much of the compositional variation between locations to subaerial fractionation influenced by the wind.

The Mt Liamuiga rocks are less potassic compared to the oldest volcanic centre on St Kitts, with a shift to lower K compositions (from up to 2.5% K₂O in the oldest volcanic centre, to ~0.5% K₂O at Mt Liamuiga) occurring within the past 2-3 Ma. This is thought to be a result of the shifting of the volcanic axis from the outer islands (e.g. Anguilla, Barbuda and Antigua) to the inner islands (e.g. Saba, St Kitts, Nevis, Monserrat, Guadeloupe and Dominica) of the Lesser Antilles and, as a result of this shift, volcanism started at a new zone. A low-K composition is more representative of a new and immature island arc. Changes from the more potassic and calc-alkaline composition to low-K composition relate to the progressive reduction in the depth of the Benioff zone as the slab began subducting at a shallower inclination (Baker, 1984; Toothill *et al.*, 2007).

The range of MgO and Al₂O₃ contents described by Toothill *et al.* (2007) suggest that the suite is comprised of several magmatic lineages, with two clear groups termed “higher-Al” and “lower-Al”. There are no stratigraphic or geographical differences between these two groups,

suggesting that both magma types were available for eruption during the period studied. As the two groups did not mix, this indicates that at least two magma types are stored below St. Kitts (Toothill *et al.*, 2007).

Major element variations suggest that in the lower-Al Mt Liamuiga deposits of Toothill *et al.* (2007) fractional crystallization of a basaltic parental magma was the source of the eruptive rocks. Given the overlap of the compositional trends of the higher-Al and lower-Al groups, it is likely that both groups originated in this way. As many Mt Liamuiga deposits are interpreted as hybrids formed from the mixing of basalt, basaltic andesite and andesite magma, open-system processes have likely overprinted magmatic processes dominated by fractional crystallization (Toothill *et al.*, 2007). The close relationship between basaltic and andesitic products from Mt Liamuiga has been considered to be the result of a basaltic andesite magma that was periodically differentiating into an andesitic composition (Baker, 1980).

Deposits showing clear variations in nature, for example, vesicularity, mineralogy and colour, have been identified in PDCs on Mt Liamuiga. These are often referred to as 'mixed magma clasts'. Roobol *et al.*, (1987) published XRF major element data for two scoriaceous juvenile clasts from a scoria and ash flow deposit from the Mansion series, located below Sadler's village. They identified large juvenile clasts containing streaks of white, more siliceous, vesicular andesite in the PDC deposits, which they attribute to the mixing of a dominant basaltic andesite with a minor andesitic component. These clasts were taken from the top and bottom of the 'mixed magma' scoria and ash flow deposits, one from lighter material (SK-165) which they concluded is andesite, and one from dark material (SK-164) which they describe as being basaltic andesite. The whole rock XRF analysis for these deposits is shown in Table 4.1. Toothill *et al.* (2007) also identified the mixed magma pumice within the

pyroclastic flows of the Mansion Series and the evidence of magma mingling, found on the eastern and north-eastern sides of the volcano. The single sample analysed (Kit35) was found to contain two end members, the dark end consisting of basalt and the light end consisting of andesite. This variation in colour could also be due to textural variation, for example, differences in vesicularity or crystallinity.

Table 4.1 - Whole rock XRF analysis (major and trace element) for the 'mixed magma' clasts in Roobol et al. (1987). SK-164 is the darker end member and SK-165 is the lighter end member.

<i>wt. %</i>	<i>SiO₂</i>	<i>Al₂O₃</i>	<i>Fe₂O₃</i>	<i>MgO</i>	<i>CaO</i>	<i>Na₂O</i>	<i>K₂O</i>	<i>TiO₂</i>	<i>P₂O₅</i>	<i>Total</i>
<i>SK-164</i>	57.64	18.59	8.45	2.71	7.71	3.5	0.57	0.72	0.1	99.99
<i>SK-165</i>	60.26	17.68	7.69	2.06	6.94	3.94	0.64	0.67	0.11	99.99

<i>ppm</i>	<i>Sc</i>	<i>V</i>	<i>Cr</i>	<i>Mn</i>	<i>Ni</i>	<i>Cu</i>	<i>Zn</i>	<i>Rb</i>	<i>Sr</i>	<i>Y</i>	<i>Zr</i>	<i>Ba</i>	<i>La</i>
<i>SK-164</i>	20	124	42	1792	11	43	72	9	232	12	78	26	10
<i>SK-165</i>	15	80	15	1725	11	62	62	12	239	19	87	55	10

4.1.1.2 Trace Elements

Trace elements typically act as impurities within mineral phases where they may substitute for major elements with a similar valence or ionic radius (Winter, 2014). Different mineral phases selectively incorporate or exclude trace elements and so they are more sensitive to fractionation processes than the major elements, with incompatible trace elements typically being concentrated within a melt as it forms, and compatible trace elements becoming comparatively enriched in the solid (Winter, 2014). Due to this, trace elements can be effective indicators of a melt source, and also of the extent of melting or crystallisation based

upon the relative enrichment of different trace elements. The trace elements seen in the St Kitts rocks are typical of subduction-related magmas, such as depletion of Nb and Ta compared to La and relatively high Ba/La and Sr/Nd ratios (Toothill *et al.*, 2007). Absolute abundances of REE, a sub-group of trace elements, increase from basalts to andesites (Toothill *et al.*, 2007).

K/Rb ratios for the St Kitts tholeiitic suit are higher than those seen in other deposits in the Lesser Antilles. The values are still comparatively low for other island arcs, around 500 (Baker, 1984; Brown *et al.*, 1977). There is no difference observed in Ti/Zr ratios between younger and older deposits on St Kitts. The values seen in the St Kitts rocks are higher than those observed on neighbouring Monserrat (Baker, 1984; Brown *et al.*, 1977).

Younger pyroclastic flows on Mt Liamuiga have relatively high Zr/Y ratios. This could be due to the nature of the source and different degrees of partial melting, though it is most likely due to the younger rocks at Mt Liamuiga have undergone greater fractionation of phases enriched in Y relative to Z (Baker, 1984). Ni concentrations are low in younger St Kitts rock. Low Th/U ratios observed in the St Kitts deposits are indicative of a depleted mantle source. Pb concentrations are comparatively low to neighbouring Montserrat (Baker, 1984).

The St Kitts basaltic rocks are low in Ba, Nb, Zr, Sr, Rb, Ni, and Cr (Baker, 1968a; Baker and Holland, 1973; Brown *et al.*, 1977; Toothill *et al.*, 2007). They have relatively high K/Rb and K/Ba ratios of 140 and 30 respectively, compared other deposits in the Lesser Antilles. St Kitts rocks are transitional towards island arc tholeiites, compared to the general trend in the Lesser Antilles, which are more typically calc-alkaline rocks (Baker, 1984; Baker and Holland, 1973). Sr is slightly concentrated in the andesites, while Ba increases with an increase in SiO₂ (Baker, 1968a).

Toothill *et al.* (2007) suggest that while the major elements suggest an open system, with evidence of magma mixing, the trace elements are more indicative of fractional crystallization in a closed system. Another explanation for the trends observed may be contamination by sediments in the crust. Pb correlated with SiO₂, Ba/La and La/Sm evidence suggesting that assimilation-fractional-crystallization may play a role.

4.1.2 Petrography of the St Kitts

Baker (1968) stated that the majority of the deposits from Mt Liamuiga were porphyritic, with plagioclase as the dominant phenocrysts. In the basaltic andesites, plagioclase with core compositions of An₇₅ is the most abundant phenocryst. Small quantities of orthopyroxene and clinopyroxene were present in basaltic andesites, and hypersthene was present in the andesites. Amphibole in the form of hornblende is typical in the andesitic pumice. Olivine is observed in the basaltic andesites, and it is occasionally seen as xenocrysts in the andesites (Baker, 1968a; Toothill *et al.*, 2007). Quartz is also listed as identified in the andesites. The groundmass of the deposit is typically composed of varying quantities of plagioclase, clinopyroxene, orthopyroxene, hypersthene, magnetite, cristobalite and/or areas of glass. In the basaltic andesites, the groundmass consists of laths of plagioclase, clinopyroxene and orthopyroxene, set in a dark glassy matrix. In the andesites, the groundmass was described as consisting of plagioclase, hypersthene, magnetite and cristobalite, with clinopyroxene only appearing as occasional microphenocrysts (Baker, 1968a; Toothill *et al.*, 2007).

The andesitic lapilli and pumices of the Mansion series are described as 'nearly aphyric', with sparse phenocrysts of plagioclase and hornblende (Baker, 1968a). The Steel Dust Series, a group of andesitic dusts on the western side of Mt Liamuiga, is considered to be the youngest

deposit from the volcano. These contain both crystalline and lithic fragments, and are similar in composition to the two-pyroxene andesites (Baker, 1968a).

4.1.3 Geochemical and petrographic background of Nevis

The volcanic deposits on Nevis have a basaltic to dacitic composition (Hutton, 1968; Hutton and Nockolds, 1978; Koon Koon, 2012). The material erupted from the main cone, Nevis Peak, is described as being composed mainly of porphyritic dacite (Hutton and Nockolds, 1978; Koon Koon, 2012). The compositional range given for this material is 58.17% SiO₂ to 60.4% SiO₂, so can be classified as andesitic (Hutton and Nockolds, 1978). The mineralogy of these rocks consists of plagioclase, hornblende and orthopyroxene phenocrysts. The plagioclase is zoned and appears as 5 mm phenocrysts to small groundmass crystals less than 0.03 mm across. Inclusions are abundant in phenocrysts. Rare crystals of quartz can be found in some rocks. The groundmass is composed of plagioclase, pyroxene, hornblende, granules of iron oxide and cristobalite, sometimes with small amounts of pale-brown glass (Hutton and Nockolds, 1978).

The two domes, one on the main crater floor and the other on the northern outer slopes of the main dome, are thought to be of relatively recent origin. Hutton and Nockolds (1978) described rocks from the dome on the northern outer slopes; these rocks are described as vitrophyric hornblende orthopyroxene dacites, which are strongly porphyritic with a pinkish-grey colour and show banding. The phenocrysts consist of plagioclase and hornblende, with some orthopyroxene and quartz and make up half of the rock. The hornblende phenocrysts locally display a parallel preferred orientation. The groundmass is mainly glass, with areas of plagioclase, orthopyroxene and iron ore microlites. Pyroclastic density current (PDC) deposits

(consisting entirely of block and ash flows) show a similar mineralogical composition to the dome rocks described (Hutton and Nockolds, 1978).

4.1.4 Microlites

Microlites are crystals with a cross-sectional area of $<100 \mu\text{m}^2$ (Clarke et al., 2007). They are formed during magma ascent from a reservoir to the surface, from an increase in the liquidus temperature due to water exsolution or vesiculation triggered by magma decompression. They provide crucial insights into the pre- and syn- eruptive conditions in a conduit, most importantly ascent rate. Microlites have been studied in deposits on neighbouring islands (Fedele *et al.*, 2021; Martel and Poussineau, 2007; Murch and Cole, 2019), but not in deposits from St Kitts and Nevis. The nature of the microlite crystals in the samples analysed from Mt Liamuiga and Nevis Peak are explored in detail in Chapter 5.

4.1.5 Glass compositions

Glass compositions can provide a record of magma recharge and mixing, magma ascent rate, and syn-eruptive mixing (Cashman and Edmonds, 2019), and reflects the composition of the original melt (Czuppon *et al.*, 2012). Brown isotropic glass occurs in the matrix of some basaltic to andesitic deposits from Mt Liamuiga. The composition of glass is commonly andesitic to rhyolitic (Toothill *et al.*, 2007). Some glass data displayed large variations in the $\text{Na}_2\text{O}/\text{K}_2\text{O}$, thought to be the result of the electron microprobe beam encroaching on microlites within the glass (Toothill *et al.*, 2007).

Residual patches of dark brown glass and devitrified glass have been identified in samples collected from Nevis Peak (Hutton and Nockolds, 1978). No glass composition data has been published for Nevis.

4.2 Method

4.2.1 Sample selection and preparation

Thirty-five samples in total were collected from St Kitts and Nevis during the 2019 fieldwork outlined in Chapter Four. Four of these were charcoal samples, seven were collected from the Steel Dust series and one consisted of a bulk lapilli sample. Twenty-four samples were collected from PDC and fallout deposits, sixteen from St Kitts and seven from Nevis. Two of the sixteen St Kitts samples were considered to be older than the target deposits, so were excluded due to being outside the scope of this study. The locations of the samples collected are shown in Figure 3.1 (Chapter 3).

4.2.2 Petrographic analysis

Both hand specimens and polished thin sections were used for petrographic analysis. Samples were washed, dried and cut to allow detailed observations to be made in hand specimens. Twenty-three hand specimens, sixteen from St Kitts and seven from Nevis, were assessed for textural characteristics and images were taken of all hand specimens using a Nikon SS900 digital camera. Mineralogy and textural characteristics of thirteen polished thin sections (eleven from St Kitts and two from Nevis) were identified and described using Nikon Alphaphot 2 YS2-Hpolarising light microscope and as well as SEM.

4.2.3 Geochemical analysis

4.2.3.1 *WD XRF*

Sample selection

Twenty samples from both St Kitts and Nevis were selected for major element Wavelength Dispersive X-ray fluorescence (WD XRF) analysis. These samples were chosen for their range

of textural characteristics to establish the compositional variation of the most recent volcanic deposits on St. Kitts and Nevis (described in appendix 1). WD XRF analysis was selected for these samples as it allowed fast and accurate data collection of major elements using a non-destructive technique (for example, no need for acid digestion). While XRF has a relatively high limit of detection (LOD), measuring parts per million (ppm) was adequate to meet the aims of this project.

XRF uses X-rays produced by a source to excite the elements within the sample. The X-rays are produced by X-ray tubes. These contain a filament and an anode within a vacuum. An electrical current is passed through the filament and releases electrons. A high voltage is applied to the filament to accelerate the electrons along the tube towards the rhodium anode. As the electrons hit the anode they are decelerated. This causes the emission of X-rays. The current and voltage applied to the filament are altered to adjust the peak on wavelengths and intensities. This excites different elements, allowing the composition of the sample to be analysed (Brouwer, 2010).

Each element emits fluorescent x-ray radiation with discrete energies. These energies are characteristic of individual elements. By measuring the energies of the radiation emitted, the elements present in the sample can be identified. Measuring the intensity of the energies allows the concentration of each element present to be determined.

The WD-XRF spectrometer performs sequential analysis from the heaviest to the lightest elements. Two detectors are used; the gas proportional detector, which measures elements Be to Cu, and the Scintillation detector, which measures elements Cu to U.

Spectrometers analyse only the sample surface, so the surface must be representative of the entire sample. Matrix effects may lead to bias, therefore must be addressed during sample

preparation and calibration. Matrix effects include particle distribution effect, sample density, sample roughness, particle size effect, mineralogical effect and critical depth. The particle distribution effect can be prevented by ensuring the sample is homogeneous and without over-representation across the surface. Analysing pressed pellets instead of loose powders reduces the particle distribution, sample roughness and particle size effects. Preparing fused glass beads reduces the mineralogical effects and provides the best sample geometry for analysis. Calibration can adjust for elements exciting each other. A Certified Reference Material (CRM) can be analysed alongside samples to assess the influence of matrix effects (Brouwer, 2010).

Preparation

Twenty samples were selected for major element XRF analysis. The samples were selected for their significant light/dark colour, as well as textural variations. Light and dark end-members were selected for the SK5, SK8 and SKN19 samples. Descriptions of each sample were made before starting the preparation process.

The samples were crushed using a jaw crusher. Samples were cut into small blocks (<50mm in length) and put through the Jaw crusher twice, reducing the size of the gap between the plates on the second run. The sample material was crushed to pieces <5mm in size. The plates in the jaw crusher were cleaned with water, dried with paper towels and left on a hot plate for 2 minutes between each sample.

The crushed sample material was milled using an agate ring and puck mill bowl in a Retsch Vibratory Disc Mill RS 100 for 7 minutes 30 seconds. Contamination of samples was avoided by maintaining a clean working environment, thoroughly cleaning the mill parts and sample dishes between uses, drying parts with paper towels and leaving on a hot plate for 2 minutes

between the milling of each sample. The milled sample powders were dried in an oven for a minimum of 2 hours at 120°C.

After an unsuccessful trial of the fusion of glass beads, with the beads cracking due to small amounts of powder remaining after fusion. All samples were milled for an additional 3 minutes using the same agate ring and puck mill bowl in the Retsch Vibratory Disc Mill RS 100. The analysis of the trial beads returned results that total over 100% in composition, suggesting a flaw in the original methodology. To correct this, all powders were dried in an oven at 120°C for 24 hours to drive off any remaining water. The flux was also dried in an oven for 24 hours to ensure it contained no moisture. Both the additional milling and extended dry time appear to have solved the preparation methodology flaws.

[Fusion of glass beads for major element analysis](#)

The preparation of glass beads was chosen to limit the mineralogical effects and to gain the best geometry for major element analysis.

0.9 grams of sample and 9 grams of lithium tetra/metaborate flux (66:34) (Claisse) were measured into a platinum crucible using a Salter ER-182A balance. The sample and flux were thoroughly mixed with a platinum spatula. Ammonium Iodide pellet was added as a releasing agent. The glass beads were fused in a Proalytics PANalytical Eagon 2 fusion system at a fusion temperature of 1200°C, with a melt time of 180 seconds and a mixing time of 420 seconds at an angle of 45°. The repeatability of the procedure was assessed by fusing three samples in triplicate.

Pressed pellets for trace element analysis

Pressed pellets were prepared for trace element analysis. Eight grams of sample and 2 grams of Ceridust binding wax were mixed in an agate bowl for 30 seconds at 300rpm using a Fritsch GmbH Planetary Mill pulverisette 5. The mixed samples were pressed at 150kN using a Herzog TP20 manual press to produce pressed pellets. The repeatability of the procedure was assessed by producing pressed pellets for three samples in triplicate.

XRF analysis

The fused glass beads and pressed pellets were analysed using Wavelength Dispersive X-ray fluorescence (WD XRF). This geochemical analysis was completed using the PANalytical Wavelength Dispersive X-Ray Fluorescence Spectrometer (WD-XRF) Axios Max in the Consolidated Radio-isotope Facility (CORIF), University of Plymouth. The samples were analysed under vacuum in 37mm cups. A Certified Reference Material (CRM), OKUM (an ultramafic rock powder, typical of an Mg-poor komatiite or komatiitic basalt), was analysed alongside the fused beads to validate the data collected.

The PANalytical Wroxi and Protrace applications were used to process the major element and trace element data respectively. The settings for these applications are shown in the Table 4.2 below.

Table 4.2 - Settings for the Wroxi applications, for major elements of interest.

Channel	Line	Collimator	Detector	kV	mA	Angle
Fe	KA	150µm	Flow	60	66	85.7634
Ca	KA	150µm	Flow	30	133	133.1152
K	KA	150µm	Flow	30	133	136.6658
Si	KA	300µm	Flow	25	160	109.0368
Al	KA	300µm	Flow	25	160	144.8480
Mg	KA	300µm	Flow	25	160	22.8722
Na	KA	300µm	Flow	25	160	27.6494

4.2.3.2 Electron Microprobe

Major element compositions of the interstitial glass, microlite crystals and plagioclase phenocrysts were determined using JEOL JXA8530F Hyperprobe field-emission electron probe microanalyser (EPMA) at the University of Bristol. Element abundances were determined using wavelength dispersive spectroscopy (WDS). Standards for calibration of the spectrometers included a range of silicates and oxides. Analyses on glass and microlites were performed using a 15kV accelerating voltage, 5 nA beam current and a defocused spot size of 5 µm. This small beam size was chosen to allow precision targeting of unaltered patches of glass and single microlite crystals. A 10 µm defocused spot size was used to perform analysis on phenocrysts.

4.2.3.3 SEM

A total of twenty-nine samples were selected for SEM analysis; thirteen polished thin sections and sixteen polished blocks.

Sixteen samples, fourteen from St Kitts and two from Nevis, were selected as typically representative of the deposits they were collected from. These samples were cut to fit resin

moulds. Epoxy resin was mixed using a resin to hardener ratio of 100:30. Resin moulds containing the sample and resin mix were placed into a Fistreem Digital Vacuum Oven for 20 minutes to ensure the removal of air from any brecciated and pumice material. Resin blocks were placed on a hot plate at 60°C for 48 hours to harden.

Thirteen polished thin sections were used for SEM analysis. These thin sections were selected from samples typical of the deposits they were collected from, or showing textural features of interest (e.g. banding or inclusions). These were prepared by the Open University rock preparation and polishing laboratories.

A 10nm carbon coat was applied to all polished blocks and thin sections using the Quorum Q150T Coating System, to prevent charging in the SEM. All samples were analysed using the JEOL JSM-7001F Field Emission Scanning Electron Microscope (SEM) at the Plymouth Electron Microscopy Centre (PEMC). Point data and element maps were collected using Energy Dispersive Spectroscopy (EDS) and analysed using Oxford Instruments Aztec. The wt. % elemental data collected was converted into wt. % oxides.

4.3 Results

4.3.1 Petrography

The polished thin sections of samples from Mt Liamuiga were studied to understand and interpret the textures and mineralogy on the microscopic scale. Thirteen samples were chosen for petrographic analysis, eleven from St Kitts and two from Nevis; SK1E, SK1, SK5, SK5D, SK8D, SK8L, SK8 (banded), SK20, SK21, SK30, SK31, SKN18, SKN19.

4.3.1.1 Petrological overview of the Mt Liamuiga samples

The St Kitts samples showed similar phenocryst phases throughout all of the samples, although the abundance of each phase varied. The main phenocryst phase in all samples was plagioclase (20-40%), and ranged from <1 mm to a maximum of 4 mm in size, although plagioclase phenocrysts typically did not exceed 2.5 mm in length (Figure 4.1). Pyroxene (10-30%) and opaque minerals were also present in every sample (Figure 4.1, and Table 4.3). Amphibole was less common (0-5%), present in three of the samples, while quartz was present only within inclusions (Table 4.3).

Complex zoning was observed in the plagioclase phenocrysts, while only some pyroxene phenocrysts showed evidence of zoning, examples of which are shown in Figures 4.2 and 4.3. Zoning was not observed in the amphibole phenocrysts. Sieve-textured plagioclase crystals were ubiquitous in the St Kitts samples (examples shown in Figures 4.2 and 4.3). Glomerocrysts composed of plagioclase and pyroxene were common, and were observed in the majority of samples (as shown in Figures 4.1 and 4.4).

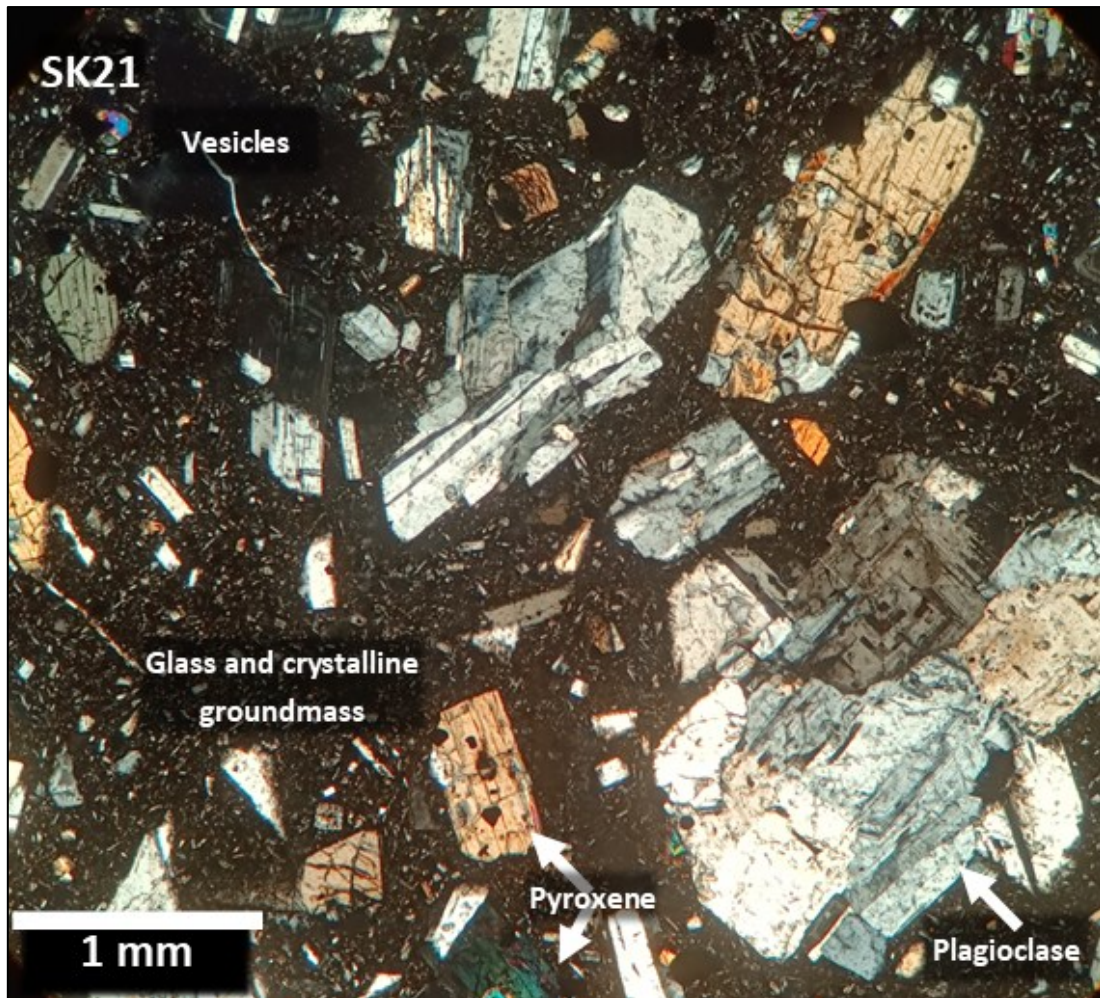


Figure 4.1 - Photomicrograph showing sample SK21 in cross polarised light. The two main phenocryst phases, plagioclase and pyroxene, and the glass and crystalline groundmass, are labelled.

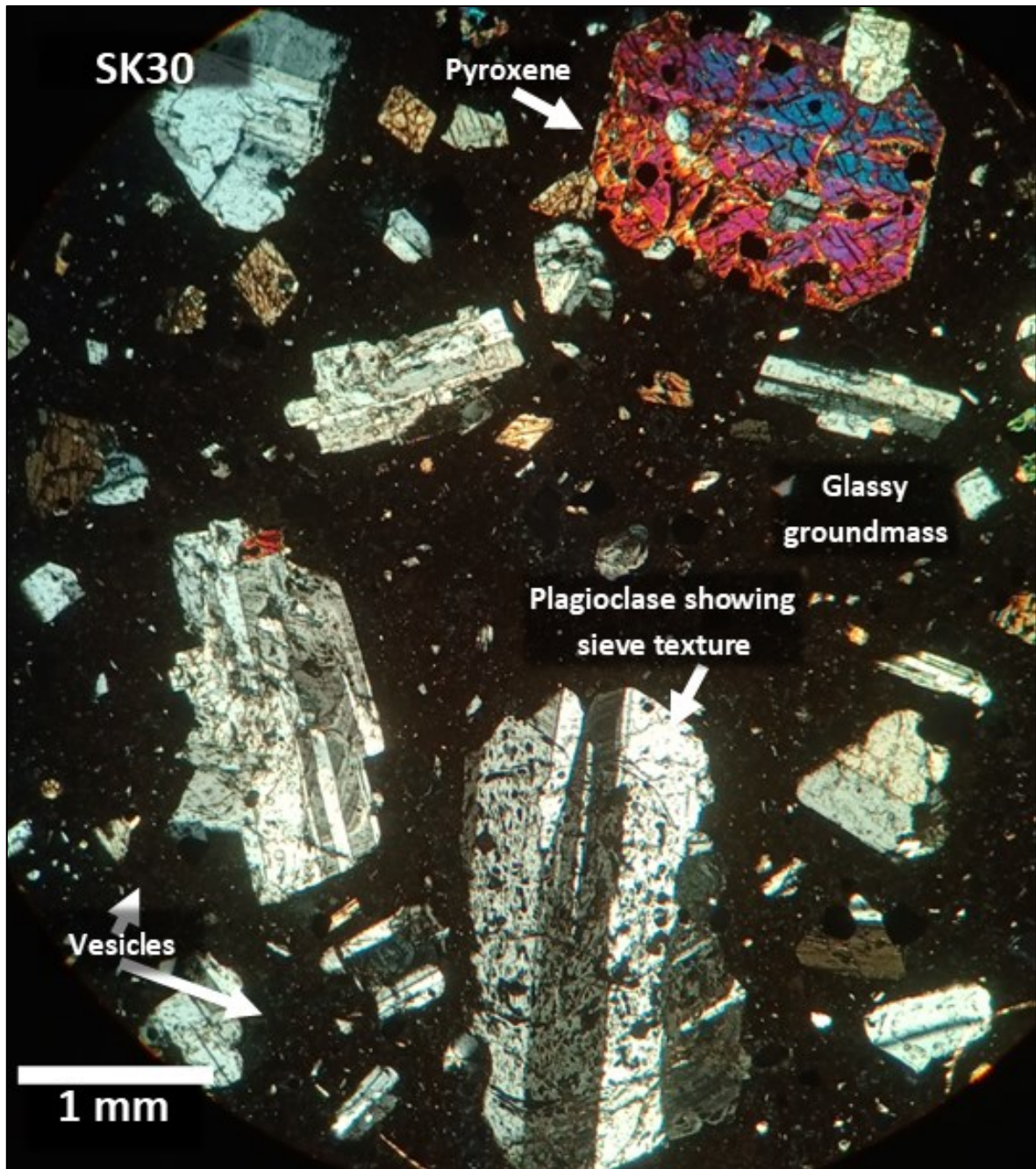


Figure 4.2 - Photomicrograph showing sample SK30 in cross polarised light. This image shows the typical phenocryst textures observed in the Mt Liamuiga samples; sieve textures, zoning and glomerocrysts.

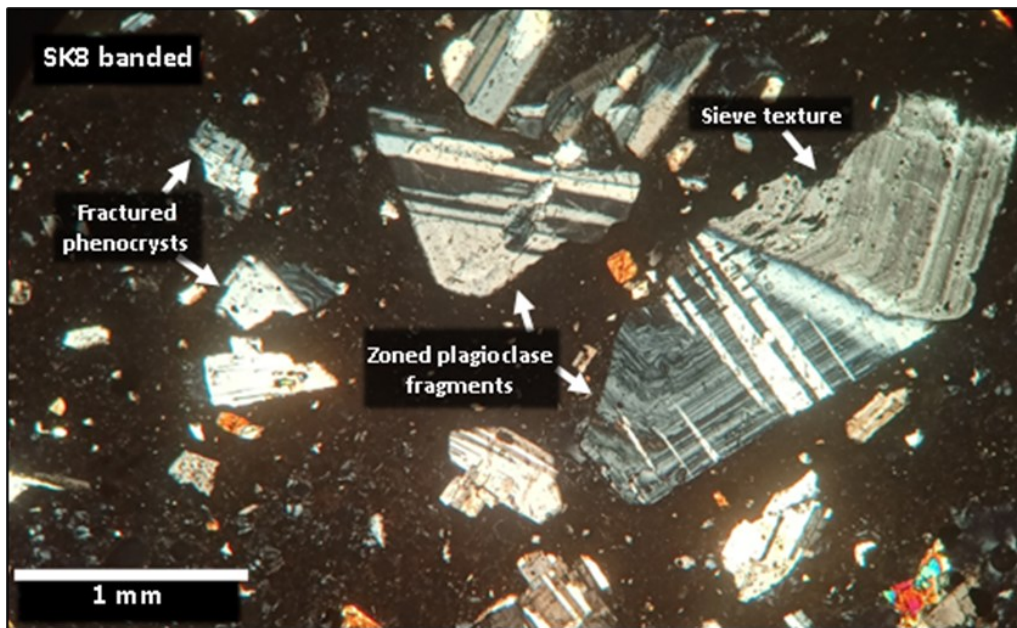


Figure 4.3 – Photomicrograph showing the typical characteristics of plagioclase phenocrysts in SK8 banded in cross-polarised light. Fine oscillatory zoning, sieve texture, reabsorbed crystals and fractured crystals are present.

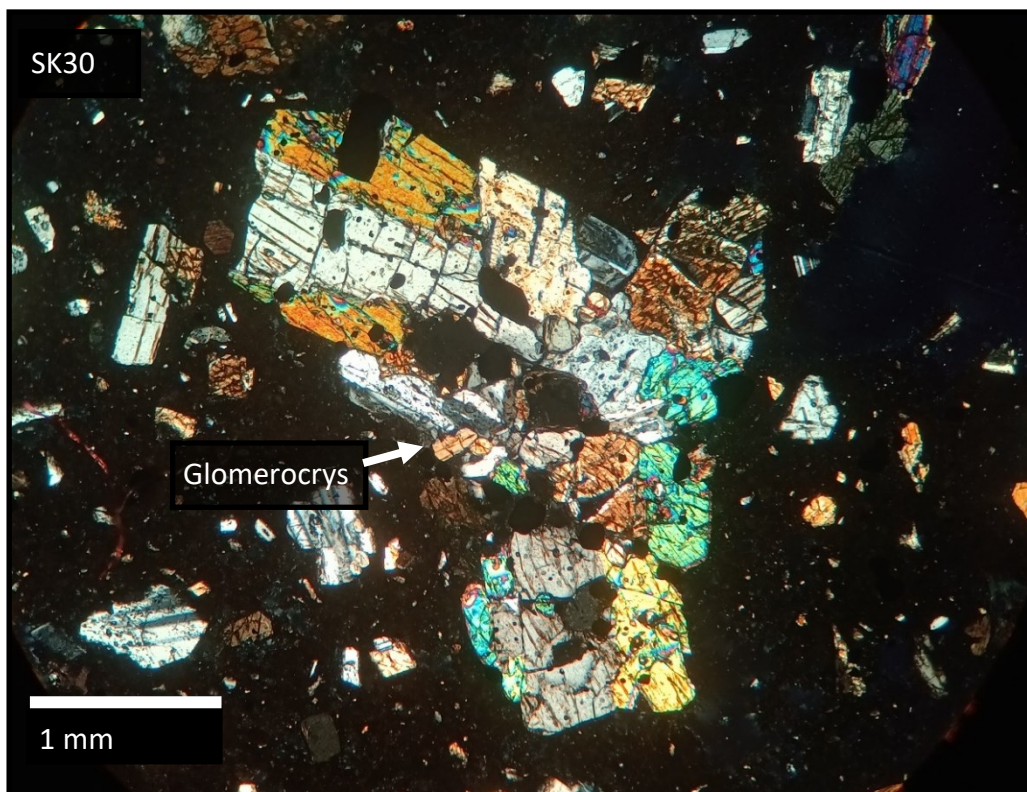


Figure 4.4 – Photomicrograph showing a large glomerocryst found in SK30, in cross polarised light.

Reaction rims were present around some amphibole phenocrysts (Figures 4.5) in samples SK1, SK5L, and SK8L. The amphibole phenocrysts in samples SK1 and SK5L showed either thin or no reaction rims. Sample SK5L contains a larger number of amphibole phenocrysts, most of which are fractured and exhibit thin reaction rims. The amphiboles in SK8L all showed thick reaction rims. In some cases, the amphibole crystals had broken down, completely dehydrating to Fe-oxides and pyroxenes.

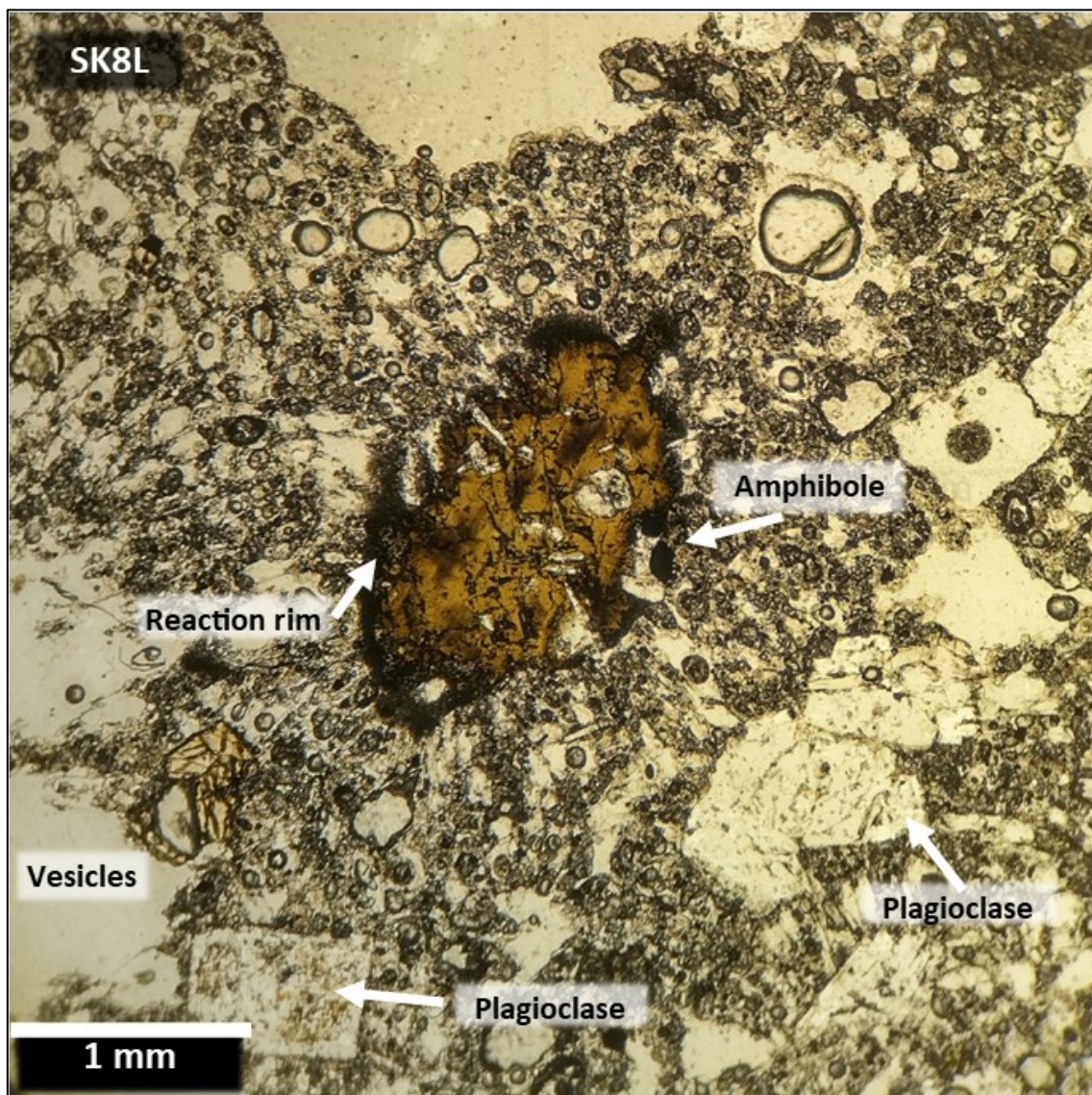


Figure 4.5 – Photomicrograph of SK8L showing reaction rim around an amphibole phenocryst.

Vesicularity varied between the samples, ranging from 5% to 50% vesicles, estimated based on visual inspection of the thin sections. High levels of vesicularity were observed in the fallout pumices, for example 50% in samples SK1 and SK11, while much lower levels of vesicularity were observed in the darker, glassier samples, for example 5-15% in samples SK20 and SK21.

The groundmass in the Mt Liamuiga samples was typically glassy, with varying levels of crystallisation. The groundmass in some samples was composed almost entirely of glass, with few crystals present, such as sample SK8L. In other samples, groundmass crystallisation was more dominant, with microphenocrysts of plagioclase, pyroxene and opaque minerals (likely magnetite) present. Microlite crystal population density varied between samples. In general, the Mt Liamuiga samples showed a low abundance of microlites, with samples commonly containing no or few microlites. Samples containing more microlites still showed low abundances compared to a typical 'microlite-rich' sample. The nature of the microlite crystals are discussed further in Chapter 5.

Enclaves were observed in the Mt Liamuiga samples SK8 and SK1 (Figures 4.6 and 4.7). A single, large enclave was examined in thin section SK1E, while smaller fragments of the same material were observed throughout SK1 and SK8. The enclaves present in both samples were similar in nature, composed mainly of quartz and plagioclase, with some amphibole and pyroxene phenocrysts. SK1E had a vein of quartz with the enclave. No chilled or baked margins were observed around any of the enclaves, and there was no evidence of any interaction with the host magma.

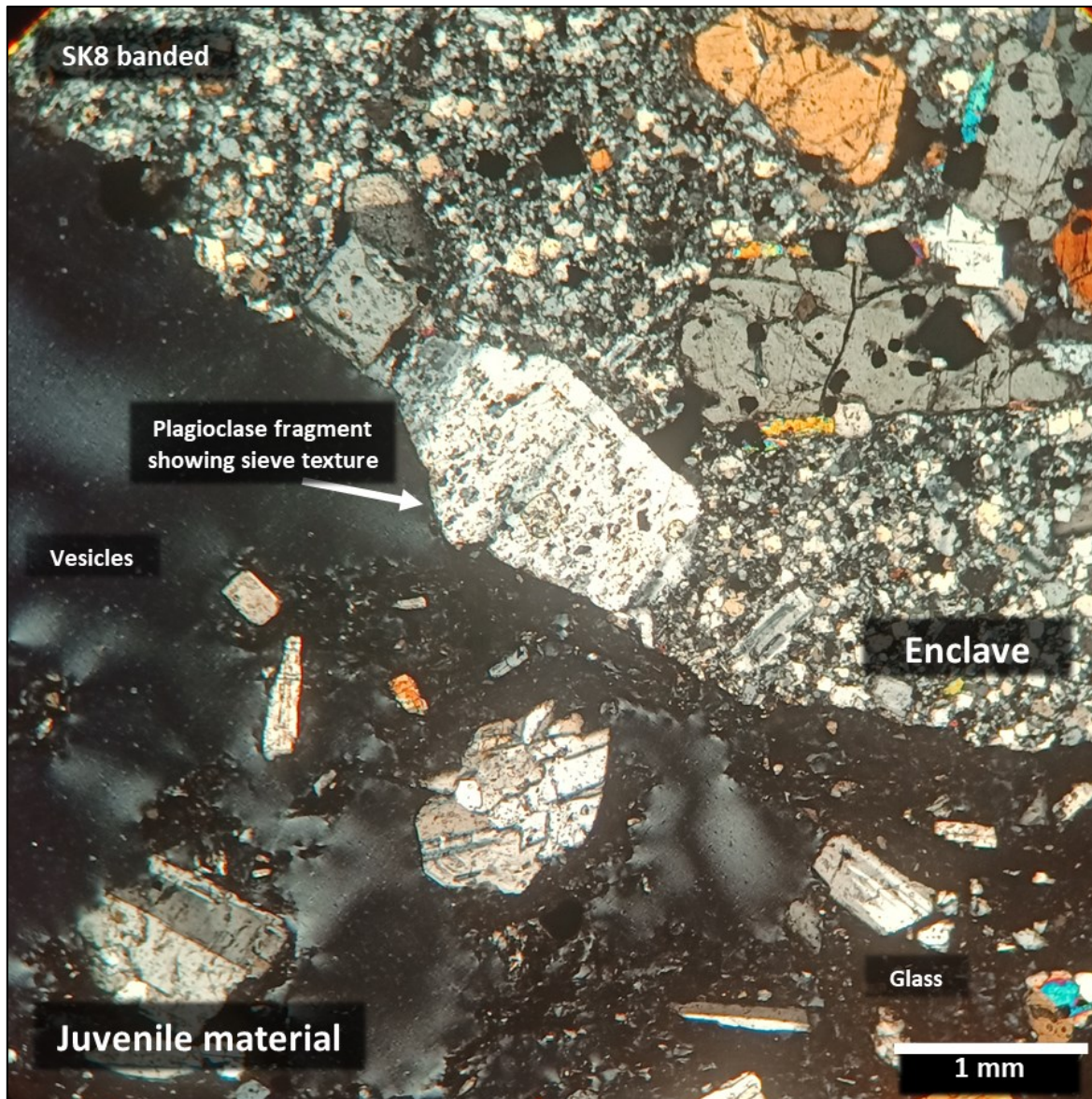


Figure 4.6 – Photomicrograph showing the difference in textures between the enclave and juvenile material in SK8, shown in cross polarised light.



Figure 4.7 – Photomicrograph showing the difference in groundmass textures between the enclaves and juvenile material (highly crystalline enclave and the glassy juvenile material) in SK1E, shown in cross polarised light.

4.3.1.2 Petrological overview of the Nevis Peak samples

The polished thin sections of samples from Nevis were studied to understand and interpret the textures and mineralogy on the microscopic scale.

The Nevis samples show different mineralogy compared to St Kitt's. The primary phase of the two Nevis samples was plagioclase (~40%), whilst they also contained an abundance of amphibole (10-30%), with pyroxenes (20-30%) and opaque minerals (~10%) also present. The plagioclase and pyroxene phenocrysts in Nevis samples appear to show little evidence of being fragmented, compared to the Mt Liamuiga samples.

Sieve-textured plagioclase crystals were prevalent in the Nevis samples (Figure 4.8).

Glomerocrysts of plagioclase and pyroxene were also common, and were observed in both of the samples from Nevis.

The groundmass found in the Nevis samples was more crystalline and contained a higher abundance of plagioclase microlites than the Mt Liamuiga samples. The microlite populations observed in the St Kitts and Nevis samples are discussed further in Chapter 5. Plagioclase, pyroxenes and opaque (inc. magnetite) minerals are also prevalent in the groundmass of these samples.

Amphibole phenocrysts in the Nevis samples showed a range of reaction rims; no or thin reaction rims were observed in SKN18, whereas a significant number of the phenocrysts in SKN19 showed thick reaction rims, although many other smaller phenocrysts showed only very thin reaction rims. In some cases, the amphibole crystals have broken down, completely dehydrating to Fe-oxides and pyroxenes. These reaction rims are shown in Figure 4.9.

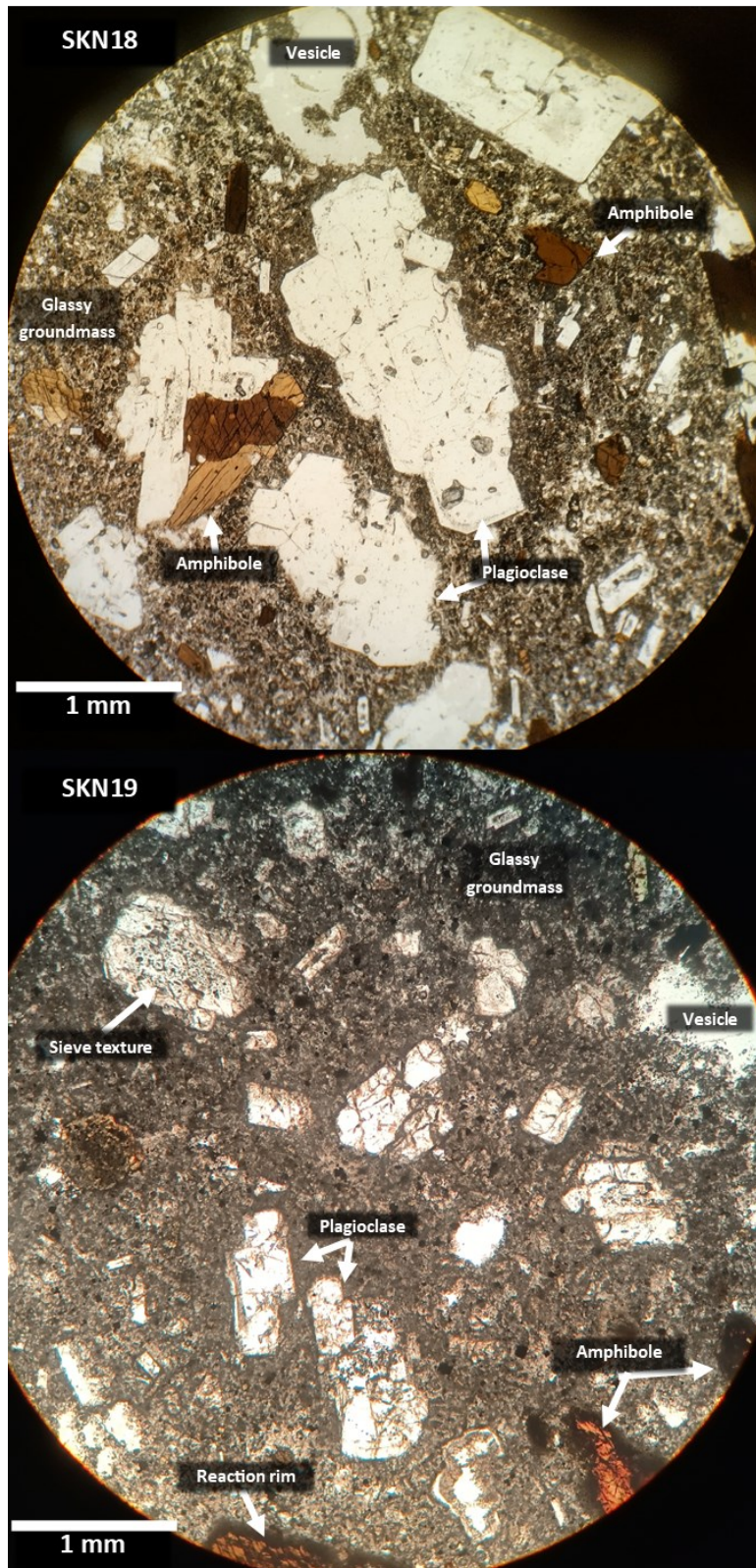


Figure 4.8 – Photomicrograph of SKN18 (top) and SKN19 (bottom) in plane polarised light. This image shows the typical texture of the Nevis Peak samples, including amphibole phenocryst with reaction rims.

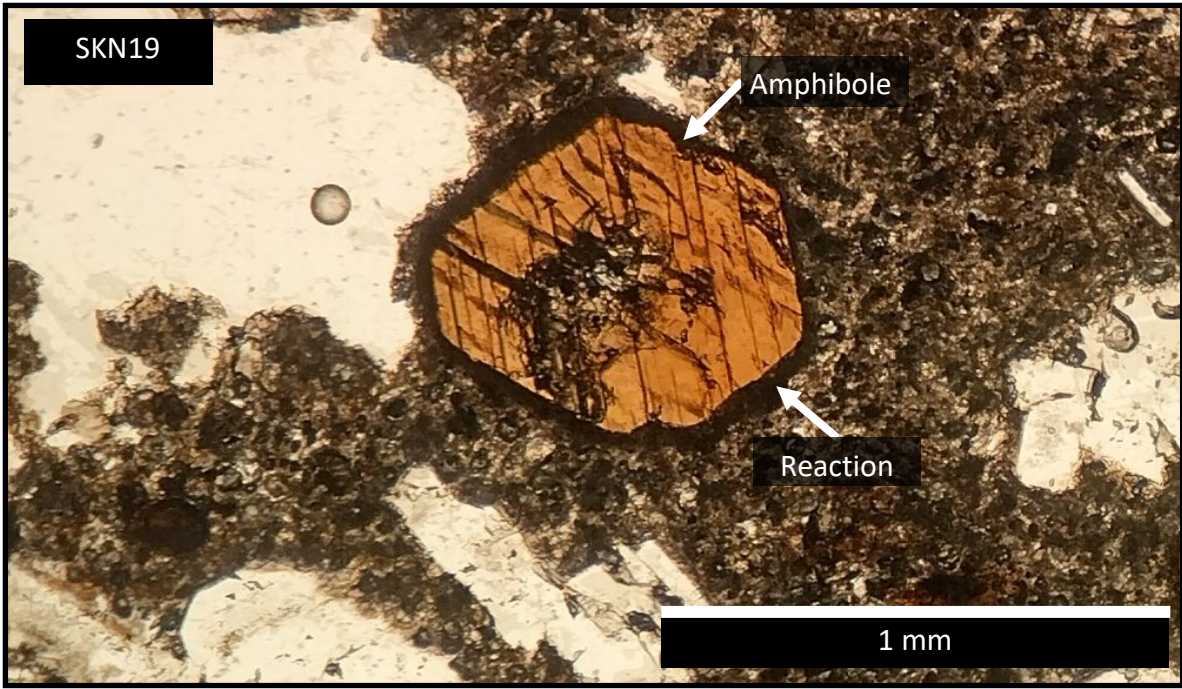


Figure 4.9 – Photomicrograph showing an amphibole phenocryst in SKN19 surrounded by a reaction rim.

Table 4.3 - Table of petrographic analysis of the Mt Liamuiga and Nevis samples. Modal abundances and vesicle areas were estimated based on a visual inspection of the sample. The number of 'x' symbols indicates the relative phenocryst abundance, for example, x = very rare and XXXX = abundant.

Sample	Rock type (TAS)	Pl	Px	Amb	Op	Other Mineralogy	Texture	Zoning	Other comments	% Vesicles	Phenocryst comments	% Plag phenocrysts	Plag size min (mm)	Plag size max (mm)	Plag phenocryst form
Mt Liamuiga SK1	Andesite pumice	XXX X	XX	tr	x	N/A	Porphyritic Vesicular Glassy	Zoning in Pl and some Px	Glomerocrysts of Pl and Px phenocrysts. Altered glass in the sample (mottled).	50%	Dominant phenocryst is Pl. Difficult to tell the difference between single or fragmented phenocrysts.	50%	<1	1.5	Subhedral to anhedral
SK1E (Main sample)	Andesite pumice	XXX X	XX	X	x	N/A	Porphyritic Vesicular Glassy	Zoning in Pl and some Px		50%	Dominant phenocryst is Pl. Basal sections of pyroxene. Sieve texture was observed in Pl phenocrysts.	50%	<1	1.5	Subhedral to anhedral
SK1E (enclave)	Andesite pumice	XXX X	X	N/A	x	Quartz	Porphyritic Crystalline groundmass	Zoning in Pl	Veins of quartz, groundmass of Pl, and mafic minerals appear almost absent.	0%	Dominant phenocryst is Pl. Few opaque phenocrysts, no other phenocrysts are present.	40%	<1	1.0	Subhedral to anhedral
SK5 Lighter end-member	Andesite	XXX X	XX	XX	x	N/A	Porphyritic Vesicular Glassy	Zoning in Pl and some Px	Glomerocrysts of Pl and Px.	30%	Dominant phenocryst is Pl. Sieve textured observed. Difficult to tell the difference between single or fragmented phenocrysts	30%	<1	2.0	Subhedral to anhedral
SK5 Darker end-member	Andesite	XXX X	XXX	tr	X	N/A	Porphyritic Vesicular Glassy	Zoning in Pl and Px	Glomerocrysts of Pl and Px.		More phenocryst rich than the lighter end-member. Sieve textured observed.	60%	<1	2.5	Subhedral to anhedral

<i>SK5D</i>	Dacite	XXX X	XX	N/A	X	N/A	Porphyritic Vesicular Glassy	Zoning in Pl		60%	Evidence of alteration. Sieve textured observed. Fragmented phenocrysts.	40%	<1	2.0	Subhedral to anhedral
<i>SK8 banded (enclave)</i>	Andesite	XXX X	X	N/A	X	Quartz	Porphyritic Vesicular Glassy	Zoning in Pl and some Px	The groundmass of Pl and quartz with phenocrysts present.	~0%	Sieve textured observed. Fragmented phenocrysts. Dissolution of phenocrysts.	80%	0.5	2.0	Subhedral to anhedral
<i>SK8 banded bands</i>	Andesite	XXX X	XX	N/A	X	N/A	Porphyritic Vesicular Glassy	Zoning in Pl and some Px	Bands show different glass content and vesicularity. Glass appears altered in the darker bands. Lighter bands contain fewer vesicles and more altered glass. No variation in crystallinity.	40%	Sieve textured observed. Fragmented phenocrysts. Dissolution of phenocrysts.	60%	<1	2.5	Subhedral to anhedral
<i>SK8D</i>	Andesite	XXX	XX	tr		N/A	Porphyritic Vesicular Glassy	Zoning in Pl and Px	Small glomerocrysts of Pl and Px. Basal sections of Px.	10%	Sieve textured observed. Fragmented phenocrysts. Dissolution of phenocrysts. Irregular shapes are common.	80%	<1	2.0	Subhedral to anhedral
<i>SK8L</i>	Andesite	XXX	X	tr	x	N/A	Porphyritic Vesicular Glassy	Zoning in Pl and Px	Small glomerocrysts of Pl and Px. More crystalline groundmass, fewer glassy areas.	15%	Sieve textured observed. Fragmented phenocrysts. Dissolution of phenocrysts.	40%	<1	2.5	Subhedral to anhedral

SK20	Andesite	XXX	XXX	N/A	X	N/A	Porphyritic Vesicular Glassy	Zoning in Pl and Px	Glass is speckled/mottled (possibly due to thickness of thin section).	15%	Sieve textured observed. Fragmented phenocrysts. Dissolution of phenocrysts.	60%	<1	2.0	Subhedral to anhedral
SK21	Andesite	XXX X	XX	N/A	x	N/A	Porphyritic Vesicular Glassy	Zoning in Pl and Px	Large glomerocrysts of Pl and Px.	5%	Sieve textured observed. Fragmented phenocrysts. Dissolution of phenocrysts.	80%	<1	3.1	Subhedral to anhedral
SK30	Andesite	XXX	XX	N/A	X	N/A	Porphyritic Vesicular Glassy	Zoning in Pl and Px	Large glomerocrysts of Pl and Px.	10%	Sieve textured observed. Fragmented phenocrysts. Dissolution of phenocrysts.	60%	<1	1.8	Subhedral to anhedral
SK31	Andesite	XXX	XX	N/A	X	N/A	Porphyritic Vesicular Glassy	Zoning in Pl and Px	Glomerocrysts of Pl and Px.	25%	Sieve textured observed. Fragmented phenocrysts. Dissolution of phenocrysts.	40%	<1	3.0	Subhedral to anhedral
<i>Nevis Peak</i> SKN18	Dacite	XX	x	XX	x	N/A	Porphyritic Vesicular Glassy	Zoning in Pl	Small glomerocrysts of Pl and Px.	10%	Sieve textured observed. Fragmented phenocrysts. Dissolution of phenocrysts.	40%	<1	2.0	Subhedral to anhedral
SKN19	Dacite	XX	X	XX	x	N/A	Porphyritic Vesicular Glassy	Zoning in Pl		5%	Sieve textured observed. Fragmented phenocrysts. Dissolution of phenocrysts.	40%	<1	1.5	Subhedral to anhedral

4.3.2 Whole-rock major and trace element analysis

The compositional breakdown from the WD XRF analysis (Section 4.2.3.1) of each sample from Mt Liamuiga and Nevis are shown below in Table 4.4, with the normalised data shown in Appendix 7.

4.3.2.1 Major element composition for Mt Liamuiga

Figure 4.10 shows a FeO*/MgO versus silica diagram, Figure 4.11 shows an AFM diagram and Figure 4.12 shows a K₂O versus silica plot. These plots can be used to distinguish between calc-alkaline and tholeiitic compositions in island arc systems. All three diagrams show that the Mt Liamuiga samples plot close to the calc-alkaline/tholeiitic boundary. The youngest Mt Liamuiga samples are typically shown to be tholeiitic, with the exception of the AMF diagram, where they plot as calc-alkaline. This is likely due to the two plots distinguishing tholeiitic from calc-alkaline compositions in similar, but not identical grounds. The FeO*/MgO versus silica diagram shows that the St Kitts samples had a medium-Fe composition.

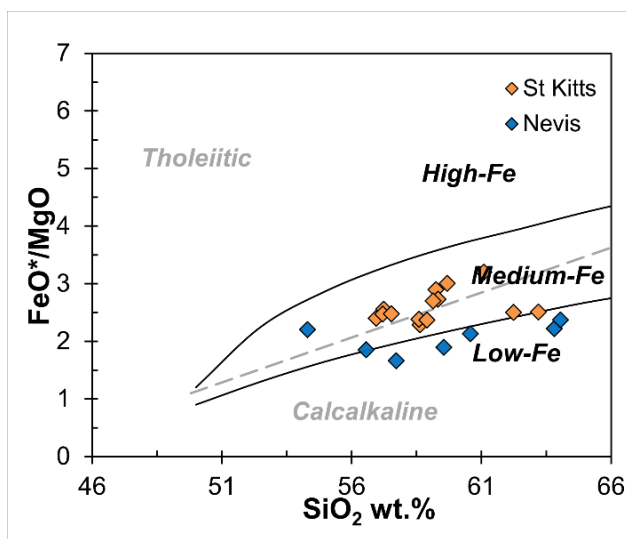


Figure 4.10 – FeO*/MgO versus silica diagram showing tholeiitic and calc-alkaline classifications.

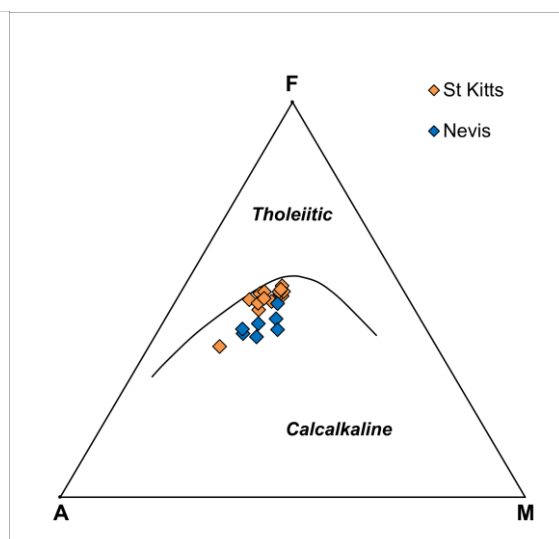


Figure 4.11 - AMF diagram showing tholeiitic and calc-alkaline classifications.

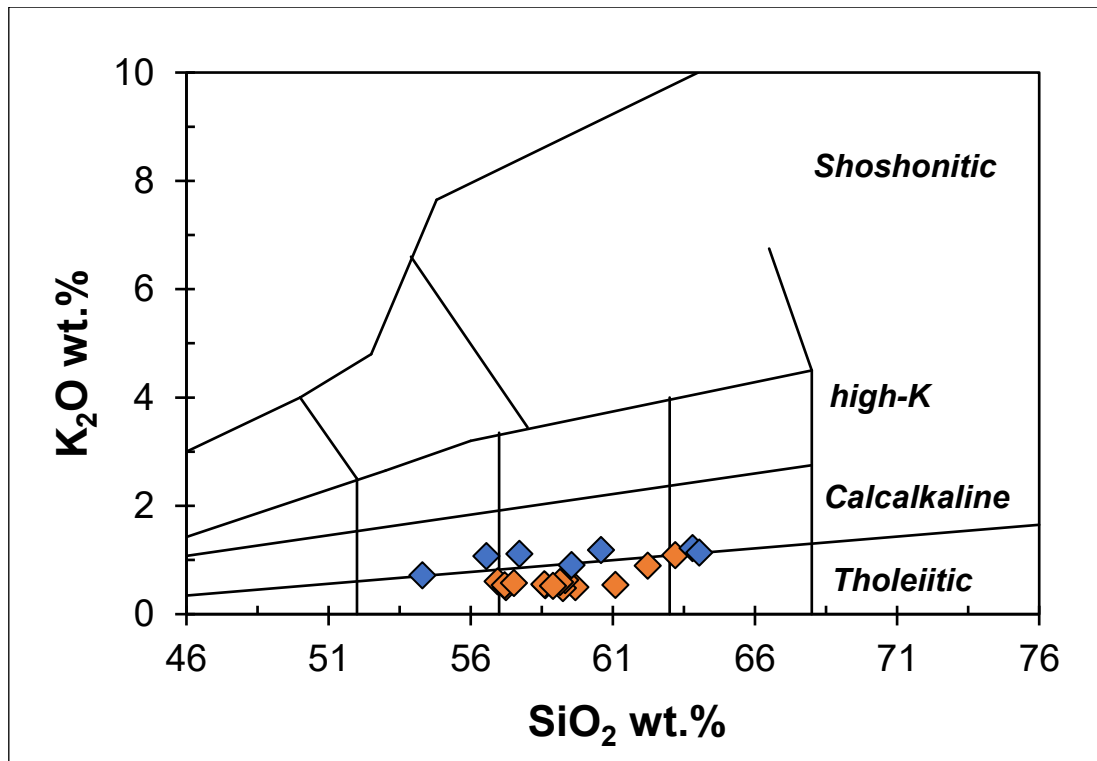


Figure 4.12 – K_2O shown against SiO_2 . This diagram shows the tholeiitic and calc-alkaline classifications.

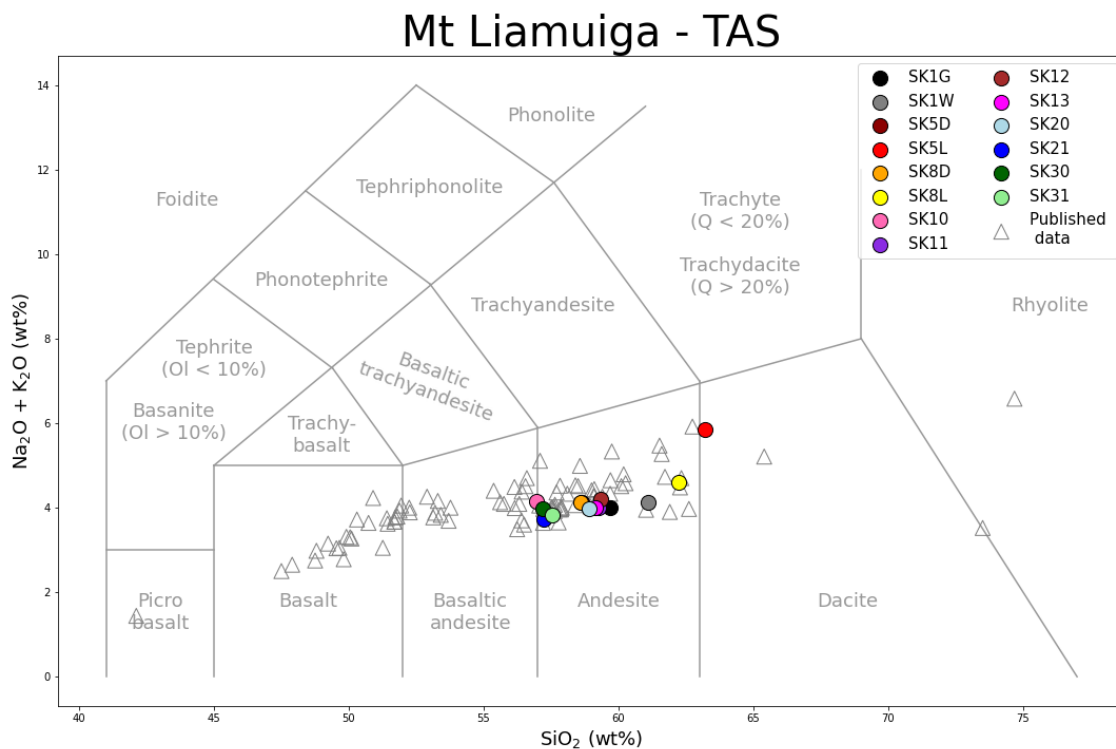


Figure 4.13 – Total Alkali-Silica (TAS) diagrams showing whole rock the chemical composition of the samples collected on Mt Liamuiga, St Kitts, with comparison to published data (Baker, 1968a, 1980, 1984, 1985; Baker and Holland, 1973; Roobol et al., 1987; Toothill et al., 2007). The samples collected are of basaltic andesite, andesitic and dacitic composition.

The chemical composition of the samples can be further classified using a TAS (total-alkali-silica) diagram (Figure 4.13). All of the Mt Liamuiga samples can be classified as andesite, with the exception of SK5L which sits on the dacitic side of the andesite/dacite boundary. R1-R2 diagrams (De la Roche *et al.*, 1980) can also be used to classify volcanic rocks. The R1-R2 diagram (Figure 4.14) shows a similar classification to the TAS diagram. Based on the R1-R2 diagrams, the Mt Liamuiga samples can be classified as andesites and dacites, though the R1-R2 plot classes more of the St Kitts samples as Dacites compared to the TAS diagram.

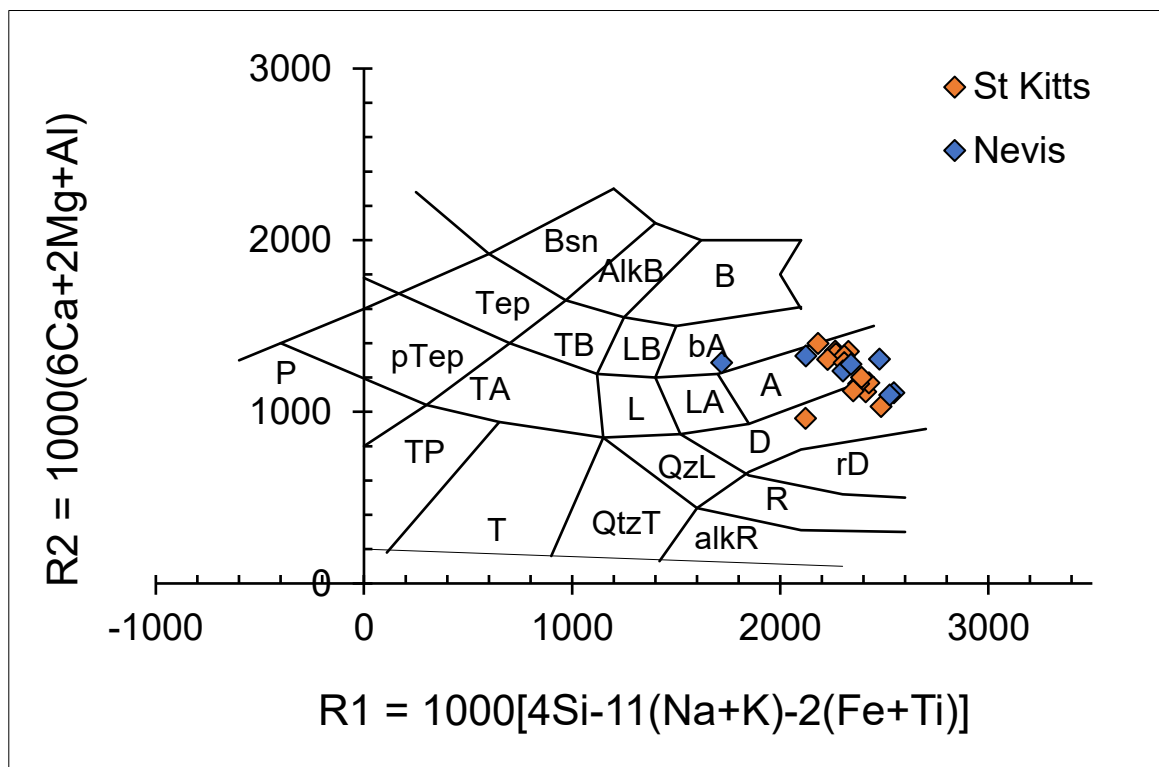


Figure 4.14 - R1-R2 diagrams (De la Roche *et al.*, 1980) showing the classification of volcanic rocks.

The mixed magma samples described in Chapter 3, and noted by Toothill *et al.* (2007) contained material of different natures, typically lighter and darker in colour. These lighter and darker components were thought to be end-members representing the maximum amount of variation within the deposit. The causes of these colour differences were unclear in the field, and may have been due to either textural or compositional variation. Light and

dark components were analysed for each of the samples, SK5 and SK8, to investigate the causes of these apparent colour differences. The compositional differences between the light and dark coloured components are shown in Figure 4.13. In both cases, the lighter coloured sample had a higher SiO₂ content than the darker coloured sample. For SK5 this was 58.63% SiO₂ in the darker coloured sample and 63.20% SiO₂ in the lighter coloured sample, and in SK8 and the percentages were 58.59% compared with 62.23%, respectively.

Fallout deposit SK1 showed colour variations, with compositions of 59.68% SiO₂ in the darker coloured sample and 61.09% in the lighter coloured sample, SK1 grey and white respectively.

The SK11 fallout sample showed similar compositions to SK1 (Figure 4.13).

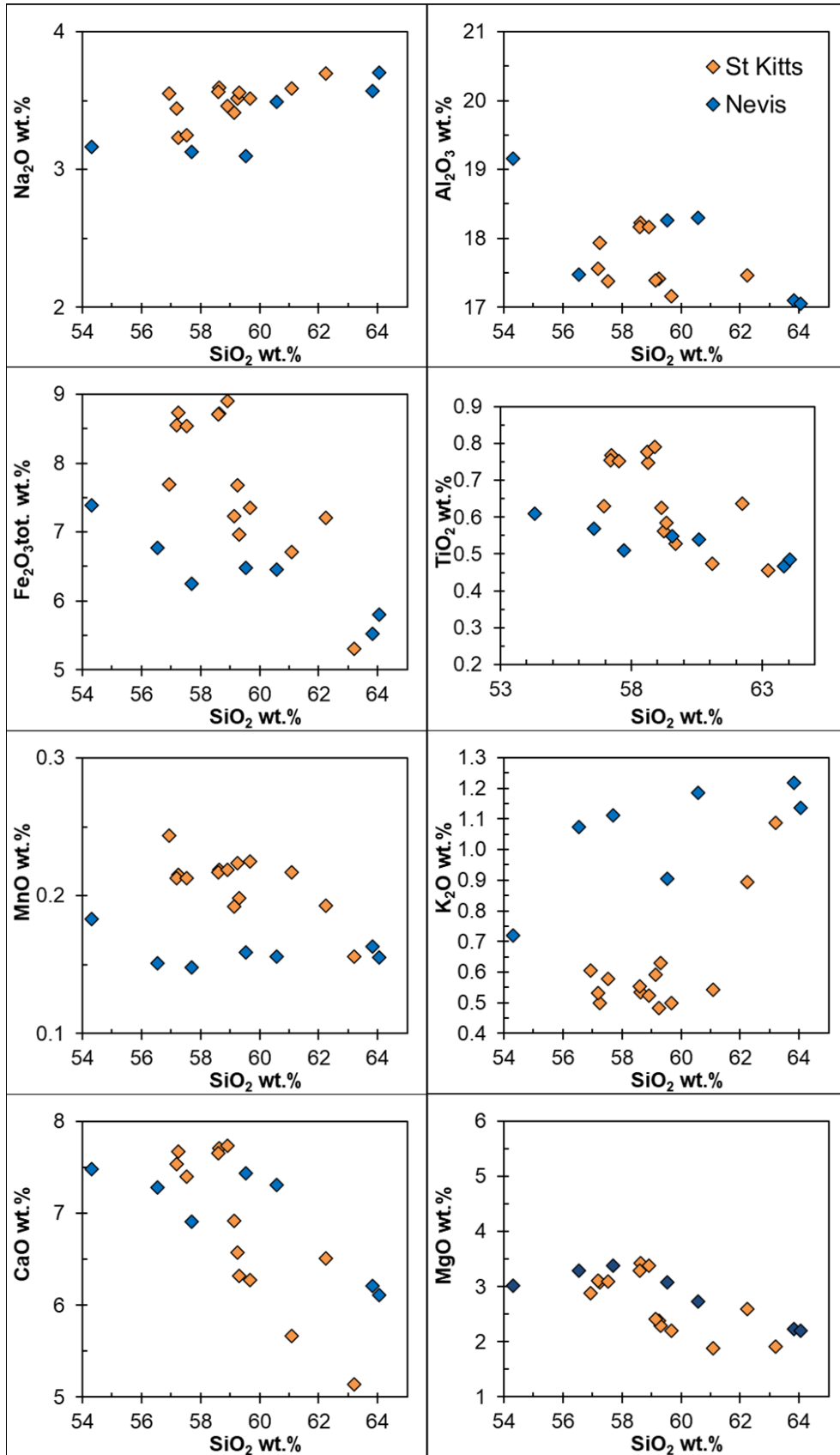


Figure 4.15 – Harker diagrams (Harker, 1909) showing major element trends plotted against SiO₂.

4.3.2.2 Major element composition for Nevis Peak

The plots shown in Figures 4.10 to 4.12 can be used to distinguish between calc-alkaline and tholeiitic compositions in island arc systems, all of which show that the Nevis samples plot close to the calc-alkaline/tholeiitic boundary. The Nevis samples can be classified as calc-alkaline or transitional. The FeO*/MgO versus silica diagram shows that the Nevis samples had a medium to low-Fe composition.

The Nevis samples show a similar composition to the Mt Liamuiga samples (as observed in the TAS diagram in Figure 4.16), though the whole-rock major element XRF data shows that the Nevis samples exhibit more variation, ranging from basaltic andesite to dacite. The R1-R2 diagram (Figure 4.14) shows a similar classification to the TAS diagram, with compositions ranging from basaltic andesite to dacite. The Nevis samples again show the full range of compositions.

Lighter and darker components were also analysed for SKN19 samples. Here, again, the lighter coloured sample had a higher SiO₂ content than the darker coloured sample; for SK19 the percentages were 56.55% for the dark sample, compared with 60.58% for the lighter sample, as shown in Figure 4.16.

Nevis Peak - TAS

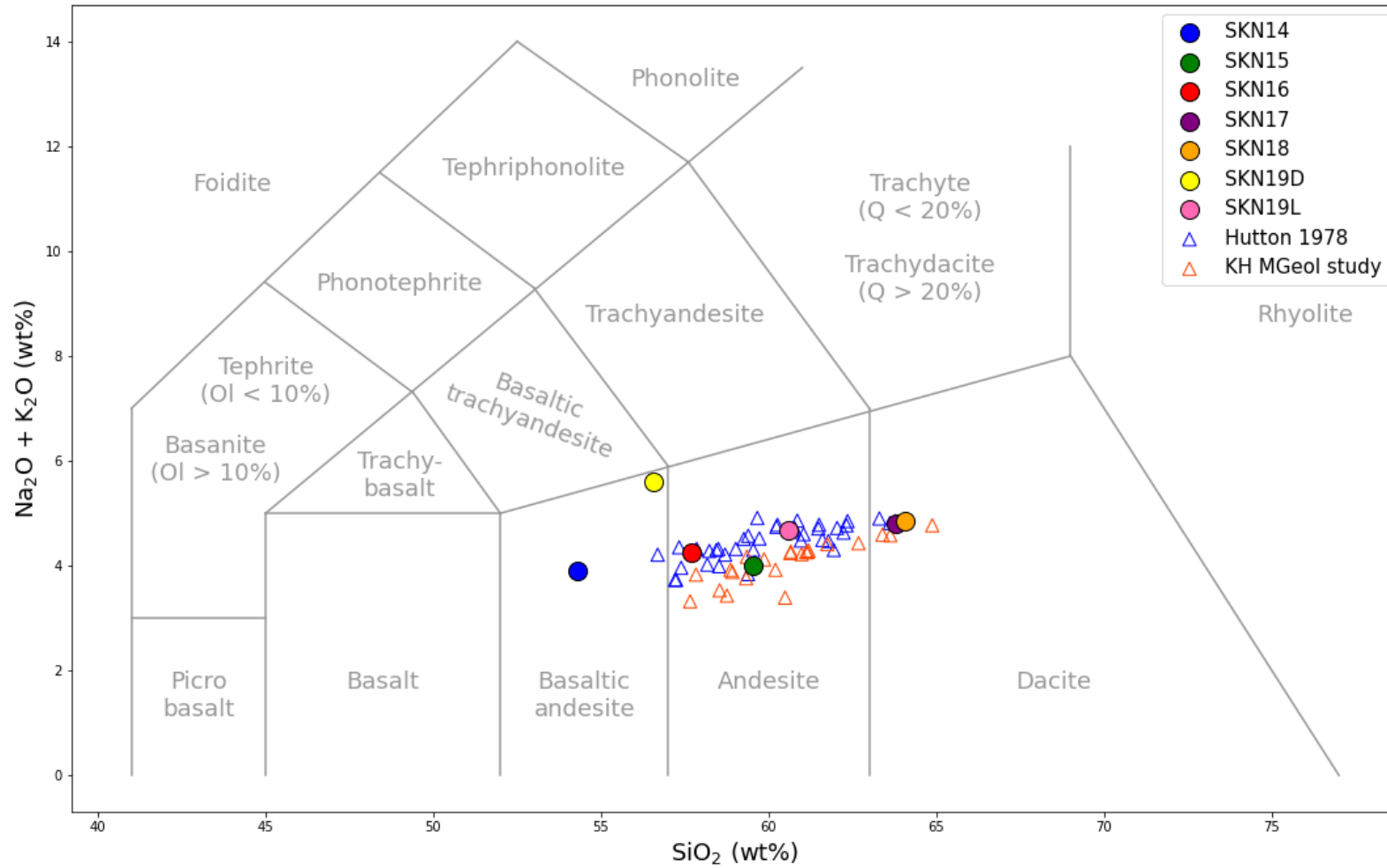


Figure 4.16 – Total Alkali-Silica (TAS) diagrams showing the chemical composition of the samples collected on Nevis Peak, Nevis. The samples collected are of basaltic andesite, andesitic and dacitic composition.

Table 4.4 – Whole rock XRF major element data for St Kitts and Nevis samples.

Sample	SiO ₂	TiO ₂	Al ₂ O ₃	Fe ₂ O ₃ tot	MnO	MgO	CaO	Na ₂ O	K ₂ O	P ₂ O ₅	LOI	Total
St Kitts												
SK1G	59.68	0.53	17.17	7.36	0.23	2.20	6.27	3.51	0.50	0.15	1.21	98.79
SK1W	61.09	0.47	16.79	6.71	0.22	1.89	5.67	3.59	0.54	0.14	1.76	98.88
SK5-DARK	58.63	0.75	18.22	8.72	0.22	3.43	7.71	3.60	0.54	0.10	0.30	102.22
SK5-LIGHT	63.20	0.46	16.15	5.31	0.16	1.91	5.14	4.75	1.09	0.09	2.77	101.02
SK8-DARK	58.59	0.78	18.17	8.71	0.22	3.29	7.65	3.56	0.55	0.11	0.00	101.65
SK8-LIGHT	62.23	0.64	17.46	7.21	0.19	2.59	6.51	3.70	0.89	0.10	0.54	102.07
SK10	56.95	0.63	16.98	7.69	0.24	2.88	8.62	3.55	0.60	0.12	0.40	98.66
SK11	59.24	0.56	17.42	7.69	0.22	2.38	6.58	3.52	0.48	0.14	1.77	100.00
SK12	59.32	0.58	16.92	6.97	0.20	2.30	6.32	3.56	0.63	0.10	2.43	99.31
SK13	59.14	0.63	17.40	7.23	0.19	2.41	6.92	3.41	0.59	0.10	1.05	99.06
SK20	58.90	0.79	18.16	8.91	0.22	3.38	7.74	3.46	0.52	0.10	0.28	102.45
SK21	57.24	0.77	17.94	8.73	0.22	3.07	7.68	3.23	0.50	0.10	-0.08	99.40
SK30	57.20	0.75	17.57	8.56	0.21	3.12	7.53	3.44	0.53	0.10	0.58	99.60
SK31	57.53	0.75	17.38	8.55	0.21	3.10	7.40	3.25	0.58	0.10	0.55	99.39
Nevis												
SKN14	54.30	0.61	19.16	7.39	0.18	3.01	7.48	3.17	0.72	0.09	3.18	99.29
SKN15	59.55	0.55	18.27	6.49	0.16	3.07	7.44	3.10	0.91	0.08	2.76	102.35
SKN16	57.71	0.51	16.83	6.25	0.15	3.38	6.91	3.13	1.11	0.08	3.33	99.39
SKN17	63.81	0.47	17.10	5.52	0.16	2.23	6.21	3.57	1.22	0.09	1.68	102.06
SKN18	64.05	0.49	17.05	5.80	0.16	2.20	6.11	3.70	1.14	0.10	0.78	101.57
SKN19-DARK	56.55	0.57	17.48	6.77	0.15	3.29	7.28	4.54	1.08	0.08	3.78	101.57
SKN19-LIGHT	60.58	0.54	18.30	6.46	0.16	2.73	7.31	3.49	1.19	0.08	1.26	102.09

4.3.3 Trace element composition

The trace element compositions of the Mt Liamuiga samples and the Nevis Peak samples were also analysed using WD XRF (Section 4.2.3.1). Figure 4.17 shows the chondrite normalised REE patterns for the St Kitts and Nevis samples. The relative enrichment compared to mid-ocean ridge basalt (MORB) is shown in Figure 4.18. The standard deviation for each element was typically < 1.4 ppm, with the exception of manganese, which was 16.8 ppm (due to its value being several orders of magnitude larger).

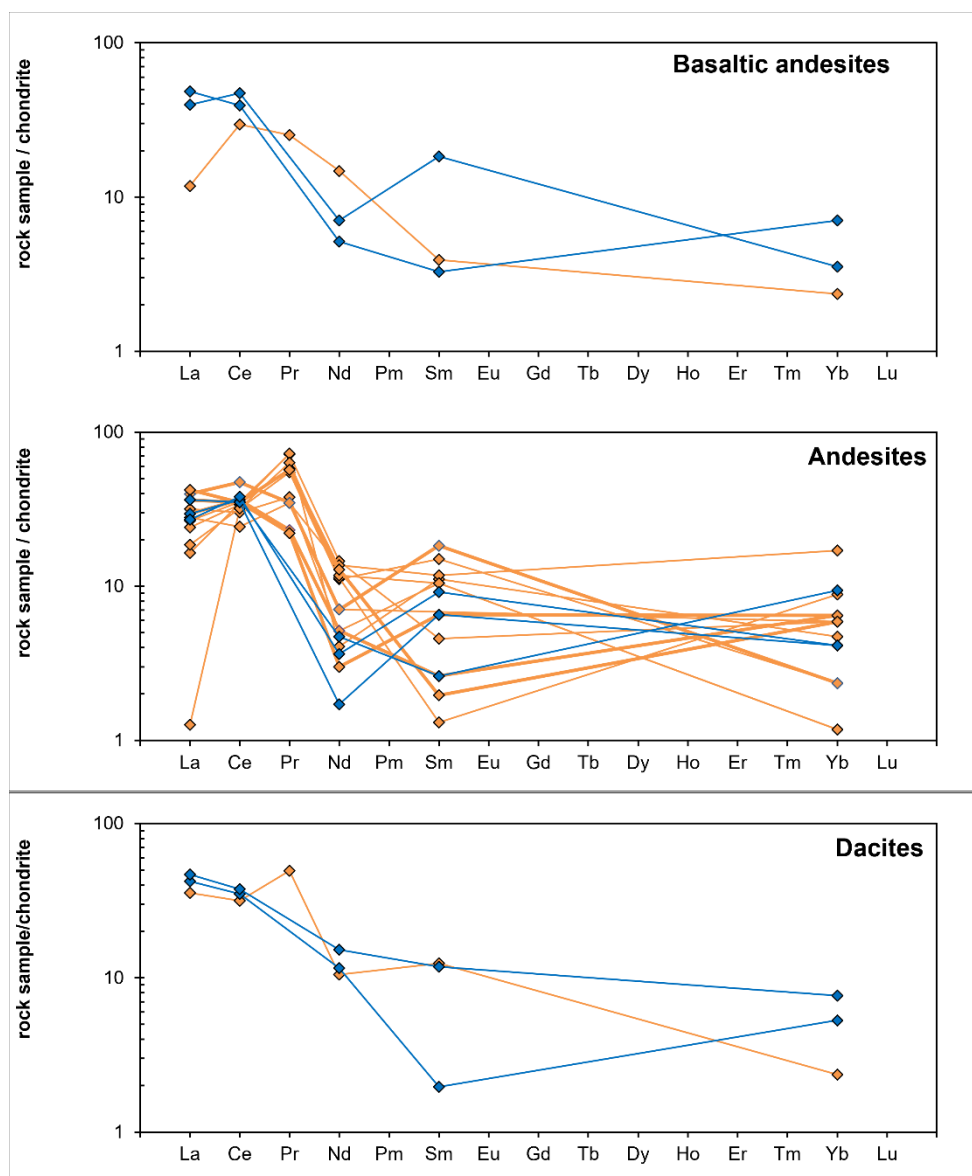


Figure 4.17 - Chondrite normalised REE patterns for the St Kitts (orange) and Nevis (blue) samples.

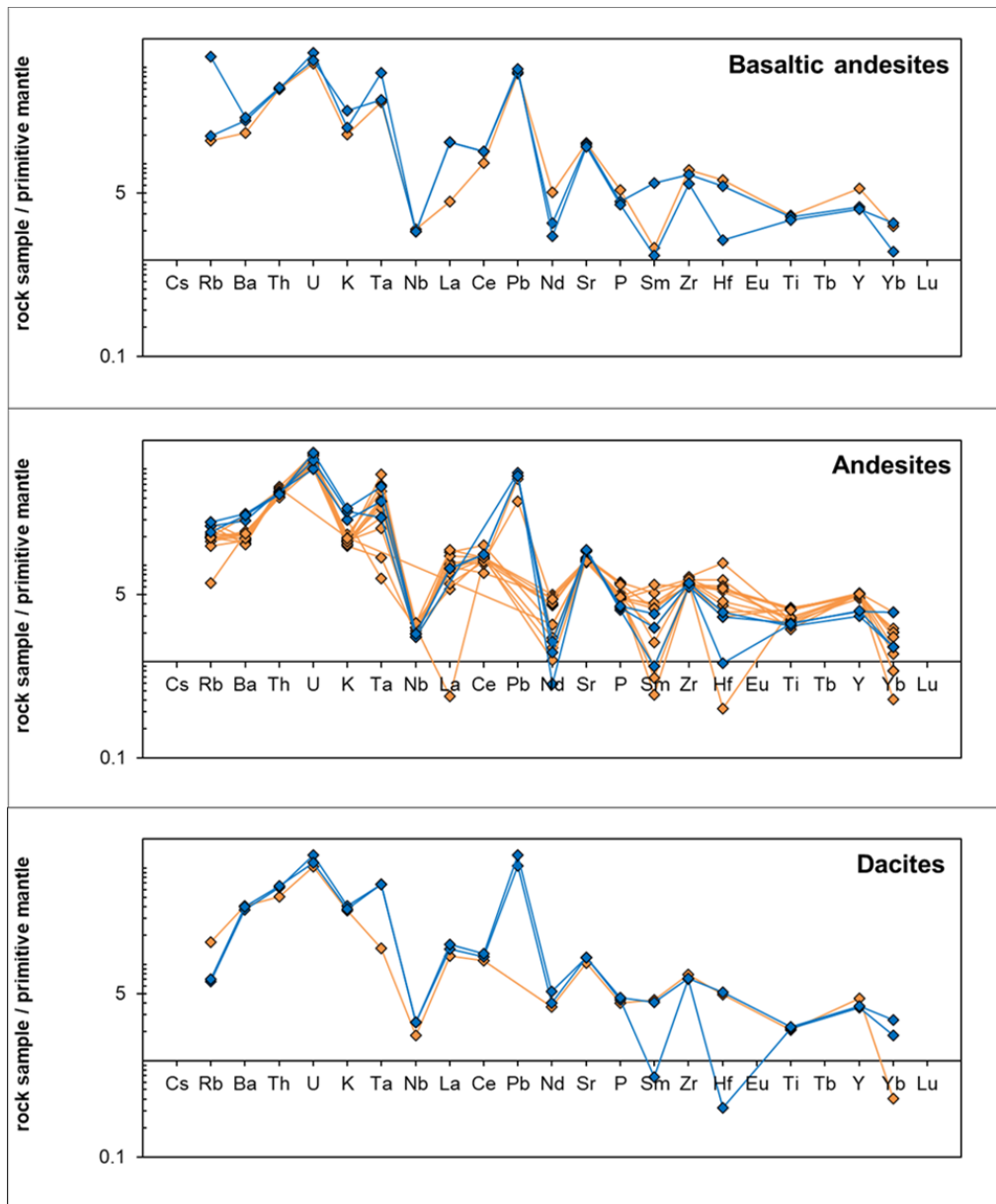


Figure 4.18 - Relative enrichment compared to mid-ocean ridge basalt (MORB) shown for St Kitts (orange) and Nevis (blue) samples.

3.3.3.1 Trace element compositions for Mt Liamuiga

The Mt Liamuiga basaltic andesites REEs show enrichment relative to chondrite of between 3 and 30, with Ce being the most enriched and the remaining elements showing the expected trend of reduced enrichment with increasing atomic weight. The andesites exhibit a range between 1 and 80. The typical trend of decreasing enrichment with increasing atomic weight

is less clear in the andesites, with Pr and Sm being proportionally more enriched. The dacites show an enrichment relative to chondrite of between 2 to 60, and a similar trend to the andesites.

The basaltic andesite trace elements show enrichment relative to MORB of between 1 and 100, with the most enriched elements being U, Ta, Pb and Sr. The least enriched elements were Nb, Nd, Sm and Yb. Both the andesites and dacites show relative enrichment of 0.3 and 150. The most consistently enriched elements in the andesites were Th, U and Ta, while Pb was relatively more enriched in two samples. The least enriched elements were Nb, Nd, Sm and Yb, with Hf and La being comparatively depleted in one sample. The most enriched elements in the dacites were Th, U and Pb, while the least enriched were the same elements as observed in the andesites.

The trace elements for St Kitts shows Pb values of between 2.7 to 6.9 ppm. Ni values showed a range from 0 to 6.4 ppm, while Cr values ranged from 0.1 to 20.8 ppm. V values ranged from 36 to 108.3 ppm. The samples showed relatively low Y and Yb concentrations.

The trace elements have been plotted on Zr/TiO₂ against Nb/Y, and Zr/TiO₂ against Ce diagrams, shown in Figure 4.19. Both of these plots suggest that the samples can be classified as andesite or dacite/andesite, as also shown by the major element classification plots. Figure 4.20 based on Barrett and MacLean (2019), shows that the St Kitts samples are tholeiitic in composition, and in agreement with the major element data.

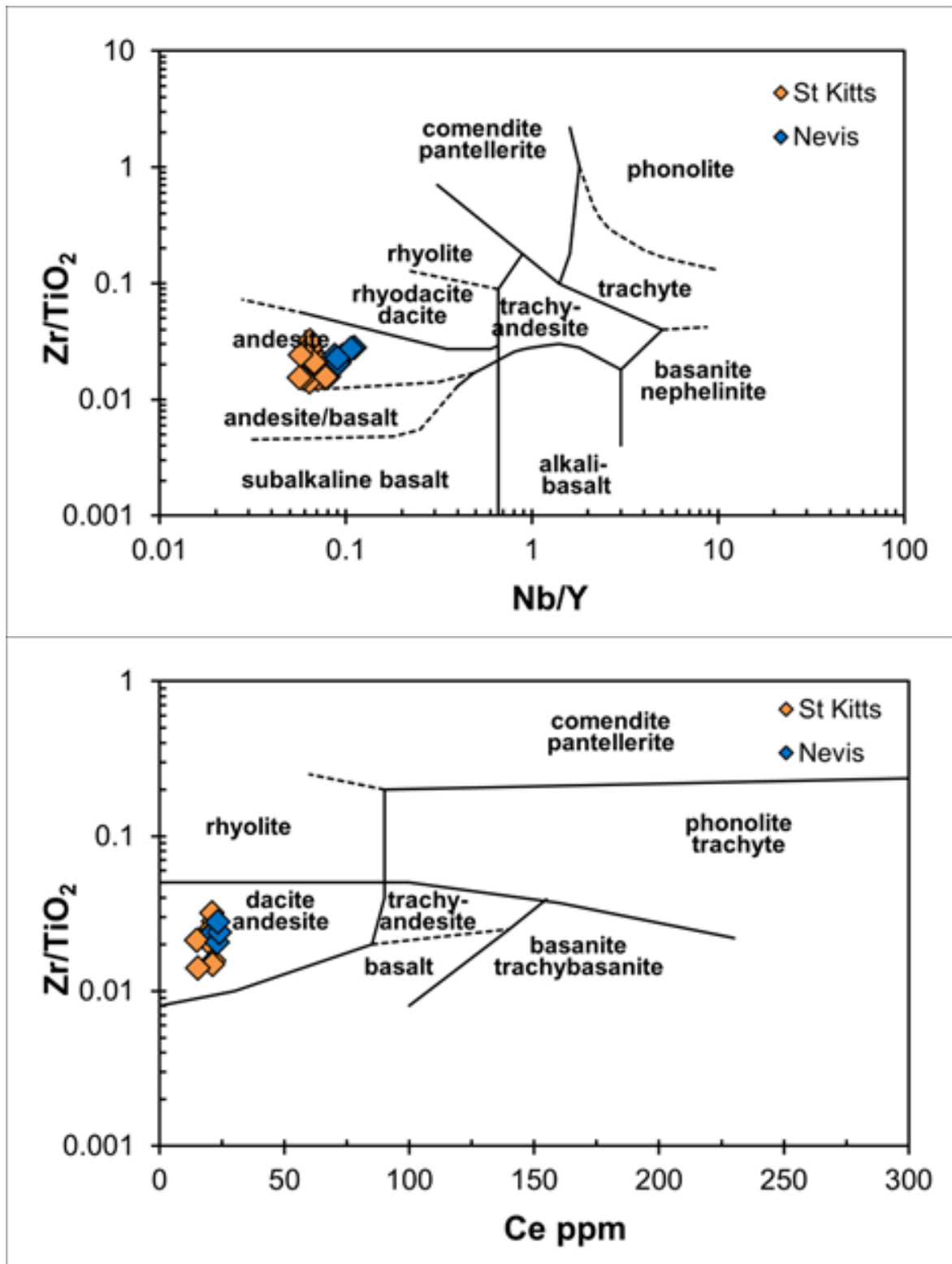


Figure 4.19 - Trace elements plotted on Zr/TiO_2 versus Nb/Y (top), and Zr/TiO_2 versus Ce (bottom) diagrams (Winchester and Floyd, 1977).

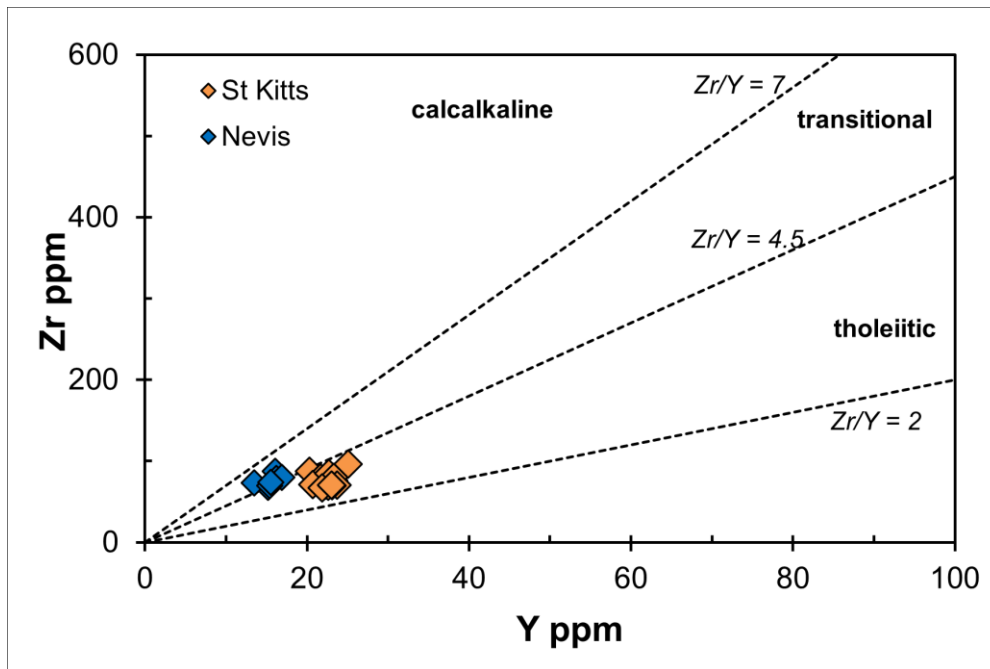


Figure 4.20 – Based on Barrett and MacLean (2019), showing Zr versus Y, classifying tholeiitic, transitional and calc-alkaline magmas.

3.3.3.2 Trace element composition for Nevis Peak

The basaltic andesites of Nevis Peak show enrichment relative to chondrite of between 3 and 50, with La and Ce being most enriched. The andesites exhibit a range between 2 and 40, with La and Ce being most enriched and Nd being least enriched. The dacites show an enrichment relative to chondrite of between 2 to 60, with the general trend of decreasing enrichment with increasing atomic weight.

The basaltic andesites show enrichment relative to MORB of between 1 and 110, while the andesites show relative enrichment of 0.7 and 110, and the dacites between 0.3 and 110. For all three compositions, the most enriched elements were the same, namely U, Ta and Pb. The least enriched elements were similar in the basaltic andesites and andesites; these were Nb, Nd and Sm. The least enriched elements in the dacites were Nb and Sm.

Trace elements for Nevis showed Pb values of 6.7 to 11 ppm. Ni values showed a range between 0.8 to 4.9 ppm while Cr values ranged from 1.6 to 12.4 ppm. V values ranged from 51.2 to 128.2 ppm. Similarly to the St Kitts samples, the Nevis samples showed relatively low Y and Yb concentrations.

The trace elements have been plotted on Zr/TiO₂ against Nb/Y, and Zr/TiO₂ against Ce diagrams, shown in Figure 4.18. Both of these plots suggest that the samples can be classified as andesite or dacite/andesite, as also shown by the major element classification plots. In Figure 4.20, based on Barrett and MacLean (2019), the Nevis samples are shown to be transitional, in contrast to the major element data which suggests they are calc-alkaline.

4.3.4 Loss on Ignition (LOI)

LOI can act as an estimation of the total volatile content in a sample. LOI was calculated for each of the St Kitts and Nevis samples (Table 4.5). All of the samples had loss on ignition, with the exception of SK21, which showed a small gain on ignition of 0.076%, most likely related to the oxidation of ferrous iron (Lechler and Desilets, 1987). The highest loss on ignition, and therefore the highest volatile content for the Mt Liamuiga samples was 2.773%. The Nevis samples had a larger loss on ignition and higher volatile content compared to the Mt Liamuiga samples, ranging between 0.781% and 3.782%.

Table 4.5 - Table showing loss on ignition (LOI) as a percentage of sample mass

St Kitts		Nevis	
Sample	LOI %	Sample	LOI %
SK1G	1.205	SKN14	3.180
SK1W	1.756	SKN15	2.755
SK5-DARK	0.302	SKN16	3.330
SK5-LIGHT	2.773	SKN17	1.681
SK8-DARK	0.004	SKN18	0.781
SK8-LIGHT	0.544	SKN19-DARK	3.782
SK10	0.398	SKN19-LIGHT	1.256
SK11	1.775		
SK12	2.425		
SK13	1.049		
SK20	0.276		
SK21	-0.076		
SK30	0.585		
SK31	0.547		

4.3.5 Interstitial glass compositions

4.3.5.1 Mt Liamuiga

Glass compositions analysed in the Mt Liamuiga samples showed large variations. The glass samples ranged from andesitic to rhyolitic, although the majority were dacitic to rhyolitic. Glass compositions varied slightly between those acquired using the SEM and those acquired using the EMPA (SEM measurements indicated by 'EDS' in Figure 4.21). The SEM appeared to show higher SiO₂ compositions compared to the EMPA, although as high silica glass can be unstable during analysis, this could be an artefact created during data collection. The EMPA is considered to be more accurate due to the method of acquisition. Overall, the spread of the data is consistent, suggesting that the data from the EMPA validates those acquired from the SEM.

The glass compositions observed in the mixed magma samples showed clear variations between the end member 'light' and 'dark' samples analysed for SK5 and SK8. The glass in the dark material had a lower SiO₂ content, with a composition of andesite to dacite, while the lighter components had a higher SiO₂ content and were rhyolitic in composition. SK8 shows more variation in composition than SK5. This variation between the identified end-members shows that the light and dark samples are compositionally different in nature.

Mt Liamuiga - Glass Compositions

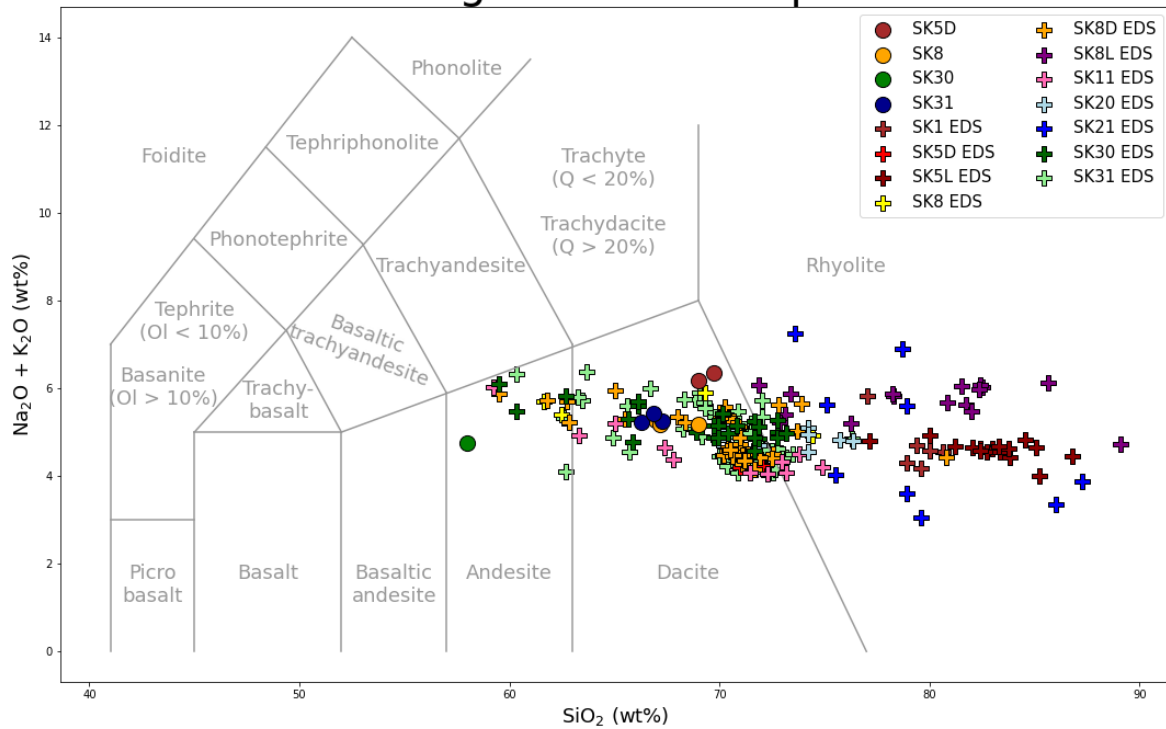


Figure 4.21 – TAS diagrams showing glass compositions for the Mt Liamuiga samples. SEM derived EDS data is shown as crosses, while microprobe derived data is shown as circles.

Mt Liamuiga - Glass Compositions

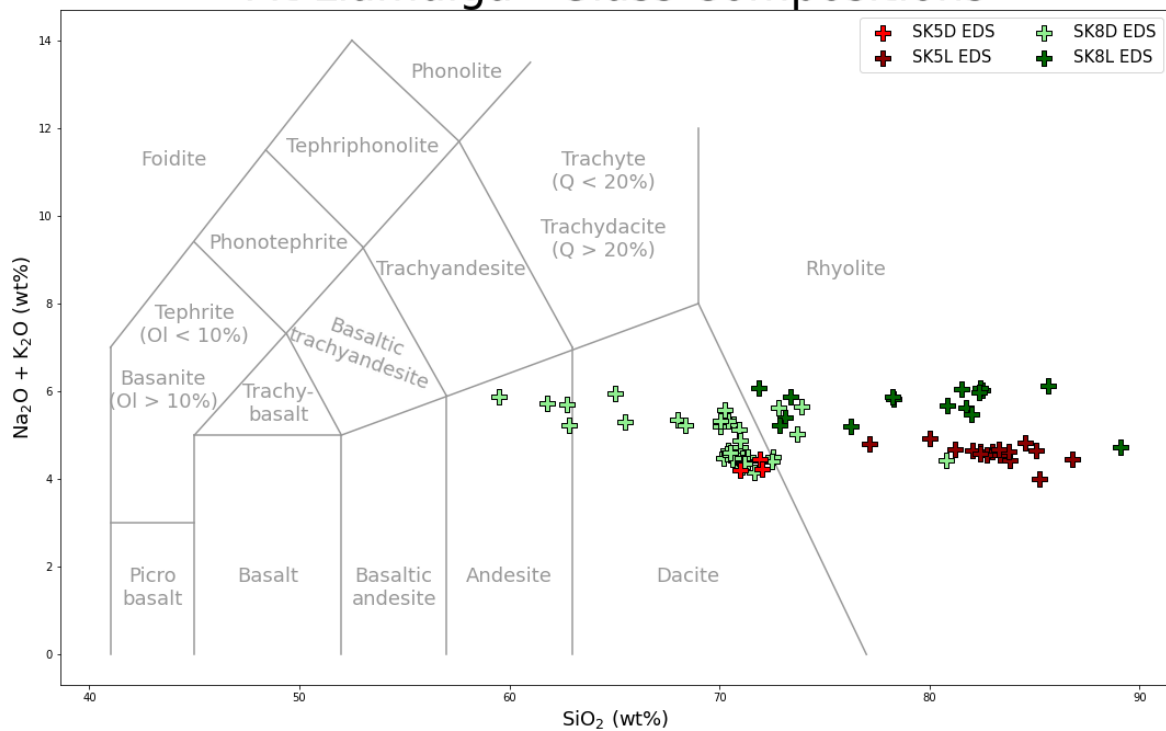


Figure 4.22 – TAS diagrams showing glass compositions derived from SEM EDS data for the 'mixed magma' Mt Liamuiga samples, SK5 and SK8.

4.3.5.2 *Nevis Peak*

Glass compositions analysed in the Nevis Peak samples showed large variations. The glass samples ranged from dacitic to rhyolitic. The glass compositions for one of the Nevis samples, SKN19, showed such a high SiO₂ wt. % that it was unstable under analysis in the microprobe. The data acquired from SEM appear to show that the compositions for SKN18 and SKN19 plot as two different groups. The data acquired from the microprobe (shown in Figure 4.23 as red and blue circles) plots much closer together. The SKN19 SEM EDS data, and the microprobe data plot relatively close together, with a rhyolitic composition. The SKN18 data acquired from SEM EDS plot in a separate group, with a dacitic composition. The cause of this variation is uncertain although, due to the high SiO₂ content of the glass, it was unstable under the microprobe beam. This may have prevented accurate results from being obtained, although it is thought that the trends are representative of the compositions.

Nevis Peak - Glass Compositions

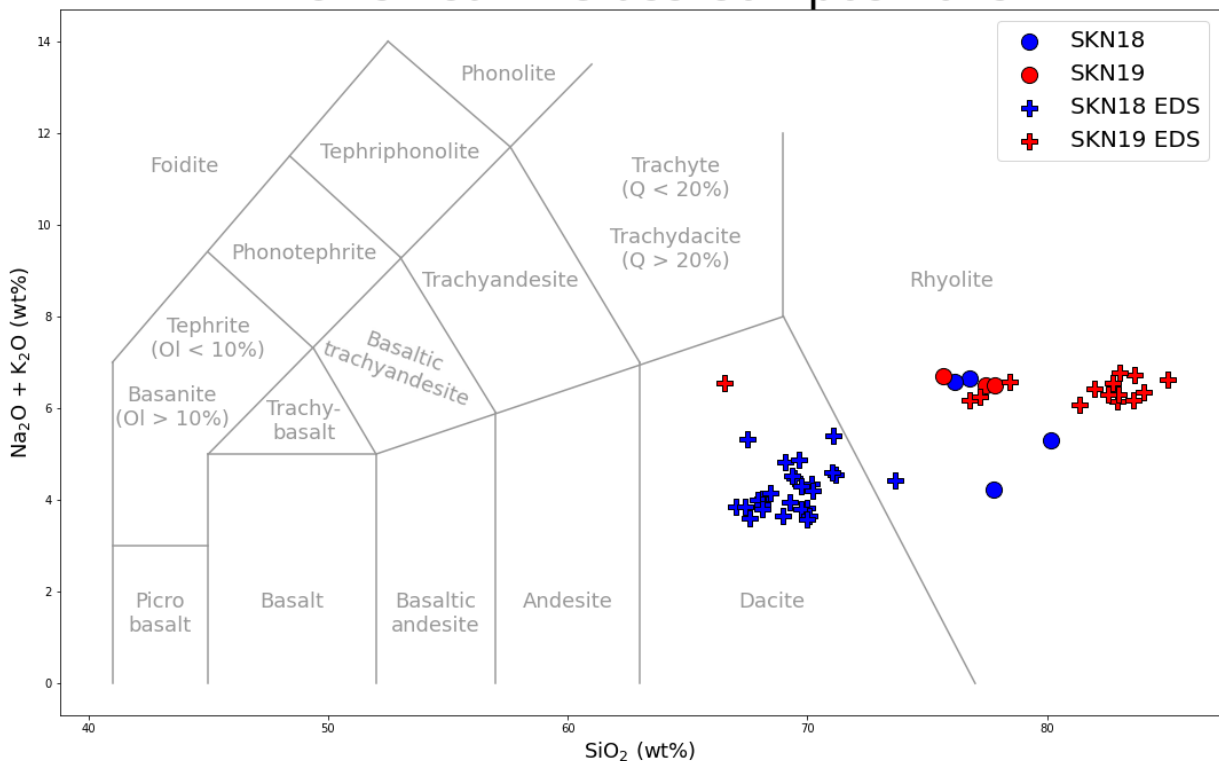


Figure 4.23 – TAS diagrams showing glass compositions for the Nevis Peak samples. SEM derived EDS data is shown as crosses, while microprobe derived data is shown as circles.

4.3.6 Phenocryst composition

The composition and classification of phenocrysts were calculated from data collected using the microprobe. The phenocrysts populations consisted of plagioclase, pyroxene, hornblende and iron oxide minerals (magnetite and titanomagnetite).

4.3.6.1 Phenocryst compositions of the Mt Liamuiga samples

In the Mt Liamuiga samples, plagioclase is the dominant phenocryst and can be classified as labradorite or bytownite (Figure 4.24). All plagioclase phenocrysts are low in K_2O , BaO and FeO. The pyroxenes are almost entirely orthopyroxene. The orthopyroxene is enstatite (Figure 4.25). The clinopyroxene present was classified as pigeonite. Fe-Ti oxides, and amphibole were also present.

Compositional data from the microprobe was also collected from complexly zoned plagioclase phenocrysts. Compositional data were collected from traverses across the phenocrysts. The plagioclases show complex core-rim zonation patterns (Figure 4.26), and multiple different styles of zonation in the same deposits. Oscillatory zoning is common in many of the plagioclases, with An values varying by up to 30% across the crystal. Normal zoning is more common, although both normal and reverse zoning can be observed in the Mt Liamuiga samples. Cores in the St Kitts samples were typically An₍₅₂₋₈₇₎, while rims were An₍₅₂₋₈₁₎.

4.3.6.2 Phenocryst compositions of the Nevis Peak samples

In the Nevis samples, plagioclase is the dominant phenocryst, and can be classified as labradorite or bytownite, with an An range of 52.8 % to 83.8 % (Figure 4.25). All plagioclase phenocrysts are low in K₂O, BaO and FeO. Two populations of pyroxene were present; orthopyroxene in the form of ferrosilite and clinopyroxene in the form of augite. Pyroxene classifications are shown in Figure 4.24. Amphibole was observed in both of the Nevis samples, this could be classified as ferro-edenite. Magnetite was also present.

The plagioclases show complex core-rim zonation patterns, and multiple different styles of zonation in the same deposits (Figure 4.26). Oscillatory zoning is common in many of the plagioclases, with An values varying by up to 30% across the crystal. Normal zoning is more common, although both normal and reverse zoning can be observed in the Nevis samples. Cores in the Nevis Peak samples, cores were An₍₅₃₋₈₂₎, while rims were An₍₅₄₋₇₆₎.

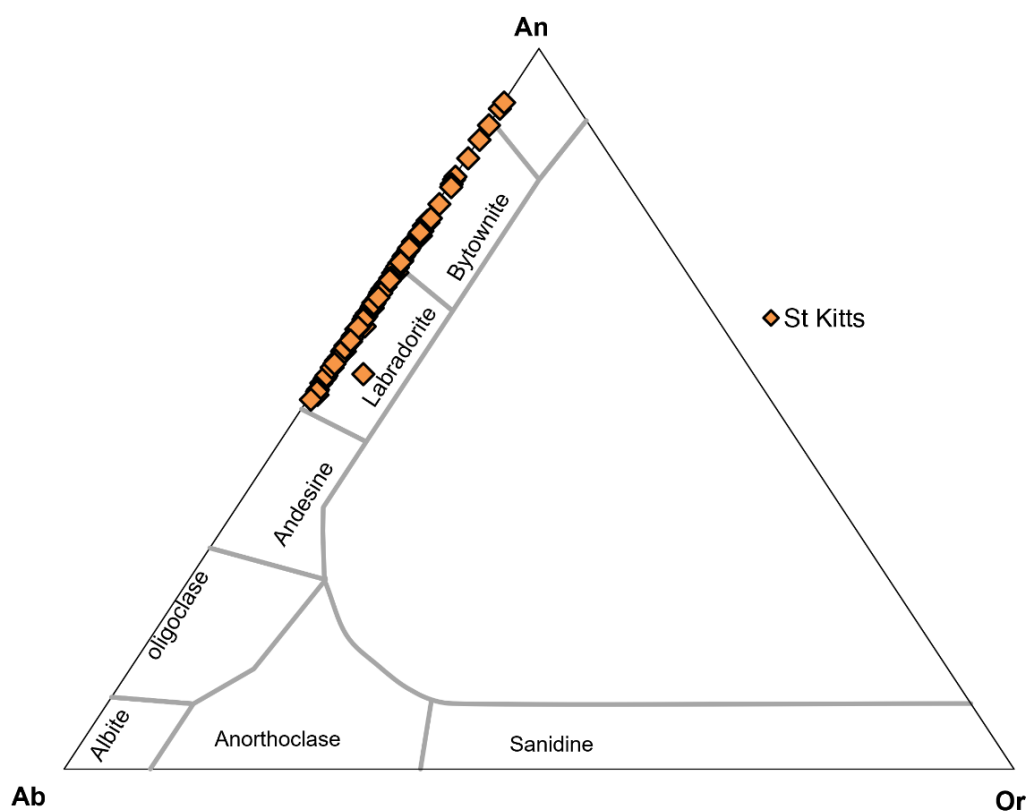
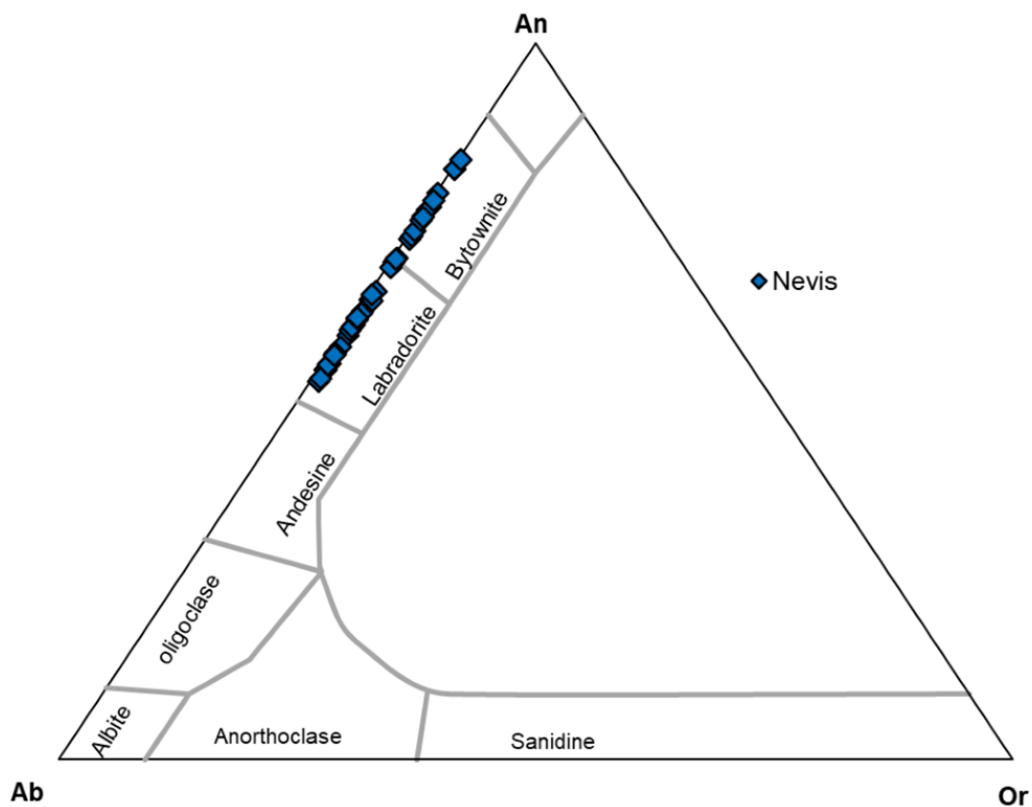


Figure 4.24 – Feldspar classification diagram (Deer et al., 1992), showing the classification of feldspar phenocrysts for the Nevis (top) and the St Kitts (bottom) samples.

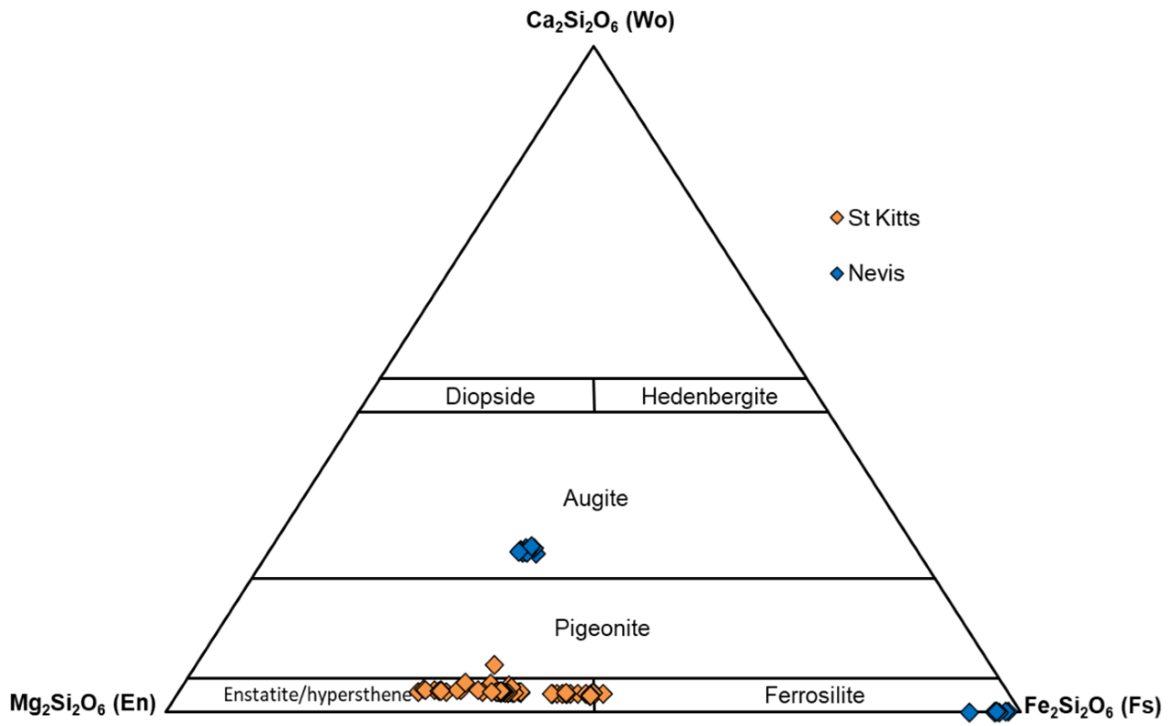


Figure 4.25 – Ternary composition diagram for pyroxene phenocrysts.

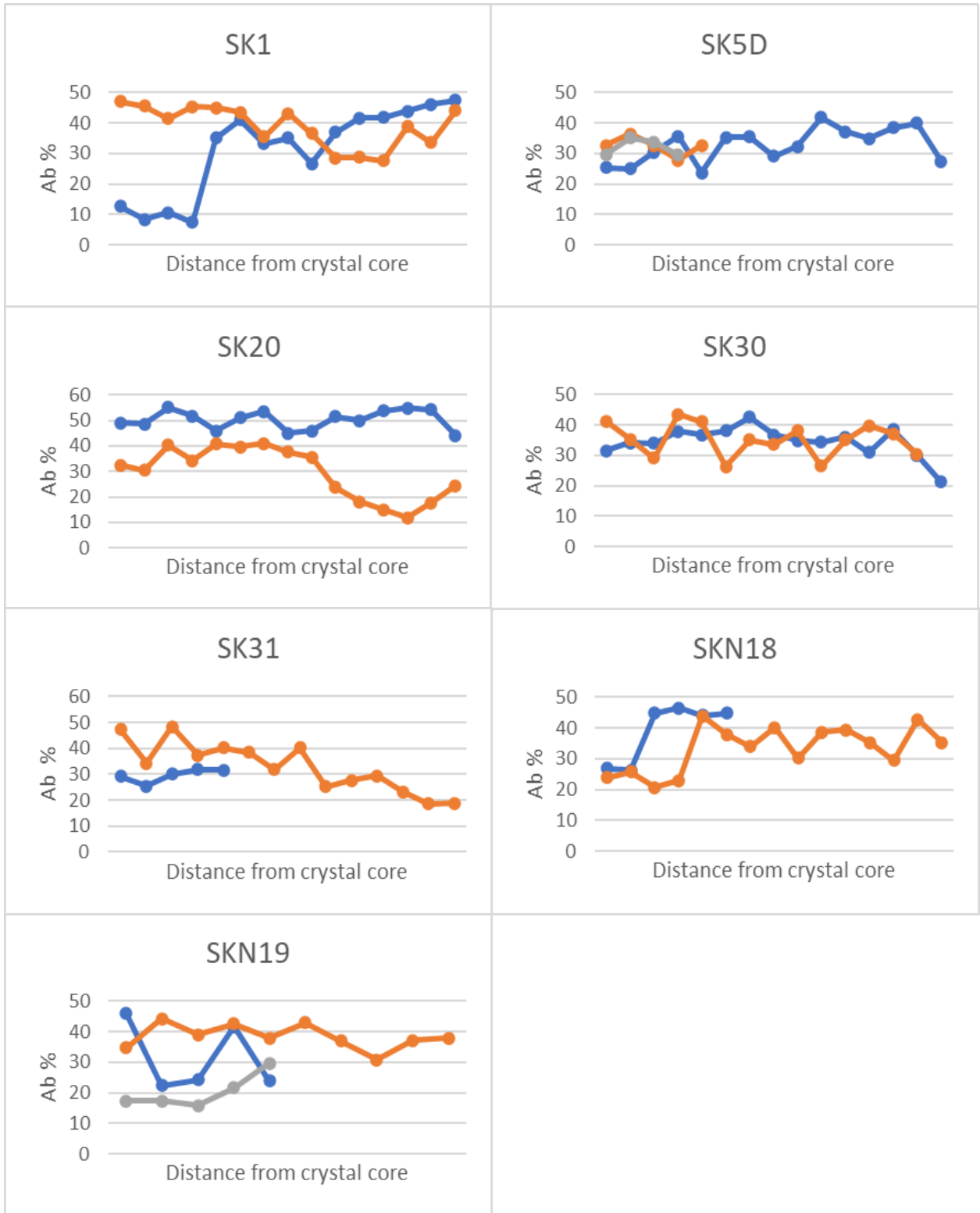


Figure 4.26 - An-Ab compositional diagrams for plagioclase phenocrysts transects, shown for the St Kitts and Nevis polished thin sections. The different coloured lines on each plot represent different transects taken on the same sample.

4.3.7 Microlite composition

4.3.7.1 Microlite composition in Mt Liamuiga samples

The composition and classification of microlite crystals were calculated using the data collected from the microprobe. The microlites in the St Kitts samples were plagioclase and pyroxene, with small amounts of magnetite. The plagioclase microlites fell into three classifications; andesine, labradorite and bytownite (Figure 4.27). Both clinopyroxene and orthopyroxene microlites were identified. The clinopyroxene microlites were classified as augite, while the orthopyroxene microlites were classified as enstatite (Figure 4.28).

4.3.7.2 Microlite composition in Nevis Peak samples

The microlites in the Nevis samples showed similar compositions to those observed in the Mt Liamuiga samples, with plagioclase microlites classified as labradorite (Figure 4.27). The clinopyroxene microlites are augite, while the orthopyroxene microlites are enstatite (Figure 4.28). The microlites in the Mt Liamuiga and Nevis Peak samples are further studied in Chapter 5.

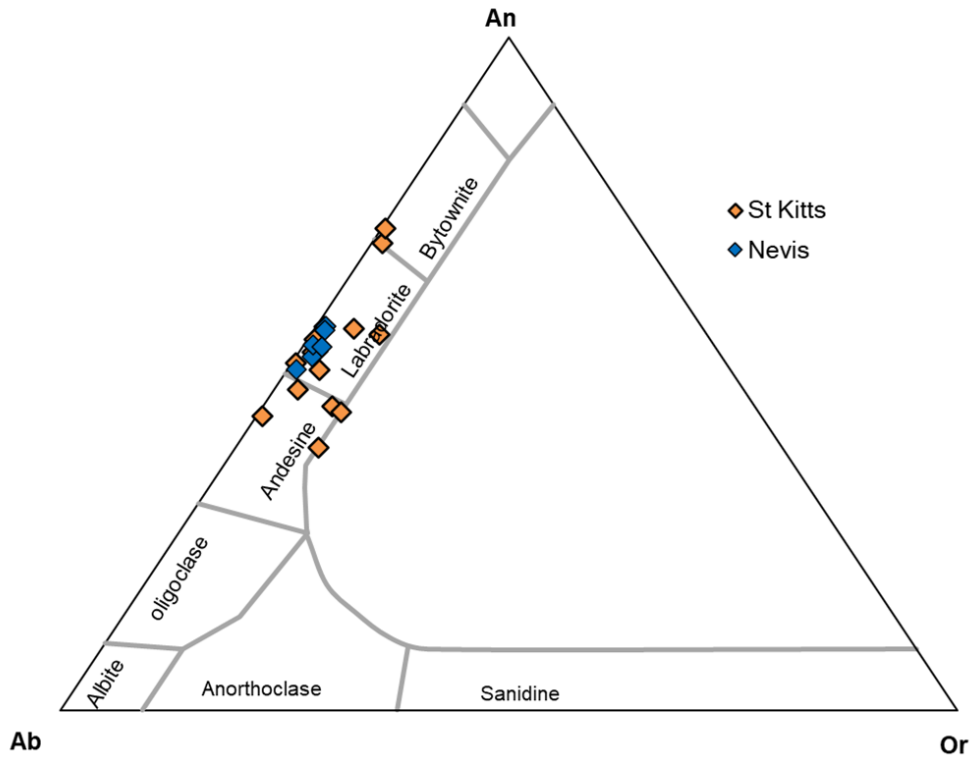


Figure 4.27 - Feldspar classification diagram (Deer et al., 1992), showing the classification of feldspar microlites for the Nevis and the St Kitts samples.

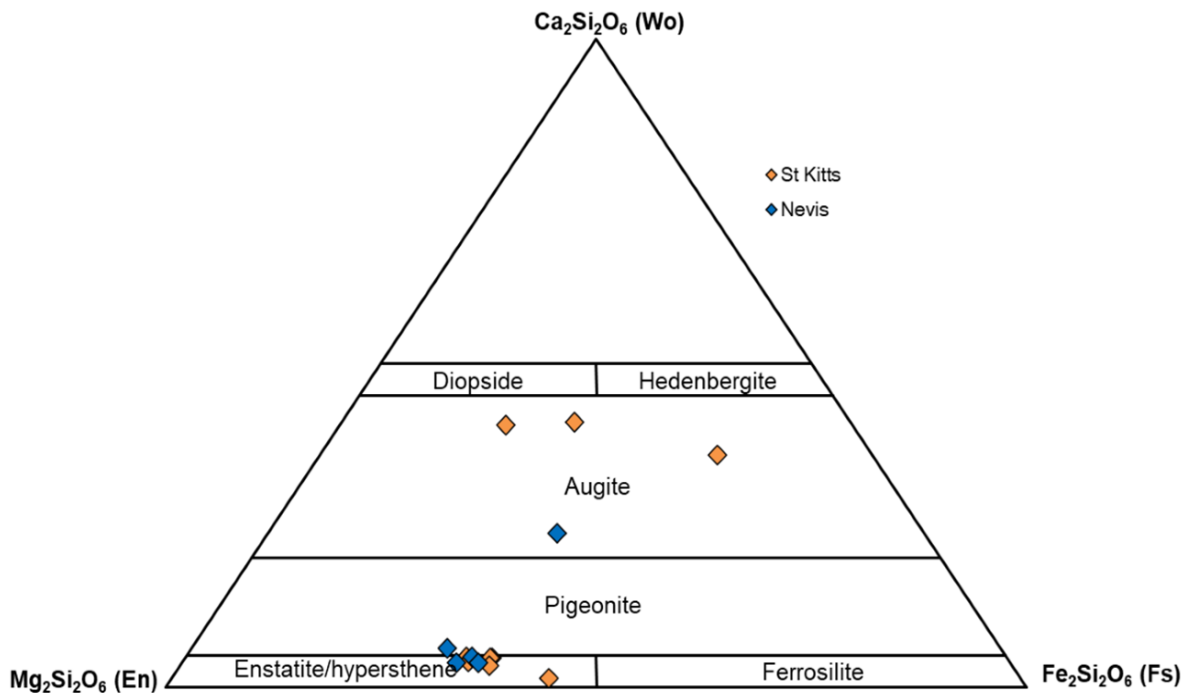


Figure 4.28 - Ternary composition diagram for pyroxene microlites.

4.4 Interpretation and comparison with published data

4.4.1 Origins of the St Kitts and Nevis magmas

The St Kitts whole rock major and trace element show that the Mt Liamuiga lavas plot in the low-K tholeiites series (Figures 4.10, 4.11, 4.12 & 4.20). This suggests that the magma source was likely depleted mantle similar to that of mid-ocean ridge basalt (MORB) (Pearce and Peate, 1995; Zimmer *et al.*, 2010). Evidence for this can be seen in Figure 4.18, where depletion in trace elements is below the normalized values for MORB. Trace elements, unlike major elements, are less affected by magma-rock/mineral interactions, therefore can tell us about the source characteristics of magmas. Enrichment of large ion lithophile (LIL) elements such as Pb and Sr, suggest a more fertile and hydrated source compared to MORB, potentially due to contributions from the subducting slab (Macdonald *et al.*, 2000; Pearce, 2008). Anhydrous, low-pressure fractional crystallization in the upper crust then differentiated the magma into the basaltic andesite and andesitic compositions observed (Juster *et al.*, 1989; Zimmer *et al.*, 2010). Variation was also controlled in part by magma mixing (Section 4.4.1.1), with injections of more primitive magma into reservoirs of cooler, more silicic magma. The Harker diagrams in Figure 4.16 show decreasing Al_2O_3 , MgO, FeO and CaO with increasing SiO_2 , indicating fractional crystallization of plagioclase and pyroxenes. The slight decrease in TiO_2 is likely due to the fractional crystallization of Fe-Ti oxides (Chin *et al.*, 2018; Zimmer *et al.*, 2010). Figure 4.13 shows medium-Fe concentration, typical in the earlier stages of differentiation. Tholeiitic arc magmas typically evolve towards Fe-enrichment (Chin *et al.*, 2018).

In comparison to the Mt Liamuiga samples, the Nevis Peak samples plotted as calc-alkaline. There are numerous theories for the generation of calc-alkaline magma (Chin *et al.*, 2018).

These theories include origins from a mantle source (Carmichael, 1991), fractional crystallization (Bowen, 1928), contamination of Si-rich, Fe-poor crustal material (Grove *et al.*, 1982), and elevated water contents fO_2 inherited from the mantle wedge, which has been hydrated and oxidised by material from the subducting slab (Brounce *et al.*, 2014; Eggins, 1993; Evans *et al.*, 2012; Kelley and Cottrell, 2009; Parkinson and Arculus, 1999). The parental magma would have had a higher H_2O content to produce the geochemical signals identified in calc-alkaline magmas (Sisson and Layne, 1993; Zimmer *et al.*, 2010). This consistent with the LOI values calculated for Mt Liamuiga and Nevis Peak (Section 4.3.3.4), where the Nevis samples show a higher estimated volatile content. Figure 4.12 shows low-Fe concentration, which is common in subduction zones. This is because calc-alkaline arc magmas typically evolve towards Fe-depletion (Chin *et al.*, 2018; Zimmer *et al.*, 2010). These low-Fe values, suggest that significant fractional crystallization occurred. Further evidence for fractional crystallization can be seen in the Harker diagrams in Figure 4.16, where Al_2O_3 , MgO, FeO and CaO decrease with increasing SiO_2 . Further variation of calc-alkaline magmas can be caused by assimilation of continental crust and mixing with primitive magmas.

Figure 4.29a from Pearce (2008) shows that the magmas are likely to have originated from a mantle/MORB-like source, but have interacted with the crust and are likely affected by subduction components (Pearce and Peate, 1995). Figures 4.29a and 4.29b suggests that the origin of the St Kitts magma is a depleted mantle similar to that of MORB, while the Nevis samples originate from a more enriched source.

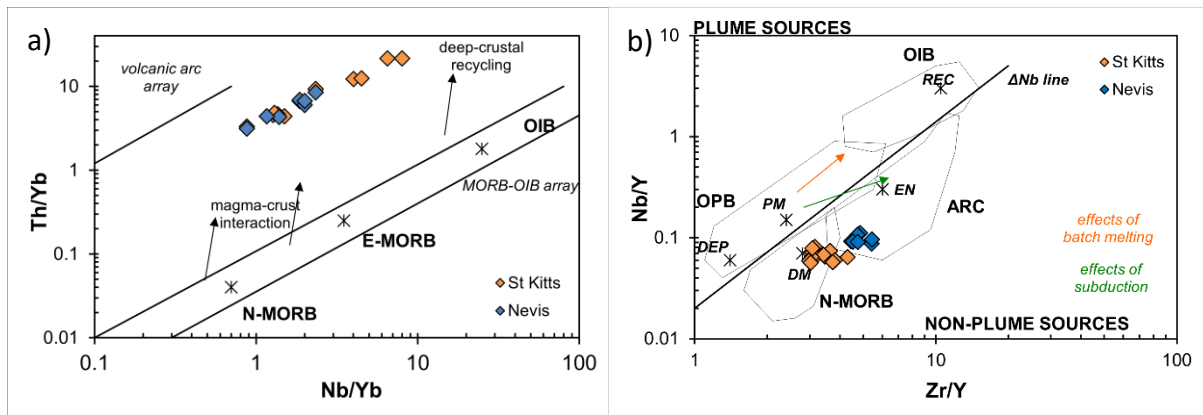


Figure 4.29 – Diagrams showing inferred origins of magma a) from Pearce (2008), b) from Pearce et al. (1984). N-MORB (normal mid-ocean ridge basalt), E-MORB (enriched mid-ocean ridge basalt), OIB (ocean island basalt), OPB (oceanic plateau basalts), DEP (deep depleted mantle), PM (primordial mantle), REC (recycled component), DM (depleted mantle), EN (enriched mantle).

Toothill et al. (2007) classified the St Kitts samples as transitional magmas, between low-k tholeiitic and calc-alkaline, suggesting that the magma source was MORB altered by sediment and fluid influx. This is also the proposed source of much of the volcanism observed in the Lesser Antilles (Macdonald *et al.*, 2000; Pichavant and Macdonald, 2003). This is in agreement with the source arc conditions interpreted by this study.

The low K-tholeiitic lavas from Mt Liamuiga differ compared to older deposits found on St Kitts. This could be due to the progressive reduction in the depth of the Benioff zone as the subducting slab adjusted to a shallower angle, caused by the earlier shift in volcanic axis (Baker, 1984). Due to this, the magma source for the most recent eruptions may differ to that from which older deposits on Mt Liamuiga originated.

4.4.2 Implications for magma storage

The samples analysed from St Kitts and Nevis exhibited a variety of petrological features, including zoning, dissolution textures, sieve textures, glomerocrysts, enclaves, and reaction

rims. This variety of features is evidence that the magma storage systems below both islands are complex, involving recharge, fractional crystallization and convection.

Zoning is a common feature in the phenocrysts observed in the Mt Liamuiga and Nevis Peak samples. Zoning in plagioclase phenocrysts reflects changes in the conditions within a magma reservoir during the residence time of the crystal. Oscillatory zoning was the most common type of zoning observed in this study. There are three main processes which can lead to the development of oscillatory zoning: kinetics, convection, and magma recharge (Humphreys *et al.*, 2006; Viccaro *et al.*, 2010). Fine oscillatory zoning on a crystal level is the result of gradual, diffusion-dependent depletion and re-enrichment of the melt surrounding the growing crystal, as a result of kinetics (Humphreys *et al.*, 2006; Viccaro *et al.*, 2010).

Oscillatory zoning may also form as a result of convection in the surrounding magma during crystallization, as the crystal is recycled through zones of cooler, more evolved melt, and hotter, less evolved melt (Humphreys *et al.*, 2006; Renjith, 2014; Viccaro *et al.*, 2010). Convection produces high amplitude, low frequency (HALF) oscillations, defined as having Am variations greater than 10% and bands greater than 20 μm in width (Viccaro *et al.*, 2010). HALF oscillations were observed in the zoned plagioclase found in the Mt Liamuiga samples. This suggests that convection influenced the growth of crystals in the magma reservoir below Mt Liamuiga. The same effects as convection may be observed when the temperature of the magma is changed but no movement has taken place.

Coarser oscillations can also develop due to magma recharge. The influx of more basic magma into the existing cooling melt can cause fluctuations in both temperature and chemical composition, which results in oscillatory zoning (Humphreys *et al.*, 2006; Renjith, 2014; Viccaro *et al.*, 2010). Further evidence for magma recharge-induced oscillatory zoning

includes resorption surfaces resulting in rounded corners and wavy zoning surfaces (Humphreys *et al.*, 2006). Whilst convection may have produced some of the oscillatory zoning observed, resorption surfaces are present in some plagioclase phenocrysts in the Mt Liamuiga and Nevis Peak samples, suggesting that magma recharge also occurred during crystal growth.

As well as the dissolution surfaces observed within zoned plagioclase phenocrysts, sieve textures and dissolution of the phenocrysts were observed in the St Kitts and Nevis samples. The rounded corners and irregular shape of the plagioclase phenocrysts suggests partial resorption of the crystal back into the melt from which it formed. Sieve textures can be attributed to advanced dissolution of a crystal and were frequently observed in plagioclase phenocrysts. Sieve texture often develops as a result of mixing with more mafic, Ca-rich melt (Humphreys *et al.*, 2006; Renjith, 2014). Prolonged dissolution occurs due to reactions with a hotter, more primitive magma and volatile-rich magma (Renjith, 2014; Viccaro *et al.*, 2010). This provides further evidence for recharge, and mixing with more primitive magma.

Small numbers of glomerocrysts were observed in the Mt Liamuiga samples. These glomerocrysts are thought to be remnants of crystal mush fragments. There are two possible ways in which these fragments could have been produced. The lack of open structures suggests that they may have been derived from compaction of the crystal mush, where spaces between crystals had been eliminated. Fragments of this compacted crystal mush may then have been entrained into the melt as it ascended (Bennett *et al.*, 2019). The second possible explanation for the formation of these glomerocrysts is via the process of synneusis, where individual crystals from within the mush adhered to other crystals during melt transport (Bennett *et al.*, 2019).

Evidence of the injection of hotter, primitive magma suggests that open-system processes are operating in the magma reservoirs below St Kitts and Nevis. Magma mixing of more mafic magmas with more fractionated silicic magmas is likely to have taken place (Humphreys *et al.*, 2006). Zoning features are consistent with a combination of convection in the magma reservoir, and periodic magma recharge. The abundance of disequilibrium features (e.g. zoning, dissolution surfaces and sieve textures, Figure 4.30) suggests that magma mixing took place on several occasions before the magma was erupted.








Type of texture	Description	Interpretation
TYPE 1 	Oscillatory-zoned	LAHF-kinetic effects at the plagioclase/melt interface HALF-crystallization in dynamic regime (i.e., convection in the open-conduit)
TYPE 2 	Dissolved or resorbed core	High rate of decompression at H ₂ O-undersaturated conditions in volatile-rich magma
TYPE 3 	Patchy core	Slow rate of decompression at H ₂ O-undersaturated conditions in volatile-poor magma
TYPE 4 	Coarsely sieved	Intermediate rate of decompression with respect to Type 2 and 3 at H ₂ O-undersaturated conditions
TYPE 5 	Resorbed rim	Recharge of more primitive, hotter and volatile-rich magma
TYPE 6 	Fine melt inclusion trains	Rapid growth due to decompression accompanied by volatile loss
TYPE 7 	Swallow-tailed	Skeletal growth due to syn-eruptive fast decompression of degassed magma

Figure 4.30 – representative diagrams of plagioclase textures and their suggested interpretations, adapted from Viccaro *et al.* (2010).

4.4.3 Interpretation of pre- and syn-eruptive processes and style of eruption

Two 'mixed magma' clasts were analysed in this study, SK5 and SK8, with the darker material found to have a lower SiO₂ content than the comparable lighter material in both whole rock and glass composition. This confirms that the 'colour' difference is a compositional difference and not a textural difference. This compositional difference suggests that magma mingling played a role in the evolution of the magmas from Mt Liamuiga, where two magmas interacted, but were not able to mix. The paucity of microlites in the lighter end members suggests that this mingling happened at shallow levels and shortly before eruption, as discussed further in Chapter 5. Sample SKN19 'LIGHT' and 'DARK' also display this trend, suggesting that similar processes may have taken place in the shallow magma plumbing system below Nevis.

As well as the basaltic andesite and andesites, this study identified three dacites, one from St. Kitts and two from Nevis. The sample from St. Kitts was taken from the lighter-coloured pumiceous material from a 'mixed magma PDC', suggesting that dacite could be an end member of the magma that erupted at that time. These samples are likely to represent the most evolved magmas erupted on St Kitts.

Enclaves were observed in two of the Mt Liamuiga samples. These enclaves lacked chilled or baked margins, and one enclave contained a quartz vein, suggesting that they were not magmatic. The most likely scenario is that the enclaves are xenoliths, fragments of country rock that have fallen into a relatively cool magma, potentially from the walls of the conduit.

Reaction rims are common on amphibole phenocrysts in both the Mt Liamuiga and Nevis peak samples. These rims are caused by amphibole crystals dehydrating and oxidising to Fe-oxides

plus pyroxene due to pressure release upon eruption of andesite (Rutherford and Hill, 1993).

The interpretation of these amphibole reaction rims are discussed further in Chapter 5.

The glass analysed in the St Kitts samples ranged in composition from andesitic to rhyolitic.

The glass in the Nevis Peak samples showed a narrower compositional range of dacitic to rhyolitic. The glass may have been the product of partial melting due to reheating or during decompression. This would provide an explanation for the differences between the whole rock and the matrix glass compositions (Zellmer *et al.*, 2003).

Analysing the St Kitts glasses in the microprobe revealed that not all of the groundmass glass was true glass. Some areas appeared to consist of fine poorly-formed crystalline material. A similar phenomenon has been identified in glass studied from the Soufrière Hills Volcano (SHV) on Montserrat and at Mt St Helens, where fine crystalline intergrowths of feldspar and quartz have been observed in patches of glass, likely the result of devitrification (Cashman, 1992; Cashman *et al.*, 2017; Couch *et al.*, 2003; Harford *et al.*, 2003; Horwell *et al.*, 2013). The Nevis glass data collected using the microprobe showed significantly high concentrations of SiO₂ of >80 wt.%. This is likely due to alteration of the glass. Typical alteration of silicic glasses involves glass matrix destruction and precipitation of secondary phases in the space left by the dissolution of the glass (Fisher and Schmincke, 1984).

4.4.4 Implications for future eruptions

The evidence gathered in this study suggests that that the magmatic systems operating below Mt Liamuiga and Nevis Peak were similar in nature. Magma differentiation begins at a deep level, from the primitive melt. Open-system processes dominated the magma reservoirs, where injections of hot, primitive magma and mixing between different batches were common. The reservoir would have been dynamic, with small and larger scale convection and

mixing. Rapid crystallization, reheating and partial melting occurred in the shallow crust, shortly before and during eruption. At Mt Liamuiga, mingling of separate magma batches took place shortly before eruption, where conditions and time scales did not allow for mixing to take place. The abundance of fragmented crystals in the Mt Liamuiga samples also suggests that the eruptions were much more explosive in nature. It is likely that similar processes control any future eruption at either Mt Liamuiga or Nevis Peak.

4.5 Conclusions

The following conclusions can be made from this chapter:

- The Mt Liamuiga and Nevis Peak samples analysed show a compositional range from basaltic andesite to andesite and dacite.
- The Mt Liamuiga deposits analysed were classified as low-K tholeiites. The source of these magmas is likely to be depleted mantle, similar to MORB, potentially contaminated by H₂O and sediments from the subducting slab.
- The Nevis Peak samples analysed were shown to be calc-alkaline. The source of the Nevis magmas is likely to be a mantle source similar to MORB, which has been contaminated by crustal material, likely from the subducting slab, and had undergone significant fractional crystallization.
- Open-system processes dominated at both St Kitts and Nevis. Recharges of hot, primitive magma injected into the reservoirs lead to mixing and magmatic differentiation.
- Rapid crystallization, reheating and partial melting occurred in the shallow crust before eruption.

- The 'Light' and 'Dark' colour in the SK5 and SK8 samples reflects a compositional difference, confirming that the colour variations are not a purely textural difference.
- The compositional difference between 'light' and 'dark' samples suggests that magma mingling took place at Mt Liamuiga shortly before eruption of the deposits SK5 and SK8 were sampled from.

5. Crystal Size Distribution Analysis for Mt Liamuiga and Nevis Peak

5.1 Introduction

Syn-eruptive magma ascent rate, together with the geometry of the conduit, has a large influence on the style in which a volcano erupts (Murch and Cole, 2019) and therefore the types of volcanic hazards that may be likely to affect the surrounding communities.

There is a significant link between the ascent rate of magma, and the explosivity of an eruption. Syn-eruptive ascent rates in the upper few hundred metres of the conduit influence the transition between effusive and explosive eruptions; generally speaking, the faster the ascent rate in the upper conduit, the more explosive the following eruption is likely to be. This also affects the resulting lava dome and lava flow morphologies (Cassidy *et al.*, 2015; Hammer *et al.*, 1999; Martel, 2012; Murch and Cole, 2019; Preece *et al.*, 2013, 2016; Rutherford, 2008; Szramek *et al.*, 2006; Toramaru *et al.*, 2008).

Several methods can be used to calculate syn-eruptive magma ascent rates. Extrusion rate can be observed during effusive eruptions. The limitations of this method are that good visibility of the eruption is needed, and the estimate of ascent rate is likely to apply to the upper few hundred metres of the conduit (Rutherford, 2008). Seismicity can also give an indication of ascent rate; real-time seismic amplitude measurements can be correlative with seismic signals at a range of depths to estimate the speed at which magma is moving (Rutherford, 2008) however, this also requires real time monitoring of the volcano.

Studying the bubble textures and degassing behaviour of volatiles during volatile exsolution can improve our understanding of magma decompression and ascent (Holloway and Blank, 1994). These techniques often require access to specialist equipment and experimental

methods beyond the scope of this study. Reaction rims formed around anhydrous minerals (e.g. pyroxene, amphibole or plagioclase) during the slow ascent of magma have been reproduced in experimental studies, allowing the analysis of these reaction rims to be used to constrain ascent rates (Devine *et al.*, 1998; Geschwind and Rutherford, 1995; Rutherford, and Hill, 1993). The study of reaction rims requires multiple crystals of the relevant minerals to be present in the samples to be studied. Groundmass crystallization, or the formation of microlite crystals (crystals less than 100 μm in size), is another indication of syn-eruptive ascent rate. Microlite size, morphology and abundance record the style and rate of magma ascent, due to the relationship between microlite nucleation rate and undercooling driven by decompression (Hammer *et al.*, 1999, 2000; Murch and Cole, 2019; Preece *et al.*, 2016; Szramek *et al.*, 2006; Toramaru *et al.*, 2008). Studying microlites requires access to a SEM (see Section 5.2). Table 5.1 shows the ascent rates calculated using the various methods listed above, for two volcanoes, Mt St Helens and Soufriere Hills Volcano. The large range in ascent rate estimates shown in Table 5.1 may be partly due to the ascent rates being calculated from different deposits from multiple eruptions. The variations between the same eruptions reflects the experimental nature of ascent rate and decompression studies. Table 5.1 also highlights the importance of using the same methods when comparing between eruptions.

Table 5.1 - Comparison of ascent rate estimates using different methods, for Mt St Helens, and Soufriere Hills.

Volcano	Source	Observation	Ascent rate (m/s)		Explosive rate (m/s)		Ascent Extrusive rate (m/s)	
			min	max	min	max	min	max
Mt St Helens (1980-86)	Browne and Szramek (2015), from Rutherford (2008)	Groundmass crystallization			1	3	0.01	0.02
Mt St Helens (1980 & 1986)	Browne and Szramek (2015), from Rutherford (2008)	Hornblende reaction rims			0.018	n/a	0.004	0.015
Mt St Helens (1980)	Cassidy et al. (2015), from Rutherford and Hill (1993)	Amphibole rims	0.002	0.015				
Mt St Helens (1980)	Browne and Szramek (2015), from Rutherford (2008)	Extrusion rate			1	2	0.0001	0.005
Mt St Helens (1980 & 1986)	Browne and Szramek (2015), from Rutherford (2008)	Seismicity			0.6	n/a	0.007	0.01
Soufriere Hills (2005-2010)	Murch and Cole (2019)	Groundmass crystallization			0.0006	0.0035	0.0057	0.014
Soufriere Hills (1995-2002)	Browne and Szramek (2015), from Rutherford (2008)	Hornblende reaction rims			0.2	n/a	0.001	0.012
Soufriere Hills (2003)	Cassidy et al. (2015), from Rutherford et al. (2003)	Amphibole rims	0.001	0.02				
Soufriere Hills (1996-1998)	Browne and Szramek (2015), from Rutherford (2008)	Extrusion rate			0.2	n/a	0.0001	0.02

This study uses analysis of groundmass (microlite) crystallization through crystal size distribution, to gain an insight into pre- and syn-eruptive ascent rates for Mt Liamuiga on St Kitts, and Nevis Peak on Nevis. While analysis of crystal size distribution (CSD) to study ascent rate conditions has not previously been attempted for any eruption productions on St Kitts or Nevis, the technique has been applied to other Caribbean volcanoes (Cassidy *et al.*, 2015; Clarke *et al.*, 2007; Martel, 2012; Martel and Poussineau, 2007; Murch and Cole, 2019). This method was chosen as microlites are present in the samples collected, and it is suitable for historic and prehistoric eruptions (i.e. eruptions with no observational data).

5.2 Methodology

Samples were chosen from a variety of eruption products (fallout and PDCs) deposited during Mt Liamuiga's most recent eruptions. These samples were set in resin, polished and carbon-coated in preparation for SEM and electron microprobe analysis.

5.2.1 Image and data acquisition

Images were acquired using the JEOL7001 scanning electron microscope at the Plymouth Electron Microscopy Centre (PEMC) at the University of Plymouth. Carbon-coated samples were imaged at 15-20kV and a working distance of 10 mm, using both secondary electron (SE) and backscatter electron (BSE) detectors. Areas for imaging were chosen for their microlite population and lack of phenocrysts.

Quantitative Microlite crystal and vesicle analysis was conducted using BSE images saved as TIFF files. These images were manually traced using Inkscape vector drawing software. The size of the area analysed varied depending on the average microlite density and size. The processed images were exported to ImageJ (version 1.53o) where measurements were

collected for the field of view area, number of crystals, mean crystal area and dimensions for plagioclase and mafic microlites. The crystal dimensions (long and short axis) were collected using the best fit ellipsoid method. Using data collected from analysis in ImageJ, N_A (plagioclase area number density) and microlite area fraction (ϕ) were calculated. Crystals that were cut off by the edge of images were excluded in the 2D ImageJ analysis but were included in the percentage area.

The major element microlite and glass compositions were acquired using a JEOL JXA8530F Hyperprobe electron microprobe at the University of Bristol. A variety of standards (silicate, oxide and metal) were used for calibration of the spectrometers; these calibrations were run at the beginning of each day of analysis to ensure precision and accuracy. Microlites were analysed using a 15 kV acceleration voltage, 20 nA beam current and a focused $\sim 10 \mu\text{m}$ beam, while glasses were analysed using a 5 nA beam current and defocussed $10 \mu\text{m}$ beam. The compositional totals were checked for each data point to ensure consistency, and those with totals outside of 97-102% were discarded. For the majority of samples, glass and microlite composition values used in the ascent rate calculations were acquired from the microprobe. The microprobe data was used to validate the reliability of the SEM qualitative composition data acquired; the validated SEM data was used in ascent rate calculation for samples that were not analysed using the microprobe (due to time constraints).

5.2.2 Ascent rates

Ascent rates were estimated using the microlite number density (MND) water exsolution rate meter of Toramaru *et al.* (2008). Both plagioclase and mafic microlites were studied for this analysis. The decompression rate was calculated as:

$$\left| \frac{dP_w}{dt} \right| = \frac{c}{b} \left(\frac{N}{a} \right)^{\frac{2}{3}}$$

Where a is a calculation combining wt.% H₂O and glass SiO₂ and can be calculated as:

$$a = 3 \times 10^{15 \pm 1 + 0.345 \Delta C_{Si} - 0.65 C_w}$$

b is a constant (40 for plagioclase, 17 for pyroxene), N is the microlite number density and c is a function of the water content:

$$c = 11.2 \times 10^6 \times C_w$$

where C_w and C_{Si} are the water content and the average glass SiO₂ for the sample.

Ascent rate was then calculated as:

$$V_n = \frac{1}{\rho g} \left| \frac{dP_w}{dz} \right|$$

Where ρ is density, g is gravity, and $\left| \frac{dP}{dz} \right|$ is the decompression rate at a given water content based on depth (z).

The most sensitive factors of this calculation are the glass composition and the plagioclase area number density (N_A), although water content (wt. % H₂O) also has an impact. Errors of 5% in C_{Si} can result in differences of up to 500% in the calculated ascent rates using this method (Murch and Cole, 2019). For all samples a wt. % H₂O of 6% was used based on water contents calculated for St Kitts in previous studies including Melekhova *et al.* (2017) and Higgins *et al.* (2021). This value was calculated from samples taken across St Kitts, and not limited to Mt Liamuiga. Water contents calculated for similar volcanoes were considered, however, values calculated from material in St Kitts were considered the most representative.

5.2.3 Crystal size distribution (CSD)

Crystal size distributions (CSD) were calculated using *CSDcorrections* (version 1.60) (Higgins, 2000). The rock fabric was set to massive, crystal shape values were estimated from data obtained from ImageJ, and crystal roundness was set to 0.1 for all samples (where 0 is rectangular and 1 is an ellipsoid). *CSDcorrections* uses the 2D length measurements of the sampled crystals as well as information on crystal habit, crystal roundness and sample foliation, to perform stereological correction of this 2D data array, providing a corrected 3D CSD (Morgan and Jerram, 2006). The areas analysed were corrected for vesicles, and any bins that contained less than 5 crystals were removed as they were considered to be imprecise (Higgins, 2000; Murch and Cole, 2019).

5.2.4 Crystallization times and Nucleation rates

Crystallization times and Nucleation rates were calculated using slope and y-intercept values calculated from CSDs, as described in Marsh (1988). Crystallisation times were calculated using the following equation:

$$slope = \frac{-1}{G\tau}$$

where τ is the crystallization time and G , the crystal growth rate, is a constant.

The nucleation rate (J) was calculated as:

$$J = n^{\circ}G$$

where n° is the y-intercept.

5.3 Results

5.3.1 Quantitative microlite analysis

The microlites identified can be classified into two categories, plagioclase microlites and mafic microlites. The mafic microlites consist of pyroxenes, amphiboles and oxides. The two groups of crystals can be identified by their distinctly different appearances in BSE images. The plagioclase crystals appear dark in colour, in some samples only faintly visible compared to the surrounding glass. The mafic microlites appear as easily identifiable, bright white crystals.

The samples collected from St Kitts contained few microlite crystals, with most containing only small populations of plagioclase microlites, and consistent, but small populations of pyroxene, amphibole and oxide microlites. The majority of plagioclase microlites were tabular, acicular or swallow-tailed (Figure 5.1). There were no significant differences in morphology between samples. Some samples contain few to no measurable plagioclase microlites.

Where present, plagioclase microlites made up between 1.94% and 63.12% of the microlite population, with an average of 17.05%, these populations correspond to between 0.06% and 11.24% of the sample area. Pyroxene, amphibole and oxides made up 36.88% to 98.06% of the microlite population. These mafic microlites were present in all samples that were seen to contain microlites, whereas plagioclase was absent from sample SK8D, and generally in lesser numbers than the mafic microlites when present.

In the Nevis samples, Plagioclase made up between 11.25% and 55.37% of the microlite population, and between 1.3% and 5.9% of the sample area. Other microlites, including

pyroxene, amphibole and oxides, made up 0.7% to 1.5% of the sample area. The microlites in the Nevis samples were mostly tabular, with a small number of swallow tail shaped microlites.

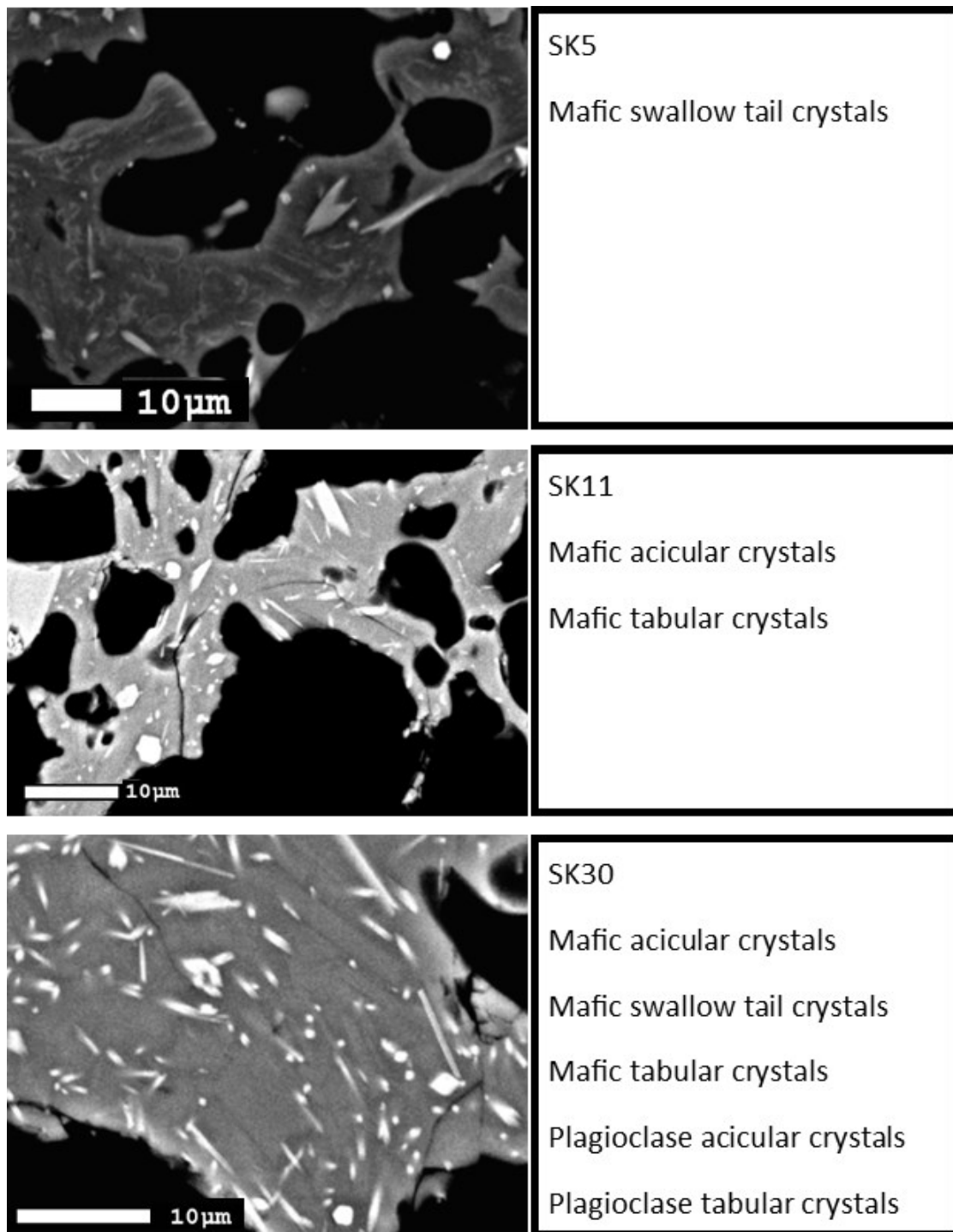


Figure 5.1 - SEM images showing key microlite textures. The mafic crystals are shown as light crystals, while the plagioclase microlites are shown as dark grey.

The mean crystal area of plagioclase microlites in each sample varied widely, ranging between $0.85 \mu\text{m}^2$ and $44.73 \mu\text{m}^2$ (Figure 5.2). The mean microlite area of the mafic microlites is comparatively smaller than plagioclase microlites, although they follow the same trend. The two samples from Nevis, showed a variation in mean crystal area values (Figure 5.2).

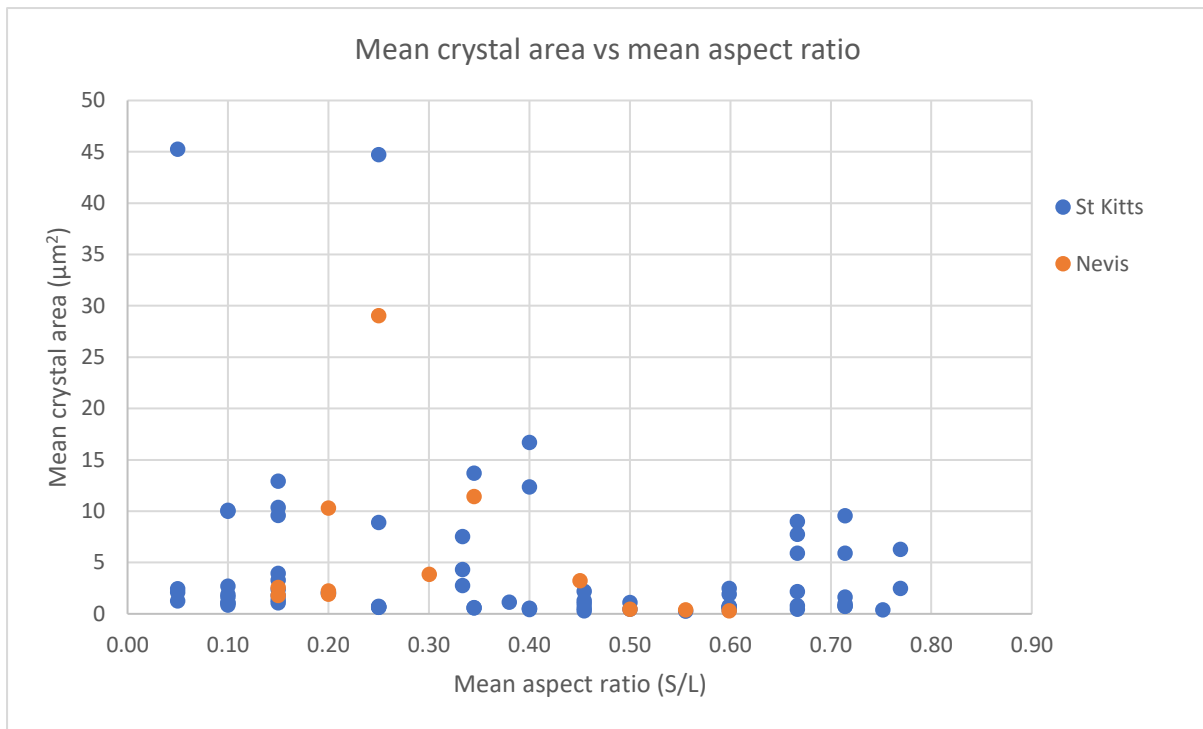


Figure 5.2 - Mean aspect ratio (S/L) against mean microlite crystal area (μm^2) for both plagioclase and mafic microlites analysed from the Mt Liamuiga and Nevis Peak samples.

The mean aspect ratio (shortest/longest value) was calculated for each sample. The values for Mt Liamuiga ranged from 0.05 to 0.40 for plagioclase microlites, and 0.25 to 0.77 for mafic microlites (Figure 5.2 and Table 5.2). Sample SK1 showed the highest mean aspect ratio for plagioclase microlites, with an average of 0.38, while samples SK11 and SK31 the lowest showed mean aspect ratio average, 0.10 for plagioclase microlites. The mean aspect ratios for mafic microlites were generally larger when compared with the plagioclase microlites. The mafic microlites observed in sample SK21 had the largest mean aspect ratio for mafic

microlites, with an average of 0.71. The lowest mean aspect ratio for mafic microlites was observed in sample SK5D with an average value of 0.3. The two samples from Nevis, showed mean aspect ratios ranging from 0.15 to 0.34 for plagioclase microlites, and 0.15 to 0.60 for mafic microlites.

Table 5.2 - Quantitative microlite data for plagioclase microlites.

Sample no.	Sample description	Total no. plagioclase microlites n	Total image area (mm ²)	Total image area (μm ²)	Total area of plagioclase crystals (μm ²)	Total area of plagioclase crystals (mm ²)	Total area of Solid Groundmass (mm ²)	Crystallinity Φ	Total area of vesicles (mm ²)	Total area of vesicles %	Plagioclase area number density (number of crystals per mm ²) NA (μm ²)	Area %	Plagioclase area fraction φ	Mean microlite area (μm ²)	Characteristic plagioclase crystal size Sn(μm)	Characteristic plagioclase crystal size Sn(mm)	MND Volumetric plagioclase number density Nv (mm ⁻³)	MND Volumetric plagioclase number density Nv (m ⁻³)	Mean aspect ratio (s/l)
SK1/1	Pumice clast from Location SK1	50	0.014	14000	110	0.00011	0.008	0.014	0.006	42.61	3.57E+09	0.79	0.01	2.75	0.0019	0.0000019	1.83E+06	1.83E+15	0.33
SK1/2	Pumice clast from Location SK1	52	0.014	14000	224	0.00022	0.007	0.033	0.007	51.37	3.71E+09	1.60	0.03	4.31	0.0030	0.0000030	1.25E+06	1.25E+15	0.33
SK1/3	Pumice clast from Location SK1	38	0.015	15400	287	0.00029	0.007	0.041	0.008	54.53	2.47E+09	1.86	0.04	7.55	0.0041	0.0000041	6.03E+05	6.03E+14	0.33
SK1/4	Pumice clast from Location SK1	74	0.015	15400	437	0.00044	0.007	0.063	0.008	54.70	4.81E+09	2.84	0.06	5.90	0.0036	0.0000036	1.33E+06	1.33E+15	0.67
SK1/5	Pumice clast from Location SK1	40	0.014	14000	357	0.00036	0.007	0.054	0.007	52.70	2.86E+09	2.55	0.05	8.92	0.0044	0.0000044	6.56E+05	6.56E+14	0.25
SK5D/01	Pumice - darker component of sample	30	0.001	1200	35	0.00003	0.001	0.033	0.000	41.17	2.50E+10	2.89	0.03	1.10	0.0012	0.0000012	2.17E+07	2.17E+16	0.10
SK5D/02	Pumice - darker component of sample	26	0.002	2000	29	0.00003	0.001	0.029	0.001	38.28	1.30E+10	1.43	0.03	1.13	0.0015	0.0000015	8.66E+06	8.66E+15	0.38
SK5D/03	Pumice - darker component of sample	49	0.017	16500	118	0.00012	0.007	0.016	0.009	52.50	2.97E+09	0.72	0.02	2.38	0.0023	0.0000023	1.28E+06	1.28E+15	0.15
SK11/01	Pumice	19	0.054	54000	31	0.00003	0.047	0.001	0.007	51.20	3.52E+08	0.06	0.00	1.65	0.0014	0.0000014	2.56E+05	2.56E+14	0.10
SK11/02	Pumice	24	0.009	8800	43	0.00004	0.004	0.010	0.004	65.00	2.73E+09	0.49	0.01	1.79	0.0019	0.0000019	1.43E+06	1.43E+15	0.15
SK11/03	Pumice	29	0.009	8800	61	0.00006	0.004	0.015	0.005	64.70	3.30E+09	0.69	0.02	2.10	0.0022	0.0000022	1.53E+06	1.53E+15	0.05
SK20/1	Moderately vesicular clast from location SK10	126	0.052	52000	1210	0.00121	0.045	0.027	0.007	39.90	2.42E+09	2.33	0.03	9.61	0.0033	0.0000033	7.29E+05	7.29E+14	0.15
SK20/2	Moderately vesicular clast	80	0.052	52000	800	0.00080	0.025	0.031	0.027	43.00	1.54E+09	1.54	0.03	10.00	0.0045	0.0000045	3.40E+05	3.40E+14	0.10

	from location SK10																		
SK20/3	Moderately vesicular clast from location SK10	82	0.052	52000	827	0.00083	0.023	0.035	0.029	46.50	1.58E+09	1.59	0.04	10.09	0.0047	0.0000047	3.33E+05	3.33E+14	0.10
SK20/4	Moderately vesicular clast from location SK10	76	0.052	52000	983	0.00098	0.023	0.042	0.029	49.90	1.46E+09	1.89	0.04	12.94	0.0054	0.0000054	2.73E+05	2.73E+14	0.15
SK20/5	Moderately vesicular clast from location SK10	66	0.030	30000	684	0.00068	0.014	0.049	0.016	35.30	2.20E+09	2.28	0.05	10.37	0.0047	0.0000047	4.68E+05	4.68E+14	0.15
SK21/1	Dense block from Location SK21	68	0.154	15400 0	3042	0.00304	0.134	0.023	0.020	13.08	4.42E+08	1.98	0.02	44.73	0.0072	0.0000072	6.16E+04	6.16E+13	0.25
SK21/2	Dense block from Location SK21	13	0.086	86000	588	0.00059	0.042	0.014	0.044	13.05	1.51E+08	0.68	0.01	45.26	0.0096	0.0000096	1.57E+04	1.57E+13	0.05
SK21/3	Dense block from Location SK21	52	0.085	85000	868	0.00087	0.038	0.023	0.047	10.70	6.12E+08	1.02	0.02	16.69	0.0061	0.0000061	1.00E+05	1.00E+14	0.40
SK21/4	Dense block from Location SK21	33	0.083	83000	453	0.00045	0.037	0.012	0.046	10.20	3.98E+08	0.55	0.01	13.72	0.0055	0.0000055	7.20E+04	7.20E+13	0.34
SK21/5	Dense block from Location SK21	15	0.083	83000	184	0.00018	0.039	0.005	0.044	12.90	1.81E+08	0.22	0.00	12.37	0.0051	0.0000051	3.53E+04	3.53E+13	0.40
SK24b/01	Steel dust sample	75	0.012	11700	203	0.00020	0.010	0.020	0.002	53.25	6.41E+09	1.73	0.02	2.70	0.0018	0.0000018	3.64E+06	3.64E+15	0.10
SK24b/02	Steel dust sample	68	0.006	6300	138	0.00014	0.003	0.045	0.003	49.20	1.08E+10	2.19	0.04	2.03	0.0020	0.0000020	5.30E+06	5.30E+15	0.20
SK24b/03	Steel dust sample	67	0.015	15000	140	0.00014	0.007	0.021	0.008	51.88	4.47E+09	0.93	0.02	2.09	0.0022	0.0000022	2.07E+06	2.07E+15	0.20
SK27a/01	Steel dust sample	166	0.002	2000	225	0.00022	0.002	0.129	0.000	29.42	8.30E+10	11.24	0.13	1.35	0.0012	0.0000012	6.65E+07	6.65E+16	0.15
SK27a/02	Steel dust sample	175	0.002	2000	189	0.00019	0.001	0.193	0.001	29.40	8.75E+10	9.46	0.19	1.08	0.0015	0.0000015	5.89E+07	5.89E+16	0.15
SK27a/03	Steel dust sample	170	0.002	2000	217	0.00022	0.001	0.241	0.001	31.43	8.50E+10	10.86	0.24	1.28	0.0017	0.0000017	5.05E+07	5.05E+16	0.05
SK30/1	Dense block from location SK12	201	0.005	4800	494	0.00049	0.004	0.118	0.001	21.40	4.19E+10	10.29	0.12	2.46	0.0017	0.0000017	2.49E+07	2.49E+16	0.05

SK30/2	Dense block from location SK12	62	0.005	5400	245	0.00025	0.003	0.093	0.003	36.90	1.15E+10	4.54	0.09	3.96	0.0028	0.0000028	4.04E+06	4.04E+15	0.15
SK30/3	Dense block from location SK12	73	0.005	5400	240	0.00024	0.002	0.099	0.003	34.60	1.35E+10	4.44	0.10	3.28	0.0027	0.0000027	5.01E+06	5.01E+15	0.15
SK31/1	Pumice from location SK12	31	0.002	2400	33	0.00003	0.002	0.016	0.000	52.60	1.29E-02	1.37	0.02	1.06	0.0011	0.0000011	1.17E+07	1.17E+16	0.10
SK31/2	Pumice from location SK12	27	0.002	2400	51	0.00005	0.001	0.044	0.001	34.50	1.13E+07	2.15	0.04	1.91	0.0020	0.0000020	5.70E+06	5.70E+15	0.10
SK31/3	Pumice from location SK12	23	0.002	2400	20	0.00002	0.001	0.018	0.001	51.30	9.58E+06	0.82	0.02	0.85	0.0014	0.0000014	6.96E+06	6.96E+15	0.10
SKN18/01	Nevis	380	0.019	19000	682	0.00068	0.017	0.041	0.002	49.30	2.00E+10	3.59	0.04	1.79	0.0014	0.0000014	1.39E+07	1.39E+16	0.15
SKN19/02	Nevis	299	0.011	11000	575	0.00057	0.005	0.107	0.006	48.00	2.72E+10	5.22	0.11	1.92	0.0020	0.0000020	1.37E+07	1.37E+16	0.20
SKN18/03	Nevis	323	0.012	12000	718	0.00072	0.005	0.133	0.007	28.57	2.69E+10	5.98	0.13	2.22	0.0022	0.0000022	1.21E+07	1.21E+16	0.20
SKN19/01	Nevis	25	0.019	19200	258	0.00026	0.017	0.015	0.003	46.99	1.30E+09	1.34	0.02	10.32	0.0034	0.0000034	3.78E+05	3.78E+14	0.20
SKN19/02	Nevis	73	0.117	11700 0	2121	0.00212	0.057	0.037	0.060	59.06	6.24E+08	1.81	0.04	29.06	0.0077	0.0000077	8.10E+04	8.10E+13	0.25
SKN19/03	Nevis	103	0.077	76800	1178	0.00118	0.035	0.034	0.042	56.87	1.34E+09	1.53	0.03	11.44	0.0050	0.0000050	2.66E+05	2.66E+14	0.34

Table 5.3 - Quantitative microlite data for mafic microlites.

Sample no.	Sample description	Total mafic microlites counted	Total image area (μm^2)	Total area of mafic crystals (μm^2)	Total area of mafic crystals (mm^2)	Total area of Solid Groundmass (μm^2)	Crystallinity Φ	Total area of vesicles (μm^2)	Total area of vesicles %	Mafic area number density (number of crystals per mm^2) N_A (μm^2)	Area %	Mafic area fraction ϕ	Mean microlite area (μm^2)	Characteristic mafic crystal size S_n ($\text{m}\mu$)	MND Volumetric mafic number density N_v (mm^{-3})	MND Volumetric mafic number density N_v (m^{-3})	Mean aspect ratio (s/l)
SK1/1	Pumice clast from Location SK1	395	14000	241	0.000240553	8120	0.030	5880	42.61	4.86E+10	1.72	0.03	0.63	0.0008	6.23E+07	6.23E+16	0.60
SK1/2	Pumice clast from Location SK1	430	14000	330	0.000330047	6860	0.048	7140	51.37	6.27E+10	2.36	0.05	0.77	0.0009	7.15E+07	7.15E+16	0.60
SK1/3	Pumice clast from Location SK1	300	15400	301	0.00030	6930	0.043	8470	54.53	4.33E+10	1.96	0.04	1.00	0.0010	4.32E+07	4.32E+16	0.71
SK1/4	Pumice clast from Location SK1	406	15400	305	0.00030	6930	0.044	8470	54.70	5.86E+10	1.98	0.04	0.75	0.0009	6.76E+07	6.76E+16	0.71
SK1/5	Pumice clast from Location SK1	340	14000	276	0.000276374	6580	0.042	7420	52.70	5.17E+10	1.97	0.04	0.81	0.0009	5.73E+07	5.73E+16	0.67
SK5D/01	Pumice - darker component of sample	61	1200	38	0.0000	1043	0.037	157	41.17	5.08E+10	3.20	0.04	0.65	0.0009	5.97E+07	5.97E+16	0.25
SK5D/02	Pumice - darker component of sample	118	2000	49	0.0000	980	0.050	1020	38.28	5.90E+10	2.47	0.05	0.42	0.0009	6.38E+07	6.38E+16	0.40
SK5D/03	Pumice - darker component of sample	193	16500	137	0.0001	7425	0.018	9075	52.50	1.17E+10	0.83	0.02	0.71	0.0013	9.32E+06	9.32E+15	0.25
SK8D/1	Pumice	1253	58800	1410	0.0014	51109	0.028	7691	42.50	2.13E+10	2.40	0.03	1.13	0.0011	1.87E+07	1.87E+16	0.50
SK8D/2	Pumice	1086	58000	1405	0.0014	28420	0.049	29580	40.90	1.87E+10	2.42	0.05	1.29	0.0016	1.15E+07	1.15E+16	0.45
SK8D/3	Pumice	563	59000	1082	0.0011	26550	0.041	32450	47.50	9.54E+09	1.83	0.04	1.92	0.0021	4.62E+06	4.62E+15	0.60
SK8D/4	Moderately vesicular clast from location SK10	1637	91000	1275	0.0013	40950	0.031	50050	44.20	1.80E+10	1.40	0.03	0.78	0.0013	1.37E+07	1.37E+16	0.71
SK8D/5	Moderately vesicular clast from location SK10	1009	78000	987	0.0010	36660	0.027	41340	44.10	1.29E+10	1.27	0.03	0.98	0.0014	8.97E+06	8.97E+15	0.45

SK11/01	Moderately vesicular clast from location SK10	555	5400	338	0.0003	4694	0.072	706	51.20	1.03E+11	6.26	0.07	0.61	0.0008	1.23E+08	1.23E+17	0.34
SK11/02	Moderately vesicular clast from location SK10	367	8800	170	0.0002	4312	0.039	4488	65.00	4.17E+10	1.93	0.04	0.46	0.0010	4.29E+07	4.29E+16	0.50
SK11/03	Moderately vesicular clast from location SK10	515	8800	196	0.0002	3960	0.049	4840	64.70	5.85E+10	2.23	0.05	0.38	0.0009	6.37E+07	6.37E+16	0.60
SK20/1	Dense block from Location SK21	491	54000	1071	0.0011	46937	0.023	7063	39.90	9.09E+09	1.98	0.02	2.18	0.0016	5.74E+06	5.74E+15	0.67
SK20/2	Dense block from Location SK21	516	52000	1141	0.0011	25480	0.045	26520	43.00	9.92E+09	2.19	0.04	2.21	0.0021	4.67E+06	4.67E+15	0.45
SK20/3	Dense block from Location SK21	393	52000	980	0.0010	23400	0.042	28600	46.50	7.56E+09	1.88	0.04	2.49	0.0024	3.21E+06	3.21E+15	0.77
SK20/4	Dense block from Location SK21	398	52000	984	0.0010	23400	0.042	28600	49.90	7.65E+09	1.89	0.04	2.47	0.0023	3.27E+06	3.27E+15	0.60
SK20/5	Dense block from Location SK21	362	30000	591	0.0006	14100	0.042	15900	35.30	1.21E+10	1.97	0.04	1.63	0.0019	6.48E+06	6.48E+15	0.71
SK21/1	Dense block from Location SK21	1056	154000	6239	0.0062	133857	0.047	20143	13.08	6.86E+09	4.05	0.05	5.91	0.0026	2.63E+06	2.63E+15	0.71
SK21/2	Dense block from Location SK21	658	86000	2960	0.0030	42140	0.070	43860	13.05	7.65E+09	3.44	0.07	9.01	0.0030	2.53E+06	2.53E+15	0.67
SK21/3	Dense block from Location SK21	612	85000	5844	0.0058	38250	0.153	46750	10.70	7.20E+09	6.88	0.15	9.56	0.0046	1.56E+06	1.56E+15	0.71
SK21/4	Dense block from Location SK21	694	83000	5389	0.0054	37350	0.144	45650	10.20	8.36E+09	6.49	0.14	7.76	0.0042	2.01E+06	2.01E+15	0.67
SK21/5	Dense block from Location SK21	677	83000	4262	0.0043	39010	0.109	43990	12.90	8.16E+09	5.13	0.11	6.30	0.0037	2.23E+06	2.23E+15	0.77
SK24b/01	Steel dust sample	374	11700	215	0.0002	10170	0.021	1530	53.25	3.20E+10	1.84	0.02	0.57	0.0008	3.93E+07	3.93E+16	0.34

SK24b/02	Steel dust sample	253	6300	143	0.0001	3087	0.046	3213	49.20	4.02E+10	2.27	0.05	0.56	0.0011	3.74E+07	3.74E+16	0.40
SK24b/03	Steel dust sample	517	15000	164	0.0002	6750	0.024	8250	51.88	3.45E+10	1.09	0.02	0.32	0.0008	4.11E+07	4.11E+16	0.45
SK27a/01	Steel dust sample	97	2000	71	0.0001	1738	0.041	262	29.42	4.85E+10	3.56	0.04	0.73	0.0009	5.28E+07	5.28E+16	0.25
SK27a/02	Steel dust sample	186	2000	94	0.0001	980	0.096	1020	29.40	9.30E+10	4.70	0.10	0.51	0.0010	9.16E+07	9.16E+16	0.40
SK27a/03	Steel dust sample	281	2000	78	0.0001	900	0.087	1100	31.43	1.41E+11	3.90	0.09	0.28	0.0008	1.79E+08	1.79E+17	0.56
SK30/1	Dense block from location SK12	410	4800	273	0.0003	4172	0.065	628	21.40	8.54E+10	5.69	0.07	0.67	0.0009	9.76E+07	9.76E+16	0.60
SK30/2	Dense block from location SK12	348	5400	202	0.0002	2646	0.076	2754	36.90	6.44E+10	3.74	0.08	0.58	0.0011	5.92E+07	5.92E+16	0.45
SK30/3	Dense block from location SK12	419	5400	273	0.0003	2430	0.112	2970	34.60	7.76E+10	5.06	0.11	0.65	0.0012	6.45E+07	6.45E+16	0.25
SK31/1	Pumice from location SK12	111	2400	73	0.0001	2086	0.035	314	52.60	4.63E+07	3.04	0.03	0.66	0.0009	5.32E+07	5.32E+16	0.60
SK31/2	Pumice from location SK12	164	2400	0	0.0000	1176	0.000	1224	34.50	6.83E+07	0.02	0.00	0.39	0.0001	9.83E+08	9.83E+17	0.75
SK31/3	Pumice from location SK12	131	2400	62	0.0001	1080	0.057	1320	51.30	5.46E+07	2.58	0.06	0.47	0.0010	5.32E+07	5.32E+16	0.67
SKN18/01	Nevis	408	19000	158	0.0002	16515	0.010	2485	49.30	2.15E+10	0.83	0.0096	0.39	0.0007	3.21E+07	3.21E+16	0.56
SKN18/02	Nevis	241	11000	108	0.0001	5390	0.020	5610	48.00	2.19E+10	0.98	0.0199	0.45	0.0010	2.30E+07	2.30E+16	0.50
SKN18/03	Nevis	399	12000	115	0.0001	5400	0.021	6600	28.57	3.33E+10	0.96	0.0213	0.29	0.0008	4.16E+07	4.16E+16	0.60
SKN19/01	Nevis	45	19200	146	0.0001	16689	0.009	2511	46.99	2.34E+09	0.76	0.01	3.24	0.0019	1.21E+09	1.21E+18	0.45
SKN19/02	Nevis	576	11700 0	2225	0.0022	57330	0.039	59670	59.06	4.92E+09	1.90	0.04	3.86	0.0028	1.75E+09	1.75E+18	0.30
SKN19/03	Nevis	288	76800	742	0.0007	34560	0.021	42240	56.87	3.75E+09	0.97	0.02	2.58	0.0024	1.57E+09	1.57E+18	0.15

Microlite abundance can be expressed by the microlite area number density (N_a), a measure of the number of microlites per measured unit, in this case mm^2 . The N_a values are shown in Table 5.2 and displayed in Figure 5.3. The largest N_a values were shown by SK30, with values range from 11481.48 mm^{-2} to 41875 mm^{-2} . The lowest value was shown by SK21 values range from 151.16 mm^{-2} to 611.76 mm^{-2} . The Steel Dust samples showed a large difference in N_a values. The two samples from Nevis show very different N_a values. SKN18 ranged from 20000 mm^{-2} to 27181.82 mm^{-2} , while SKN19 ranged from 623.93 mm^{-2} to 1341.15 mm^{-2} .

Plagioclase microlite crystallinity (ϕ) is expressed as a fraction of the groundmass area, excluding areas of vesicles and phenocrysts. Plagioclase microlite crystallinity (ϕ) was calculated based on Hammer *et al.* (1999), and is shown in Table 5.2 and plotted in Figure 5.3. The Mt Liamuiga samples show a consistent crystallinity, with values ranging between 0.015 and 0.250, and the majority of samples ranging between 0.015 and 0.050, the mean value was 0.058, with 1 s.d. of 0.057. Crystallinity plotted against N_a is shown in Figure 5.3. The two samples from Nevis showed crystallinity varied between 0.00873 and 0.13300 (Figure 5.3).

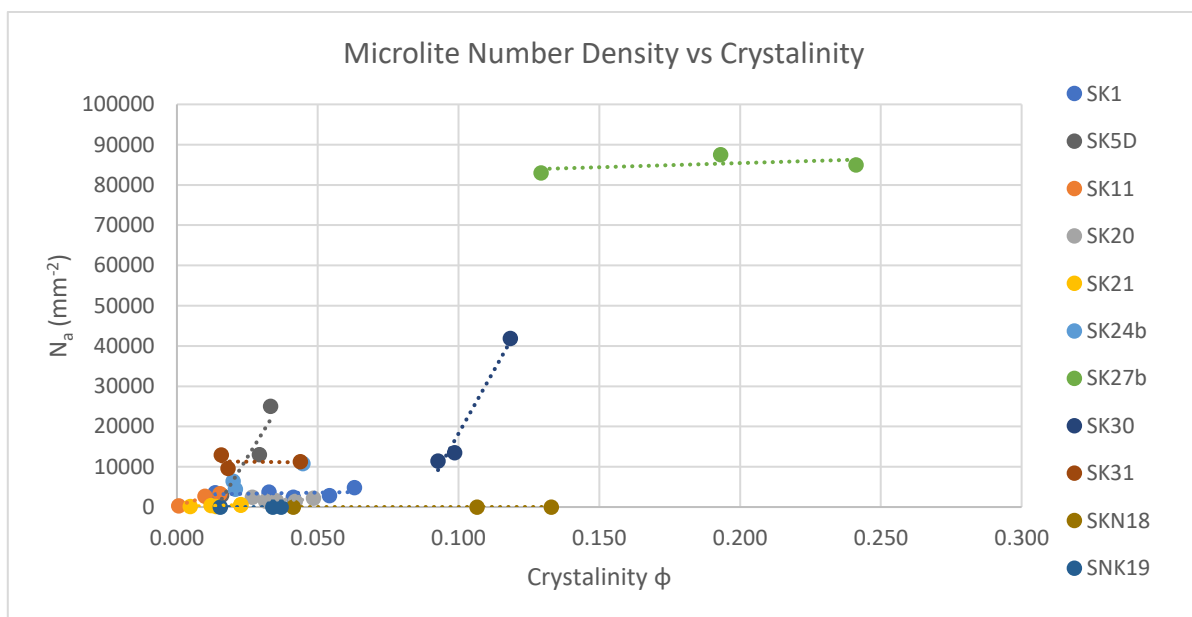


Figure 5.3 - Microlite area number density (N_a) shown against crystallinity (ϕ) for Mt Liamuiga and Nevis samples.

5.3.2 Crystal size distributions (CSD)

Studying plagioclase microlite distribution allows 2-dimensional data to be converted into 3-dimensional data, providing a more complete picture of the crystal growth patterns in the sample, and allowing for the identification of spatial relationships that may not be apparent in a 2D analysis. 2-dimensional microlite data, calculated from ImageJ, was imported into CSD corrections to generate crystal size distribution (CSD) plots. These plots show population density (number of crystals per unit volume) against crystal size.

The CSD plots produced for the Mt Liamuiga samples are either concave or convex in shape and can be split into two or three separate straight lines (Figures 5.4 to 5.7, where each line represents a different analysed point on a sample). The y-intercept values (n°) and slope values calculated for the entire plots and straight-line sections are shown in Table 5.4. The y-intercept (n°) varies from 14.79 mm^{-4} to 25.54 mm^{-4} for plagioclase microlites. The lowest values are shown by sample SK21 (Figure 5.4), varying between 14.79 mm^{-4} and 18.66 mm^{-4} . Other SK20 and SK30, similarly to SK21, show higher values (Figure 5.4). The samples collected from the Steel dust show the highest y-intercept values, as shown in Figures 5.4, and Table 5.4.

The slope values vary greatly throughout the Mt Liamuiga samples. The lowest value is -95, while the highest value is -941, as shown in Table 5.4. Variation in slope was observed in individual samples. SK1 shows an average slope value of -287, while SK11 shows an average slope value of -789. SK24b and SK27a show average slope values of -753 and -860 respectively. Samples SK20, SK21 and SK30 show average slope values of -299, -278 and -560 respectively. SK5D shows an average slope value of -729, while sample SK31 showed an average slope value of -425.

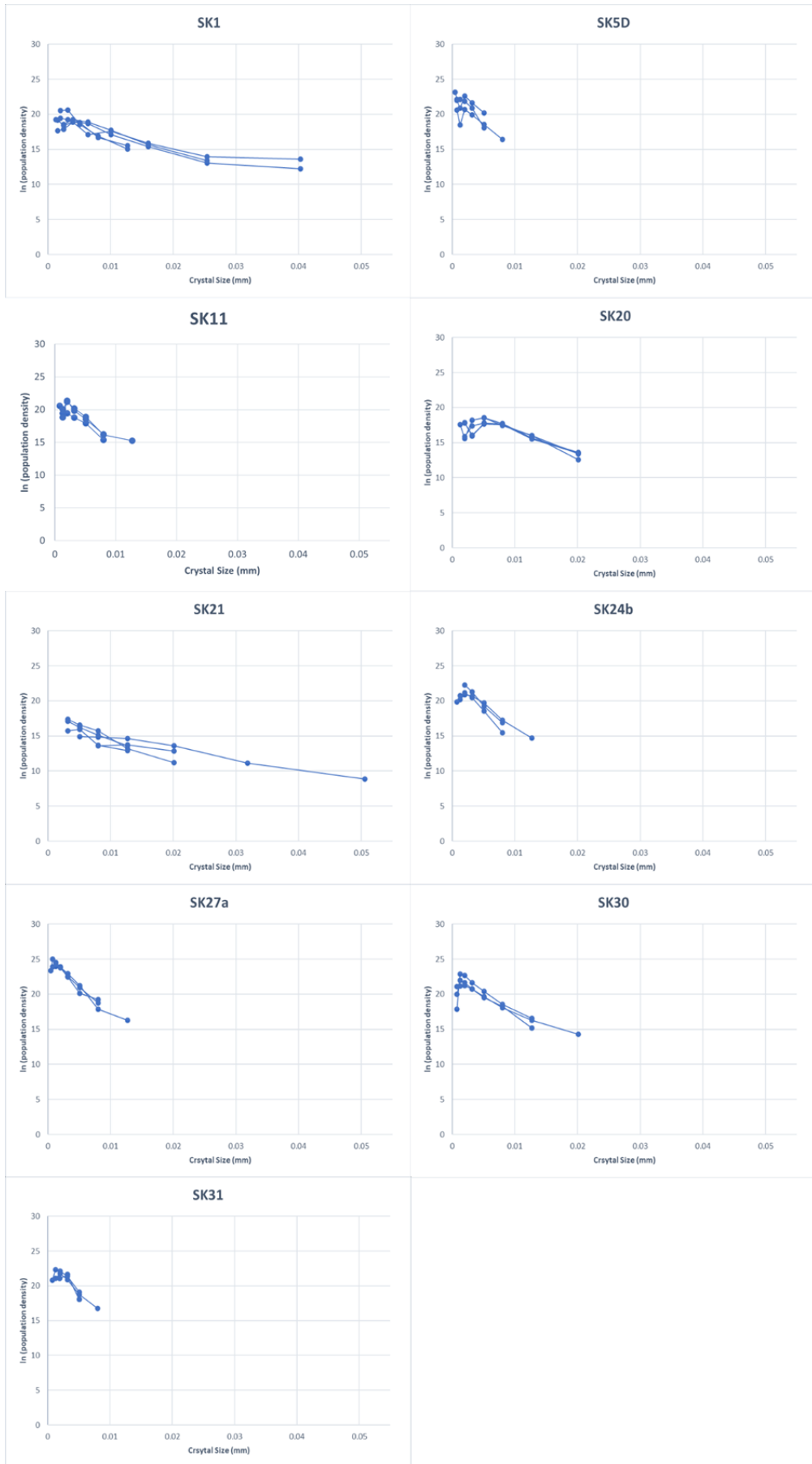


Figure 5.4 - CSD plot for plagioclase microlites in the St Kitts samples.

The CSD plots produced for the Nevis samples show a straight line, with a very slight concave shape seen in SKN18, as shown in Figures 5.5. The y-intercept values (n°) and slope values for the entire plots and straight-line sections are shown in Table 5.6. The y-intercept (n°) varies from 18.28 mm^{-4} to 24.31 mm^{-4} for plagioclase microlites. The slope values range from -713 to -825 in SKN18, to -226 to -369 in SKN19.

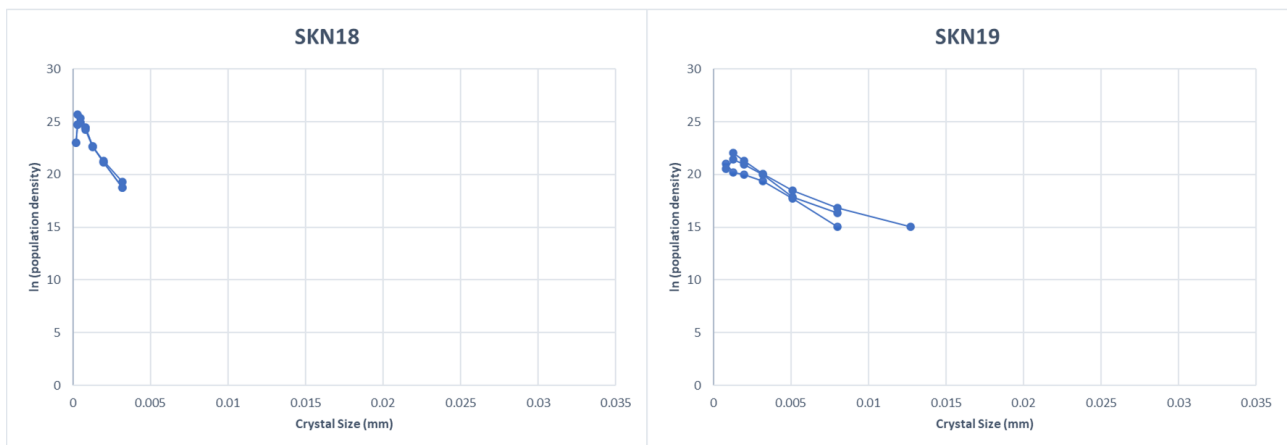


Figure 5.5 - CSD plot for plagioclase microlites in the Nevis samples.

Table 5.4 - Crystal Size Distribution (CSD) data for plagioclase microlites in Mt Liamuiga samples.

Sample no.	N (number of samples)	Measured area (μm^2)	Aspect Ratio	Section 1		Section 2		Section 3		Plot average	
				$\ln(n^\circ)$ (mm^{-4})	Slope ($^\circ$)	$\ln(n^\circ)$ (mm^{-4})	Slope ($^\circ$)	$\ln(n^\circ)$ (mm^{-4})	Slope ($^\circ$)	$\ln(n^\circ)$ (mm^{-4})	Slope ($^\circ$)
SK1-01	50	0.01539	1:1.5:5	19.21	83.3	20.87	-351	17.77	-147	20.45	-313
SK1-02	52	0.01447	1:1.5:3	19.76	-137	21.02	-330	21.33	-354	20.00	-257
SK1-03	36	0.01488	1:1.5:3	19.53	-197	20.15	-257	18.7	-132	18.99	-148
SK1-04	75	0.01632	1:1.5:1.5	22.52	-664	22.60	-673			21.05	-299
SK1-05	39	0.01529	1:4:4	19.88	-204	21.10	-464			20.71	-416
SK5D-01	30	0.00120	1:10:10	20.6	-1000			24.12	-772	24.12	-772
SK5D-02	26	0.00200	1:2.9:2.9	23.77	-1287	23.17	-701	22.92	-632	23.26	-734
SK5D-03	49	0.01650	1:1.67:1.67	21.04	-576			22.14	-708	22.01	-680
SK11-01	19	0.01492	1:10:10	21.7	-930	20.36	-485	20.26	-463	20.60	-541
SK11-02	24	0.00889	10:6.67:6.67	33.84	-1250	23.84	-1250	22.03	-684	23.10	-927
SK11-03	29	0.00903	1.0:20:20	22.86	-833	22.63	-742	22.38	-684	22.63	-742
SK20-01	126	0.05111	1:6.67:6.67	15.47	854	17.63	179	20.43	-355	20.13	-313
SK20-02	80	0.05083	1:10:10	17.88	-41.9	17.76	-17.2	20.49	-365	19.56	-286
SK20-03	82	0.05097	1:10:10	17.92	-25.8	17.98	-37.9	20.52	-361	19.62	-285
SK20-04	76	0.05068	1:6.67:6.67	16.71	215	19.30	-256	20.19	-334	19.45	-272
SK20-05	66	0.02966	1:6.67:6.67			20.22	-336	20.02	-317	20.22	-336
SK21-01	68	0.14840	1:4:4	15.15	-40.7	16.88	-169	17.84	-210	16.27	-140
SK21-02	13	0.08320	1:20:20					14.79	-95.6	14.79	-95
SK21-03	52	0.08601	1:2.5:2.5	18.36	-331	18.72	-396	20.07	-540	18.66	-388
SK21-04	33	0.08129	1:2.9:2.9							18.18	-371
SK21-05	15	0.08326	1:2.5:2.5	18.81	-596			17.94	-416	17.78	-398
SK24b-01	75	0.01199	1:10:10	18.91	986	21.07	-114	22.94	-669	22.39	-565
SK24b-02	68	0.00627	1:5:5							24.20	-941
SK24b-03	67	0.01491	1:5:5	21.83	-407			22.96	-826	22.68	-752

SK27a-01	166	0.00170	1:6.67:6.67	25.04	-644	25.68	-874	25.87	-1002	25.42	-810
SK27a-02	173	0.00174	1:6.67:6.67	25.08	-571			25.63	-906	25.54	-882
SK27a-03	170	0.00176	1:6.67:6.68	25.82	-1020	25.94	-1107	25.56	-863	25.54	-888
SK30-01	201	0.00541	1:20:20	23.36	-357	23.88	-676	23.61	-596	23.72	-622
SK30-02	62	0.00550	10:6.67:6.67	21.01	100	22.23	-495	21.96	-464	22.18	-487
SK30-03	73	0.00556	10:6.67:6.67	22.73	-557			22.66	-571	22.66	-571
SK31-01	31	0.00261	1:10:10	22.75	-314			24.08	-910	23.76	-820
SK31-02	21	0.00272	1:10:10					23.73	-925	23.60	-889
SK31-03	23	0.00268	1:10:10							20.19	433

Table 5.5 - Crystal Size Distribution (CSD) data for plagioclase microlites in Nevis samples.

Sample no.	N (number of samples)	Measured area (μm^2)	Aspect Ratio	Section 1		Section 2		Section 3		Plot average	
				$\ln(n^2)$ (mm^{-4})	Slope ($^\circ$)	$\ln(n^2)$ (mm^{-4})	Slope ($^\circ$)	$\ln(n^2)$ (mm^{-4})	Slope ($^\circ$)	$\ln(n^2)$ (mm^{-4})	Slope ($^\circ$)
SKN18-01	381	0.01929	1:6.67:6.67	21.71	1027	24.21	-868	21.88	-476	23.78	-713
SKN18-02	299	0.01172	1:5:5			24.49	-886	23.15	-655	24.31	-825
SKN18-03	323	0.01192	1:5:5	20.09	2120	24.04	-946	23.27	-723	23.68	-800
SKN19-01	25	0.01904	1:5:5							20.01	-369
SKN19-02	73	0.1165	1:4:4							18.28	-226
SKN19-03	103	0.07713	1:2.9:2.9	16.69	1236			19.79	-362	19.79	-362

The y-intercepts for the CSD plots generated from analysis of the mafic microlites show a similar trend to the plots generated from the plagioclase microlites (Figures 5.6). The y-intercept (n°) varies from 21.40 mm^{-4} to 27.74 mm^{-4} . These values are shown in Table 5.6. SK21 again shows the lowest values (Figure 5.6), between 21.40 mm^{-4} and 21.89 mm^{-4} , while SK27a shows the highest values (Figure 5.6), between 26.02 mm^{-4} to 27.74 mm^{-4} .

The slope values calculated using the mafic microlites vary across the suite of samples (Table 5.6). The lowest value is -496, while the highest value is -2230. Variation in slope was observed in individual samples. SK1 shows an average slope value of -1085, while SK11 shows an average slope value of -1729. SK24b and SK27a show average slope values of -1640 and -1883 respectively. Samples SK20, SK21 and SK30 show average slope values of -921, -557 and -1422 respectively. SK8D shows an average value of -1332. SK5D shows an average slope value of -1790, while sample SK31 showed an average slope value of -2007.

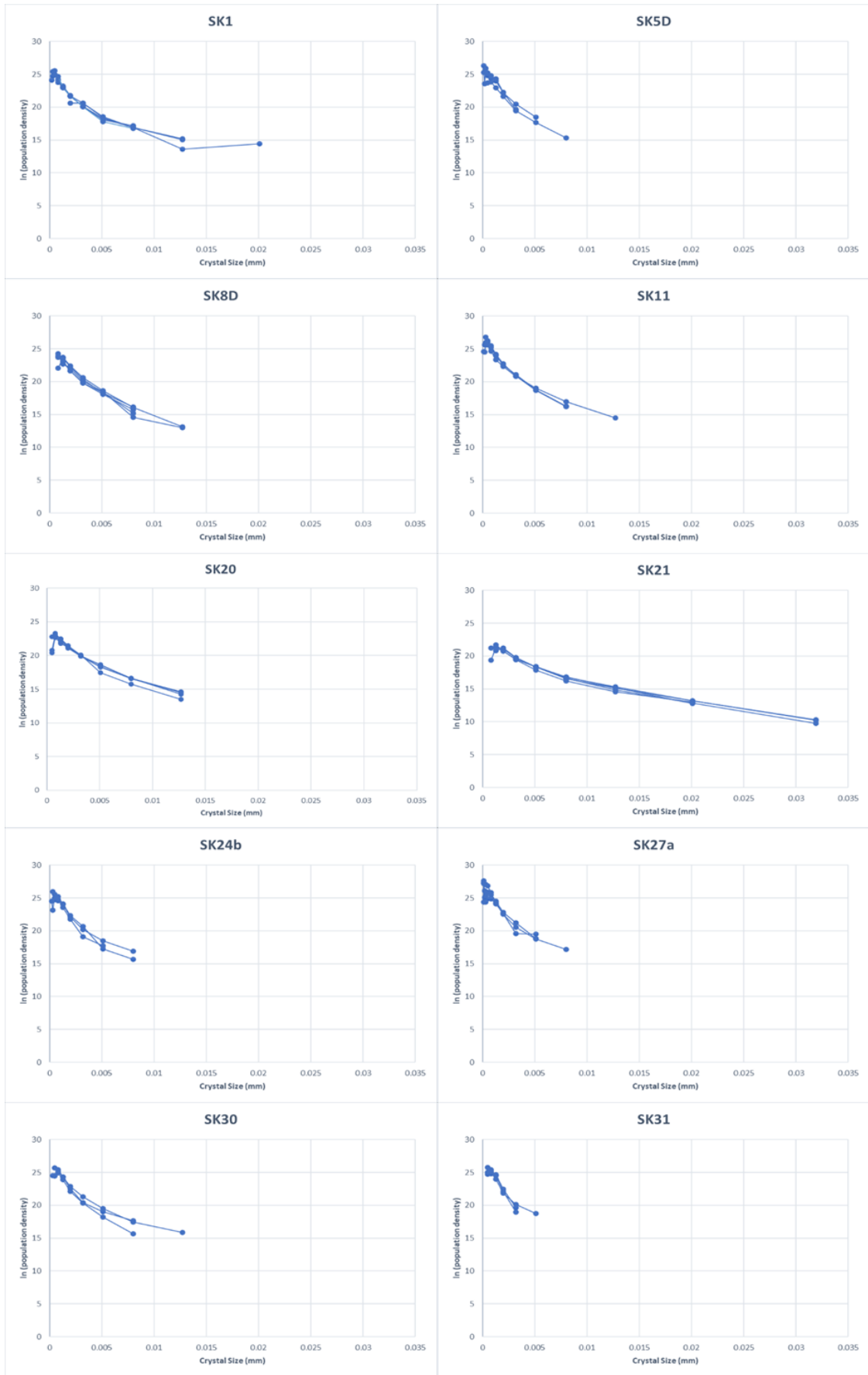


Figure 5.6 - CSD plot for mafic microlites in the St Kitts samples.

Nevis samples show similar trends to the Mt Liamuiga samples (Figure 5.7). The y-intercept (n°) varies from 21.48 mm^{-4} to 26.36 mm^{-4} for mafic microlites (Table 5.7). The slope values range from -1890 to -2489 in SKN18, to -704 to -812 in SKN19.

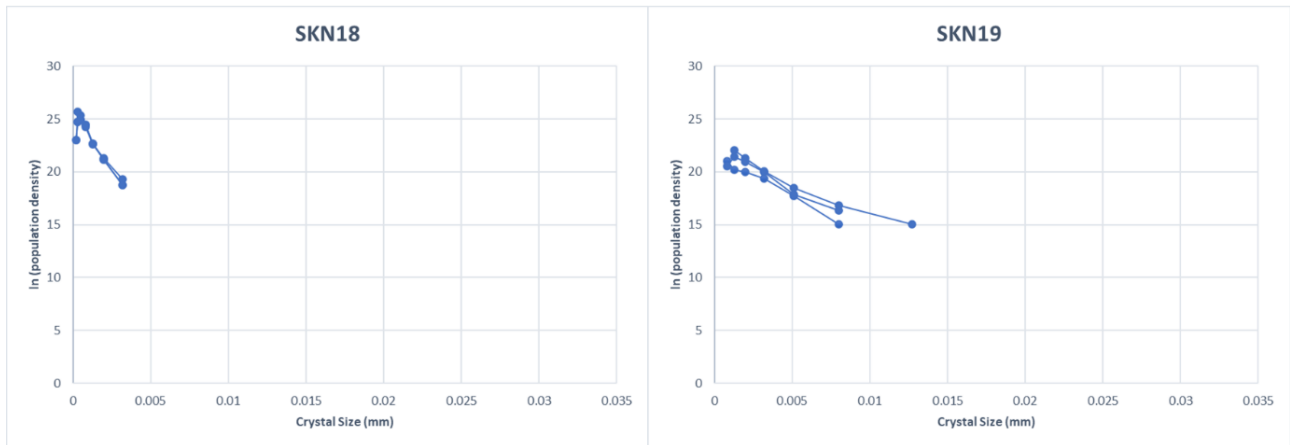


Figure 5.7 - CSD plot for mafic microlites in the Nevis samples.

Table 5.6 - Crystal Size Distribution (CSD) data for mafic microlites in Mt Liamuiga samples.

Sample	N (number of samples)	Measured area (μm^2)	Aspect Ratio	Section 1		Section 2		Section 3		Plot average	
				$\ln(n^\circ)$ (mm^{-4})	Slope ($^\circ$)	$\ln(n^\circ)$ (mm^{-4})	Slope ($^\circ$)	$\ln(n^\circ)$ (mm^{-4})	Slope ($^\circ$)	$\ln(n^\circ)$ (mm^{-4})	Slope ($^\circ$)
SK1-01	395	0.01581	1:1.67:1.67	26.21	-2850	24.34	-1129	18.55	-205	24.21	-771
SK1-02	430	0.01548	1:1.67:1.67	27.05	-3366	25.34	-1611	21.97	-631	25.6	-1436
SK1-03	300	0.01495	1:1.4:1.4	25.88	-2137	23.88	-1049	20.62	-444	24.97	-1115
SK1-04	74	0.01632	1:1.5:1.5	22.74	-756	23.17	-827	20.9	-477	22.38	-648
SK1-05	340	0.01523	1:1.5:1.5	26.62	-2670	24.79	-1457			25.41	-1456
SK5D-01	61	0.0012	1:4:4	26.53	-2200	25.19	-924	26.51	-1995	26.11	-1809
SK5D-02	118	0.0020	1:2.5:2.5	23.77	7039.915	25.71	-1072	27.79	-2690	26.54	-1962
SK5D-03	193	0.0165	1:4:4	24.81	-1369	25.36	-1849	22.53	-958	24.99	-1601
SK8D-01	1253	0.05807	1:2:2	25.27	-1378			23.09	-876	25.16	-1310
SK8D-02	1086	0.05797	1:2.2:2.2	25.78	-1719			23.29	-937	25.1	-1340
SK8D-03	566	0.05802	1:1.67:1.67	24.24	-1182					24.24	-1182
SK8D-04	1637	0.09186	1:1.4:1.4	25.76	-1964			22.5	-857	25.15	-1497
SK8D-05	1009	0.07799	1:2.2:2.2	25.11	-1689			22.54	-847	24.6	-1332
SK11-01	555	0.01504	1:2.9:2.9	25.47	313	26.21	-1843	23.39	-827	25.76	-1425
SK11-02	367	0.008849	1:2:2	27.1	-2206	27.13	-2346	24.99	-1223	26.59	-1781
SK11-03	515	0.009004	1:1.67:1.67	27.54	-2576	27.15	-2108	24.6	-1153	27.07	-1981
SK20-01	491	0.05428	1:1.5:1.5	23.74	-1142			20.82	-507	23.18	-857
SK20-02	516	0.05081	1:2.2:2.2	24.11	-1299			22.02	-656	23.44	-908
SK20-03	393	0.05094	1:1.3:1.3	23.5	-1144			21.78	-631	22.87	-816

SK20-04	398	0.05085	1:1.67:1.67	23.8	-1243			21.78	-610	23.06	-830
SK20-05	362	0.02951	1:1.4:1.4	24.19	-1315			20.43	-586	23.96	-1193
SK21-01	1056	0.148	1:4:4	22.12	-725			19.22	-329	21.62	-559
SK21-02	658	0.08825	1:1.5:1.5	22.94	-1041			19.45	-355	21.87	-602
SK21-03	615	0.08558	1:1.4:1.4	22.11	-700			19.14	-297	21.4	-496
SK21-04	694	0.08363	1:1.5:1.5	22.66	-858			19.48	-335	21.87	-569
SK21-05	677	0.08331	1:1.3:1,3	23.1	-965			18.87	-290	21.89	-560
SK24b-01	374	0.01209	1:2.9:2.9	25.31	-927	26.43	-1878	26.49	-1815	25.96	-1655
SK24b-02	253	0.006353	1:2.5:2.5	27.25	-2527	24.55	-1256	22.44	-722	24.74	-1079
SK24b-03	517	0.01486	1:2.2:2.2	26.79	-2482			26.77	-2432	26.53	-2188
SK27a-01	97	0.00171	1:4:4	28.8	-1568	26.18	-1718	24.57	-1016	26.02	-1470
SK27a-02	186	0.001744	1:2.5:2.5	27.12	-2076			25.47	-1322	26.86	-1803
SK27a-03	281	0.001775	1:1.8:1.8	27.58	-1579	28.23	-2966	23.66	-973	27.74	-2376
SK30-01	410	0.00543	1:1.67:1.67	26.94	-2120	27.11	-2184	22.14	-573	25.8	-1271
SK30-02	348	0.005594	1:2.2:2.2	26.82	-2320	26.41	-1997	23.9	-1121	26.12	-1773
SK30-03	419	0.005579	1:4:4	26.89	-1971	25.93	-1370	23.3	-679	26	-1222
SK31-01	111	0.002619	1:1.67:1.67	24.9	-189			28.34	-2857	26.79	-1934
SK31-02	164	0.002721	1:1.33:1.33	27.15	-2536			23.79	-1029	26.51	-1857
SK31-03	131	0.00271	1:1.5:1.5	26.43	-1444			27.6	-2536	27.18	-2230

Table 5.7 - Crystal Size Distribution (CSD) data for mafic microlites in Nevis samples.

Sample	N (number of samples)	Measured area (μm^2)	Aspect Ratio	Section 1		Section 2		Section 3		Plot average	
				$\ln(n^\circ)$ (mm^{-4})	Slope ($^\circ$)	$\ln(n^\circ)$ (mm^{-4})	Slope ($^\circ$)	$\ln(n^\circ)$ (mm^{-4})	Slope ($^\circ$)	$\ln(n^\circ)$ (mm^{-4})	Slope ($^\circ$)
SKN18-01	408	0.02014	1:1.8:1.8	26.07	-2268			23.69	-1234	25.67	-1890
SKN18-02	241	0.0117	1:2:2	26.64	-2931			25.32	-2059	26.25	-2489
SKN18-03	399	0.01195	1:1.67:1.67	26.86	-3236			24.84	-1737	26.36	-2480
SKN19-01	45	0.01908	1:2.2:2.2	21.2	-575			22.15	-863	21.48	-704
SKN19-02	576	0.1162	1:3.3:3.3	23.24	-963			20.73	-460	22.64	-708
SKN19-03	288	0.07822	1:6.67:6.67	22.36	-722			22.55	-821	22.52	-812

5.3.3 Crystallization times and nucleation rate

Crystal growth rate values were estimated from Brugger and Hammer (2010), allowing crystallization times (τ) and nucleation rate (J) to be calculated. Three sets of crystallisation times and nucleation rates were calculated using crystal growth rate values of $10^{-6} \text{ mm s}^{-1}$, $10^{-7} \text{ mm s}^{-1}$ and $10^{-8} \text{ mm s}^{-1}$ (shown in Appendix 16), with $10^{-7} \text{ mm s}^{-1}$ considered the most suitable value as this is the most commonly used value for plagioclase in ascending andesite (Brugger and Hammer, 2010; Mastrolorenzo and Pappalardo, 2006; Salisbury *et al.*, 2008). The results using $10^{-7} \text{ mm s}^{-1}$ are summarised here.

A large range of crystallisation times and nucleation rates were observed from the Mt Liamuiga samples. Crystallisation times vary from 2.95 hours to 29.24 hours, with the majority of calculated times falling between 3 and 9 hours. Individual samples also showed large variations, with crystallization times for SK21 ranging between 6.98 hours and 29.24 hours. Sample SK21 also showed the slowest crystallization times. Sample SK24b showed the fastest value, 2.95 hours. The average crystallization time was 7.41 hours.

Nucleation rates showed a very similar trend to crystallization times. Values calculated ranged from $0.26 \text{ mm}^{-3} \text{ s}^{-1}$ to $12356 \text{ mm}^{-3} \text{ s}^{-1}$, with SK21 showing the highest value and SK27a showing the lowest value. Values calculated for individual samples also showed a significant variation.

Table 5.8 - Calculated crystallisation times and nucleation rate for the Mt Liamuiga and Nevis samples.

Sample no.	N (number of microlites)	Slope (°)	n° (mm ⁻⁴)	Crystallisation time (hours)	Nucleation rate (l) mm ⁻³ s ⁻¹
SK1-01	50	-313	7.61E+08	8.87	76.09
SK1-02	52	-257	4.85E+08	10.81	48.52
SK1-03	36	-148	1.77E+08	18.77	17.67
SK1-04	75	-299	1.39E+09	9.29	138.64
SK1-05	39	-416	9.87E+08	6.68	98.68
SK5D-01	30	-772	2.99E+10	3.60	2986.64
SK5D-02	26	-734	1.26E+10	3.78	1263.83
SK5D-03	49	-680	3.62E+09	4.08	362.09
SK11-01	19	-541	8.84E+08	5.13	88.40
SK11-02	24	-927	1.08E+10	3.00	1076.97
SK11-03	29	-742	6.73E+09	3.74	673.11
SK20-01	126	-313	5.53E+08	8.87	55.25
SK20-02	80	-286	3.12E+08	9.71	31.25
SK20-03	82	-285	3.32E+08	9.75	33.18
SK20-04	76	-272	2.80E+08	10.21	27.99
SK20-05	66	-336	6.05E+08	8.27	60.46
SK21-01	68	-140	1.16E+07	19.84	1.16
SK21-02	13	-95	2.65E+06	29.24	0.26
SK21-03	52	-388	1.27E+08	7.16	12.70
SK21-04	33	-371	7.86E+07	7.49	7.86
SK21-05	15	-398	5.27E+07	6.98	5.27
SK24b-01	75	-565	5.29E+09	4.92	529.48
SK24b-02	68	-941	3.24E+10	2.95	3235.39
SK24b-03	67	-752	7.08E+09	3.69	707.62
SK27a-01	166	-810	1.10E+11	3.43	10958.87
SK27a-02	173	-882	1.24E+11	3.15	12356.09
SK27a-03	170	-888	1.24E+11	3.13	12356.09
SK30-01	201	-622	2.00E+10	4.47	2002.00
SK30-02	62	-487	4.29E+09	5.70	429.19
SK30-03	73	-571	6.94E+09	4.86	693.61
SK31-01	31	-820	2.08E+10	3.39	2083.71
SK31-02	21	-889	1.78E+10	3.12	1775.62
SK31-03	23	-433	5.87E+08	6.42	58.67
SKN18-01	381	-713	2.13E+10	3.89	2125.80
SKN18-02	299	-825	3.61E+10	3.36	3611.59
SKN18-03	323	-800	1.92E+10	3.47	1923.50
SKN19-01	25	-369	4.90E+08	7.52	49.00
SKN19-02	73	-226	8.69E+07	12.29	8.68
SKN19-03	103	-362	3.93E+08	7.67	39.32

Crystallization times (τ) and nucleation rate (J) were calculated for the Nevis samples (Table 5.8). SKN18 had an average crystallization time of 3.58 hours, and nucleation rates ranging from $1923.51 \text{ mm}^{-3} \text{ s}^{-1}$ to $3611.59 \text{ mm}^{-3} \text{ s}^{-1}$. SKN19 showed crystallization times ranging between 7.53 hours and 12.29 hours. The nucleation rates calculated for SKN19 ranged from $8.69 \text{ mm}^{-3} \text{ s}^{-1}$ to $49 \text{ mm}^{-3} \text{ s}^{-1}$.

5.3.4 Magma decompression and ascent rates

Experimental decompression rates and ascent rates were calculated using both the Mt Liamuiga and Nevis Peak samples. The method for calculating decompression rate, and ascent rate from the decompression rate is described in Section 5.2.2. Two sets of decompression and ascent rates were calculated for each sample, one using plagioclase microlites and the other using mafic microlites. The values calculated using the mafic microlites consistently returned larger values than those calculated using plagioclase microlites (except for SK1 where the values overlapped, and SK8D where too few microlites were present to calculate decompression and ascent rate using plagioclase microlites). Two samples, SK5L and SK8L, contained no microlite populations, therefore decompression and ascent rates could not be calculated for these samples. The estimated ascent rates for Mt Liamuiga, calculated using plagioclase and mafic microlites are shown in Table 5.9 and 5.10, and in Figure 5.8.

The decompression rates calculated for Mt Liamuiga ranged from 0.02 Pa s^{-1} to $1395.23 \text{ Pa s}^{-1}$ when calculated using plagioclase microlites. These values are shown in Table 5.9. SK1 and SK11, both samples collected from beds of fallout, had comparative decompression rates. Samples from the steel dust showed a large difference in decompression rates. Samples SK20 and SK21 show a much slower decompression rate than the other samples. Sample SK30

shows a faster decompression rate compared to SK20 and SK21, and is more similar to SK1, SK5D and SK11.

Table 5.9 – Decompression and ascent rates estimated for Mt Liamuiga and Nevis using plagioclase microlites.

Sample no.	Sample description	Total no. plagioclase microlites n	Csi	Cw	a	b	c	N	Decompression rate $c/b*(N/a)^{2/3}$ Pa/s	Ascent rate ($m\ s^{-1}$)
SK1/1	Pumice clast from Location SK1	50	74.5	2	4.26208E+22	40	22400000	1.83E+15	6.87	0.0003
SK1/2	Pumice clast from Location SK1	52	74.5	2	1.07059E+20	40	22400000	1.25E+15	288.48	0.012
SK1/3	Pumice clast from Location SK1	38	74.5	2	1.07059E+20	40	22400000	6.03E+14	177.20	0.007
SK1/4	Pumice clast from Location SK1	74	74.5	2	1.07059E+20	40	22400000	1.33E+15	299.88	0.012
SK1/5	Pumice clast from Location SK1	40	74.5	2	1.07059E+20	40	22400000	6.56E+14	187.49	0.008
SK5D/01	Pumice - darker component of sample	30	71.65	2	4.42967E+21	40	67200000	2.17E+16	484.05	0.02
SK5D/02	Pumice - darker component of sample	26	71.65	2	4.42967E+21	40	67200000	8.66E+15	262.72	0.01
SK5D/03	Pumice - darker component of sample	49	71.65	2	4.42967E+21	40	67200000	1.28E+15	73.54	0.003
SK11/01	Pumice	19	69.2	2	6.32588E+20	40	67200000	2.56E+14	91.84	0.004
SK11/02	Pumice	24	69.2	2	6.32588E+20	40	67200000	1.43E+15	289.17	0.012
SK11/03	Pumice	29	69.2	2	6.32588E+20	40	67200000	1.53E+15	302.31	0.012
SK20/1	Moderately vesicular clast from location SK10	126	73.4	2	1.77878E+22	40	67200000	7.29E+14	19.97	0.0008
SK20/2	Moderately vesicular clast from location SK10	80	73.4	2	1.77878E+22	40	67200000	3.40E+14	12.02	0.0005
SK20/3	Moderately vesicular clast from location SK10	82	73.4	2	1.77878E+22	40	67200000	3.33E+14	11.85	0.0005
SK20/4	Moderately vesicular clast from location SK10	76	73.4	2	1.77878E+22	40	67200000	2.73E+14	10.36	0.0004
SK20/5	Moderately vesicular clast from location SK10	66	73.4	2	1.77878E+22	40	67200000	4.68E+14	14.87	0.0006
SK21/1	Dense block from Location SK21	68	79.3	2	1.93028E+24	40	22400000	6.16E+13	0.06	0.000002
SK21/2	Dense block from Location SK21	13	79.3	2	1.93028E+24	40	22400000	1.57E+13	0.02	0.000001

SK21/3	Dense block from Location SK21	52	79.3	2	1.93028E+24	40	22400000	1.00E+14	0.08	0.000003
SK21/4	Dense block from Location SK21	33	79.3	2	1.93028E+24	40	22400000	7.20E+13	0.06	0.000003
SK21/5	Dense block from Location SK21	15	79.3	2	1.93028E+24	40	22400000	3.53E+13	0.04	0.000002
SK24b/01	Steel dust sample	75	70	2	1.19432E+21	40	22400000	3.64E+15	117.62274 8	0.005
SK24b/02	Steel dust sample	68	70	2	1.19432E+21	40	22400000	5.30E+15	151.29117 4	0.006
SK24b/03	Steel dust sample	67	70	2	1.19432E+21	40	22400000	2.07E+15	80.899977	0.003
SK27a/01	Steel dust sample	166	70	2	1.19432E+21	40	22400000	6.65E+16	816.41	0.03
SK27a/02	Steel dust sample	175	70	2	1.19432E+21	40	22400000	5.89E+16	753.03	0.03
SK27a/03	Steel dust sample	170	70	2	1.19432E+21	40	22400000	5.05E+16	679.29	0.03
SK30/1	Dense block from location SK12	201	68.9	2	4.9845E+20	40	22400000	2.49E+16	759.60	0.03
SK30/2	Dense block from location SK12	62	68.9	2	4.9845E+20	40	22400000	4.04E+15	225.97	0.01
SK30/3	Dense block from location SK12	73	68.9	2	4.9845E+20	40	22400000	5.01E+15	260.65	0.01
SK31/1	Pumice from location SK12	31	66.8	2	9.39986E+19	40	22400000	1.17E+16	1395.23	0.06
SK31/2	Pumice from location SK12	27	66.8	2	9.39986E+19	40	22400000	5.70E+15	864.56	0.04
SK31/3	Pumice from location SK12	23	66.8	2	9.39986E+19	40	22400000	6.96E+15	987.11	0.04
SKN18/01	Nevis	380	77.7	1.5	1.14451E+24	40	16800000	1.39E+16	2.22	0.00009
SKN19/02	Nevis	299	77.7	1.5	1.14451E+24	40	16800000	1.37E+16	2.20	0.00009
SKN18/03	Nevis	323	77.7	1.5	1.14451E+24	40	16800000	1.21E+16	2.02	0.00008
SKN19/01	Nevis	25	77	1.5	6.56328E+23	40	16800000	3.78E+14	0.29	0.00001
SKN19/02	Nevis	73	77	1.5	6.56328E+23	40	16800000	8.10E+13	0.10	0.000004
SKN19/03	Nevis	103	77	1.5	6.56328E+23	40	16800000	2.66E+14	0.23	0.00001

Table 5.10 - Decompression and ascent rates estimated for Mt Liamuiga and Nevis using mafic microlites

Sample no.	Sample description	Total plagioclase microlites	no. n	Csi	Cw	a	b	c	N	Decompression rate c/b*(N/a)^2/3) Pa/s	Ascent rate (m s ⁻¹)
SK1/1	Pumice clast from Location SK1	395		74.5	2	4.26208E+22	17	22400000	6.23E+16	169.78	0.0069
SK1/2	Pumice clast from Location SK1	430		74.5	2	4.26208E+22	17	22400000	7.15E+16	186.11	0.008
SK1/3	Pumice clast from Location SK1	300		74.5	2	4.26208E+22	17	22400000	4.32E+16	132.96	0.005
SK1/4	Pumice clast from Location SK1	406		74.5	2	4.26208E+22	17	22400000	6.76E+16	179.23	0.007
SK1/5	Pumice clast from Location SK1	340		74.5	2	4.26208E+22	17	22400000	5.73E+16	160.53	0.007
SK5D/01	Pumice - darker component of sample	61		71.65	2	4.42967E+21	17	22400000	5.97E+16	746.26	0.03
SK5D/02	Pumice - darker component of sample	118		71.65	2	4.42967E+21	17	22400000	6.38E+16	780.02	0.03
SK5D/03	Pumice - darker component of sample	193		71.65	2	4.42967E+21	17	22400000	9.32E+15	216.37	0.009
SK8D/1	Dense block from location SK5	1253		67.7	2	1.92142E+20	17	22400000	1.87E+16	2790.53	0.114
SK8D/2	Dense block from location SK5	1086		67.7	2	1.92142E+20	17	22400000	1.15E+16	2018.67	0.082
SK8D/3	Dense block from location SK5	563		67.7	2	1.92142E+20	17	22400000	4.62E+15	1097.30	0.045
SK8D/4	Dense block from location SK5	1637		67.7	2	1.92142E+20	17	22400000	1.37E+16	2262.59	0.0923
SK8D/5	Dense block from location SK5	1009		67.7	2	1.92142E+20	17	22400000	8.97E+15	1707.83	0.0696
SK11/01	Pumice	555		69.2	2	6.32588E+20	17	22400000	1.23E+17	4416.21	0.1801
SK11/02	Pumice	367		69.2	2	6.32588E+20	17	22400000	4.29E+16	2190.22	0.0893
SK11/03	Pumice	515		69.2	2	6.32588E+20	17	22400000	6.37E+16	2850.76	0.1162
SK20/1	Moderately vesicular clast from location SK10	491		73.4	2	1.77878E+22	17	67200000	5.74E+15	185.96	0.007582
SK20/2	Moderately vesicular clast from location SK10	516		73.4	2	1.77878E+22	17	67200000	4.67E+15	162.10	0.006609
SK20/3	Moderately vesicular clast from location SK10	393		73.4	2	1.77878E+22	17	67200000	3.21E+15	126.24	0.005147
SK20/4	Moderately vesicular clast from location SK10	398		73.4	2	1.77878E+22	17	67200000	3.27E+15	127.69	0.005207
SK20/5	Moderately vesicular clast from location SK10	362		73.4	2	1.77878E+22	17	67200000	6.48E+15	201.55	0.008218
SK21/1	Dense block from Location SK21	1056		79.3	2	1.93028E+24	17	22400000	2.63E+15	1.579056	0.000
SK21/2	Dense block from Location SK21	658		79.3	2	1.93028E+24	17	22400000	2.53E+15	1.536754	0.000

SK21/3	Dense block from Location SK21	612	79.3	2	1.93028E+24	17	22400000	1.56E+15	1.116133	0.000
SK21/4	Dense block from Location SK21	694	79.3	2	1.93028E+24	27	22400000	2.01E+15	1.32	0.00
SK21/5	Dense block from Location SK21	677	79.3	2	1.93028E+24	17	22400000	2.23E+15	1.41	0.00
SK24b/01	Steel dust sample	374	70	2	1.19432E+21	17	22400000	3.93E+16	1353.80	0.06
SK24b/02	Steel dust sample	253	70	2	1.19432E+21	17	22400000	3.74E+16	1309.28	0.05
SK24b/03	Steel dust sample	517	70	2	1.19432E+21	17	22400000	4.11E+16	1393.02	0.06
SK27a/01	Steel dust sample	97	70	2	1.19432E+21	17	22400000	5.28E+16	1647.56	0.07
SK27a/02	Steel dust sample	186	70	2	1.19432E+21	17	22400000	9.16E+16	2377.76	0.10
SK27a/03	Steel dust sample	281	70	2	1.19432E+21	17	22400000	1.79E+17	3716.59	0.15
SK30/1	Dense block from location SK12	410	68.9	2	4.9845E+20	17	22400000	9.76E+16	4442.96	0.18
SK30/2	Dense block from location SK12	348	68.9	2	4.9845E+20	17	22400000	5.92E+16	3184.13	0.12983
SK30/3	Dense block from location SK12	419	68.9	2	4.9845E+20	27	22400000	6.45E+16	2121.39	0.08650
SK31/1	Pumice from location SK12	111	66.8	2	9.39986E+19	17	22400000	5.32E+16	9013.58	0.36753
SK31/2	Pumice from location SK12	164	66.8	2	9.39986E+19	17	22400000	9.83E+17	62996.88	2.56868
SK31/3	Pumice from location SK12	131	66.8	2	9.39986E+19	17	22400000	5.32E+16	9018.89	0.36774 3
SKN18/01	Nevis	408	77.7	1.5	1.14451E+24	17	16800000	3.21E+16	9.13	0.00037
SKN18/02	Nevis	241	77.7	1.5	1.14451E+24	17	16800000	2.29611E+16	7.141598188	0.00029 1197
SKN18/03	Nevis	399	77.7	1.5	1.14451E+24	17	16800000	4.15629E+16	10.60728559	0.00043 2509
SKN19/01	Nevis	45	77	1.5	6.56328E+23	17	16800000	1.21455E+18	148.9555153	0.00607 3619
SKN19/02	Nevis	576	77	1.5	6.56328E+23	17	16800000	1.75333E+18	190.2631528	0.00775 7927
SKN19/03	Nevis	288	77	1.5	6.56328E+23	17	16800000	1.56702E+18	176.5344293	0.00719 8142

The decompression rates calculated using the mafic microlites present showed a similar trend to those calculated using the plagioclase microlites. The decompression rates calculated for Mt Liamuiga ranged from 1.58 Pa s^{-1} to $62996.88 \text{ Pa s}^{-1}$ when calculated using mafic microlites. These decompression rates are shown in Table 5.10. SK1 and SK11 showed a little more differentiation, with SK11 showing much higher decompression rates. The Steel Dust samples, SK24b and SK27a, showed less variation than observed using the plagioclase microlites. Sample SK31 also showed the fastest decompression rate when using the mafic microlites.

Sample SK20 and SK21 continued to show the lowest values. Decompression rates estimated for SK8D were calculated using only mafic microlites due to the absence of plagioclase microlites in the sample.

The ascent rates follow a similar trend to the decompression rates. The ascent rates calculated using the mafic microlites were faster than those calculated with the plagioclase microlites. These ascent rate values are shown in Tables 5.9 and 5.10, and displayed in Figure 5.7. Ascent rate values were calculated using only mafic microlites for SK8D. Sample SK31, showed the fastest ascent rate when calculated using the plagioclase microlites, and the mafic microlites. When calculated using mafic microlites, values for SK20 and SK21 were an order of magnitude faster when calculated using the plagioclase microlites. When calculated using the mafic microlites, SK11 showed faster values compared with SK1. Samples collected from the Steel Dust show a significant difference, with SK24b showing slower ascent rate values and SK27b showing a faster ascent rate. SK24b was an order of magnitude faster when calculated using mafic microlites.

The samples collected from Nevis show much slower decompression and ascent rates compared to the data collected for Mt Liamuiga on St Kitts. Sample SKN18 shows a faster decompression rate compared to SKN19. The ascent rate values show the same trend, with SKN18 faster than SKN19. The ascent rate estimates for Nevis are given in Tables 5.9 and 5.10 and shown in Figure 5.8.

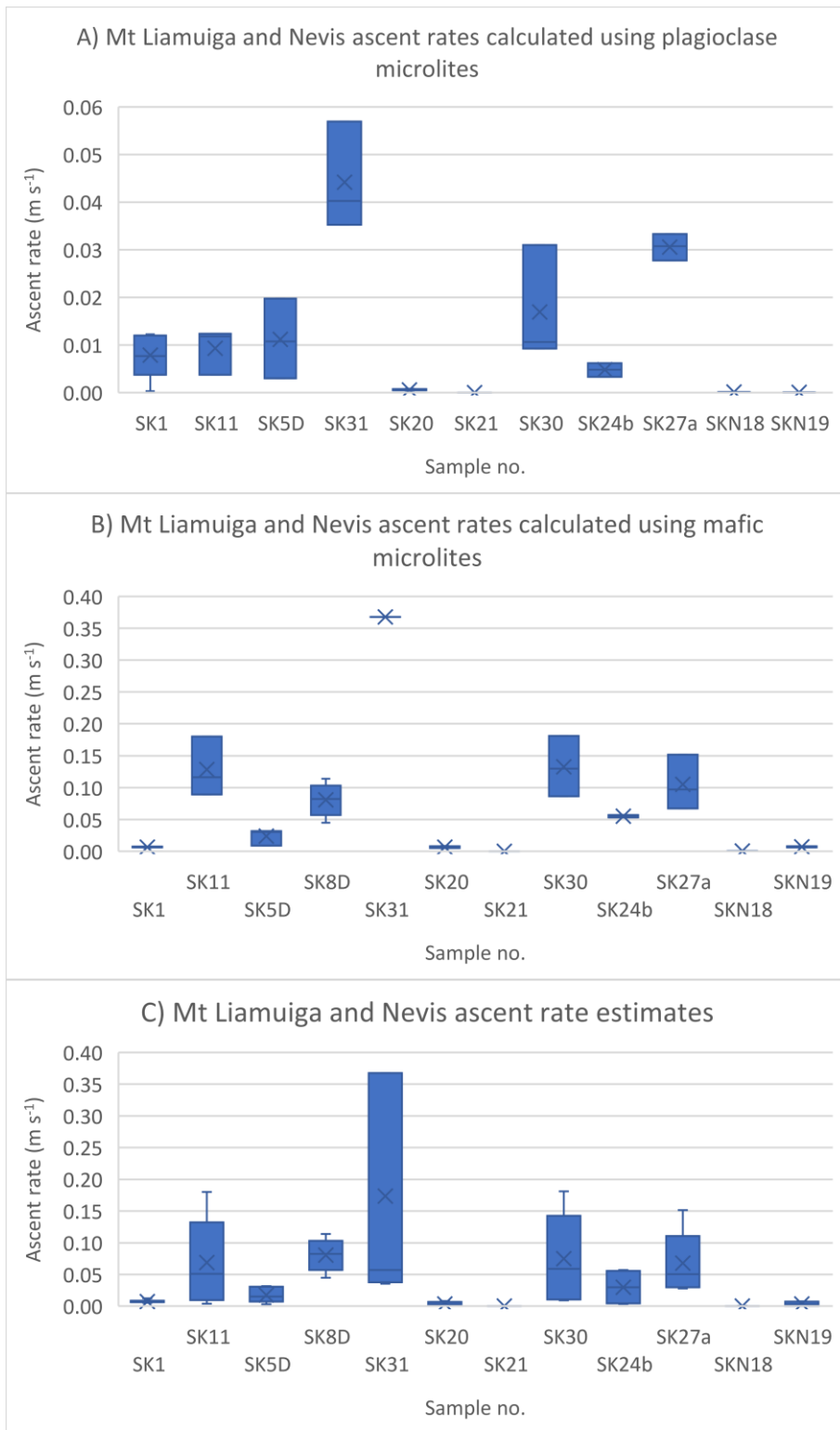


Figure 5.8 - Box plot showing the estimated ascent rates for Mt Liamuiga and Nevis based on A) plagioclase microlites, B) mafic microlites and C) average of the plagioclase and mafic microlites from different areas of each sample. SK1 & SK11 – Pumice lapilli. SK5D, SK8D and SK31 – Pumice and ash flows. SK20, SK21 & SK30 – Block and ash flows. SK24b & SK27a – Steel dust. SKN18 & SKN19 – Nevis samples. The box plots show the range, first quartile, median, third quartile and the mean (x).

5.4 Discussion

5.4.1 Microlite textural variations within the youngest deposits on Mt Liamuiga.

Studying microlite populations in volcanic deposits can improve our understanding of the shallow conduit processes and the properties of the pre- and syn-eruption melt (Hammer *et al.*, 1999, 2000; Murch and Cole, 2019; Preece *et al.*, 2016; Szramek *et al.*, 2006; Toramaru *et al.*, 2008).

Microlite crystallisation is controlled by the degree of undercooling (ΔT) of magma in the conduit. During decompression of magma in the conduit, water exsolution raises the liquidus temperature of a water-rich magma. Magma that was above or at the liquidus line at high pressure becomes significantly undercooled (Martel and Poussineau, 2007; Murch and Cole, 2019). Magma source depth, decompression and ascent rate, conduit geometry and near-surface degassing can also have an impact on ΔT . High degrees of ΔT cause a nucleation dominated regime, leading to the development of many small crystals. Nucleation regimes tend to dominate at low pressure or with high decompression rates. Lower degrees of ΔT allow for a growth dominated regime, producing fewer crystals, but allowing crystals to grow much larger. These crystal growth regimes are dominant at high pressure, or low decompression rates (Hammer *et al.*, 2000; Martel and Poussineau, 2007; Murch and Cole, 2019; Preece *et al.*, 2013). Very high rates of ΔT may result in negligible rates of nucleation and growth as crystallisation is prevented by limited rates of diffusion. This means that the melt may not crystallise, leading to eruptive products containing large volumes of glass with very few or no crystals (Martel and Poussineau, 2007). The microlite textures, including the size and number of crystals, seen in the products at Mt Liamuiga are indicative of ΔT of the magma. This reflects the near-surface processes in the conduit.

Microlites are known to form during a sudden period of nucleation as water is exsolved from the magma. If the magma erupts soon after this nucleation takes place, we expect to see products with many small crystals. If the melt is allowed to re-equilibrate after microlite formation, the system may transition to a growth dominated system. Hammer *et al.* (2000) suggest that this re-equilibration may happen due to a drop in the degree of ΔT after microlite nucleation.

The values of N_a and ϕ are thought to reflect nucleation conditions of the magma (Hammer *et al.*, 2000). By analysing N_a and ϕ , we can gain an understanding of the dominant style of crystallisation. A low N_a and high ϕ would suggest a growth dominated regime, while a high N_a and low ϕ suggest a nucleation dominated regime (Martel and Poussineau, 2007).

The diagram shown in Figure 5.9 from Hammer *et al.* (2000) shows the relationship between N_a and ϕ , and the implications for crystallisation. Line 1 in Figure 5.9 shows a linear positive correlation, which represents a nucleation dominated regime. The initial steep sections of lines 2A and 2B also suggest a nucleation dominated regime. The upper, shallowing section of 2A and 2B show the transition to a growth dominated regime. 2b shows a more rapid change from nucleation to growth. This transition from nucleation to growth can occur at any point, producing a range of N_a values. Where a system is entirely dominated by a nucleation regime, the trend line will intercept the origin. This would not be observed when the system has transitioned from a nucleation dominated regime, to a growth dominated regime.

The samples analysed for Mt Liamuiga were collected from a range of different deposits, produced by an unknown number of eruptions. As a result, it is only possible to comment on individual samples and compare between types of deposits

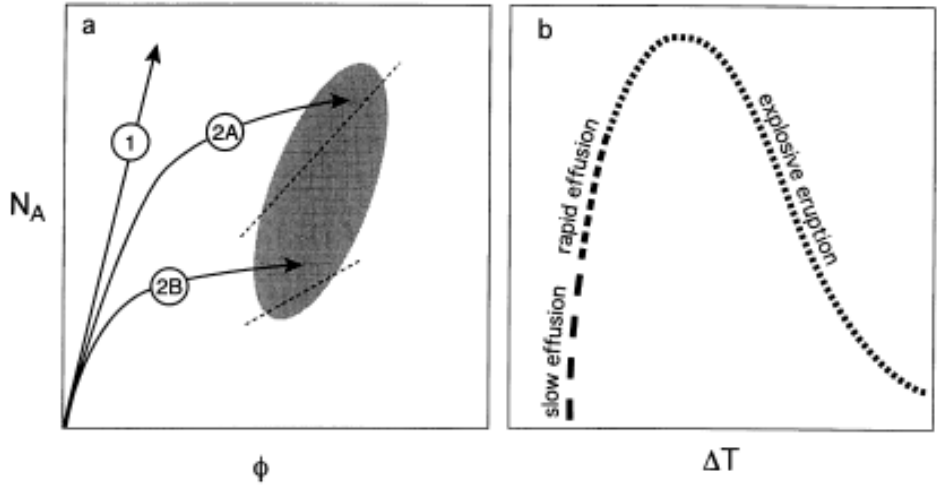


Figure 5.9 - Modified from Hammer et al. (2000) a) Schematic diagram showing crystallisation paths of erupting lavas. Path 1 shows a nucleation dominated regime, while 2A and 2B show nucleation dominated regimes, followed by a transition to growth dominated regimes. b) Hypothetical curve modified from Swanson (1977) relating N_a and ΔT , showing over low degrees of undercooling, microlite population density is proportional to the rate of undercooling. As ΔT increases, the rate of nucleation peaks then declines, resulting in a much larger potential range of textures produced by explosive eruptions (Swanson, 1977).

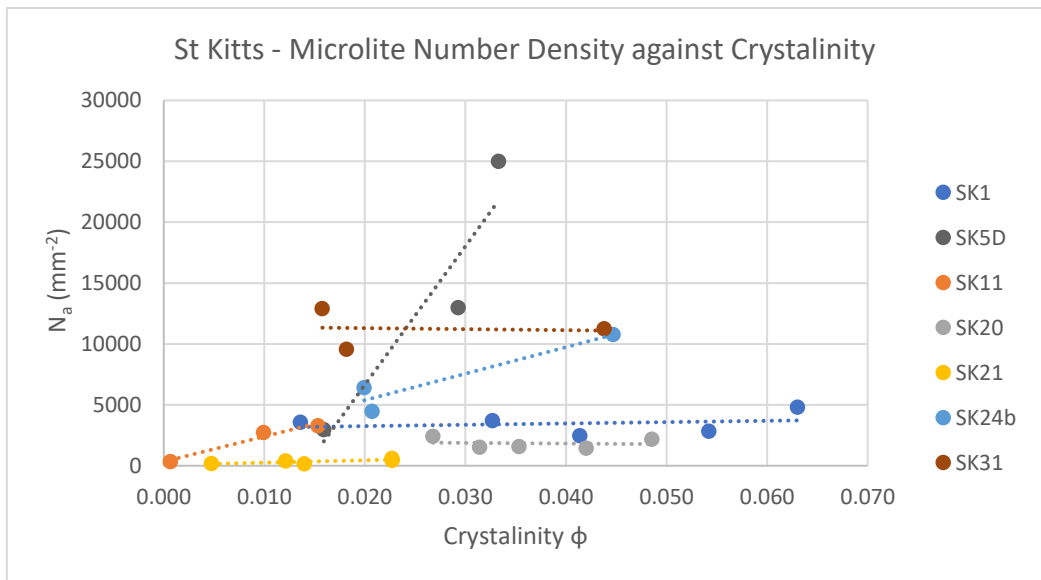


Figure 5.10 - Microlite number density (N_a) shown against crystallization (ϕ). This graph shows the same values as Figure 5.3, with SK27a and SK30 removed to allow the trends to be seen with more clarity.

The positive correlation between N_a and ϕ and the lack of a zero y-axis intercept shown by the majority of the Mt Liamuiga samples suggests that the microlite evolution within the magmas involved started as a nucleation dominated regime. The re-equilibration of the system after this original burst of nucleation would have allowed growth dominated crystallisation to dominate. One sample, SK11, shows a potential zero y-axis intercept, suggesting it may have been erupted after the initial burst of nucleation. This may be an artefact of the low number of samples analysed, as SK1, is thought to be from the same deposit, but shows a shift towards a growth driven regime. The large variations in N_a and ϕ observed for the Mt Liamuiga samples suggest there were significant differences in the nucleation conditions, and in the subsequent growth periods within the magma. This is expected considering the samples are thought to represent several different types of eruptions.

Similarities can be observed in deposits of the same type. The pumice fallout samples (SK1 & SK11) both show low N_a , but a more varied ϕ , with shallow positive trend lines. This suggests the system was dominated by nucleation rather than growth dominated regimes, creating small crystals, or in the case of SK11, a small number of small crystals. In comparison, the pumice and ash flow samples (SK5D & SK30) show a steeper N_a/ϕ trend line compared to the other samples. This suggests a shorter period where the system was dominated by nucleation, before changing to a growth driven regime. The block and ash flow samples (SK20, SK21 & SK31) also show similar shallow trends, although the very low N_a shown by SK20 and SK21 suggests a much shorter period of nucleation before moving to a growth driven regime. SK31 shows similar values of ϕ , with higher N_a values, suggesting a slower transition from nucleation to growth dominated regimes. The Steel Dust samples (SK24b & SK27a) show vast

differences, with one showing relatively low N_a and ϕ , while the other shows a relatively high N_a and ϕ .

Similarities in N_a and ϕ were observed in the Nevis samples (Figure 5.3). Both samples (SKN18 and SKN19) showed similar shallow trend lines, and lacked a zero y-intercept, suggesting nucleation followed by a growth dominated regime. SKN18 showed a higher N_a and a slightly higher ϕ suggesting it has a longer period of nucleation compared with SKN19.

Figure 5.11 compares the microlite number volume (N_v) with crystallinity (ϕ) for St Kitts and Nevis, and for several other volcanoes. For this graph, the trend of samples from a volcano are interpreted collectively (Cashman, 2020). The St Kitts samples show a positive, broadly linear trend in N_v and ϕ , indicating a nucleation dominated regime, as may be expected in open channel processes (Cashman, 2020), suggesting faster ascent rates. It is more difficult to draw a conclusion for the Nevis samples as there are fewer data points, however, the samples that have been plotted show the same general trend as the St Kitts samples (i.e. nucleation dominated). In contrast, a growth dominated regime (often slower ascent rates), such as in a lava lake, would show a shallow, negative linear trend, representing a more significant increase in ϕ rather than N_v .

Figure 5.11 suggests that the youngest eruptive products of Mt Liamuiga typically show low values of ϕ . The range of N_v values observed is comparable to those observed at other volcanoes, suggesting that a large range for N_v is a common phenomenon. The Nevis samples show a relatively low ϕ and a range of variation of N_v which is comparable to the other volcanoes described in Figure 5.11. The high N_v and low ϕ trends are most similar to those observed for Pinatubo, where the high N_v values have been interpreted to record rapid decompression (Cashman, 2020). CSD analysis of microlites from Mt Pinatubo suggest that

crystallisation was initially nucleation dominated, although growth of existing crystals surpassed nucleation in importance through time, indicated by the flattening of the trend (Hammer *et al.*, 1999). In contrast to Pinatubo, the N_v against ϕ trend does not significantly flatten in the Mt Liamuiga samples, suggesting that nucleation continued to dominate as the primary process for increasing crystallinity. Together these indicate that the syn-eruptive processes at Mt Liamuiga show similarities to those that occurred at the 1991 eruption at Mt Pinatubo.

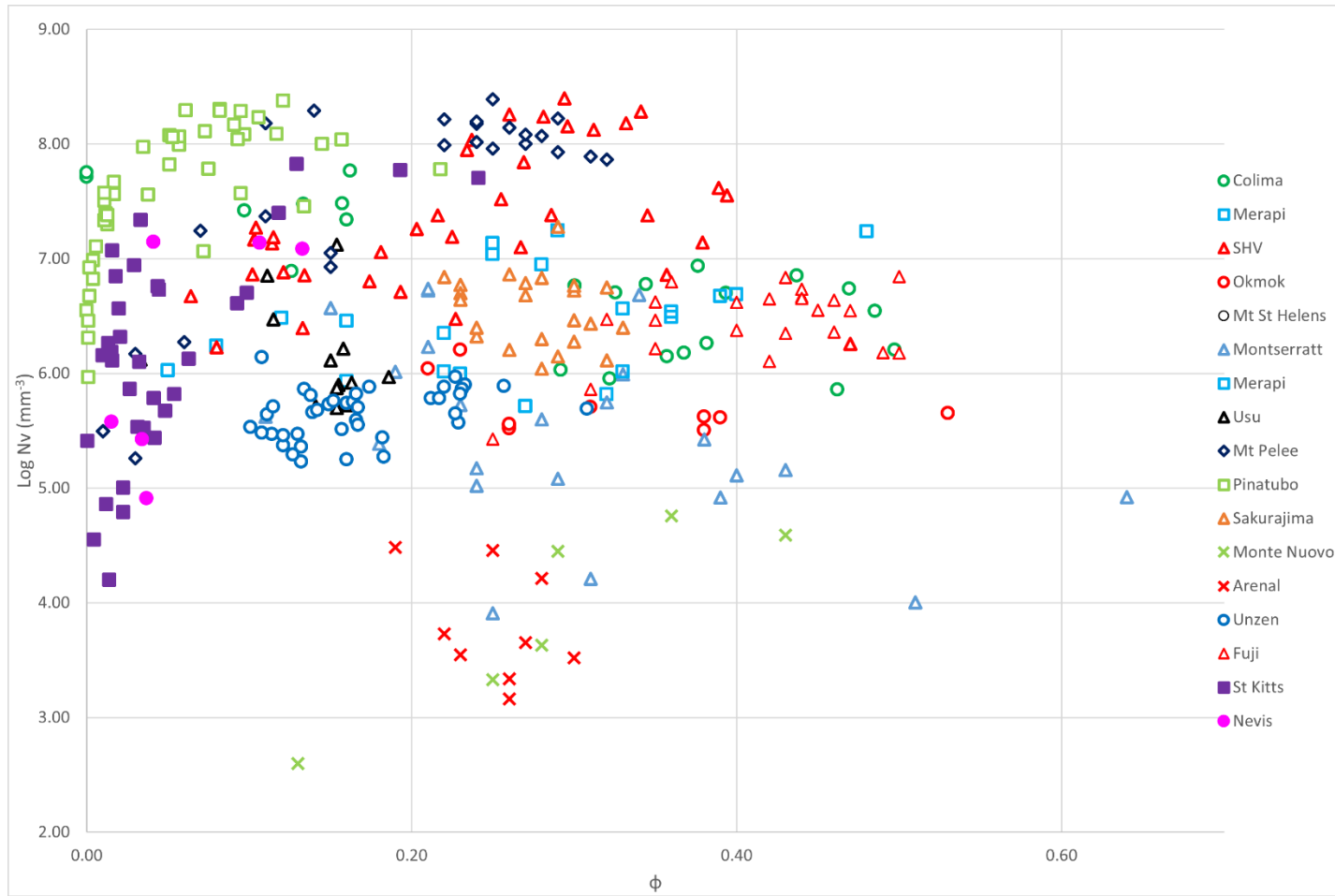


Figure 5.11 - Comparison of global microlite number volume (N_v) against crystallinity (ϕ) on a vesicle free basis, based on (Cashman, 2020). (Cashman and McConnell, 2005; Clarke et al., 2007; Hammer et al., 1999; Martel and Poussineau, 2007; Miwa et al., 2009; Murch and Cole, 2019; Piochi et al., 2005; Preece et al., 2013, 2016; Suzuki et al., 2006; Suzuki and Fujii, 2010; Szramek et al., 2006; Wong and Larsen, 2009).

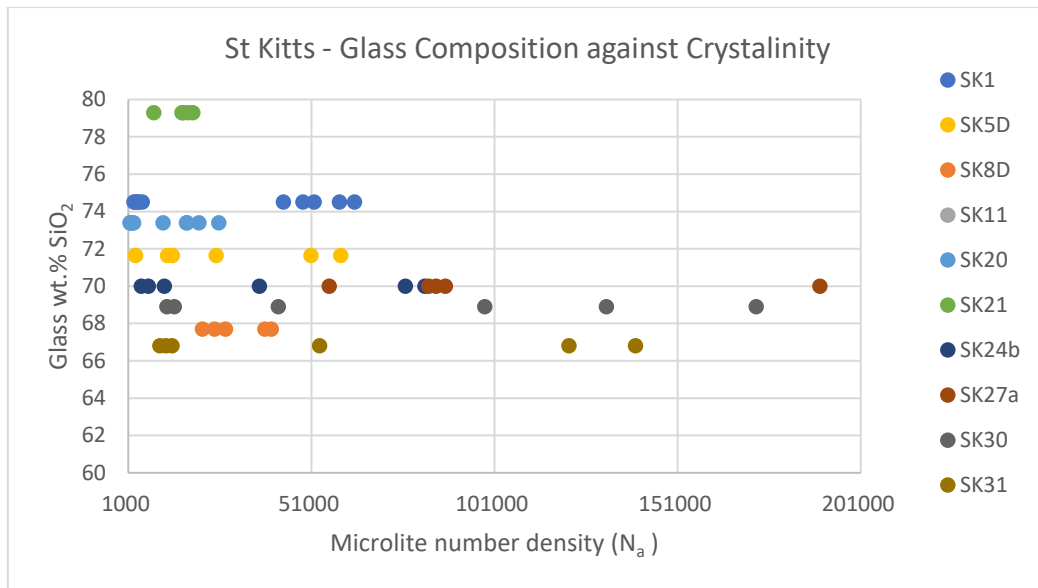


Figure 5.12 - Glass composition shown against microlite number density (N_a) for the Mt Liamuiga samples.

Figure 5.12 shows the glass wt.% SiO₂ against N_a for the Mt Liamuiga samples. The increasing glass wt.% SiO₂ with a decreasing N_a suggests that the geochemical composition of the melt has some control on microlite nucleation and growth. The data suggest that samples containing glass with a higher wt.% SiO₂ contained fewer microlite crystals. This is because crystal nucleation selectively uses SiO₂ from the melt in crystal formation and growth, causing a relative depletion of SiO₂ in the remaining glass. Where there are no microlites, the SiO₂ has not been removed from the melt, leading to a higher SiO₂ content in the glass (Couch *et al.*, 2003).

5.4.2 Crystal Size Distribution (CSD)

Crystal size distributions (CSD) record the changes in crystallisation processes during magma ascent (Marsh, 1998; Melnik *et al.*, 2011; Murch and Cole, 2019). Larger crystals tend to form at deeper depths, where slower decompression rates produce growth dominated regimes (Marsh, 1998; Melnik *et al.*, 2011). Decompression rates are typically much faster in the shallow conduit, allowing nucleation to dominate (Clarke *et al.*, 2007; Geschwind and

Rutherford, 1995; Hammer *et al.*, 1999). Changes in the crystallisation process (e.g. crystal growth and nucleation) as magma decompresses and ascends are reflected in the shape of the CSD produced.

The deeper magma storage system (>2 km depth) (Murch and Cole, 2019) is typically characterised by a small number of larger microlites typical in growth dominated regimes. This is represented on a CSD plot by low values of population density and high values of crystal length, which will generate a shallower curve. In the shallow conduit (< 1km depth) (Murch and Cole, 2019), nucleation dominates creating smaller crystals. This is represented by low values of population density and high values of crystal length, which will generate a steeper CSD plot. The different crystallisation processes at different depths are reflected in the different areas of the CSD plots.

A number of assumptions are required to be made in order to analyse and interpret CSD data, one of the most significant of which is that the crystals exhibit a constant growth rate (Marsh, 1988; Melnik *et al.*, 2011), reducing the complexity of what is likely a variable growth rate in reality. Another significant assumption is that the relatively small fields of view capable of being studied under a sufficiently powered microscope are representative of deposits orders of magnitude larger in volume. Crystal shape and volume significantly influence the resulting CSD; it is typically assumed that all crystals of a given phase (e.g. plagioclase) exhibit similar shapes, and that these shapes remain constant as the volume increases with crystal growth (Marsh, 1988; Melnik *et al.*, 2011; Rannou and Caroff, 2010). However, these crystal shapes are likely to vary over the course of crystal nucleation and growth, with crystal impingement potentially becoming more significant as the crystal fraction increases (Schiavi *et al.*, 2009).

The CSDs produced for Mt Liamuiga are linear or concave upwards, reflecting the change in crystallisation from nucleation to growth as the magma decompressed. The plots are typically smooth in shape, and lack any kinks, suggesting a progressive change in crystallisation and ΔT during ascent (Marsh, 1998). Where the CSD plots have been divided into sections, section 1 is the steepest section while section 3 is the shallowest section. Section 1 represents the formation of small microlites in the shallow conduit, while sections 2 and 3 represent the larger crystal sizes formed at greater depths compared to section 1.

There is little variation in CSD plots between the different types of deposits. The two fallout pumice samples (SK1 & SK11) show slightly concave up curves, with a steeper upper section and a shallower lower section, suggesting a gradual change from a nucleation dominated regime to a growth dominated system. The Steel Dust samples (SK24b & SK27a) show very slightly concave upwards curves and follow the shapes and observations seen in the fallout samples. This suggests they are the result of similar processes. The CSD plot of the pumice and ash flow samples (SK5D and SK31) shows a shallower, more constant gradient than the fallout and pumice and ash flow samples, which have a steeper, varying gradient. The block and ash flow samples (SK20, SK21 & SK30) plot a shallow, rather linear curve, suggesting that there was little microlite nucleation and rather growth regimes dominated. This is reflected in the N_a/ϕ analysis, which supports this interpretation.

Using the linear regression of the CSD plots, it is possible to calculate crystallisation time and nucleation rates (Brugger and Hammer, 2010). Calculating crystallization time (τ) and nucleation rates (J) is only possible when crystal growth rates (G) are known. For this study, estimates of G were taken from Brugger and Hammer (2010). Studies have found that G values for crystal growth resulting from rapid decompression and water exsolution range

from 10^{-8} mm s⁻¹ to 10^{-6} mm s⁻¹ (e.g. Genareau *et al.*, 2009; Mastrolorenzo and Pappalardo, 2006; Noguchi *et al.*, 2006; Piochi *et al.*, 2005; Salisbury *et al.*, 2008). Microlite crystal growth under these conditions is thought to be as high as 10^{-7} mm s⁻¹ to 10^{-6} mm s⁻¹ (Brugger and Hammer, 2010; Couch *et al.*, 2003; Gardner *et al.*, 1998; Geschwind and Rutherford, 1995; Hammer *et al.*, 1999). The most commonly used value for plagioclase in ascending andesite is 10^{-7} mm s⁻¹ (Brugger and Hammer, 2010; Mastrolorenzo and Pappalardo, 2006; Salisbury *et al.*, 2008). For this study, 10^{-6} mm s⁻¹, 10^{-7} mm s⁻¹ and 10^{-8} mm s⁻¹ were calculated using CSDs (Appendix 16). Taking into account the literature and the context of the ascent conditions of this study, 10^{-7} mm s⁻¹ was considered the most suitable value for G when calculating τ and J.

Table 5.8 shows the crystallisation times and nucleation rates calculated for Mt Liamuiga. As crystal growth rate is not a constant over time due to continuously changing conditions in the conduit, it cannot be used to accurately calculate crystallisation times. However, this value can be estimated based on observations and estimates from experiments and other volcanoes. Taking into account the literature and the context of the ascent conditions of this study, 10^{-7} mm s⁻¹ was considered the most suitable value for G when calculating τ and J (Brugger and Hammer, 2010; Couch *et al.*, 2003; Gardner *et al.*, 1998; Genareau *et al.*, 2009; Geschwind and Rutherford, 1995; Hammer *et al.*, 1999; Mastrolorenzo and Pappalardo, 2006; Piochi *et al.*, 2005; Salisbury *et al.*, 2008). Using this value, an estimated average crystallisation time of 2.95 hours to 29.24 hours was calculated, an order of magnitude of time variation. This suggests that groundmass crystallisation took place over a very short time (less than a day) after decompression. The block and ash flows showed the slowest crystallization times, while the fallout pumices, pumice and ash flows and the steel dust showed faster times (a few hours). This same trend was reflected in the nucleation rates, with the pumices showing the faster nucleation rates, and the dense blocks from the block and ash flows showing the

slowest nucleation rates. The Nevis samples also showed a fast crystallization time. These crystallisation times are shown in Table 5.8.

The crystallisation times and nucleation rates are comparable to those calculated for Soufriere Hills volcano on Montserrat, where it is thought that crystallization must have occurred within 8 hours, or with 4 hours for samples lacking microlites formed due to degassing induced crystallisation (Couch *et al.*, 2003). The estimates of maximum discharge rates and the lack of amphibole reaction rims suggest that the pumice samples took ~4 days to reach the surface, with a maximum decompression period of 1-2 days (Couch *et al.*, 2003).

As stated previously, these crystallization times and nucleation rates are estimated based on a value of G estimated from the literature. Taking this into account, the crystallisation times varied from a couple of hours to over a week. The variation in nucleation rates was two orders of magnitude between the slowest and fastest rates. As a result, the crystallisation times and nucleation rates should be interpreted with caution.

5.4.3 Ascent rates

An estimation of the magma ascent rates at the microlite nucleation depth were made using the microlite number density (MND) decompression rate metre as described in Toramaru *et al.* (2008). Microlite textures are a product of the undercooling conditions in which they nucleated and grew, and can therefore be used to infer decompression conditions during magma ascent. The calculation of decompression and ascent rates using the Toramaru *et al.* (2008) method is considered experimental, although studies have found that the values calculated are comparable to those observed in the field and laboratory experiments. The most sensitive factors of the calculation are the glass composition (C_{Si}) and the plagioclase number density (N_A). Water content (wt. % H_2O) also has an impact. Errors of 5% in C_{Si} can

result in differences of up to 500% in the calculated ascent rates using this method (Murch and Cole, 2019). The accuracy of the MND decompression rate metre decreases with fewer microlites (Toramaru *et al.*, 2008). The low crystallinity seen in the Mt Liamuiga samples may have had an impact on the final ascent rates calculated.

The two samples of pumice collected from beds of fallout, SK1 and SK11, showed similar ascent rates. This is seen most clearly in the ascent rates estimated from the plagioclase microlites, shown in Figure 5.8A and Table 5.9. When the mafic microlites are also considered, SK11 shows a much larger range of ascent rates compared with SK1. This is shown in Figure 5.8B. While SK1 and SK11 were collected from different locations, it was thought that they were from the same layer of fallout. This is confirmed by their similar geochemical compositions, and the similarity shown by CSD and ascent rate data. Similar ascent rates were observed in SK5D, and the Steel Dust sample SK24b. The other Steel Dust sample, SK27a showed a slightly faster average ascent rate compared to SK24b (Tables 5.9 and 5.10).

The slowest ascent rates were seen in, SK20 and SK21, two samples thought to be from block and ash flows (Figure 5.8). Slow ascent rate estimates were expected as the block and ash flows are thought to be generated by the collapse of a lava dome, and the material sampled is likely from the lava dome itself. Lava domes erupt at a considerably slower rate compared to explosive events. SK30, also thought to represent material from a block and ash flow, shows considerably faster ascent rates than SK20 and SK21 and similar ascent rates to the other samples collected from Mt Liamuiga. Similar observations have been observed at Soufriere Hills Volcano, where ascent rates calculated from block and ash flows samples were faster than those calculated for Vulcanian explosions and ash venting (Murch and Cole, 2019). Murch and Cole (2019) suggest that the atypical trend observed could be a result of microlite

populations from the various types of eruptive activity sampling from different windows during magma ascent. It is difficult to draw any conclusions from the single sample taken from Mt Liamuiga, however, alternative explanations could include that the deposit has been incorrectly labelled as a block and ash flow, or that the material sampled was not juvenile in the context of the deposit it was sampled from. The only sample to show a significantly faster ascent rate was SK31 (Figure 5.8), collected from a pumice and ash flow located below the block and ash flow from which SK30 was collected. SK5D, also sampled from a pumice and ash flow, showed ascent rates more similar to the fallout pumices and SK30, a much slower ascent rate compared to SK31. SK30 appears to be the outlier here, with the expectation that it would have shown similar ascent rates to SK20 and SK21, but appears to show a significantly faster ascent rate. These patterns are shown in Tables 5.9 and 5.10.

Some samples observed in the Mt Liamuiga suite contained no microlites, with the groundmass consisting entirely of glass. SK8L and SK5L, both samples from pumice and ash flows, contained no microlites, while SK5D, from the same pumice and ash flow as SK5L, contained no plagioclase microlites. Ascent rates could not be calculated using these samples due to the lack of microlites, however, the lack of microlites itself would suggest a rapid ascent rate, less than 4 hours (Couch *et al.*, 2003). This suggests that the ascent rate values for Mt Liamuiga are underestimated.

A comparison plot of ascent rates and crystallisation times from St Kitts shows that the samples with the fastest ascent rate tend to have shorter crystallisation times (Figure 5.13), as may be expected if an approximately equal starting depth is assumed. The agreement of these two separate calculations lends further credence to the validity of the results described here.

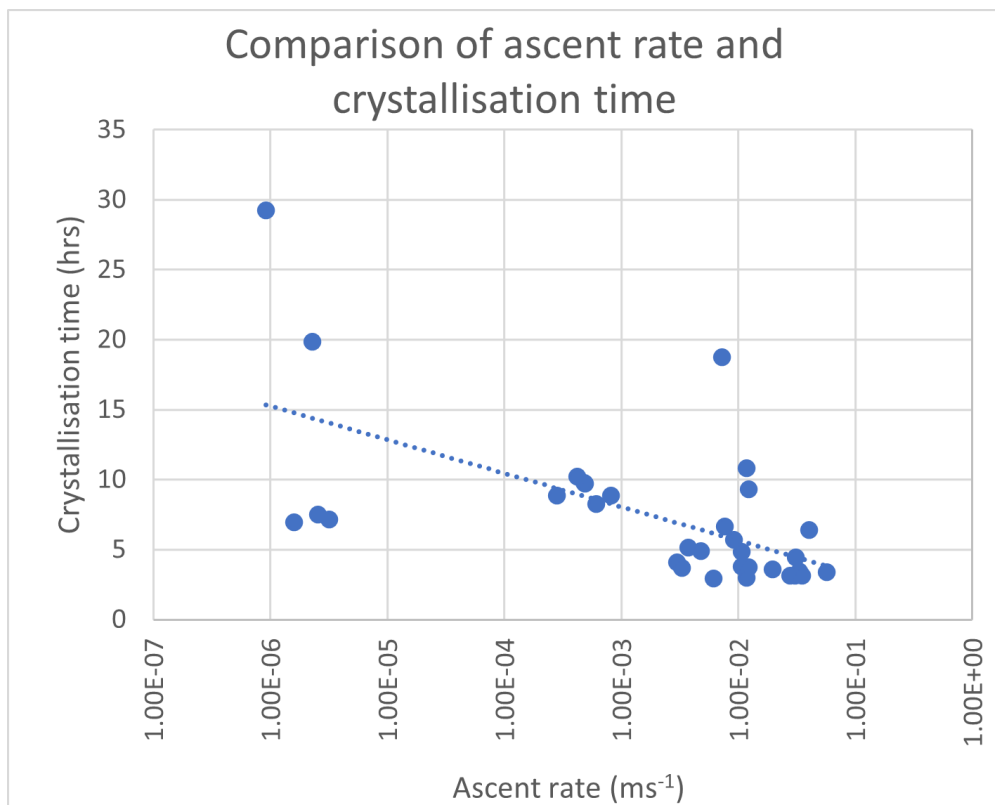


Figure 5.13 - Comparison graph showing the relationship between ascent rate and crystallisation time.

Due to the prehistoric age of the samples collected, it is unknown whether they were erupted under explosive or effusive conditions. The majority of existing studies into ascent rates focus on samples with a known eruptive time or style. The controls on silicic eruption styles can be schematically simplified into ascent rate, and outgassing efficiency (Cassidy *et al.*, 2018). Factors which affect the ascent rate include overpressure, stress fields, the radius of the conduit, magma viscosity, and buoyancy, whereas outgassing efficiency is largely a function of viscosity, pressure, time, bubble nucleation, permeability of magma and wall rock, and fragmentation processes (Cassidy *et al.*, 2018). The use of microlites has allowed ascent rates within the samples studied here to be well-constrained, whereas parameters associated with outgassing efficiency have not been similarly quantified. Evidence reported here in

association with outgassing efficiency is limited to the deposit type a sample was collected from, and its relative vesicularity. By combining the calculated ascent rates with broad generalisations on outgassing efficiency, based on field observations of eruption deposits described in Chapter 3, inferences on the eruption style that produced the respective deposit can be made. Figures 5.14 and 5.15 compare ascent rates for volcanoes with known eruption styles with the ascent rates calculated for St Kitts and Nevis, allowing inferences to be made on past eruption styles at St Kitts and Nevis based on direct comparisons.

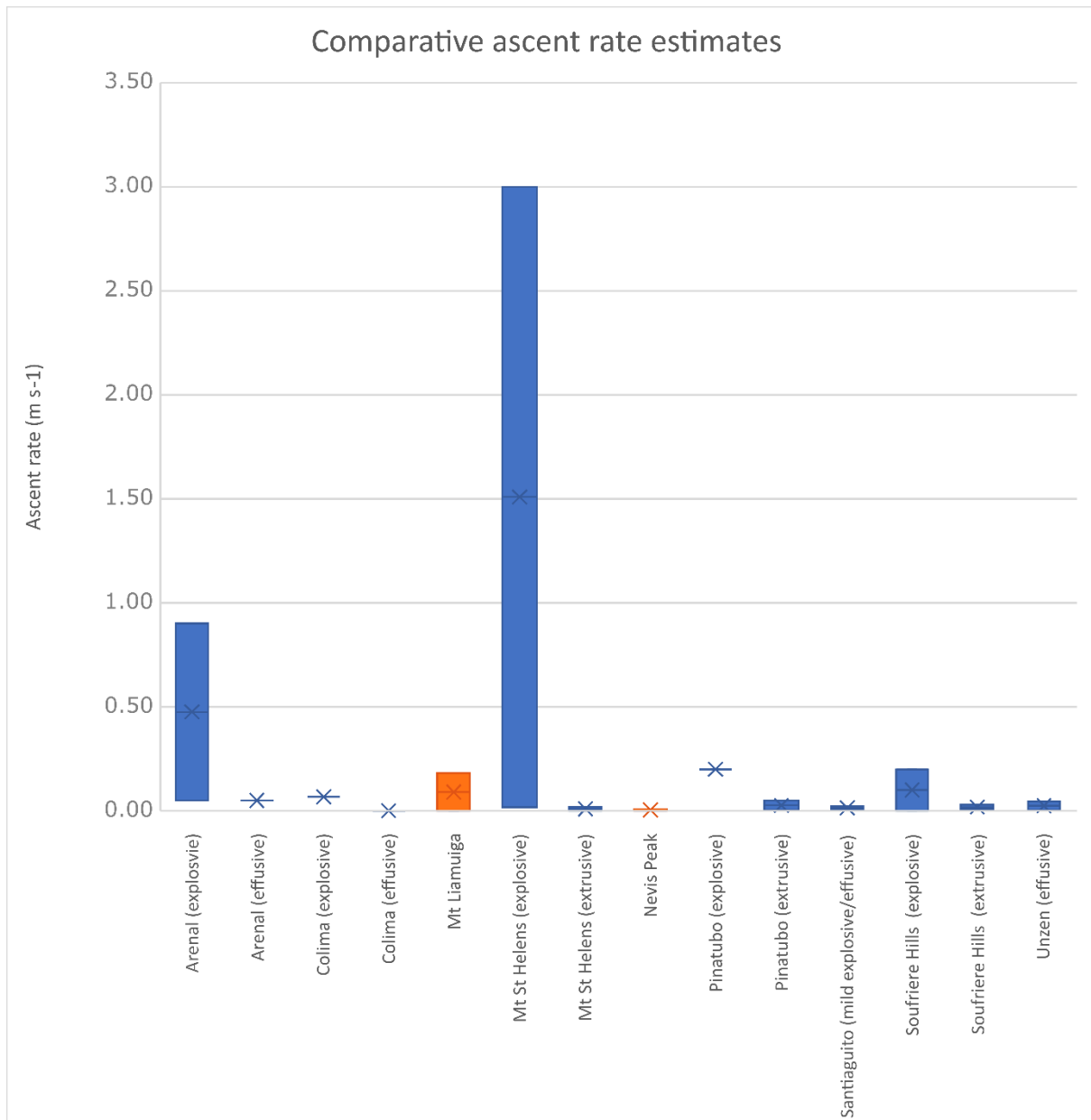


Figure 5.14 - Ascent rate estimates for different volcanoes, with the bars representing the range of the data, and the x symbols indicating the mean value. Where explosive/extrusive is not specified, the values are combined into one dataset. (Baker, 1968b; Brown and Andrews, 2015; Cassidy et al., 2015; Geschwind and Rutherford, 1995; Hammer et al., 1999; Murch and Cole, 2019; Noguchi et al., 2008; Scott et al., 2012; Szramek et al., 2006).

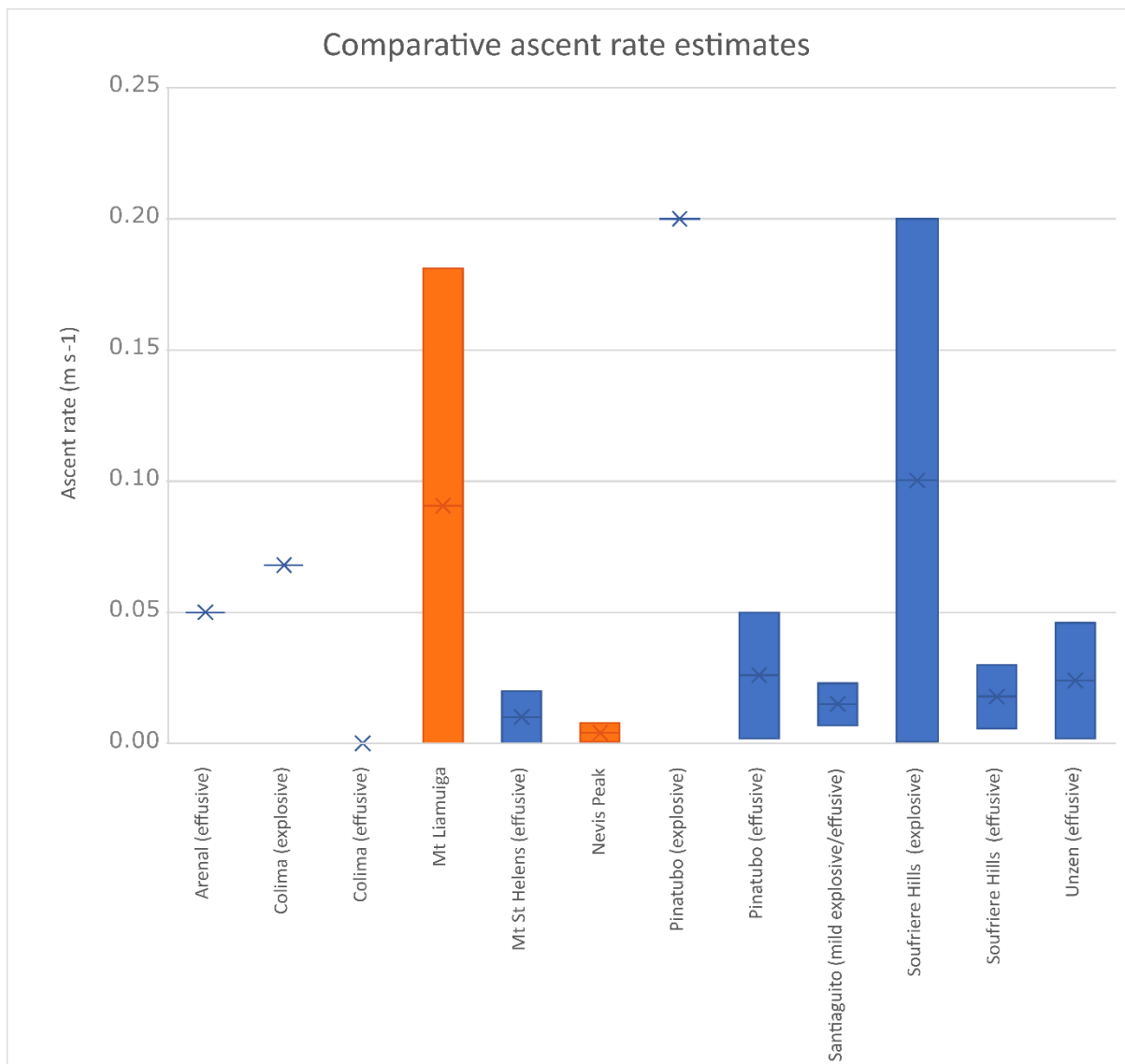


Figure 5.15 – Ascent rate estimates for different volcanoes with the outliers shown in Figure 5.14 removed, with the bars representing the range of the data, and the x symbols indicating the mean value. Where explosive/extrusive is not specified, the values are combined into one dataset. (Brown and Andrews, 2015; Cassidy et al., 2015; Geschwind and Rutherford, 1995; Hammer et al., 1999; Murch and Cole, 2019; Noguchi et al., 2008; Scott et al., 2012; Szramek et al., 2006).

The graphs shown in Figures 5.14 and 5.15 shows the estimations of ascent rates for eight volcanoes: Arenal, Colima, Mt St Helens, Pinatubo, Santiaguigo, Soufriere Hills and Unzen, as well as the values for Mt Liamuiga and Nevis Peak calculated in this study. All seven of these volcanoes are known to have erupted material with a composition of basaltic

andesite/andesite. Soufriere Hills on Montserrat and Nevis share the same tectonic setting as Mt Liamuiga, the remainder are located on continental crust at subduction zones. The studies from which these data originate use a number of methods to calculate ascent rates. These methods include groundmass crystallization/MND (as used in this study), amphibole reaction rims, magnetite zonation, seismicity and extrusion rate.

Mt Liamuiga shows ascent rates similar to those calculated at the volcanoes in Figures 5.14 and 5.15. The most similarity is shown with ascent rates for effusive eruptions. The maximum ascent rate values calculated for Mt Liamuiga are similar to the values calculated for Soufriere Hills explosive eruptions. The explosive eruptions by Arenal, Mt St Helens and Pinatubo have a faster ascent rate than those observed at Mt Liamuiga. Looking at these comparisons, it can be suggested that the material from which ascent rates were calculated for Mt Liamuiga could be products of both effusive and/or explosive eruptions. This is summarised in Figure 5.16.

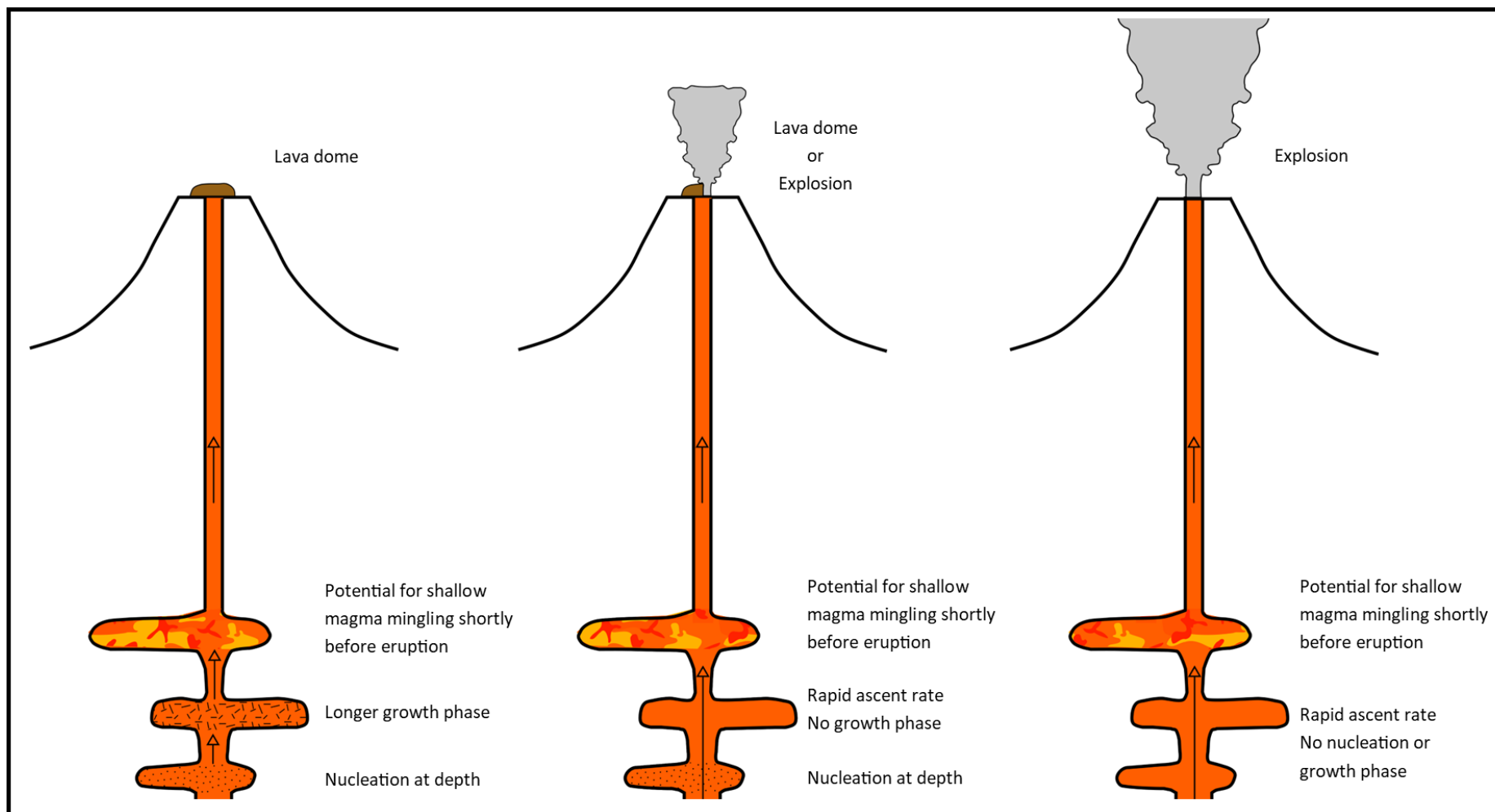


Figure 5.16 - Summary diagram showing three microlite evolution pathways and their corresponding eruption styles. The different shades of orange represents different magma types with the potential to mingle at shallow levels of the magma reservoir.

Samples SK1 and SK11 were identified in field observations (Chapter 3) as pumice lapilli fallout, which is a product of explosive eruptions, therefore we know the ascent rates calculated for these samples are indicative of ascent rates during explosive eruptions.

SK5D and SK8D show similar ascent rates, and were classified as pumice and ash flows in Chapter 3, suggesting that they were also products of explosive eruptions, which supports the hypothesis that these pumice and ash flows may have been formed due to column collapse. SK31, also thought to be from a pumice and ash flow, shows a overlapping and faster ascent rate, further suggesting that it was also a product of an explosive eruption. Comparing the ascent rates estimates suggests that SK24b and SK27a, both sampled from the Steel Dust Series, are products of similar explosive eruptions. SK20 and SK21 show significantly slower ascent rates suggesting that they may be products of different types of eruptions, more likely effusive events. This supports the idea that they were sampled from block and ash flows that were the result of a lava dome collapse. Based on observations in the field, SK30 was also thought to represent a block and ash flow, although it shows a much faster ascent rate in comparison to SK20 and SK21. As block and ash flows and pumice and ash flows represent the end members of PDC classification, it is likely that SK30 represents a more intermediate deposit. The deposit from which SK30 was collected contained horizons of pumice, not typical in end member block and ash flows. This combined with the decompression and ascent rate evidence (faster than expected, Section 5.3.4), suggests that the deposit from which SK30 was sampled, originated from an explosive eruption, and simply contains more clasts of denser material than the end member pumice and ash flows.

The samples from Nevis, show significantly slower ascent rates compared to Mt Liamuiga, and compared to many of the volcanoes shown in Figures 5.14 and 5.15, supporting the field

observations that they represent typical block and ash flows resulting from a lava dome collapse. The Nevis Peak samples shows a similar range of values to other effusive eruptions at similar volcanoes.

5.4.4 Amphibole reaction rims

Reaction rims on amphibole crystals also be used to estimate ascent rates (Devine *et al.*, 1998; Geschwind and Rutherford, 1995; Rutherford and Hill, 1993). The development of reaction rims is caused by the decreasing pressure of an H₂O-rich magma containing amphibole. A decrease in H₂O content tends to cause a reaction between the phenocrysts and the melt, initiating the breakdown of OH-bearing amphibole. Generally speaking, thicker reaction rims indicate a longer ascent from deep storage to the surface, while thinner or a lack of reaction rims suggest a more rapid ascent. Thicker reaction rims may represent the slow movement of the entire magma body, slow-moving magma close to the active flow zones, or remobilization of conduit wall material (Rutherford and Hill, 1993). Amphibole reaction rims are also thought to form in response to heating (De Angelis *et al.*, 2015). Reaction rim growth rates increase with increasing temperature, although it is challenging to differentiate between reaction rims formed by heating and by decompression (De Angelis *et al.*, 2015). In this study, it has been assumed that the reaction rims have formed due to decompression, as described above, therefore amphibole reaction rims can be measured and used to estimate ascent rates (De Angelis *et al.*, 2015; Devine *et al.*, 1998; Rutherford and Hill, 1993). Reaction rims were not measured and used to calculate ascent in this study due to the lack of amphibole crystals found in the Mt Liamuiga samples. Instead, the presence and qualitative description of reaction rim size and their implications for ascent rate are discussed.

Amphibole phenocrysts were not present in many of the Mt Liamuiga samples. The only samples to contain amphibole crystals were SK1, SK5L and SK8L. SK1 contained a small number of amphibole phenocrysts with no or thin reaction rims. SK5L contains a larger number of amphibole phenocrysts. Although most of these are fractured, most phenocrysts show thin reaction rims. SK8L contains amphibole phenocrysts, all with large reaction rims. In some cases, the amphibole crystals have broken down completely. The lack of amphibole crystals in the majority of Mt Liamuiga samples is likely due to magma geochemistry, rather than conduit conditions and processes related to decompression.

The lack of reaction rims observed in SK1 and SK5L suggests that the magma associated with these samples travelled from magma storage to the surface rapidly, likely in a matter of days (Rutherford and Hill, 1993). This supports the ascent rates estimated from the microlite populations found in SK1. The large reaction rims observed surrounding amphiboles in sample SK8L (Figure 5.17) suggest that the magma which corresponds to the deposits in which SK8L was collected rose from storage to the surface much slower. This is in direct contrast to the fast ascent rates suggested by the lack of microlites and the large volume of glass within the sample. This difference could be due to different ascent rates at different points in the shallow plumbing system of Mt Liamuiga shortly before and during the eruption of SK8L. The presence of amphibole reaction rims could suggest a slow ascent from storage to more shallow depths, while the lack of microlites suggests a fast ascent rate through the shallow conduit. The lack of microlites with the presence of amphibole reaction rims in SK8L, and the lack of amphibole crystals and presence of microlites in SK8D suggests that magma mingling took place at very shallow depths in the upper conduit shortly before an eruption occurred. This is also likely to apply to SK5L and SK5D. Evidence for this mingling is also apparent in the geochemical data

acquired from whole rock major element XRF analysis, where the geochemical composition of the 'lighter' (L samples) and 'darker' (D samples) were significantly different.

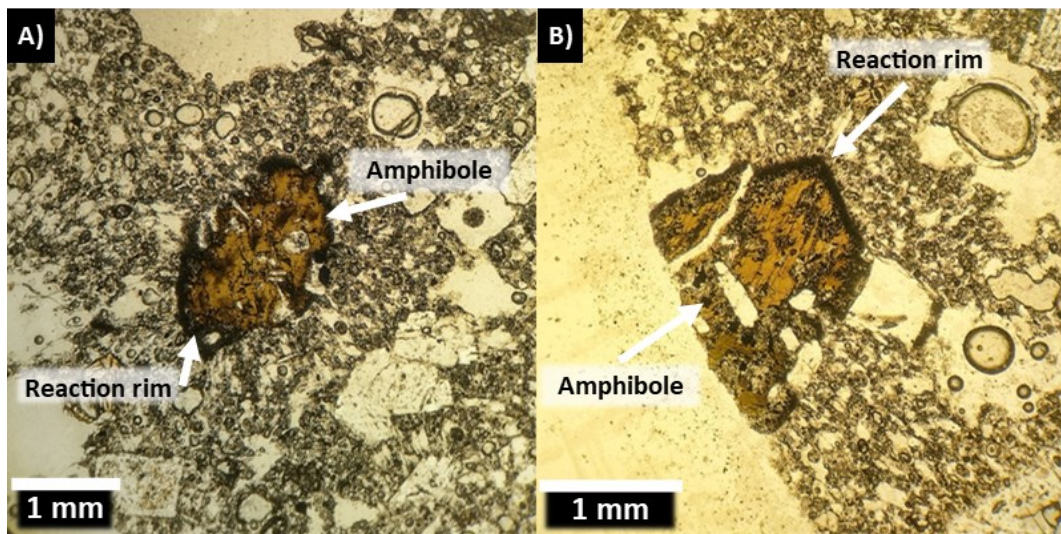


Figure 5.17 - Amphibole phenocrysts in SK8L. The thicker reaction rims are visible.

The Nevis samples contain an abundance of amphibole. Amphibole phenocrysts in SKN18 show no or thin reaction rims across the thin section studied (Figure 5.17). A significant number of the phenocrysts in SKN19 show thick reaction rims (Figure 5.18), although many other smaller phenocrysts show only very thin reaction rims. The presence of larger reaction rims suggests a slow ascent rate from storage to the surface.

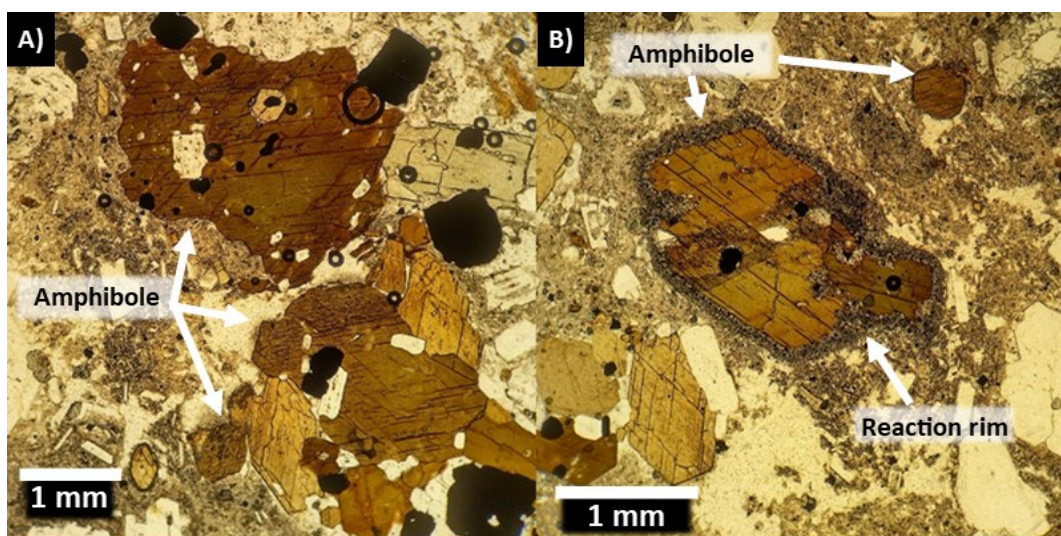


Figure 5.18 - Amphibole phenocrysts found in SKN18 and SKN19. A) Amphibole in SKN18 showing no or thin reaction rims. B) Amphibole with a thick reaction rim, other amphibole crystals in the same image show thin reaction rims.

5.5 Conclusions

The following conclusions can be drawn from this chapter:

- N_a and ϕ values suggest that most samples underwent a short period of nucleation followed by re-equilibration of the system allowing change to a growth dominated regime. Some samples lacked a growth phase, and were erupted after a burst of microlite nucleation. Samples lacking any microlites (e.g. SK5L and SK8L) were likely erupted after a rapid decompression and ascent, with no time to allow microlite nucleation.
- Estimated average crystallisation times for Mt Liamuiga ranged from 2.95 to 29.24 hours, while times for Nevis ranged from 3.58 to 12.29 hours. These values suggest fairly short periods of crystallisation, and are comparable to those observed at Soufriere Hills.
- Ascent rate estimates suggest that the majority of the Mt Liamuiga deposits studied were the products of explosive eruptions. The exceptions were SK20 and SK21, which were more likely to have originated from a collapsed lava dome.
- Ascent rate estimates calculated for the Nevis samples suggest a much slower decompression and ascent rate compared to the Mt Liamuiga samples, confirming field observations that they are typical block and ash flow deposits originating from a lava dome collapse.
- Microlite and amphibole evidence from SK8 and SK5 samples suggest that amphibole reaction rims and microlite nucleation occurred at different depths, during different stages of magma ascent. The evidence also suggests that magma mingling occurred at close to the surface in the shallow conduit, shortly before an eruption.

6. Hazard Analysis of Pyroclastic Density Currents

6.1 Introduction

This chapter aims to utilise an existing computer program to model pyroclastic density currents (PDCs) originating from Mt Liamuiga, to gain insights into the likely behaviour, paths and inundation areas of future events. The findings of the fieldwork and ascent rate calculations were considered when determining the model parameters. When considering parameters, it has been assumed that the ascent rates calculated previously (Section 5.4.3) are indicative of explosive activity, and so an explosive column-collapse eruption style was modelled, producing pumice and ash flows and transitional ash flows with a significant pumice component. The results of these models will be used to create maps of inundation area and thickness, to allow hazard analysis of the threat posed to St Kitts by PDCs.

6.1.1 Computer models for PDC hazard analysis

Several different programmes now exist for the numerical modelling of pyroclastic density currents. While modelling PDCs is difficult due to their complex nature, several different models attempt to use simplified rheological laws to reproduce the general behaviour of PDCs, including PyFlow (Dioguardi and Mele, 2018), Energy Line/Cones (Clarke *et al.*, 2020; Malin and Sheridan, 1982), PFZ (Widiwijayanti *et al.*, 2009), Titan2D (Patra *et al.*, 2005; Pitman *et al.*, 2003) and VolcFlow (Kelfoun, 2017; Kelfoun *et al.*, 2017; Gueugneau *et al.*, 2019).

PyFlow is one such programme available to model PDCs, although its main purpose is to calculate flow properties (e.g. velocity, thickness, etc.), and “impact parameters” of dilute PDCs (DPDC) at a sampled outcrop, rather than PDC inundation area (Dioguardi and Mele, 2018). These impact parameters include the dynamic pressure of a DPDC, particle volumetric

concentration, and the deposition time (Dioguardi and Mele, 2018). Rather than forward modelling of potential PDC scenarios, PyFlow instead uses input data from existing PDC deposits to calculate the previously mentioned parameters. As this programme does not model PDC inundation area, and requires extensive field campaigns and laboratory analyses of existing PDC deposits (e.g. particle analysis) to function as inputs, it was not deemed suitable to achieve the objectives of this study.

The energy line/cone model is a simplistic approach to modelling the maximum PDC footprint of an eruption and is based on three inputs: Vent location; collapse height; and a mobility parameter which essentially characterises how rapidly the potential energy from a column collapse is converted during horizontal PDC dispersion (Clarke *et al.*, 2020; Malin and Sheridan, 1982). From these inputs, a cone can be defined around a volcano, and where this cone intersects the topography defines the maximum PDC inundation area, predicting where PDCs would stop. Due to the simplicity of this model it can be effectively applied to locations with little prior knowledge, and it is computationally light, allowing for many different scenarios to be modelled in a relatively short time (Clarke *et al.*, 2020). However, this method cannot account for individual PDCs, nor for other flow factors such as channelisation of a PDC, and so was not considered appropriate for this study.

PFZ is a modified version of LAHARZ calibrated to better represent PDCs, particularly BAFs (Widiwijayanti *et al.*, 2009). This piece of software produces inundation footprints by filling in the topography downstream of a user defined point. This is achieved by creating a surface drainage grid, calculating the energy line/cone, and modelling the inundation area. The resulting inundation footprints can appear similar to real-world examples, however PFZ does not accurately represent flow characteristics for PDCs, resulting in cross-sectional thicknesses

that do not correspond to real-world deposits (Widiwijayanti *et al.*, 2009). This made PFZ unsuitable for use in this study.

Two freely available geophysical mass flow models (GMFMs) were considered potentially suitable for calculating PDC run out and thicknesses from Mt Liamuiga, Titan2D (Patra *et al.*, 2005; Pitman *et al.*, 2003) and VolcFlow (Kelfoun, 2017; Kelfoun *et al.*, 2017; Gueugneau *et al.*, 2019). Both of these models treat the granular mass flows as fluids, and are based on using shallow-water momentum conservation equations to represent their flow. VolcFlow was chosen over Titan2D as Charbonnier and Gertisser (2012) showed that, whilst both models were able to reproduce morphology and distribution of deposits, VolcFlow more accurately reproduced the timing of emplacement and flow velocity when compared to Titan2D. The Two-phase (dense and dilute PDCs) version of VolcFlow was used to allow the modelling of both dense PDCs and dilute pyroclastic surges.

VolcFlow was initially created to model single fluid flow of the 7.5 ka Socompa rock avalanche, in Chile (Kelfoun and Druitt, 2005), but has since been developed into three freely-available versions: Single-fluid, Two-fluids (Debris avalanche and tsunami), Two-fluids (dense PDCs and surges). A strength of VolcFlow has been identified in its ability to replicate PDC inundation area well, as it has also been shown to be useful for producing scenario-based hazard maps (Ogburn and Calder, 2017). It has previously been used for determining the rheological behaviour of dense PDCs, volcanic hazard mapping, and simulation of dense and dilute PDCs. It has also been applied to debris avalanches, tsunamis and lava flows (Kelfoun, 2017; Kelfoun *et al.*, 2016)

VolcFlow has been used to model PDC inundation areas on other Caribbean islands, including Montserrat (Gueugneau *et al.*, 2019), Mt Pelée (Gueugneau *et al.*, 2020), and most recently

the 2021 Eruption of La Soufriere on St Vincent (Gueugneau, in press). No numerical modelling of PDCs has yet been performed for Mt Liamuiga on St Kitts.

6.1.2 Hazard assessments of Mt Liamuiga

As stated in previous chapters, Mt Liamuiga is the only volcanic centre on St Kitts thought to have the potential for future activity (Robertson, 2005; Simpson and Shepherd, 2001). Past activity on St. Kitts suggests that Mt Liamuiga is capable of generating both explosive and effusive eruptions (Baker, 1985). Both types of eruptions are capable of producing volcanic hazards, including PDCs, ash fall, and lahars, as explored in Chapters 3, 4 and 5.

Baker (1985) produced a 'pyroclast flow hazard map' based on field mapping of PDCs, defining hazard zones based on the distribution of prehistoric deposits, taking into account the present day morphology of the volcano. The zones are approximated, and give some indication of the likely recurrence interval of PDC activity within different sectors of the volcano, ranging from 1500 – 3500 years. Baker (1985) identified the zone of maximum hazard as a triangular region extending from the lowest point of the crater rim towards the NW, with an estimated PDC recurrence interval of 1500 years. According to Baker (1985), the towns of Dieppe Bay Town, Sandy Bay, and Sandy Point Town, all lie within the next lowest hazard region, with a recurrence interval of 2000 years. However, the maps produced by Baker (1985) were simplistic and focussed on an estimate of past frequency rather than quantitative consideration of future eruption scenarios.

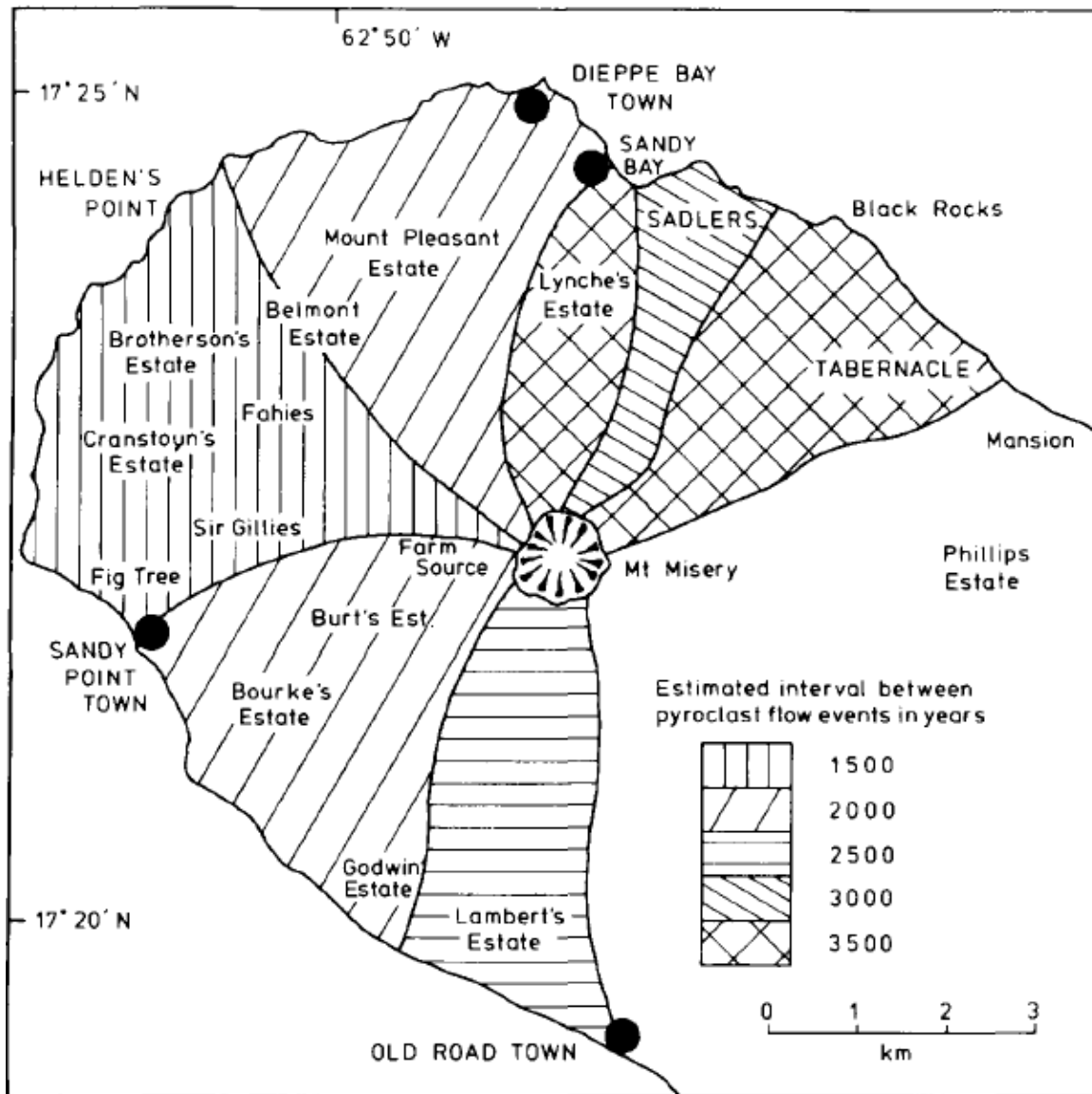


Figure 6.1 – Pyroclast flow hazard map for NW St Kitts from Baker (1985).

The most recent volcanic hazard assessment for St Kitts resulted in the creation of the two pyroclastic flow/surge hazard maps shown in Figures 6.2 & 6.3 (Simpson and Shepherd, 2001; Robertson, 2005). These hazard maps were solely qualitative, and so only broadly categorise pyroclastic flow/surge hazard into 'high', 'medium', and 'low to negligible' categories, with lahars simply indicated in valleys. This broad categorisation results in the entire north-western area of the island being highlighted as a 'high' hazard from PDCs in an explosive scenario, with no information given on possible PDC inundation area pathways.



Figure 6.2 - Volcanic hazard map for an explosive eruption at Mt Liamuiga, St. Kitts (Robertson, 2005).



Figure 6.3 - Volcanic hazard map for an effusive dome forming eruption at Mt Liamuiga, St. Kitts (Robertson, 2005).

The area between Mt. Liamuiga and Verchild's Mt, in a northeast-southwest oriented band, is categorised as having a 'Moderate' PDC hazard, with the remainder of the island falling into the 'Low to negligible' category (Robertson, 2005), as shown in Figure 6.2. For the effusive 'dome forming' scenario, the 'High' hazard band is very similar, with the 'Moderate' zone

being wider, and less of the island categorised as 'Low to negligible' PDC hazard, shown in Figure 6.3.

Explosive eruptions are likely to take place from an open crater and may start with phreatic activity. This style of activity was observed at Montserrat in 1995 (Robertson *et al.*, 2000; Young *et al.*, 1998) and Mt Pelée in 1902 (Fisher and Heiken, 1982; Gueugneau *et al.*, 2020). Large eruption columns and extensive ash fall are likely to be associated with this eruption type, with PDCs potentially developing from column collapses and explosions. The current volcanic hazard map for an explosive scenario is shown in Figure 6.2.

Effusive dome eruptions may take the form of dome-building events, with the primary hazard posed by this type of eruption being from PDCs arising from a dome collapse (Baker, 1985; Simpson, 2005; Simpson and Shepherd, 2001). The current volcanic hazard map for an effusive eruption is shown in Figure 6.3.

Previous works (Robertson, 2005) have noted the need for continuous revision of the produced hazard maps, which the modelling performed in this study will contribute to.

6.1.3 Towns, Population and infrastructure

When considering volcanic hazard, it is important to take into account the location of settlements and their populations, as well as key infrastructure. Population data based on the 2011 Census, is generally available only to the parish level and not for individual towns on St Kitts, except for Basseterre. The parishes containing towns discussed herein, and their respective populations, are included in Table 6.1, below. Approximately one third of the population of St Kitts is located in the capital, Basseterre, and the surrounding areas of the southeast, whereas the northwestern area of the island discussed herein typically has a lower

population density (Department of Statistics, 2011). The infrastructure on the island of St Kitts is relatively limited, with an orbital main road following the circumference of the island, which is also the main route for utilities, including water, electricity and some telecoms. The island hosts a single international airport, Robert L. Bradshaw Airport, one hospital to serve the whole island, and the main passenger port, all of which are located at Basseterre in the south of the island.

Table 6.1 – Parishes and towns in St Kitts, with their respective populations (Department of Statistics, 2011)

Parish/Town	Population
St George Basseterre (incl. Basseterre)	12,635
Basseterre (Town only)	11,400
St Thomas Middle Island (incl. Old Road Town)	2,535
Christ Church Nichola Town (incl. Nichola Town and Mansion)	2,020
St Paul Capisterre (incl. most of Newton Ground, Heldens, and Dieppe Bay)	2,432
St John Capisterre (incl. Saddlers Village, Tabernacle)	2,962
St Anne Sandy Point (incl. Sandy Point Town, remainder of Newton Ground)	1,922

6.2 Methodology

6.2.1 Digital elevation model (DEM)

The digital elevation model (DEM) used for this study was based on satellite data, and was provided by the St Kitts and Nevis Department of Physical Planning and Environment. The DEM had a spatial resolution of 1 m covering much of the island of St Kitts, with the exception of the mountain peaks in the centre of the island which had a resolution of 30 m due to frequent cloud cover preventing high-resolution satellite data collection. The provided DEM was then resampled to a 20 m resolution using a cubic convolution, as this method results in a smoother and less distorted raster than one produced by a “nearest neighbour” resampling algorithm, which doesn’t account for all surrounding values. The resampled DEM was cropped to the northwest region of the island surrounding Mt Liamuiga in order to reduce the file size and improve the calculation time in VolcFlow.

6.2.2 VolcFlow

As described in the introduction (Section 1.2), VolcFlow is a model used to simulate the inundation area and emplacement of dense and dilute PDCs. VolcFlow is distributed as an un-editable P-code file, which is executed within the MATLAB environment. An input file was written, based on the Merapi example file distributed as part of the VolcFlow package, using input parameters published in the literature (Charbonnier and Gertisser, 2012; Deng *et al.*, 2019; Kelfoun *et al.*, 2017) and suggested by expert users of VolcFlow (Gueugneau, 2022, personal communication). Charbonnier and Gertisser (2012) included a list of “best fit” parameters, which were used to help decide the starting values used in the modelling of this study. The significant input parameters are shown in Table 6.2.

Table 6.2 - VolcFlow input parameters chosen for the Mt Liamuiga dense PDC and surge models.

Input parameters	Name in VolcFlow	Value
Source area radius	rdome	650 m
Particle density	rhop	2400 kg m ⁻³
Atmosphere density	rhoa	1 kg m ⁻³
Basal part density	rhoD	1200 - 1400 kg m ⁻³
Particle mean diameter	d_part	0 ϕ
Drag coefficient (Cd)	coef_Cd	1
Total deposit volume	V	$1 \times 10^5 - 1 \times 10^8 \text{ m}^3$
Collapse duration	talim	10 s
Mixture density	rho_m	5 kg m ⁻³
Voellmy drag coefficient	coef_u2 (1)	0.01
Surge drag coefficient	coef_u2 (2)	0.05
Surge production coefficient	coef_a3	0.001 - 0.01

6.2.2.1 Defined parameters

The full range of potential parameters cannot be explored in studies with limited time and computing resources, and so ‘starting points’ must be chosen from the literature on similar scenarios, and these then used to guide modelling decisions. An expert in VolcFlow was consulted to ensure that appropriate values were used, to reduce the need for trial and error and maximise the outputs, as the modelling conducted in this thesis was time constrained (Gueugneau, 2022, personal communication).

An atmospheric density of 1 kg m^{-3} was chosen, as this is an approximation of the average atmospheric density on Earth, as suggested by Kelfoun *et al.* (2017). Similarly, a particle density of 2400 kg m^{-3} , representing the density of each modelled particle in the flows, was used, based on similar modelling in the literature of BAFs and surges (Kelfoun *et al.*, 2017).

Mixture density, controlling the density of the mixing that leaves the dense PDC to supply the surge, can again range from 0 to 100. A value of 5 kg m^{-3} was used in this study, selected based on the values used in Kelfoun *et al.* (2017), who used values ranging from $3 - 8 \text{ kg m}^{-3}$, a mean value was used (Gueugneau, 2022, personal communication).

The drag coefficient, *coef_cd*, affects particle settling and can range in value from 0 to 100, although it does not exceed 32 where specified in the available literature. A value of 1 was used as a starting point in this study, and it was not considered necessary to be changed further (Gueugneau, 2022, personal communication).

Two further drag coefficients are defined together, 'Voellmy' and 'Surge', and are used to control the turbulent or collisional stresses that act to retard the flow (Kelfoun *et al.*, 2009; Ogburn and Calder, 2017). Here, values of 0.01 and 0.05 were used, based on those in Kelfoun *et al.* (2017) (Gueugneau, 2022, personal communication).

As particle analysis was not performed on the samples collected from the field campaign, the particle mean diameter value was estimated. The particle sizes found in the field samples were estimated to range from ash, to block sized. Ash formed the majority of the material collected in the field, and so a particle size of 1.6 mm, equivalent to a phi value of 0, or a coarse ash, was used for the particle mean diameter value (Gueugneau, 2022, personal communication).

6.2.2.2 Chosen variables

While each input parameter is capable of influencing the output of the model, three were chosen as variables to be used in this study; total deposit volume (V), basal part density (ρ_D), and the surge production coefficient (coef_{a_3}). The total deposit volume was changed in each scenario run to reflect varying sizes of eruptions thought to be possible at Mt Liamuiga. Minimum and maximum volumes were initially informed by literature, with the absolute values determined experimentally. The minimum volume modelled was $1 \times 10^5 \text{ m}^3$, as this was the largest volume modelled that did not leave the crater to produce PDCs. Deposit volumes in the region of $1 \times 10^7 \text{ m}^3$ are used to model single PDCs in each of Charbonnier and Gertisser (2012), Deng *et al.* (2019) and Gueugneau *et al.* (2019). These volumes fell between the minimum and maximum feasible scenarios calculated as part of this study. The maximum modelled total deposit volume was $1 \times 10^8 \text{ m}^3$, which produced PDCs that covered the majority of the northwest of St Kitts, and was larger than the deposit volumes commonly seen in the literature for similar volcanoes.

The second modelled variable, basal part density, representing the density of the PDC deposits, was changed to reflect the Pumice and ash flows, and transitional PDC classifications. These PDC types were observed in the field on St Kitts (described in Chapter 3) and considered feasible for future eruption scenarios. A density of 1200 kg m^{-3} was used to represent the pumice and ash flows, and 1400 kg m^{-3} for the transitional flows (Brown and Andrews, 2015).

The third modified variable, the surge production coefficient, controls the rate at which surges are formed within the model. Two values were used for this, one value producing

relatively small surges (lower surge production coefficient), and one value resulting in the generation of larger surges (higher surge production coefficient), 0.001 and 0.01, respectively. The chosen values are within the range of those described in Kelfoun *et al.* (2017).

6.2.2.3 Source conditions

Both column collapse and dome collapse PDC sources can be modelled using VolcFlow. To model a dome collapse scenario, the PDC source is defined as a single point of origin, whereas for a column collapse scenario the source is defined as a sustained input of material over a defined area in a given time (Kelfoun, 2017). The column height itself cannot be modelled, but the rate at which material is released and the area over which this occurs can be used to approximate different column sizes, e.g. a prolonged emission over a larger area could simulate a larger column collapsing.

The model specifically relates only to the material forming parts of the PDCs, and does not account for the size of the explosion or the height of the associated eruption column produced. For the column collapse scenario the model simulates directly emplacing material onto the flanks of the volcano, which then generates PDCs (Kelfoun, 2017).

In the first trial models, a small source region was used which did not extend beyond the crater rim, due to this the resulting PDCs simply infilled the crater rather than flow down the flanks. Following this the source region was revised to extend slightly beyond the crater rim as a circle with a radius of 650 m (Figure 6.4), so that material would be emplaced on the upper flanks, allowing PDCs to flow beyond the crater. The 650 m radius from the centre of the crater was used as the source region for all models discussed in this chapter. If further modelling were to be undertaken, larger source areas, along with larger volumes, could be

used to simulate larger eruptions with higher eruption columns. This would likely increase the size of the resulting PDCs modelled.

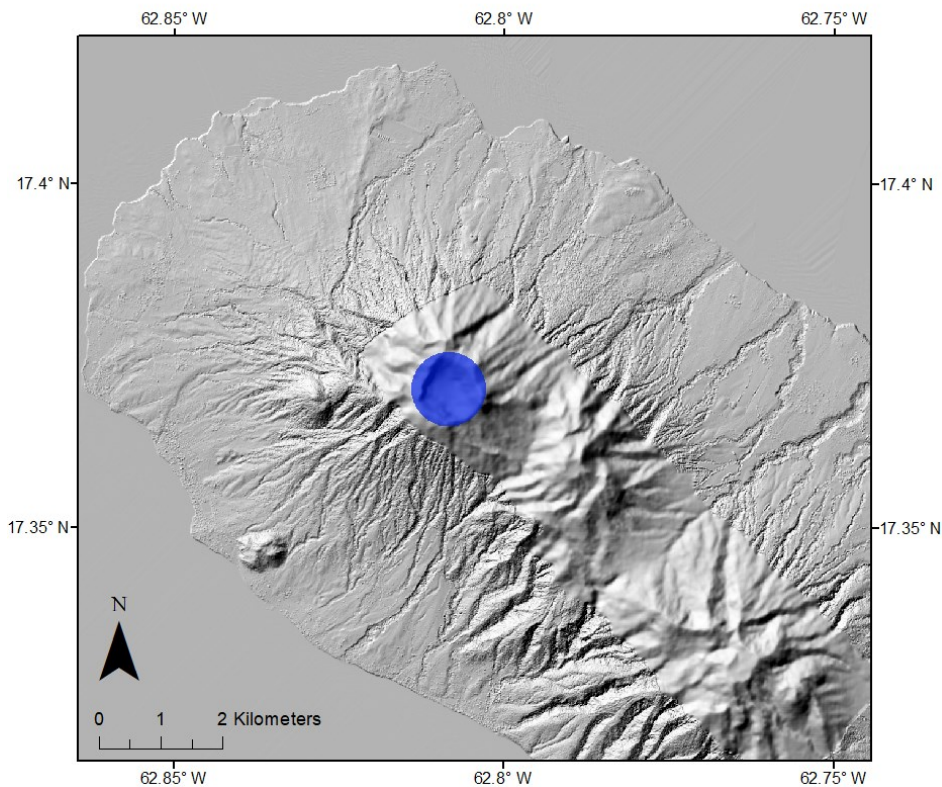


Figure 6.4 - Map of Mt Liamuiga showing the source area, a circle with a radius of 650 m centred on the crater, indicated in blue.

In trial models, the source supply duration was experimented with to determine the effects this had on PDC inundation areas, using longer supply times for larger volumes, with the inverse for smaller volumes. Changing the supply duration did not significantly affect the resulting PDCs.

6.2.3 ArcMap

The dense PDC and surge outputs from VolcFlow were imported into ArcMap. These output files were georeferenced and overlain onto the DEM to generate inundation area and

thickness maps of each modelled scenario. Infrastructure data sourced from OpenStreetMap were imported into ArcMap to gain insight into the potential vulnerability of St Kitts to PDCs.

6.3 Results

Twenty-two eruption scenarios were modelled using VolcFlow. For each deposit volume, two densities were modelled; 1200 kgm^{-3} representing pumice and ash flows, and 1400 kg m^{-3} representing transitional flows, as described in the methodology (Section 6.2.2). These are collectively referred to as the 'dense deposits'.

Studies of actual PDCs at various volcanoes, including Merapi (Charbonnier *et al.*, 2013; Lerner *et al.*, 2022; Widiwijayanti *et al.*, 2009) and Soufriere Hills Volcano (Cole *et al.*, 2002, 2014) have shown that the extent of any dilute PDC current (surge) is extremely variable between events. Some PDCs have only a minimal dilute current, whereas others have extensive dilute currents. To take this into account with this modelling, for six volumes, two types of dilute current were modelled 'low production' and 'high production' coefficient scenarios (Section 6.2.2.2).

A topographic map in Figure 6.5 shows the locations of the towns and topographic features referenced in this chapter when describing the inundation area of dense and surge PDCs.

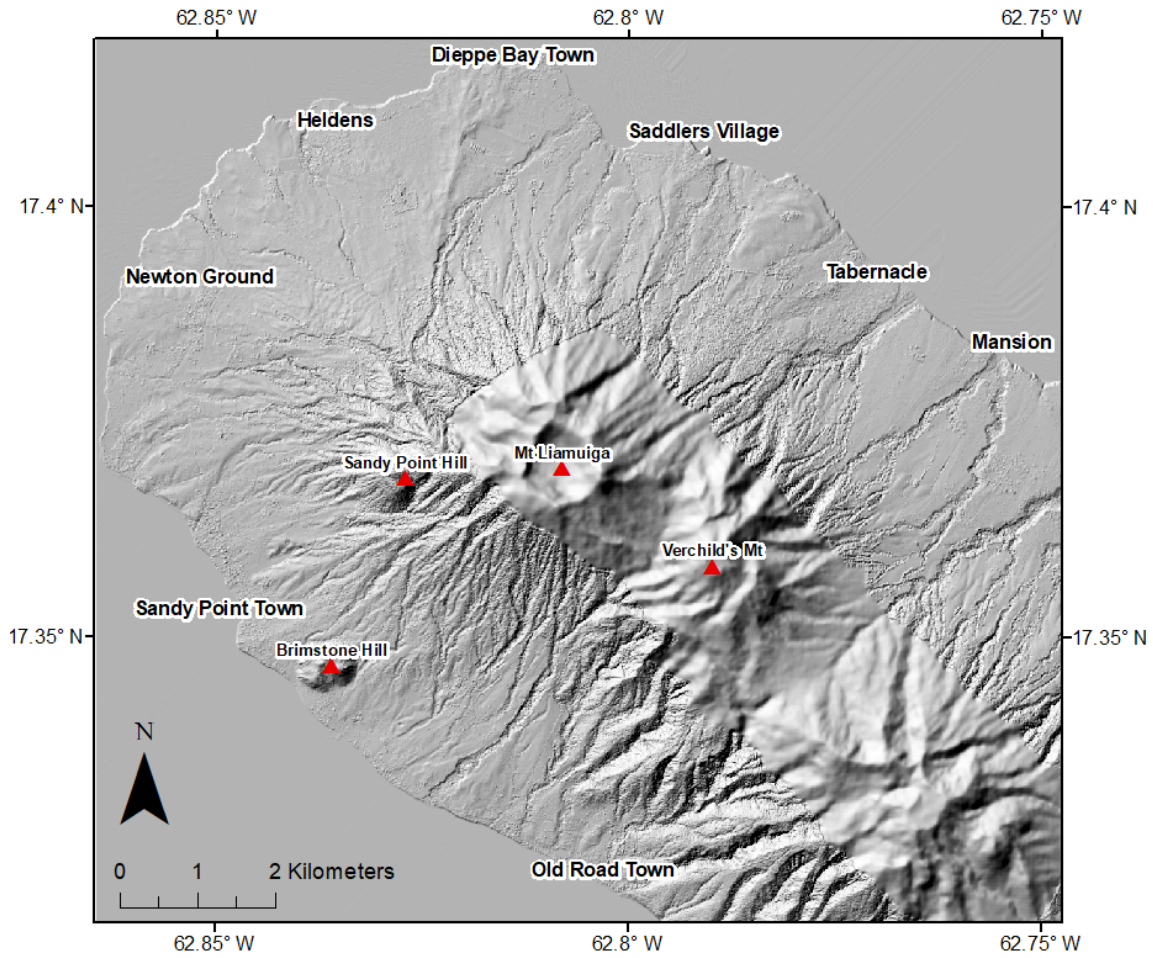


Figure 6.5 - Topographic map of Northern St Kitts showing the towns and topographic features referenced in this chapter.

6.3.1 Dense PDC deposits

The dense PDC deposit inundation areas generated by the low and high production coefficient scenarios were similar, exhibiting similar inundation area pathway directions at similar volumes, although the inundation areas of the high production coefficient scenarios were typically shorter due to more material lost to the surges. The inundation areas of the dense deposits are shown in Figures 6.6, 6.7 and 6.8. The model outputs can be divided into four broad categories, based on their PDC inundation area distances; crater-confined, upper flanks, lower flanks, and coastal.

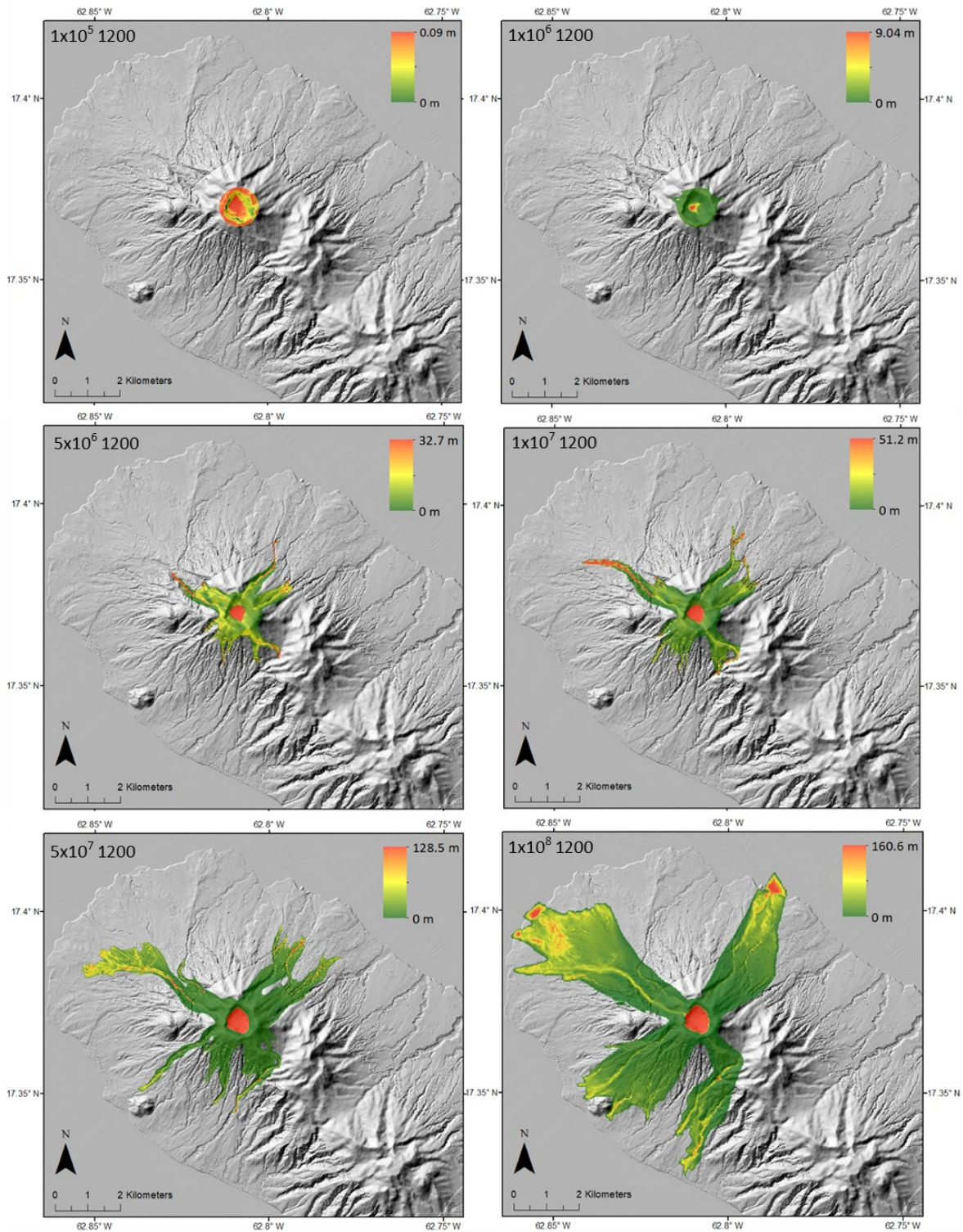


Figure 6.6 - Maps showing examples of deposits from dense PDCs from the low surge production scenarios with basal part densities of 1200 kg m^{-3} . The inundation area and deposit thickness is shown for each scenario, with the respective total deposit volume (m^3) and basal part densities ($kg m^{-3}$) indicated in the upper left of each map.

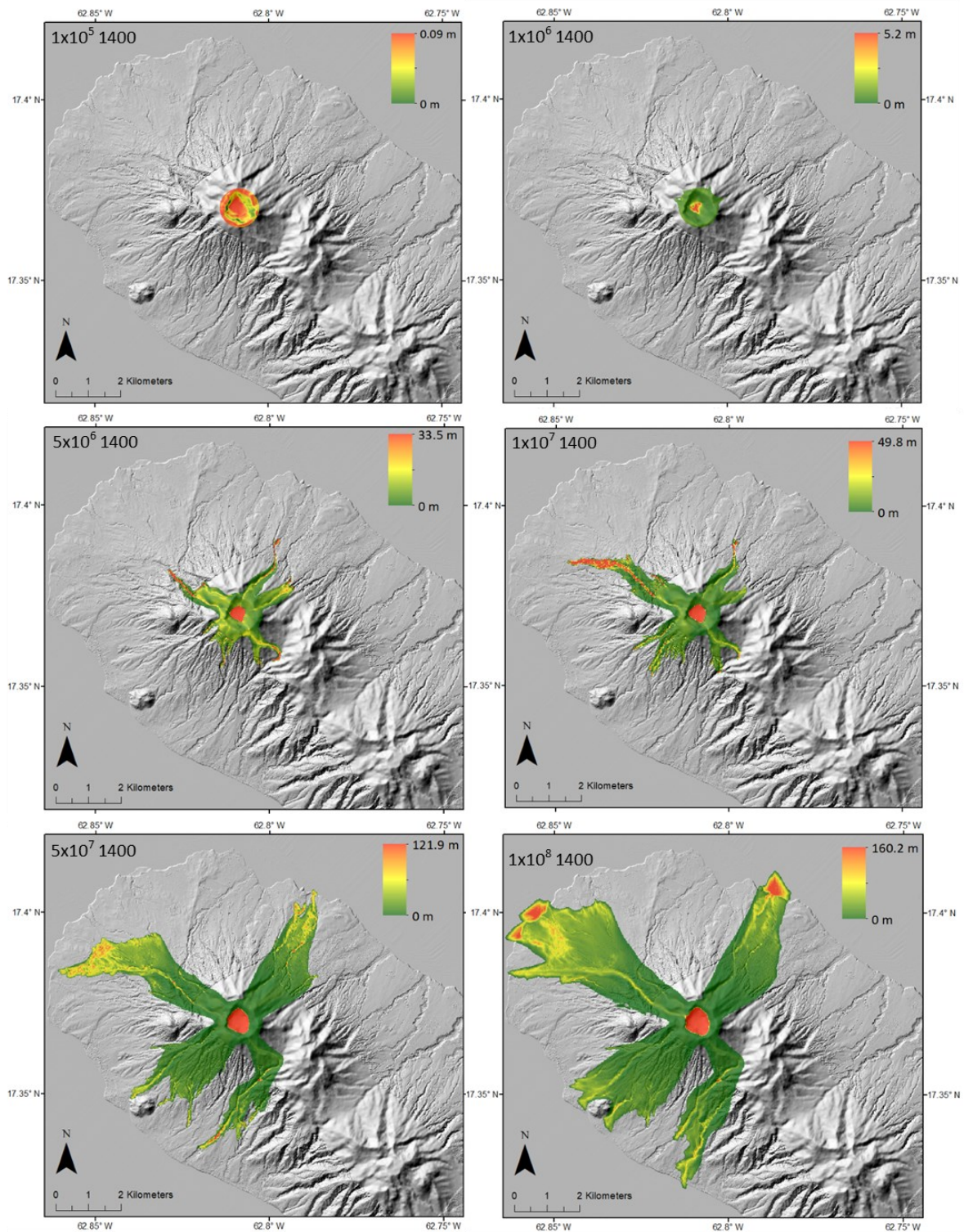


Figure 6.7 - Maps showing examples of deposits from dense PDCs from the low surge production scenarios with basal part densities of $1400\ kg\ m^{-3}$. The inundation area and deposit thickness is shown for each scenario, with the respective total deposit volume (m^3) and basal part densities ($kg\ m^{-3}$) indicated in the upper left of each map.

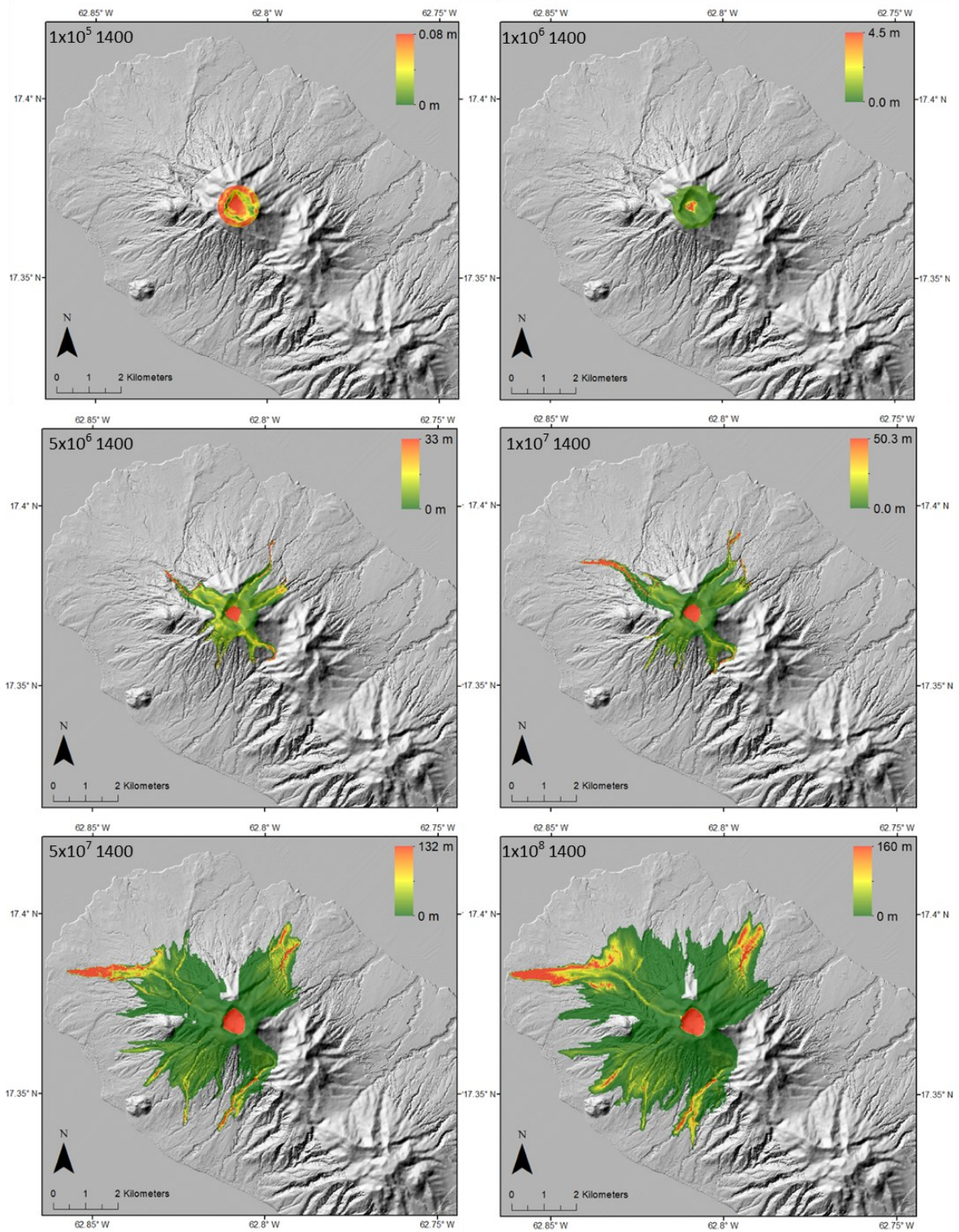


Figure 6.8 - Maps showing examples of deposits from dense PDCs from the high surge production scenarios with basal part densities of 1400 kg m⁻³. The inundation area and deposit thickness is shown for each scenario, with the respective total deposit volume (m³) and basal part densities (kg m⁻³) indicated in the upper left of each map.

6.3.1.1 Crater-confined PDCs

This category encompasses the smallest PDCs that were not large enough to leave the crater.

Low surge production scenarios

Both densities of the $1 \times 10^5 \text{ m}^3$ low production coefficient scenarios generated PDCs that remained within the crater (Figure 6.6 & 6.7). The resulting deposits are a thin up to 0.09 m in thickness across the crater. There is no significant difference between the 1200 or 1400 kg m^{-3} basal part density scenarios.

High surge production scenarios

The 1×10^5 and $1 \times 10^6 \text{ m}^3$ high production coefficient scenarios (Figure 6.8) can be classified as crater-confined. For the $1 \times 10^5 \text{ m}^3$ scenario the resulting deposits are a thin coating across the crater, up to 0.08 m in thickness. In the $1 \times 10^6 \text{ m}^3$ scenario, the dense deposits have a maximum thickness of 4.5 m in the centre of the crater, and are thinner on the crater walls and around the crater rim. This scenario produced a small dense PDC to the west of the crater.

6.3.1.2 Upper Flank PDCs

The PDCs in this category were large enough to overtop the crater but did not travel further than the volcano's upper flanks (approximately 2.5 km from the centre of the crater).

Low surge production scenarios

For the low surge production scenario, the upper flank PDCs includes all modelled scenarios with total deposit volumes between 1×10^6 to $5 \times 10^6 \text{ m}^3$ (Figures 6.6 and 6.7).

A total deposit volume of $1 \times 10^6 \text{ m}^3$ (Figures 6.6 and 6.7) resulted in PDCs which barely overtopped the crater rim, resulting in small PDCs in three directions, towards the northwest,

north, and east-northeast. To the northwest PDC moved out of the crater's lowest point, whereas towards the north and east-northeast the PDCs travelled over the steepest section of the crater rim. These PDCs extend no further than 0.5 km from the crater rim.

The two $5 \times 10^6 \text{ m}^3$ scenarios produced PDCs in the same directions as the $1 \times 10^6 \text{ m}^3$ scenarios (Figures 6.6 and 6.7), but with two additional lobes, one towards the southwest, and one towards the south. Each of these lobes has a inundation area length greater than 1 km, though they were still restricted to the upper flanks of the volcano, and remained strongly valley confined. Notably, the 1400 kg m^{-3} scenarios (Figure 6.7) exhibit inundation areas up to 0.5 km longer than the 1200 kg m^{-3} equivalents (Figure 6.6), with the $5 \times 10^6 \text{ m}^3$ 1400 kg m^{-3} model (Figure 6.7) beginning to show the southern PDCs being deflected towards the southwest by Verchild's Mt (Figure 6.5).

High surge production scenarios

For the high surge production scenario, the upper flank PDCs includes all modelled scenarios with total deposit volumes from 5×10^6 to $1 \times 10^7 \text{ m}^3$ (Figure 6.8)

The $5 \times 10^6 \text{ m}^3$ scenario produced lobes in multiple directions: two directed to the northeast, one to the northwest, one towards the southeast, and one towards the south (Figure 6.8). Each of these has a inundation area length greater than 1 km, though they were still restricted to the upper flanks of the volcano, and remained valley confined. The dense deposits are typically thickest in the valley bottoms, particularly towards the advancing edge of the PDCs, with thicknesses of up to 33 m in the $5 \times 10^6 \text{ m}^3$ model, and of up to 50.3 m in the $1 \times 10^7 \text{ m}^3$ model.

The $5 \times 10^6 \text{ m}^3$ model run (Figure 6.8) shows the south-eastern PDC being deflected towards the southwest by Verchild's Mt (Figure 6.5) slightly with the $1 \times 10^7 \text{ m}^3$ showing a similar deflection, with the dense PDCs continuing further down the valley (Figure 6.8).

6.3.1.3 Lower Flank PDCs

The 'Lower Flanks' category describes the scenarios which produced PDCs extending down to the lower flanks and base of the volcano (approximately 2.5 km to 5.3 km from the centre of the crater).

Low surge production scenarios

For the low surge production coefficient scenarios, the lower flank PDCs category includes deposit volumes ranging from 1×10^7 to $5 \times 10^7 \text{ m}^3$ (Figures 6.6 and 6.7).

The primary PDC directions remain similar to those described in Section 3.1.2, though with extended inundation area paths. The two PDCs towards the north and northeast overlap to produce a single larger deposit from volumes $2 \times 10^7 \text{ m}^3$ and greater. As volumes increase, the PDC oriented northwest from the crater is initially directed westwards as it follows a valley, although at $5 \times 10^7 \text{ m}^3$ the dense deposits then also spread northwards as the topography flattens. The PDC moves southeast from the crater follows the valley as it turns to the southwest, with any potential lateral deposits prevented from accumulating further east by Verchild's Mt (Figure 6.5). As described previously, the scenarios with a basal part density of 1400 kgm^{-3} (Figure 6.7) have marginally longer inundation areas than the 1200 kgm^{-3} equivalent (Figure 6.6).

The thickest dense deposits typically occur in the valley bottoms, especially towards the distal end of the deposit. However, in the larger volume scenarios, the distal edge of the deposits begins to spread out and thin, having maximum thicknesses of approximately 90 m.

High surge production scenarios

For the high surge production scenario, the lower flank PDCs includes all modelled scenarios with total deposit volumes from 5×10^7 to $1 \times 10^8 \text{ m}^3$ (Figure 6.8).

The dense deposits produced in these two scenarios extend in all directions out from the crater, resulting in the upper flanks being completely inundated. Despite this, the primary travel directions remain similar to those in the 'Upper Flanks' category, though with significantly extended inundation areas. The lobe initially oriented to the northwest from the crater is deflected to the west after approximately 2.5 km as it follows a channel, though in the $1 \times 10^8 \text{ m}^3$ scenario dense deposits continue to accumulate to the north of this (Figure 6.8). The deflected south-eastern lobe continues to the southwest, almost overlapping with the southwestern PDC in the $1 \times 10^8 \text{ m}^3$ scenario (Figure 6.8). Potential lateral dense deposits are prevented from accumulating further to the east by Verchild's Mt (Figure 6.5). At the volumes modelled in these scenarios, the dense deposits are less valley confined, although the inundation area is still controlled by topography, and are thickest in the valleys.

There are three significant topographical barriers to dense PDCs: a ridge to the north of the crater, Verchild's Mt., and Sandy Point Hill (Figure 6.5). These topographical barriers prevent the dense deposits from passing over, or deflect the dense PDCs around them, with Sandy Point Hill protecting an area directly to the west of the crater from dense PDCs, and Verchild's Mt. protecting the southeast. However, in the largest modelled scenario, $1 \times 10^8 \text{ m}^3$ (Figure

6.8), the north-eastern and north-western PDCs overlap slightly beyond the ridge to the north of the crater.

In the larger volume scenarios, the distal edge of the deposits begins to spread out and thin, having maximum thicknesses of > 100 m. The thickest deposits, shown in red, at the most distal point of a PDC are likely an 'artefact' from the model not running to completion, and instead ending prematurely due to a NaN error. These NaN errors are discussed further in Section 4.1.3. This does not affect the general interpretation of the modelling, as the PDC has just not run to its full extent leaving a thicker than expected deposit at the advancing edge of a lobe.

6.3.1.4 Coastal PDCs

This category encompasses the largest modelled scenarios which generated dense deposits that reached the sea.

Low surge production scenarios

In the low surge production model scenarios, total deposit volumes ranging from 6×10^7 to 1×10^8 m³ (Figures 6.6 and 6.7) generated lobes that reached the sea.

Scenario 6×10^7 m³ 1200 kg m⁻³ (Figure 6.6) is the smallest modelled volume to produce a PDC extending to the coast, with the north-eastern lobe entering the sea near Saddlers village. The largest modelled scenario, 1×10^8 m³ shows that ultimately each of the PDCs will reach the sea. The north-western lobe reaches the sea along an approximately 1.5 km wide section of the coast in scenario 1×10^8 m³ 1400 kg m⁻³ (Figure 6.7) . The southwestern lobes enter the sea on either side of Brimstone Hill, and the initially south-easterly lobe enters the sea following the valley through Old Road Town (Figures 6.5 and 6.7).

In these largest eruption scenarios, the majority of the upper flanks are inundated by dense deposits, except for areas beyond Verchild's Mt. to the east, Sandy Point Hill to the west, and a crater lip to the north.

The dense deposits continued to be thickest in the valley bottoms, and towards the distal end of the deposits, particularly where they meet the sea. The deposits are generally at their thinnest on the upper flanks of the volcano, where the steeper gradient prevents thick accumulations from forming.

High surge production scenarios

No 'high surge production' scenarios generated PDCs that reached the sea (Figure 6.8), primarily as a result of NaN errors, this is considered further in section 4. Coastal PDCs could likely be generated by 'high surge production' scenarios, however, due to limited computing resources and time constraints on the project, it was not feasible to run models to natural completion.

6.3.2 Surge deposits generated by a lower surge production coefficient

The surges described in this section were modelled using a surge production coefficient of 0.001, and produced small surges that followed, or extended a short distance beyond, the dense PDCs.

The first modelled surges large enough to leave the crater were in the $1 \times 10^6 \text{ m}^3$ scenarios, in which small deposits formed around the crater rim, and in the uppermost valleys on the flanks of the volcano. The largest scenario modelled had a total deposit volume of $1 \times 10^8 \text{ m}^3$, as this volume is at least an order of magnitude larger than examples typically given in the literature volumes larger than this inundating the entire flanks of Mt Liamuiga, and into the sea. Larger

volumes also caused frequent errors which prematurely terminated the model runs, and addressing these errors within VolcFlow was outside the scope of this study.

Surges are confined to the same inundation area paths as the dense PDCs, up to a total volume of $4 \times 10^7 \text{ m}^3$, from which the surge deposits start to extend beyond the topographically-confined dense deposits.

The lower surge production coefficient model outputs can be divided into four broad categories, based on the inundation area distance of the surges produced; crater-confined, upper flanks, lower flanks, and coastal. The inundation areas of the surge deposits are shown in Figures 6.9 and 6.10.

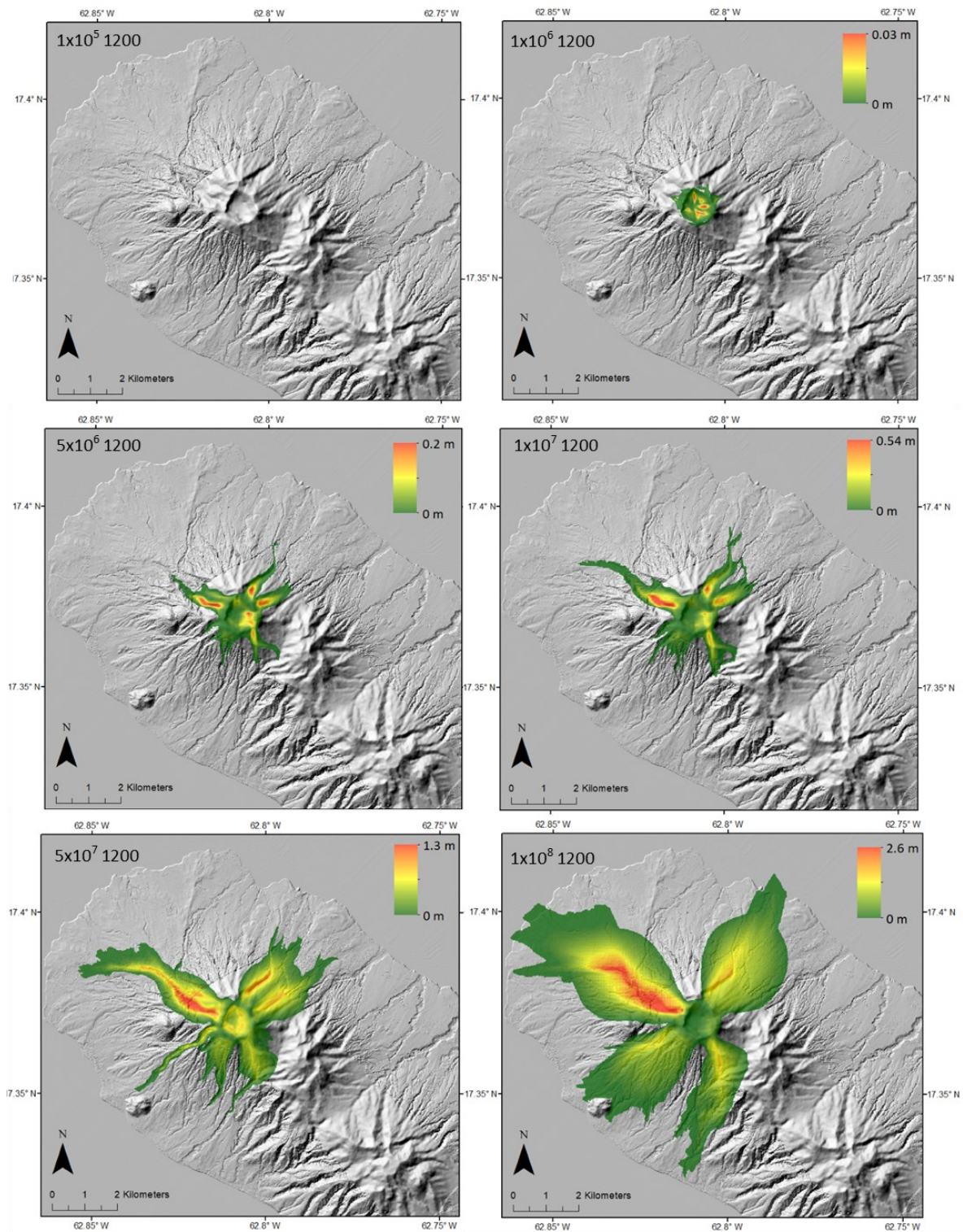


Figure 6.9 – Maps showing examples of surge deposits from the low surge production scenarios with basal part densities of $1200\ kg\ m^{-3}$. The inundation area and deposit thickness is shown for each scenario, with the respective total deposit volume (m^3) and basal part densities ($kg\ m^{-3}$) in the upper left of each map.

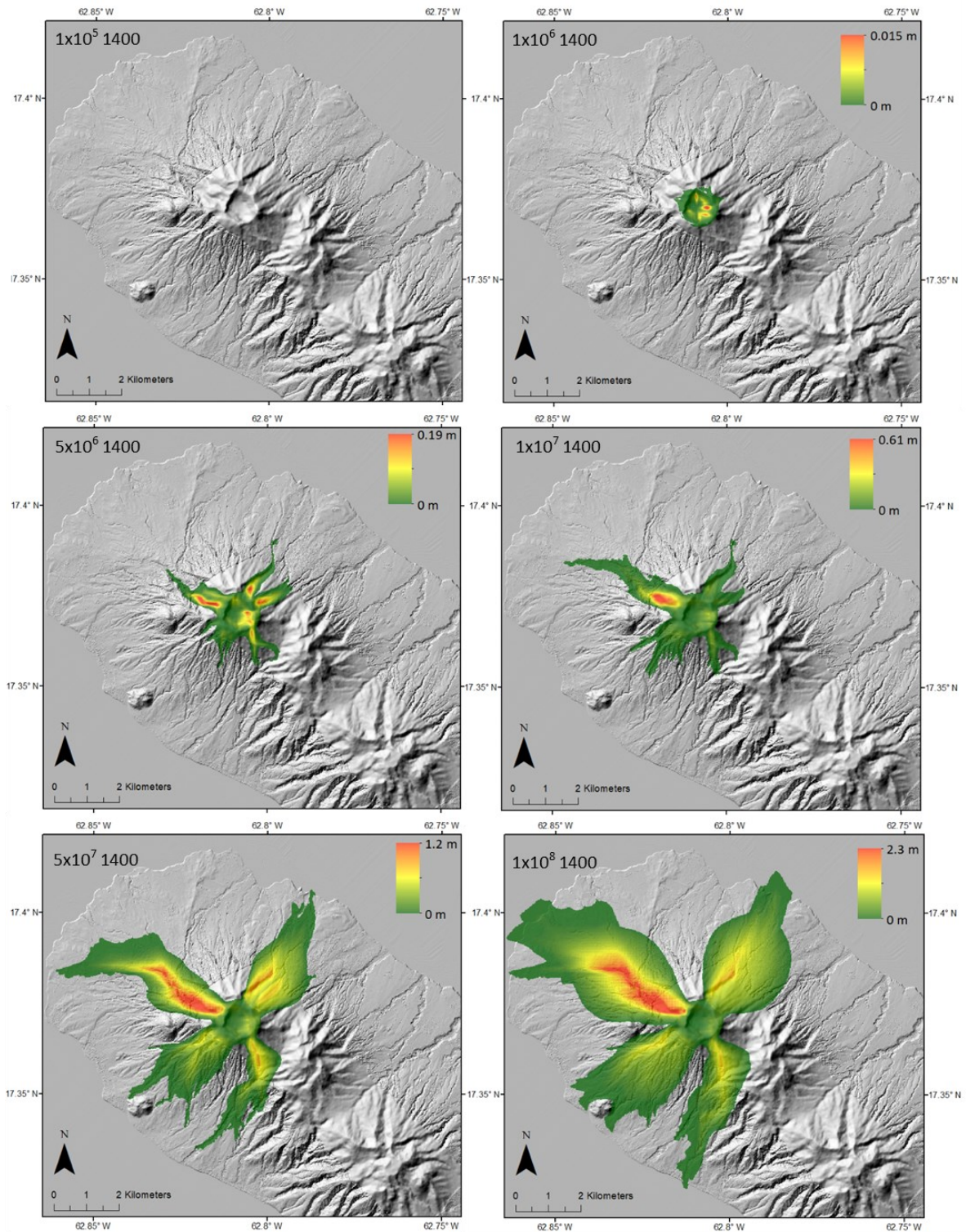


Figure 6.10 – Maps showing examples of surge deposits from the low surge production scenarios with basal part densities of 1400 kg m^{-3} . The inundation area and deposit thickness is shown for each scenario, with the respective total deposit volume (m^3) and basal part densities (kg m^{-3}) indicated in the upper left of each map.

6.3.2.1 No surges

The modelled scenarios with a total deposit volume of $1 \times 10^5 \text{ m}^3$ did not produce any surge deposits (Figures 6.9 and 6.10).

6.3.2.2 Upper flank surges

Scenarios with a total deposit volume of $1 \times 10^6 \text{ m}^3$ produced only minor surges, just overtopping the crater walls. In the $5 \times 10^6 \text{ m}^3$ scenarios the surges were generally valley-confined, following paths to the northeast, southeast, and southwest (Figures 6.9 and 6.10).

The surge deposit oriented towards the northwest appears to flow directly downslope from the lowest section of the crater rim, rather than following a valley (Figures 6.9 and 6.10).

The resulting surge deposit thicknesses in the $1 \times 10^6 \text{ m}^3$ scenario were very thin, with a 0.01 m layer of surge deposits in and around the crater rim, and a maximum thickness of 0.03 m within the crater itself (Figures 6.9 and 6.10). In the larger volume scenario, $5 \times 10^6 \text{ m}^3$, the resulting surge deposits had a maximum thickness of approx. 0.20 m in the upper parts of the valleys (Figures 6.9 and 6.10). Unlike the dense deposits, the thickest parts of the surge deposits do not lie within the crater.

6.3.2.3 Lower flank surges

Scenarios with total deposit volumes between $1 \times 10^7 \text{ m}^3$ and $4 \times 10^7 \text{ m}^3$ comprise this category (Figures 6.9 and 6.10). Here the surge deposits inundate the volcano's upper flanks and extend to the lower flanks, and base of the volcano. As first shown in the smaller deposit volume scenarios, surges continue to be produced in the same four directions, northeast, northwest, southeast, and southwest. As the total deposit volumes increase, the surges begin to be deflected towards the southwest by Verchild's Mt (Figure 6.5).

The surge deposits towards the northeast, southeast, and southwest, are typically thickest in the valleys, where the dense deposits are also at their thickest. The surge towards the northwest differed somewhat, with the thickest portion of the deposits towards the centre of the surge, particularly on the upper flanks. In this 'Lower Flanks' category, the maximum deposit thicknesses for each scenario were of the order of 1 m, with the maximum thickness modelled occurring in scenario $4 \times 10^7 \text{ m}^3$ 1200 kg m^{-3} (Figure 6.9), where it was 1.2 m. The scenarios with a basal part density of 1200 kg m^{-3} , simulating pumice and ash flows, tended to produce marginally thicker surge deposits than 1400 kg m^{-3} (Figure 6.10), representing transitional flows.

6.3.2.4 Coastal surges

This category consists of scenarios in which surge deposit inundation areas extended to the coastline, these were scenarios with total deposit volumes of $5 \times 10^7 \text{ m}^3$ and above (Figures 6.9 and 6.10). As modelled for the dense deposits, the surge deposits also entered the sea near Sadler's Village, Old Road Town, near Brimstone Hill, and along a section of coastline to the northwest (Figure 6.5).

Within this category, as volumes increased, surges tended to be more topography independent than in the smaller volume scenarios. This tendency was particularly apparent to the north-eastern and north-western regions in scenarios of $6 \times 10^7 \text{ m}^3$ and larger, where lobes up to 3 km wide formed and crossed between valleys (Figures 6.9 and 6.10). These lobes appear to initiate as the gradient of the slope decreases. The surge deposits oriented towards the southeast and southwest remained more topographically-confined, with Verchild's Mt. continuing to deflect the south-eastern lobe towards the southwest.

The maximum thicknesses of these surge deposits were up to 2.6 m in the central portion of the north-western lobe, which thinned smoothly towards the edge of the lobe. A similar thickness pattern was also modelled for the north-eastern surge lobe. The two more topographically-restricted surges, towards the southeast and southwest, were generally thinner, with maximum thicknesses of approximately 1.3 m on the upper flanks. The trend of the less dense scenarios to produce thicker surge deposits than their denser equivalents continued to occur with the larger volumes modelled in this category.

6.3.3 Surge deposits generated by a higher surge production coefficient

The surges described in this section were modelled using a surge production coefficient of 0.01. This larger surge production coefficient produced larger surges that were topography independent and extended far beyond the inundation areas of the dense PDCs.

In the high surge production series of models, six volumes ranging from 1×10^5 to 1×10^8 m³ were modelled, with a larger surge production coefficient (Figure 6.11). The model outputs for surges with a high production coefficient can be divided into three categories, based on the inundation area distance of the surges produced; no surge, small and large surge. The inundation areas of the surge deposits are shown in Figure 6.11.

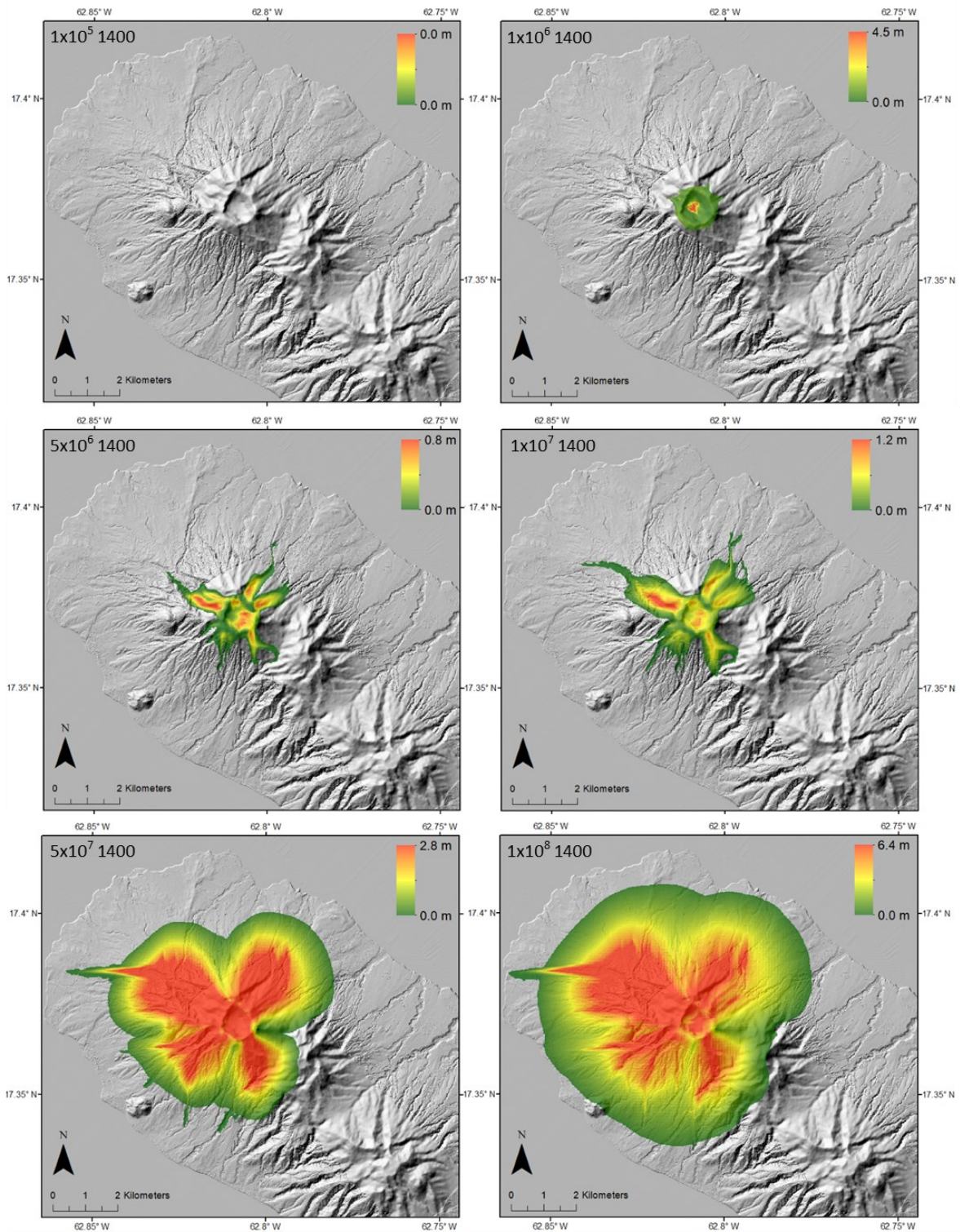


Figure 6.11 - Maps showing examples of surge deposits from the high surge production scenarios with basal part densities of 1400 kg m⁻³. The inundation area and deposit thickness is shown for each scenario, with the respective total deposit volume (m³) and basal part densities (kg m⁻³) indicated in the upper left of each map.

6.3.3.1 No surge

No surges were produced in the $1 \times 10^5 \text{ m}^3$ scenario (Figure 6.11), with only thin surge deposits directly above the dense deposits being produced in the $1 \times 10^6 \text{ m}^3$ scenario.

6.3.3.2 Small surges

In scenario $5 \times 10^6 \text{ m}^3$ (Figure 6.11) surges were only produced directly above the dense deposits, extending to the upper flanks of the volcano as described in Section 3.2.1.2. However, in the $1 \times 10^7 \text{ m}^3$ scenario (Figure 6.11), surge deposits began to be produced that extended beyond the footprint of the dense deposits, particularly associated with the north-eastern and north-western lobes. As such, these surge deposits remain mostly topographically controlled. These surges extended further laterally than the dense PDCs, producing lobe-shaped deposits with thicknesses of up to 1.2 m in the centres, and thinning towards the edges of the lobe.

6.3.3.3 Large surges

In scenarios $5 \times 10^7 \text{ m}^3$ and $1 \times 10^8 \text{ m}^3$ (Figure 6.11), extensive surge deposits are formed, extending up to 2 km beyond the dense deposits. The surge deposits in the $5 \times 10^7 \text{ m}^3$ scenario (Figure 6.11) produced lobes extending in each of the main flow directions of the dense deposits, these lobes were up to 3 km in diameter, with maximum thicknesses of 2.8 m. In the $1 \times 10^8 \text{ m}^3$ scenario (Figure 6.11), the lobes are so large as to effectively overlap, although the four lobes can still be identified in the thickness map.

There are fewer topographic barriers affecting the distribution of the larger surge deposits compared to those in smaller volume scenarios. Sandy Point Hill (Figure 6.5) is engulfed by surges in both of the 'large surge' scenarios, and surges also inundate Brimstone Hill in the 1

$\times 10^8 \text{ m}^3$ scenario (Figure 6.11). Notably, Verchild's Mt. remains an effective topographic barrier for surge deposits in the $5 \times 10^7 \text{ m}^3$ scenario (Figure 6.11), although the largest modelled scenario begins to overtop it. Surges to the northwest, northeast, and southwest appear to be topography independent, with Verchild's Mt. remaining a significant topographic control on surge deposit distribution in the southeast (Figure 6.5).

6.4 Discussion

6.4.1 Comparison between pumice and ash flows and transitional flows

For each modelled total deposit volume in the low surge production scenarios, two different types of PDC were modelled: pumice and ash flows represented by a basal part density of 1200 kgm^{-3} , and transitional flows represented by a basal part density of 1400 kgm^{-3} . The transitional flows are an intermediate between pumice and ash flows and block and ash flows, as described in Chapter 3. The resulting outputs from these two different basal densities were quite similar, with near-negligible differences in inundation area or surge production, shown in Figures 6.12 and 6.13. Although these differences were only minor, the transitional flows tended to result in slightly longer inundation areas than the pumice and ash flows. The pumice and ash flows produced slightly thicker surge deposits than the transitional flows.

Block and ash flows were not modelled, as no end-member block and ash flow deposits were observed in the field (Chapter 3). It is considered likely that any block and ash flows, with a typical density of 1600 kgm^{-3} (Brown and Andrews, 2015) would continue to follow a similar trend, producing thinner surge deposits, but with slightly longer inundation areas than the transitional flows. Due to these similarities in both inundation area and deposit thicknesses, it is likely that the hazard posed by block and ash flows will also be similar.

In both of the modelled basal flow densities of the low surge production scenarios, it was observed that the resulting surge deposits were far smaller than would be expected for the respective volume. As basal part density had little influence on surge production, only the surge production coefficient was changed for the second series of models.

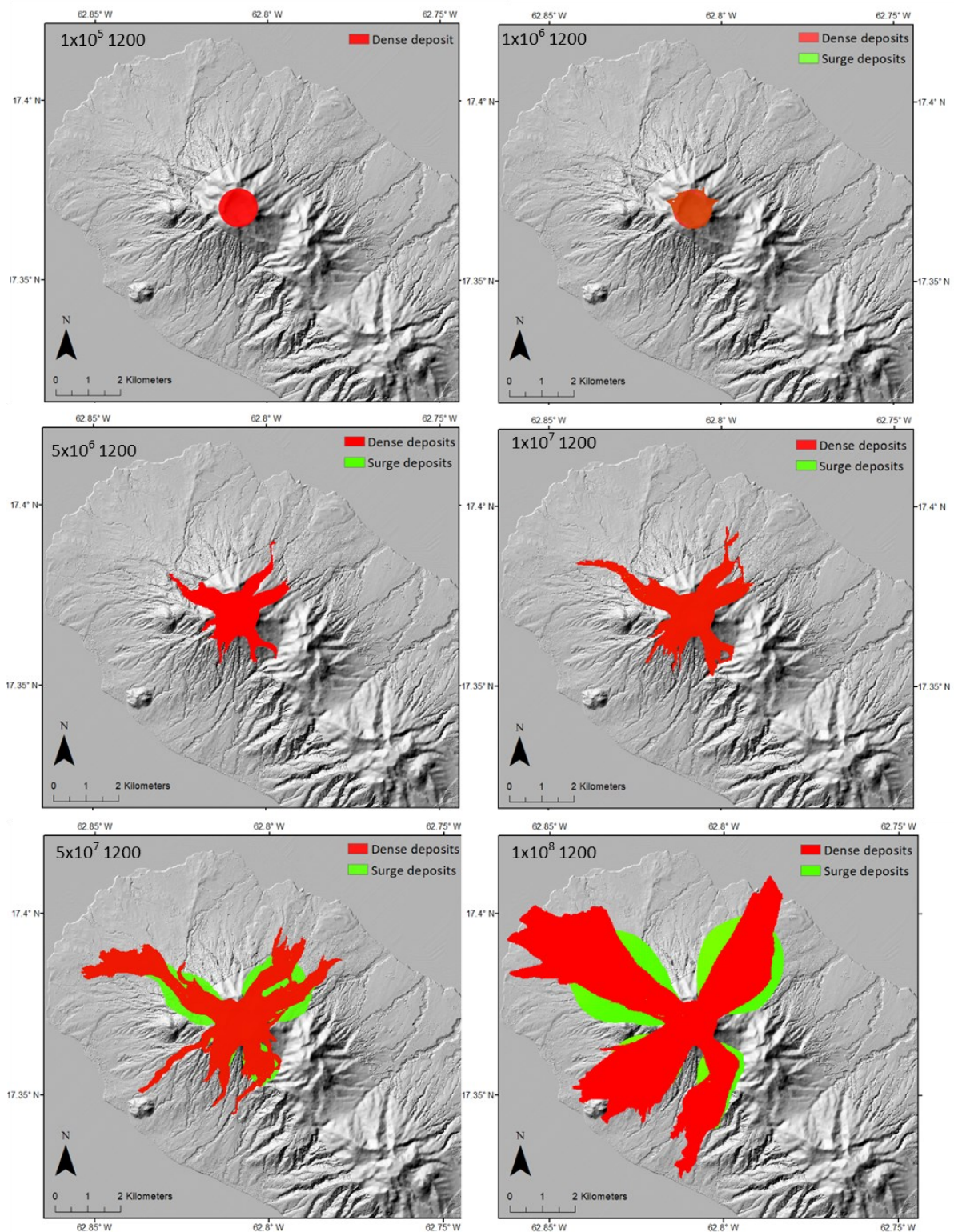


Figure 6.12 – Combined dense deposits and surge deposits maps from the low surge production scenarios with basal part densities of 1200 kg m^{-3} , with the respective total deposit volume (m^{-3}) and basal part densities (kg m^{-3}) indicated in the upper left of each map.

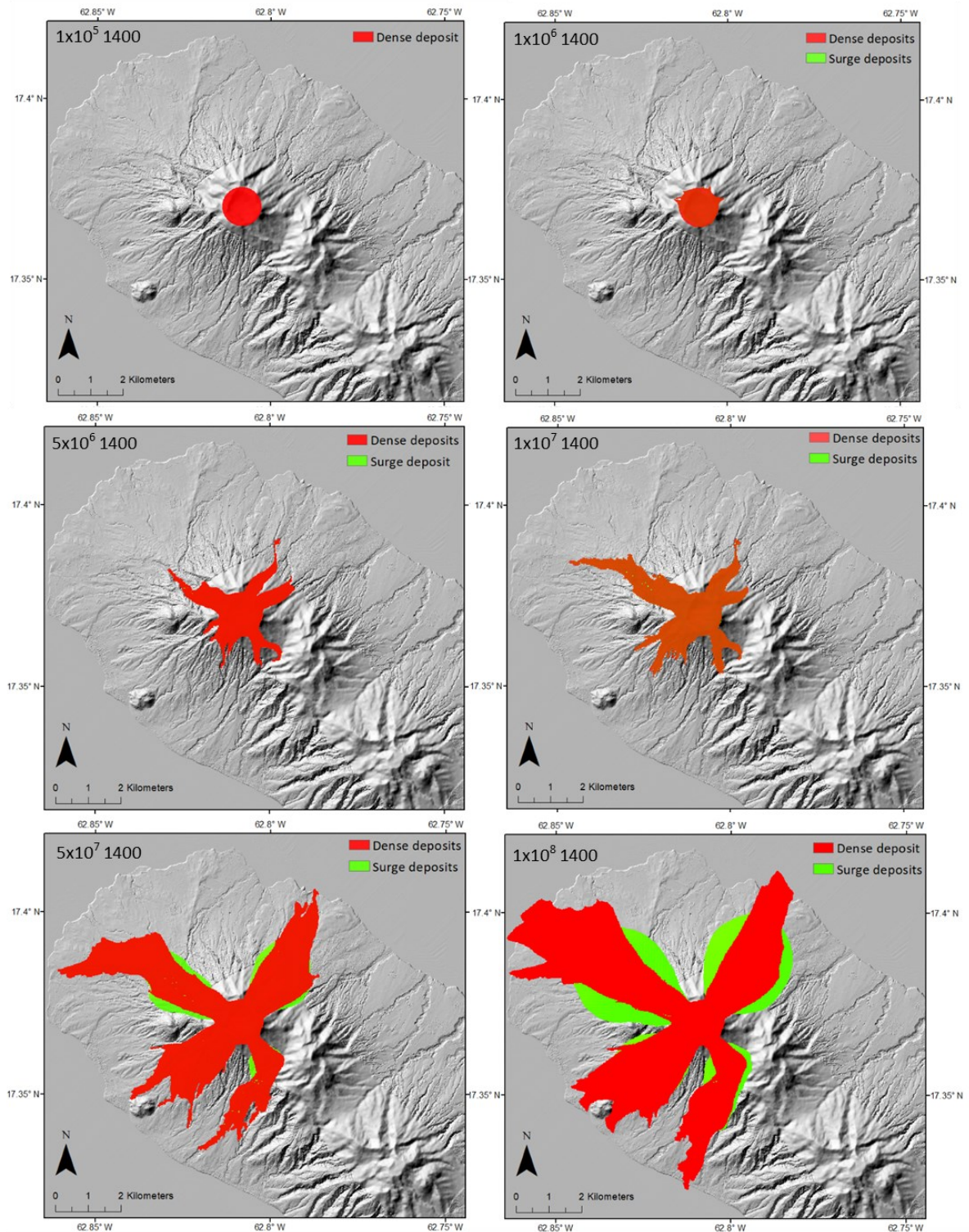


Figure 6.13 – Combined dense deposits and surge deposits maps from the low surge production scenarios with basal part densities of 1400 kg m^{-3} , with the respective total deposit volume (m^3) and basal part densities (kg m^{-3}) indicated in the upper left of each map.

6.4.2 Comparison between low and high surge production scenarios models

The objective of the models with the higher surge production coefficients, was to produce more typical surges for the modelled volumes, compared to the small surges produced by the low surge production coefficient. These are shown in Figure 6.14. To achieve this, a surge production coefficient of 0.01 was used. Compared to the low surge production scenarios, the surges here were much larger producing lobes that extended several kilometres laterally beyond the dense PDCs. This is in contrast to the low surge production scenarios where even in the $1 \times 10^8 \text{ m}^3$ scenario, surges extended less than 1 km from the dense PDCs. The surges in the high surge production scenarios produced topographically independent lobes up to 6 km in diameter, that inundated areas such as Sandy Point Hill in the largest volumes. These larger surge deposits, multiple kilometres in width, are considered more feasible for the modelled volumes, and are similar in size to surges produced in the 1902 eruption of Mt. Pelée, Martinique (Gueugneau *et al.*, 2020), and Soufrière Hills, Montserrat (Cole *et al.*, 2002; Druitt *et al.*, 2002).

Significant surge lobes also began to form at much smaller volumes in the high surge production scenarios, from volumes of $1 \times 10^7 \text{ m}^3$ and above, whereas equivalent surges were only produced from volumes of $5 \times 10^7 \text{ m}^3$ and above in the low surge production scenarios.

As a result of the greater surge production in the high surge production scenarios, the inundation area of the dense PDCs was generally notably shorter than equivalent scenarios in the low surge production scenarios. This shorter inundation area is likely related to significantly more material being lost from the dense PDCs into the surges, meaning that less material was available to continue the dense inundation area.

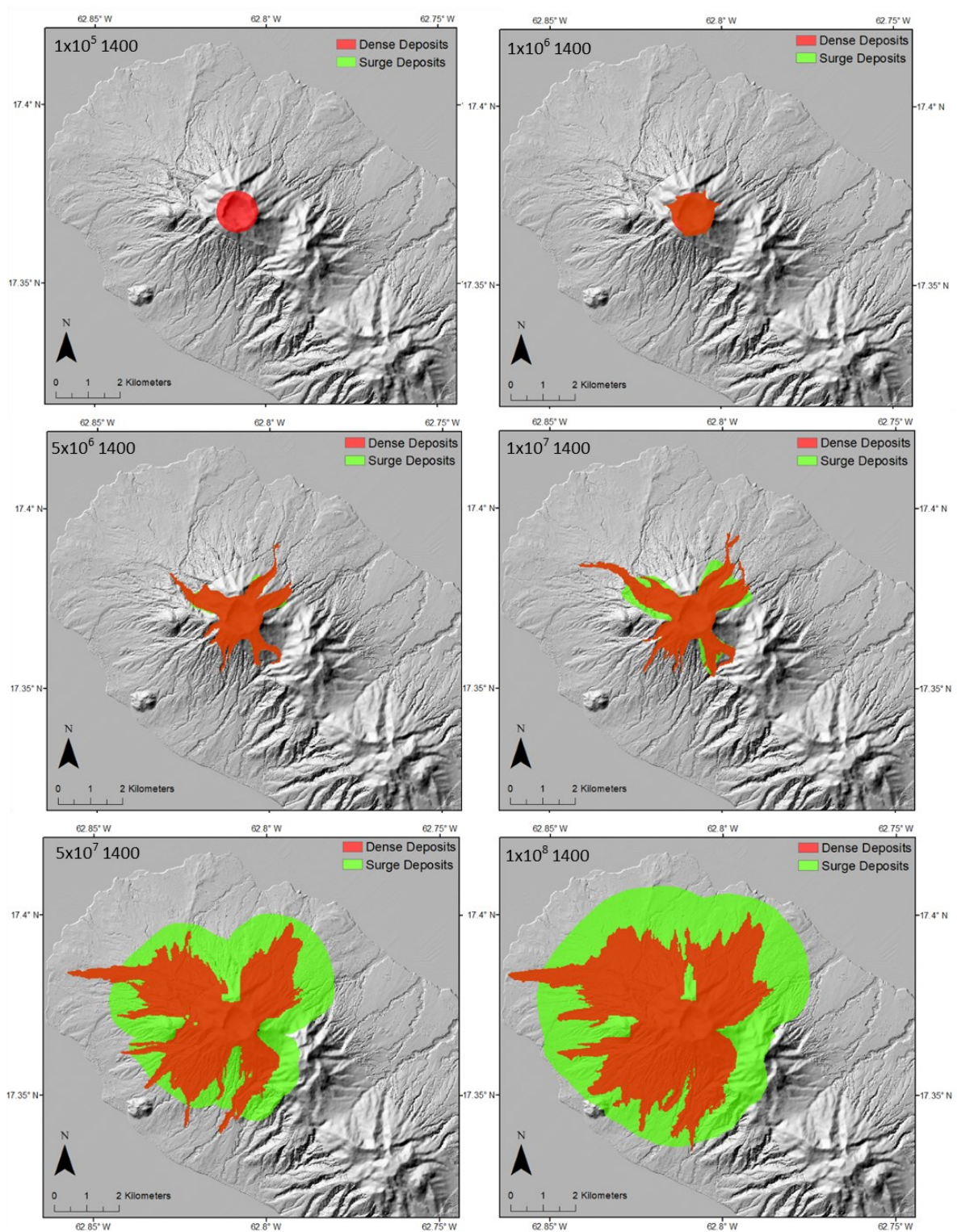


Figure 6.14 – Combined dense deposits and surge deposits maps from the high surge production scenarios with basal part densities of 1400 kg m^{-3} , with the respective total deposit volume (m^{-3}) and basal part densities (kg m^{-3}) indicated in the upper left of each map.

6.4.3 Comparison to field observations

The models presented here show a broad distribution of deposits across the north-eastern end of the island, originating from the crater in four main directions: northeast, northwest, southwest, and southeast. This distribution of deposits is similar to those observed in the field (Chapter 3), where deposits have been described primarily between Brimstone Hill and Saddlers Village (Baker, 1985). The modelling undertaken here potentially supports the hypothesis in Chapter 3 that the deposits at Nicola Town, near Mansion (Sample SK2), did not originate from Mt. Liamuiga, as it is unlikely that PDCs could overtop the ridge to the east. Although the general trend of PDC emplacement directions is similar between the model outputs and the field observations, modern topography differs from that of when the PDCs observed in the field were generated, > 1620 B.P. (Baker, 1985). This difference in topography may account for some of the differences in distribution. Also, the effects of factors such as wind, or lateral blasts, were not accounted for here.

The surges produced in both the high and low surge production coefficient scenarios show similar thicknesses at their most distal edges to those observed in the field (< 0.5 m). However, the modelled surges do not reach the coast unlike those described in the fieldwork chapter, this is likely related to the largest scenario in the high surge production scenarios, $1 \times 10^8 \text{ m}^3$ terminating prematurely due to a NaN error. If this scenario ran to completion, it would have resulted in thin surge deposits at the coast, and dense deposits reaching the coast in valleys. In this case, the $1 \times 10^8 \text{ m}^3$ scenario would most resemble the deposits observed in the field campaign. Future work on refining the $1 \times 10^8 \text{ m}^3$ volume from the high surge production scenarios would likely produce models similar to field observations, and this model provides an approximation for the potential outcomes of a vulcanian to plinian eruption.

In both model series, the dense PDCs are far thicker than those observed in the field. In the larger scenarios this is likely related to the NaN errors, and models ending prematurely before the thick PDCs finished flowing and thinning out.

6.4.4 Factors influencing inundation area and thickness

Three major topographical barriers exert a large influence on the inundation areas of the PDCs modelled. The largest of these topographical barriers is Verchild's Mt., which forms a ridge to the east of Mt. Liamuiga, which deflects PDCs eastward towards the north and south, preventing them from reaching the east of the island. In larger volume scenarios, the PDCs extended further up the ridge, though none modelled here were large enough to overtop it.

The second major topographic barrier is Sandy Point Hill, which lies immediately to the west of the crater, and prevents the northwest and southwest lobes from merging. Sandy Point Hill also disrupts the southwards spread of surge deposits from the north-western lobes in the largest eruption scenarios i.e. those reaching the coast. A high point to the north of the crater act as the third major topographical barrier, preventing PDCs from flowing in that direction, and instead flowing down the valleys on either side.

Brimstone Hill, approximately 200 m tall, creates a more minor topographical barrier, with PDCs flowing on either side of the hill, with even the largest scenario not producing PDCs capable of overtopping the hill.

6.4.5 PDC Hazard implications for St Kitts

Maps were created to illustrate the PDC hazard posed by several different scenarios, 5×10^6 m³, 5×10^7 m³, and 1×10^8 m³, examples of the small (Figure 6.15), medium (Figure 6.16), and large (Figure 6.17) total deposit volume scenarios, respectively. The northwest of the island

is the most vulnerable, northwest of Old Road Town and Tabernacle. The PDC inundation areas identified in this study can be used to refine areas of differing PDC hazard that were previously grouped together in past hazard assessments as maximum hazard regions (Robertson, 2005; Simpson and Shepherd, 2001).

There are a number of settlements that lie directly in the path of the PDCs modelled, including: Old Road Town (Parish population: 2,535), Sandy Point Town (Parish population: 1,922), Newton Ground (Parish population: 2,432), and Saddlers Village (Parish population: 2,962). Sandy Point Hill appears to deflect dense PDCs away from Sandy Point town, at least in the modelled scenarios up to a deposit volume of $5 \times 10^7 \text{ m}^3$. Only in the largest scenarios, $1 \times 10^8 \text{ m}^3$, is Sandy Point Town itself met with a dense PDC, at the southern end near Brimstone Hill, and also becomes inundated by surge deposits.

Whilst a PDC does not reach Newton Ground in the smaller volume scenario mapped, the dense deposits extend to within 0.5 km of the town. In this scenario, lahars may be the more significant hazard if heavy rainfall were to occur during, or soon after, the eruption. In the medium and large volume scenarios shown in Figures 6.16 and 6.17, Newton Ground lies directly within the inundation area pathway of the dense PDCs.

Saddlers Village is in the path of dense PDCs in the large volume scenario, though within the small and medium volume scenario it remains at risk of lahars due to the presence of PDC deposits higher in the valley where the river that runs through the village originates.

The modelled PDCs do not reach Old Road Town, although it may be affected in the large volume scenario where both dense PDCs and surges reach within less than 1 km of the town, and the road. This is in apparent agreement with previous hazard maps (Robertson 2005;

Simpson and Shepherd, 2001) that have considered the town as only in the 'moderate' or borderline 'low to negligible' PDC hazard category.

The towns of Dieppe Bay and Tabernacle are at comparatively lower risk from PDC hazards than other towns in the area, as no PDCs reach either town in any of the modelled scenarios. However, in the largest scenarios the surge deposits extend a large distance laterally from the primary flow direction of the dense PDCs, and come to within approximately 1 km of Dieppe Bay.

The major circular road on the island is the main route connecting each town to the next, and so serves as an important piece of infrastructure on the island. In the large volume scenario, this road is intercepted by a surge near to Saddlers Village approximately 100 s after eruption initiation. According to the large volume scenario (Figure 6.17), this orbital road is threatened, or crossed, by PDCs in four different locations within five minutes of the eruption initiation, which may severely impede its use in emergency response. A possible consequence of this is that maritime evacuations may be required, as were used in the 2021 eruption of La Soufrière, St Vincent, or the entire NW part of the island, up to 9,850 people based on 2011 census data (Department of Statistics, 2011), may require evacuation prior to the onset of volcanic activity.

The categorisation of the island to the southeast of Old Road Town and Tabernacle as a 'Low to Negligible' PDC hazard (Robertson, 2005; Simpson and Shepherd, 2001) is supported by the modelling results shown here. Verchild's Mt. and the Middle Range effectively deflect any southeast-oriented PDCs away from this area of the island, meaning that the SE portion of St Kitts appears safe from PDCs of the volumes modelled here. As the capital of St Kitts, Basseterre, is located in this area at the southeast of the island, alongside critical

infrastructure including the international airport, largest passenger port, and the hospital, the governance of the island and response to an eruption should not be significantly hindered.

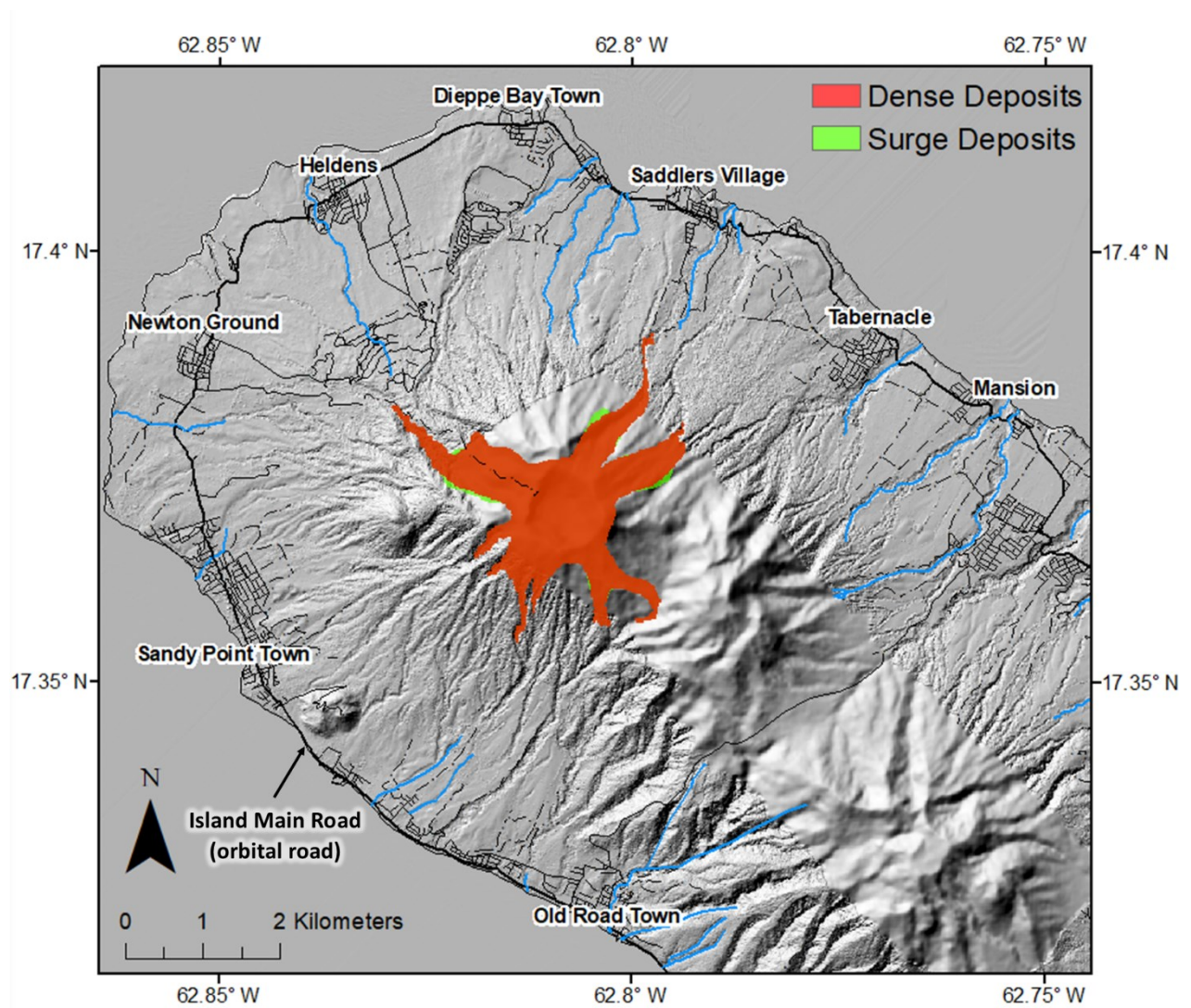


Figure 6.15 - Map showing the locations of the main settlements, roads and rivers surrounding Mt Liamuiga. The inundation area of PDCs in a small volume scenario is shown.

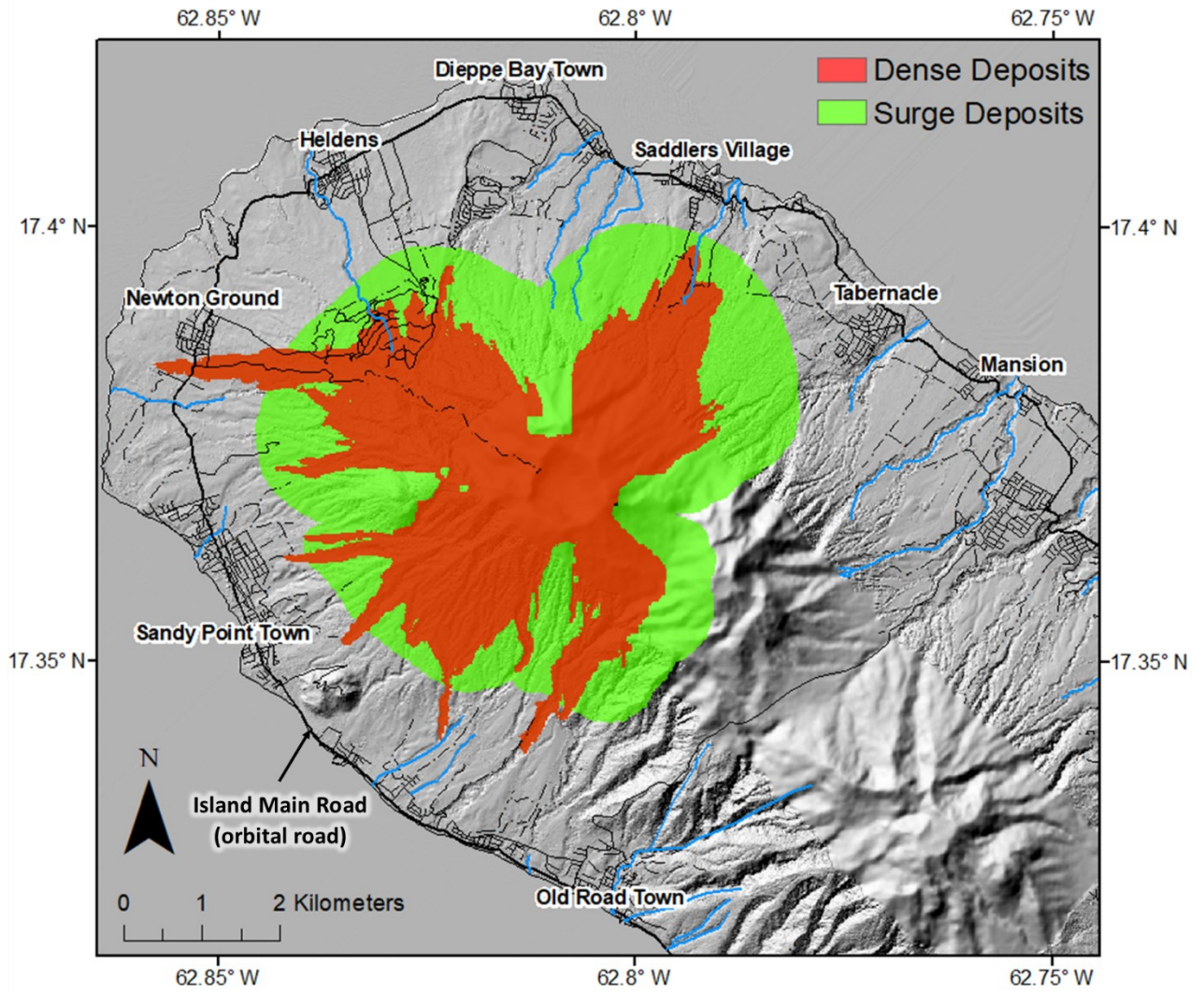


Figure 6.16 - Map showing the locations of the main settlements, roads and rivers surrounding Mt Liamuiga. The inundation area of PDCs in a medium volume scenario is shown.

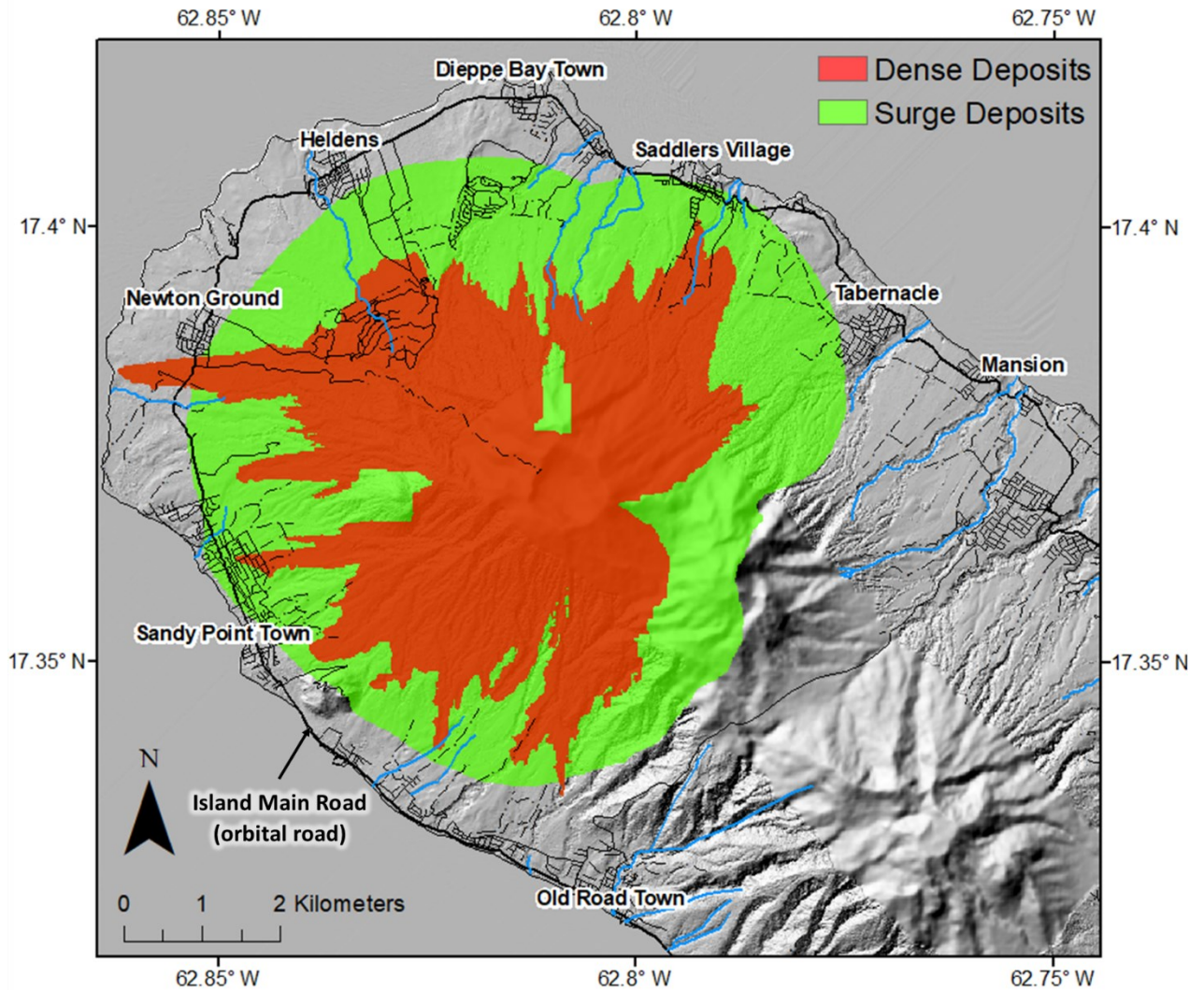


Figure 6.17 - Map showing the locations of the main settlements, roads and rivers surrounding Mt Liamuiga. The inundation area of PDCs in a large volume scenario is shown.

6.4.6 Discussion of VolcFlow

6.4.6.1 Limited variables changed

Whilst only the total deposit volumes and basal part densities were used as variables throughout this study, the model outputs generally align with both field observations (Chapter 3) and the wider literature. However, VolcFlow allows numerous other variables to be changed as part of the input file, as described in Section 2.2, but time and computational limits prevented making use of these during this study. Experimenting with more variables may enable models to be further refined to produce PDCs more representative to those observed in the field, whereas this study focuses on larger-scale trends.

The modelled timescale for each scenario was up to 60 minutes, which was typically long enough for the maximum flow velocity to reduce to below 1 ms^{-1} (or for the model to be terminated by a NaN error). Beyond this, it was considered that any remaining PDCs would be confined to river beds and the bottoms of valleys, where they would flow until exhausted, or until they reached the sea. The majority of the PDCs occurred during the first five minutes of the eruption scenario, although future work could model the PDCs until the maximum flow velocity reaches 0 ms^{-1} . This is typical of most Vulcanian explosions, which tend to be short-lived with resulting PDCs lasting up to tens of minutes. Such events have been witnessed at Soufriere Hill Volcano between 2008 and 2010, where events lasted between 4 and 20 minutes (Cole *et al.*, 2014), and at Merapi in 2010, where PDCs of 2 to 33 minutes were recorded, with one exception recorded to have lasted 90 minutes (Cronin *et al.*, 2013; Kelfoun *et al.*, 2017).

As mentioned previously, the source area, volume, and supply rate can all be experimented with to simulate different column collapse scenarios. Many of the parameters used in this

study were informed by the literature, such as Kelfoun *et al.* (2017), but a trial-and-error approach to varying these parameters could allow the flow properties to be more precisely defined to match those in the field. In particular, parameters relating to the flow properties may be of interest to future modelling studies, including the mixture density, surge production coefficient, cohesion, and the drag coefficients. Additionally, values such as the mean particle size could be determined empirically in future by performing particle size analysis on material collected from the field, which may result in more representative model outputs.

Another potential avenue for future work is to focus on modelling of individual PDCs, rather than of the entire volcano. Many similar studies have been performed for other volcanoes (e.g. Kelfoun *et al.*, 2017; Gueugneau *et al.*, 2019; Gueugneau *et al.*, 2020), and would allow for more granular control of each PDC. Such models may also potentially use higher resolution DEMs and smaller time steps, as they would focus on a smaller area.

6.4.6.2 DEM

As described in Section 2.1, the uneven resolution of the original DEM necessitated resampling it to a lower resolution. A consistently high-resolution DEM extending to cover the whole island could help to improve the accuracy of the models, particularly in the upper flanks of the volcano, and reduce any artefacts associated with the transition between the high and lower-resolution areas.

6.4.6.3 NaN errors

NaN, of 'Not a Number' errors, prevented some models from reaching completion of the total run time. These errors typically occurred with the larger volume scenarios. While every effort

was made to resolve these errors, such as by reducing the calculation step times and checking the DEM for errors, the extent of coding required and the closed-source nature of VolcFlow made fully resolving these errors beyond the scope of this study. Despite these errors, the models used for this chapter generally either completed the planned run times, or had their maximum velocities fall to less than 2 ms^{-1} .

6.5. Conclusions

- Whilst only the total deposit volumes, basal part densities, and surge production coefficient were used as variables throughout this study, the model outputs generally align with field observations.
- Surges and dense deposits had similar spatial distributions up to volume $1 \times 10^7 \text{ m}^3$ in the high surge production scenarios models, where surge deposits began to separate and form more independent lobes.
- In the larger volumes of the high surge production scenarios, surges extended several kilometres laterally away from the dense PDCs, presenting a significant additional risk to areas that may not be in the inundation area pathway of the dense PDCs.
- Pumice and ash flows produced thicker surge deposits than the transitional flows.
- Transitional flows resulted in marginally longer inundation areas than the pumice and ash flows, particularly in the larger volume scenarios.
- If it were it not for NaN errors terminating the model before completion, the $1 \times 10^8 \text{ m}^3$ model in the high surge production scenarios would be most comparable to the PDCs observed during the field campaign.
- PDC inundation areas were oriented in four main directions from the crater, northwest, southwest, southeast, and northeast.

- Topographical barriers, Sandy Point Hill, Verchild's Mt., the northern crater rim, and Brimstone Hill, significantly influence the inundation area of PDCs.
- The main hazard from PDCs is in the northwest of the island, whilst the southeast has low to negligible PDC hazard as Verchild's Mt. prevents PDC inundation areas from extending further east.
- Multiple settlements lie directly in the path of the PDCs modelled, including Old Road Town, Newton Ground, Saddlers Village, and the southern portion of Sandy Point Town in the larger volume scenarios. The main circular road of the island is cut off in multiple locations by dense PDCs and surges, during the larger-volume scenarios.

7. Conclusions

7.1 Concluding remarks

Following the analysis and interpretation of the data collected, the following concluding remarks can be made:

7.1.1 Historic volcanic activity

It is likely that no eruption occurred at Mt Liamuiga, or anywhere else on the Island of St Kitts during 1692, and that the single record of the eruption has misidentified the activity for that of La Soufriere on Guadeloupe. It is possible that a small phreatic eruption associated with an earthquake may have occurred in 1843 although, without further written records or physical evidence in the crater, it is unlikely that this eruption can be proven or disproven. No historical eruptions have taken place on Nevis.

7.1.2 Prehistoric volcanic activity

7.1.2.1 Magma source and storage conditions

The Mt Liamuiga and Nevis Peak samples analysed show a compositional range from basaltic andesite to andesite and dacite. The Mt Liamuiga deposits analysed were classified as low-K tholeiites. The source of these magmas is likely to be depleted mantle, similar to MORB, potentially contaminated by H₂O and sediments from the subducting slab. The Nevis Peak samples analysed were shown to be calc-alkaline. The source of the Nevis magmas is likely to be a mantle source similar to MORB, which has been contaminated by crustal material, likely from the subducting slab, and had undergone significant fractional crystallization.

Open-system processes dominated at both Mt Liamuiga and Nevis. Recharges of hot, primitive magma injected into the reservoirs lead to mixing and magmatic differentiation. Rapid crystallization, reheating and partial melting occurred in the shallow crust before eruption.

7.1.2.2 Pre- and syn- eruptive processes

The compositional difference between 'light' and 'dark' samples collected from a single layer of deposits on Mt Liamuiga provide evidence that magma mingling took place shortly before the corresponding eruption.

CSD analysis suggest that most samples underwent a short period of microlite nucleation followed by re-equilibration of the system allowing for transition to a growth-dominated regime. Some samples lacked a growth phase, and were erupted after a burst of microlite nucleation. Samples lacking any microlites were likely erupted after a rapid decompression and ascent, with no time to allow for microlite nucleation. Estimated average crystallisation times calculated using microlites from Mt Liamuiga ranged from 2.95 to 29.24 hours, while times for Nevis ranged from 3.58 to 12.29 hours. These values suggest fairly short periods of crystallisation.

7.1.2.3 Eruption Styles

Rather than the end-members of block and ash flow vs pumice and ash flow, Mt Liamuiga exhibits more transitional PDCs skewed towards the pumice and ash flow end of the scale. These pumice and ash-flows were the result of fountain collapse during explosive activity. The rapid ascent rate estimates calculated for Mt Liamuiga provide further evidence of explosive eruptions. Transitional nature PDCs were more likely to have originated from lava dome

growth and collapse, which may have included explosive activity. The Steel Dust series identified in the field are likely deposits from a pyroclastic surge.

The block and ash flows on Nevis formed primarily from dome collapse events, with secondary explosive activity associated with them, evidenced from vesicular components. Ascent rate estimates calculated for the Nevis samples suggest a much slower decompression and ascent rate compared to the Mt Liamuiga samples, confirming field observations that they are typical block and ash flow deposits originating from a lava dome collapse.

7.1.3 Future volcanic hazards

Based on evidence gathered from prehistoric volcanic activity at Mt Liamuiga, future eruptions are likely to be explosive in nature. Activity at Nevis Peak will most likely be related to lava dome formation.

Future eruptive scenarios modelled using VolcFlow show that surge and dense deposits typically exhibit similar spatial distributions in the small volume eruption scenarios. The distribution of the surge and dense deposits begin to differ significantly in the medium volume scenarios, and in the larger volume scenarios surges extend up to several kilometres laterally away from the dense PDCs, presenting a significant additional risk to areas that may not be in the inundation area pathway of the dense PDCs. The resulting PDC inundation areas were oriented in four main directions from the crater, northwest, southwest, southeast, and northeast. These inundation areas were significantly influenced by topographical barriers including Sandy Point Hill, Verchild's Mt., the northern crater rim, and Brimstone Hill.

The main hazard from PDCs is in the northwest of the island, whilst the southeast has low to negligible PDC hazard as Verchild's Mt. prevents PDC inundation areas from extending further

east. Multiple settlements lie directly in the path of the PDCs modelled, including Old Road Town, Newton Ground, Saddlers Village, and the southern portion of Sandy Point Town in the larger volume scenarios. The main circular road of the island is intersected in multiple locations by dense PDCs and surges, during the larger-volume scenarios.

7.2 Limitations and future work

An important limitation of the archival study is that no historic documents held within archives from the Caribbean were studied, largely due to the limited time spent visiting St Kitts and Nevis. Instead, this study consulted material held within British archives where more records are preserved compared to the archives in the Caribbean, due to a poor history of document preservation in humid conditions and frequent changes in the islands' governance. Future research may benefit from expanding the archival study to include information from more diverse sources, particularly using local archives where potentially important documentation may still be held.

The most significant limitation on the fieldwork was the short time spent on St Kitts and Nevis. An initial one week reconnaissance campaign was completed, with a second, longer campaign planned, however this was not undertaken due to the Covid-19 pandemic. Future research could perform more extensive field mapping of PDCs with modern classifications, and work to fully delineate the extent of the Steel Dust Series and resolve its stratigraphic position. As only one location on Nevis was studied here, it is difficult to evaluate how representative the findings are for other PDC deposits on the island. Additional sampling of Nevis would help to further refine the conclusions of this study.

The concentrations of several potentially useful trace elements, such as Eu, were below the limit of detection in the XRF analysis of pressed pellets. Further research using acid digestion

coupled with ICPMS would enable the limit of detection for numerous elements to be lowered, and so additional trace elements may be considered to aid the interpretation of magma sources.

Due to the short amount of time available on the EMPA, only a small dataset was able to be collected. In future, studies would benefit from analysing more samples, as well as larger areas within each sample, in order to confirm the conclusions made in this study are representative of the wider PDC deposits at Mt Liamuiga and Nevis Peak, rather than individual samples. Similarly, SEM analysis would also benefit from a larger sample set.

The modelling performed in this study aimed to model future eruption scenarios, and identify areas of high PDC hazard. To achieve this three parameters were considered: deposit volume, basal part density, and surge production coefficient. Whilst varying these three parameters was sufficient to meet this study's aims, there remains a significant potential for the models to be further refined to better reflect PDCs observed in the field. Modelling of dome collapse scenarios, in addition to the explosive scenarios modelled here, would also contribute to the characterisation of PDC hazards on St Kitts. The use of alternative modelling software packages may provide additional insight into PDC properties that aren't modelled by VolcFlow.

As this study focussed on the forward modelling of future eruptions, it did not reconstruct the past eruptions that produced the deposits observed in the field. This is in part due to the lack of a DEM being available from before the deposits on the island formed, due to their pre-historic nature, and so past PDCs could not be effectively modelled. One possible solution to this would be to artificially manipulate the DEM to "subtract" the existing PDC deposits from the modern topography, and to then use modelling to recreate the runout of the existing

deposits. This would allow the model to be validated based on field observations, and the variables used could be applied to forward modelling of potential future scenarios to ensure they are as realistic as possible, although it should be considered that every eruption event is different. Where VolcFlow has been used on more recently active volcanoes (e.g. St Vincent in 2021), significant time has been dedicated to refining the model to identically match the observed deposition of the deposits and their mapped runout. The detailed extent of previous eruptions at St Kitts were not known, so such comparisons were not possible.

References

Alexander, W. H. (1899) THE FLOOD OF JANUARY, 1880, AT BASSETERRE, ST. KITTS, W. I. *Monthly Weather Review* 27(5): 196–196.

Anonymous (1690) An account of the late dreadful earth-quake in the islands of Mevis and St. Christophers, &c. Which happen'd in the beginning of April, of this present 1690, In a letter to a friend in London. London: A. Smith.

Anonymous (1843) *A narrative of the late awful and calamitous earthquake in the West India islands of Antigua, Montserrat, Nevis, St. Christopher, Guadeloupe &c. &c. on February 8th 1843. Written by an eye-witness.* London.

Baker, D. M., Taylor, M., and Jiang, L. (2019) Local Residents' Attitudes Toward the Impacts of Tourism Development in the Caribbean Nation of St. Kitts & Nevis. *Revista de turism - studii si cercetari in turism* 0(28).

Baker, P. E. (1968a) Petrology of Mt. Misery Volcano, St. Kitts, West Indies. *LITHOS* 1(2): 124–150.

Baker, P. E. (1968b) Comparative volcanology and petrology of the atlantic island-arcs. *Bulletin Volcanologique* 32(1): 189–206.

Baker, P. E. (1969) The geological history of Mt Misery Volcano, St Kitts, West Indies.

Baker, P. E. (1980) Geology and geochemistry of the mansion pyroclast fall succession, St. Kitts. *Bulletin Volcanologique* 43(2): 303–310.

Baker, P. E. (1984) Geochemical evolution of St Kitts and Montserrat, Lesser Antilles. *Journal of the Geological Society* 141(3): 401–411.

Baker, P. E. (1985) Volcanic hazards on St Kitts and Montserrat, West Indies. *Journal of the Geological Society* 142(2): 279–295.

Baker, P. E., and Holland, J. G. (1973) Geochemical variations in a pyroclastic succession on St. Kitts, west Indies. *Bulletin Volcanologique* 37(4): 472–490.

Barclay, J., Few, R., Armijos, M. T., Phillips, J. C., Pyle, D. M., Hicks, A., Brown, S. K., and Robertson, R. E. A. (2019) Livelihoods, Wellbeing and the Risk to Life During Volcanic Eruptions. *Frontiers in Earth Science* 7.

Barclay, J., Robertson, R., Scarlett, J. P., Pyle, D. M., and Armijos, M. T. (2022) Disaster aid? Mapping historical responses to volcanic eruptions from 1800–2000 in the English-speaking Eastern Caribbean: their role in creating vulnerabilities. *Disasters* 46(S1): S10–S50.

Barclay, J., Wilkinson, E., White, C. S., Shelton, C., Forster, J., Few, R., Lorenzoni, I., Woolhouse, G., Jowitt, C., Stone, H., and Honychurch, L. (2019) Historical Trajectories of Disaster Risk in Dominica. *International Journal of Disaster Risk Science* : 1–17. doi:10.1007/s13753-019-0215-z.

Barrett, T. J., and MacLean, W. H. (2019) Volcanic Sequences, Lithochemistry, and Hydrothermal Alteration in Some Bimodal Volcanic-Associated Massive Sulfide Systems. In *Volcanic Associated Massive Sulfide Deposits_{title>Processes and Examples in Modern and Ancient Settings}*. Society of Economic Geologists doi:10.5382/rev.08.05.

Belousov, A., Voight, B., and Belousova, M. (2007/June) Directed blasts and blast-generated pyroclastic density currents: A comparison of the Bezymianny 1956, Mount St Helens 1980, and Soufrière Hills, Montserrat 1997 eruptions and deposits. *Bulletin of Volcanology*.

Bennett, E. N., Lissenberg, C. J., and Cashman, K. V. (2019) The significance of plagioclase

textures in mid-ocean ridge basalt (Gakkel Ridge, Arctic Ocean). *Contributions to Mineralogy and Petrology* 174(6): 1–22.

Bowen, N. L. (1928) *The Evolution of the Igneous Rocks*. Dover Publications. New York: Dover Publications doi:10.1038/124474a0.

Brounce, M. N., Kelley, K. A., and Cottrell, E. (2014) Variations in Fe³⁺/PFe of Mariana Arc Basalts and Mantle Wedge fO₂. *Journal of Petrology* 55(12): 2514–2536.

Brouwer, P. (2010) Theory of XRF. *The Netherlands: PANalytical B.V.*

Brown, G. M., Holland, J. G., Sigurdsson, H., Tomblin, J. F., and Arculus, R. J. (1977) Geochemistry of the Lesser Antilles volcanic island arc. *Geochimica et Cosmochimica Acta* 41(6): 785–801.

Brown, R. J., and Andrews, G. D. M. (2015) Deposits of Pyroclastic Density Currents. In Sigurdsson, H., Houghton, B., McNutt, S., Rymer, H., and Stix, J. (eds.). (Eds.), *Encyclopedia of Volcanoes*. (2nd ed.). Academic Press doi:10.1029/00eo00168.

Brown, R. J., and D. M. Andrews, G. (2015) Deposits of Pyroclastic Density Currents. *The Encyclopedia of Volcanoes* : 631–648. doi:10.1016/B978-0-12-385938-9.00036-5.

Browne, B., and Szramek, L. (2015) Rates of Magma Ascent and Storage. In *The Encyclopedia of Volcanoes*. doi:10.1016/b978-0-12-385938-9.00009-2.

Brugger, C. R., and Hammer, J. E. (2010) Crystal size distribution analysis of plagioclase in experimentally decompressed hydrous rhyodacite magma. *Earth and Planetary Science Letters* 300(3–4): 246–254.

Burns, F. A., Bonadonna, C., Pioli, L., Cole, P. D., and Stinton, A. (2017) Ash aggregation during

the 11 February 2010 partial dome collapse of the Soufrière Hills Volcano, Montserrat. *Journal of Volcanology and Geothermal Research* 335: 92–112.

Capadose, H. (1845) *Sixteen years in the West Indies*.

Carmichael, I. S. E. (1991) The redox states of basic and silicic magmas: a reflection of their source regions? *Contributions to Mineralogy and Petrology* 1991 106:2 106(2): 129–141.

Case, B., and Mayfield, M. (1990) Atlantic hurricane season of 1989. *Monthly Weather Review* 118(5): 1165–1177.

Cashman, K. V., and McConnell, S. M. (2005) Multiple levels of magma storage during the 1980 summer eruptions of Mount St. Helens, WA. *Bulletin of Volcanology* 2005 68:1 68(1): 57–75.

Cashman, Katharine V. (1992) Groundmass crystallization of Mount St. Helens dacite, 1980–1986: a tool for interpreting shallow magmatic processes. *Contributions to Mineralogy and Petrology* 1992 109:4 109(4): 431–449.

Cashman, Katharine V. (2020/10/July) Crystal Size Distribution (CSD) Analysis of Volcanic Samples: Advances and Challenges. *Frontiers in Earth Science*. Frontiers Media S.A.

Cashman, Katharine V., and Edmonds, M. (2019) Mafic glass compositions: a record of magma storage conditions, mixing and ascent. *Philosophical Transactions of the Royal Society A* 377(2139).

Cashman, Katharine V., Sparks, R. S. J., and Blundy, J. D. (2017) Vertically extensive and unstable magmatic systems: A unified view of igneous processes. *Science* 355(6331).

Cassidy, M., Cole, P. D., Hicks, K. E., Varley, N. R., Peters, N., and Lerner, A. H. (2015) Rapid

and slow: Varying magma ascent rates as a mechanism for Vulcanian explosions. *Earth and Planetary Science Letters* 420: 73–84.

Cassidy, M., Manga, M., Cashman, K., and Bachmann, O. (2018) Controls on explosive-effusive volcanic eruption styles. *Nature Communications* 2018 9:1 9(1): 1–16.

Cervený, R. (2016) Hamilton and the Hurricane. *Weatherwise* 69(5): 42–48.

Charbonnier, S. J., Germa, A., Connor, C. B., Gertisser, R., Preece, K., Komorowski, J. C., Lavigne, F., Dixon, T., and Connor, L. (2013) Evaluation of the impact of the 2010 pyroclastic density currents at Merapi volcano from high-resolution satellite imagery, field investigations and numerical simulations. *Journal of Volcanology and Geothermal Research* 261: 295–315.

Charbonnier, S. J. J., and Gertisser, R. (2012) Evaluation of geophysical mass flow models using the 2006 block-and-ash flows of Merapi Volcano, Java, Indonesia: Towards a short-term hazard assessment tool. *Journal of Volcanology and Geothermal Research* 231–232: 87–108.

Chenoweth, M. (2006) A Reassessment of Historical Atlantic Basin Tropical Cyclone Activity, 1700–1855. *Climatic Change* 76(1–2): 169–240.

Chin, E. J., Shimizu, K., Bybee, G. M., and Erdman, M. E. (2018) On the development of the calc-alkaline and tholeiitic magma series: A deep crustal cumulate perspective. *Earth and Planetary Science Letters* 482: 277–287.

Clarke, A. B., Stephens, S., Teasdale, R., Sparks, R. S. J., and Diller, K. (2007) Petrologic constraints on the decompression history of magma prior to Vulcanian explosions at the Soufrière Hills volcano, Montserrat. *Journal of Volcanology and Geothermal Research* 161(4): 261–274.

Clarke, B., Tierz, P., Calder, E., and Yirgu, G. (2020) Probabilistic Volcanic Hazard Assessment

for Pyroclastic Density Currents From Pumice Cone Eruptions at Aluto Volcano, Ethiopia. *Frontiers in Earth Science* 8: 348.

Cole, P. D., Calder, E. S., Druitt, T. H., Hoblitt, R., Robertson, R., Sparks, R. S. J., and Young, S. R. (1998) Pyroclastic flows generated by gravitational instability of the 1996–97 Lava Dome of Soufriere Hills Volcano, Montserrat. *Geophysical Research Letters* 25(18): 3425–3428.

Cole, P. D., Calder, E. S., Sparks, R. S. J., Clarke, A. B., Druitt, T. H., Young, S. R., Herd, R. A., Harford, C. L., and Norton, G. E. (2002) Deposits from dome-collapse and fountain-collapse pyroclastic flows at Soufrière Hills Volcano, Montserrat. *Geological Society Memoir* 21(1): 231–262.

Cole, P. D., Smith, P. J., Stinton, A. J., Odbert, H. M., Bernstein, M. L., Komorowski, J. C., and Stewart, R. (2014) Chapter 5 Vulcanian explosions at Soufrière Hills Volcano, Montserrat between 2008 and 2010. *Geological Society, London, Memoirs* 39(1): 93–111.

Colonial Office (1843) Blue Book (St. Christopher (St. Kitts), Nevis and Anguilla). Available via: CO 243/31, The National Archives, London.

Couch, S., Harford, C. L., Sparks, R. S. J., and Carroll, M. R. (2003) Experimental constraints on the conditions of formation of highly calcic plagioclase microlites at the Soufrière Hills Volcano, Montserrat. *Journal of Petrology* 44(8): 1455–1475.

Couch, S., Sparks, R. S. J., and Carroll, M. R. (2003) The Kinetics of Degassing-Induced Crystallization at Soufrière Hills Volcano, Montserrat. *Journal of Petrology* 44(8): 1477–1502.

Cronin, S. J., Lube, G., Dayudi, D. S., Sumarti, S., Subrandiyo, S., and Surono (2013) Insights into the October–November 2010 Gunung Merapi eruption (Central Java, Indonesia) from the stratigraphy, volume and characteristics of its pyroclastic deposits. *Journal of Volcanology and*

Geothermal Research 261: 244–259.

Czuppon, G., Lukács, R., Harangi, S., Mason, P. R. D., and Ntaflos, T. (2012) Mixing of crystal mushes and melts in the genesis of the Bogács Ignimbrite suite, northern Hungary: An integrated geochemical investigation of mineral phases and glasses. *Lithos* 148: 71–85.

Day, C. W. (1852) *Five years' residence in the West Indies, Volume II*. London: Colburn and Co. Publishers.

De Angelis, S. H., Larsen, J., Coombs, M., Dunn, A., and Hayden, L. (2015) Amphibole reaction rims as a record of pre-eruptive magmatic heating: An experimental approach. *Earth and Planetary Science Letters* 426: 235–245.

De la Roche, H., Leterrier, J., Grandclaude, P., and Marchal, M. (1980) A classification of volcanic and plutonic rocks using R1R2-diagram and major-element analyses — Its relationships with current nomenclature. *Chemical Geology* 29(1–4): 183–210.

Deer, W., Howie, R., and Zussman, J. (1992) *An introduction to the rock-forming minerals*.

Defant, M. J., Sherman, S., Maury, R. C., Bellon, H., De Boer, J., Davidson, J., and Kepezhinskas, P. (2001) The geology, petrology, and petrogenesis of Saba Island, Lesser Antilles. *Journal of Volcanology and Geothermal Research* 107(1–3): 87–111.

Deng, F., Rodgers, M., Xie, S., Dixon, T. H., Charbonnier, S., Gallant, E. A., López Vélez, C. M., Ordoñez, M., Malservisi, R., Voss, N. K., and Richardson, J. A. (2019) High-resolution DEM generation from spaceborne and terrestrial remote sensing data for improved volcano hazard assessment — A case study at Nevado del Ruiz, Colombia. *Remote Sensing of Environment* 233: 111348.

Department of Statistics, M. of S. D. (/2011) Households, Population and Average Household

Size by Parish 2001 - 2011. Accessed: 3rd October 2023

<<https://www.stats.gov.kn/topics/demographic-social-statistics/population/households-population-and-average-household-size-by-parish-2001-2011/>>.

Devine, J. D., Rutherford, M. J., and Gardner, J. E. (1998) Petrologic determination of ascent rates for the 1995–1997 Soufriere Hills Volcano andesitic magma. *Geophysical Research Letters* 25(19): 3673–3676.

Dioguardi, F., and Mele, D. (2018) PYFLOW_2.0: a computer program for calculating flow properties and impact parameters of past dilute pyroclastic density currents based on field data. *Bulletin of Volcanology* 80(3): 1–16.

Dobson, T. (1853) XIV. On the Connexion between Volcanic Eruptions and Hurricanes. *Papers and Proceedings of the Royal Society of Tasmania* 2(2): 225–243.

Druitt, T. H., Calder, E. S., Cole, P. D., Hoblitt, R. P., Loughlin, S. C., Norton, G. E., Ritchie, L. J., Sparks, R. S. J., and Voight, B. (2002) Small-volume, highly mobile pyroclastic flows formed by rapid sedimentation from pyroclastic surges at Soufrière Hills Volcano, Montserrat: an important volcanic hazard. *Geological Society Memoir* 21(1): 263–279.

Dyde, B. (2005) *Out of the crowded vagueness : a history of the islands of St Kitts, Nevis & Anguilla*. Macmillan Caribbean.

Eggins, S. M. (1993) Origin and differentiation of picritic arc magmas, Ambae (Aoba), Vanuatu. *Contributions to Mineralogy and Petrology* 114(1): 79–100.

Evans, K. A., Elburg, M. A., and Kamenetsky, V. S. (2012) Oxidation state of subarc mantle. *Geology* 40(9): 783–786.

Fedele, L., Cole, P. D., Scarpati, C., and Robertson, R. E. A. (2021) Petrological insights on the

last 1000 years of explosive activity at La Soufrière volcano, St. Vincent (Lesser Antilles). *Lithos* 392–393: 106150.

Feuillet, N., Beauducel, F., and Tapponnier, P. (2011) Tectonic context of moderate to large historical earthquakes in the Lesser Antilles and mechanical coupling with volcanoes. *Journal of Geophysical Research: Solid Earth* 116(10): 1–26.

Fink, L. K. (1975) St. Christopher-Nevis-Anguilla. *World Regional Geology* : 439–443. doi:10.1007/3-540-31081-1_95.

Fisher, R. V., and Heiken, G. (1982) Mt. Pelée, martinique: may 8 and 20, 1902, pyroclastic flows and surges. *Journal of Volcanology and Geothermal Research* 13(3–4): 339–371.

Fisher, R. V., and Schmincke, H.-U. (1984) Alteration of Volcanic Glass. *Pyroclastic Rocks* : 312–345. doi:10.1007/978-3-642-74864-6_12.

Gardner, C. A., Cashman, K. V., and Neal, C. A. (1998) Tephra-fall deposits from the 1992 eruption of Crater Peak, Alaska: implications of clast textures for eruptive processes. *Bulletin of Volcanology* 1998 59:8 59(8): 537–555.

Garriott, E. B. (1900) *West Indian Hurricanes*. Washington: U.S. Department of Agriculture.

Genareau, K., Clarke, A. B., and Hervig, R. L. (2009) New insight into explosive volcanic eruptions: Connecting crystal-scale chemical changes with conduit-scale dynamics. *Geology* 37(4): 367–370.

Geological Survey (1974) *Earthquake Information Bulletin, Volumes 6-7*. Geological Survey.

Geschwind, C. H., and Rutherford, M. J. (1995) Crystallization of microlites during magma ascent: the fluid mechanics of 1980–1986 eruptions at Mount St Helens. *Bulletin of*

Volcanology 1995 57:5 57(5): 356–370.

Gordon, J. (1987) *Nevis Queen of the Caribees*. London: Macmillan Publishers Ltd.

Graham, O., Thomas, T., Hicks, A., Edwards, S., Juman, A., Ramroop, A., and Robertson, R. (2024) Facts, Faith and Facebook: Science communication during the 2020–2021 La Soufrière, St. Vincent volcanic eruption. *Geological Society, London, Special Publications* 539(1).

Grove, T. L., Gerlach, D. C., and Sando, T. W. (1982) Origin of calc-alkaline series lavas at Medicine Lake Volcano by fractionation, assimilation and mixing. *Contributions to Mineralogy and Petrology* 1982 80:2 80(2): 160–182.

Gueugneau, V., Kelfoun, K., Charbonnier, S., Germa, A., and Carazzo, G. (2020) Dynamics and Impacts of the May 8th, 1902 Pyroclastic Current at Mount Pelée (Martinique): New Insights From Numerical Modeling. *Frontiers in Earth Science* 8: 279.

Gueugneau, V., Kelfoun, K., and Druitt, T. (2019) Investigation of surge-derived pyroclastic flow formation by numerical modelling of the 25 June 1997 dome collapse at Soufrière Hills Volcano, Montserrat. *Bulletin of Volcanology* 2019 81:4 81(4): 1–14.

Hammer, J. E., Cashman, K. V., Hoblitt, R. P., and Newman, S. (1999) Degassing and microlite crystallization during pre-climactic events of the 1991 eruption of Mt. Pinatubo, Philippines. *Bulletin of Volcanology* 1999 60:5 60(5): 355–380.

Hammer, J. E., Cashman, K. V., and Voight, B. (2000) Magmatic processes revealed by textural and compositional trends in Merapi dome lavas. *Journal of Volcanology and Geothermal Research* 100(1–4): 165–192.

Harford, C. L., Sparks, R. S. J., and Fallick, A. E. (2003) Degassing at the Soufrière Hills Volcano, Montserrat, Recorded in Matrix Glass Compositions. *Journal of Petrology* 44(8): 1503–1523.

- Harker, A. (1909) *The Natural History of Igneous Rocks*. London: Methuen and Co.
- Harkness, D. D., Roobol, M. J., Smith, A. L., Stipp, J. J., and Baker, P. E. (1994) Radiocarbon redating of contaminated samples from a tropical volcano: the Mansion 'Series' of St Kitts, West Indies. *Bulletin of Volcanology* 56(5): 326–334.
- Haynes, R. (1934) *The Barbadian Diary of Gen. Robert Haynes, 1787-1836*. Barbados: Azania Press.
- Higgins, M. D. (2000) Measurement of crystal size distributions. *American Mineralogist* 85(9): 1105–1116.
- Higgins, O., Sheldrake, T., and Caricchi, L. (2021) Machine learning thermobarometry and chemometry using amphibole and clinopyroxene: a window into the roots of an arc volcano (Mount Liamuiga, Saint Kitts). *Contributions to Mineralogy and Petrology* 2021 177:1 177(1): 1–22.
- Hincks, T., Sparks, S., Dunkley, P., and Cole, P. (2005) Montserrat. In *Volcanic Hazard Atlas of the Lesser Antilles*.
- Holloway, J. R., and Blank, J. G. (1994) Application of experimental results to C-O-H species in natural melts | Reviews in Mineralogy and Geochemistry | GeoScienceWorld. *Reviews in Mineralogy and Geochemistry* 30(1): 187–230.
- Horwell, C. J., Williamson, B. J., Llewelin, E. W., Damby, D. E., and Le Blond, J. S. (2013) The nature and formation of cristobalite at the Soufrière Hills volcano, Montserrat: Implications for the petrology and stability of silicic lava domes. *Bulletin of Volcanology* 75(3): 1–19.
- Houghton, B., and Carey, R. J. (2015) Pyroclastic Fall Deposits. *The Encyclopedia of Volcanoes* : 599–616. doi:10.1016/B978-0-12-385938-9.00034-1.

House of Commons Parliamentary Papers (1843) Papers relative to the Earthquake in the West Indies. Accessed via: The House of Commons Parliamentary Papers Online: London: Printed by William Clowes and Sons, Stamford Street, for Her Majesty's Stationery Office.

Hubbard, V. K. (2002a) *A history of St Kitts : the sweet trade*. Macmillan.

Hubbard, V. K. (2002b) *Swords, Ships & Sugar: History of Nevis*. (Vol. 2). Premiere Editions International.

Humphreys, M. C. S., Blundy, J. D., and Sparks, R. S. J. (2006) Magma evolution and open-system processes at Shiveluch Volcano: Insights from phenocryst zoning. *Journal of Petrology* 47(12): 2303–2334.

Hurricane damage | National Archives St. Kitts & Nevis (n.d.). Accessed: 7th April 2020 <<http://www.nationalarchives.gov.kn/966>. >.

Hutton, C. O. (1968) The mineralogy and petrology of Nevis, Leeward Islands, British West Indies: A progress report. *Transactions of the Fourth Caribbean Geological Conference* : 383–388.

Hutton, C. O., and Nockolds, S. R. (1978) The Petrology of Nevis, Leeward Islands, West Indies. *Overseas Geology and Mineral Resources* 52.

Juster, T. C., Grove, T. L., and Perfit, M. R. (1989) Experimental constraints on the generation of FeTi basalts, andesites, and rhyodacites at the Galapagos Spreading Center, 85°W and 95°W. *Journal of Geophysical Research: Solid Earth* 94(B7): 9251–9274.

Kelfoun, K (2017) A two-layer depth-averaged model for both the dilute and the concentrated parts of pyroclastic currents. *Journal of Geophysical Research: Solid Earth* 122(6): 4293–4311.

Kelfoun, K, and Druitt, T. H. (2005) Numerical modeling of the emplacement of Socompa rock avalanche, Chile. *Journal of Geophysical Research: Solid Earth* 110(12): 1–13.

Kelfoun, Karim, Gueugneau, V., Komorowski, J. C., Aisyah, N., Cholik, N., and Merciecca, C. (2017) Simulation of block-and-ash flows and ash-cloud surges of the 2010 eruption of Merapi volcano with a two-layer model. *Journal of Geophysical Research: Solid Earth* 122(6): 4277–4292.

Kelfoun, Karim, Samaniego, P., Palacios, P., and Barba, D. (2009) Testing the suitability of frictional behaviour for pyroclastic flow simulation by comparison with a well-constrained eruption at tungurahua volcano (Ecuador). *Bulletin of Volcanology* 71(9): 1057–1075.

Kelfoun, Karim, and Vallejo Vargas, S. (2016) VolcFlow capabilities and potential development for the simulation of lava flows. *Geological Society Special Publication* 426(1): 337–343.

Kelley, K. A., and Cottrell, E. (2009) Water and the oxidation state of subduction zone magmas. *Science* 325(5940): 605–607.

Komorowski, J.-C., Boudon, G., Michel-Semet, Beauducel, F., Anténor-Habazac, C., Bazin, S., and Hammouya, G. (2005) Guadeloupe. In *Volcanic Hazard Atlas of the Lesser Antilles*.

Koon Koon, R. R. (2012) Geothermal energy prospecting for the caribbean islands of Nevis and Montserrat. *GHC Bulletin* 31(August): 23–27.

Lawrence, M. B. (1996) *Preliminary Report - Hurricane Luis*.

Lechler, P. J., and Desilets, M. O. (1987) A review of the use of loss on ignition as a measurement of total volatiles in whole-rock analysis. *Chemical Geology* 63(3–4): 341–344.

Lerner, G. A., Jenkins, S. F., Charbonnier, S. J., Komorowski, J. C., and Baxter, P. J. (2022) The

hazards of unconfined pyroclastic density currents: A new synthesis and classification according to their deposits, dynamics, and thermal and impact characteristics. *Journal of Volcanology and Geothermal Research* 421: 107429.

Lindsay, J. M., and Robertson, R. E. A. (2018) Integrating volcanic hazard data in a systematic approach to develop volcanic hazard maps in the lesser antilles. *Frontiers in Earth Science* 6: 366255.

Longshore, D. (2000) *Encyclopedia of hurricanes, typhoons, and cyclones*. Checkmark Books.

Lockett, R., Loughlin, S., De Angelis, S., and Ryan, G. (2008) Volcanic seismicity at Montserrat, a comparison between the 2005 dome growth episode and earlier dome growth. *Journal of Volcanology and Geothermal Research* 177(4): 894–902.

Macdonald, R., Hawkesworth, C. J., and Heath, E. (2000) The Lesser Antilles volcanic chain: a study in arc magmatism. *Earth-Science Reviews* 49(1–4): 1–76.

Malin, M. C., and Sheridan, M. F. (1982) Computer-Assisted Mapping of Pyroclastic Surges. *Science* 217(4560): 637–640.

Marsh, B. D. (1988) Crystal size distribution (CSD) in rocks and the kinetics and dynamics of crystallization. *Contributions to Mineralogy and Petrology* 1988 99:3 99(3): 277–291.

Marsh, B. D. (1998) On the interpretation of crystal size distributions in magmatic systems. *Journal of Petrology* 39(4): 553–599.

Martel, C. (2012) Eruption Dynamics Inferred from Microlite Crystallization Experiments: Application to Plinian and Dome-forming Eruptions of Mt. Pelée (Martinique, Lesser Antilles). *Journal of Petrology* 53(4): 699–725.

Martel, C., and Poussineau, S. (2007) Diversity of eruptive styles inferred from the microlites of Mt Pelée andesite (Martinique, Lesser Antilles). *Journal of Volcanology and Geothermal Research* 166(3–4): 233–254.

Marx, R. F. (1987) *Shipwrecks in the Americas*. Dover Publications.

Mastrolorenzo, G., and Pappalardo, L. (2006) Magma degassing and crystallization processes during eruptions of high-risk Neapolitan-volcanoes: Evidence of common equilibrium rising processes in alkaline magmas. *Earth and Planetary Science Letters* 250(1–2): 164–181.

Melekhova, E., Blundy, J., Martin, R., Arculus, R., and Pichavant, M. (2017) *Petrological and experimental evidence for differentiation of water-rich magmas beneath St. Kitts, Lesser Antilles*. *Contributions to Mineralogy and Petrology* (Vol. 172). Springer Berlin Heidelberg.

Melnik, O. E., Blundy, J. D., Rust, A. C., and Muir, D. D. (2011) Subvolcanic plumbing systems imaged through crystal size distributions. *Geology* 39(4): 403–406.

Meniketti, M. G. (2016) *Sugar cane capitalism and environmental transformation : an archaeology of colonial Nevis, West Indies*. The University of Alabama Press.

Minor, D. K. (eds) (1833) *American Railroad Journal*. 2: 237.

Miwa, T., Toramaru, A., and Iguchi, M. (2009) Correlations of volcanic ash texture with explosion earthquakes from vulcanian eruptions at Sakurajima volcano, Japan. *Journal of Volcanology and Geothermal Research* 184(3–4): 473–486.

Morgan, D. J., and Jerram, D. A. (2006) On estimating crystal shape for crystal size distribution analysis. *Journal of Volcanology and Geothermal Research* 154(1–2): 1–7.

Mulcahy, M. (2006) *Hurricanes and society in the British greater caribbean, 1624-1783*.

Hurricanes and Society in the British Greater Caribbean, 1624-1783. Johns Hopkins University Press.

Murch, A. P., and Cole, P. D. (2019) Using microlites to gain insights into ascent conditions of differing styles of volcanism at Soufrière Hills Volcano. *Journal of Volcanology and Geothermal Research* 384: 221–231.

Neely, W. (2014) *The Great Okeechobee Hurricane of 1928*.

Neely, W. (2016) *The greatest and deadliest hurricanes of the Caribbean and the Americas : the stories behind the great storms of the North Atlantic*.

Noguchi, S., Toramaru, A., and Nakada, S. (2008) Groundmass crystallization in dacite dykes taken in Unzen Scientific Drilling Project (USDP-4). *Journal of Volcanology and Geothermal Research* 175(1–2): 71–81.

Noguchi, S., Toramaru, A., and Shimano, T. (2006) Crystallization of microlites and degassing during magma ascent: Constraints on the fluid mechanical behavior of magma during the Tenjo Eruption on Kozu Island, Japan. *Bulletin of Volcanology* 68(5): 432–449.

Ogburn, S. E., and Calder, E. S. (2017) The relative effectiveness of empirical and physical models for simulating the dense undercurrent of pyroclastic flows under different emplacement conditions. *Frontiers in Earth Science* 5: 83.

Parkinson, I. J., and Arculus, R. J. (1999) The redox state of subduction zones: Insights from arc-peridotites. *Chemical Geology* 160(4): 409–423.

Partagas, J. F. (1966) *Year 1899. Atlantic Oceanographic and Meteorological Laboratory*. Miami, Florida: National Oceanic and Atmospheric Administration.

Pasch, R. J. (1999) *Preliminary Report - Hurricane Jose*.

Patra, A. K., Bauer, A. C., Nichita, C. C., Pitman, E. B., Sheridan, M. F., Bursik, M., Rupp, B., Webber, A., Stinton, A. J., Namikawa, L. M., and Renschler, C. S. (2005) Parallel adaptive numerical simulation of dry avalanches over natural terrain. *Journal of Volcanology and Geothermal Research* 139(1–2): 1–21.

Pearce, J. A. (2008) Geochemical fingerprinting of oceanic basalts with applications to ophiolite classification and the search for Archean oceanic crust. *Lithos* 100(1–4): 14–48.

Pearce, J. A., and Peate, D. W. (1995) Tectonic implications of the composition of volcanic arc magmas. *Annual Review of Earth & Planetary Sciences* 23: 251–285.

Pichavant, M., and Macdonald, R. (2003) Mantle genesis and crustal evolution of primitive calc-alkaline basaltic magmas from the Lesser Antilles arc. *Geological Society, London, Special Publications* 219(1): 239–254.

Piochi, M., Mastrolorenzo, G., and Pappalardo, L. (2005) Magma ascent and eruptive processes from textural and compositional features of Monte Nuovo pyroclastic products, Campi Flegrei, Italy. *Bulletin of Volcanology* 2005 67:7 67(7): 663–678.

Pitman, E. B., Nichita, C. C., Patra, A., Bauer, A., Sheridan, M., and Bursik, M. (2003) Computing granular avalanches and landslides. *Physics of Fluids* 15(12): 3638.

Post Impact Report #1 - Hurricane Lenny - Anguilla | ReliefWeb (/1999) *Caribbean Disaster Emergency Response Agency*. Accessed: 8th April 2020 <<https://reliefweb.int/report/anguilla/post-impact-report-1-hurricane-lenny>>.

Preece, K., Barclay, J., Gertisser, R., and Herd, R. A. (2013) Textural and micro-petrological variations in the eruptive products of the 2006 dome-forming eruption of Merapi volcano,

Indonesia: Implications for sub-surface processes. *Journal of Volcanology and Geothermal Research* 261: 98–120.

Preece, K., Gertisser, R., Barclay, J., Charbonnier, S. J., Komorowski, J. C., and Herd, R. A. (2016) Transitions between explosive and effusive phases during the cataclysmic 2010 eruption of Merapi volcano, Java, Indonesia. *Bulletin of Volcanology* 78(8): 1–16.

Rannou, E., and Caroff, M. (2010) Crystal Size Distribution in Magmatic Rocks: Proposition of a Synthetic Theoretical Model. *Journal of Petrology* 51(5): 1087–1098.

Rappaport, E. N., and Fernandez-Partagas, J. (1995) *The Deadliest Atlantic Tropical Cyclones, 1492-1996*.

Renjith, M. L. (2014) Micro-textures in plagioclase from 1994–1995 eruption, Barren Island Volcano: Evidence of dynamic magma plumbing system in the Andaman subduction zone. *Geoscience Frontiers* 5(1): 113–126.

Robertson, R. (2005) St Kitts. In *Volcanic Hazard Atlas of the Lesser Antilles*.

Robertson, R. (2009) Antilles geology. In Gillespie, R. and Clague, D. (Eds.), *Encyclopedia of Islands*. University of California Press.

Robertson, R. E. A., Aspinall, W. P., Herd, R. A., Norton, G. E., Sparks, R. S. J., and Young, S. R. (2000) The 1995-1998 eruption of the Soufrière Hills volcano, Montserrat, WI. *Philosophical Transactions of the Royal Society A: Mathematical, Physical and Engineering Sciences* 358(1770): 1619–1637.

Robson, G. R. (1964) An Earthquake Catalogue for the Eastern Caribbean. *Bulletin of the Seismological Society of America* 54(2): 785–832.

Roobol, M. J., Smith, A. L., and Wright, J. V. (1985) Dispersal and characteristics of pyroclastic fall deposits from Mt. Misery Volcano, West Indies. *Geologische Rundschau* 74(2): 321–335.

Roobol, M. J., Smith, A. L., and Wright, J. V. (1981) Revisions in the pyroclastic stratigraphy of Mt Misery volcano, St. Kitts, Lesser Antilles: 14 C ages and recognition of pyroclastic flow deposits. *Journal of the Geological Society* 138(6): 713–718.

Roobol, M. John, Smith, A. L., and Wright, J. V. (1987) Lithic breccias in pyroclastic flow deposits on St. Kitts, West Indies. *Bulletin of Volcanology* 49(5): 694–707.

Roobol, M.J. (1985) Discussion on differences in radiocarbon ages reported from St. Kitts, West Indies. *Journal of the Geological Society* 144(1): 205–206.

Rutherford, M. J. (2008) Magma ascent rates. *Reviews in Mineralogy and Geochemistry* 69(1): 241–271.

Rutherford, M. J., and Hill, P. M. (1993) Magma ascent rates from amphibole breakdown: An experimental study applied to the 1980–1986 Mount St. Helens eruptions. *Journal of Geophysical Research: Solid Earth* 98(B11): 19667–19685.

Rutherford, Malcolm J., and Devine, J. D. (2003) Magmatic Conditions and Magma Ascent as Indicated by Hornblende Phase Equilibria and Reactions in the 1995–2002 Soufrière Hills Magma. *Journal of Petrology* 44(8): 1433–1453.

Salisbury, M. J., Bohron, W. A., Clynne, M. A., Ramos, F. C., and Hoskin, P. (2008) Multiple Plagioclase Crystal Populations Identified by Crystal Size Distribution and in situ Chemical Data: Implications for Timescales of Magma Chamber Processes Associated with the 1915 Eruption of Lassen Peak, CA. *Journal of Petrology* 49(10): 1755–1780.

Schiavi, F., Walte, N., and Keppler, H. (2009) First in situ observation of crystallization

processes in a basaltic-andesitic melt with the moissanite cell. *Geology* 37(11): 963–966.

Schwartz, S. B. (2015) *Sea of storms: A history of hurricanes in the Greater Caribbean from Columbus to Katrina*. *Sea of Storms: A History of Hurricanes in the Greater Caribbean from Columbus to Katrina*.

Scott, J. A. J., Mather, T. A., Pyle, D. M., Rose, W. I., and Chigna, G. (2012) The magmatic plumbing system beneath Santiaguito Volcano, Guatemala. *Journal of Volcanology and Geothermal Research* 237–238: 54–68.

Simpson, K. (2005) Nevis. In *Volcanic Hazard Atlas of the Lesser Antilles*.

Simpson, K., and Shepherd, J. B. (2001) *Volcanic-hazard assessment for St. Kitts, Lesser Antilles*.

Sisson, T. W., and Layne, G. D. (1993) H₂O in basalt and basaltic andesite glass inclusions from four subduction-related volcanoes. *Earth and Planetary Science Letters* 117(3–4): 619–635.

Sloane, H. (1694) I. A letter from Hans Sloane, M. D. and S. R. S: with several accounts of the earthquakes in Peru October the 20th. 1687. and at Jamaica, February 19th. 1687/8 and June the 7th. 1692. *Philosophical Transactions of the Royal Society of London* 18(209): 78–100.

Smith, L. (1835) Despatches from Lionel Smith, governor of Barbados, dated August to December 1835. Available via: CO 28/116, The National Archives, London.

Smith, W. (1745) *A natural history of Nevis, and the rest of the English Leeward Charibee Islands in America : with many other observations on nature and art*. London: J. Bentham, sold by W. Thurlbourn; S. Birt, C. Bathurst, and J. Beecroft.

St. Kitts declared disaster area with damage over 1 Billion EC dollars - Saint Kitts and Nevis |

ReliefWeb (/1998) OCHA. Accessed: 7th April 2020 <<https://reliefweb.int/report/saint-kitts-and-nevis/st-kitts-declared-disaster-area-damage-over-1-billion-ec-dollars>. >.

Stinton, A. J., Cole, P. D., Stewart, R. C., Odbert, H. M., and Smith, P. (2014) Chapter 7 The 11 February 2010 partial dome collapse at Soufrière Hills Volcano, Montserrat. *Geological Society, London, Memoirs* 39(1): 133–152.

Stødle, K., Metcalfe, C. A., Brunner, L. G., Saliani, J. N., Flage, R., and Guikema, S. D. (2021) Dependent infrastructure system modeling: A case study of the St. Kitts power and water distribution systems. *Reliability Engineering & System Safety* 209: 107421.

Suzuki, Y., and Fujii, T. (2010) Effect of syneruptive decompression path on shifting intensity in basaltic sub-Plinian eruption: Implication of microlites in Yufune-2 scoria from Fuji volcano, Japan. *Journal of Volcanology and Geothermal Research* 198(1–2): 158–176.

Suzuki, Y., Gardner, J. E., and Larsen, J. F. (2006) Experimental constraints on syneruptive magma ascent related to the phreatomagmatic phase of the 2000AD eruption of Usu volcano, Japan. *Bulletin of Volcanology* 2006 69:4 69(4): 423–444.

Swanson, S. E. (1977) Relation of nucleation and crystal-growth rate to the development of granitic textures | American Mineralogist | GeoScienceWorld. *American Mineralogist* 62(9–10): 966–978.

Sword-Daniels, V., Wilson, T. M., Sargeant, S., Rossetto, T., Twigg, J., Johnston, D. M., Loughlin, S. C., and Cole, P. D. (2014) Chapter 26 Consequences of long-term volcanic activity for essential services in Montserrat: challenges, adaptations and resilience. *Geological Society, London, Memoirs* 39(1): 471–488.

Szramek, L., Gardner, J. E., and Larsen, J. (2006) Degassing and microlite crystallization of

basaltic andesite magma erupting at Arenal Volcano, Costa Rica. *Journal of Volcanology and Geothermal Research* 157(1–3): 182–201.

The Christian remembrancer; or, The Churchman's Biblical, ecclesiastical & literary miscellany (1844). doi:papers2://publication/uuid/87EA1D0A-9812-4998-9941-BFA7A9D09877.

The Disastrous Floods at St. Kitts (1880/1/April) *The Maitland Mercury and Hunter River General Advertiser*: 6. New South Wales.

The Times (1843) Dreaful Earthquake in the West Indies (from The Times). *The South Australian*. Accessed via: The National library of Austraila.

Toothill, J., Williams, C. A., MacDonald, R., Turner, S. P., Rogers, N. W., Hawkesworth, C. J., Jerram, D. A., Ottley, C. J., and Tindle, A. G. (2007) A complex petrogenesis for an arc magmatic suite, St Kitts, Lesser Antilles. *Journal of Petrology* 48(1): 3–42.

Toramaru, A., Noguchi, S., Oyoshihara, S., and Tsune, A. (2008) MND(microlite number density) water exsolution rate meter. *Journal of Volcanology and Geothermal Research* 175(1–2): 156–167.

Treasury (1843) Treasury: papers - A letter from The Govenor of Barbados. Avaliable via: T 1/494, The National Archives, London.

Viccaro, M., Giacomoni, P. P., Ferlito, C., and Cristofolini, R. (2010) Dynamics of magma supply at Mt. Etna volcano (Southern Italy) as revealed by textural and compositional features of plagioclase phenocrysts. *Lithos* 116(1–2): 77–91.

Wadge, G. (1986) The dykes and structural setting of the volcanic front in the Lesser Antilles island arc. In *Bulletin of Volcanology* (Vol. 48). Springer-Verlag.

Widiwijayanti, C., Voight, B., Hidayat, D., and Schilling, S. P. (2009) Objective rapid delineation of areas at risk from block-and-ash pyroclastic flows and surges. *Bulletin of Volcanology* 71(6): 687–703.

Willmore, P. L. (1952) The Earthquake Series in St. Kitts - Nevis, 1950-51: With Notes on Soufrière Activity in the Lesser Antilles. *Nature* 169(4306): 770–772.

Winchester, J. A., and Floyd, P. A. (1977) Geochemical discrimination of different magma series and their differentiation products using immobile elements. *Chemical Geology* 20(C): 325–343.

Winter, J. D. (2014) Chapter 9 Chemical Petrology II: Trace Elements and Isotopes. In *Principles of Igneous and Metamorphic Petrology* (2nd ed.). Pearson Education Inc.

Wong, L. J., and Larsen, J. F. (2009) The Middle Scoria sequence: A Holocene violent strombolian, subplinian and phreatomagmatic eruption of Okmok volcano, Alaska. *Bulletin of Volcanology* 2009 72:1 72(1): 17–31.

Young, S. R., Sparks, R. S. J., Aspinall, W. P., Lynch, L. L., Miller, A. D., Robertson, R. E. A., and Shepherd, J. B. (1998) Overview of the eruption of Soufriere Hills Volcano, Montserrat, 18 July 1995 to December 1997. *Geophysical Research Letters* 25(18): 3389–3392.

Zacek, N. A. (2010) *Settler society in the english Leeward Islands, 1670–1776. Settler Society in the English Leeward Islands, 1670-1776.* Cambridge University Press doi:10.1017/CBO9780511760907.

Zellmer, G. F., Hawkesworth, C. J., Sparks, R. S. J., Thomas, L. E., Harford, C. L., Brewer, T. S., and Loughlin, S. C. (2003) Geochemical Evolution of the Soufrière Hills Volcano, Montserrat, Lesser Antilles Volcanic Arc. *Journal of Petrology* 44(8): 1349–1374.

Zimmer, M. M., Plank, T., Hauri, E. H., Yogodzinski, G. M., Stelling, P., Larsen, J., Singer, B., Jicha, B., Mandeville, C., and Nye, C. J. (2010) The Role of Water in Generating the Calc-alkaline Trend: New Volatile Data for Aleutian Magmas and a New Tholeiitic Index. *Journal of Petrology* 51(12): 2411–2444.

Appendices

Appendix 1 - List of Libraries and Archives consulted

- National Archives, Kew Gardens
- Plymouth City Records Office
- The Bodleian Libraries, University of Oxford
- The Parliamentary Archives, online access
- Caird Library, Royal Museums Greenwich
- British Library, London




Appendix 2 - St. Kitts field locations and Latitude/Longitude




Location	Latitude	Longitude
SK1	17.348031	-62.720695
SK2	17.380760	-62.750976
SK3	17.403852	-62.780720
SK4	17.408393	-62.797731
SK5	17.410295	-62.842876
SK6	17.398266	-62.854530
SK7	17.402573	-62.851068
SK8	17.362673	-62.853016
SK10	17.831456	-62.863086
SK11	17.356261	-62.843975
SK12	17.416726	-62.819973
SK13	17.416958	-62.817780


Appendix 3 - Maximum axis collected from clasts in the upper layer of pumice lapilli at location SK2.




	X (mm)	Y (mm)	Z (mm)	Average (mm)
Axes of pumice clasts	92	65	56	71.0
	104	70	50	74.7
	90	65	40	65.0
	75	53	46	58.0
	74	50	43	55.7
	87	60.6	47	64.9
Average				
Axes of dense clasts	50	40	32	40.7
	40	25	20	28.3
	43	33	18	31.3
	35	25	20	26.7
	28	26	15	27.0
	39.2	29.8	21	30.8
Average				



Appendix 4 - Description of the samples chosen for XRF analysis.




Sample	Description	Photo
SK1	<p>Highly vesicular light/whitish in coloured pumice.</p> <p>Porphyritic with a small number of phenocrysts in an aphanitic fine-grained groundmass.</p> <p>A higher proportion of mafic phenocrysts, with a small number of felsic phenocrysts. Max. length of phenocrysts 4 mm.</p>	
SK1 GREY	<p>Highly vesicular light grey in coloured pumice. White and grey clasts clearly distinguishable.</p> <p>Porphyritic with an aphanitic fine-grained groundmass.</p> <p>Mafic and felsic phenocrysts with a max. length of 10 mm.</p>	
SK5 DARK	<p>Dark grey in colour and vesicular.</p> <p>Dark end-member of SK5.</p> <p>Porphyritic with an aphanitic fine-grained groundmass.</p> <p>Feldspar phenocrysts with a max. length of 3 mm.</p>	




<p>SK5 LIGHT</p>	<p>White/light grey in colour. Light end-member of SK5. Evidence of mingling between light and dark material. Porphyritic with an aphanitic fine-grained groundmass. Feldspar phenocrysts and mafic phenocrysts (pyroxenes) with a max. length of 7 mm.</p>	
<p>SK8 DARK</p>	<p>Dark grey in colour and mildly vesicular. Porphyritic with an aphanitic fine-grained groundmass. Feldspar phenocrysts with a max. length of 5 mm.</p>	
<p>SK8 LIGHT</p>	<p>Light in colour and vesicular. Porphyritic with an aphanitic fine-grained groundmass. Felsic (feldspar) and mafic phenocrysts with a max. length of 3 mm.</p>	




<p>SK8 Mixed</p>	<p>Dark grey in colour, with streaks/bands and multiple inclusions. Generally vesicular, with some bands more vesicular than others. Grain size varies across the sample.</p> <p>Dark coloured inclusions - Mafic and felsic phenocrysts in fine-grained groundmass. Felspar phenocrysts of 2 to 4 mm. Few vesicles. No banding/flow indicators.</p> <p>Grey inclusion – Felsic phenocrysts with a max. length of 5mm, mafic phenocrysts with a max. length of 1mm, fine-grained groundmass, few vesicles.</p> <p>Coarse bands – Large number of number feldspar and mafic in a fine-grained groundmass. No preferred orientation of phenocrysts. Bands appear to mingle.</p>	
------------------	---	---

<p>SK10</p>	<p>Dark in colour. Porphyritic, crystalline and dense with no vesicles. Feldspar phenocrysts with a max. length of 5 mm. Mafic phenocrysts with a max. length of 3 mm.</p>	
<p>SK11</p>	<p>Light grey in colour and pumiceous. Porphyritic with an aphanitic fine-grained groundmass. Even proportions of felsic and mafic phenocrysts, with a max. length of 6 mm.</p>	
<p>SK12</p>	<p>Light grey in colour and highly vesicular, pumice. Porphyritic with a fine-grained groundmass. Large feldspar phenocrysts with a max. of length of 4 mm. Mafic phenocrysts with a max. length of 2 mm.</p>	

<p>SK13</p>	<p>Light in colour with a grey/pink tinge, mildly vesicular. Porphyritic with a fine-grained groundmass. Felsic phenocrysts with a max. length of 2mm and mafic phenocrysts with a max length of 4 mm. Slight preferred orientation to vesicles/phenocrysts identified.</p>	
<p>SK14</p>	<p>Light in colour and highly vesicular. Porphyritic. Felsic (feldspar) phenocrysts with a max. length of 3 mm, and mafic phenocrysts with a tabular, elongated shape and a max. length of 4 mm.</p>	

<p>SK16</p>	<p>Light in colour and vesicular. Porphyritic. Felsic phenocrysts with a max. of length of 3 mm. Mafic phenocrysts with a tabular, elongated shape and a max. length of 7 mm. No preferential orientation of phenocrysts.</p>	
<p>SKN17</p>	<p>White/light grey in colour. Porphyritic with an aphanitic fine-grained groundmass. Equal ratio of mafic and felsic phenocrysts. Feldspar and mafic phenocrysts with max. length of 7 mm. Small cluster of dark phenocrysts, this could be a Xenolith. Groundmass consistent with the bulk of the sample.</p>	
<p>SKN18</p>	<p>Light pinkish/grey in colour. Porphyritic with an aphanitic fine-grained groundmass. Feldspar and rectangular mafic phenocrysts with a max. length of 12 mm.</p>	

<p>SKN19 DARK</p>	<p>Dark in colour and mildly vesicular. Porphyritic with an aphanitic fine-grained groundmass. Felsic phenocrysts with a max. length of 6 mm and mafic phenocrysts with a max. length of 10 mm.</p>	
<p>SKN19 LIGHT</p>	<p>White/light grey in colour and mildly vesicular. No differences in vesicularity between SKN19 LIGHT and SKN19 DARK. Porphyritic with an aphanitic fine-grained groundmass. Felsic phenocrysts and mafic phenocrysts with a max. length of 7 mm.</p>	
<p>SK20</p>	<p>Dark grey in colour and mildly vesicular. Porphyritic with an aphanitic fine-grained groundmass. Felsic phenocrysts with a max. length of 4 mm. Two 7 mm x 4 mm inclusions of lighter grey material with felsic and mafic phenocrysts in a fine-grained, aphanitic groundmass.</p>	

SK21	<p>Dark grey in colour with few to no vesicles. Homogeneous sample. Porphyritic with a fine-grained groundmass. Felsic phenocrysts with a max. length 5mm.</p>	
SK30	<p>Very dark grey in colour. Porphyritic with a fine-grained aphanitic groundmass. Felsic and mafic phenocrysts, with an approximate 70:30 ratio. Feldspar and mafic phenocrysts with a max. length of 4 mm. Denser than other 'SK' samples.</p>	
SK31	<p>Light grey to brownish in colour and highly vesicular. Porphyritic with a fine-grained aphanitic groundmass. Equal amounts of felsic and mafic phenocrysts with a max. length of 4 mm. Colour variation across sample, small amount of streakiness with no change in phenocrysts or vesicularity.</p>	

Appendix 5 – Thin section scans

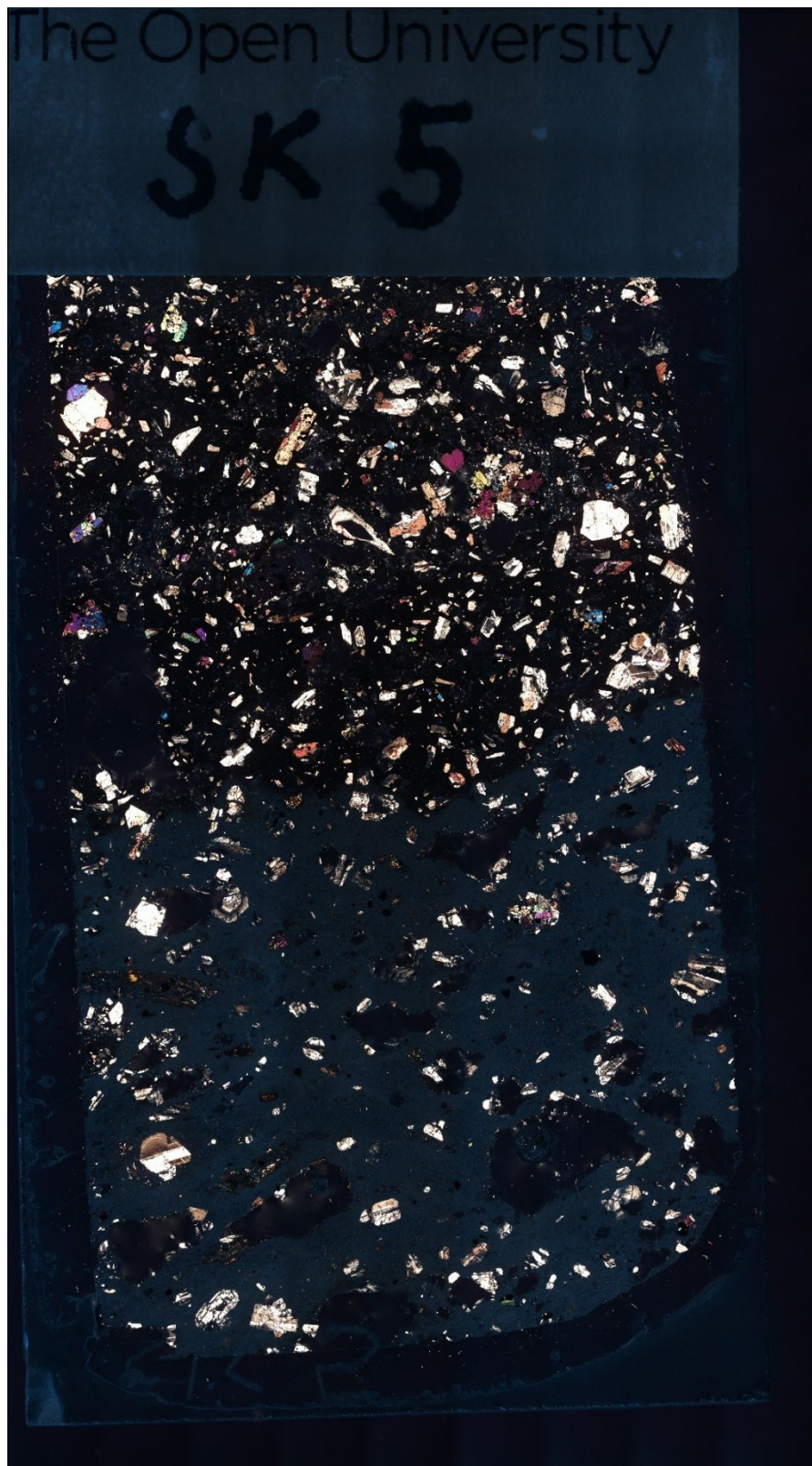
SK1



SK1E



SK5



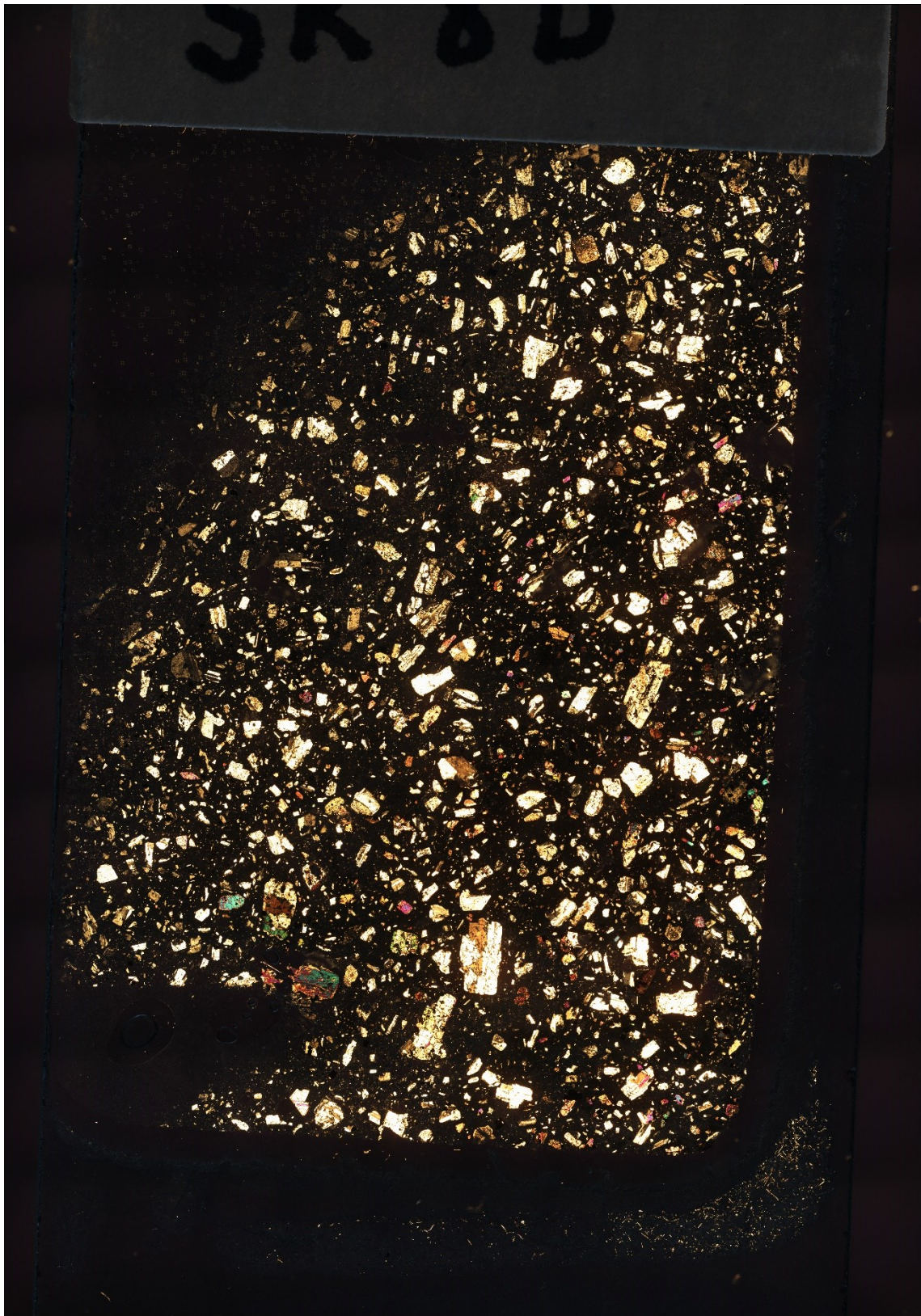
SK5D



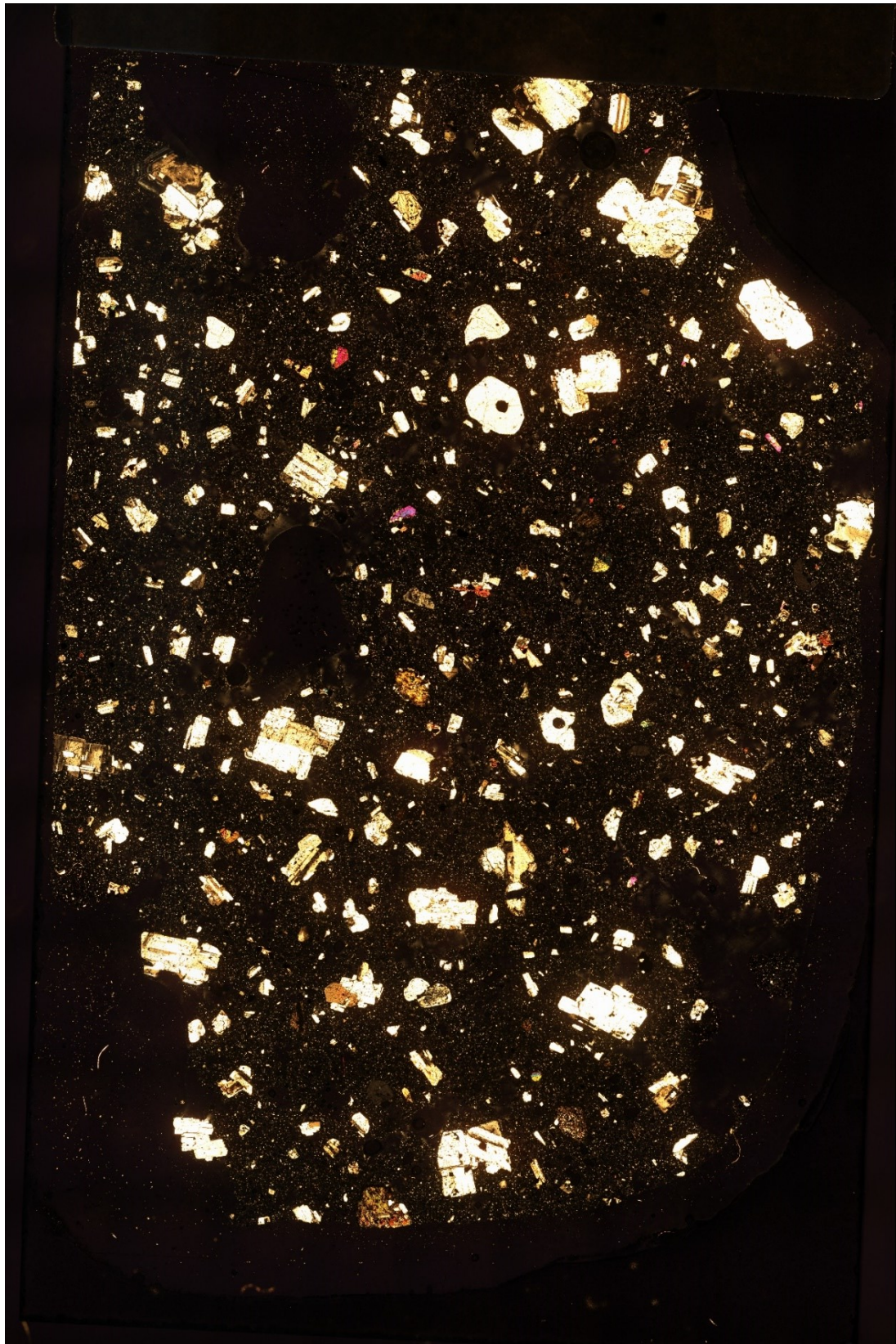
SK8 Banded



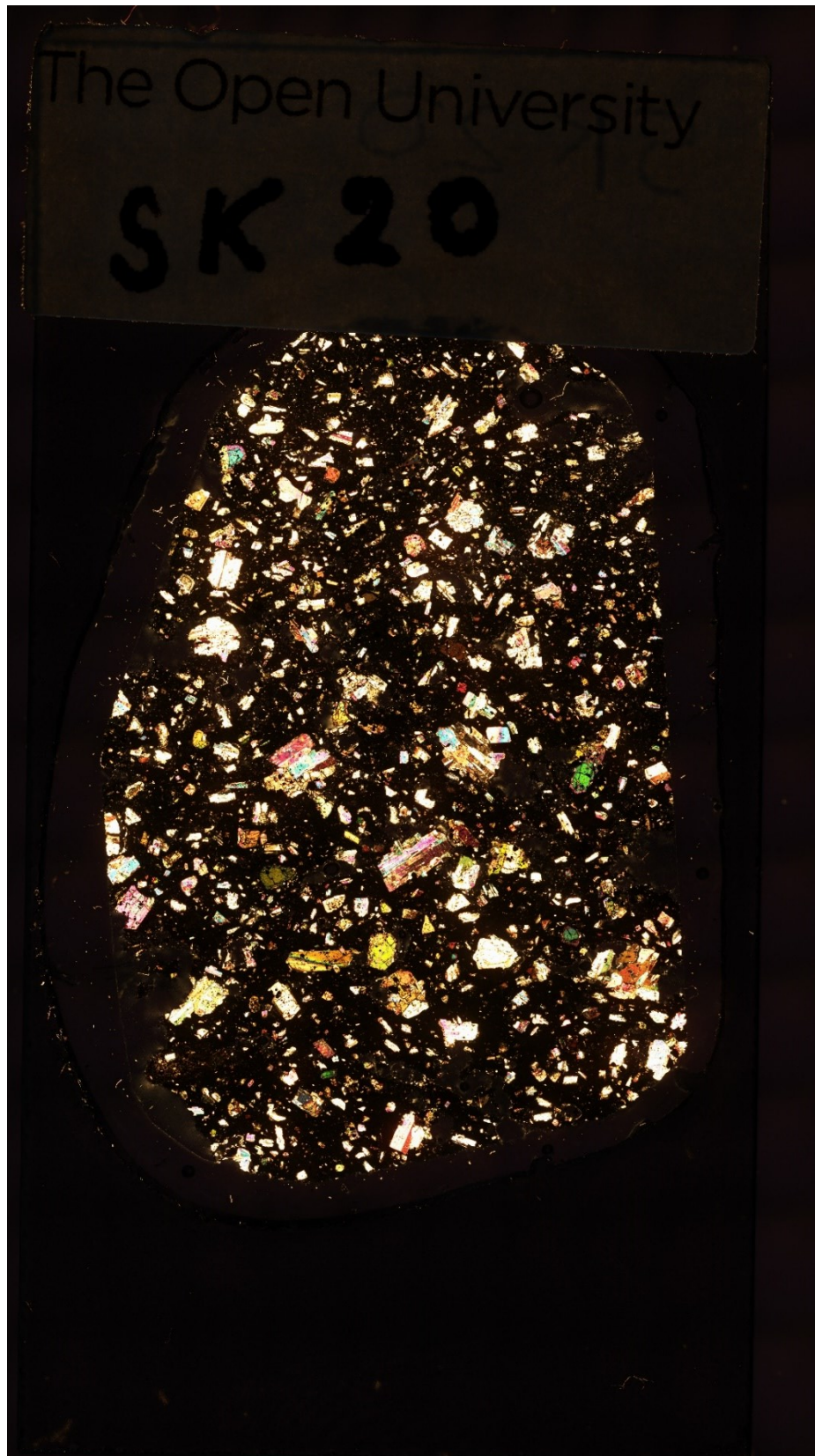
SK8D



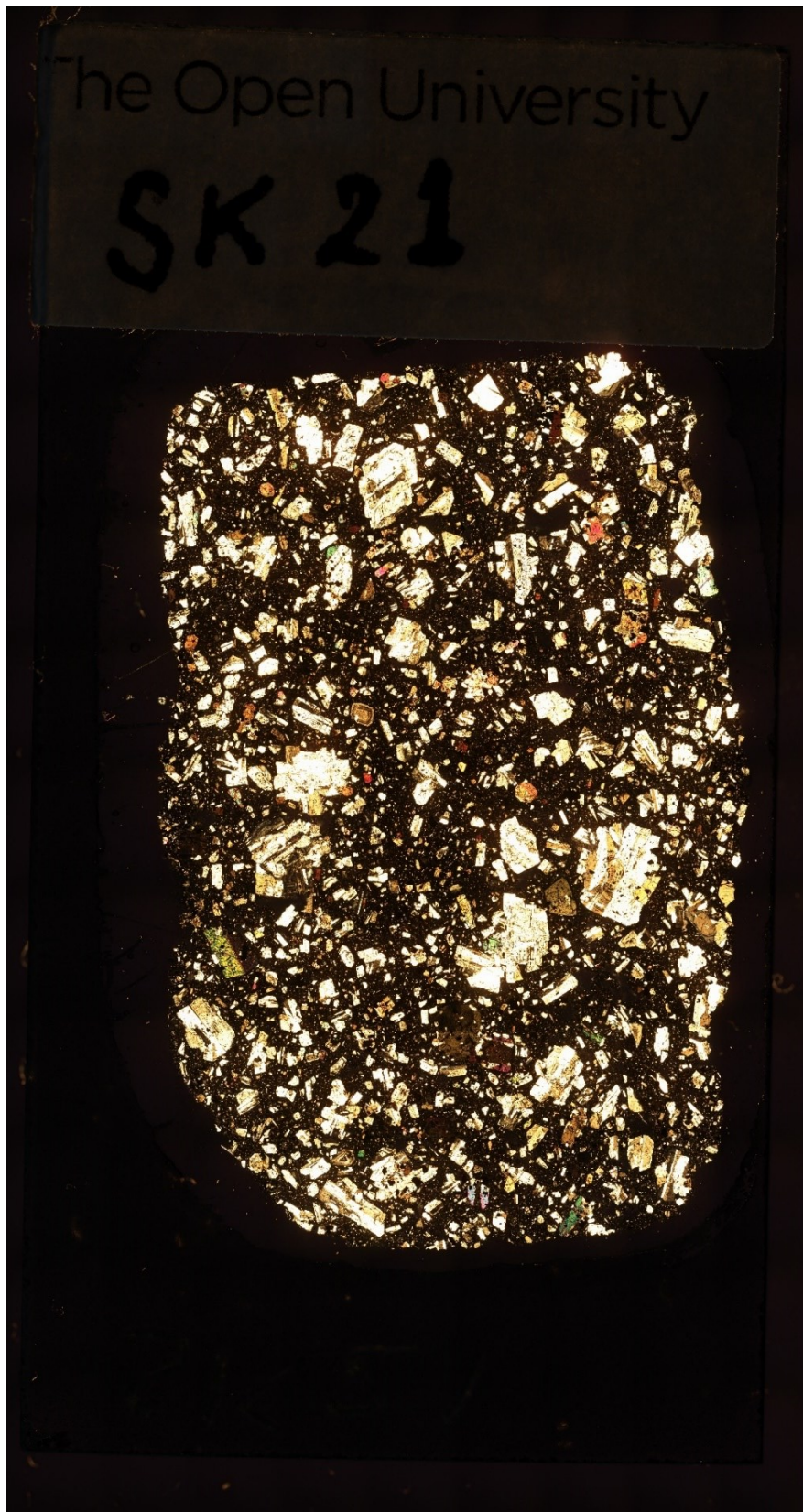
SK8L



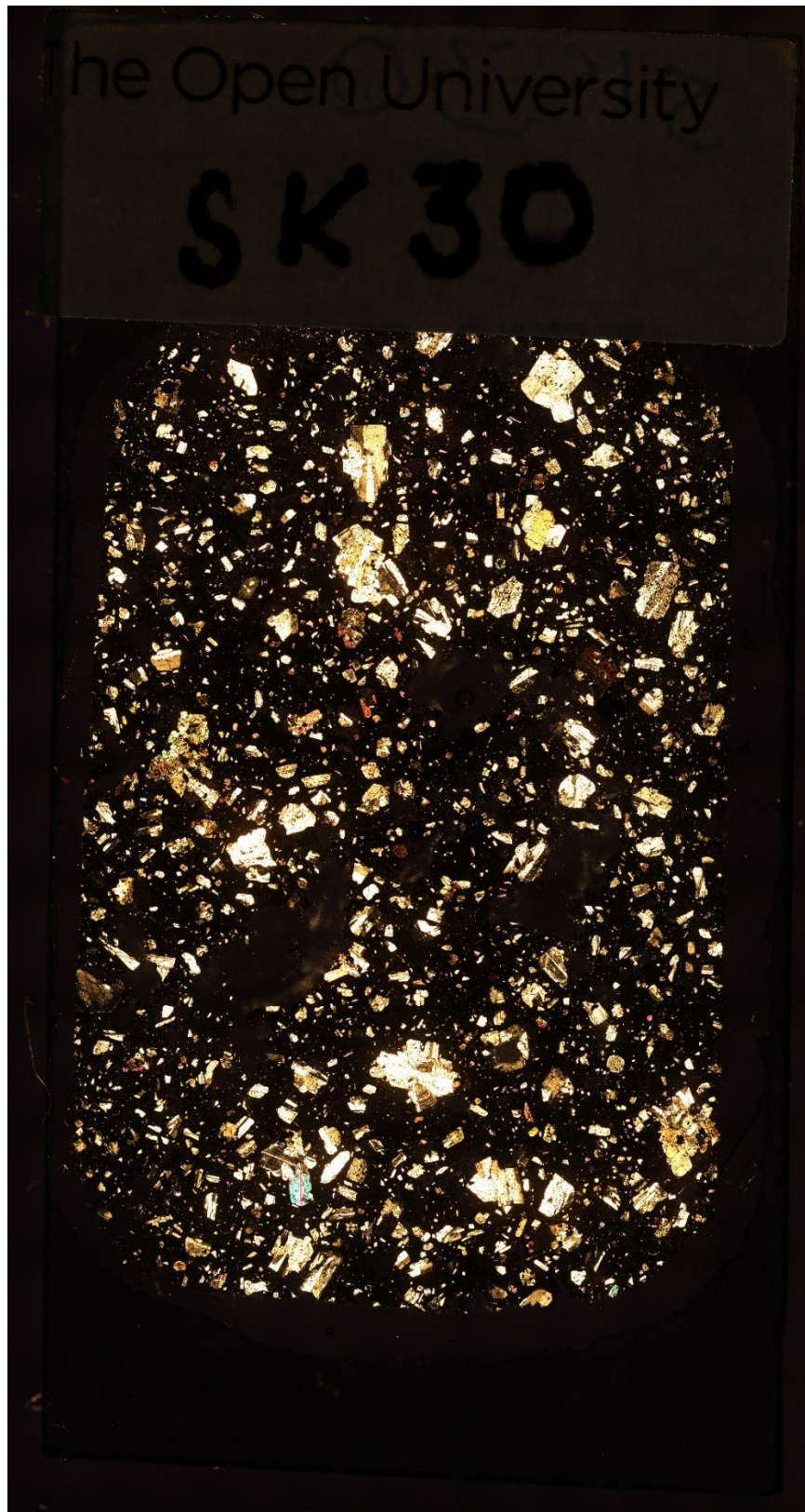
SK20



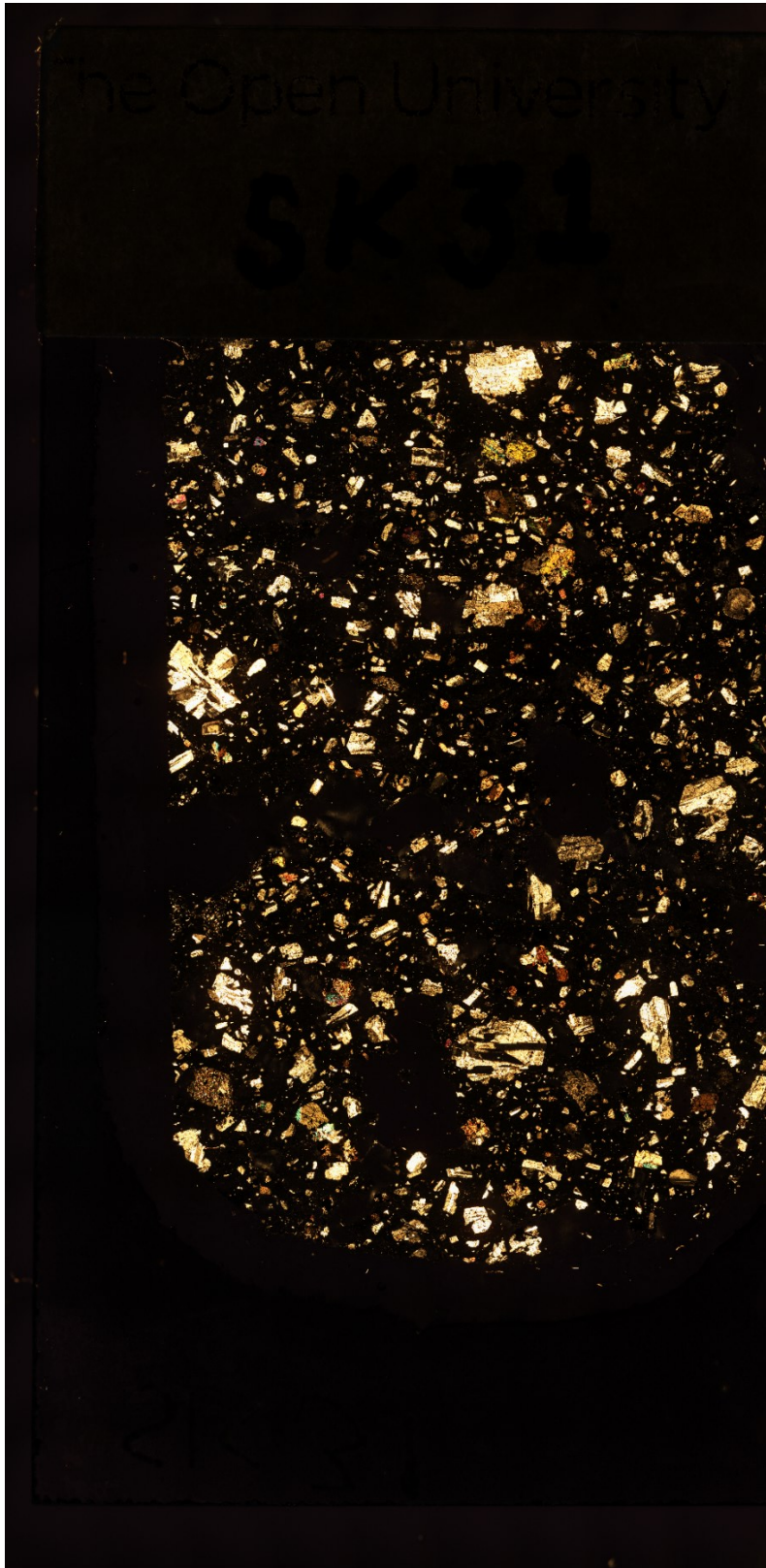
SK21



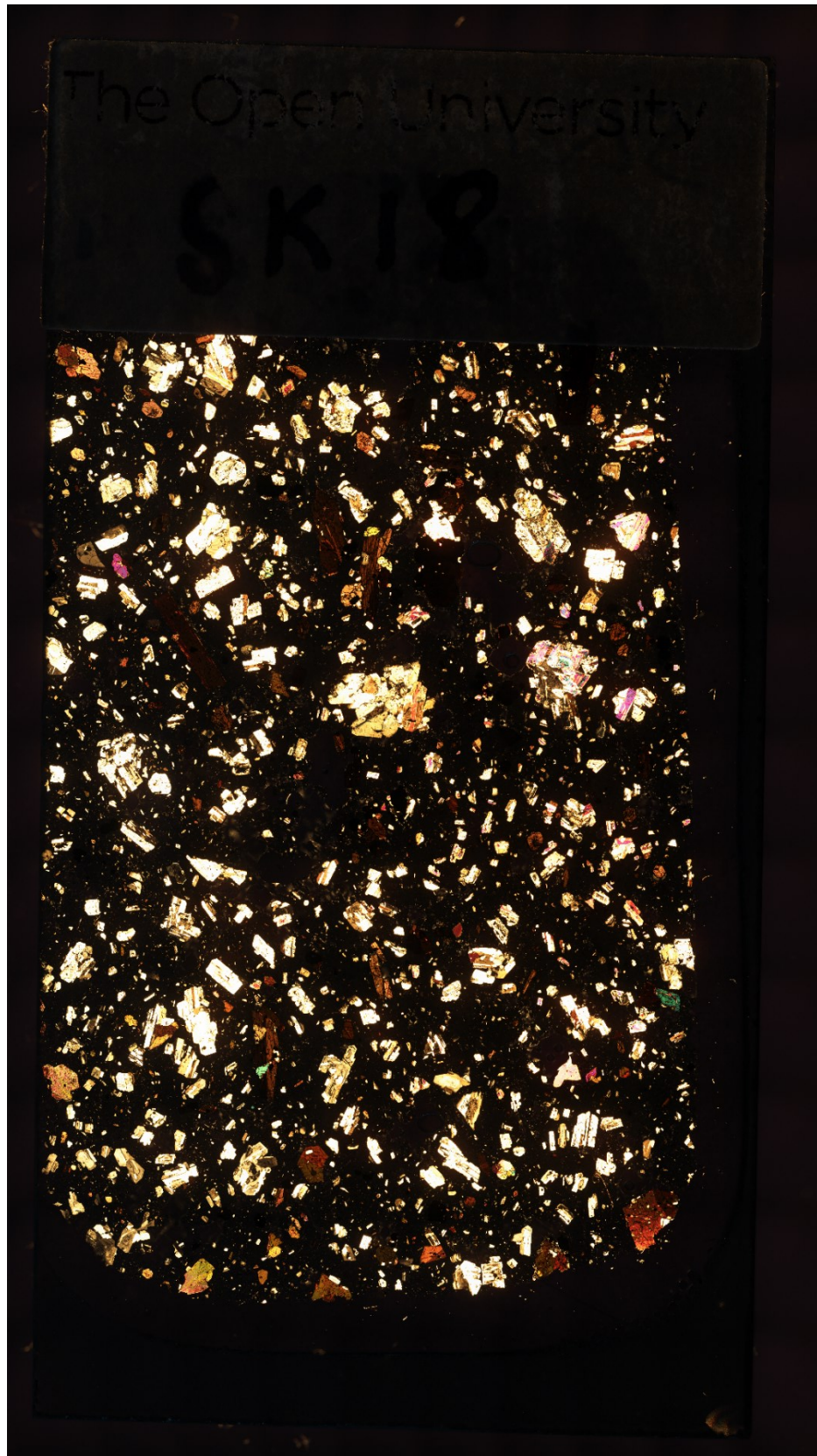
SK30



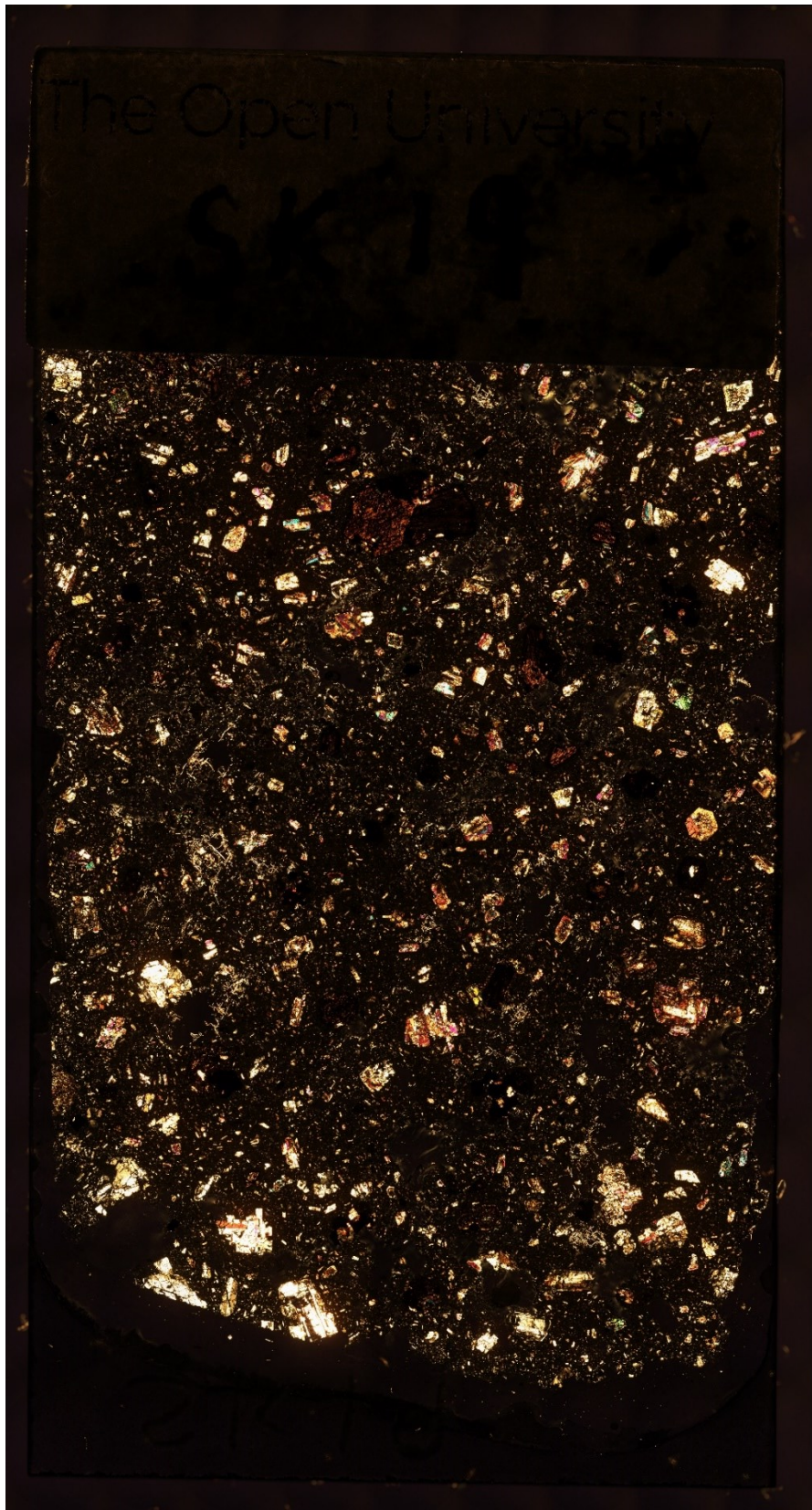
SK31



SKN18



SKN19



Appendix 6 - XRF whole rock major element data

Raw data	Result type	SiO2	TiO2	Al2O3	Fe2O3	Mn3O4	MgO	CaO	Na2O	K2O	P2O5	SO3	V2O5	Cr2O3	SrO	ZrO2	BaO	NiO	CuO	ZnO	PbO	HfO2	LOI	SUM
Sample name		Si	Ti	Al	Fe	Mn	Mg	Ca	Na	K	P	S	V	Cr	Sr	Zr	Ba	Ni	Cu	Zn	Pb	Hf		
		(%)	(%)	(%)	(%)	(%)	(%)	(%)	(%)	(%)	(%)	(%)	(%)	(%)	(%)	(%)	(%)	(%)	(%)	(%)	(%)	(%)	(%)	(%)
SK1G	Concentration	59.679	0.527	17.166	7.357	0.225	2.202	6.272	3.513	0.500	0.146	0.007	0.012	0.002	0.024	0.006	0.014	0.000	0.002	0.008	0.010	0.002	1.205	98.871
SK1W	Concentration	61.090	0.473	16.792	6.712	0.217	1.889	5.670	3.591	0.543	0.143	0.002	0.011	0.000	0.025	0.007	0.011	0.002	0.001	0.007	0.010	0.003	1.756	98.945
SK5-DARK	Concentration	58.628	0.748	18.222	8.721	0.219	3.429	7.713	3.596	0.535	0.103	0.017	0.028	0.004	0.022	0.005	0.015	0.000	0.004	0.008	0.001	0.000	0.302	102.320
SK5-DARK/3	Concentration	58.684	0.761	18.332	8.622	0.220	3.250	7.682	3.636	0.538	0.102	0.015	0.026	0.001	0.029	0.004	0.014	0.001	0.002	0.007	0.001	0.002	0.302	102.225
SK5-DARK/2	Concentration	58.643	0.744	18.496	8.568	0.212	3.264	7.744	3.575	0.529	0.104	0.015	0.026	0.001	0.027	0.004	0.016	0.001	0.002	0.008	0.000	0.002	0.302	102.277
SK5-LIGHT	Concentration	63.198	0.456	16.154	5.311	0.156	1.907	5.138	4.750	1.088	0.086	0.115	0.013	0.000	0.013	0.010	0.027	0.001	0.002	0.006	0.001	0.002	2.773	101.199
SK5-LIGHT/3	Concentration	63.877	0.453	16.315	5.344	0.154	1.891	5.163	4.860	1.103	0.096	0.113	0.013	0.001	0.032	0.009	0.026	0.001	0.000	0.005	0.001	0.002	2.773	102.226
SK5-LIGHT/2	Concentration	63.799	0.447	16.224	5.288	0.155	1.879	5.150	4.789	1.102	0.092	0.111	0.015	0.001	0.026	0.008	0.028	0.002	0.001	0.005	0.002	0.000	2.773	101.893
SK8-DARK	Concentration	58.591	0.777	18.172	8.713	0.217	3.289	7.654	3.564	0.554	0.110	0.009	0.028	0.000	0.024	0.006	0.012	0.000	0.002	0.008	0.001	0.002	0.004	101.733
SK8-LIGHT	Concentration	62.234	0.637	17.462	7.208	0.193	2.590	6.514	3.696	0.893	0.099	0.001	0.022	0.002	0.024	0.010	0.024	0.000	0.003	0.007	0.003	0.002	0.544	102.164
SK10	Concentration	56.949	0.631	16.975	7.694	0.244	2.884	8.618	3.550	0.604	0.117	0.007	0.020	0.000	0.040	0.008	0.013	0.001	0.002	0.016	0.007	0.001	0.398	98.777

SK11	Concentration	59.240	0.563	17.417	7.685	0.224	2.383	6.575	3.515	0.482	0.138	0.037	0.013	-	0.002	0.032	0.006	0.017	-	0.002	0.001	0.008	0.011	0.001	1.775	100.117
SK12	Concentration	59.321	0.584	16.918	6.967	0.198	2.295	6.319	3.556	0.630	0.098	0.028	0.019	-	0.001	0.020	0.006	0.016	-	0.002	0.002	0.007	0.006	0.003	2.425	99.409
SK13	Concentration	59.141	0.626	17.396	7.232	0.192	2.409	6.915	3.412	0.591	0.098	0.009	0.020	-	0.002	0.026	0.003	0.016	-	0.001	0.002	0.007	0.006	0.001	1.049	99.146
SKN14	Concentration	54.302	0.609	19.162	7.386	0.183	3.013	7.480	3.166	0.719	0.089	0.052	0.028	-	0.003	0.036	0.006	0.020	-	0.001	0.003	0.008	0.008	0.002	3.180	99.444
SKN15	Concentration	59.545	0.548	18.267	6.487	0.159	3.074	7.440	3.096	0.905	0.075	0.014	0.026	-	0.001	0.032	0.005	0.021	-	0.001	0.002	0.007	0.007	0.000	2.755	102.463
SKN16	Concentration	57.713	0.511	16.831	6.246	0.148	3.379	6.912	3.130	1.111	0.079	0.069	0.028	-	0.002	0.035	0.006	0.023	-	0.001	0.005	0.007	0.009	0.001	3.330	99.568
SK20	Concentration	58.899	0.791	18.161	8.906	0.219	3.379	7.738	3.459	0.523	0.104	0.001	0.030	-	0.001	0.030	0.007	0.014	-	0.000	0.005	0.007	0.000	0.002	0.276	102.548
SK21	Concentration	57.240	0.767	17.939	8.731	0.215	3.073	7.677	3.234	0.499	0.103	0.001	0.027	-	0.001	0.031	0.004	0.014	-	0.000	0.003	0.007	0.007	0.001	0.076	99.494
SK30	Concentration	57.197	0.754	17.566	8.558	0.213	3.116	7.533	3.444	0.532	0.101	0.030	0.027	-	0.000	0.022	0.004	0.014	-	0.002	0.001	0.006	0.007	0.000	0.585	99.708
SK31	Concentration	57.527	0.753	17.375	8.545	0.213	3.098	7.404	3.251	0.577	0.102	0.004	0.025	-	0.002	0.022	0.004	0.012	-	0.002	0.001	0.007	0.007	0.003	0.547	99.465
SK31/2	Concentration	57.384	0.760	17.368	8.574	0.211	3.082	7.423	3.247	0.564	0.100	0.007	0.025	-	0.002	0.028	0.007	0.013	-	0.002	0.001	0.008	0.006	0.004	0.547	99.347
SK31/3	Concentration	57.386	0.749	17.390	8.548	0.206	3.096	7.405	3.253	0.570	0.101	0.006	0.029	-	0.000	0.018	0.007	0.013	-	0.001	0.001	0.007	0.006	0.002	0.547	99.335
SKN17	Concentration	63.810	0.468	17.098	5.518	0.163	2.233	6.208	3.569	1.218	0.093	0.024	0.017	-	0.003	0.028	0.005	0.029	-	0.000	0.004	0.005	0.004	0.001	1.681	102.177
SKN17/2	Concentration	63.216	0.463	17.050	5.581	0.168	2.335	6.246	3.523	1.187	0.096	0.022	0.017	-	0.001	0.029	0.007	0.031	-	0.002	0.002	0.005	0.002	0.001	1.681	101.659
SKN17/3	Concentration	62.943	0.479	17.057	5.929	0.163	2.326	6.299	3.504	1.170	0.100	0.020	0.018	-	0.002	0.026	0.007	0.029	-	0.001	0.002	0.007	0.000	0.003	1.681	101.758
SKN18	Concentration	64.046	0.486	17.053	5.804	0.155	2.200	6.111	3.703	1.137	0.098	0.012	0.018	-	0.001	0.026	0.008	0.026	-	0.001	0.004	0.006	0.003	0.002	0.781	101.677

SKN19-DARK	Concentration	56.554	0.569	17.480	6.771	0.151	3.289	7.282	4.538	1.075	0.082	0.253	0.033	0.002	0.033	0.006	0.021	0.001	0.006	0.007	0.000	0.000	3.782	101.935		
SKN19-LIGHT	Concentration	60.579	0.540	18.296	6.459	0.156	2.731	7.310	3.491	1.187	0.083	0.035	0.027	0.000	0.038	0.005	0.026	-	0.001	0.006	0.007	0.003	-	0.002	1.256	102.232

Appendix 7 - Normalised XRF whole rock major element data

Normalised data	Result type	SiO2	TiO2	Al2O3	Fe2O3	Mn3O4	MgO	CaO	Na2O	K2O	P2O5	SO3	V2O5	Cr2O3	SrO	ZrO2	BaO	NiO	CuO	ZnO	PbO	HfO2	LOI	SUM	
Sample name		Si	Ti	Al	Fe	Mn	Mg	Ca	Na	K	P	S	V	Cr	Sr	Zr	Ba	Ni	Cu	Zn	Pb	Hf			
		(%)	(%)	(%)	(%)	(%)	(%)	(%)	(%)	(%)	(%)	(%)	(%)	(%)	(%)	(%)	(%)	(%)	(%)	(%)	(%)	(%)	(%)	(%)	
SK1G	Concentration	60.360	0.533	17.362	7.441	0.228	2.227	6.344	3.553	0.506	0.148	0.007	0.012	-	0.002	0.024	0.006	0.014	0.000	0.002	0.008	0.010	0.002	1.219	100.000
SK1W	Concentration	61.742	0.478	16.971	6.784	0.219	1.909	5.730	3.629	0.549	0.145	0.002	0.011	0.000	0.025	0.007	0.011	0.002	0.001	0.007	0.010	0.003	1.774	100.000	
SK5-DARK	Concentration	57.299	0.731	17.809	8.523	0.214	3.351	7.538	3.514	0.523	0.101	0.017	0.027	0.004	0.022	0.005	0.015	0.000	0.004	0.008	0.001	0.000	0.295	100.000	
SK5-DARK/3	Concentration	57.407	0.744	17.933	8.434	0.215	3.179	7.515	3.557	0.526	0.100	0.015	0.025	0.001	0.028	0.004	0.014	0.001	0.002	0.007	0.001	0.002	0.295	100.000	
SK5-DARK/2	Concentration	57.338	0.727	18.084	8.377	0.207	3.191	7.572	3.495	0.517	0.102	0.015	0.025	0.001	0.026	0.004	0.016	0.001	0.002	0.008	0.000	0.002	0.295	100.000	
SK5-LIGHT	Concentration	62.449	0.451	15.963	5.248	0.154	1.884	5.077	4.694	1.075	0.085	0.114	0.013	0.000	0.013	0.010	0.027	0.001	0.002	0.006	0.001	0.002	2.740	100.000	
SK5-LIGHT/3	Concentration	62.486	0.443	15.960	5.228	0.151	1.850	5.051	4.754	1.079	0.094	0.111	0.013	0.001	0.031	0.009	0.025	0.001	0.000	0.005	0.001	0.002	2.713	100.000	
SK5-LIGHT/2	Concentration	62.614	0.439	15.923	5.190	0.152	1.844	5.054	4.700	1.082	0.090	0.109	0.015	0.001	0.026	0.008	0.027	0.002	0.001	0.005	0.002	0.000	2.722	100.000	
SK8-DARK	Concentration	57.593	0.764	17.862	8.565	0.213	3.233	7.524	3.503	0.545	0.108	0.009	0.028	0.000	0.024	0.006	0.012	0.000	0.002	0.008	0.001	0.002	0.004	100.000	
SK8-LIGHT	Concentration	60.916	0.624	17.092	7.055	0.189	2.535	6.376	3.618	0.874	0.097	0.001	0.022	0.002	0.023	0.010	0.023	0.000	0.003	0.007	0.003	0.002	0.533	100.000	
SK10	Concentration	57.654	0.639	17.185	7.789	0.247	2.920	8.725	3.594	0.611	0.118	0.007	0.020	0.000	0.040	0.008	0.013	0.001	0.002	0.016	0.007	0.001	0.403	100.000	

SK11	Concentration	59.171	0.562	17.397	7.676	0.224	2.380	6.567	3.511	0.481	0.138	0.037	0.013	-	0.002	0.032	0.006	0.017	-	0.002	0.001	0.008	0.011	-	0.001	1.773	100.000
SK12	Concentration	59.673	0.587	17.019	7.008	0.199	2.309	6.357	3.577	0.634	0.099	0.028	0.019	-	0.001	0.020	0.006	0.016	-	0.002	0.002	0.007	0.006	-	0.003	2.440	100.000
SK13	Concentration	59.650	0.631	17.546	7.294	0.194	2.430	6.975	3.441	0.596	0.099	0.009	0.020	-	0.002	0.026	0.003	0.016	-	0.001	0.002	0.007	0.006	-	0.001	1.058	100.000
SK14	Concentration	54.605	0.612	19.269	7.427	0.184	3.030	7.522	3.184	0.723	0.089	0.052	0.028	-	0.003	0.036	0.006	0.020	-	0.001	0.003	0.008	0.008	-	0.002	3.198	100.000
SK15	Concentration	58.114	0.535	17.828	6.331	0.155	3.000	7.261	3.022	0.883	0.073	0.014	0.025	-	0.001	0.031	0.005	0.020	-	0.001	0.002	0.007	0.007	-	0.000	2.689	100.000
SK16	Concentration	57.964	0.513	16.904	6.273	0.149	3.394	6.942	3.144	1.116	0.079	0.069	0.028	-	0.002	0.035	0.006	0.023	-	0.001	0.005	0.007	0.009	-	0.001	3.344	100.000
SK20	Concentration	57.436	0.771	17.710	8.685	0.214	3.295	7.546	3.373	0.510	0.101	0.001	0.029	-	0.001	0.029	0.007	0.014	-	0.000	0.005	0.007	0.000	-	0.002	0.269	100.000
SK21	Concentration	57.531	0.771	18.030	8.775	0.216	3.089	7.716	3.250	0.502	0.104	0.001	0.027	-	0.001	0.031	0.004	0.014	-	0.000	0.003	0.007	0.007	-	0.001	0.076	100.000
SK30	Concentration	57.365	0.756	17.617	8.583	0.214	3.125	7.555	3.454	0.534	0.101	0.030	0.027	-	0.000	0.022	0.004	0.014	-	0.002	0.001	0.006	0.007	-	0.000	0.587	100.000
SK31	Concentration	57.836	0.757	17.468	8.591	0.214	3.115	7.444	3.268	0.580	0.103	0.004	0.025	-	0.002	0.022	0.004	0.012	-	0.002	0.001	0.007	0.007	-	0.003	0.550	100.000
SK31/2	Concentration	57.761	0.765	17.482	8.630	0.212	3.102	7.472	3.268	0.568	0.101	0.007	0.025	-	0.002	0.028	0.007	0.013	-	0.002	0.001	0.008	0.006	-	0.004	0.551	100.000
SK31/3	Concentration	57.770	0.754	17.506	8.605	0.207	3.117	7.455	3.275	0.574	0.102	0.006	0.029	-	0.000	0.018	0.007	0.013	-	0.001	0.001	0.007	0.006	-	0.002	0.551	100.000
SKN17	Concentration	62.450	0.458	16.734	5.400	0.160	2.185	6.076	3.493	1.192	0.091	0.023	0.017	-	0.003	0.027	0.005	0.028	-	0.000	0.004	0.005	0.004	-	0.001	1.645	100.000
SKN17/2	Concentration	62.184	0.455	16.772	5.490	0.165	2.297	6.144	3.466	1.168	0.094	0.022	0.017	-	0.001	0.029	0.007	0.030	-	0.002	0.002	0.005	0.002	-	0.001	1.654	100.000
SKN17/3	Concentration	61.855	0.471	16.762	5.827	0.160	2.286	6.190	3.443	1.150	0.098	0.020	0.018	-	0.002	0.026	0.007	0.028	-	0.001	0.002	0.007	0.000	-	0.003	1.652	100.000
SKN18	Concentration	62.990	0.478	16.772	5.708	0.152	2.164	6.010	3.642	1.118	0.096	0.012	0.018	-	0.001	0.026	0.008	0.026	-	0.001	0.004	0.006	0.003	-	0.002	0.768	100.000

SKN19-DARK	Concentration	55.481	0.558	17.148	6.642	0.148	3.227	7.144	4.452	1.055	0.080	0.248	0.032	0.002	0.032	0.006	0.021	0.001	0.006	0.007	0.000	0.000	3.710	100.000		
SKN19-LIGHT	Concentration	59.256	0.528	17.896	6.318	0.153	2.671	7.150	3.415	1.161	0.081	0.034	0.026	0.000	0.037	0.005	0.025	-	0.001	0.006	0.007	0.003	-	0.002	1.229	100.000

Appendix 8 - Plagioclase phenocryst compositions (An, Ab, Or) calculated from microprobe data

		1	2	3	4	5	6	7	8	9	10	11	12	13	14	15
SK1 pheno2	An	87.34	91.67	89.36	92.52	64.73	58.75	66.60	53.79	73.15	62.84	58.15	57.95	55.71	53.56	51.91
	Ab	12.61	8.30	10.59	7.41	35.09	40.99	33.22	35.05	26.68	36.93	41.58	41.76	43.88	46.13	47.38
	Or	0.05	0.03	0.05	0.06	0.18	0.26	0.18	11.16	0.17	0.23	0.27	0.28	0.41	0.31	0.71
SK1 pheno4	An	52.66	54.19	58.00	54.37	54.62	56.26	64.03	56.64	63.24	71.33	71.17	72.29	61.03	66.15	55.73
	Ab	46.95	45.49	41.42	45.29	45.05	43.40	35.48	43.06	36.54	28.48	28.68	27.55	38.72	33.63	43.97
	Or	0.39	0.32	0.58	0.35	0.33	0.35	0.49	0.30	0.22	0.19	0.15	0.16	0.26	0.22	0.31
SK5D pheno1	An	74.00	74.71	68.90	64.03	75.88	64.37	64.20	70.71	67.50	57.66	62.48	64.79	61.14	59.70	72.37
	Ab	25.41	24.90	30.47	35.63	23.69	35.33	35.50	29.07	32.19	41.83	37.18	34.89	38.47	39.87	27.43
	Or	0.59	0.38	0.62	0.34	0.43	0.30	0.30	0.23	0.31	0.51	0.34	0.32	0.39	0.43	0.20
SK5D pheno3	An	67.06	63.30	67.02	71.99	66.96										
	Ab	32.67	36.44	32.70	27.77	32.70										
	Or	0.27	0.26	0.27	0.24	0.34										
SK5D pheno4	An	70.21	64.64	66.01	70.28											
	Ab	29.60	35.05	33.67	29.46											
	Or	0.19	0.31	0.32	0.27											
SK20 pheno1	An	50.16	50.70	43.59	47.40	53.06	48.20	45.69	54.43	53.47	47.81	49.34	45.46	44.25	44.92	55.23
	Ab	49.12	48.57	55.11	51.81	45.91	51.03	53.45	44.95	45.90	51.46	49.93	53.63	54.85	54.22	44.15
	Or	0.72	0.72	1.30	0.80	1.03	0.77	0.86	0.62	0.63	0.72	0.73	0.91	0.90	0.86	0.61
SK5D pheno4	An	67.30	69.32	59.31	65.54	58.84	60.13	58.74	61.43	63.87	76.13	81.85	84.82	73.20	82.25	75.42
	Ab	32.43	30.44	40.34	34.15	40.76	39.54	40.87	37.61	35.69	23.67	18.01	15.06	11.85	17.69	24.41
	Or	0.27	0.24	0.36	0.32	0.39	0.32	0.38	0.96	0.44	0.20	0.14	0.12	14.96	0.07	0.17
SK30 pheno1	An	68.12	65.46	65.81	61.80	62.96	61.58	57.12	62.83	64.79	65.34	63.67	68.84	61.17	69.63	78.46

	Ab	31.59	34.21	33.89	37.82	36.70	38.04	42.51	36.79	34.90	34.38	35.97	30.95	38.45	30.04	21.25
	Or	0.29	0.32	0.30	0.38	0.34	0.38	0.37	0.38	0.31	0.29	0.36	0.21	0.38	0.32	0.29
SK30 pheno4	An	58.43	64.43	70.71	56.28	54.84	73.50	64.66	66.10	61.60	73.28	64.57	59.97	62.49	69.39	
	Ab	41.21	35.24	29.05	43.41	41.09	26.24	35.06	33.53	38.06	26.40	35.09	39.67	37.16	30.35	
	Or	0.36	0.33	0.25	0.31	4.07	0.26	0.28	0.37	0.34	0.32	0.34	0.36	0.35	0.26	
SK30 pheno1	An	70.47	74.21	69.77	67.84	68.21										
	Ab	29.16	25.50	30.03	31.79	31.50										
	Or	0.37	0.29	0.20	0.37	0.29										
SK30 pheno4	An	52.42	65.46	51.31	62.39	59.37	61.29	67.89	59.51	74.49	72.31	70.34	76.46	81.17	80.79	
	Ab	47.17	34.18	48.35	37.28	40.12	38.37	31.75	40.07	25.29	27.51	29.39	23.14	18.61	18.87	
	Or	0.41	0.35	0.35	0.33	0.51	0.34	0.36	0.42	0.22	0.17	0.27	0.40	0.22	0.34	
SKN18 pheno3	An	72.72	73.18	54.47	52.81	55.34	54.42									
	Ab	26.82	26.35	44.79	46.39	43.97	44.83									
	Or	0.45	0.47	0.74	0.80	0.69	0.75									
SKN18 pheno7	An	75.86	73.84	79.04	76.70	55.28	61.46	65.43	59.24	69.45	60.74	59.99	64.22	70.10	56.64	64.00
	Ab	23.82	25.75	20.69	22.99	43.94	37.95	34.03	40.10	30.15	38.65	39.42	35.25	29.53	42.69	35.18
	Or	0.32	0.41	0.27	0.30	0.78	0.59	0.54	0.66	0.41	0.61	0.59	0.53	0.36	0.67	0.82
SKN19 pheno1	An	53.31	77.23	75.37	57.70	75.81										
	Ab	45.92	22.44	24.30	41.65	23.89										
	Or	0.77	0.33	0.33	0.65	0.30										
SKN19 pheno2	An	64.92	55.09	60.38	56.75	61.61	56.41	62.63	68.79	62.26	61.66					
	Ab	34.65	44.20	39.03	42.59	37.85	42.90	36.85	30.78	37.17	37.81					
	Or	0.44	0.71	0.59	0.65	0.54	0.69	0.52	0.42	0.57	0.52					
SKN19 pheno3	An	82.45	82.45	83.83	78.07	69.95										
	Ab	17.31	17.31	15.92	21.63	29.61										
	Or	0.24	0.25	0.25	0.30	0.44										

Appendix 9 - Pyroxene phenocryst compositions (Wo, En, Fs) calculated from microprobe data

		1	2	3	4	5	6	7	8	9	10	11	12	13	14
SK1 pheno1	Wo	2.76	2.68	2.73	2.72	2.69	2.70	2.80	2.69	2.72					
	En	53.41	52.94	52.21	51.26	50.45	49.55	48.87	48.40	47.45					
	Fs	43.83	44.39	45.06	46.02	46.87	47.75	48.33	48.91	49.83					
SK1 pheno3	Wo	2.80	2.68	2.78	2.82	2.71									
	En	53.54	51.85	51.70	51.75	48.82									
	Fs	43.66	45.47	45.52	45.44	48.47									
SK1 pheno5	Wo	2.75	2.84	2.61	2.50	2.47									
	En	48.88	48.59	48.98	49.20	49.05									
	Fs	48.37	48.56	48.42	48.30	48.48									
SK5d pheno2	Wo	3.10	3.05	3.03	2.97	3.32	4.25	3.07	2.96	3.23	3.23				
	En	57.89	58.26	58.74	59.51	63.83	59.82	65.61	69.01	66.99	64.32				
	Fs	39.01	38.70	38.23	37.52	32.84	35.92	31.32	28.03	29.77	32.45				
SK20 pheno3	Wo	3.09	2.99	3.07	3.08	3.01	3.12	3.09	3.08	3.47	3.26				
	En	58.34	58.00	58.05	58.28	58.48	58.70	59.77	61.42	68.10	66.19				
	Fs	38.57	39.01	38.88	38.64	38.51	38.18	37.14	35.50	28.43	30.54				
SK20 pheno5	Wo	3.29	3.15	4.41	3.37										
	En	68.03	66.44	62.73	61.75										
	Fs	28.67	30.42	32.86	34.88										
SK20 pheno6	Wo	2.92	3.01	2.97	2.93	2.94	3.98	2.95	3.78	3.16					
	En	57.09	57.23	56.98	57.97	57.76	57.86	58.46	57.67	59.21					
	Fs	40.00	39.75	40.05	39.10	39.30	38.16	38.59	38.55	37.63					
SK30 pheno2	Wo	2.89	2.84	7.02	3.00	3.01	3.04	2.99	2.87	3.01	2.98	3.00	3.10	2.99	3.11

		En	58.54	58.85	58.04	59.08	59.02	59.17	59.10	59.42	59.53	59.73	59.29	59.27	60.40	66.30
		Fs	38.57	38.31	34.94	37.92	37.96	37.79	37.92	37.71	37.46	37.29	37.71	37.63	36.61	30.60
SK31 pheno3		Wo	56.92													
		En	7.24													
		Fs	35.85													
SK18 pheno1	zoned	Wo	24.50	24.33	24.65	24.24	23.74									
		En	45.67	46.34	45.53	46.34	44.79									
		Fs	29.83	29.33	29.82	29.42	31.47									
SK18 pheno2	zoned	Wo	24.09	24.65	24.51	23.86	51.93	23.94	24.82	24.11						
		En	45.92	44.62	45.19	46.39	22.40	45.73	44.81	46.67						
		Fs	29.99	30.72	30.29	29.75	25.66	30.32	30.37	29.22						
SK19 pheno2	zoned	Wo	0.06	0.01	0.06	0.04	0.00	0.05	0.03							
		En	3.02	3.00	1.34	1.70	2.46	2.77	2.83							
		Fs	96.92	96.99	98.60	98.26	97.54	97.18	97.14							

Appendix 10 - Microprobe analysis of plagioclase phenocryst compositions

SAMPLE	SiO2	TiO2	Al2O3	FeO	CaO	Na2O	K2O	MgO	MnO
SK1 pheno2	45.488	0.013	33.832	0.497	18.028	1.438	0.008	0.000	0.000
SK1 pheno2	44.566	-0.003	34.635	0.464	18.621	0.931	0.005	0.000	0.000
SK1 pheno2	44.972	0.020	34.283	0.451	18.233	1.194	0.009	0.000	0.000
SK1 pheno2	44.159	0.011	34.716	0.481	18.669	0.826	0.011	0.000	0.000
SK1 pheno2	51.321	-0.002	29.854	0.390	13.167	3.944	0.031	0.000	0.000
SK1 pheno2	52.890	0.037	28.892	0.386	12.037	4.641	0.046	0.000	0.000
SK1 pheno2	50.773	0.033	30.512	0.424	13.692	3.774	0.031	0.000	0.000
SK1 pheno2	13.532	0.066	3.919	0.935	1.668	0.601	0.291	0.000	0.000
SK1 pheno2	48.983	0.031	31.283	0.433	14.776	2.978	0.028	0.000	0.000
SK1 pheno2	51.899	-0.006	29.505	0.389	12.758	4.143	0.040	0.000	0.000
SK1 pheno2	53.243	0.002	28.679	0.360	11.833	4.675	0.047	0.000	0.000
SK1 pheno2	53.178	0.004	28.890	0.357	11.808	4.702	0.049	0.000	0.000
SK1 pheno2	53.619	0.011	28.378	0.337	11.306	4.921	0.070	0.000	0.000
SK1 pheno2	54.233	0.022	28.394	0.351	11.084	5.276	0.054	0.000	0.000
SK1 pheno2	56.014	0.016	26.730	0.587	10.200	5.144	0.117	0.000	0.000
SK1 pheno4	56.558	0.009	29.314	0.369	11.031	5.436	0.069	0.000	0.000
SK1 pheno4	54.147	0.013	28.059	0.391	11.041	5.122	0.054	0.000	0.000
SK1 pheno4	36.545	0.021	18.809	0.300	8.930	3.524	0.075	0.000	0.000
SK1 pheno4	54.084	-0.012	28.227	0.356	11.194	5.152	0.060	0.000	0.000
SK1 pheno4	54.231	0.033	28.215	0.340	11.209	5.109	0.058	0.000	0.000
SK1 pheno4	53.915	-0.008	28.417	0.388	11.444	4.878	0.059	0.000	0.000
SK1 pheno4	42.042	0.014	22.197	0.342	10.429	3.194	0.067	0.000	0.000
SK1 pheno4	53.631	0.014	28.420	0.356	11.622	4.882	0.052	0.000	0.000
SK1 pheno4	51.893	0.012	29.951	0.380	13.005	4.152	0.038	0.000	0.000
SK1 pheno4	49.763	0.019	31.125	0.411	14.502	3.200	0.032	0.000	0.000
SK1 pheno4	49.727	0.018	30.950	0.490	14.470	3.222	0.026	0.000	0.000
SK1 pheno4	49.548	0.008	31.177	0.496	14.678	3.091	0.028	0.000	0.000
SK1 pheno4	52.488	0.022	29.275	0.420	12.520	4.389	0.044	0.000	0.000
SK1 pheno4	51.075	-0.008	30.258	0.423	13.537	3.804	0.037	0.000	0.000
SK1 pheno4	53.583	0.002	28.402	0.387	11.361	4.953	0.053	0.000	0.000
SK5D zoned pheno1	52.373	0.034	30.145	0.784	14.324	2.718	0.096	0.121	0.029
SK5D zoned pheno1	49.399	0.006	31.170	0.565	14.879	2.741	0.064	0.051	0.011
SK5D zoned pheno1	52.025	0.035	31.599	0.680	13.953	3.410	0.106	0.116	0.008

SK5D zoned pheno1	51.945	0.020	29.647	0.513	12.773	3.928	0.057	0.054	0.006
SK5D zoned pheno1	50.170	0.019	29.682	0.572	13.422	2.316	0.064	0.040	0.020
SK5D zoned pheno1	52.384	0.027	29.908	0.486	12.823	3.889	0.050	0.058	0.007
SK5D zoned pheno1	53.522	0.008	30.658	0.509	13.063	3.992	0.051	0.043	0.014
SK5D zoned pheno1	49.785	0.008	31.015	0.488	14.190	3.224	0.038	0.024	0.007
SK5D zoned pheno1	50.929	-0.002	30.324	0.502	13.451	3.544	0.052	0.025	0.006
SK5D zoned pheno1	53.111	0.021	28.723	0.536	11.618	4.657	0.085	0.081	0.000
SK5D zoned pheno1	53.949	0.037	30.850	0.522	12.713	4.180	0.058	0.043	0.013
SK5D zoned pheno1	51.410	0.019	29.989	0.509	12.837	3.820	0.053	0.034	0.006
SK5D zoned pheno1	49.975	0.007	28.093	0.522	11.962	4.159	0.064	0.058	0.007
SK5D zoned pheno1	48.786	0.013	27.583	0.574	12.011	4.433	0.073	0.082	0.003
SK5D zoned pheno1	49.751	0.021	31.444	0.561	14.616	3.061	0.035	0.053	0.018
SK5D zoned pheno3	51.640	0.037	30.437	0.604	13.454	3.622	0.046	0.045	0.000
SK5D zoned pheno3	52.838	0.031	29.837	0.636	12.779	4.065	0.044	0.067	0.007
SK5D zoned pheno3	51.581	0.020	30.545	0.688	13.767	3.712	0.047	0.070	0.014
SK5D zoned pheno3	50.296	0.034	31.226	0.693	14.380	3.066	0.040	0.063	0.010
SK5D zoned pheno3	51.910	0.053	30.378	0.762	13.310	3.592	0.057	0.056	0.018
SK5D zoned pheno4	50.515	0.008	30.860	0.545	14.018	3.266	0.032	0.041	0.004
SK5D zoned pheno4	51.998	0.012	29.838	0.524	12.704	3.806	0.051	0.048	0.015
SK5D zoned pheno4	50.821	0.025	29.623	0.547	12.952	3.651	0.053	0.039	0.021
SK5D zoned pheno4	50.377	0.011	30.949	0.603	14.019	3.247	0.045	0.031	0.014
SK20 pheno1	56.308	0.028	28.298	0.186	10.454	5.658	0.126	-0.010	0.000
SK20 pheno1	56.292	0.028	28.215	0.181	10.385	5.497	0.124	-0.002	0.000
SK20 pheno1	58.314	0.031	25.546	0.169	8.489	5.931	0.213	-0.008	0.000
SK20 pheno1	56.983	-0.004	27.507	0.173	9.713	5.867	0.137	-0.008	0.000
SK20 pheno1	49.988	0.008	24.065	0.189	9.619	4.599	0.157	-0.006	0.000
SK20 pheno1	56.784	0.007	27.596	0.162	9.923	5.805	0.133	0.004	0.000
SK20 pheno1	57.387	0.007	27.367	0.174	9.437	6.101	0.148	-0.009	0.000
SK20 pheno1	55.191	-0.016	28.756	0.177	11.179	5.102	0.107	-0.005	0.000
SK20 pheno1	54.444	0.020	28.260	0.184	10.785	5.115	0.107	0.002	0.000
SK20 pheno1	55.256	-0.007	27.553	0.172	10.181	6.056	0.129	-0.008	0.000
SK20 pheno1	56.045	-0.015	28.061	0.182	10.076	5.634	0.125	0.000	0.000
SK20 pheno1	57.237	-0.001	27.119	0.192	9.225	6.014	0.154	-0.006	0.000
SK20 pheno1	57.459	-0.008	27.081	0.186	9.058	6.205	0.156	-0.025	0.000
SK20 pheno1	57.266	0.001	26.952	0.208	9.108	6.076	0.147	0.001	0.000
SK20 pheno1	54.469	0.023	27.812	0.759	11.238	4.965	0.105	0.088	0.000
SK20 pheno4	51.593	0.007	30.647	0.516	13.832	3.683	0.046	0.037	0.000
SK20 pheno4	51.375	0.018	30.765	0.526	14.003	3.398	0.041	0.040	0.000
SK20 pheno4	54.014	0.036	29.299	0.533	12.234	4.598	0.062	0.051	0.000

SK20 pheno4	52.537	0.025	30.119	0.529	13.210	3.803	0.053	0.049	0.000
SK20 pheno4	54.089	0.006	29.054	0.523	12.031	4.605	0.067	0.064	0.000
SK20 pheno4	53.616	0.015	29.449	0.516	12.435	4.519	0.056	0.037	0.000
SK20 pheno4	54.216	-0.014	28.907	0.522	12.014	4.620	0.066	0.035	0.000
SK20 pheno4	54.696	0.069	28.117	0.889	12.037	4.072	0.158	0.069	0.000
SK20 pheno4	52.863	0.029	29.502	0.659	12.938	3.995	0.075	0.064	0.000
SK20 pheno4	49.166	0.015	32.176	0.583	15.663	2.691	0.035	0.034	0.000
SK20 pheno4	47.673	0.030	33.053	0.585	16.821	2.046	0.024	0.020	0.000
SK20 pheno4	46.956	0.016	33.727	0.594	17.439	1.712	0.021	0.026	0.000
SK20 pheno4	19.130	0.422	4.157	5.822	2.442	0.218	0.419	0.099	0.000
SK20 pheno4	47.628	0.003	33.231	0.574	16.905	2.009	0.012	0.018	0.000
SK20 pheno4	49.332	0.029	31.809	0.658	15.455	2.764	0.030	0.045	0.000
SK30 pheno1	50.327	0.041	29.286	0.533	13.497	3.459	0.049	0.061	0.000
SK30 pheno1	52.154	0.022	30.209	0.546	13.321	3.848	0.055	0.043	0.000
SK30 pheno1	52.464	0.021	30.737	0.545	13.615	3.875	0.052	0.056	0.000
SK30 pheno1	52.946	0.041	30.100	0.542	12.814	4.334	0.066	0.063	0.000
SK30 pheno1	53.184	0.031	30.409	0.504	13.276	4.277	0.060	0.077	0.000
SK30 pheno1	53.987	0.026	30.110	0.538	12.795	4.368	0.066	0.050	0.000
SK30 pheno1	54.612	0.022	28.911	0.545	11.789	4.849	0.065	0.035	0.000
SK30 pheno1	53.067	0.026	29.571	0.569	12.758	4.128	0.065	0.066	0.000
SK30 pheno1	52.694	0.024	30.462	0.567	13.511	4.022	0.055	0.060	0.000
SK30 pheno1	52.138	0.045	30.449	0.591	13.417	3.901	0.050	0.052	0.000
SK30 pheno1	51.533	-0.007	29.903	0.557	13.153	4.107	0.062	0.093	0.000
SK30 pheno1	51.223	0.005	30.853	0.650	13.826	3.435	0.036	0.064	0.000
SK30 pheno1	53.484	0.018	29.771	0.697	12.650	4.394	0.066	0.067	0.000
SK30 pheno1	50.787	0.030	30.449	0.676	14.018	3.342	0.055	0.066	0.000
SK30 pheno1	48.282	0.027	31.919	0.746	15.832	2.370	0.049	0.130	0.000
SK30 pheno4	53.760	0.023	29.115	0.489	12.097	4.714	0.063	0.042	0.000
SK30 pheno4	52.020	0.045	30.051	1.576	13.081	3.954	0.056	0.094	0.000
SK30 pheno4	50.807	0.025	31.236	0.517	14.418	3.273	0.042	0.021	0.000
SK30 pheno4	58.616	0.011	32.572	0.524	12.442	5.303	0.057	0.061	0.000
SK30 pheno4	59.174	0.187	22.724	2.481	8.733	3.616	0.545	0.606	0.000
SK30 pheno4	49.861	0.057	31.904	0.574	15.124	2.984	0.046	0.045	0.000
SK30 pheno4	52.056	0.016	30.351	0.515	13.343	3.998	0.048	0.049	0.000
SK30 pheno4	51.724	0.044	30.368	0.539	13.484	3.780	0.063	0.030	0.000
SK30 pheno4	53.035	0.025	29.524	0.488	12.509	4.271	0.058	0.053	0.000
SK30 pheno4	67.360	0.573	11.933	5.694	3.016	2.257	1.395	1.282	0.000
SK30 pheno4	48.825	0.007	30.749	0.477	14.525	2.891	0.053	0.066	0.000
SK30 pheno4	52.108	0.041	30.425	0.527	13.227	3.972	0.059	0.032	0.000

SK30 pheno4	53.426	0.005	29.400	0.508	12.205	4.462	0.062	0.029	0.000
SK30 pheno4	53.024	0.012	29.769	0.529	12.760	4.193	0.060	0.047	0.000
SK30 pheno4	51.167	-0.014	30.931	0.544	14.207	3.434	0.045	0.057	0.000
SK31 zoned pheno1	50.620	-0.002	30.379	0.511	13.574	3.104	0.061	0.029	0.000
SK31 zoned pheno1	42.872	0.012	25.846	0.561	13.064	2.481	0.043	0.027	0.000
SK31 zoned pheno1	50.840	0.007	30.752	0.493	13.862	3.297	0.034	0.039	0.000
SK31 zoned pheno1	53.326	0.040	30.886	0.524	13.396	3.469	0.061	0.050	0.000
SK31 zoned pheno1	51.596	0.025	30.585	0.496	13.513	3.448	0.048	0.032	0.000
SK31 zoned pheno3	56.620	-0.013	28.380	0.435	10.707	5.324	0.071	0.029	0.000
SK31 zoned pheno3	53.349	0.006	31.426	0.485	13.314	3.842	0.060	0.034	0.000
SK31 zoned pheno3	60.013	0.023	33.271	0.496	11.763	6.126	0.067	0.064	0.000
SK31 zoned pheno3	50.450	0.015	26.937	0.448	11.787	3.892	0.052	0.032	0.000
SK31 zoned pheno3	50.882	0.011	27.055	0.436	11.449	4.275	0.083	0.049	0.000
SK31 zoned pheno3	53.640	-0.002	30.469	0.447	12.576	4.351	0.058	0.049	0.000
SK31 zoned pheno3	50.935	0.002	28.748	0.477	12.753	3.296	0.057	0.027	0.000
SK31 zoned pheno3	52.401	0.002	28.138	0.469	11.413	4.247	0.067	0.036	0.000
SK31 zoned pheno3	41.402	0.007	26.278	0.458	13.627	2.556	0.034	0.040	0.000
SK31 zoned pheno3	47.644	0.018	31.401	0.481	14.451	3.038	0.029	0.046	0.000
SK31 zoned pheno3	51.858	0.030	30.545	0.526	13.464	3.109	0.043	0.047	0.000
SK31 zoned pheno3	48.753	0.044	31.839	0.612	15.278	2.555	0.067	0.031	0.000
SK31 zoned pheno3	45.880	-0.001	29.358	0.564	15.146	1.919	0.034	0.019	0.000
SK31 zoned pheno3	30.996	0.014	18.563	0.532	12.661	1.634	0.045	0.015	0.000
SK18 zoned pheno3	49.823	-0.015	31.787	0.293	14.623	2.980	0.077	0.016	0.000
SK18 zoned pheno3	49.629	0.029	31.805	0.275	14.639	2.913	0.079	-0.007	0.000
SK18 zoned pheno3	54.490	-0.004	28.670	0.230	11.022	5.008	0.127	0.004	0.000
SK18 zoned pheno3	55.179	-0.010	28.196	0.248	10.701	5.195	0.136	-0.021	0.000
SK18 zoned pheno3	54.268	0.023	28.833	0.250	11.247	4.938	0.118	-0.002	0.000
SK18 zoned pheno3	54.730	-0.014	28.618	0.277	10.968	4.993	0.127	0.004	0.000
SK18 zoned pheno7	48.950	0.027	32.386	0.280	15.250	2.647	0.054	0.001	0.000
SK18 zoned pheno7	49.205	-0.001	31.845	0.344	14.678	2.829	0.069	0.002	0.000
SK18 zoned pheno7	47.972	-0.009	33.056	0.285	16.053	2.321	0.047	0.006	0.000
SK18 zoned pheno7	48.544	-0.019	32.470	0.264	15.463	2.561	0.051	0.004	0.000
SK18 zoned pheno7	54.158	-0.011	28.407	0.233	10.992	4.828	0.131	-0.001	0.000
SK18 zoned pheno7	52.938	-0.001	29.849	0.256	12.496	4.264	0.101	0.005	0.000
SK18 zoned pheno7	51.947	0.010	30.473	0.264	13.167	3.784	0.092	0.000	0.000
SK18 zoned pheno7	53.398	0.025	29.566	0.246	12.082	4.519	0.113	0.002	0.000
SK18 zoned pheno7	50.676	0.008	31.321	0.264	13.978	3.353	0.069	-0.003	0.000
SK18 zoned pheno7	52.871	-0.015	29.684	0.236	12.376	4.351	0.105	0.020	0.000
SK18 zoned pheno7	53.024	0.014	29.590	0.248	12.142	4.409	0.100	0.008	0.000

SK18 zoned pheno7	52.003	0.001	30.392	0.227	12.974	3.936	0.090	0.014	0.000
SK18 zoned pheno7	50.655	0.022	31.264	0.277	14.148	3.293	0.062	0.013	0.000
SK18 zoned pheno7	54.209	0.026	29.116	0.240	11.561	4.815	0.115	-0.011	0.000
SK18 zoned pheno7	47.621	0.041	24.913	0.237	11.043	3.354	0.119	0.000	0.000
SK19 zoned plag1	55.311	0.008	28.645	0.234	10.760	5.122	0.130	0.008	0.000
SK19 zoned plag1	48.983	0.035	32.465	0.575	15.451	2.480	0.055	0.052	0.000
SK19 zoned plag1	49.809	0.005	32.121	0.596	15.141	2.698	0.056	0.074	0.000
SK19 zoned plag1	54.475	0.016	29.180	0.376	11.544	4.605	0.110	0.025	0.000
SK19 zoned plag1	49.446	0.047	32.160	0.548	15.080	2.626	0.050	0.061	0.000
SK19 zoned plag2	52.527	-0.011	30.611	0.251	12.970	3.826	0.073	-0.001	0.000
SK19 zoned plag2	55.239	0.029	28.892	0.247	11.108	4.925	0.119	0.005	0.000
SK19 zoned plag2	53.467	0.017	30.014	0.254	12.225	4.368	0.100	-0.002	0.000
SK19 zoned plag2	54.842	-0.005	29.130	0.269	11.363	4.713	0.110	0.017	0.000
SK19 zoned plag2	53.571	-0.002	30.334	0.286	12.458	4.229	0.092	0.002	0.000
SK19 zoned plag2	54.532	-0.012	29.206	0.265	11.428	4.803	0.118	0.000	0.000
SK19 zoned plag2	52.849	0.027	30.192	0.275	12.508	4.067	0.087	0.003	0.000
SK19 zoned plag2	51.414	-0.009	31.082	0.315	13.769	3.405	0.071	0.003	0.000
SK19 zoned plag2	53.151	0.020	30.039	0.325	12.505	4.126	0.096	0.010	0.000
SK19 zoned plag2	53.111	-0.004	30.082	0.287	12.519	4.242	0.089	0.008	0.000
SK19 zoned pheno1	47.881	-0.011	33.483	0.550	16.549	1.921	0.040	0.028	0.000
SK19 zoned pheno1	47.781	0.023	33.555	0.546	16.634	1.930	0.042	0.035	0.000
SK19 zoned pheno1	47.330	0.012	33.714	0.530	16.914	1.775	0.042	0.042	0.000
SK19 zoned pheno1	48.971	0.024	32.455	0.566	15.725	2.407	0.051	0.057	0.000
SK19 zoned pheno1	51.071	0.017	31.104	0.576	14.223	3.327	0.075	0.062	0.000

Appendix 11 - Microprobe analysis of pyroxene phenocryst compositions

SAMPLE	SiO2	TiO2	Al2O3	Cr2O3	FeO	MnO	MgO	CaO	Na2O	K2O
SK1 pheno1	50.802	0.159	0.607	0.012	26.059	1.208	18.583	1.336	0.017	0.002
SK1 pheno1	50.432	0.145	0.617	0.007	26.319	1.186	18.340	1.291	0.006	-0.001
SK1 pheno1	50.372	0.123	0.477	0.003	26.709	1.307	18.135	1.317	0.014	0.003
SK1 pheno1	50.028	0.164	0.600	-0.040	27.228	1.301	17.745	1.311	0.014	0.007
SK1 pheno1	49.967	0.150	0.526	-0.032	27.608	1.324	17.396	1.289	0.016	0.000
SK1 pheno1	49.647	0.155	0.588	0.005	28.128	1.380	17.086	1.297	0.029	-0.005
SK1 pheno1	49.335	0.128	0.555	0.001	28.283	1.377	16.739	1.334	0.013	0.002
SK1 pheno1	49.385	0.115	0.411	0.003	28.568	1.423	16.567	1.280	0.013	0.004
SK1 pheno1	49.040	0.114	0.566	-0.017	29.167	1.448	16.249	1.298	0.011	0.004
SK1 pheno1	13.793	0.066	2.550	0.011	0.539	0.033	0.041	0.435	0.436	0.185
SK1 pheno3	50.791	0.192	0.639	-0.007	26.112	1.193	18.715	1.362	0.000	0.004
SK1 pheno3	50.607	0.193	0.582	0.006	26.999	1.254	18.011	1.295	0.024	-0.002
SK1 pheno3	50.257	0.141	0.546	0.028	26.855	1.256	17.842	1.334	0.030	0.009
SK1 pheno3	50.072	0.126	0.666	-0.003	26.643	1.252	17.766	1.345	0.009	0.004
SK1 pheno3	49.458	0.179	0.704	0.011	28.188	1.424	16.662	1.289	0.004	0.007
SK1 pheno5	49.858	0.159	0.509	0.001	28.267	1.470	16.784	1.316	0.058	0.011
SK1 pheno5	49.583	0.119	0.540	0.004	28.474	1.412	16.688	1.359	0.032	0.011
SK1 pheno5	49.968	0.154	0.498	-0.022	28.322	1.453	16.836	1.246	0.007	0.006
SK1 pheno5	49.849	0.127	0.459	0.005	28.163	1.446	16.855	1.190	0.035	0.009
SK1 pheno5	50.023	0.134	0.463	-0.033	28.027	1.479	16.706	1.171	0.055	0.020
SK5D zoned pheno2	50.529	0.274	1.222	0.028	23.254	0.933	20.072	1.496	0.035	0.007
SK5D zoned pheno2	51.361	0.204	1.360	-0.024	23.269	0.918	20.391	1.485	-0.008	0.002
SK5D zoned pheno2	51.661	0.155	0.712	0.021	22.939	0.900	20.518	1.472	0.057	-0.002
SK5D zoned pheno2	52.165	0.196	0.679	0.002	22.822	0.943	21.118	1.466	-0.007	-0.006
SK5D zoned pheno2	52.676	0.199	0.899	0.022	20.253	0.763	22.871	1.657	0.029	-0.001
SK5D zoned pheno2	46.088	0.156	0.771	0.010	17.656	0.544	17.219	1.703	0.002	0.005
SK5D zoned pheno2	52.822	0.220	1.245	0.019	19.292	0.677	23.444	1.525	0.035	0.000
SK5D zoned pheno2	54.072	0.172	1.518	0.007	17.699	0.500	25.123	1.500	0.025	0.008
SK5D zoned pheno2	53.164	0.132	0.906	0.013	18.488	0.586	24.060	1.616	0.000	0.002
SK5D zoned pheno2	52.930	0.177	0.776	0.024	19.910	0.716	22.937	1.605	-0.006	0.001
SK20 pheno3	52.495	0.152	0.671	0.005	23.314	0.958	20.589	1.520	0.052	0.001
SK20 pheno3	52.274	0.206	0.766	0.011	23.511	0.969	20.410	1.462	0.050	0.000
SK20 pheno3	52.535	0.187	0.724	-0.005	23.426	0.983	20.465	1.504	-0.011	-0.005
SK20 pheno3	52.545	0.175	0.663	-0.027	23.329	1.001	20.584	1.513	0.034	0.006
SK20 pheno3	52.744	0.147	0.638	0.011	23.321	1.000	20.712	1.483	0.051	0.002
SK20 pheno3	54.850	0.215	1.023	0.001	23.059	0.957	20.847	1.540	0.023	0.005

SK20 pheno3	52.655	0.227	0.994	0.003	22.519	0.915	21.157	1.520	0.027	0.008
SK20 pheno3	53.358	0.197	0.652	0.029	21.556	0.888	21.823	1.520	0.015	0.006
SK20 pheno3	53.968	0.189	0.855	0.027	17.746	0.587	24.646	1.748	0.031	-0.001
SK20 pheno3	53.906	0.182	0.712	0.040	18.964	0.644	23.856	1.637	0.038	0.003
SK20 pheno5	52.274	0.257	2.487	0.004	17.695	0.499	24.182	1.629	0.004	0.004
SK20 pheno5	52.544	0.302	2.066	0.002	18.707	0.652	23.680	1.561	0.063	0.007
SK20 pheno5	52.069	0.339	1.712	-0.037	20.053	0.710	22.196	2.171	0.057	0.000
SK20 pheno5	52.192	0.279	1.285	-0.015	21.024	0.784	21.662	1.645	0.037	0.008
SK20 pheno5	64.443	0.543	15.137	0.019	4.583	0.139	1.596	5.069	3.512	0.817
SK20 pheno6	51.700	0.171	0.701	-0.026	23.866	1.076	19.947	1.418	0.047	0.004
SK20 pheno6	51.942	0.157	0.631	-0.006	23.816	1.094	20.103	1.473	0.015	0.004
SK20 pheno6	51.396	0.155	0.810	-0.041	23.928	1.047	19.903	1.445	0.002	-0.003
SK20 pheno6	51.495	0.162	0.615	0.014	23.406	1.029	20.291	1.427	0.018	0.000
SK20 pheno6	51.103	0.174	0.844	0.029	23.553	1.032	20.214	1.432	0.009	0.006
SK20 pheno6	50.535	0.143	0.605	-0.013	22.971	1.015	20.295	1.944	0.030	0.000
SK20 pheno6	50.430	0.187	0.840	-0.022	23.025	0.974	20.307	1.427	0.042	-0.002
SK20 pheno6	53.166	0.238	2.815	0.013	20.613	0.884	18.288	1.670	0.380	0.174
SK20 pheno6	50.506	0.247	1.549	0.004	21.984	0.928	20.186	1.500	0.120	0.048
SK30 pheno2	52.427	0.164	0.691	0.007	23.489	0.980	20.805	1.427	0.016	0.007
SK30 pheno2	52.438	0.162	0.649	0.005	23.242	0.984	20.859	1.399	0.024	0.005
SK30 pheno2	51.872	0.174	0.998	0.009	22.606	0.954	21.693	3.650	0.052	0.014
SK30 pheno2	52.485	0.146	0.612	0.009	23.108	0.994	21.028	1.484	0.060	0.003
SK30 pheno2	52.376	0.167	0.754	-0.009	23.124	0.982	20.993	1.492	0.004	0.011
SK30 pheno2	52.615	0.167	0.741	-0.045	23.004	0.966	21.039	1.503	0.021	-0.001
SK30 pheno2	52.496	0.189	0.836	-0.004	23.150	0.933	21.023	1.478	0.047	0.007
SK30 pheno2	52.413	0.186	0.814	-0.002	23.048	0.900	21.130	1.419	0.044	0.008
SK30 pheno2	52.434	0.227	0.748	0.004	22.896	0.932	21.207	1.492	0.049	-0.001
SK30 pheno2	52.515	0.148	0.772	-0.002	22.883	0.913	21.342	1.481	0.016	0.002
SK30 pheno2	52.596	0.195	0.868	-0.039	23.078	0.915	21.130	1.487	0.036	0.006
SK30 pheno2	51.710	0.193	0.984	-0.005	22.702	0.955	20.851	1.517	0.059	0.005
SK30 pheno2	52.078	0.201	0.822	0.021	22.448	0.942	21.567	1.484	0.057	0.003
SK30 pheno2	53.617	0.155	1.008	0.027	19.143	0.596	23.966	1.563	0.063	0.008
SK31 zoned pheno3	7.351	0.027	0.994	0.004	0.550	-0.001	0.072	0.787	0.182	0.127
SK18 zoned pheno1	46.950	1.124	7.418	0.017	15.163	0.595	13.483	10.066	1.175	0.169
SK18 zoned pheno1	47.341	1.125	7.399	-0.027	15.012	0.526	13.724	10.026	1.232	0.155
SK18 zoned pheno1	47.015	1.165	7.707	0.011	15.217	0.557	13.461	10.141	1.186	0.175
SK18 zoned pheno1	48.316	1.100	7.338	0.017	15.111	0.582	13.851	10.082	1.200	0.161
SK18 zoned pheno1	46.244	1.148	8.240	-0.042	15.964	0.612	13.145	9.695	1.303	0.188
SK18 zoned pheno2	47.628	1.080	7.498	0.029	15.416	0.589	13.696	9.999	1.227	0.165

SK18 zoned pheno2	46.284	1.215	8.468	0.026	15.594	0.562	13.068	10.047	1.384	0.207
SK18 zoned pheno2	46.925	1.172	8.133	-0.016	15.425	0.585	13.341	10.069	1.236	0.179
SK18 zoned pheno2	47.772	1.011	7.182	-0.020	15.359	0.601	13.918	9.959	1.164	0.145
SK18 zoned pheno2	70.424	0.248	11.628	0.046	2.447	0.135	1.495	4.821	0.708	1.073
SK18 zoned pheno2	47.168	1.124	7.720	-0.004	15.650	0.604	13.663	9.955	1.315	0.197
SK18 zoned pheno2	46.534	1.239	8.170	0.028	15.536	0.561	13.232	10.200	1.339	0.192
SK18 zoned pheno2	47.701	1.142	7.135	0.009	14.941	0.550	13.840	9.951	1.254	0.160
SK19 zoned pheno2	0.090	7.153	2.085	-0.033	80.666	0.489	1.030	0.028	0.005	0.008
SK19 zoned pheno2	0.033	7.149	2.115	0.030	82.374	0.403	1.042	0.004	0.019	0.000
SK19 zoned pheno2	0.124	7.141	2.151	0.025	81.574	0.110	0.453	0.028	0.019	-0.001
SK19 zoned pheno2	0.046	7.173	2.171	0.016	82.350	0.217	0.582	0.018	0.016	-0.001
SK19 zoned pheno2	0.005	7.142	2.094	0.056	82.411	0.350	0.849	0.000	-0.002	0.004
SK19 zoned pheno2	0.025	7.193	1.739	0.034	81.258	0.387	0.946	0.023	-0.030	-0.002
SK19 zoned pheno2	0.042	6.162	1.809	0.036	82.450	0.429	0.974	0.012	-0.017	-0.005

Appendix 12 - Microprobe analysis of plagioclase microlites, compositions and classifications

SAMPLE	SiO2	TiO2	Al2O3	Cr2O3	FeO	MnO	MgO	CaO	Na2O	K2O	NiO	O	TOTAL		
SK1 m1	55.32	0.01	27.36	0.01	0.58	0.01	0.06	10.36	5.32	0.08	-0.02	0.00	99.11	Plagioclase	Labradorite
SK1 m2	45.06	1.68	10.85	0.00	14.63	0.34	12.29	9.38	2.00	0.18	0.00	0.00	96.43	Amphibole	Hornblende
SK1 m3	58.38	0.02	25.97	0.02	0.53	0.01	0.03	8.83	6.22	0.11	0.01	0.00	100.13	Plagioclase	Andesine
SK1 m5	55.12	0.32	3.73	-0.01	18.25	1.08	11.90	10.03	0.77	0.18	-0.01	0.00	101.37	Clinopyroxene	Augite
SAMPLE	SiO2	TiO2	Al2O3	Cr2O3	FeO	MnO	MgO	CaO	Na2O	K2O	NiO	O	TOTAL		
SK5D mm1	52.26	0.39	2.25	0.00	10.94	0.52	13.48	18.91	0.48	0.07	-0.01	0.00	99.28	Clinopyroxene	Augite
SK5D mm2	54.05	0.27	2.16	0.03	20.33	0.85	20.14	2.11	0.21	0.10	0.00	0.00	100.26	Orthopyroxene	Hypersthene
SK5D mm3	55.83	0.59	9.92	0.07	8.17	0.29	6.01	10.66	1.69	0.52	-0.01	0.00	93.75	Clinopyroxene	Augite
SAMPLE	SiO2	TiO2	Al2O3	Cr2O3	FeO	MnO	MgO	CaO	Na2O	K2O	NiO	O	TOTAL		
SK8b mm1	17.73	2.66	4.68	0.03	54.69	0.49	0.37	1.02	2.36	0.49	0.00	0.00	84.53	Magnetite	
SK8b mm2	19.64	7.14	6.25	0.06	56.52	0.42	2.14	1.22	2.01	0.32	0.00	0.00	95.70	Magnetite	
SK8b mm3	21.29	7.18	6.14	0.01	51.79	0.43	1.60	1.40	2.54	0.44	-0.01	0.00	92.81	Magnetite	
SK8b fm1	54.41	0.10	28.57	0.01	1.29	0.03	0.26	13.24	3.11	0.19	0.00	0.00	101.21	Plagioclase	Labradorite
SAMPLE	SiO2	TiO2	Al2O3	Cr2O3	FeO	MnO	MgO	CaO	Na2O	K2O	NiO	O	TOTAL		
SK20 m1	57.94	0.21	25.58	-0.02	1.70	0.04	0.18	10.01	4.64	0.31	-0.01	0.00	100.59	Plagioclase	Labradorite
SK20 m2	59.60	0.30	22.53	-0.01	2.41	0.07	0.27	8.63	4.32	0.51	0.00	0.00	98.62	Plagioclase	Labradorite
SK20 m3	58.39	0.14	23.72	0.01	1.94	0.07	0.79	9.68	4.56	0.23	0.00	0.00	99.52	Plagioclase	Labradorite
SK20 m3	0.32	13.77	2.17	0.01	75.06	0.60	1.62	0.15	0.05	0.02	-0.01	0.00	93.76	Magnetite	
SK20 m4	56.00	0.08	27.32	0.00	1.12	0.02	0.32	11.27	4.61	0.15	-0.01	0.00	100.88	Plagioclase	Labradorite
SK20 m5	54.66	0.24	1.87	-0.01	21.06	0.85	20.91	2.20	0.27	0.05	0.01	0.00	102.12	Orthopyroxene	Hypersthene
SK20 m6	62.64	0.69	9.69	0.00	4.87	0.16	1.27	3.51	1.90	1.21	0.01	0.00	85.97	Clinopyroxene	Augite
SK20 m7	56.34	0.08	28.01	0.02	0.93	0.02	0.10	11.16	4.94	0.13	0.00	0.00	101.75	Plagioclase	Labradorite
SAMPLE	SiO2	TiO2	Al2O3	Cr2O3	FeO	MnO	MgO	CaO	Na2O	K2O	NiO	O	TOTAL		
SK24a m1	51.79	0.18	1.34	0.00	25.94	0.91	18.87	0.69	0.18	0.03	-0.01	0.00	99.93	Orthopyroxene	Hypersthene
SK24a m2	58.33	0.02	26.52	-0.03	0.44	0.02	0.02	9.48	5.48	0.44	0.01	0.00	100.70	Plagioclase	Labradorite
SK24a m3	0.69	11.08	2.78	0.07	74.38	0.54	1.37	0.12	0.05	0.00	0.00	0.00	91.09	Magnetite	
SAMPLE	SiO2	TiO2	Al2O3	Cr2O3	FeO	MnO	MgO	CaO	Na2O	K2O	NiO	O	TOTAL		
SK30 fm1	63.79	0.78	10.35	0.06	12.22	0.46	8.04	5.95	2.16	0.68	0.02	0.00	104.51	Plagioclase	Labradorite

SK30 fm2	60.71	0.41	6.39	-0.02	19.10	0.76	16.87	2.23	1.29	0.32	0.01	0.00	108.08	Plagioclase	Labradorite
SK30 fm3	58.95	0.25	3.54	-0.02	16.95	0.52	22.90	2.02	0.77	0.13	0.00	0.00	106.00	Plagioclase	Labradorite
SK30 m1	53.90	0.30	2.32	-0.05	19.37	0.72	21.80	2.30	0.21	0.09	0.00	0.00	100.96	Orthopyroxene	Hypersthene
SK30 m2	53.11	0.22	1.35	0.04	21.62	0.89	21.37	1.68	0.12	0.04	0.01	0.00	100.44	Orthopyroxene	Hypersthene
SK30 m3	0.26	9.32	3.06	0.03	77.11	0.49	2.05	0.15	0.03	0.02	0.01	0.00	92.54	Magnetite	
SK30 m4	52.11	0.28	2.13	-0.01	20.09	0.71	22.12	1.96	0.04	0.02	-0.02	0.00	99.45	Orthopyroxene	Hypersthene
SAMPLE	SiO2	TiO2	Al2O3	Cr2O3	FeO	MnO	MgO	CaO	Na2O	K2O	NiO	O	TOTAL		
SK31 fm1	68.57	0.75	14.23	0.00	5.17	0.16	0.90	4.15	3.04	1.04	0.00	0.00	98.00	Plagioclase	Andesine
SK31 fm2	65.51	0.69	15.58	-0.03	4.88	0.16	0.75	4.87	2.83	1.02	0.01	0.00	96.28	Plagioclase	Labradorite
SK31 fm3	50.90	0.03	31.39	0.00	0.57	0.02	0.05	14.30	3.09	0.07	-0.01	0.00	100.42	Plagioclase	Bytownite
SK31 mm2	59.46	0.59	8.29	-0.03	15.91	0.69	8.40	2.90	1.70	0.53	0.00	0.00	98.45	Clinopyroxene	Augite
SK31 mm3	0.21	9.74	2.94	0.05	77.21	0.48	2.06	0.16	0.02	0.02	0.00	0.00	92.88	Magnetite	
SAMPLE	SiO2	TiO2	Al2O3	Cr2O3	FeO	MnO	MgO	CaO	Na2O	K2O	NiO	O	TOTAL		
SK19 fm1	55.00	0.03	28.74	0.03	0.63	0.01	0.04	11.47	4.65	0.17	0.00	0.00	100.77	Plagioclase	Labradorite
SK19 fm2	54.46	0.03	28.28	-0.01	0.80	0.02	0.05	11.29	4.67	0.21	0.00	0.00	99.79	Plagioclase	Labradorite
SK19 fm3	55.96	0.04	26.96	0.01	0.62	0.00	0.05	10.23	4.92	0.30	0.01	0.00	99.11	Plagioclase	Labradorite
SK19 mm1	1.94	8.64	2.45	0.06	74.08	0.79	1.65	0.76	0.16	0.08	0.00	0.00	90.62	Magnetite	
SK19 mm2	57.93	0.20	2.50	-0.01	19.52	0.84	21.58	2.25	0.51	0.47	0.01	0.00	105.80	Orthopyroxene	Hypersthene
SK19 mm3	55.06	0.18	1.32	-0.01	19.71	0.86	21.00	1.76	0.13	0.21	0.00	0.00	100.23	Orthopyroxene	Hypersthene
SAMPLE	SiO2	TiO2	Al2O3	Cr2O3	FeO	MnO	MgO	CaO	Na2O	K2O	NiO	O	TOTAL		
SK18 fm1	55.76	0.00	28.39	-0.05	0.26	0.00	0.00	10.92	4.98	0.16	0.00	0.00	100.42	Plagioclase	Labradorite
SK18 fm2	57.92	0.06	27.16	-0.02	0.71	0.03	0.09	10.56	4.75	0.36	0.00	0.00	101.60	Plagioclase	Labradorite
SK18 fm3	59.43	0.07	25.41	0.00	0.71	0.03	0.11	9.70	5.13	0.17	0.00	0.00	100.76	Plagioclase	Labradorite
SK18 mm1	54.44	0.18	1.75	0.01	19.00	0.71	22.49	1.85	0.24	0.08	0.00	0.00	100.76	Orthopyroxene	Hypersthene
SK18 mm2	57.13	0.19	2.78	0.01	17.64	0.63	22.50	2.97	0.39	0.08	0.01	0.00	104.32	Orthopyroxene	Hypersthene
SK18 mm3	55.90	1.00	9.68	-0.03	13.30	0.53	10.19	7.93	1.98	0.75	0.00	0.00	101.23	Clinopyroxene	Augite

Appendix 13 - Microprobe analysis of glass compositions

SAMPLE	K2O	CaO	TiO2	SiO2	Al2O3	Na2O	MgO	FeO	MnO	Cr2O3	P2O5	NiO	SO3	Cl	O	TOTAL
SK5D gl3	1.063	2.851	0.660	69.737	15.453	5.284	0.337	4.056	0.133	-0.004	0.264	-0.014	0.061	0.237	0.000	100.118
SK5D gl4	1.179	2.932	0.574	69.012	15.036	4.997	0.506	4.464	0.188	0.098	0.168	0.002	0.078	0.218	0.000	99.453
SK5D mean	1.121	2.891	0.617	69.375	15.245	5.141	0.421	4.260	0.161	0.047	0.216	-0.006	0.069	0.227	0.000	99.786
SK8b gl1	1.366	4.466	0.668	66.977	14.340	3.907	1.289	5.460	0.131	-0.005	0.165	0.016	0.035	0.206	0.000	99.021
SK8b gl2	1.214	4.370	0.721	67.180	14.941	3.966	1.389	5.237	0.172	0.025	0.204	-0.010	-0.014	0.157	0.000	99.553
SK8b gl3	1.287	4.117	0.586	69.005	14.125	3.894	1.112	5.081	0.180	-0.060	0.180	0.011	0.036	0.166	0.000	99.720
SK8b mean	1.289	4.318	0.658	67.721	14.469	3.922	1.263	5.260	0.161	-0.014	0.183	0.006	0.019	0.176	0.000	99.431
SK30 gl1	0.133	13.265	0.064	54.112	29.301	3.806	0.126	0.995	0.015	-0.075	0.019	-0.014	0.014	0.015	0.000	101.776
SK30 gl2	0.183	11.207	0.098	56.383	27.398	4.567	0.222	1.322	0.011	0.002	0.025	-0.010	0.035	0.020	0.000	101.464
SK30 gl3	0.042	14.684	-0.011	51.146	31.480	3.207	0.099	0.721	0.013	-0.060	0.035	-0.019	0.017	-0.002	0.000	101.353
SK30 gl4	0.036	15.793	0.032	49.732	32.156	2.692	0.061	0.719	0.018	0.042	-0.008	0.012	0.017	0.007	0.000	101.308
SK30 mean	0.098	13.737	0.046	52.843	30.084	3.568	0.127	0.939	0.014	-0.023	0.018	-0.008	0.021	0.010	0.000	101.475
SK31 gl1	1.007	4.436	0.647	67.299	15.417	4.240	0.915	4.512	0.150	-0.038	0.136	-0.018	0.021	0.128	0.000	98.851

SK31 gl2	0.960	4.829	0.507	66.307	15.787	4.256	0.936	4.454	0.115	0.034	0.170	-0.007	-0.011	0.139	0.000	98.476
SK31 gl3	0.872	5.107	0.540	66.834	16.546	4.547	1.031	4.234	0.097	0.023	0.175	-0.014	0.028	0.119	0.000	100.140
SK31 mean	0.946	4.791	0.565	66.813	15.917	4.348	0.961	4.400	0.121	0.006	0.160	-0.013	0.013	0.128	0.000	99.156
SK18 gl1	0.270	1.890	0.128	80.173	12.280	5.026	0.119	1.184	0.063	0.022	0.006	-0.011	-0.029	0.241	0.000	101.360
SK18 gl3	3.293	0.885	0.144	76.751	12.373	3.369	0.134	1.445	0.062	-0.063	0.029	-0.015	0.014	0.227	0.000	98.648
SK18 gl4	3.416	0.803	0.065	76.134	12.367	3.153	0.153	1.521	0.125	-0.103	0.017	0.023	0.022	0.184	0.000	97.880
SK18 gl5	0.135	10.567	0.013	55.870	28.573	5.281	0.030	0.284	0.005	-0.056	0.008	-0.024	-0.049	0.002	0.000	100.639
SK18 gl7	0.270	2.720	0.111	77.780	11.750	3.957	0.050	0.825	0.038	0.003	0.012	-0.014	0.033	0.190	0.000	97.724
SK18 Mean	1.477	3.373	0.092	73.342	15.469	4.157	0.097	1.052	0.058	-0.039	0.014	-0.008	-0.002	0.169	0.000	99.250
SK19 gl2	3.373	0.850	0.313	77.446	11.088	3.132	0.108	1.232	0.058	-0.022	0.003	-0.007	0.013	0.139	0.000	97.726
SK19 gl3	3.227	1.373	0.322	77.821	11.587	3.277	0.107	1.230	0.055	-0.004	0.003	-0.010	0.000	0.173	0.000	99.161
SK19 gl4	3.352	0.841	0.280	75.667	10.676	3.340	0.088	1.256	0.041	-0.075	-0.012	-0.026	0.007	0.218	0.000	95.653
SK19 gl6	0.056	15.303	0.032	50.198	32.210	2.790	0.068	0.666	0.025	-0.058	0.030	0.011	-0.007	-0.011	0.000	101.314
SK19 gl7	0.044	13.958	0.028	52.181	30.839	3.593	0.036	0.628	0.043	-0.080	0.008	-0.016	-0.059	-0.002	0.000	101.202
SK19 mean	2.011	6.465	0.195	66.662	19.280	3.227	0.081	1.002	0.045	-0.048	0.006	-0.009	-0.009	0.104	0.000	99.011

Appendix 14 - SEM analysis of glass compositions

Weight %	SiO2	Al2O3	K2O	CaO	TiO2	MnO	FeO	Na2O	MgO	Cl
SK1G glass	79.585	12.471	1.084	2.379	0.334	0.000	3.216	3.100	0.000	0.300
SK1G glass	78.943	13.226	1.205	2.798	0.334	0.000	2.444	3.100	0.000	0.200
SK1G glass	77.018	17.761	0.964	4.617	0.000	0.000	1.801	4.853	0.000	0.200
SK1G glass	79.371	12.660	1.325	2.518	0.334	0.000	2.702	3.370	0.332	0.200
SK1G glass	95.202	13.793	1.686	2.658	0.000	0.000	2.573	3.505	0.000	0.700
SK1G glass	80.655	12.282	1.325	2.239	0.334	0.000	2.702	3.235	0.000	0.300
SK1G glass	80.013	13.038	1.084	2.798	0.334	0.000	2.444	3.505	0.000	0.300
SK1E glass	74.686	12.830	0.795	3.022	0.284	0.000	2.599	2.912	0.000	0.400
SK1E glass	80.056	12.905	1.144	2.337	0.384	0.000	3.178	2.763	0.000	0.230
SK1E glass	76.483	15.343	0.783	4.141	0.284	0.000	3.023	3.356	0.000	0.150
SK1E glass	68.396	17.364	0.614	5.639	0.451	0.000	5.545	4.543	0.000	0.360
SK1E glass	75.563	13.888	0.831	3.792	0.417	0.000	2.817	2.467	0.000	0.230
SK1E glass	77.296	15.815	0.747	4.002	0.350	0.000	2.161	3.815	0.000	0.190
SK1E glass	73.680	17.894	0.759	5.247	0.334	0.000	2.637	4.219	0.000	0.000
SK1E glass	79.756	14.417	1.084	3.344	0.367	0.000	2.033	2.831	0.000	0.260
SK1E glass	75.541	18.253	0.699	5.219	0.384	0.000	2.239	3.626	0.000	0.000
SK1E glass	75.135	12.055	0.964	3.176	0.451	0.000	6.986	2.723	0.000	0.160
SK1E glass	70.493	11.016	0.940	1.945	0.000	0.000	1.955	1.806	0.000	1.910
SK1E glass	88.378	15.626	1.361	7.052	0.601	0.000	6.574	2.615	0.000	0.000
SK1E glass	63.176	10.959	0.867	2.896	0.267	0.000	2.264	3.977	0.000	0.180
SK1E glass	78.045	13.453	1.084	2.994	0.451	0.000	2.637	3.019	0.000	0.280
SK1E glass	78.280	12.508	1.373	2.616	0.384	0.000	2.998	2.615	0.000	0.190
SK1E glass	76.568	14.587	0.855	4.016	0.384	0.000	4.619	3.181	0.000	0.200
SK1E glass	55.089	0.661	0.000	21.435	0.000	0.000	14.795	0.337	0.000	0.000
SK5A glass	68.246	19.651	1.084	7.136	0.501	0.258	3.602	3.640	0.663	0.600
SK5A glass	68.888	15.683	0.723	5.177	1.001	0.000	6.561	4.448	1.161	0.000
SK5A glass	55.838	13.793	1.325	2.658	0.667	0.129	3.602	4.314	1.824	0.400
SK5A glass	61.186	13.226	2.168	13.152	2.836	0.646	18.526	2.292	0.829	0.200
SK5A glass	69.530	16.250	0.964	5.876	1.001	0.258	6.947	4.044	1.492	0.200
SK5A glass	69.744	14.927	0.964	5.317	1.168	0.258	8.362	3.774	1.990	0.200
SK5A glass	69.744	15.872	0.843	5.177	1.001	0.000	8.105	3.774	1.492	0.200
SK5A glass	64.395	16.250	0.843	4.617	0.667	0.000	5.146	4.179	1.990	0.300
SK5A glass	70.386	17.194	0.964	5.876	0.834	0.000	5.532	3.909	1.161	0.200
SK5A glass	80.441	13.415	2.289	2.379	0.000	0.000	2.187	3.100	0.000	0.100
SK5A glass	81.510	13.604	2.289	2.379	0.334	0.000	1.930	3.100	0.332	0.200
SK5A glass	81.938	13.604	2.289	2.518	0.000	0.000	2.058	3.100	0.000	0.200

SK5A glass	81.938	13.604	2.168	2.379	0.000	0.000	2.058	3.235	0.332	0.200
SK5A glass	82.366	13.415	2.289	2.518	0.334	0.000	1.930	2.831	0.332	0.200
SK5A glass	81.510	13.604	2.168	2.379	0.000	0.000	2.316	2.966	0.332	0.200
SK5A glass	78.943	14.360	2.168	3.078	0.334	0.000	2.702	3.235	0.332	0.200
SK5A glass	78.515	14.171	2.168	2.798	0.334	0.000	2.830	3.235	0.497	0.200
SK5A glass	78.943	14.549	2.048	2.798	0.334	0.000	2.702	3.100	0.332	0.200
SK5A glass	65.893	16.061	0.723	7.275	1.001	0.258	8.234	4.044	2.322	0.100
SK5A glass	72.739	15.683	1.566	4.757	0.834	0.000	5.918	3.235	1.161	0.200
SK5A glass	72.311	15.872	1.446	4.337	0.834	0.000	5.661	3.235	1.161	0.200
SK5A glass	67.390	22.485	0.482	7.555	0.667	0.000	5.017	4.044	0.332	0.000
SK5A glass	80.227	13.982	2.168	2.518	0.000	0.000	2.187	3.505	0.332	0.100
SK5A glass	78.943	4.724	2.048	2.798	0.334	0.000	2.702	3.370	0.332	0.200
SK5A glass	81.938	4.535	2.289	3.218	0.334	0.000	3.088	2.831	0.332	0.200
SK5A glass	67.604	5.857	1.566	2.239	0.334	0.000	1.672	4.179	0.497	0.000
SK5A glass	67.818	6.046	1.686	2.379	0.334	0.000	1.801	4.314	0.663	0.200
SK5A glass	79.585	4.535	2.168	3.218	0.501	0.000	2.702	3.235	0.497	0.200
SK5A glass	80.441	4.157	2.168	2.518	0.000	0.000	2.187	2.966	0.497	0.200
SK5 glass	68.139	15.154	1.000	5.457	0.968	0.000	8.980	3.019	0.000	0.220
SK5 glass	67.476	17.062	0.614	5.107	0.768	0.000	4.516	4.718	0.000	0.130
SK5 glass	71.156	16.193	0.928	5.764	0.934	0.000	6.818	3.626	0.000	0.170
SK5 glass	69.466	15.966	1.036	5.778	0.801	0.000	7.166	3.451	0.000	0.130
SK5 glass	70.000	15.040	1.012	5.569	1.034	0.000	7.886	2.804	0.000	0.120
SK5 glass	69.359	16.514	0.831	5.862	0.834	0.000	5.815	3.707	0.000	0.170
SK5 glass	70.193	15.815	0.843	5.890	0.884	0.000	7.307	3.518	0.000	0.270
SK5 glass	69.273	14.833	1.036	5.834	1.018	0.000	8.066	2.912	0.000	0.170
SK5 glass	67.947	15.910	0.988	6.002	0.818	0.000	7.256	3.019	0.000	0.200
SK5 glass	71.049	16.269	1.096	4.603	0.784	0.000	5.403	3.505	0.000	0.320
SK5 glass	68.118	14.795	0.952	5.708	1.101	0.000	8.324	2.952	0.000	0.140
SK5 glass	68.460	15.022	0.891	5.736	1.168	0.000	8.530	3.249	0.000	0.200
SK5 glass	69.744	15.872	0.964	5.415	0.968	0.000	7.886	3.343	0.000	0.130
SK5 glass	71.092	17.780	0.855	5.694	0.734	0.000	4.966	4.543	0.000	0.220
SK5 glass	69.722	15.683	0.964	5.792	0.918	0.000	7.938	2.831	0.000	0.120
SK5 glass	67.583	14.474	1.000	5.149	1.034	0.000	9.494	2.602	0.000	0.160
SK5 glass	68.096	15.475	1.072	5.009	1.085	0.000	9.482	2.736	0.000	0.180
SK5 glass	70.086	15.532	0.831	6.114	1.001	0.000	7.204	2.831	0.000	0.200
SK5 glass	68.974	15.607	0.855	5.974	1.085	0.000	7.346	2.790	0.000	0.130
SK5 glass	69.059	17.837	0.940	6.394	0.884	0.000	5.905	3.882	0.000	0.130
SK5 glass	33.717	13.226	0.325	2.546	4.622	0.000	47.627	2.332	0.000	0.000
SK5 glass	73.659	15.872	0.988	4.211	0.901	0.000	5.841	3.437	0.000	0.340

SK5 glass	70.214	16.552	0.940	6.156	0.968	0.000	6.150	3.262	0.000	0.140
SK5 glass	67.027	15.362	1.012	5.373	0.901	0.000	9.057	2.844	0.000	0.200
SK5 glass	70.000	14.644	1.108	5.135	0.901	0.000	8.542	2.467	0.000	0.180
SK5 glass	61.486	15.116	0.626	8.633	1.018	0.000	10.060	2.993	0.000	0.000
SK5 glass	67.412	14.927	1.132	5.275	1.085	0.000	8.748	2.723	0.000	0.230
SK5 glass	69.637	16.174	0.976	5.904	0.834	0.000	7.243	3.909	0.000	0.210
SK5D glass	70.985	15.078	0.964	4.967	1.001	0.000	9.340	3.249	0.000	0.300
SK5D glass	71.926	15.702	0.952	4.813	1.018	0.000	8.594	3.491	0.000	0.260
SK5D glass	72.054	15.872	1.000	5.009	0.934	0.000	9.572	3.222	0.000	0.250
SK5L glass	86.816	14.020	2.084	2.448	0.000	0.000	2.110	2.359	0.000	0.250
SK5L glass	84.570	13.680	2.108	2.085	0.000	0.000	128.651	2.709	0.000	0.000
SK5L glass	85.233	14.058	1.891	2.253	0.000	0.000	128.651	2.103	0.000	0.140
SK5L glass	85.104	13.548	1.939	2.379	0.000	0.000	2.161	2.723	0.000	0.180
SK5L glass	82.409	13.378	1.843	2.295	0.000	0.000	128.651	2.777	0.000	0.140
SK5L glass	83.842	13.340	1.795	2.393	0.000	0.000	128.651	2.629	0.000	0.000
SK5L glass	82.986	13.283	1.927	2.281	0.000	0.000	2.161	2.709	0.000	0.000
SK5L glass	82.730	13.699	1.867	2.448	0.000	0.000	128.651	2.696	0.000	0.000
SK5L glass	82.067	13.170	1.795	2.197	0.000	0.000	128.651	2.858	0.000	0.000
SK5L glass	82.409	13.491	1.783	2.001	0.000	0.000	1.763	2.804	0.000	0.000
SK5L glass	83.372	13.321	1.903	2.253	0.000	0.000	128.651	2.642	0.000	0.280
SK5L glass	83.778	13.718	1.927	2.183	0.384	0.000	128.651	2.696	0.000	0.210
SK5L glass	83.286	13.567	1.855	2.127	0.000	0.000	1.853	2.831	0.000	0.190
SK5L glass	81.232	13.245	1.686	2.127	0.000	0.000	128.651	2.993	0.000	0.000
SK5L glass	77.125	15.418	1.638	3.764	0.634	0.000	3.988	3.154	0.000	0.150
SK5L glass	80.013	14.663	1.903	3.176	0.000	0.000	128.651	3.033	0.000	0.160
SK8 glass	74.450	15.872	1.566	5.457	1.001	0.000	5.789	3.370	1.161	0.100
SK8 glass	62.470	14.549	0.964	3.778	0.501	0.000	4.631	4.448	1.658	0.000
SK8 glass	61.614	14.738	0.843	3.358	0.334	0.000	3.731	4.853	1.327	0.000
SK8 glass	69.316	14.738	1.325	3.638	0.501	0.258	3.474	4.583	0.829	0.100
SK8 glass	55.410	13.793	0.843	2.798	0.334	0.000	2.187	5.122	0.829	0.100
SK8D glass	70.065	17.421	1.000	5.848	0.734	0.000	4.863	4.192	0.779	0.000
SK8D glass	70.685	17.780	1.012	5.680	0.734	0.000	4.438	4.233	0.614	0.000
SK8D glass	71.370	14.058	1.277	4.673	1.018	0.000	7.578	3.222	1.426	0.300
SK8D glass	62.855	24.186	0.518	9.682	0.000	0.000	2.071	4.718	0.497	0.000
SK8D glass	70.920	15.928	0.964	5.177	0.834	0.000	6.059	4.152	1.045	0.210
SK8D glass	80.804	15.059	1.903	5.555	1.168	0.000	9.044	2.534	1.211	0.250
SK8D glass	65.508	14.927	0.855	4.589	0.651	0.000	5.082	4.448	1.227	0.170
SK8D glass	68.032	14.870	1.144	3.596	0.684	0.000	4.001	4.206	0.895	0.000
SK8D glass	65.037	23.468	0.578	7.667	0.384	0.000	2.702	5.378	0.398	0.000

SK8D glass	61.807	13.472	0.952	2.658	0.551	0.000	3.782	4.772	1.111	0.140
SK8D glass	73.723	16.080	1.048	5.107	0.868	0.000	4.966	3.977	0.929	0.000
SK8D glass	59.475	14.549	0.759	3.274	0.601	0.000	2.612	5.122	0.895	0.140
SK8D glass	72.546	14.304	1.217	4.743	0.901	0.000	6.999	3.276	1.277	0.190
SK8D glass	77.360	15.022	1.735	6.870	1.118	0.000	6.342	2.265	0.895	2.740
SK8D glass	73.916	15.040	1.313	3.288	0.751	0.000	4.914	4.327	0.978	0.340
SK8D glass	62.727	22.561	0.578	7.387	0.417	0.000	2.277	5.122	0.398	0.000
SK8D glass	56.907	14.474	0.723	3.274	0.484	0.000	2.920	5.473	1.260	0.130
SK8D glass	55.945	14.492	0.687	3.064	0.551	0.000	2.727	5.635	0.962	0.100
SK8D glass	70.407	16.212	1.048	4.925	0.834	0.000	5.442	4.273	0.763	0.180
SK8D glass	68.396	13.415	1.253	2.742	0.751	0.000	3.744	3.977	1.012	0.620
SK8D glass	72.824	17.383	1.048	5.373	0.701	0.000	4.644	4.570	0.895	0.000
SK8D glass	72.482	14.360	1.265	4.505	1.101	0.000	7.256	3.127	1.277	0.000
SK8D glass	70.407	14.965	1.337	5.009	1.034	0.000	7.732	3.316	1.277	0.310
SK8D glass	70.920	14.304	1.301	4.673	1.034	0.000	7.706	3.127	1.293	0.250
SK8D glass	70.985	14.908	1.361	4.953	0.834	0.000	7.513	3.356	1.426	0.280
SK8D glass	70.364	15.324	1.289	4.757	0.968	0.000	6.471	3.289	1.426	0.200
SK8D glass	70.214	14.870	1.361	4.771	0.884	0.000	7.320	3.114	1.675	0.250
SK8D glass	70.920	14.738	1.144	4.967	0.901	0.000	7.616	3.276	1.492	0.280
SK8D glass	70.535	14.322	1.241	4.953	1.118	0.000	7.011	3.316	1.128	0.250
SK8D glass	63.197	12.244	0.663	6.114	0.901	0.000	12.003	2.292	8.640	0.000
SK8D glass	70.985	14.681	0.879	5.177	0.918	0.000	7.153	4.004	1.526	0.190
SK8D glass	71.092	14.663	0.928	4.925	0.884	0.000	7.873	3.343	1.443	0.300
SK8D glass	71.947	14.870	1.156	4.561	0.818	0.000	6.677	3.262	1.343	0.220
SK8D glass	70.621	15.910	1.144	5.275	0.734	0.000	6.330	3.316	1.360	0.140
SK8D glass	71.113	14.436	1.217	4.547	0.984	0.000	7.809	3.249	1.592	0.240
SK8D glass	71.134	14.322	1.144	4.813	1.001	0.000	7.912	3.235	1.459	0.240
SK8D glass	70.514	15.078	0.916	5.429	0.968	0.000	7.037	3.680	1.327	0.210
SK8D glass	71.198	13.888	1.301	4.575	0.934	0.000	7.616	3.060	1.592	0.260
SK8D glass	70.279	18.253	0.879	5.862	0.667	0.000	3.872	4.704	0.597	0.000
SK8D glass	70.065	15.796	1.084	4.561	0.634	0.000	4.734	4.233	0.779	0.160
SK8D glass	71.648	15.267	1.337	4.743	1.001	0.000	6.021	2.817	1.443	0.250
SK8L glass	82.516	12.055	2.927	1.105	0.000	0.000	1.827	3.100	0.000	0.170
SK8L glass	96.850	2.626	0.000	0.630	0.000	0.000	0.000	0.903	0.000	0.000
SK8L glass	73.381	17.440	1.964	4.071	0.350	0.000	1.840	3.909	0.000	0.000
SK8L glass	73.124	15.777	2.024	4.099	0.000	0.000	1.402	3.383	0.000	0.170
SK8L glass	85.661	12.452	3.180	0.756	0.400	0.000	1.711	2.939	0.000	0.000
SK8L glass	81.746	11.431	3.120	0.881	0.000	0.000	1.930	2.507	0.000	0.270
SK8L glass	78.301	14.587	2.241	2.770	0.350	0.000	1.467	3.586	0.000	0.180

SK8L glass	78.258	16.798	1.903	3.736	0.284	0.000	1.158	3.963	0.000	0.000
SK8L glass	82.409	11.507	3.192	0.895	0.400	0.000	1.775	2.871	0.000	0.180
SK8L glass	89.105	9.202	2.433	0.658	0.350	0.000	1.570	2.305	0.000	0.150
SK8L glass	60.908	13.661	6.409	0.881	0.000	0.000	0.708	2.804	0.000	0.100
SK8L glass	80.868	12.754	2.686	1.693	0.284	0.000	1.711	2.993	0.000	0.000
SK8L glass	76.247	15.645	2.108	3.680	0.350	0.000	1.351	3.100	0.000	0.000
SK8L glass	81.553	11.866	3.084	0.909	0.284	0.000	1.724	2.979	0.000	0.150
SK8L glass	82.024	11.620	2.879	0.979	0.400	0.000	1.711	2.602	0.000	0.200
SK8L glass	72.846	15.777	1.879	3.988	0.300	0.000	1.351	3.356	0.000	0.160
SK8L glass	82.387	11.715	3.132	0.853	0.317	0.000	1.968	2.844	0.000	0.210
SK8L glass	71.883	18.045	1.723	4.673	0.000	0.000	1.261	4.354	0.000	0.000
SK11 glass	72.953	14.360	0.964	4.477	0.501	0.000	5.275	3.370	1.327	0.200
SK11 glass	67.390	20.973	0.602	8.255	0.501	0.000	2.444	4.044	0.332	0.100
SK11 glass	71.455	15.305	0.843	5.177	0.667	0.000	6.690	3.235	2.487	0.200
SK11 glass	72.311	14.171	0.964	3.638	0.667	0.000	4.374	3.100	0.497	0.300
SK11 glass	73.809	18.706	0.723	6.016	0.334	0.000	2.573	3.774	0.332	0.100
SK11 glass	65.037	22.863	0.482	8.395	0.334	0.000	3.345	4.718	0.829	0.100
SK11 glass	67.818	17.950	0.602	6.716	0.501	0.000	5.275	3.774	1.658	0.100
SK11 glass	63.326	20.596	0.482	7.136	0.334	0.000	2.316	4.448	0.663	0.000
SK11 glass	59.261	19.651	0.361	5.457	0.167	0.000	1.801	5.662	0.497	0.000
SK11 glass	73.167	15.116	0.843	5.037	0.834	0.000	4.760	3.235	0.829	0.200
SK11 glass	74.878	14.171	0.964	4.337	0.501	0.000	4.503	3.235	0.995	0.200
SK20 glass	74.236	15.872	1.325	4.477	0.834	0.000	4.889	3.774	0.663	0.200
SK20 glass	70.386	18.895	0.843	6.716	0.501	0.000	3.602	4.179	0.497	0.100
SK20 glass	75.734	13.604	1.446	3.778	0.834	0.000	5.146	3.370	0.829	0.100
SK20 glass	74.236	13.604	1.446	4.057	0.834	0.000	5.017	3.100	0.497	0.200
SK20 glass	69.958	12.471	1.325	3.218	0.834	0.000	5.017	3.505	0.829	0.200
SK20 glass	76.376	13.415	1.566	3.358	0.834	0.258	5.275	3.235	0.663	0.200
SK20 glass	71.883	15.872	1.205	5.317	0.834	0.000	5.275	3.505	0.663	0.200
SK20 glass	74.236	13.793	1.446	3.638	0.834	0.000	5.017	3.505	0.663	0.000
SK21 glass	78.943	13.226	0.602	2.938	0.501	0.000	4.889	4.988	0.332	0.200
SK21 glass	86.003	8.125	0.241	1.679	1.001	0.000	5.146	3.100	0.332	0.000
SK21 glass	75.520	18.139	0.241	6.576	0.000	0.000	0.772	3.774	0.000	0.000
SK21 glass	78.729	12.093	2.048	1.679	0.834	0.000	3.860	4.853	0.000	0.000
SK21 glass	87.287	11.715	0.241	2.798	0.334	0.000	1.029	3.640	0.000	0.000
SK21 glass	78.943	15.872	0.241	5.597	0.000	0.000	0.772	3.370	0.000	0.000
SK21 glass	79.585	14.171	0.361	5.736	0.000	0.000	0.901	2.696	0.000	0.000
SK21 glass	75.092	20.218	0.241	6.296	0.000	0.000	1.029	5.392	0.000	0.000
SK21 glass	73.595	13.038	2.530	3.218	0.667	0.000	5.403	4.718	0.497	0.300

SK30 glass	72.739	14.360	1.084	4.057	1.001	0.258	6.304	3.909	0.497	0.300
SK30 glass	72.739	14.171	0.964	4.197	1.001	0.000	6.561	3.909	0.663	0.300
SK30 glass	70.172	17.761	1.084	5.736	0.834	0.000	4.889	4.314	0.497	0.200
SK30 glass	71.669	14.927	1.084	4.757	1.001	0.000	5.532	3.505	0.663	0.200
SK30 glass	69.744	16.817	0.964	4.757	0.667	0.000	4.117	3.909	0.332	0.100
SK30 glass	69.744	18.328	0.843	5.317	0.667	0.000	4.631	4.314	0.497	0.200
SK30 glass	73.167	14.360	1.205	6.016	1.168	0.000	6.433	3.774	0.829	0.200
SK30 glass	72.739	16.250	0.964	4.057	0.834	0.000	4.631	4.314	0.332	0.000
SK30 glass	69.958	18.517	0.964	4.617	0.667	0.000	4.245	4.179	0.000	0.100
SK30 glass	68.888	14.927	1.084	6.156	0.834	0.000	3.988	3.909	0.995	0.000
SK30 glass	65.679	14.927	0.843	4.757	0.667	0.000	3.860	4.448	0.663	0.100
SK30 glass	62.684	13.604	0.964	3.778	0.667	0.000	3.602	4.853	1.161	0.100
SK30 glass	70.386	15.494	1.205	3.078	0.834	0.000	6.047	3.774	1.492	0.200
SK30 glass	70.172	18.328	0.843	5.037	0.667	0.000	3.731	4.583	0.000	0.200
SK30 glass	71.669	16.439	1.084	6.016	0.834	0.000	4.760	4.179	0.497	0.200
SK30 glass	66.107	22.674	0.602	5.177	0.334	0.000	2.959	4.988	0.332	0.100
SK30 glass	71.883	13.982	1.084	7.835	1.168	0.000	7.076	4.044	0.829	0.200
SK30 glass	71.883	13.793	1.084	4.337	1.001	0.000	6.947	3.774	0.663	0.200
SK30 glass	71.669	15.305	0.964	4.617	1.001	0.000	5.661	3.909	0.663	0.200
SK30 glass	59.475	15.305	0.843	5.037	0.501	0.000	3.216	5.257	0.663	0.000
SK30 glass	70.813	16.628	0.964	3.638	0.834	0.000	4.760	4.179	0.332	0.200
SK30 glass	60.330	27.209	0.482	5.317	0.000	0.000	2.187	4.988	0.000	0.000
SK30 glass	71.883	14.738	1.205	10.354	1.001	0.000	6.304	3.909	0.829	0.100
SK30 glass	65.893	20.973	0.602	4.477	0.501	0.000	3.345	4.179	0.332	0.100
SK30 glass	69.958	16.817	0.843	8.255	0.834	0.000	4.889	4.044	0.497	0.200
SK30 glass	66.107	15.872	0.843	5.597	0.667	0.000	4.374	4.853	0.663	0.200
SK30 glass	70.813	16.628	0.964	5.317	0.834	0.000	4.760	4.179	0.332	0.200
SK30 glass	60.330	27.209	0.482	10.354	0.000	0.000	2.187	4.988	0.000	0.000
SK30 glass	71.883	14.738	1.205	4.477	1.001	0.000	6.304	3.909	0.829	0.100
SK30 glass	65.893	20.973	0.602	8.255	0.501	0.000	3.345	4.179	0.332	0.100
SK30 glass	69.958	16.817	0.843	5.597	0.834	0.000	4.889	4.044	0.497	0.200
SK30 glass	66.107	15.872	0.843	4.337	0.667	0.000	4.374	4.853	0.663	0.200
SK31 glass	71.819	13.944	1.060	4.491	1.068	0.000	8.362	3.154	0.000	0.200
SK31 glass	69.594	18.271	1.000	5.625	0.617	0.000	4.786	4.475	0.000	0.190
SK31 glass	71.755	14.681	1.241	4.827	0.934	0.000	7.204	3.208	0.000	0.180
SK31 glass	71.519	14.530	1.241	4.645	1.151	0.000	8.208	3.222	0.000	0.220
SK31 glass	71.990	14.568	1.397	4.309	0.801	0.000	7.127	3.316	0.000	0.200
SK31 glass	72.504	14.946	1.277	4.687	0.751	0.000	7.127	3.289	0.000	0.160
SK31 glass	71.049	14.870	1.349	4.659	0.901	0.000	7.963	3.046	0.000	0.200

SK31 glass	71.284	15.078	1.132	4.799	0.951	0.000	7.552	3.303	0.000	0.220
SK31 glass	68.845	20.596	0.650	7.443	0.417	0.000	2.740	5.095	0.000	0.000
SK31 glass	71.305	14.398	1.181	4.393	1.051	0.000	7.294	3.060	0.000	0.170
SK31 glass	72.546	14.474	1.168	4.827	0.901	0.000	6.999	2.912	0.000	0.210
SK31 glass	72.632	14.738	1.289	4.575	0.968	0.000	7.269	2.858	0.000	0.240
SK31 glass	72.011	18.423	0.916	6.044	0.617	0.000	3.834	4.812	0.000	0.160
SK31 glass	70.899	17.308	1.012	5.736	0.801	0.000	4.914	4.475	0.000	0.170
SK31 glass	70.878	14.833	1.144	4.883	0.934	0.000	8.298	2.925	0.000	0.320
SK31 glass	71.348	14.795	1.096	4.771	0.868	0.000	7.616	3.303	0.000	0.230
SK31 glass	65.615	14.474	1.132	3.442	0.701	0.000	5.185	4.475	0.000	0.130
SK31 glass	72.910	15.891	1.181	4.911	0.551	0.000	6.137	3.356	0.000	0.220
SK31 glass	71.776	15.475	1.542	4.547	0.834	0.000	7.436	2.790	0.000	0.210
SK31 glass	71.327	14.984	1.458	4.561	0.751	0.000	7.475	3.006	0.000	0.250
SK31 glass	64.930	15.569	0.952	4.323	0.567	0.000	4.078	3.923	0.000	0.210
SK31 glass	69.893	18.120	0.795	6.156	0.751	0.000	5.172	4.354	0.000	0.180
SK31 glass	70.407	19.896	0.687	6.870	0.484	0.000	3.100	4.448	0.000	0.000
SK31 glass	72.183	13.831	1.289	4.575	0.984	0.000	7.912	2.952	0.000	0.170
SK31 glass	71.498	18.328	0.867	5.974	0.684	0.000	4.065	4.165	0.000	0.160
SK31 glass	72.653	14.984	1.373	4.673	0.868	0.000	6.252	2.588	0.000	0.200
SK31 glass	71.498	17.950	0.952	6.128	0.634	0.000	4.220	4.260	0.000	0.000
SK31 glass	71.498	15.267	1.301	4.743	0.884	0.000	7.732	2.858	0.000	0.210
SK31 glass	70.364	15.154	1.385	4.071	0.818	0.000	6.317	2.844	0.000	0.250
SK31 glass	73.167	15.815	1.156	5.079	0.751	0.000	5.133	3.276	0.000	0.140
SK31 glass	71.327	15.040	1.385	4.715	0.884	0.000	7.050	2.979	0.000	0.210
SK31 glass	72.011	18.366	0.879	6.324	0.467	0.000	4.117	4.475	0.000	0.000
SK31 glass	71.691	15.475	1.446	4.589	0.818	0.000	6.986	3.073	0.000	0.200
SK31 glass	71.691	15.343	1.241	4.617	0.818	0.000	7.269	3.046	0.000	0.220
SK31 glass	72.118	14.908	1.373	4.715	0.768	0.000	6.793	3.087	0.000	0.000
SK31 glass	72.161	15.853	1.024	5.471	0.701	0.000	5.648	3.572	0.000	0.190
SK31 glass	72.097	15.022	1.084	4.883	0.918	0.000	6.703	3.073	0.000	0.190
SK31 glass	70.343	14.644	1.289	4.701	0.851	0.000	7.899	3.168	0.000	0.210
SK31 glass	71.177	15.022	1.446	4.561	0.884	0.000	7.719	2.952	0.000	0.260
SK31 glass	73.488	16.439	1.181	4.995	0.667	0.000	5.918	3.330	0.000	0.150
SK31 glass	71.027	18.101	0.916	5.932	0.667	0.000	4.104	3.990	0.000	0.000
SK31 glass	62.598	11.904	0.675	6.730	0.968	0.000	12.698	2.251	0.000	0.130
SK31 glass	70.920	19.254	0.807	6.744	0.551	0.000	3.551	4.394	0.000	0.000
SK31 glass	70.856	18.914	0.867	6.576	0.567	0.000	3.757	4.138	0.000	0.180
SK31 glass	72.504	13.982	1.205	4.659	0.934	0.000	7.590	2.534	0.000	0.300

SK31 glass	71.733	16.646	1.048	5.680	0.651	0.000	5.725	3.114	0.000	0.180
SK31 glass	63.475	17.024	0.663	4.295	0.501	0.000	2.908	5.055	0.000	0.130
SK31 glass	69.166	15.721	1.000	4.491	0.584	0.000	4.207	3.896	0.000	0.000
SK31 glass	66.727	19.197	0.711	5.708	0.467	0.000	3.088	5.298	0.000	0.000
SK31 glass	60.330	17.421	0.590	4.449	0.434	0.000	2.689	5.729	0.000	0.000
SK31 glass	63.668	18.139	0.675	4.897	0.350	0.000	2.444	5.688	0.000	0.000
SK31 glass	68.268	17.213	0.687	5.149	0.584	0.000	3.242	4.381	0.000	0.120
SK31 glass	63.240	17.213	0.807	4.099	0.467	0.000	2.470	5.001	0.000	0.000
SK31 glass	72.739	16.892	0.928	5.163	0.801	0.000	4.786	3.693	0.000	0.170
SK31 glass	62.662	21.502	0.482	8.843	0.284	0.000	2.431	3.626	0.000	0.000
SK31 glass	76.290	16.514	0.928	4.883	0.717	0.000	5.326	3.923	0.000	0.000
SK31 glass	57.956	28.758	0.301	13.767	0.000	0.000	1.634	3.019	0.000	0.000
SK31 glass	62.577	14.738	0.819	3.596	0.567	0.000	4.040	4.502	0.000	0.160
SK31 glass	65.593	15.343	0.759	5.974	0.734	0.000	8.542	2.939	0.000	0.000
SK31 glass	70.642	14.455	1.313	4.645	1.118	0.000	8.465	3.060	0.000	0.270
SK31 glass	71.220	13.623	1.409	4.085	1.051	0.000	7.912	3.046	0.000	0.290
SK31 glass	71.477	16.080	1.108	5.009	0.784	0.000	6.265	3.869	0.000	0.240
SK31 glass	71.455	14.492	1.253	4.855	0.801	0.000	7.745	2.939	0.000	0.210
SK31 glass	69.273	19.764	0.711	6.730	0.484	0.000	3.358	4.961	0.000	0.000
SK31 glass	70.771	16.760	0.928	5.694	0.768	0.000	5.043	3.963	0.000	0.150
SK31 glass	69.337	18.687	0.843	6.436	0.601	0.000	3.808	4.718	0.000	0.000
SK31 glass	69.979	14.379	1.313	4.645	1.118	0.000	8.247	3.127	0.000	0.250
SK31 glass	65.700	17.478	0.747	6.968	0.651	0.000	6.690	3.815	0.000	0.000
SK31 glass	70.300	18.007	1.024	5.848	0.717	0.000	4.786	4.381	0.000	0.190
SK31 glass	70.086	16.949	1.048	5.583	0.934	0.000	6.613	4.165	0.000	0.190
SK31 glass	68.310	20.444	0.807	7.024	0.517	0.000	3.821	4.934	0.000	0.000
SK31 glass	71.755	15.872	1.217	5.387	0.918	0.000	5.892	3.909	0.000	0.000
SK31 glass	69.038	19.707	0.988	6.310	0.667	0.000	4.709	4.920	0.000	0.150
SK31 glass	71.712	15.135	1.144	4.141	0.884	0.000	6.921	3.356	0.000	0.160
SK31 glass	70.172	14.171	1.156	4.533	1.068	0.000	9.211	3.316	0.000	0.270
SK31 glass	69.765	18.630	0.771	6.772	0.634	0.000	4.065	4.570	0.000	0.000
SKN18 glass	83.029	15.626	0.494	3.974	0.267	0.000	0.489	4.071	0.000	0.000
SKN18 glass	76.761	11.526	2.229	3.036	0.417	0.000	6.008	1.712	0.000	0.140
SKN18 glass	83.778	12.490	3.084	1.161	0.000	0.000	1.003	2.211	0.000	0.000
SKN18 glass	83.243	12.338	3.337	0.867	0.317	0.000	0.926	2.157	0.000	0.130
SKN18 glass	86.688	13.453	0.181	3.624	0.000	0.000	0.360	3.572	0.000	0.000
SKN18 glass	83.350	13.113	2.915	1.315	0.317	0.000	0.939	2.602	0.000	0.130
SKN18 glass	82.730	12.131	3.264	0.937	0.000	0.000	1.184	1.955	0.000	0.180
SKN18 glass	81.596	15.928	0.000	4.617	0.000	0.000	1.711	4.516	0.000	0.000

SKN18 glass	85.746	12.735	0.470	3.246	0.267	0.000	0.952	3.046	0.000	0.000
SKN18 glass	84.891	12.282	2.987	0.909	0.234	0.000	0.772	2.305	0.000	0.000
SKN18 glass	83.757	12.792	2.686	1.301	0.250	0.000	0.952	2.251	0.000	0.000
SKN18 glass	82.794	12.679	1.144	2.490	0.000	0.000	3.126	3.316	0.000	0.000
SKN18 glass	83.200	12.565	3.024	1.119	0.000	0.000	1.312	2.453	0.000	0.170
SKN18 glass	81.382	14.020	2.096	2.211	0.000	0.000	0.849	3.006	0.000	0.000
SKN18 glass	83.136	12.527	2.614	1.413	0.317	0.000	1.081	2.116	0.000	0.160
SKN18 glass	82.109	12.112	2.674	1.175	0.000	0.000	0.836	2.494	0.000	0.200
SKN18 glass	79.435	16.987	1.939	3.666	0.000	0.000	0.476	3.532	0.000	0.000
SKN18 glass	83.243	12.660	2.819	1.385	0.000	0.000	1.016	2.143	0.000	0.200
SKN18 glass	78.344	12.074	2.759	0.881	0.000	0.000	0.849	2.858	0.000	0.140
SKN19 glass	82.751	11.299	4.132	0.867	0.451	0.000	1.312	2.426	0.000	0.200
SKN19 glass	76.782	12.017	2.999	1.511	0.400	0.000	1.595	3.168	0.000	0.140
SKN19 glass	83.650	11.356	4.204	0.993	0.484	0.000	1.415	2.521	0.000	0.180
SKN19 glass	78.451	10.978	3.710	0.784	0.350	0.000	1.068	2.871	0.000	0.220
SKN19 glass	66.535	10.222	2.530	0.644	0.267	0.000	0.875	4.017	0.000	0.200
SKN19 glass	82.944	11.205	3.638	0.728	0.451	0.000	1.570	2.521	0.000	0.220
SKN19 glass	77.210	10.959	3.036	0.839	0.350	0.000	1.055	3.222	0.000	0.190
SKN19 glass	83.008	11.356	4.397	0.811	0.467	0.000	1.325	2.372	0.000	0.180
SKN19 glass	82.986	11.431	3.879	1.007	0.551	0.000	1.351	2.413	0.000	0.140
SKN19 glass	84.013	11.280	3.746	0.784	0.417	0.000	1.428	2.602	0.000	0.200
SKN19 glass	83.607	11.469	3.710	0.784	0.000	0.000	1.492	2.453	0.000	0.260
SKN19 glass	81.339	13.226	3.349	1.847	0.317	0.000	1.325	2.723	0.000	0.210
SKN19 glass	85.040	11.583	4.578	1.105	0.434	0.000	1.389	2.049	0.000	0.190
SKN19 glass	82.559	11.677	3.987	1.021	0.451	0.000	1.454	2.319	0.000	0.170
SKN19 glass	81.960	11.526	3.638	1.483	0.350	0.000	1.389	2.777	0.000	0.260

Appendix 15 - XRF whole rock trace element compositions

			SK1G/1	SK1W	SK5L	SK5D	SK8L	SK8D	SK10	SK11	SK12	SK20	SK21	SK30	SK31	SKN14	SKN15	SKN16	SKN17	SKN18	SKN19L	SKN19D
Sum	of conc.	(%)	13.079	11.632	8.393	14.089	11.706	14.933	16.424	13.698	13.023	14.829	15.754	15.714	15.355	14.215	13.116	11.431	9.615	10.292	12.186	12.553
CaO	Ca	(%)	5.75	5.04	3.71	6.68	5.26	6.92	8.46	6.05	5.86	7.06	7.81	7.29	6.92	6.78	6.83	5.57	5.1	5.1	6.12	5.99
Sc	Sc	(ppm)	9.1	6.7	6.4	11.6	11.4	14.4	12.4	9.6	9.9	15	13.6	14.5	15.8	14.9	11.9	11.7	7.9	8.3	11.6	13.8
TiO2	Ti	(%)	0.55	0.48	0.37	0.71	0.58	0.79	0.7	0.59	0.64	0.73	0.75	0.82	0.82	0.66	0.54	0.51	0.38	0.44	0.54	0.59
V	V	(ppm)	50.2	36	41.5	87.5	75.9	99.3	100.1	58.7	72.8	102.5	101.5	110	108.3	128.2	111.3	102.5	51.2	63.7	111.3	127.5
Cr	Cr	(ppm)	1.6	0.8<@LL	2.9	5.1	3.5	1.7	20.8	0.1<LL	1.5<@LL	4.7	11.9	2.9	1.1	2.6	1.6	5.1	4.8	12.4	6	2.1
Mn	Mn	(ppm)	1697.3	1621.1	1081.9	1402	1301.6	1528.7	1957.9	1727.7	1500.6	1450.9	1517.5	1581.8	1596	1442.5	1215.4	1116	1116.5	1180.3	1114.2	1133.5
Fe2O3	Fe	(%)	6.53	5.87	4.12	6.48	5.65	7	6.96	6.81	6.29	6.82	6.97	7.36	7.38	6.53	5.53	5.14	3.94	4.54	5.32	5.75
Co	Co	(ppm)	9.6	8.9	7.7	11.6	11.8	10.5	12.2	11.4	10.7	13.9	15.5	12.7	12.7	16.9	14	12.7	6.8	9.5	14.3	15.8
Ni	Ni	(ppm)	1.4	0.4<LL	1.2	1	0.0<LL	1.6	6.4	0.1<@LL	1.1	1.5	0.3<LL	0.4<@LL	1.4	4.9	2.2	2.9	1.5	0.8<LL	0.8<LL	3.2
Cu	Cu	(ppm)	15.6	18.9	12.2	35.2	32.2	20.7	17.2	18.4	21.2	29.3	30.7	18.9	15.5	31.2	25.4	47.1	18.8	26	38.7	60.7
Zn	Zn	(ppm)	54.9	50.5	33.2	45.2	38.5	48.3	122.4	54.8	50.8	44.7	47	52.3	50.8	48.6	40.1	42	30.6	30.5	40.3	44
Ga	Ga	(ppm)	14.2	14	12.4	14.3	13.4	14.4	14.7	14.9	13.9	14.1	15.8	14.7	14.7	15.7	13.5	13.1	12.4	12.4	13.7	13.6
Ge	Ge	(ppm)	-0.3<LL	0.4	0.8	0.4<LL	0.1<@LL	0.2<LL	0.7	0.1<LL	0.5	0.3<LL	0.6	0.1<LL	0.5	0.5	0.9	0.2<LL	0.5	0.3<@LL	0.5	0.1<LL
As	As	(ppm)	0.9<LL	1.6	1.0<LL	0.7<LL	1.2<LL	1.7	0.7<LL	1.5	1.6	1.9	2.9	2.5	3.4	4	2.1	2.5	2.7	1.0<LL	1.0<LL	1.1<LL
Se	Se	(ppm)	1.1<@LL	1.3<@LL	1.4<@LL	1.2<@LL	0.8<@LL	0.9<@LL	0.6<@LL	0.7<@LL	0.9<@LL	0.4<@LL	0.1<@LL	0.5<@LL	0.4<@LL	0.7<@LL	0.7<@LL	1.3<@LL	0.9<@LL	1.1<@LL	0.6<@LL	-1<@LL
Br	Br	(ppm)	2.4	2.6	48.9	5.9	1.1	4.4	5.7	8	12	1.3	1.6	19.3	3.5	30.9	3.3	61.7	4.2	4.5	14	82.4
Rb	Rb	(ppm)	11.8	12.1	23.5	11.5	18.3	12.1	10.1	10.9	13.3	11.6	11.1	12.3	12.6	12.4	16.4	17.9	22.6	23.9	18.9	17.2
Sr	Sr	(ppm)	252.3	239.4	218.1	238.4	227.2	239.5	347.2	252.4	229.1	233.5	246	242.7	233	334.2	298.8	294.3	249.1	249.2	308.6	316

Y	Y	(ppm)	22.5	23.1	20.3	22.3	21.7	22.6	25.1	20.7	22.7	21.9	23.7	23.1	23	16.1	15.2	13.5	16.2	16.9	15.5	15.4			
Zr	Zr	(ppm)	75.1	79.9	87.3	70.3	79	69.3	96	70.8	84.7	67	70.5	69.8	70.7	87.1	67.7	73.3	78.5	79.9	73.6	69.6			
Nb	Nb	(ppm)	1.3	1.5	1.6	1.4	1.9	1.2	1.8	1.3	1.6	1.2	1.5	1.4	1.3	1.4	1.4	1.3	1.8	1.8	1.4	1.4			
Mo	Mo	(ppm)	1.3	0.8	1.3	1	1.9	1.2	3.3	1.2	1.4	1.2	1	1.2	1.4	0.6	1.2	1.2	1.6	1.7	1.1	1.5			
Ag	Ag	(ppm)	1.7<LL	0.4<LL	-	1.3<LL	0.2<LL	2.1	0.8<LL	2.2	1.4<LL	2.3	2.2	-	0.1<@LL	1.9<LL	-	0.3<@LL	2	2.9	0.3<LL	1.2<LL	2.5	1.0<LL	
Cd	Cd	(ppm)	6.2	4.1	3.2	5.6	3.5	5.6	6	6.2	5.2	5.2	5.9	4.4	5.9	3.1	6.1	6.5	4.4	5.1	7	4.5			
Sn	Sn	(ppm)	17.1	15.1	15.8	19.2	19	18.4	18	17.7	17.9	19.7	17.4	17.5	17.4	16.1	17.6	16.5	16.2	18.3	18.5	18.3			
Sb	Sb	(ppm)	1.5<LL	1.9<LL	2.1	2.3	3.2	1.2<LL	0.7<LL	2.3	1.0<LL	2.3	2.9	3.2	1.8<LL	1.9<LL	2.2	0.7<LL	1.9<LL	2.4	2	3.1			
Te	Te	(ppm)	-	-	-	-	-	-	-	-	-	-	-	-	-	-	-	-	-	-	-	-	-		
I	I	(ppm)	4.7<@LL	3.3<@LL	3.7<@LL	4.6<@LL	-4<@LL	5.4<@LL	7.5<@LL	5.4<@LL	6.3<@LL	4.2<@LL	5.6<@LL	5.3<@LL	6.8<@LL	5.5<@LL	4.7<@LL	-7<@LL	5.3<@LL	-4<@LL	6.2<@LL	4.1<@LL			
l	l	(ppm)	4.4	4.7	5.1	5.4	5.4	3.1	4.4	6.6	3.4	5	4.7	3.3	4.8	7.1	7.6	5.9	2.7	2.8	4.2	6.8			
Cs	Cs	(ppm)	-1<@LL	1.9<@LL	-	0.7<@LL	3.4<@LL	1.6<@LL	0.5<LL	-	2.4<@LL	2.2<@LL	-1<@LL	1.2<@LL	1.4<@LL	2.5<@LL	3.2<@LL	-4<@LL	0.8<@LL	1.1<LL	-	1.4<@LL	0.6<@LL	1.6<LL	0.8<@LL
Ba	Ba	(ppm)	140.9	157.5	285.2	126.8	229.3	145.9	147.6	134.2	143.6	119.4	115.9	132.9	148.8	196.3	206.3	243.1	260.2	279.3	234.2	211.4			
La	La	(ppm)	7.4	6.3	9.7	6.6	7.8	6.1	5.7	8.4	3.9	5.5	2.8<LL	7.5	4.4	9.4	7	8.6	10	11.1	6.4	11.5			
Ce	Ce	(ppm)	16.8	21.6	20.9	21.6	20.2	21.1	20.7	19.3	21.1	15.4	18.1	18.4	19.6	28.9	22.2	21.4	21.4	23	23.3	24			
Nd	Nd	(ppm)	5.9	6.8	4.9	5.6	6.4	5.3	6.9	4.7	5.5	3.3	2.4	3.6	6	3.3	2.2	2.1	5.4	7.1	1.7<LL	2.4			
Sm	Sm	(ppm)	6.3	0.7<LL	1.4<LL	0.4<LL	2.5	1.4<LL	1.7<LL	1.9<LL	-	0.2<@LL	1.5<LL	0.6<LL	1.6<@LL	0.1<@LL	2.8<@LL	0.4<LL	1.0<LL	-	0.3<@LL	1.8<LL	1.4<@LL	0.5<LL	
Yb	Yb	(ppm)	-	0.3<@LL	1.0<LL	0.4<LL	0.8<@LL	2.9<@LL	1.5<@LL	0.4<LL	0.2<LL	0.2<LL	0.4<@LL	1.1<@LL	1.1<LL	-1<@LL	0.6<LL	1.6<@LL	0.7<LL	0.9<LL	1.3<LL	0.7<@LL	1.2<@LL		
Hf	Hf	(ppm)	1.6	2.2	2.2	1.2<LL	0.1<@LL	0.2<LL	1.8	1.5	1.7	0.4<LL	2.1	1.9	3.3	1.8	-	0.9<@LL	1.0<LL	0.1<LL	1.6	0.3<LL	0.5<LL		
Ta	Ta	(ppm)	1.5	1.0<LL	1.2<LL	3.3	0.4<LL	2.1	2	0.6<LL	1.6	1.9	1.8	-	0.5<@LL	2.4	3.6	1.9	1.3<LL	2.8	2.8	2.7	1.9		
W	W	(ppm)	2.2	1.8	1.6	1.6	0.1<LL	4	2.4	2.2	2.5	1.9	0.7<LL	0.4<LL	1.6	0.1<LL	2.7	1.6	2.6	1.4<LL	2.2	2			
Pt	Pt	(ppm)	1.3<LL	1.5	2	0.2<LL	1.2<LL	1.0<LL	1.2<LL	1.1<LL	1.6	0.5<LL	1.1<LL	0.0<LL	0.5<LL	0.8<LL	1.7	1.4<LL	1.0<LL	1.7	1.1<LL	1.8			

Au	Au	(ppm)	0.7<LL	0.4<LL	-	0.1<@LL	0.2<LL	1.1	0.8	0.0<LL	0.7<LL	0.6<LL	0.4<LL	1.5	1.4	1	0.8	1.2	0.5<LL	0.7<LL	1	1.4	0.5<LL		
Hg	Hg	(ppm)	3.4	4.8	6.2	4.9	4.6	5.2	5.2	5	5.6	6.1	6	5.3	6	5.2	5.6	5	4.8	4.3	5.3	4.9			
Tl	Tl	(ppm)	-	0.9	-	1.4<@LL	0.6<LL	0.7<LL	-	0.4<@LL	1.2<@LL	0.6<LL	0.2<LL	0.0<LL	0.3<LL	0.6<LL	0.7<LL	0.1<LL	0.8	0.7<LL	0.8	-	0.1<@LL	0.3<LL	0.7<LL
Pb	Pb	(ppm)	3.4	5.9	2.9	6.4	6.5	6.4	2.7	6.2	3.3	3.1	6.9	6.3	3.7	7.1	6.8	7.3	8.3	10.9	6.7	7.6			
Bi	Bi	(ppm)	-	-	-	-	-	-	-	-	-	-	-	-	-	-	-	-	-	-	-	-	-	-	
			1.2<@LL	1.6<@LL	2.6<@LL	1.1<@LL	0.7<@LL	0.9<@LL	0.5<@LL	0.6<@LL	0.6<@LL	0.2<@LL	0.2<@LL	0.1<LL	0.0<LL	0.5<@LL	1.2<@LL	1.5<@LL	-1<@LL	1.2<@LL	0.6<@LL	1.5<@LL			
Th	Th	(ppm)	4.8	4.4	5.1	4.4	5.2	4.8	4.8	4.5	4.6	4.8	5	4.3	4.3	5.1	5	4.8	5.4	5.6	4.7	5.3			
U	U	(ppm)	2	2.7	2.3	2.5	3.1	2.2	3.1	2.2	2.2	2.5	2.3	2.3	2.4	3	2.1	2.6	2.9	2.4	3.1	2.5			

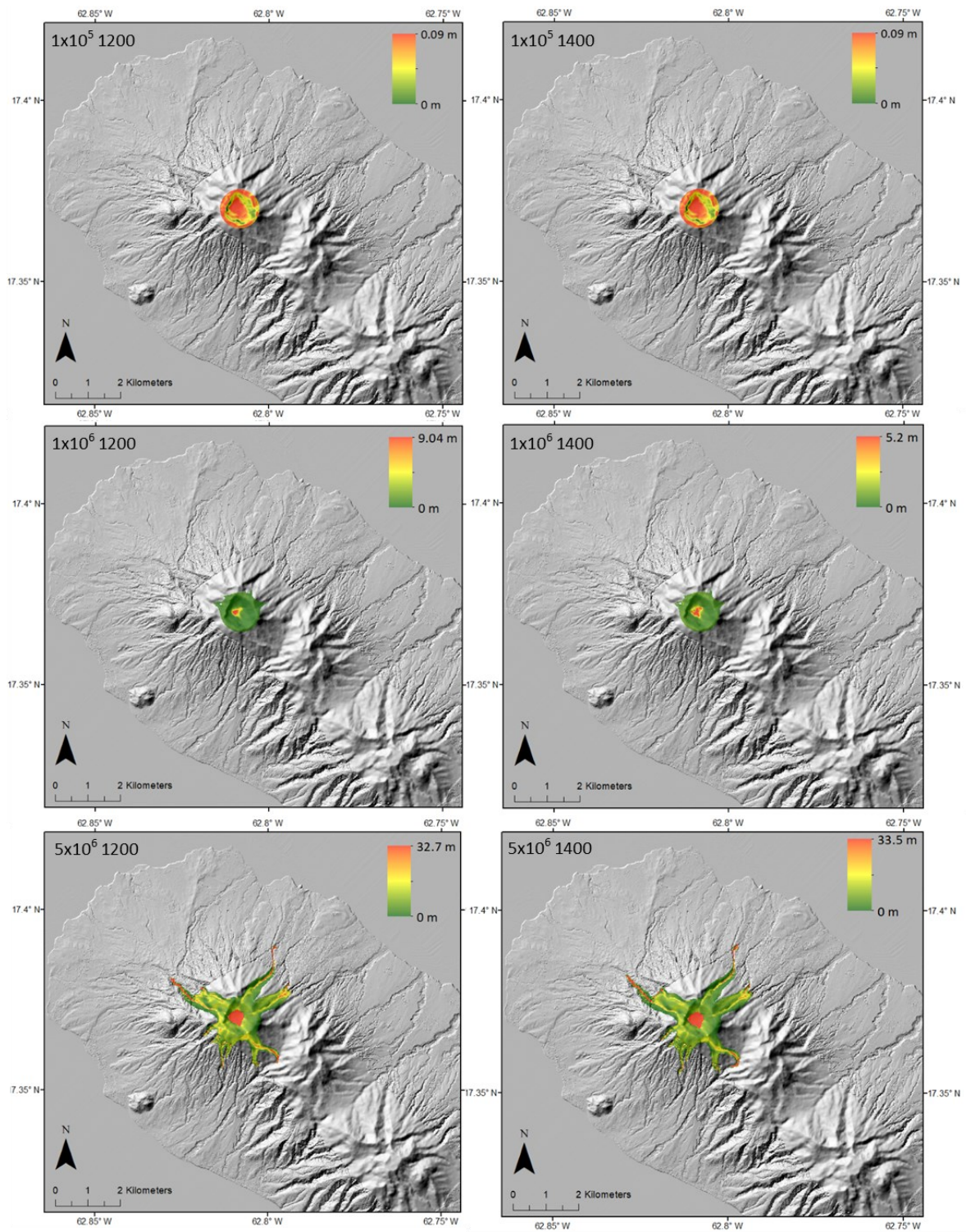
Appendix 16 – Growth rate and nucleation rate calculations

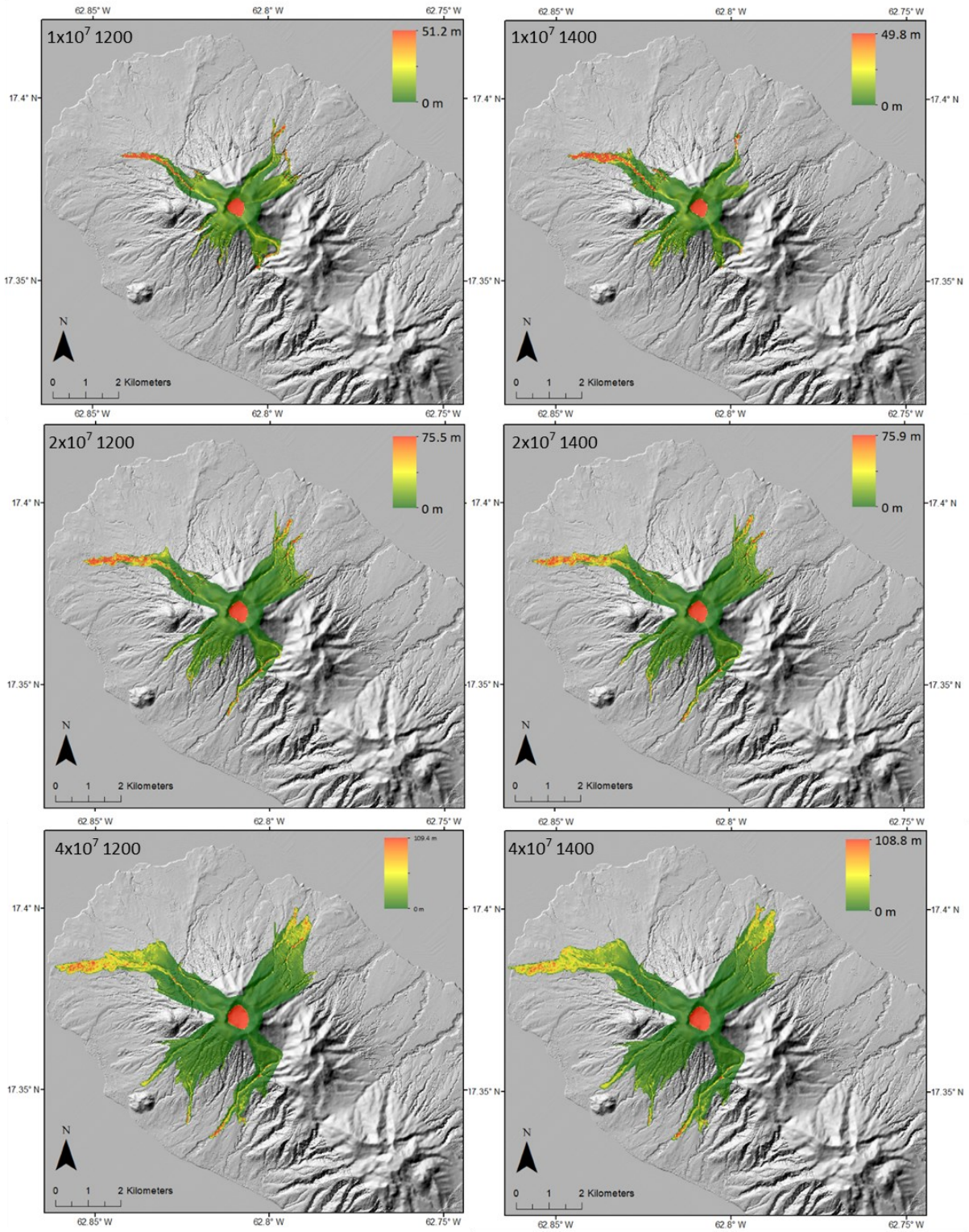
Sample no.	N (number of microlites)	Slope (°)	n° (mm ⁻⁴)	Crystallisation				Nucleation rate(J) G = 10 ⁻⁸	Nucleation rate(J) G = 10 ⁻⁷	Nucleation rate(J) G = 10 ⁻⁶
				time (t)	time (t)	time (t)	time (t)			
				hours G = 10 ⁻⁸	Days G = 10 ⁻⁸	hours G = 10 ⁻⁷	hours G = 10 ⁻⁶			
SK1-01	50	-313	760890487.9	88.75	3.70	8.87	0.89	7.61	76.09	760.89
SK1-02	52	-257	485165195.4	108.08	4.50	10.81	1.08	4.85	48.52	485.17
SK1-03	36	-148	176706372.4	187.69	7.82	18.77	1.88	1.77	17.67	176.71
SK1-04	75	-299	1386432863	92.90	3.87	9.29	0.93	13.86	138.64	1386.43
SK1-05	39	-416	986821766.5	66.77	2.78	6.68	0.67	9.87	98.68	986.82
SK5D-01	30	-772	29866401803	35.98	1.50	3.60	0.36	298.66	2986.64	29866.40
SK5D-02	26	-734	12638328778	37.84	1.58	3.78	0.38	126.38	1263.83	12638.33
SK5D-03	49	-680	3620941819	40.85	1.70	4.08	0.41	36.21	362.09	3620.94
SK11-01	19	-541	884028623.9	51.35	2.14	5.13	0.51	8.84	88.40	884.03
SK11-02	24	-927	10769673371	29.97	1.25	3.00	0.30	107.70	1076.97	10769.67
SK11-03	29	-742	6731070286	37.44	1.56	3.74	0.37	67.31	673.11	6731.07
SK20-01	126	-313	552519895.1	88.75	3.70	8.87	0.89	5.53	55.25	552.52
SK20-02	80	-286	312464056.1	97.13	4.05	9.71	0.97	3.12	31.25	312.46
SK20-03	82	-285	331785754.2	97.47	4.06	9.75	0.97	3.32	33.18	331.79
SK20-04	76	-272	279915967.5	102.12	4.26	10.21	1.02	2.80	27.99	279.92
SK20-05	66	-336	604553060.5	82.67	3.44	8.27	0.83	6.05	60.46	604.55
SK21-01	68	-140	11640488.89	198.41	8.27	19.84	1.98	0.12	1.16	11.64
SK21-02	13	-95	2649813.982	292.40	12.18	29.24	2.92	0.03	0.26	2.65
SK21-03	52	-388	127038405	71.59	2.98	7.16	0.72	1.27	12.70	127.04

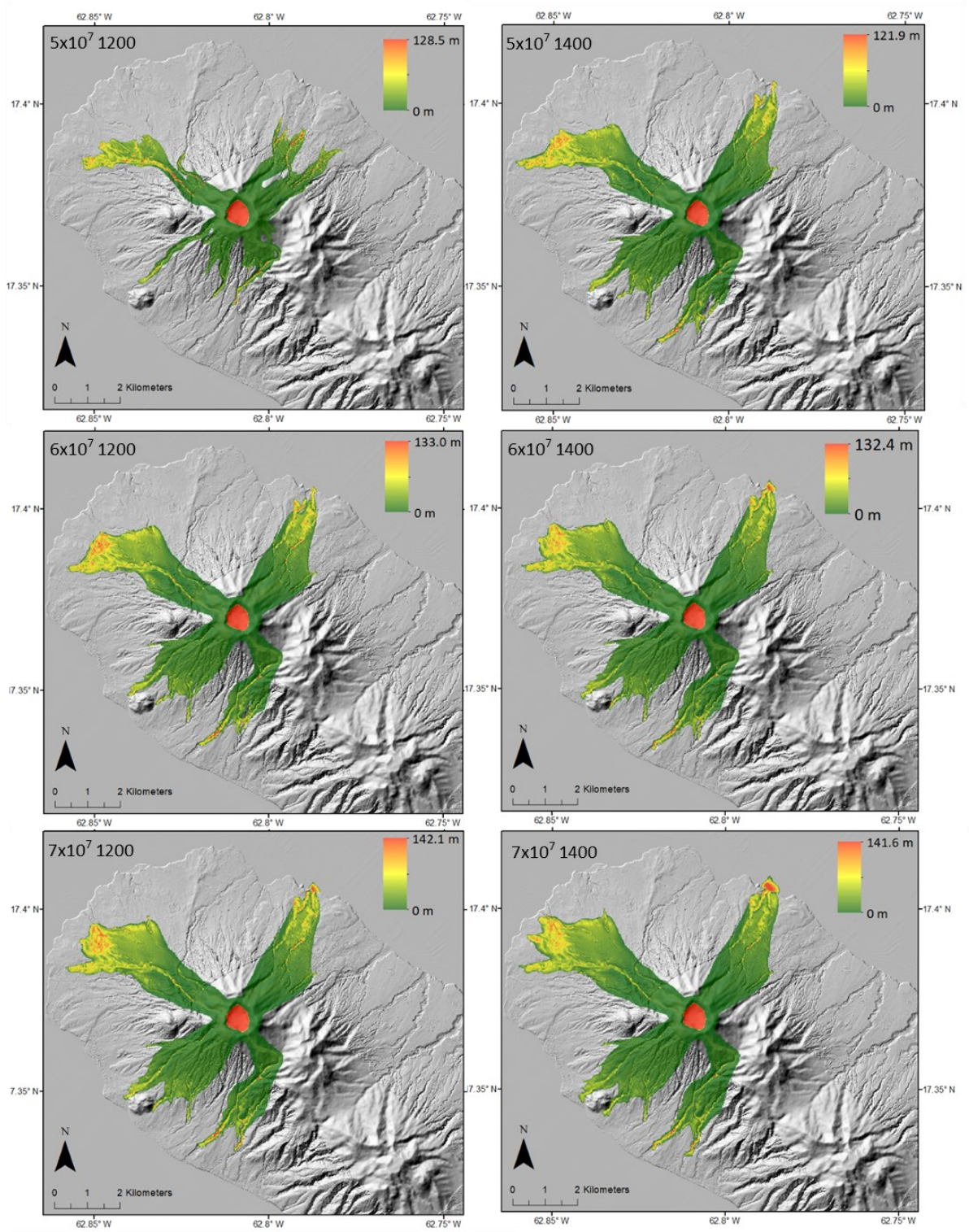
SK21-04	33	-371	78609255.11	74.87	3.12	7.49	0.75	0.79	7.86	78.61
SK21-05	15	-398	52693359.51	69.79	2.91	6.98	0.70	0.53	5.27	52.69
SK24b-01	75	-565	5294847421	49.16	2.05	4.92	0.49	52.95	529.48	5294.85
SK24b-02	68	-941	32353886831	29.52	1.23	2.95	0.30	323.54	3235.39	32353.89
SK24b-03	67	-752	7076179639	36.94	1.54	3.69	0.37	70.76	707.62	7076.18
SK27a-01	166	-810	1.09589E+11	34.29	1.43	3.43	0.34	1095.89	10958.87	109588.69
SK27a-02	173	-882	1.23561E+11	31.49	1.31	3.15	0.31	1235.61	12356.09	123560.90
SK27a-03	170	-888	1.23561E+11	31.28	1.30	3.13	0.31	1235.61	12356.09	123560.90
SK30-01	201	-622	20020047831	44.66	1.86	4.47	0.45	200.20	2002.00	20020.05
SK30-02	62	-487	4291919905	57.04	2.38	5.70	0.57	42.92	429.19	4291.92
SK30-03	73	-571	6936061894	48.65	2.03	4.86	0.49	69.36	693.61	6936.06
SK31-01	31	-820	20837081483	33.88	1.41	3.39	0.34	208.37	2083.71	20837.08
SK31-02	21	-889	17756189566	31.25	1.30	3.12	0.31	177.56	1775.62	17756.19
SK31-03	23	-433	586685817.3	64.15	2.67	6.42	0.64	5.87	58.67	586.69

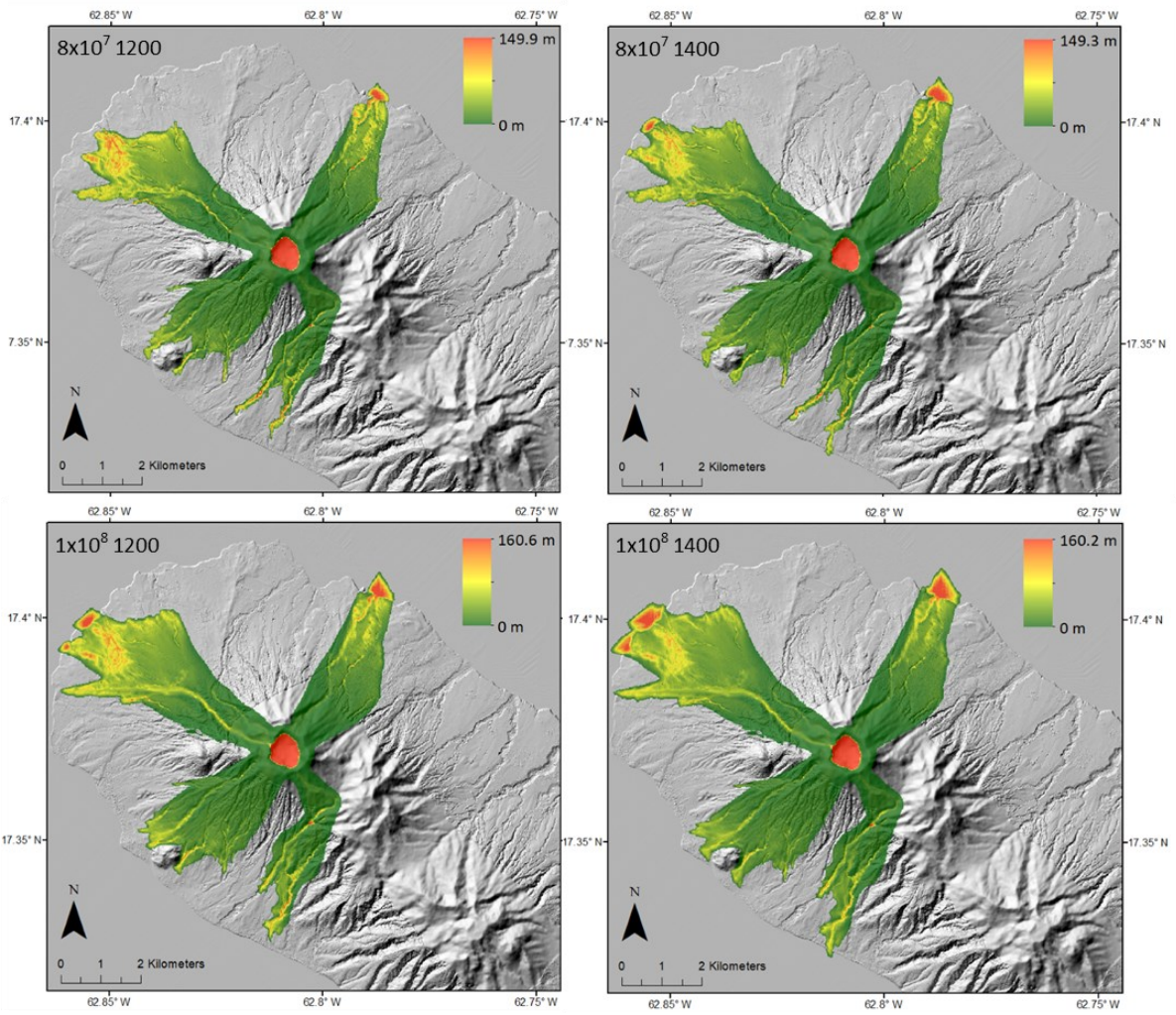
Sample no.	N (number of samples)	Slope (°)	n° (mm ⁻⁴)	Crystallisation time (t) hours G = 10 ⁻⁸	Crystallisation time (t) Days G = 10 ⁻⁹	Crystallisation time (t) hours G = 10 ⁻⁷	Crystallisation time (t) hours G = 10 ⁻⁶	Nucleation rate(J) G = 10 ⁻⁸	Nucleation rate(J) G = 10 ⁻⁷	Nucleation rate(J) G = 10 ⁻⁶	
SKN18-01	381	-713	21258018451	38.96	1.62	3.90	0.39	212.58	2125.80	21258.02	
SKN18-02	299	-825	36115934363	33.67	1.40	3.37	0.34	361.16	3611.59	36115.93	
SKN18-03	323	-800	19235050528	34.72	1.45	3.47	0.35	192.35	1923.51	19235.05	
SKN19-01	25	-369	490041187	75.28	3.14	7.53	0.75	4.90	49.00	490.04	
SKN19-02	73	-226	86876663	122.91	5.12	12.29	1.23	0.87	8.69	86.88	
SKN19-03	103	-362	393267264	76.73		3.20	7.67	0.77	3.93	39.33	393.27

Appendix 17 - Lower surge production coefficient - dense deposits

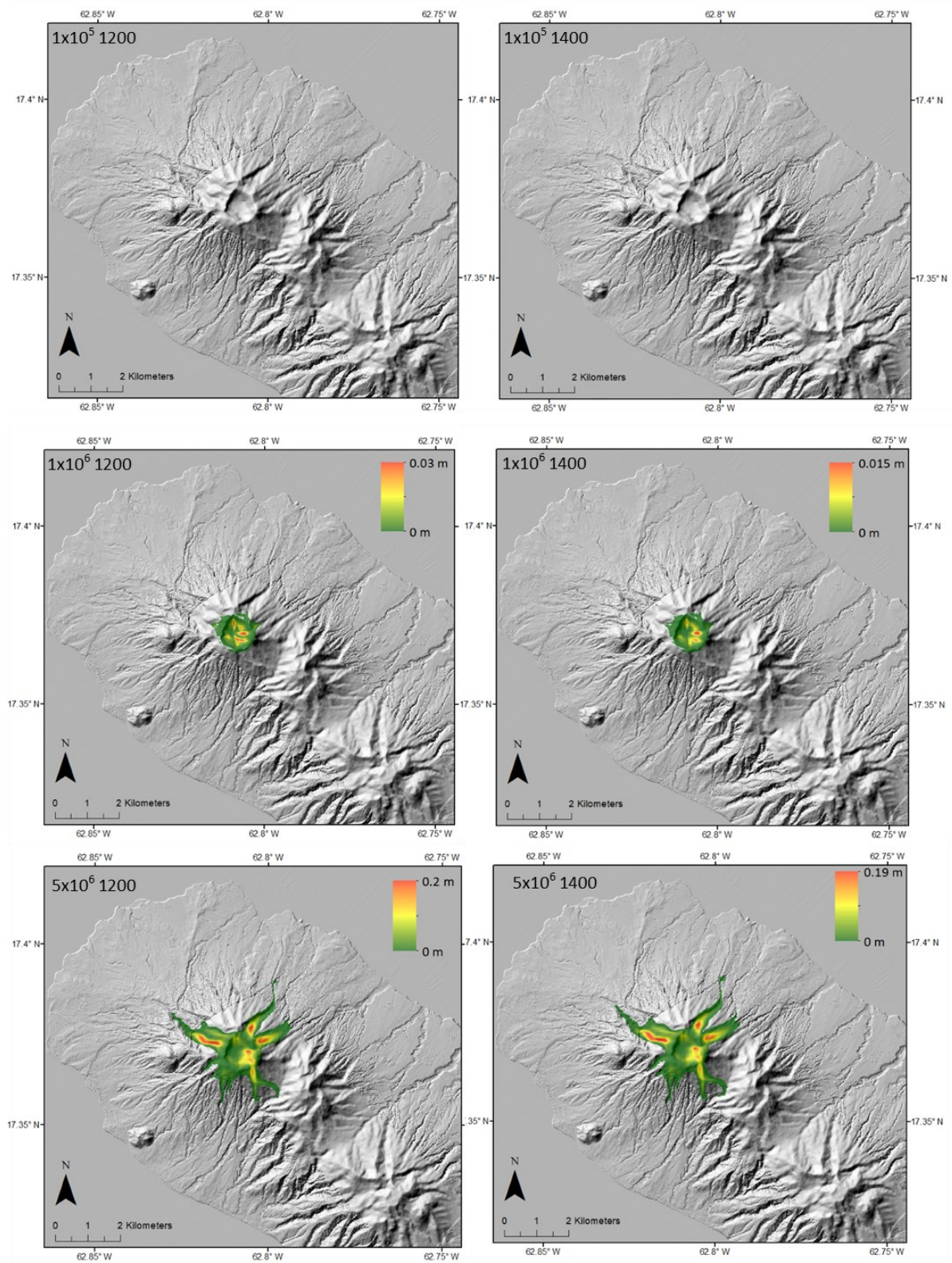


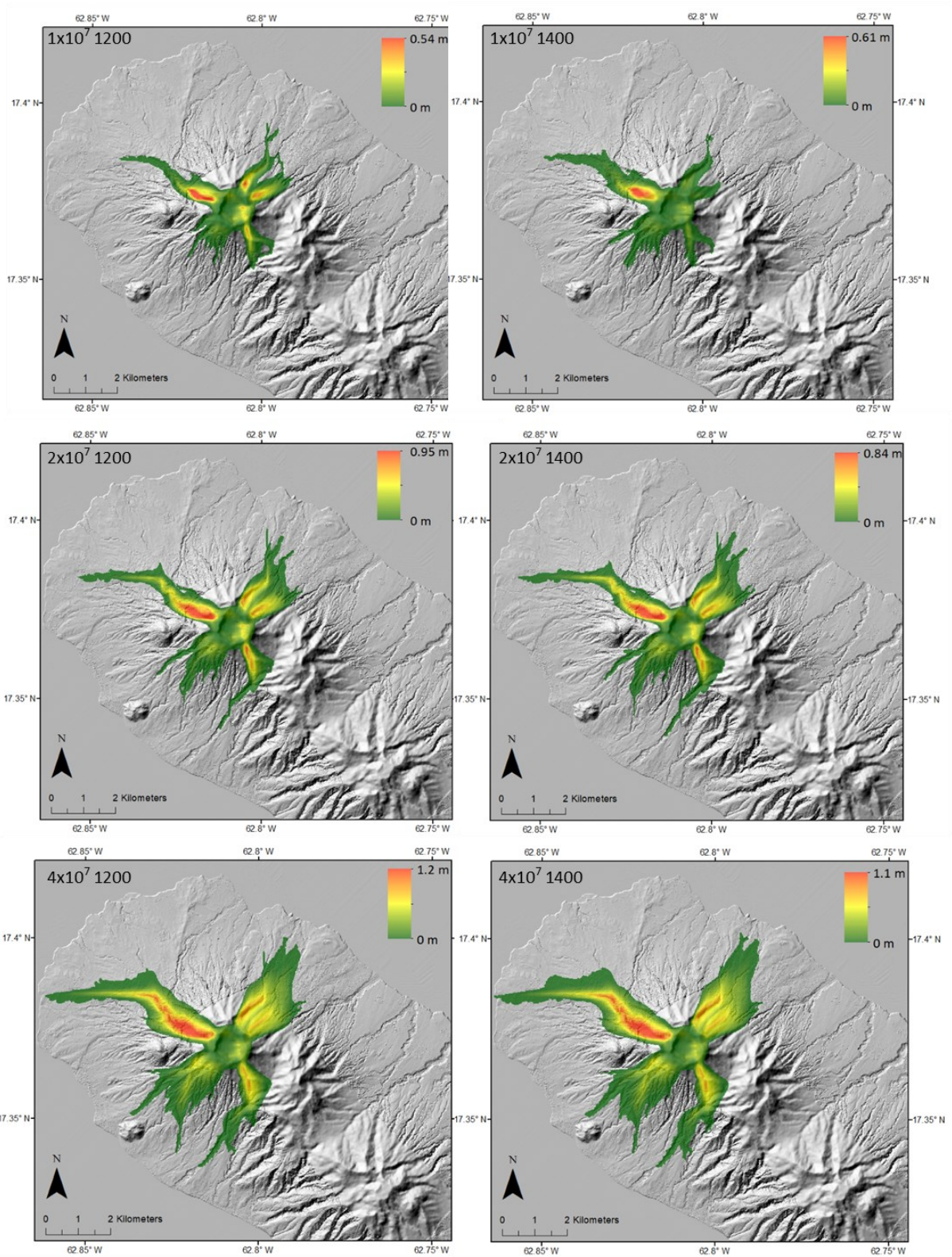


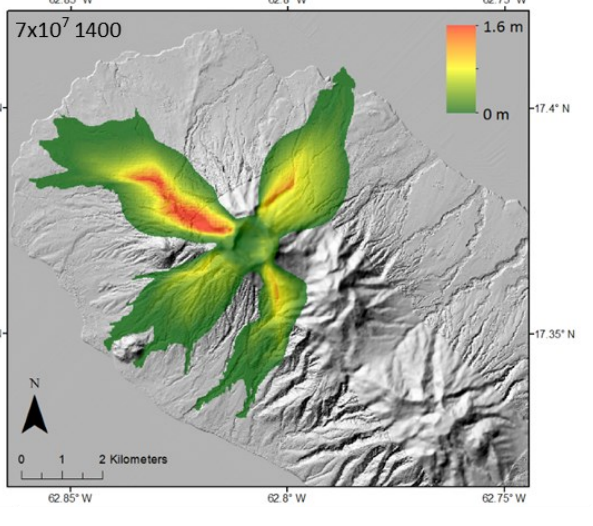
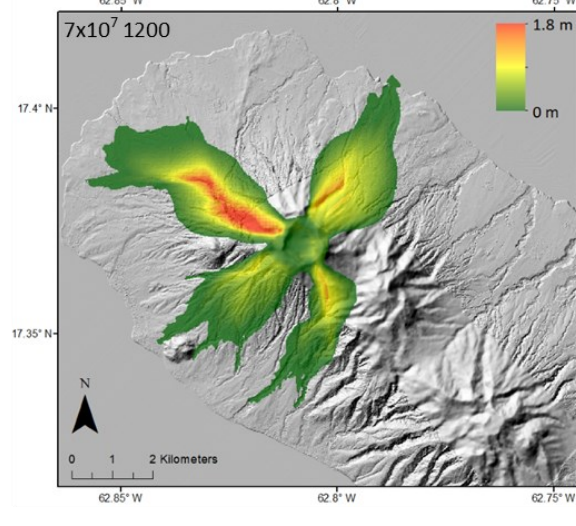
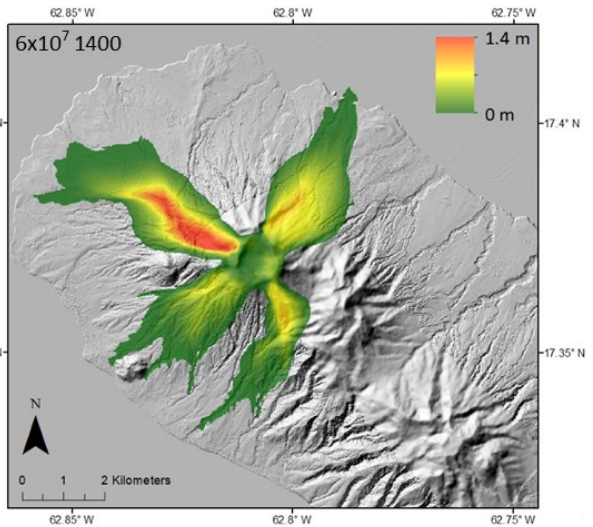
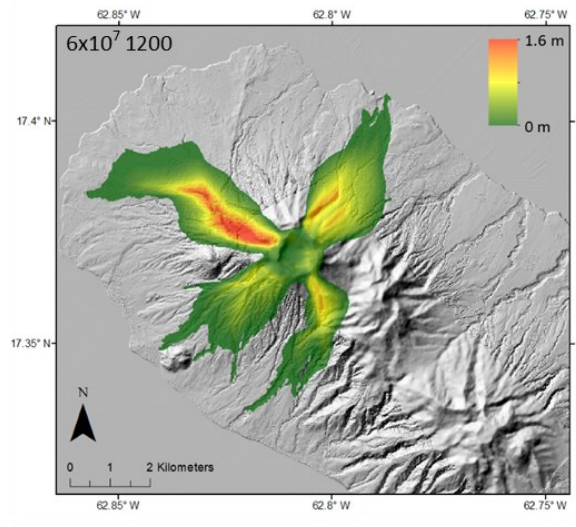
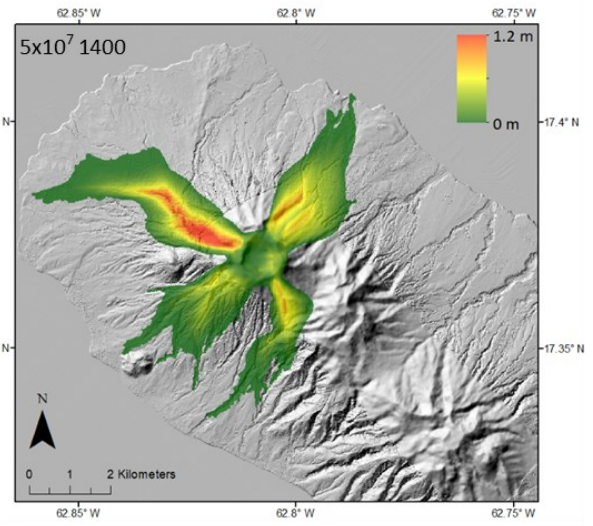
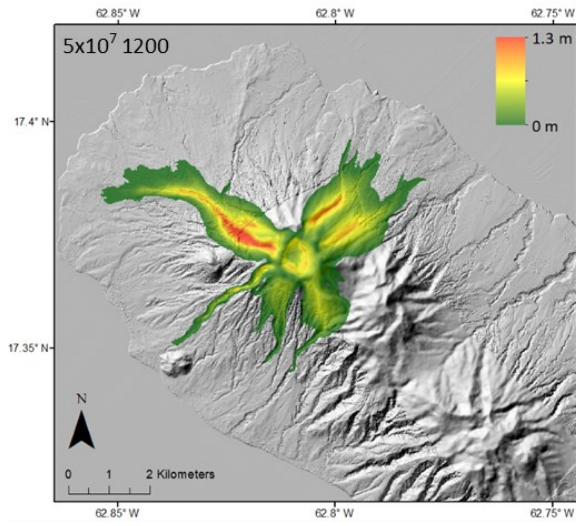


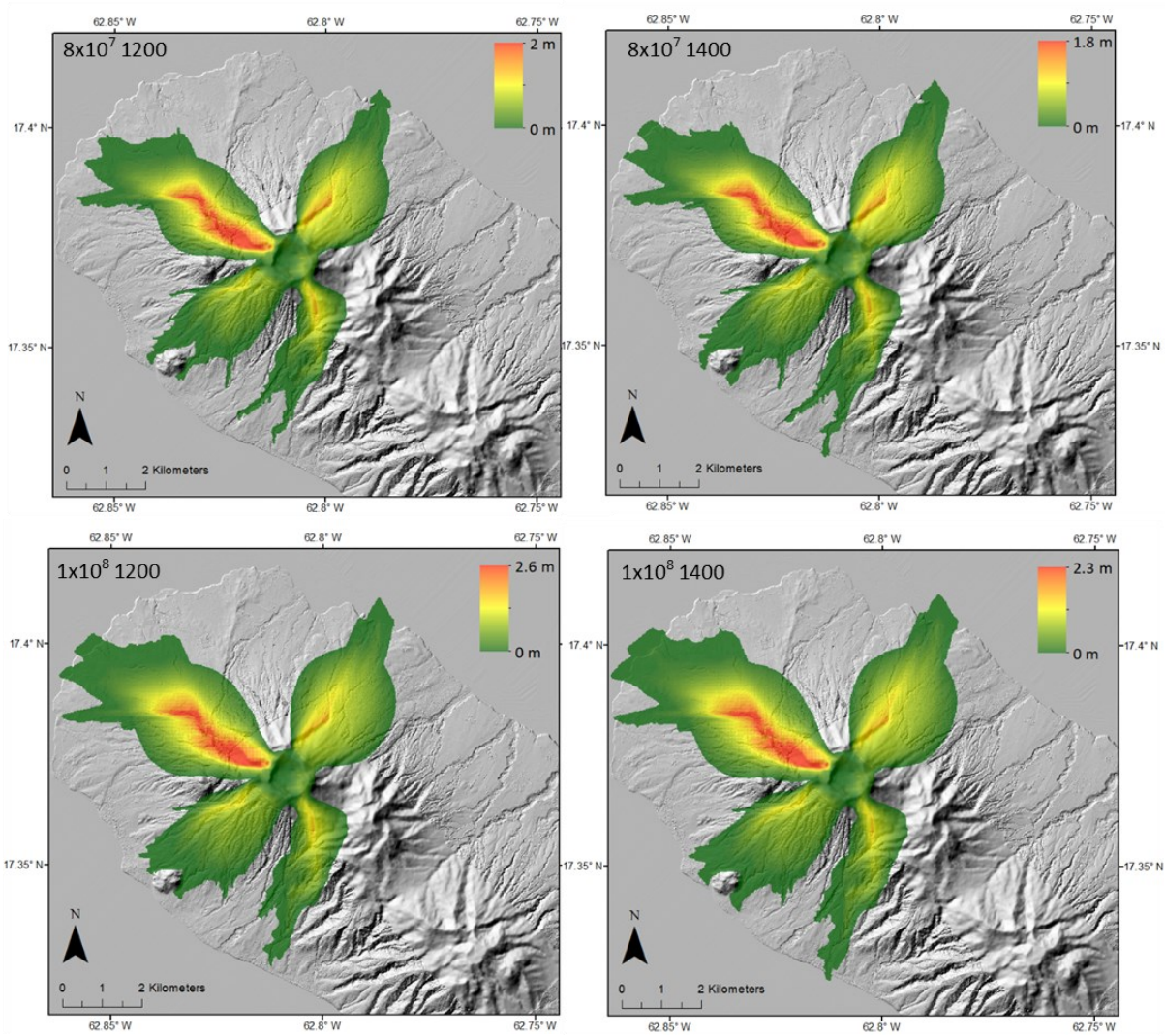


Appendix 18 - Lower surge production coefficient - surge deposits

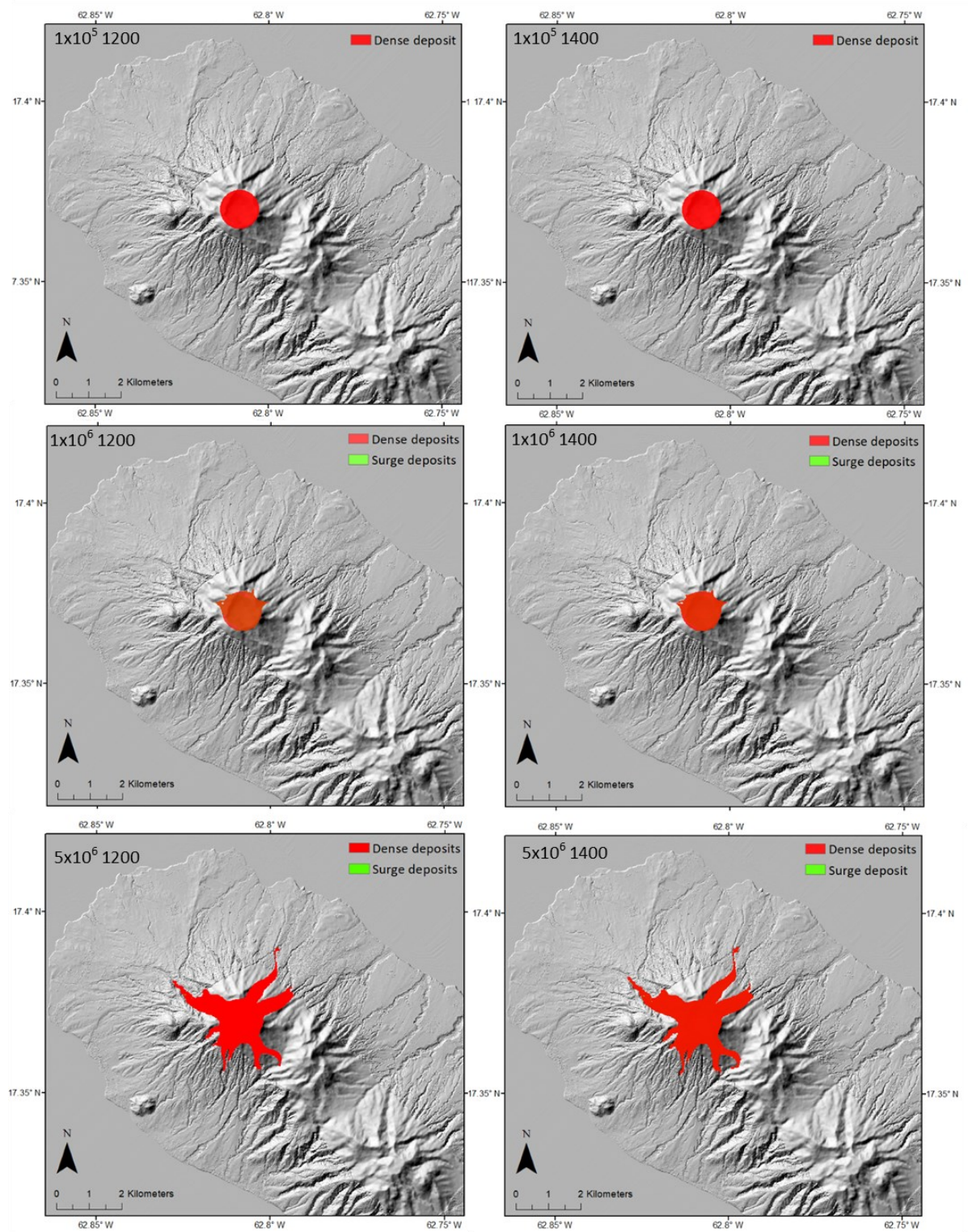


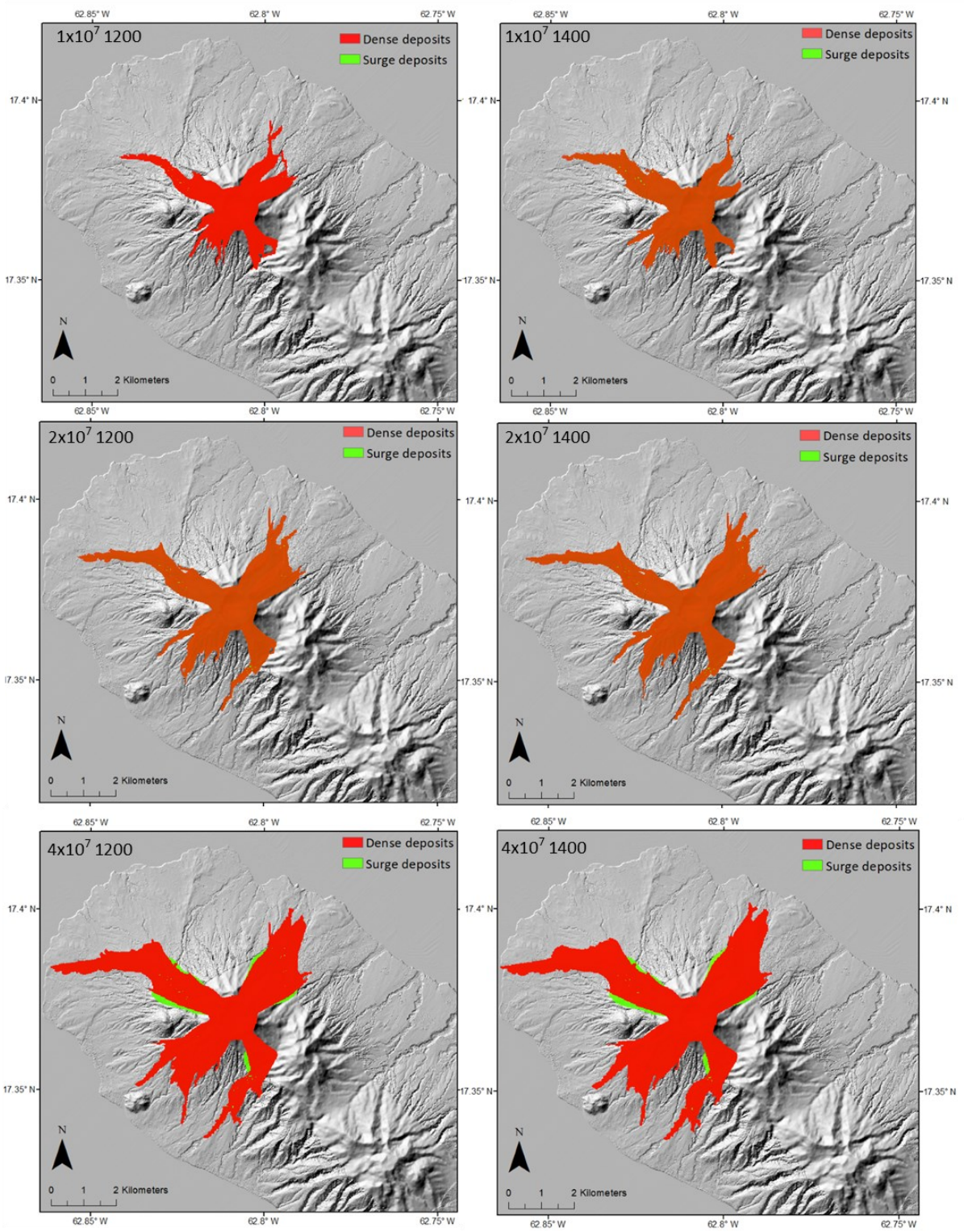


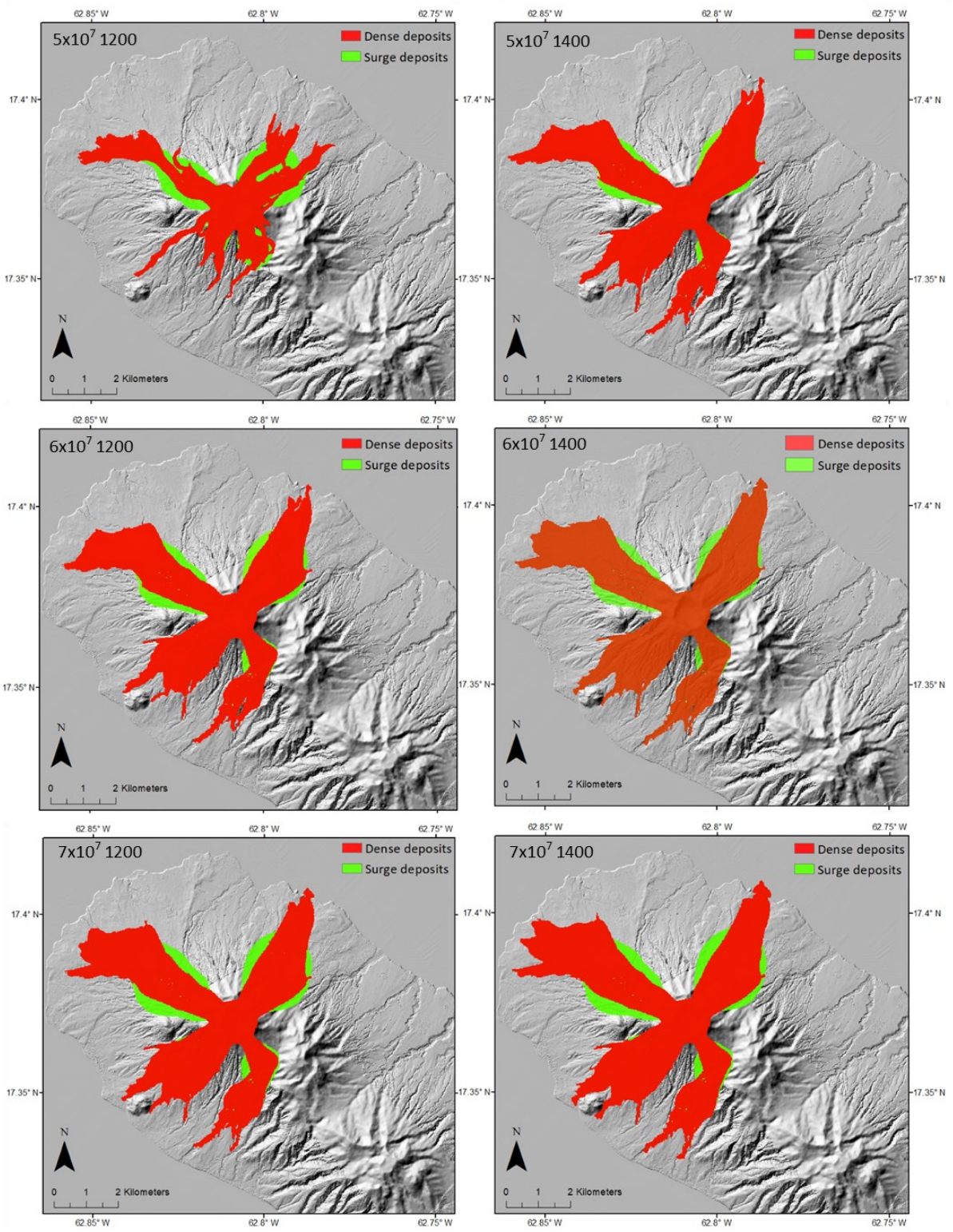


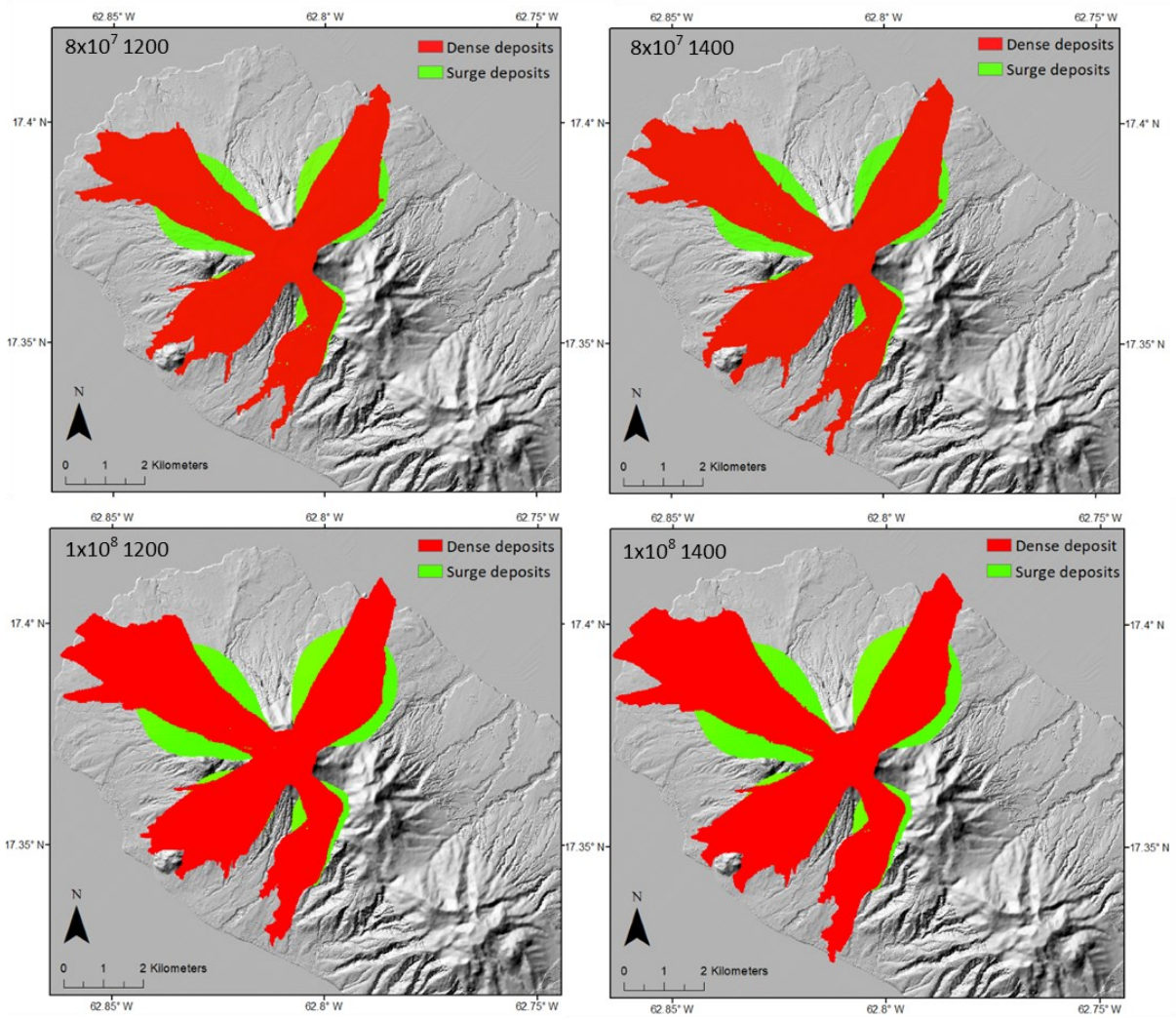


Appendix 19 - Lower surge production coefficient - surge and dense deposits

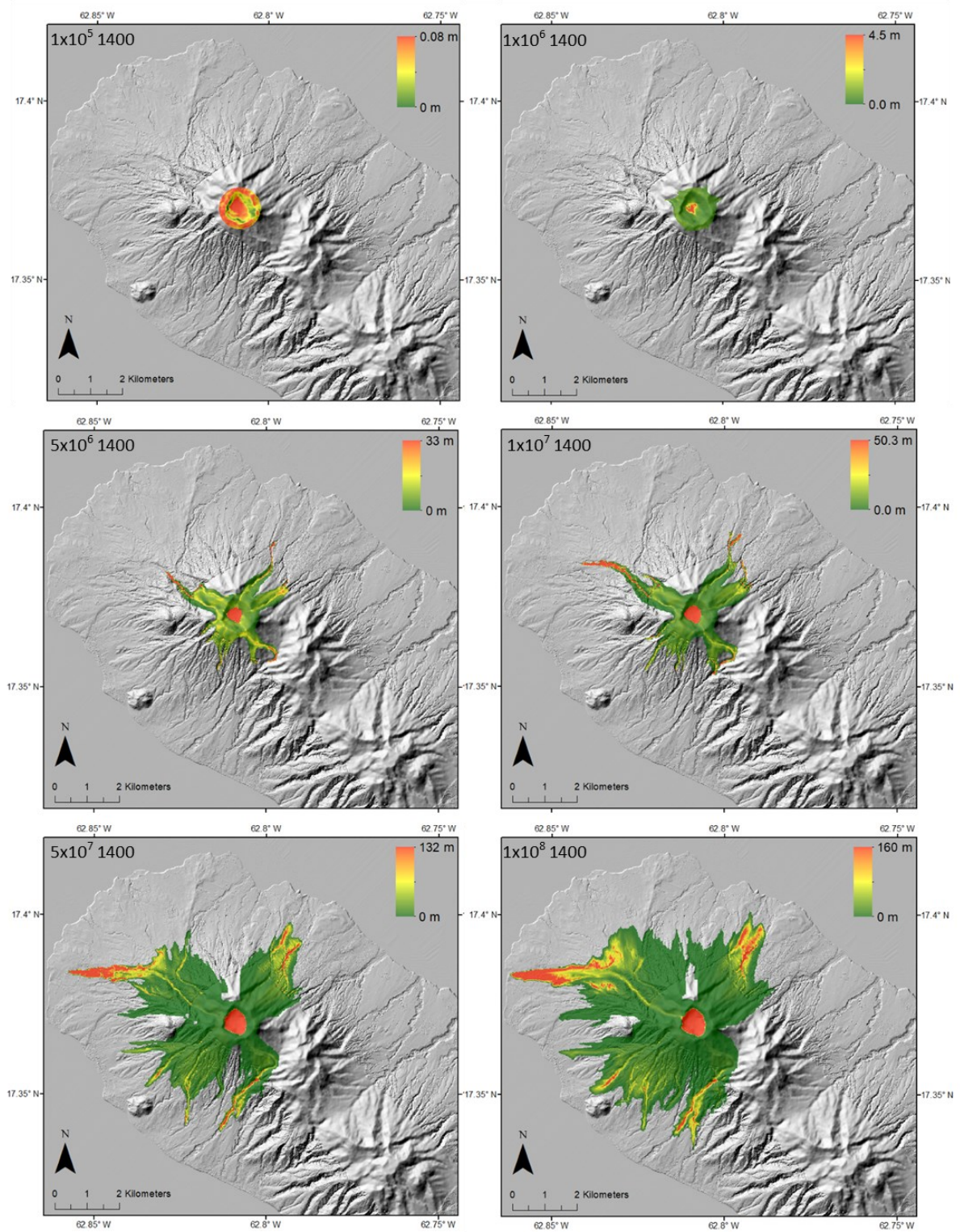




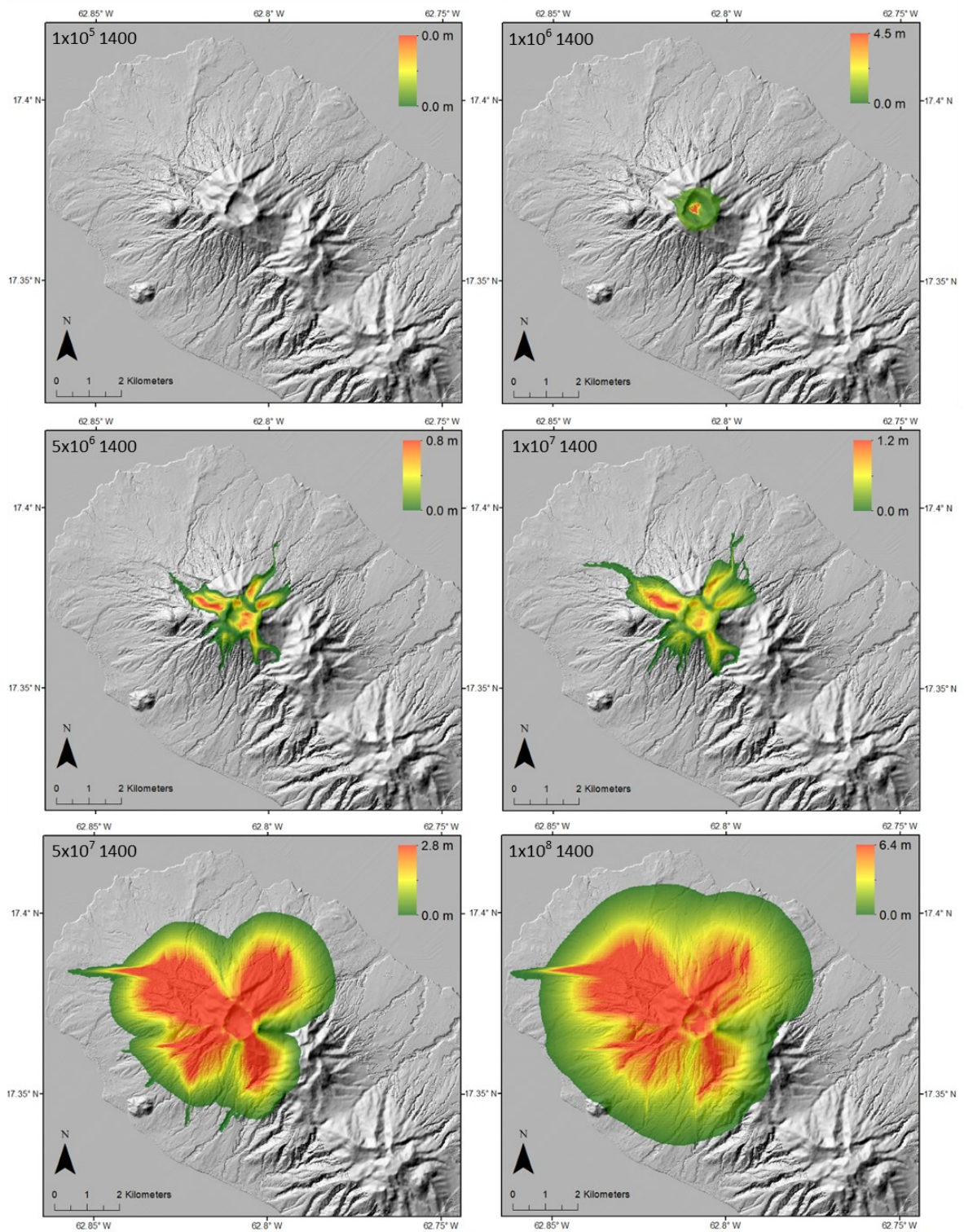




Appendix 20 - Higher surge production coefficient - dense deposits



Appendix 21 - Higher surge production coefficient - surge deposits



Appendix 22 - Higher surge production coefficient - surge and dense deposits

